RUSSIAN ACADEMY OF SCIENCES
INSTITUTE FOR PROBLEMS IN MECHANICAL ENGINEERING
PETER THE GREAT ST. PETERSBURG POLYTECHNIC UNIVERSITY

Proceedings of the XLV Summer School – Conference

ADVANCED PROBLEMS IN MECHANICS

A P M 2 0 1 7

St. Petersburg

http://apm-conf.spb.ru

St. Petersburg, 2017

Scientific Committee and Editorial Board

Preface

Dear Reader,

in this book you will find the Proceedings of the Summer School – Conference "Advanced Problems in Mechanics (APM) 2017". The conference had been started in 1971. The first Summer School was organized by Prof. Ya.G. Panovko and his colleagues. In the early years the main focus of the School was on nonlinear oscillations of mechanical systems with a finite number of degrees of freedom. Since 1994 the Institute for Problems in Mechanical Engineering of the Russian Academy of Sciences organizes the Summer School. The traditional name of "Summer School" has been kept, but the topics covered by the School have been much widened, and the School has been transformed into an international conference. Now it is held under the patronage of the Russian Academy of Sciences. The topics of the conference cover now almost all fields of mechanics, being concentrated around the following main scientific directions:

— aerospace mechanics;
— computational mechanics;
— dynamics of rigid bodies and multibody dynamics;
— fluid and gas;
— mechanical and civil engineering applications;
— mechanics of media with microstructure;
— mechanics of granular media;
— nanomechanics;
— nonlinear dynamics, chaos and vibration;
— molecular and particle dynamics;
— phase transitions;
— solids and structures;
— wave motion.

The Summer School – Conference has two main purposes: to gather specialists from different branches of mechanics to provide a platform for cross-fertilization of ideas, and to give the young scientists a possibility to learn from their colleagues and to present their work. Thus the Scientific Committee encouraged the participation of young researchers, and did its best to gather at the conference leading scientists belonging to various scientific schools of the world.

We believe that the significance of Mechanics as of fundamental and applied science should much increase in the eyes of the world scientific community, and we hope that APM conference makes its contribution into this process.

The Conference is organized by Institute for Problems in Mechanical Engineering of Russian Academy of Sciences (IPME RAS) and Peter the Great St.Petersburg Polytechnic University (SPbPU) under the patronage of Russian Academy of Sciences (RAS), St.Petersburg Scientific Center, Ministry of Education and Science of Russian Federation and the University of Seville (Universidad de Sevilla). APM 2017 is partially supported by Russian Foundation for Basic Research. Minisymposium in memoriam of Antonio Castellanos Mata is partially sponsored by the Vicerrectorado de Investigacion de la Universidad de Sevilla (Vice-Rectorate for Research, University of Seville, Spain).

We hope that you will find the materials of the conference interesting, and we cordially invite you to participate in the coming APM conferences. You may find the information on the future "Advanced Problems in Mechanics" Schools – Conferences at our website:

`http://apm-conf.spb.ru`

With kind regards,

Co-Chairmen of APM 2017

Dmitri A. Indeitsev, Anton M. Krivtsov

Contents

Dynamics of Gravitating System of Gas and Dust Cloud

M. Abobaker, A. M. Krivtsov, A. Murachev

mhmdbb@yahoo.com

Abstract

Due to the gravitational force, cloud of dust and gas can contract and form planet. Here we present a simple model for the dynamics of one dimensional of self-gravitating spherical symmetrical gas and dust cloud.
We present analytic, similarity solution for the one dimensional of self-gravitating spherical symmetrically gas and dust cloud. In this paper we used a Cole-Hopf transformation to simplify the equations of dynamics and thereafter we applied method of characteristics to reduce partial differential equation to a system of completely solvable ordinary differential equations. The similarity solution method is applied to reduce the partial differential equations to a system of completely solvable ordinary differential equations. The Runga-Kutta method has been used for numerical calculation of the problem.
KEYWORDS: Cole-Hopf transformation, Self-Gravitating; Gas-Dust System; Similarity Reductions; Planet Formation

1 Introduction

Mechanical theories of gas-dust systems of cloud can be developed from two quite different starting points: We can introduce either the model of N gravitating mass points, or the model of a compressible fluid streaming in the phase space. The motion of this fluid will be determined by the gravitational fluid produced by itself. In this work we will study a model of a compressible fluid of dust and gas. Magnetic field, radiation force, rotation probably play important roles but to simplify the problem in this work we will ignoring these factors. The gravitational collapse of spheres has received considerable theoretical attention in literature,particularly in connection with the problem of star formation ([1] , [2]).
We shall consider spherically symmetric, self-gravitating dust-gas cloud. All the physical quantities will depend on two independent variables; radius and time $(r;t)$. Let $P(r,t)$, $\rho(r,t)$, $v(r,t)$ and $\Phi(r,t)$ be the pressure, mass density, radial velocity and gravitational potential respectively.

2 Fundamental Equations

The motion of the spherically symmetrical compressible fluid flow of self-gravitating dust-gas is governed by the following equations [3], [11]:

$$\rho_t + v\rho_r + \rho v_r + \frac{2}{r}v\rho = 0, \tag{1}$$

$$v_t + vv_r + \frac{1}{\rho}P_r + \Phi_r = 0, \tag{2}$$

$$\Phi_{rr} + \frac{2}{r}\Phi_r = 4\pi G\rho, \tag{3}$$

where G is Newton's gravitational constant.
These nonlinear partial differential equations are quite complicated and the general solution cannot be obtained. Here we will use two methods for finding particular solution, Hopf-Cole transformation method and finite-different numerical method.

3 Hopf-Cole Solution

Let us first consider one dimensional flow of fluid in self-gravitating field without pressure, the equation of dust state ($P = 0$). let $\sigma = r^2\rho$, now we can rewrite the equation (1)−(3) as:

$$\frac{\partial\sigma}{\partial t} + \frac{\partial(\sigma v)}{\partial r} = 0, \tag{4}$$

$$\frac{\partial v}{\partial t} + v\frac{\partial v}{\partial r} = -\frac{\partial\Phi}{\partial r}, \tag{5}$$

$$\frac{\partial}{\partial r}\left(r^2\frac{\partial\Phi}{\partial r}\right) = 4\pi G\sigma. \tag{6}$$

It is an amazing fact that the equations like (4)−(6) may be solved exactly using a trick discovered independently by Cole J. D. [5] and E. Hopf [6] about 1950. After hopf and Cole introduced the transformation, several attempts have been made to generalised Cole-Hopf transformation, we shall use here modified generalized Cole-Hopf method [7]. The trick is to change the dust velocity in the following form:

$$v(r,t) = -\frac{\theta_t}{\theta_r}, \tag{7}$$

where $\theta = \theta(r,t)$ is the auxiliary function, $\theta_t = \frac{\partial\theta}{\partial t}$, $\theta_r = \frac{\partial\theta}{\partial r}$.
Let consider θ_r to be

$$\theta_r = \sigma = r^2\rho, \tag{8}$$

By using generalised Cole-Hopf transformation we can find [Appendix]:

$$v(r,t) = -\frac{\theta_t}{\theta_r} = \pm\sqrt{b + r^{-1}}\sqrt{8\pi G}\sqrt{\theta}, \tag{9}$$

or

$$\theta_t \pm \sqrt{b + r^{-1}}\sqrt{8\pi G}\sqrt{\theta}\theta_r = 0, \tag{10}$$

where b is constant of integration.
By the substitution of new variable

$$\xi(r) = \int (b + r^{-1})^{-1/2} dr, \tag{11}$$

to equation (10), it takes the form

$$\theta_t \pm \sqrt{8\pi G}\sqrt{\theta}\theta_\xi = 0. \tag{12}$$

We use the method of characteristics to solve (12). The method will reduce PDE to ODE.
The characteristics of the PDE (12) are

$$\frac{dt}{1} = \pm\frac{d\xi}{\sqrt{8\pi G}\sqrt{\theta}} = \frac{d\theta}{0}, \tag{13}$$

From here we find the general solution

$$\xi \pm \sqrt{8\pi G}\sqrt{\theta}t = F(\theta). \tag{14}$$

4 Initial and Boundary Conditions

One of the main problems with model calculations the formation of planets is fact that initial conditions of the cloud are not known. It is obvious for the density become zero at the surface of the cloud, then let we look for the solution of the problem with initial conditions

$$\rho(r, 0) = \frac{1}{r^2}\frac{\partial\theta_0(r)}{\partial r} \tag{15}$$

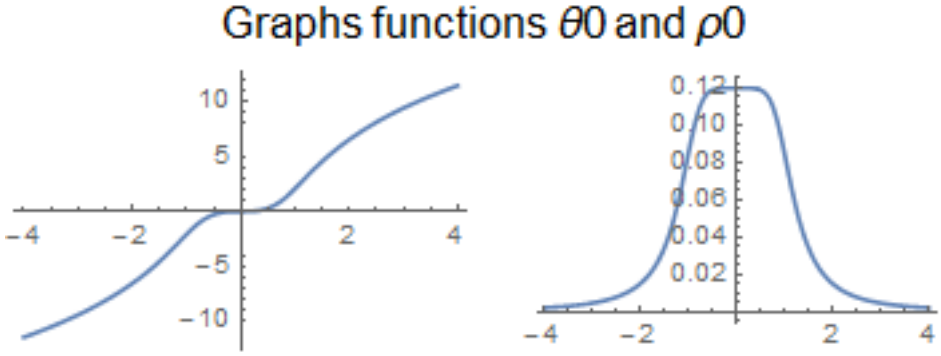

Figure 1

where $\theta_0(r) = \theta(r, 0)$.
Let

$$\theta_0(r) = \frac{M}{4\pi}\,\mathrm{arsinh}(r^3), \tag{16}$$

where M is mass of cloud.
Differentiating equation (16) and using (8), we find $\rho(r, 0)$, (see Figure 1).

$$\rho_0 = \rho(r, 0) = \frac{3M}{4\pi(r^6 + 1)^{1/2}} > 0, \tag{17}$$

$$v(r, 0) = 0; \tag{18}$$

and assume that we have boundary condition

$$\Phi(R, t) = -\frac{GM}{R}, \tag{19}$$

where R is radius of the cloud.

5 Analytical Solution of Fundamental Equations

Now we want to get the solution of the equation (12) with initial condition (16) and (17).
By plugging initial condition (16) into equation (12), we get

$$\theta - \frac{M}{4\pi}\,\mathrm{arsinh}(\frac{3}{2}(\xi \pm \sqrt{8\pi G}\sqrt{\theta}t))^2 = 0, \tag{20}$$

When $b = 0$ in equation (11) we obtain

$$\xi(r) = \frac{2}{3}r^{\frac{3}{2}}. \tag{21}$$

Now we can rewrite (20) as

$$\theta - \frac{M}{4\pi}\,\mathrm{arsinh}(r^{3/2} \pm \frac{3}{2}\sqrt{8\pi G}\sqrt{\theta}t)^2 = 0, \tag{22}$$

this is hyperbolic transcendental equation, we can solve it numerically to find θ.
Differentiating the equation (22) with respect to r, we find

$$\theta_r = \frac{6M\sqrt{\theta}w(r, t)\sqrt{r}}{8\pi\sqrt{\theta}\sqrt{1 + w^4} - 3M\lambda t w(r, t)}, \tag{23}$$

where

$$w(r, t) = (r^{\frac{3}{2}} \pm \frac{3}{2}\lambda\sqrt{\theta}t), \qquad \lambda = \sqrt{8\pi G}. \tag{24}$$

Now we can calculate density ρ through function $\theta(r, t)$

$$\rho = \frac{1}{r^2}\theta_r = \frac{6M\sqrt{\theta}(r^{\frac{3}{2}} \pm \frac{3}{2}\lambda t\sqrt{\theta})r^{-\frac{3}{2}}}{8\pi\sqrt{\theta}\sqrt{1 + (r^{\frac{3}{2}} \pm \frac{3}{2}\lambda\sqrt{\theta}t)^4} - 3M\lambda t(r^{\frac{3}{2}} \pm \frac{3}{2}\lambda\sqrt{\theta}t)}. \tag{25}$$

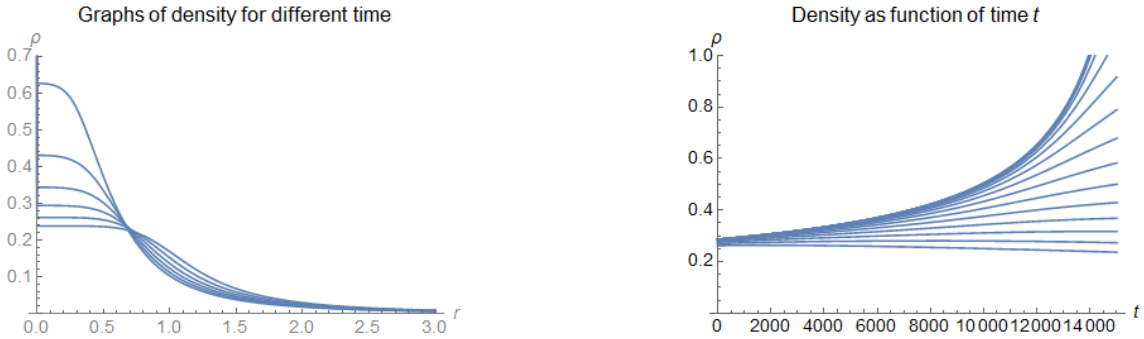

(a) (b)

Figure 2

Differentiating equation (20) with respect to t, we obtain

$$\theta_t = \frac{6M\theta w(r,t)}{8\pi\sqrt{\theta}\sqrt{1+w^4} - 3M\lambda t w(r,t)}. \tag{26}$$

Now we can calculate velocity v through function θ

$$v(r,t) = -\frac{\theta_t}{\theta_r} = -\frac{\lambda\theta^{\frac{1}{2}}}{r^{\frac{1}{2}}}. \tag{27}$$

From equations (5) and (19)

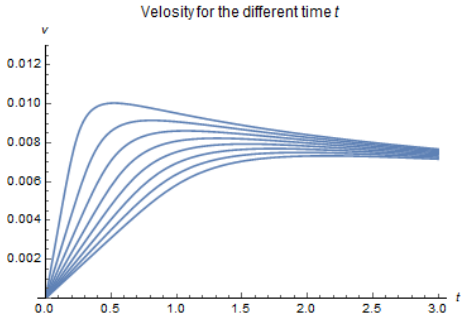

Figure 3

$$\Phi(r,t) = \lambda^2\theta. \tag{28}$$

6 Similarity Solution

In this section we are seeking solution of the equations of spherically symmetrical compressible fluid flow of self-gravitating dust-gas (1)−(3).
Let for example we look for the solution of the problem with boundary conditions

$$v(0,t) = 0, \tag{29}$$

$$\rho(0,t) = \rho_0, \tag{30}$$

$$\Phi(0,t) = 0 \tag{31}$$

By introducing the similarity variable [2] [1]

$$\xi = \frac{r}{\sqrt{4\lambda\pi G t}} \tag{32}$$

and seek a solution in the following form

$$v(r,t) = \sqrt{4\lambda\pi G} w(\xi), \tag{33}$$

$$\rho(r,t) = \frac{q(\xi)}{4\pi G t^2}, \tag{34}$$

$$\Phi(r,t) = 4\lambda\pi G \Psi(\xi) \tag{35}$$

Here λ - some dimensional factor, functions w, q, Ψ are dimensionless functions
Let we denote

$$\Psi' = \Omega \tag{36}$$

Let us first we seeking solution for the problem without pressure, which corresponds

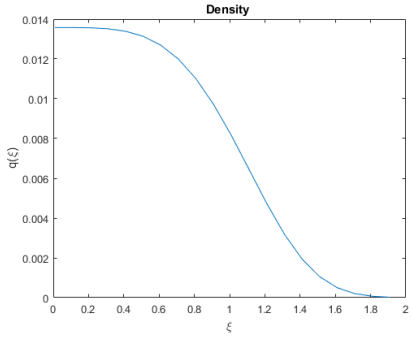

Figure 4

to the equation of state (P = 0).
Using the introduced dimensionless variables, after some manipulation we can reduce

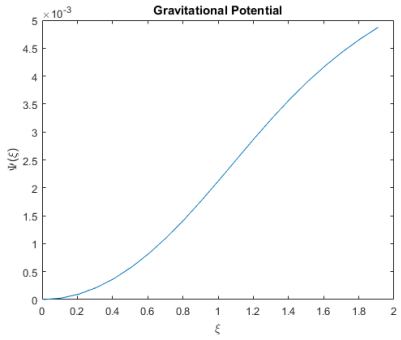

(a)

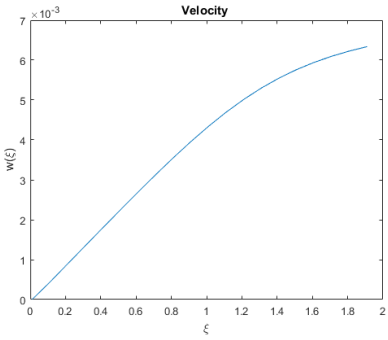

(b)

Figure 5

the system of fundamental equations (1), (2) and (3) to the following system of ordinary differential equations:

$$\Psi^{'} = \Omega, \tag{37}$$

$$w^{'} = \frac{\Omega}{\xi - w}, \tag{38}$$

$$\Omega^{'} = \frac{\xi q - 2\Omega}{\xi}, \tag{39}$$

$$q^{'} = q\frac{\Omega\xi - 2(\xi - w)^2}{\xi(\xi - w)^2} \tag{40}$$

where the prime denotes differentiation with respect to the ξ.
In term of the similarity variables the boundary conditions take the form

$$w(\xi = 0) = 0 \tag{41}$$

$$q(\xi = 0) = 4\pi G\rho_0 t^2, \tag{42}$$

$$\Psi^{'}(\xi = 0) = 0 \tag{43}$$

We obtain the similarity solution by integrating equations (37)−(40) by numerical

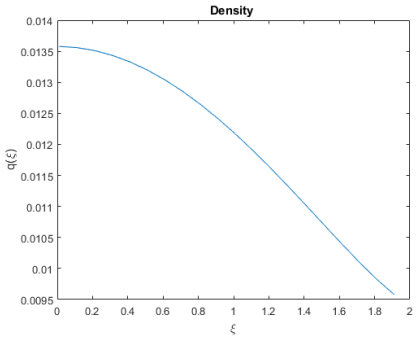

Figure 6

methods.
Now we try to find solution when the equation of state of flow which is a mixture of gas and small solid particle is taken to be

$$P = K\rho \tag{44}$$

where K is a constant physically characterizes the central pressure and central density in our model.
Similar equations to (37)−(40) obtained when taking into account the equation of state (44)

$$\Psi^{'} = \Omega, \tag{45}$$

$$w^{'} = \frac{(\xi\Omega - 2)(w - \xi)}{\xi(1 - (w - \xi)^2)}, \tag{46}$$

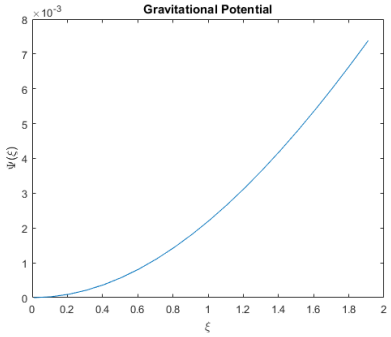

(a) Gravitational Potential

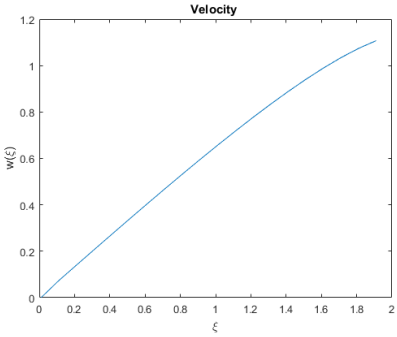

(b) Velocity

Figure 7

$$\Omega^{'} = \frac{\xi q - 2\Omega}{\xi}, \tag{47}$$

$$q^{'} = q\frac{\xi\Omega - 2(\xi - w)^2}{((\xi - w)^2 - 1)\xi} \tag{48}$$

Similarly we can find numerical solution of the equations (45)−(48) for boundary conditions (41)−(43).
Equations (37)−(40) and (45)−(48) have been integrated by Runge-Kutta method for boundary conditions (41)−(43). The graphs of flow variable are given in Figure 4 , Figure 5a , Figure 5b , Figure 6 , Figure 7a and Figure 7b . It is clear from the graphs that the density increases as we move towards the centre, while velocity and gravitational potential decreases.

7 Summary

We investigated the The motion of the spherically symmetrical compressible fluid flow of self-gravitating dust-gas cloud, In certain cases we have tried to find solution for the system of equations presented in (1)−(3). In the case when $P = 0$, we find particular analytical solution with help of modified Cole-Hopf transformation and special initial condition.
In this work, similarity solutions are obtained for one dimensional flow of fluid in self-gravitating field without pressure and with pressure.
Further possible study my be the investigation of the system (1)−(3) with other possible equation of state, which my be different than the ones considered here.

8 Appendix

Following [7], let us consider the representation for dust velocity in the following form:

$$v(r,t) = -\frac{\theta_t}{\theta_r} \tag{49}$$

where $\theta = \theta(r,t)$ is the auxiliary function (generalized Cole-Hopf transformation) The equivalent representation (49) has the form of the equation

$$\theta_t + v(r,t)\theta_r = 0 \tag{50}$$

There are several simple identities that follow from (50) and hold for any differentiable function $\theta(r,t)$ [7] , the first of them has the form

$$\left[\frac{\partial}{\partial t} + v(r,t)\frac{\partial}{\partial r}\right] F(\theta) = F'(\theta)(\theta_t + v\theta_r) \tag{51}$$

Differentiating (50) with respect to r, we obtain

$$\frac{\partial}{\partial t}\theta_r + \frac{\partial}{\partial r}\left[v(r,t)\theta_r\right] = 0 \tag{52}$$

From (50) and (51) there follows anther identity of the form

$$\frac{\partial}{\partial t}\left[f(r)F(\theta)\right] + v\frac{\partial}{\partial r}\left[f(r)F(\theta)\right] = f'(r)F(\theta)v \tag{53}$$

Relation (52) takes the form of continuity equation if the density $\rho(r,t)$ is considered to be

$$\rho(r,t) = \frac{1}{r^2}\theta_r \tag{54}$$

In this case (52) is equivalent to the continuity equation (4)

$$\frac{\partial \sigma}{\partial t} + \frac{\partial}{\partial r}(v\sigma) = 0, \tag{55}$$

We reduce the Poisson equation (6) to the form

$$\Phi_r = \frac{1}{r^2}4\pi G\theta \tag{56}$$

From equation (5) and (56), we obtain

$$\frac{\partial v}{\partial t} + v\frac{\partial v}{\partial r} = -\frac{4\pi G\theta}{r^2} \tag{57}$$

Let

$$v = S(r)T(\theta) \tag{58}$$

where $S(r)$ and $T(\theta)$ are so far undefined functions. Using the identities we obtain

$$\frac{\partial v}{\partial t} + v\frac{\partial v}{\partial r} = S'(r)T(\theta)v = S'(r)S(r)T^2(\theta) \tag{59}$$

Comparing (57) and (59), we obtain

$$T(\theta) = \sqrt{4\pi G}\sqrt{\theta} \tag{60}$$

$$S(r) = \pm\sqrt{2}\sqrt{b + r^{-1}} \tag{61}$$

where b is constant of integration.
From (49), (58), (60), and (61)

$$v(r,t) = -\frac{\theta_t}{\theta_r} = \pm\sqrt{b + r^{-1}}\sqrt{8\pi G}\sqrt{\theta} \tag{62}$$

or

$$\theta_t \pm \sqrt{b + r^{-1}}\sqrt{8\pi G}\sqrt{\theta}\theta_r = 0 \tag{63}$$

References

[1] Shu Frank H., Self-similar collapse of isothermal spheres and star formation, The Astrophysical Journal, 214: 488-497, 1977.

[2] Penston M. V. Dynamics of self-gravitating gaseous sphere, I. Royal Greenwich Observatory Bulletins, 117: 299-312, 1966.

[3] Avinash K., Eliasson B., Shukla P.K. Dynamics of self-gravitating dust clouds and the formation of planetesimals.

[4] Michael P. Brenner and Thomas P. Witelski. On spherically symmetric gravitational collapse. Journal of statistical physics, 93(3-4): 863-899, 1998.

[5] Cole J.D. Quart. Appl. Math. 1951. Vol. 9. P. 225-236.

[6] Hopf E. The partial differential equation $u_t + uu_x = \mu u_{xx}$, Comm. Pure Appl. Math. 1950. Vol. 3. P. 201-230.

[7] Zhuravlev M. The Application of Generalized Cole-Hopf Substitutions in Compressible Fluid Hydrodynamics Nonlinear Hydrodynamics, Physics of Wave Phenomena, December 2010, Volume 18, Issue 4, pp 245-250.

[8] Chandrasekhar S. Introduction to the Study of Stellar Structure, 1939

[9] Fridman A. M., Polyachenko V. L. Physics of gravitating systems, 1984.

[10] Safronov V. S. Evolution of the protoplanetary cloud and formaton of the Earth and Planets, 1972.

[11] Ogorodnikov K. F. Dynamics of Stellar Systems, Oxford, 1965.

[12] Andrei D. Polyanin, Valentin F.Zaitsev, Handbook of Nonlinear Partial Differential Equations, Second Edition, page 1503.

[13] Yuri E. Litvinenko, *A similarity reduction of Grad-Shafranov equation*, PHYSICS OF PLASMAS 17, 074502 2010

[14] Ogorodnikov K. F., Dynamics of steller systems. Oxford: Pergamon, edited by Beer, Arthur,1, 1965.

[15] Horedt G. P., Polytropes: Applications in Astrophysics and Related Fields, 2004.

[16] Papaloizou John C. B. , Caroline Terquem, Planet formation and migration, Institute of Physics Publishing, Rep. Prog. Phys. 69 p. 119вГУ180, 2006.

[17] Galimov E. M., Krivtsov A. M. Origin of the Moon. New Concept Geochemistry and Dynamics, De Gruyter, 2012.

M. Abobaker, Department of Theoretical and Applied Mechanics, St Petersburg, Russia
A. M. Krivtsov, Department of Theoretical and Applied Mechanics, St Petersburg, Russia
A. Murachev, Department of Theoretical and Applied Mechanics, St Petersburg, Russia

The solutions of nonlinear equations of flat deformation of the crystal media allowing martensitic transformations

E. L. Aero, A. N. Bulygin, Yu. V. Pavlov

bulygin_an@mail.ru

Abstract

Mathematical methods of the solution of the equations of statics of flat nonlinear deformation of the crystal media with a complex lattice allowing martensitic transformations are developed. The equations of a statics represent system of four connected nonlinear equations. The vector of macroshifts is looked in the Papkovish-Neuber form. The system of the connected nonlinear equations is reduced to system of the separate equations. The vector of microshifts can be found from the sine Gordon equation with variable coefficient (amplitude) before the sine and Poisson equation. The class of doubly periodic solutions expressing in the Jacobi elliptic functions is found for a case of constant amplitude. It is shown that the nonlinear theory possesses a set of solutions which describe fragmentation of the crystal medium, emergence of defects of structure of different types, phase transformations and other topological features of the deformation which are implemented under the influence of intensive power loadings and which can't be described by classical mechanics of the continuous medium. Features of the found solutions are discussed.

1 Introduction

In recent years nanotechnologies are intensively developed. Practically all modern technologies for metals and alloys with ultrafine-grained structure are based on use of superhigh external impacts on material. The structure of material is significantly changed under the influence of intensive plastic deformations. Medium breaks up on separate nanoscale grains which are variously oriented. Grains divide big-angle borders in which defects like micropores and local consolidations are formed. The superlattice is formed and there are phase transformations.

Modern problems of technologies of obtaining and studying of the new materials set new problems for mechanics of continuous media. New analytical models are necessary for modern technologies of obtaining the new materials with the designated operational properties.

The classical continual model isn't adequate any more to those new problems which have arisen in connection with deep penetration into area the nano-scales. In works [1, 2] nonlinear model of deformation of crystal media with a complex lattice is offered. The offered model allows to describe specific processes of deformation, which are implemented in modern technologies of obtaining new materials.

2 Nonlinear model of deformation of crystal media with a complex lattice

In nonlinear model [1]–[3] deformation of crystal medium is described by vector of acoustic mode $\mathbf{U}(x,y,z,t)$ and vector of optical mode $\mathbf{u}(x,y,z,t)$. Equations of motion defining $\mathbf{U}(x,y,z,t)$ and $\mathbf{u}(x,y,z,t)$, are derived from LagrangeŸs variation principle. They have the form

$$\rho\ddot{U}_i = \sigma_{il,l}, \tag{1}$$

$$\sigma_{il} = \lambda_{ilmn}e_{mn} + C_{ilmn}\varepsilon_{mn} - s_{il}\Phi(u_s), \tag{2}$$

$$\mu\ddot{u}_i = \chi_{il,l} - \mathcal{P}\frac{\partial\Phi(u_s)}{\partial u_i}, \tag{3}$$

$$\chi_{il} = k_{ilmn}\varepsilon_{mn} + C_{ilmn}e_{mn}. \tag{4}$$

In Eqs. (1)–(4) and further the over point denotes time derivative while a comma in indexes defines spatial derivative. Besides, the following designations are entered: ρ, μ are density and the specified density of mass of couple of atoms, σ_{il}, χ_{il} are tensors of macro- and microstresses, λ_{ilmn}, k_{ilmn}, C_{ilmn} are the coefficients of elasticity, microelasticity and modules of interaction of acoustic and optical modes, e_{il}, ε_{il} are tensors of deformation and microdeformation

$$e_{il} = \frac{1}{2}\left(U_{i,l} + U_{l,i}\right), \qquad \varepsilon_{il} = \frac{1}{2}\left(u_{i,l} + u_{l,i}\right), \tag{5}$$

$\Phi(u_s)$ is the energy of interaction of sublattices. In pioneer work [4] and in majority of modern works [5, 6] one is accepted, that

$$\Phi(u_s) = 1 - \cos u_s. \tag{6}$$

The argument is

$$u_s = \mathbf{B}\cdot\mathbf{u}, \tag{7}$$

where $\mathbf{B}$ is the vector of inverse lattice [7]. For crystal of cubic system with length of elementary cell b one has

$$\mathbf{B} = \frac{1}{b}(\mathbf{i}+\mathbf{j}+\mathbf{k}), \tag{8}$$

$$u_s = \frac{1}{b}(u_x + u_y + u_z). \tag{9}$$

Multiplier $\mathcal{P} = p - s_{il}e_{il}$ is an effective interatomic barrier, where p is half of energy of activation of rigid shift of lattices, and s_{il} is a tensor of nonlinear mechanostriction. For the cubic crystal one has $s_{il} = s\delta_{il}$, and

$$\mathcal{P} = p - s\,\mathrm{div}\,\mathbf{U}, \tag{10}$$

The material tensors λ_{ilmn}, k_{ilmn}, C_{ilmn} have only three independent components for this crystal. Let they will be in Voigt's designations [8]

$$\lambda_{11}, \lambda_{12}, \lambda_{44}, \quad k_{11}, k_{12}, k_{44}, \quad C_{11}, C_{12}, C_{44}.$$

Take for a measure of anisotropy of a cubic crystal [9]

$$a_1 = \frac{2\lambda_{44}}{\lambda_{11} - \lambda_{12}}, \quad a_2 = \frac{2k_{44}}{k_{11} - k_{12}}, \quad a_3 = \frac{2C_{44}}{C_{11} - C_{12}}. \tag{11}$$

For isotropic medium we have

$$a_1 = a_2 = a_3 = 1. \tag{12}$$

Material ratios for the media of cubic system have the form

$$\sigma_{il} = \begin{cases} (\lambda_{11} - \lambda_{12})e_{il} + (C_{11} - C_{12})\varepsilon_{il} + (\lambda_{12}e + C_{12}\varepsilon - s\Phi(u_s))\delta_{il} \ (i = l), \\ 2\lambda_{44}e_{il} + 2C_{44}\varepsilon_{il} \ (i \neq l), \end{cases} \tag{13}$$

$$\chi_{il} = \begin{cases} (k_{11} - k_{12})\varepsilon_{il} + (C_{11} - C_{12})e_{il} + (k_{12}\varepsilon + C_{12}e)\delta_{il} \ (i = l), \\ 2k_{44}\varepsilon_{il} + 2C_{44}e_{il} \ (i \neq l), \end{cases} \tag{14}$$

$$e = e_{xx} + e_{yy} + e_{zz}, \quad \varepsilon = \varepsilon_{xx} + \varepsilon_{yy} + \varepsilon_{zz}. \tag{15}$$

3 Flat deformation. Statics equations

We will call the deformed state as statically flat and parallel to an axis x_3 if

$$U_x = U_x(x, y), \quad U_y = U_y(x, y), \quad U_z = 0, \tag{16}$$

$$u_x = u_x(x, y), \quad u_y = u_y(x, y), \quad u_z = 0. \tag{17}$$

Taking into account (16), (17) in material ratios (13) and (14), and substituting the expressions for σ_{il} and χ_{il} in Eqs. (1) and (3), we find the equations of static in movements for flat deformation of nonlinear model:

$$\begin{aligned} &\lambda_{44}\Delta\mathbf{U} + (\lambda_{12} + \lambda_{44})\,\mathrm{grad}\,\mathrm{div}\mathbf{U} + \\ &C_{44}\Delta\mathbf{u} + (C_{12} + C_{44})\,\mathrm{grad}\,\mathrm{div}\,\mathbf{u} - s\,\mathrm{grad}\,\Phi(u_s) = 0, \end{aligned} \tag{18}$$

$$\begin{aligned} &k_{44}\Delta\mathbf{u} + (k_{12} + k_{44})\,\mathrm{grad}\,\mathrm{div}\,\mathbf{u} + \\ &C_{44}\Delta\mathbf{U} + (C_{12} + C_{44})\,\mathrm{grad}\,\mathrm{div}\,\mathbf{U} - \mathbf{B}(p - s\,\mathrm{div}\,\mathbf{U})\sin u_s = 0. \end{aligned} \tag{19}$$

In Eqs. (18) and (19) one has

$$\mathbf{U} = U_x\mathbf{i} + U_y\mathbf{j}, \quad \mathbf{u} = u_x\mathbf{i} + u_y\mathbf{j}, \quad \mathbf{B} = \frac{\mathbf{i} + \mathbf{j}}{b}, \quad \Delta = \frac{\partial^2}{\partial x^2} + \frac{\partial^2}{\partial y^2}$$

and, besides, restrictions (12) are accepted.

3.1 General solution of the equations of statics

The equations of static (18), (19) are a system of four coupled nonlinear equations. We will seek a vector of macroshifts $\mathbf{U}$ in Papkovish-Neuber form

$$\mathbf{U} = a\mathbf{A} + \operatorname{grad}\chi. \tag{20}$$

Here $(a, \chi, \mathbf{A})$ are an arbitrary constant, a scalar function $\chi(x, y)$ and a vector function $\mathbf{A}(x, y)$. If one substitutes the expression (20) in Eq. (18), then it will be solved if vectors $\mathbf{A}$ and $\mathbf{u}$ are satisfy to equation

$$a\lambda_{44}\Delta\mathbf{A} + C_{44}\Delta\mathbf{u} = 0, \tag{21}$$

and the scalar function χ is a solution of the Poisson equation

$$\Delta\chi = \frac{1}{\lambda_{12} + 2\lambda_{44}} \left[s\Phi(u_s) - a(\lambda_{12} + \lambda_{44}) \operatorname{div}\mathbf{A} - (C_{12} + C_{44}) \operatorname{div}\mathbf{u}\right]. \tag{22}$$

After substitution Eq. (20) in Eq. (19), we can see that this equation will be solved if

$$\operatorname{div}\mathbf{A} = \operatorname{div}\mathbf{u}, \quad a = \frac{k_{12} + k_{44} - C(C_{12} + C_{44})}{(\lambda_{12} + \lambda_{44})C - (C_{12} + C_{44})}, \quad C = \frac{C_{12} + 2C_{44}}{\lambda_{12} + 2\lambda_{44}}, \tag{23}$$

$$k_{44}\Delta\mathbf{u} + aC_{44}\Delta\mathbf{A} + sC \operatorname{grad}\Phi(u_s) - \mathbf{B}(p - s \operatorname{div}\mathbf{U}) \sin u_s = 0. \tag{24}$$

One can exclude $\Delta\mathbf{A}$ from Eq. (24) with help (21). Then the components of microshift vector (u_x, u_y) are the solutions of the equations

$$\begin{aligned} K\Delta u_x + sC\frac{b^2}{2} \sin u_s \frac{\partial u_s}{\partial x} - \mathbf{B}(p - s \operatorname{div}\mathbf{U}) \sin u_s = 0, \\ K\Delta u_y + sC\frac{b^2}{2} \sin u_s \frac{\partial u_s}{\partial y} - \mathbf{B}(p - s \operatorname{div}\mathbf{U}) \sin u_s = 0, \end{aligned} \tag{25}$$

$$K = \frac{b^2}{2}\left(k_{44} - \frac{C_{44}^2}{\lambda_{44}}\right).$$

Eqs. (25) can be transformed to more simple form. After summation of (25) and elementary algebraic transformations we find the equation for u_s

$$\begin{aligned} &K\Delta u_s = P \sin u_s, \\ &P = p - \frac{s}{\lambda_{12} + 2\lambda_{44}} \left[\operatorname{div}\mathbf{u}_+ + s\Phi(u_s)\right], \\ &\mathbf{u}_+ = (a\lambda_{44} - C_{12} - C_{44})\,\mathbf{u} + \frac{b^2}{2}(C_{12} + 2C_{44})\,\mathbf{B}u_s. \end{aligned} \tag{26}$$

To find a vector of microshifts $\mathbf{u}$ it is necessary to add the equation for u_x and u_y to the Eq. (26). They have the form

$$\Delta\left(u_x - \frac{b}{2}u_s\right) = f, \quad \Delta\left(u_y - \frac{b}{2}u_s\right) = -f, \tag{27}$$

where

$$f = \lambda \left(\frac{\partial u_s}{\partial y} - \frac{\partial u_s}{\partial x} \right) \sin u_s, \qquad \lambda = \frac{s}{4K} C\, b^2. \tag{28}$$

Thus, realization of nonlinear model is reduced to the solution of the equation (26). If function u_s is found, then the functions u_x and u_y can be found from the Poisson equation with the known function f, as we can see from (27) and (28). Problems of finding of scalar function χ and vector $\mathbf{A}$ from Eq. (21) also lead to Poisson equation

$$\Delta\chi = \frac{1}{\lambda_{12} + 2\lambda_{44}} \left\{ s\Phi(u_s) - [(C_{12} + C_{44}) + a(\lambda_{12} + \lambda_{44})] \operatorname{div} \mathbf{u} \right\}. \tag{29}$$

3.2 Solutions of the equations of optical mode and structures of microdeformation corresponding to them

In literature there are no analytical methods for solution of sine Gordon (SG) equation with a variable amplitude. Functionally invariant solutions of the (2+1)- and (3+1)-dimensional SG equations are constructed for a wide, but specific type of amplitudes in [10]–[12]. The Eq. (26) can be reduced to well studied cases if to make some restrictions for model or for the field of microdeformations. So, if not to consider dependence of potential of interaction of sublattices on deformation of the medium, i.e. to accept $s = 0$, then Eq. (28) becomes the SG equation with constant coefficients (K, p)

$$K\Delta u_s = p \sin u_s. \tag{30}$$

Also it will be if

$$\operatorname{div} \mathbf{u}_+ + \frac{s}{\lambda_{12} + 2\lambda_{44}} \Phi(u_s) = 0. \tag{31}$$

In literature the method of the solution of the SG equation (30) based on substitution

$$u_s = 4 \operatorname{arctg} (\mathrm{G(x, y)}), \quad \mathrm{G(x, y)} = \Phi_1(\mathrm{x})\Phi_2(\mathrm{y}), \tag{32}$$

is widely known. The solution (32) assumes that $K > 0$. If $K < 0$, then solution of Eq. (30) is

$$u_s = \pi + 4 \operatorname{arctg} (\mathrm{G(x, y)}). \tag{33}$$

The solution (32) is connected with G. L. Lamb Jr. [13], though the first time it was used by Steuerwald [14].

The functions $\Phi_1(x)$ and $\Phi_2(y)$ can be found by inversion of the corresponding elliptic integrals by Legendre's method. The Legendre method is rather difficult. In [15] the method of finding of functions $\Phi_1(x)$ and $\Phi_2(y)$ is offered based on the differential equations which satisfy elliptic functions of Jacobi (the modified Lamb method). The offered approach allows to receive a wide class of doubly periodic solutions of

the SG equation. Two solutions from this class are given below

$$\mathbf{1)}\quad A\frac{\mathrm{cn}(\xi,\nu_1)}{\mathrm{cn}(\eta,\nu_2)},\qquad \begin{aligned} H^2 &= \frac{\nu_1^2(1+A^2)\left[(1+A^2)\nu_2^2-1\right]}{A^4\nu_2^2}\,\mathrm{K}^2(\nu_1),\\ B^2 &= \frac{(1+A^2)\left[(1+A^2)\nu_2^2-1\right]}{A^2}\,\mathrm{K}^2(\nu_2),\\ A^4 &= \frac{\nu_1^2(1-\nu_2^2)}{\nu_2^2(1-\nu_1^2)}, \end{aligned} \tag{34}$$

$$\mathbf{2)}\quad \frac{A}{\mathrm{cn}(\xi,\nu_1)}\frac{\mathrm{sn}(\eta,\nu_2)}{\mathrm{dn}(\eta,\nu_2)},\qquad \begin{aligned} H^2 &= \frac{(1-\nu_1^2)(\nu_2^2-A^2)(A^2+1-\nu_2^2)}{A^4}\,\mathrm{K}^2(\nu_1),\\ B^2 &= \frac{(\nu_2^2-A^2)(A^2+1-\nu_2^2)}{A^2}\,\mathrm{K}^2(\nu_2),\\ A^4 &= \frac{\nu_2^2(1-\nu_1^2)(1-\nu_2^2)}{\nu_1^2},\quad \nu_1^2+\nu_2^2>1, \end{aligned} \tag{35}$$

In examples (34), (35) values $\mathrm{K}(\nu_1)$, $\mathrm{K}(\nu_2)$ are full elliptic integrals of the first sort and variables are

$$\xi = \frac{x}{lH}\,\mathrm{K}(\nu_1),\quad \eta = \frac{y}{lB}\,\mathrm{K}(\nu_2),\quad l=\sqrt{K/p}. \tag{36}$$

On Fig. 1 and Fig. 2 microdeformations corresponding to the solutions (34) and (35) are shown. As we can see, the solution (34) describes creating in crystal lattice

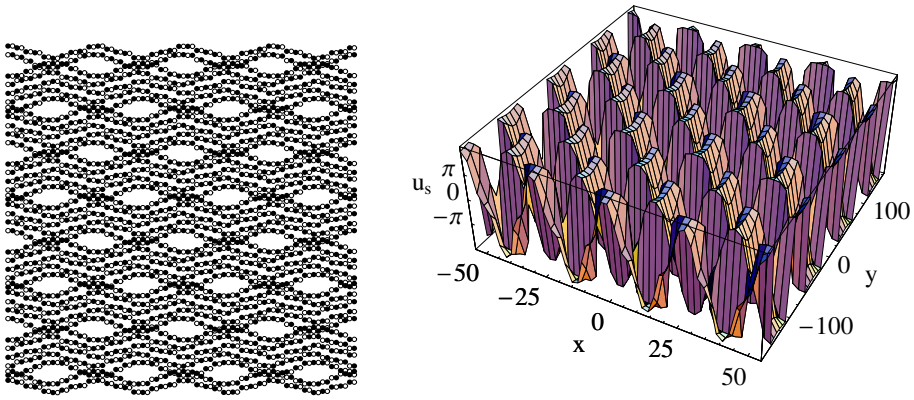

Figure 1: Microdeformations of crystal and solution (34) for $\nu_1 = 0.99999$, $\nu_2 = 0.9$.

of system of regularly located micropores, and (35) describes of system of regularly located microconsolidations.

The modified method allows to construct solutions which are expressed through circular or hyperbolic functions from solutions which are expressed through elliptic functions of Jacobi. It can be done, if to use the known limit ratios

$$\begin{aligned} &\mathbf{1}.\quad \nu\to 0,\ \ \mathrm{sn}(u,\nu)\to \sin u,\ \ \mathrm{cn}(u,\nu)\to\cos u,\ \ \mathrm{dn}(u,\nu)\to 1,\\ &\mathbf{2}.\quad \nu\to 1,\ \ \mathrm{sn}(u,\nu)\to \mathrm{th}\,u,\ \ \mathrm{cn}(u,\nu)\to\frac{1}{\mathrm{ch}\,u},\ \ \mathrm{dn}(u,\nu)\to\frac{1}{\mathrm{ch}\,u}. \end{aligned} \tag{37}$$

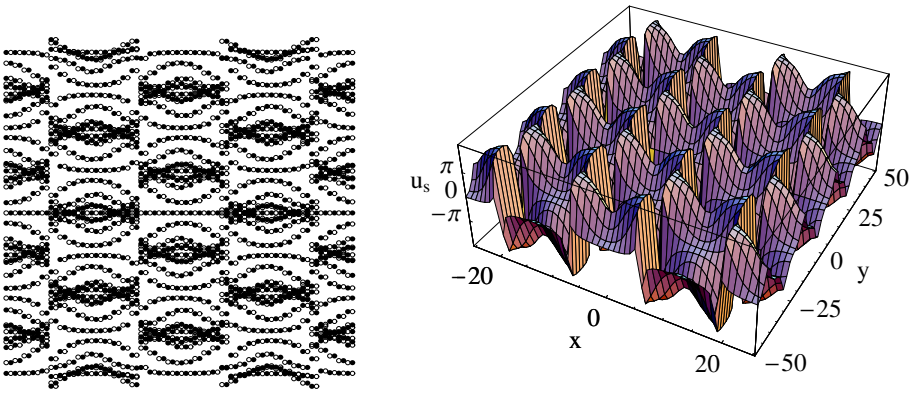

Figure 2: Microdeformations of crystal and solution (35) for $\nu_1 = \nu_2 = 0.999$.

Using (37), one finds

$$G = \begin{cases} \operatorname{tg}\psi \dfrac{\operatorname{sh}(x\cos\psi)}{\operatorname{sh}(y\sin\psi)} \\ \operatorname{tg}\psi \dfrac{\operatorname{ch}(\mathrm{x}\cos\text{-})}{\operatorname{ch}(\mathrm{y}\sin\text{-})}, \\ \dfrac{1}{\operatorname{th}\psi}\dfrac{\cos(x\operatorname{sh}\psi)}{\operatorname{sh}(y\cosh\psi)}, \end{cases} \tag{38}$$

where ψ is an arbitrary constant.
On Fig. 3–5 microdeformations corresponding to the solutions (38) are shown. For

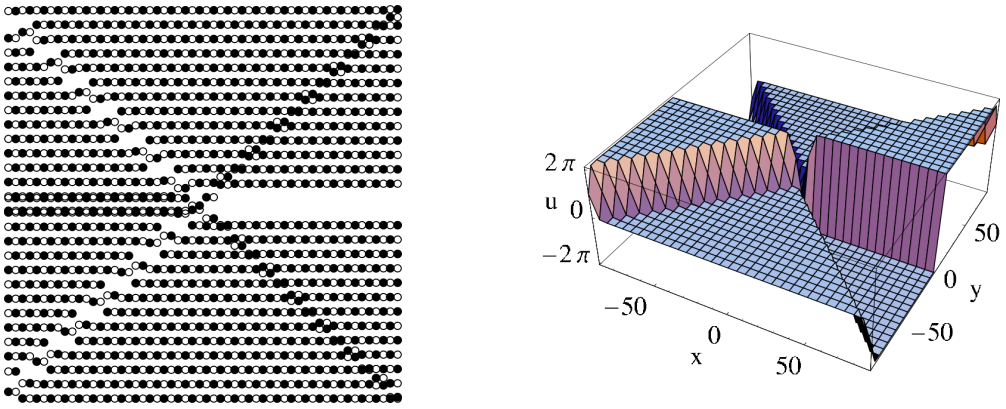

Figure 3: Microdeformations and solutions for the first case in (38) with $\psi = \pi/4$.

the first solution the plane of $y = 0$ is the plane with defects. On half-plane $x > 0$ defect like the main crack is formed, half-plane $x < 0$ contains the defects caused by introduction of the excess crystal planes. It is visible that defects are also the inclined planes. For the second solution the plane of $y = 0$ is not the singular plane. The third solution (38) describes system of micropores which are located in $y = 0$ plane.
The given examples show that the nonlinear model describes features of deformation which are implemented in the field of big external tension, are observed on experience and not described by classical mechanics of the continuous medium.

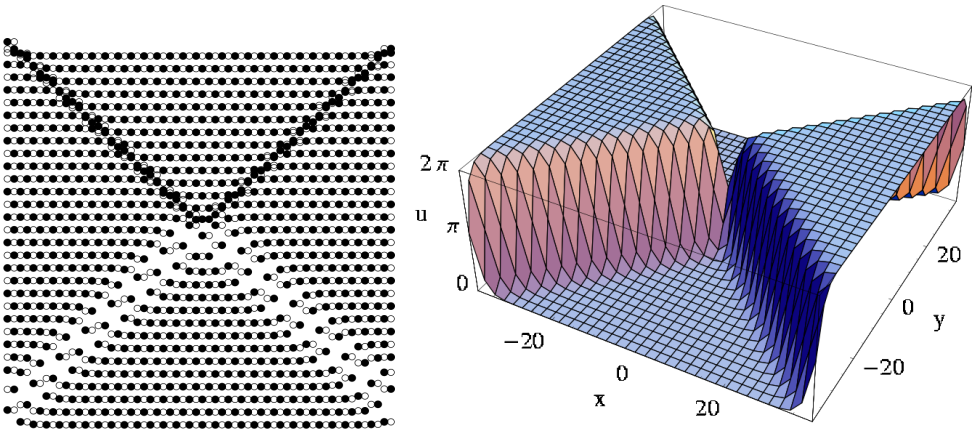

Figure 4: Microdeformations and solutions for the second case in (38) with $\psi = \pi/4$.

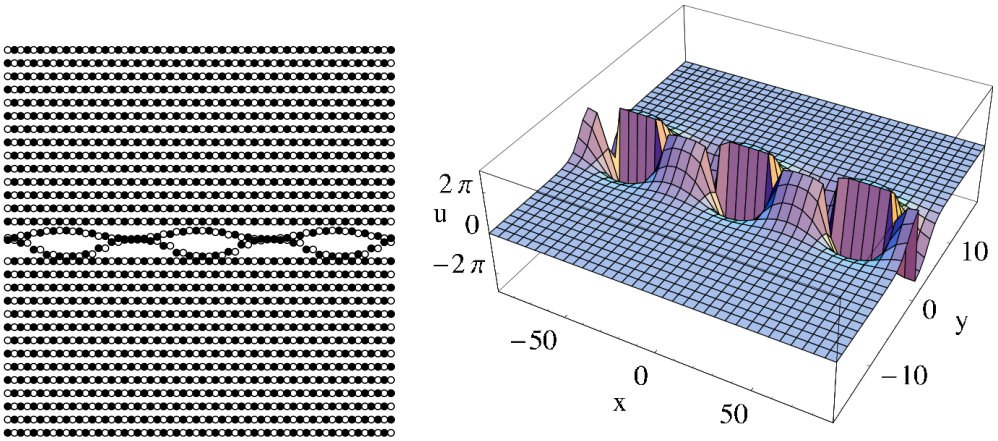

Figure 5: Microdeformations and solutions for third case in (38) with $\psi = 0.1$.

4 Conclusion

The flat deformation plays an extremely important role in classical mechanics of continuous medium. It is caused by the fact that effective analytical and numerical methods are developed for the solution of problems of flat deformation. The problems of flat deformation can be reduced to boundary problems of theory of the functions of complex variable. It allowed for their solution to apply both methods of classical mathematical physics, and the methods of the theory of functions of complex variable (conformal mappings, Riemann problem, theory of singular integrable equations, etc.) As a result exact analytical solutions of a large number of concrete cases of deformation of one- and multiply connected domains have been found [16]. The found solutions have formed a scientific basis of modern materials science.

However the linear classical model of the continuous medium doesn't answer inquiries of modern technologies of materials with internal structure. It doesn't describe processes of deformation and specific nanoscale changes (defects, phase transformations, fragmentation, etc.) which are implemented in the field of intensive plastic deformations. More adequately these processes can be described by the nonlinear theory of deformation of crystal media with a complex lattice. However, the development

of mathematical methods for realization of the nonlinear model is necessary that it became a scientific basis for engineering calculations in modern technologies.

Acknowledgements

This work was supported by RFBR, grants 16-01-00068-a, 17-01-00230-a and 17-02-00365-a.

References

[1] E. L. Aero. Microscale deformations in a two-dimensional lattice: Structural transitions and bifurcations at critical shear. *Phys. Solid State* **42**, (2000) 1147–1153.

[2] E. L. Aero. Significantly nonlinear micromechanics of the medium with changeable periodic structure. *Uspekhi Mekhaniki* **1**, (2002) 130–176.

[3] E. L. Aero, A. N. Bulygin, Yu. V. Pavlov. Nonlinear model of deformation of crystal media with complex lattice: mathematical methods of model implementation. *Math. Mech. Solids* **21**, (2016) 19–36.

[4] J. Frenkel, T. Kontorova. On the theory of plastic deformation and twinning. *ZhETF* **8**, (1938) 89.

[5] O. M. Braun, Y. S. Kivshar. The Frenkel-Kontorova Model. Concepts, Methods, and Applications. Springer, New York, 2004.

[6] A. V. Porubov, E. L. Aero, G. A. Maugin. Two approaches to study essentially nonlinear and dispersive properties of the internal structure of materials. *Phys. Rev. E* **79**, (2009) 046608.

[7] M. P. Shaskol'skaya. Crystallography [In Russian]. Vysshaya Shkola, Moscow, 1984.

[8] W. Voigt. Lehrbuch der Kristalphysik. Leipzig, 1910.

[9] C. Kittel. Introduction to Solid State Physics. Wiley, New York, 1956.

[10] E. L. Aero, A. N. Bulygin, Yu. V. Pavlov. New approach to solution of sine-Gordon equation with variable amplitude. *Proc. Int. Conf. "Days on Diffraction 2010"*, p. 10 –15.

[11] E. L. Aero, A. N. Bulygin, Yu. V. Pavlov. New approach to the solution of the classical sineЦGordon equation and its generalizations. *Differential Equations* **47**, (2011) 1442–1452.

[12] E. L. Aero, A. N. Bulygin, Yu. V. Pavlov. Solutions of sine-Gordon equation with variable amplitude. *Theor. Math. Phys.* **184**, (2015) 961–972.

[13] G. L. Lamb, Jr. Analytical Descriptions of Ultrashort Optical Pulse Propagation in a Resonant Medium. *Rev. Mod. Phys.* **43**, (1971) 99–124.

[14] R. Steuerwald. Über Enneper'sche Flächen und Bäcklund'sche Transformationen. *Abh. Bayer. Akad. Wiss., N. F.* **40**, (1936) 1–105.

[15] E. L. Aero, A. N. Bulygin, Yu. V. Pavlov. Mathematical methods for solution of nonlinear model of deformation of crystal media with complex lattice. *Proc. Int. Conf. "Days on Diffraction 2015"*, p. 8–13.

[16] N. I. Muskhelishvili. Some base problems of the theory of elasticity [In Russian]. Nauka, Moscow, 1966.

E. L. Aero, *A. N. Bulygin, Yu. V. Pavlov,*
Institute for Problems in Mechanical Engineering of Russian Academy of Sciences,
61 Bol'shoy, V.O., Saint Petersburg, 199178, Russia

Formulation Of Rheologycal Equations Of The Elastic-Viscous Plastic Medium Taking Into Account The Current Value Of The Lateral Deformation

Alexander R. Arutyunyan, Robert A. Arutyunyan
r.arutyunyan@spbu.ru

Abstract

On the stress-strain diagram, which is obtained in experiments on a simple tension of metal specimens, there is a region of instability due to the formation of the neck. In the theory of plasticity are defined conditions for the transition to an unstable state and appearance of the maximum point on the stress-strain diagram. In the derivation of this condition assumption of incompressibility of the material is accepted. However, this assumption cannot be justified, since in the neck region there are numerous damages (pores, micro-cracks), i.e. the material is compressible. In this paper, the condition for the transition to the unstable state for a compressible plastic medium is formulated. Incompressibility condition is also used in the formulation of nonlinear elastic and viscous-elastic equations generalizing linear models of Hooke and Maxwell.

1 Introduction.

In solid mechanics, the main mechanical characteristics of materials are determined, in particular, from experiments on simple tension. According to the results of measurements of force, current length and diameter of the specimen are calculated the values of true stress $\sigma = P/F = \sigma_0 F_0/F$ and logarithmic strain $\varepsilon = \ln l/l_0$ (P is force, $\sigma_0 = P/F_0$ is engineering stress, l_0, F_0 are initial and l, F are the current length and the cross section area of the specimen). Typical stress-strain diagrams for metallic specimen are shown on Fig. 1.
It is usually assumed that the change in the cross section area of the specimen during deformation can be neglected, then $\sigma \approx \sigma_0$ and stress-strain curves are plotted in $\sigma_0 - \varepsilon$ coordinates (ε is engineering strain). At the point M on Fig. 1 engineering stress reaches maximum, neck is occurs on specimen and the deformation becomes unstable. The drop-down region of the $\sigma_0 - \varepsilon$ curve is the result of a sharp cross section area reduction of the specimen due to the necking. The nature of the neck is determined by the properties of the material and is various for different materials (metals, polymers).

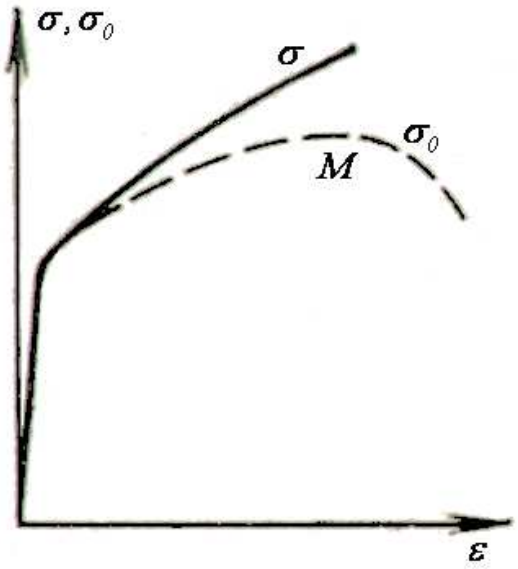

Figure 1: Stress-strain diagrams. Solid line corresponds to tension diagram plotted in true stresses and the dotted line is diagram plotted in engineering stresses.

2 Definition of maximum point achievement on the stress-strain curve for incompressible and compressible plastic medium.

To determine the conditions of the maximum achievement at the point M (Fig. 1) in the literature [1, 2] the material is considered as incompressible, then $l_0F_0 = lF$ and $P = \sigma F = \sigma F_0\, e^{-\varepsilon}$. Differentiating the last expression for the ε we will have

$$\frac{dP}{d\varepsilon} = F_0\, e^{-\varepsilon} \left(\frac{d\sigma}{d\varepsilon} - \sigma \right). \tag{1}$$

Under $\frac{dP}{d\varepsilon} = 0$, from (1) follows the ratio

$$\frac{d\sigma}{d\varepsilon} = \sigma, \tag{2}$$

which is the condition for maximum achievement at the point M (Fig. 1).
Let's note that in derivation of the expression (2) is used the assumption of incompressibility of the material, resulting in a fixed maximum point on the stress-strain diagram. At the same time in real metallic materials during plastic deformation, particularly in the area of instability, the maximum point shifts, numerous damages (pores, cracks) are occurred, so the assumption of incompressibility of the material in the general case cannot be considered as reasonable.
The condition of compressibility is determined by using the current value of the lateral deformation ν: $\nu = -\varepsilon_y/\varepsilon_x = -\varepsilon_z/\varepsilon_x$ (ε_x is longitudinal, ε_y, ε_z are transverse deformations of a cylindrical specimen). Then, taking into account the geometric relation $F_0/F = (l/l_0)^{2\nu}$ [3], we will have

$$P = \sigma F = \sigma F_0 \, e^{-2\nu\varepsilon}. \tag{3}$$

Approximately taking that $\nu = \nu(\sigma_0) = const$ and differentiating (3) for the ε, we receive the following relation

$$\frac{dP}{d\varepsilon} = F_0 \, e^{-2\nu\varepsilon} \left(\frac{d\sigma}{d\varepsilon} - 2\nu\sigma \right), \tag{4}$$

from which is follows the condition for maximum achievement

$$\frac{d\sigma}{d\varepsilon} = 2\nu\sigma. \tag{5}$$

For an incompressible material $\nu = 1/2$ and the relation (5) will coincide with the formula (2). According to the formula (5) the position of the maximum point M on the stress-strain curve will be vary depending on the material state.
In the case of elastic-plastic media $d\varepsilon = d\varepsilon^e + d\varepsilon^p$ (ε^e, ε^p are the components of the elastic and plastic deformation, $\varepsilon^e = \sigma/E$, E is Young modulus). The ratio between stress and deformation can be determined by the following equation

$$\frac{dl}{l} = \frac{d\sigma}{E} + \varphi(\sigma)d\sigma. \tag{6}$$

Integrating equation (6), we will receive

$$\ln \varepsilon = \frac{\sigma}{E} + \int_0^\sigma \varphi(\sigma)d\sigma. \tag{7}$$

In the general case, inserting at (6) a relation $\sigma = \sigma_0 \, e^{2\nu\varepsilon}$, we can obtain the equation written through the value of the lateral deformation ν. For different values of ν, we can plot a non-monotonic $\sigma_0 - \varepsilon$ diagrams and, thus, to describe experimental curves for metallic materials in engineering stress-strain coordinates. Further, this approach is applied for the case of rigid-plastic Ludwig medium with nonlinear hardening

$$\sigma = \sigma_T + b\varepsilon^m, \tag{8}$$

where σ_T is the yield stress, b, m are constants.
Let's write equation (8) through σ_0

$$\sigma_0 = (\sigma_T + b\varepsilon^m) \, e^{-2\nu\varepsilon}. \tag{9}$$

The theoretical curves according formula (9) for $\sigma_T = 200 \; MPa$, $b = 5 \cdot 10^2 \; MPa$, $m = 0,5$ and for different ν values are shown on Fig. 2.

3 Formulation of nonlinear equations for compressible elastic and elastic-viscous medium.

Next, let's formulate nonlinear equations for compressible viscoelastic medium based on the linear relations of Hooke's law and viscous Newton media. It is well known

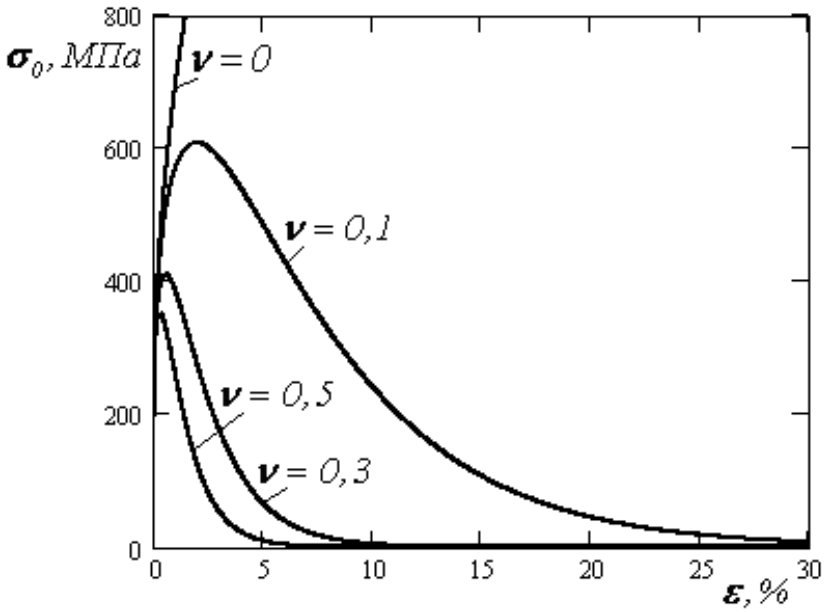

Figure 2: The theoretical curves according formula (9).

that using the linear relations the mechanical behavior of materials, in particular, polymers can be described only in limited temperature and force actions. In general case, we should operate the non-linear rheological equations. Under the proposed approach, will be considered the behavior of a compressible elastic-viscous medium, which generalized linear models of Hooke and Maxwell.

In the case of Hooke's law, nonlinear version of the equations for the elastic medium written using the current value of the transverse deformation has the form

$$\sigma_0 = E\varepsilon e^{-2\nu\varepsilon}. \tag{10}$$

Using equation (10) the nonlinear effects observed in experiments on simple tension can be described. When $\nu = 1/2$ relation (10) is described the behavior of an incompressible nonlinear medium. When $\nu = 0$ the medium is linearly elastic. Intermediate cases will correspond to the elastic materials with different mechanical properties. Diagrams $\sigma_0 - \varepsilon$ for different values of lateral deformation coefficient are shown on Fig. 3.

Let's consider a rheological Maxwell model for nonlinear elastic-viscous medium. With this aim, the classical linear Maxwell's equation

$$\frac{d\varepsilon}{dt} = \frac{1}{E}\frac{d\sigma}{dt} + \frac{\sigma}{\eta} \tag{11}$$

will be written through the stress σ_0, considering that the material is compressible and introducing the current value of the lateral deformation

$$\frac{d\varepsilon}{dt} = \frac{2\sigma_0\nu}{E}\, e^{2\nu\varepsilon}\frac{d\varepsilon}{dt} + \frac{\sigma_0}{\eta}\, e^{2\nu\varepsilon}. \tag{12}$$

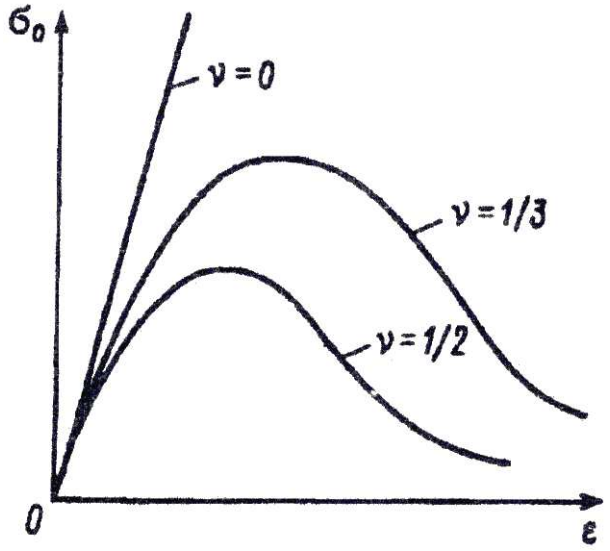

Figure 3: Diagrams $\sigma_0 - \varepsilon$ for different values of lateral deformation coefficient: incompressible non-linear medium ($\nu = 1/2$), linear-elastic medium ($\nu = 0$).

From equation (11) when $\sigma = const$ is follows a linear dependence for creep deformation $\varepsilon = \frac{\sigma}{\eta}t$, which is known to be bad fit with the experimental results. Solving the equation (12) the nonlinear equations for creep strain can be obtained. Considering that $\nu = \nu(\sigma_0) = const$ from the solution of equation (12) with the initial conditions $t = 0$, $\varepsilon = 0$, we can obtain

$$t = \eta\left(\frac{1 - e^{-2\nu\varepsilon}}{2\nu\sigma_0} - \frac{2\nu\varepsilon}{E}\right). \tag{13}$$

The theoretical creep curves for a given stress level and different values of ν according to the formula (13) are shown on Fig. 4.
For $\nu \to 0$ from (13) follows the linear Maxwell relation for creep deformation. In the general case, creep curves are nonlinear and qualitatively described the corresponding experimental curves.

4 Conclusion.

In the article, the condition for the transition to instable state in the region of necking for compressible metal specimen is formulated. For an incompressible material Hill was first who described this condition. The effect of compressibility is determined by using the current value of the lateral deformation. Taking into account this coefficient the rheological equations for compressible media are obtained, which generalized well-known equations for an incompressible plastic, elastic and elastic-viscous medium. Analytical solutions were obtained, constructed the corresponding theoretical stress-strain curves and creep curves dependent on the current value of lateral deformation coefficient. In particular, it is shown that for a compressible material in the region of instability, the maximum point is shifted. In the case of

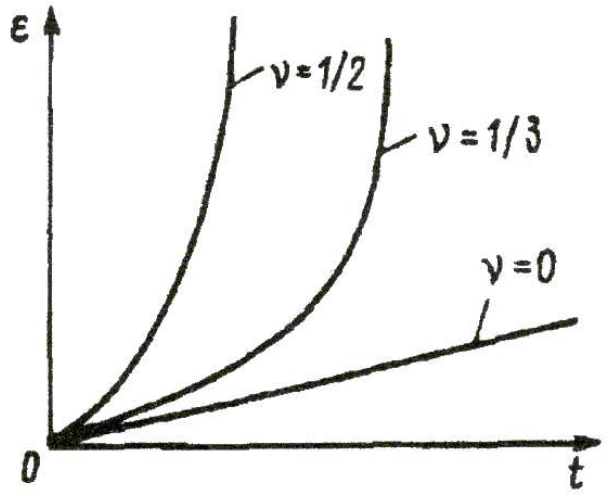

Figure 4: Theoretical creep curves for different values of ν according to the formula (13).

the Hill solution the maximum point of the stress-strain curve is fixed.

Acknowledgements

Financial support of the Russian scientific Fund (Grant N 17-79-20361) is gratefully acknowledged.

References

[1] Hill R. Mathematical theory of plasticity. M: Gostekhizdat. 1956. 408p. (in Russian).

[2] Kachanov L.M. Fundamentals of fracture mechanics. Moscow: Nauka. 1974. 311p. (in Russian).

[3] Arutyunyan R.A. The problem of deformation aging and prolonged fracture in mechanics of materials. St.-Petersburg: Publishing house of St. Petersburg state University. 2004. 253p. (in Russian).

Alexander R. Arutyunyan, Robert A. Arutyunyan, Universitetskii pr., 28, Faculty of Mathematics and Mechanics Sankt-Petersburg State University, Sankt-Petersburg, Petrodvoretz, 198504, Russia.

Formulation And Experimental Justification Of The Long-Term Strength Criterion

Robert A. Arutyunyan
r.arutyunyan@spbu.ru

Abstract

The new results on the effect of thermal embrittlement (embrittlement of structural metallic materials under prolonged action of relatively low stresses and high temperatures) are obtained. The main attention is focused on the formulation of the relations for the damage parameter and the development of the long-term strength criterion. For comparison of the obtained relations with the experimental results observational studies were performed on the determination of damage accumulation under high temperature creep conditions for various metals and alloys: copper, aluminum, Magnox AL80, Nickel and 0.1% palladium alloy, various heat resistant alloys. The experiments were carried out at different temperatures and levels of tensile stresses. Theoretical curves of density change were compared with the experimental results for some of these metals and alloys. At the time interval 30-500 hours the damage function is expressed as a straight line. The theoretical curves have the general character irrespective of the material and the temperature-power effects, which indicates the existence of a common law of damage processes and indirectly confirms the selection of a physical damage parameter as the ratio of the current density of the material to the initial density.

For the description of brittle fractures the conception of continuity (Kachanov [1]) and damage (Rabotnov [2, 3]) was developed. To materialize the damage parameter various definitions were offered [4-6]. In the paper the parameter of continuity is determined by the ratio $\psi = \rho/\rho_0$ (ρ_0 is initial, ρ is current density) and it is an integral measure of the accumulation of structural microdefects during long-term high-temperature loading [7-14]. In the initial conditions $t = 0$, $\rho = \rho_0$, $\psi = 1$, at the fracture time $t = t_f$, $\rho = 0$, $\psi = 0$.

In the brittle model of Kachanov it is supposed that creep deformation doesn't influence to fracture processes, and the kinetic equation of the continuity parameter is taken as a power function of effective stress [1]

$$\frac{d\psi}{dt} = -A\left(\frac{\sigma_{\max}}{\psi}\right)^n, \tag{1}$$

where $A > 0$, $n \geq 0$ are constants, $\sigma_{\max}/\psi$ is effective stress.

The tension problem of specimen under the action of constant load P is solved. It is considered that brittle fracture happens at small deformations therefore it is

possible to neglect change of specimen cross section, i.e. the conditions $F = F_0$, $\sigma_{\max} = \sigma = P/F = P/F_0 = \sigma_0 = \text{const}$, ($\sigma$ is true stress, σ_0 is nominal stress, F_0, F are the initial and current cross section area of a specimen) are accepted. At these assumptions the equation (1) can be expressed in the form

$$\frac{d\psi}{dt} = -A\left(\frac{\sigma_0}{\psi}\right)^n. \tag{2}$$

In the Rabotnov's brittle fracture model [3] the damage parameter ω ($0 \le \omega \le 1$) is defined by the following kinetic equation

$$\frac{d\omega}{dt} = A\sigma^n. \tag{3}$$

The damage parameter is introduced as $\omega = F_T/F_0$ (F_T is the total area of pores). From condition $F = F_0 - F_T$, we have $F = F_0(1-\omega)$, $\sigma = P/F = \sigma_0 F_0/F = \sigma_0/(1-\omega)$. Taking into account these relations the kinetic equation (3) can be written as

$$\frac{d\omega}{dt} = A\left(\frac{\sigma_0}{1-\omega}\right)^n, \tag{4}$$

The equations (2) and (4) are identical at $\omega = 1 - \psi$, $d\psi = -d\omega$. From the solution of these equations under the initial conditions $t = 0$, $\psi = 1$, $\omega = 0$ we have

$$\psi = 1 - \omega = \left[1 - (n+1)A\sigma_0^{nt}\right]^{\frac{1}{n+1}}. \tag{5}$$

Accepting the fracture conditions $t = t_f^b$, $\psi = 0$, $\omega = 1$ (in the general case, the fracture occurs when $\rho = \rho_*$, $\psi = \psi_*$, $\omega = \omega_*$ where the asterisk indicated the limit values of density and damage parameters), from (5) follows the criterion

$$t_f^b = \frac{1}{(n+1)\cdot A\sigma_0^n}. \tag{6}$$

Such approach can give to the parameter of Kachanov the physical content. However from condition $F = F_0$, which is used in Kachanov's theory, follows $\omega = 0$, i.e. the concept of damage loses meaning. Thus, similar interpretation of Kachanov's continuity parameter isn't represented fully correct. The development of the conception of damage received in work [3], where the system of equations for the creep deformation ε and damage parameter ω was proposed. When the criterion of ductile-brittle fracture is determined using this system of equations, the condition of incompressibility, which is contrary to the damage conception, is accepted.

To overcome these contradictions a system of equations for the creep rate and damage, based on the continuity parameter $\psi = \rho/\rho_0$, is proposed. Let's consider the following system of equations

$$\psi^\beta \frac{d\varepsilon}{dt} = B\sigma^m, \tag{7}$$

$$\psi^\alpha \frac{d\psi}{dt} = -A\sigma^n, \tag{8}$$

where B, A, α, β are constants.
Taking into account the mass conservation law $\rho_0 l_0 F_0 = \rho l F$ the true stress can be expressed as $\sigma = \sigma_0 \psi e^{\varepsilon}$. Taking into account this relation the equations (7)-(8) can be written in the form

$$\frac{d\varepsilon}{dt} = B\sigma_0^m \psi^{m-\beta} e^{m\varepsilon}, \tag{9}$$

$$\frac{d\psi}{dt} = -A\sigma_0^n \psi^{n-\alpha} e^{n\varepsilon}. \tag{10}$$

The system of equations (9)-(10) can be solved approximately, for example, for the case of purely brittle fracture and small deformations, when the approximations $e^{m\varepsilon} \approx 1$, $e^{n\varepsilon} \approx 1$ can be considered. In this case, using the initial conditions $t = 0$, $\psi = 1$, $\omega = 0$ we can receive the following analytical solutions

$$\psi = \left[1 - (\alpha - n + 1) A\sigma_0^{nt}\right]^{\frac{1}{\alpha - n + 1}}, \tag{11}$$

$$\varepsilon = \frac{B\sigma_0^{m-n}}{A\gamma} \left\{1 - \left[1 - (\alpha - n + 1) A\sigma_0^{nt}\right]^{\frac{\gamma}{\alpha - n + 1}}\right\}, \tag{12}$$

where $\gamma = m - \beta + \alpha - n + 1$.
Consider the approximate and exact solutions for the damage function $\psi(\varepsilon)$. Taking $e^{m\varepsilon} \approx 1$, $e^{n\varepsilon} \approx 1$ from the system of equations (9)-(10) we get

$$\frac{d\psi}{d\varepsilon} = -\frac{A}{B}\sigma_0^{n-m} \psi^{n-\alpha-m+\beta}. \tag{13}$$

The solution of equation (13) with initial conditions $\psi = 1$, $\varepsilon = 0$ has the form

$$\psi(\varepsilon) = \left[1 - \frac{A\sigma_0^{n-m}\,(1 - n + \alpha + m - \beta)}{B}\varepsilon\right]^{\frac{1}{1-n+\alpha+m-\beta}}. \tag{14}$$

The exact solution of equations (9)-(10) for function $\psi(\varepsilon)$ can be received. Dividing (10) to (9), we will obtain the following equation

$$\frac{d\psi}{d\varepsilon} = -\frac{A}{B}\sigma_0^{n-m} \psi^{n-\alpha-m+\beta} e^{(n-m)\varepsilon}. \tag{15}$$

Using the initial conditions $\psi = 1$, $\varepsilon = 0$ and solving (15) we receive

$$\psi(\varepsilon) = \left[1 + \frac{A\sigma_0^{n-m}(1 - n + \alpha + m - \beta)}{B(n - m)}(1 - e^{(n-m)\varepsilon})\right]^{\frac{1}{1-n+\alpha+m-\beta}}. \tag{16}$$

On Fig. 1 the curves $\psi(\varepsilon)$ according formulas (14) and (16) for different values of parameter α ($\alpha = 6$ - curves 1, 1', $\alpha = 4$ - curves 2, 2' и $\alpha = 2$ - curves 3, 3') are shown. In the calculations the following values of coefficients were used: $A = 10^{-9}[MPa]^{-2}$, $B = 5 \cdot 10^{-14}[MPa]^{-4}$, $\sigma_0 = 100\,MPa$, $n = 2$, m $= 4$, $\beta = 1$.
As can be seen from Fig. 1 the damage curves for formulas (14) and (16) are identical.
Taking the fracture conditions $t = t_f$, $\psi = 0$, from (11) we obtain the creep fracture criterion

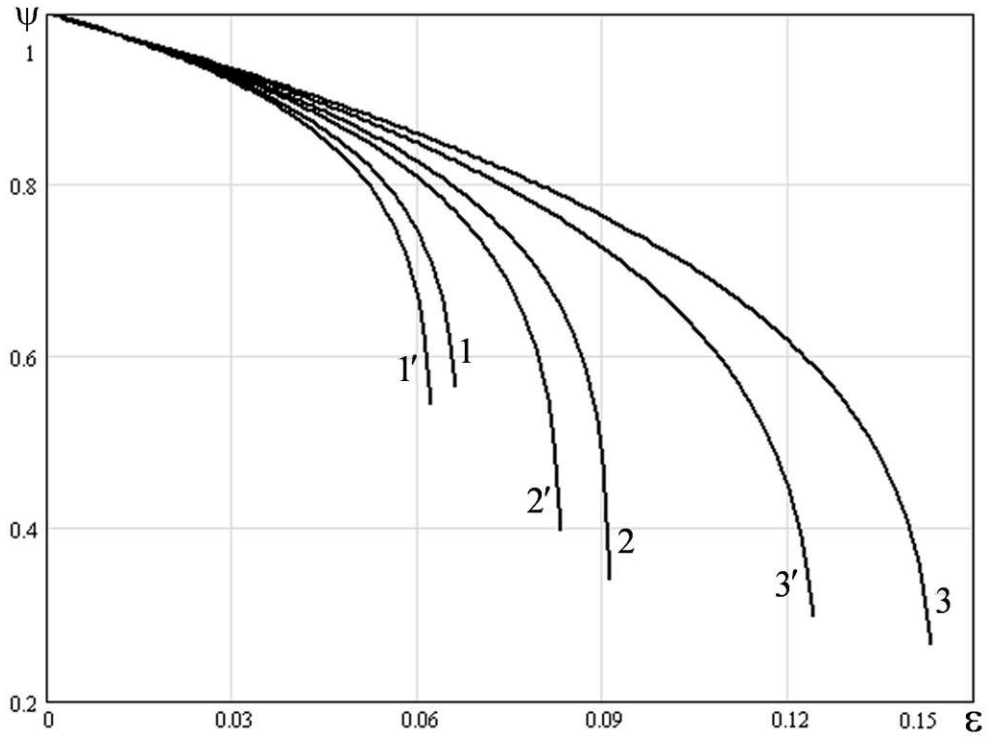

Figure 1: The curves $\psi(\varepsilon)$ according formulas (14) and (16) for different values of parameter α: $\alpha = 6$ - curves 1, 1', $\alpha = 4$ - curves 2, 2' и $\alpha = 2$ - curves 3, 3'.

$$t_f^b = \frac{1}{(\alpha - n + 1) \cdot A\sigma_0^n}. \tag{17}$$

When $\alpha = 2n$ the criterion (17) coincides with the Kachanov-Rabotnov criterion.
In Fig. 2 are shown the theoretical creep deformation curves according to the relation (12) for different values of the coefficient α ($\alpha = 6$ - curve 1, $\alpha = 4$ - curve 2 и $\alpha = 2$ - curve 3). As can be seen from this figure, the system of equations (9)-(10) is able to describe the third phase of creep curves, which is determined by the processes of damage accumulation. In the calculations the following values of coefficients were used: $A = 10^{-9}[MPa]^{-2}$, $B = 5 \cdot 10^{-17}[MPa]^{-4}$, $\sigma_0 = 100\,MPa$, $n = 2$, m $= 4$, $\beta = 1$.
For comparison of the obtained relations with the experimental results observational studies were performed on the determination of damage accumulation under high temperature creep conditions for various metals and alloys: copper, aluminum, Magnox AL80, Nickel and 0.1% palladium alloy, various heat resistant alloys [8-14]. The experiments were carried out at different temperatures and levels of tensile stresses. Dwell times under load to failure were within 30-500 hours. Theoretical curves of density change were compared with the experimental results for some of these metals and alloys. On Fig. 3 theoretical curves $\psi(\varepsilon)$ (solid line) and experimental points of density changes of pure copper during creep under 500° C [8] (circle points) and 250° C [10] (cross points) are shown.
On Fig. 4 theoretical curves $\psi(t)$ (solid line) and experimental points of density

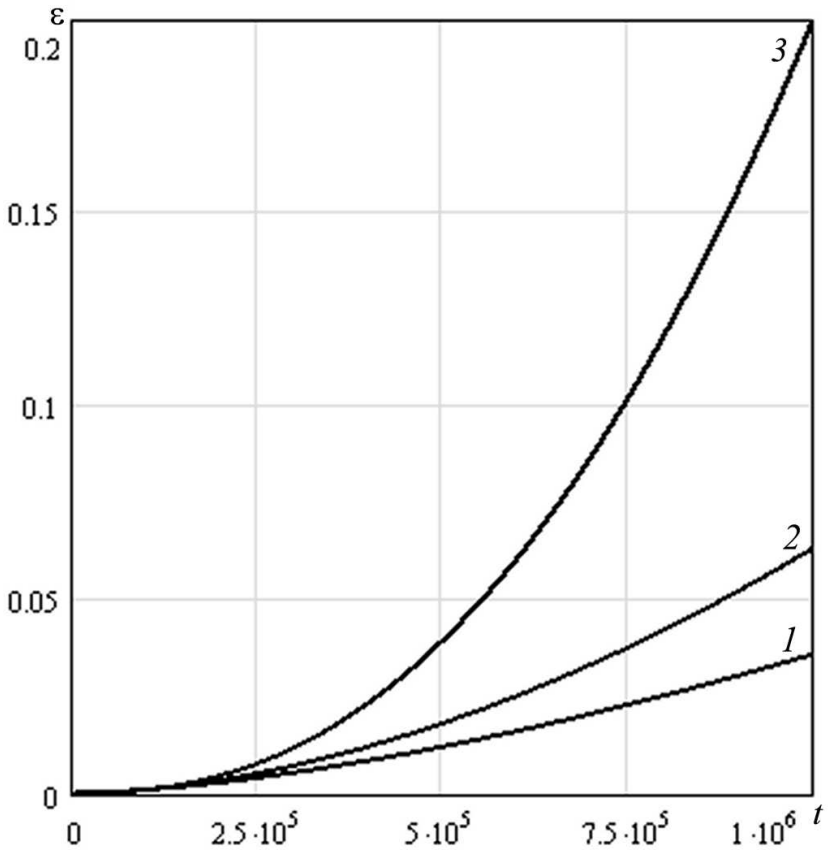

Figure 2: The theoretical creep deformation curves according to the relation (12) for different values of the coefficient α: ($\alpha = 6$ - curve 1, $\alpha = 4$ - curve 2 и $\alpha = 2$ - curve 3.

changes of pure aluminum during creep under 250° C [9] (circle points) and nickel alloy under 503° C [13] (cross points) are shown.
From Fig. 3-4 it follows that the experimental points are described well by straight lines and have the general character for different metals tested under various temperature and force conditions. These results allow us to consider the damage parameter $\psi = \rho/\rho_0$ as universal characteristic of porosity accumulation in the creep process.

Acknowledgements

Financial support of the Russian Foundation for Basic Research (Grant N 15-01-03159) is gratefully acknowledged.

References

[1] Kachanov L.M. Time of fracture under creep // Proceedings USSR Academy of Sciences. OTN. 1958. N 8. P. 26-31. (in Russian).

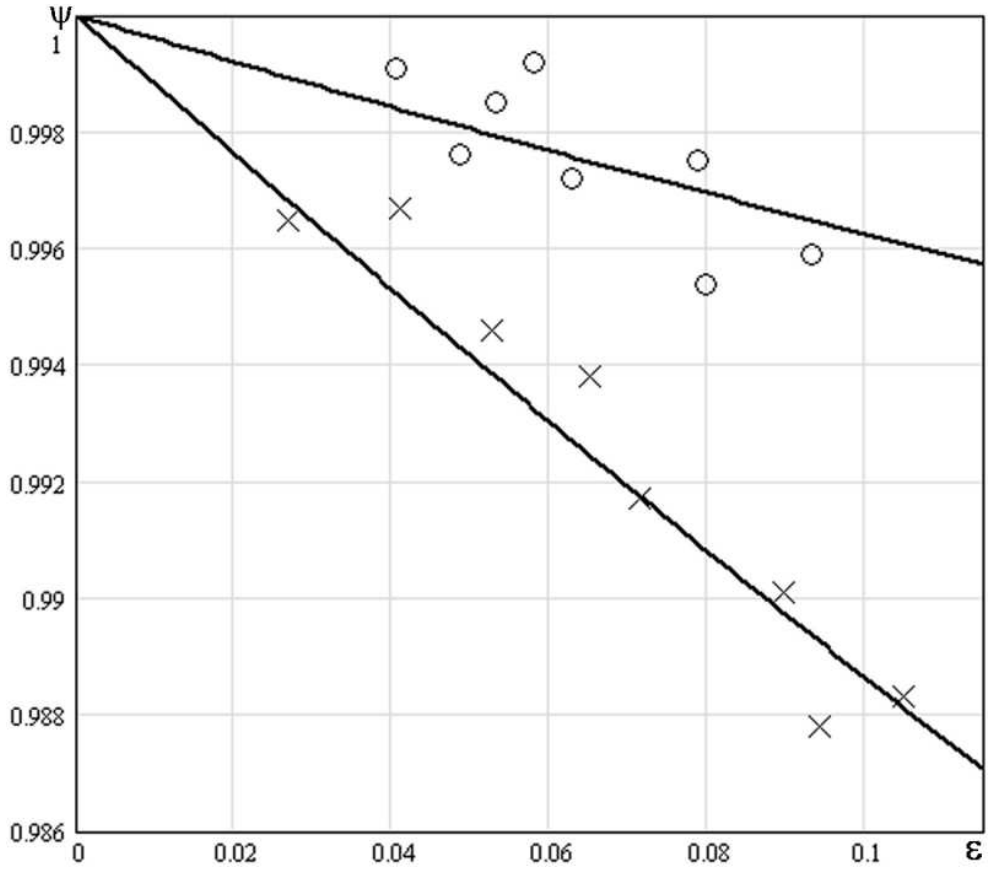

Figure 3: Theoretical curves $\psi(\varepsilon)$ (solid line) and experimental points of density changes of pure copper during creep under 500° C [8] (circle points) and 250° C [10] (cross points).

[2] Rabotnov Y.N. On the mechanism of long-term fracture // Problems of strength of materials and structures. M.: Publishing House of the USSR Academy of Sciences. 1959. P. 5-7. (in Russian).

[3] Rabotnov Y.N. Creep of elements of designs: M.: Nauka. 1966. 752 p. (in Russian).

[4] Novozhilov V.V. On plastic loosening // Applied Mathematics and Mechanics. 1965. N 4. P. 681-689. (in Russian).

[5] Arutyunyan R.A. The problem of strain aging and long-term fracture in mechanics of materials. SPb.: Publishing House of the St. Petersburg State University. 2004. 252p. (in Russian).

[6] Arutyunyan R.A. High-temperature embrittlement and long-term strength of metallic materials // Mechanics of solids. 2015. Volume 50. Issue 2. P. 191-197.

[7] Arutyunyan R.A. Embrittlement problem in mechanics of materials. // Vestn. St. Petersburg. Univ. 2009. ser. 1. vol. 1. P. 54-57. (in Russian).

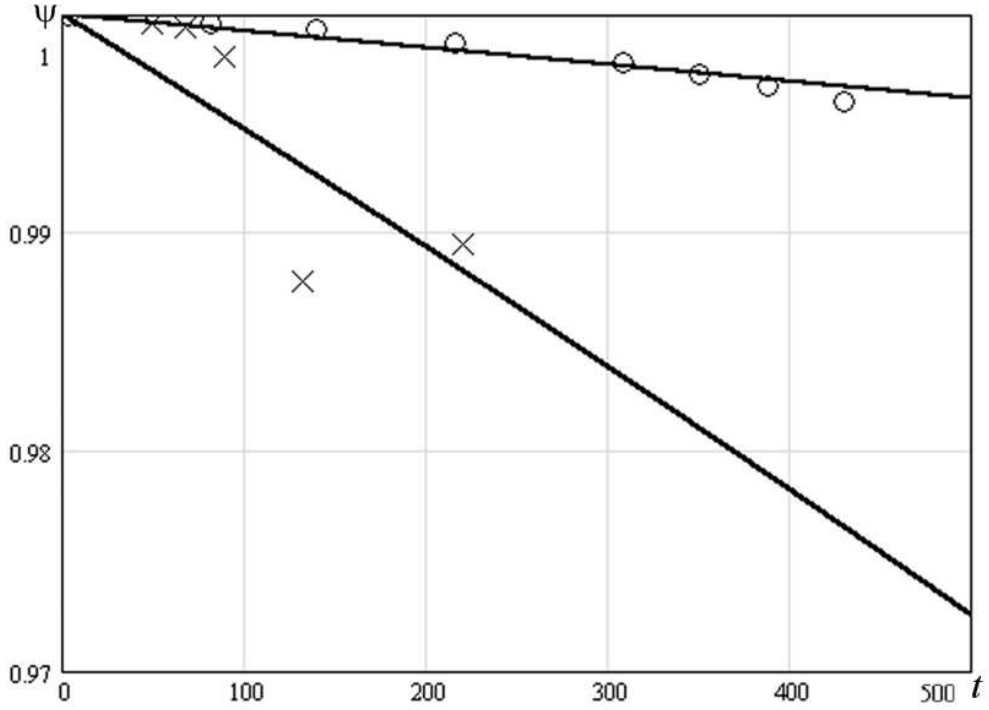

Figure 4: Theoretical curves $\psi(t)$ (solid line) and experimental points of density changes of pure aluminum during creep under 250° C [9] (circle points) and nickel alloy under 503° C [13] (cross points).

[8] Boethner R.C., Robertson W.D. A study of the growth of voids in copper during the creep process by measurement of the accompanying change in density // Trans. of the Metallurg. Society of AIME. 1961. vol. 221. N 3. P. 613-622.

[9] Beghi C., Geel C., Piatti G. Density measurements after tensile and creep tests on pure and slightly oxidised aluminium // J. Mat. Sci. 1970. vol. 5. N 4. P. 331-334.

[10] Brathe L. Macroscopic measurements of creep damage in metals // Scand. J. Metal. 1978. vol. 7. N 5. P. 199-203.

[11] Ratcliffe R.T., Greenwood G.W. Mechanism of cavitation in magnesium during creep // Phil. Mag. 1965. vol. 12. P. 59-69.

[12] Woodford D.A. Density changes during creep in nickel // Metal science journal. 1969. vol. 3. N 11. P. 234-240.

[13] Bowring P., Davies P.W., Wilshire B. The strain dependence of density changes during creep // Metal science journal. 1968. vol. 2. N 9. P. 168-171.

[14] Kumanin V.I., Kovalev L.A., Alekseev S.V. The durability of the metal in the creep conditions. M.: Metallurgy. 1988. 223p. (in Russian).

Robert A. Arutyunyan, Universitetskii pr., 28, Faculty of Mathematics and Mechanics Sankt-Petersburg State University, Sankt-Petersburg, Petrodvoretz, 198504, Russia.

Thermoelasticity of micropolar thin plates

Aslanyan N.S., Sargsyan S.H.

asnaira73@mail.ru

Abstract

The problems of the stress state caused by uneven heating are of great importance for the analysis of the strength and correct functioning of the structures of the new technology, including micro and nano techniques, operating under conditions of unevenly distributed temperature fields. Three-dimensional theory of temperature stresses in the micropolar theory of elasticity was developed by Novacki [1] [2]. In papers [3][4] system of asymptotically justified hypotheses is developed and on the basis of them applied theories of micropolar elastic thin plates and shells are constructed. In paper [5] applied theory of thermoelasticity of micropolar thin shells is constructed. Developing this direction in current paper theory of thermal stresses of bending deformation of micropolar elastic thin plates is introduced and on the basis of this theory problems of thermoelastic bending of rectangular and circular plates are studied, which are brought to final numerical results. Effective properties of micropolar material rigidity are revealed compared with classical case.

1 Problem statement

Isotropic elastic plate of constant thickness $2h$ is considered as three-dimensional body. Axes x_1, x_2 are referred to the plate middle plane. We proceed from main equations of three-dimensional asymmetric linear theory of quasistatic thermoelasticity [2]:
Equilibrium equations:

$$\sigma_{ji,j} = 0,\ \mu_{ji,j} + \epsilon_{ijk}\sigma_{jk} = 0 \tag{1.1}$$

Geometric relations:

$$\gamma_{ji} = u_{i,j} - \epsilon_{kji}\omega_k,\ \chi_{ji} = \omega_{i,j} \tag{1.2}$$

Physical relations of elasticity:

$$\begin{aligned}\sigma_{ji} &= (\mu+\alpha)\gamma_{ji} + (\mu-\alpha)\gamma_{ij} + (\lambda\gamma_{kk} - \alpha_T T)\delta_{ij},\\ \mu_{ji} &= (\gamma+\varepsilon)\chi_{ji} + (\gamma-\varepsilon)\chi_{ij} + \beta\chi_{kk}\delta_{ij}.\end{aligned} \tag{1.3}$$

Here σ_{ij} are stresses, μ_{ij}-momental stresses, u_i-displacements, ω_i re body points rotations during the deformation, γ_{ij} are deformations, χ_{ij}-bending-torsions, $\lambda, \mu, \alpha, \gamma, \varepsilon, \beta$ -elastic constants, α_T is the linear coefficient of temperature expansion of body material $(i, j = 1, 2, 3)$.
Boundary conditions should be added to the above mentioned equations. σ_{3i}, σ_{33}, μ_{3i}, $\mu_{33}(i = 1, 2)$ are given on the facial planes, stresses or displacements and rotations can be given on the lateral surface, or mixed boundary conditions can be given on different parts of the surface.
Energy balance equation in three-dimensional micropolar thermoelasticity has the following form:

$$\int\int_S \int_{-h}^{h} W dx_1 dx_2 dx_3 = A, \tag{1.4}$$

where W is the density of deformation potential energy:

$$\begin{aligned} W = \frac{1}{2}(&\sigma_{11}\gamma_{11} + \sigma_{22}\gamma_{22} + \sigma_{33}\gamma_{33} + \sigma_{12}\gamma_{12} + \sigma_{21}\gamma_{21} + \sigma_{13}\gamma_{13} + \\ &+\sigma_{23}\gamma_{23} + \sigma_{32}\gamma_{32} + \mu_{11}\chi_{11} + \mu_{22}\chi_{22} + \mu_{33}\chi_{33} + \mu_{12}\chi_{12} + \mu_{13}\chi_{13} + \\ &+\mu_{31}\chi_{31} + \mu_{23}\chi_{23} + \mu_{32}\chi_{32}) - \frac{\alpha_t T}{2}(\sigma_{11} + \sigma_{22} + \sigma_{33}), \end{aligned} \tag{1.5}$$

A is the work of external forces and moments on displacements and rotations of deformation:

$$\begin{aligned} A = \frac{1}{2}\Bigg\{ &\Bigg[\int_{-h}^{h} dx_3 \int_{l_1} \left(\sigma_{21}^0 u_1 + \sigma_{22}^0 u_2 + \sigma_{23}^0 u_3 + \mu_{21}^0 \omega_1 + \mu_{22}^0 \omega_2 + \mu_{23}^0 \omega_3\right) dx_1 + \\ &+ \int_{-h}^{h} dx_3 \int_{l_2} \left(\sigma_{11}^0 u_1 + \sigma_{12}^0 u_2 + \sigma_{13}^0 u_3 + \mu_{11}^0 \omega_1 + \mu_{12}^0 \omega_2 + \mu_{13}^0 \omega_3\right) dx_2\Bigg] + \\ &+ \Bigg[\iint_{S^+} \left(p_1^+ u_1 + p_2^+ u_2 + p_3^+ u_3 + m_1^+ \omega_1 + m_2^+ \omega_2 + m_3^+ \omega_3\right) dx_1 dx_2 + \\ &+ \iint_{S^-} \left(p_1^- u_1 + p_2^- u_2 + p_3^- u_3 + m_1^- \omega_1 + m_2^- \omega_2 + m_3^- \omega_3\right) dx_1 dx_2\Bigg]\Bigg\}. \end{aligned} \tag{1.6}$$

On the basis of Hook's law (1.3) density (1.5) of deformation potential energy can be expressed by components of tensors of deformation and bending-torsions, or by components of force and moment stresses. Let's introduce the density W of deformation potential energy by by components of tensors of deformation and bending-torsions:

$$\begin{aligned} W = \frac{1}{2}\Big\{&2\mu\left(\gamma_{11}^2 + \gamma_{22}^2 + \gamma_{33}^2\right) + \lambda\left(\gamma_{11} + \gamma_{22} + \gamma_{33}\right)^2 + \\ &+ (\mu + \alpha)\left(\gamma_{12}^2 + \gamma_{21}^2 + \gamma_{13}^2 + \gamma_{31}^2 + \gamma_{23}^2 + \gamma_{32}^2\right) + \\ &+2(\mu - \alpha)(\gamma_{12}\gamma_{21} + \gamma_{13}\gamma_{31} + \gamma_{23}\gamma_{32}) + 2\gamma\left(\chi_{11}^2 + \chi_{22}^2 + \chi_{33}^2\right) + \\ &+\beta\left(\chi_{11} + \chi_{22} + \chi_{33}\right)^2 + (\gamma + \varepsilon)\left(\chi_{12}^2 + \chi_{21}^2 + \chi_{13}^2 + \chi_{31}^2 + \chi_{23}^2 + \chi_{32}^2\right) + \\ &+2(\gamma - \varepsilon)(\chi_{12}\chi_{21} + \chi_{13}\chi_{31} + \chi_{23}\chi_{32})\Big\} - (3\lambda + 2\mu)\alpha_T T(\gamma_{11} + \gamma_{22} + \gamma_{33}) \end{aligned} \tag{1.7}$$

As it is accepted in the classical theory of elasticity, as well as in the micropolar theory of elasticity, the application of variation methods is effective during the determination of temperature stresses. General variation principle in micropolar theory of thermoelasticity is studied, the functional of which is the following :

$$
\begin{aligned}
I = \iint_S \int_{-h}^{h} \Bigg\langle W - \Bigg\{ & \sigma_{11}\left(\gamma_{11} - \frac{\partial u_1}{\partial x_1}\right) + \sigma_{22}\left(\gamma_{22} - \frac{\partial u_2}{\partial x_2}\right) + \sigma_{33}\left(\gamma_{33} - \frac{\partial u_3}{\partial x_3}\right) + \\
& + \sigma_{12}\left[\gamma_{12} - \left(\frac{\partial u_2}{\partial x_1} - \omega_3\right)\right] + \sigma_{21}\left[\gamma_{21} - \left(\frac{\partial u_1}{\partial x_2} + \omega_3\right)\right] + \\
& + \sigma_{13}\left[\gamma_{13} - \left(\frac{\partial u_3}{\partial x_1} + \omega_2\right)\right] + \sigma_{31}\left[\gamma_{31} - \left(\frac{\partial u_1}{\partial x_3} - \omega_2\right)\right] + \\
& + \sigma_{23}\left[\gamma_{23} - \left(\frac{\partial u_3}{\partial x_2} - \omega_1\right)\right] + \sigma_{32}\left[\gamma_{32} - \left(\frac{\partial u_2}{\partial x_3} + \omega_1\right)\right] + \\
& + \mu_{11}\left(\chi_{11} - \frac{\partial \omega_1}{\partial x_1}\right) + \mu_{22}\left(\chi_{22} - \frac{\partial \omega_2}{\partial x_2}\right) + \mu_{33}\left(\chi_{33} - \frac{\partial \omega_3}{\partial x_3}\right) + \\
& + \mu_{12}\left(\chi_{12} - \frac{\partial \omega_2}{\partial x_1}\right) + \mu_{21}\left(\chi_{21} - \frac{\partial \omega_1}{\partial x_2}\right) + \mu_{13}\left(\chi_{13} - \frac{\partial \omega_3}{\partial x_1}\right) + \\
& + \mu_{23}\left(\chi_{23} - \frac{\partial \omega_3}{\partial x_2}\right) + \mu_{31}\left(\chi_{31} - \frac{\partial \omega_1}{\partial x_3}\right) + \mu_{32}\left(\chi_{32} - \frac{\partial \omega_2}{\partial x_3}\right) \Bigg\} \Bigg\rangle dx_1 dx_2 dx_3 - \\
& - \iint_{s^+} \left[p_1^+ u_1 + p_2^+ u_2 + p_3^+ u_3 + m_1^+ \omega_1 + m_2^+ \omega_2 + m_3^+ \omega_3\right]_{x_3 = h} dx_1 dx_2 + \\
& + \iint_{s^-} \left[p_1^- u_1 + p_2^- u_2 + p_3^- u_3 + m_1^- \omega_1 + m_2^- \omega_2 + m_3^- \omega_3\right]_{x_3 = -h} dx_1 dx_2 + \\
& + \int_{-h}^{+h} dx_3 \int_{l_1'} \left(\sigma_{21}^0 u_1 + \sigma_{22}^0 u_2 + \sigma_{23}^0 u_3 + \mu_{21}^0 \omega_1 + \mu_{22}^0 \omega_2 + \mu_{23}^0 \omega_3\right) dx_1 + \\
& + \int_{-h}^{+h} dx_3 \int_{l_1''} \left[\sigma_{21}\left(u_1 - u_1^0\right) + \sigma_{22}\left(u_2 - u_2^0\right) + \sigma_{23}\left(u_3 - u_3^0\right) + \right. \\
& \left. + \mu_{21}\left(\omega_1 - \omega_1^0\right) + \mu_{22}\left(\omega_2 - \omega_2^0\right) + \mu_{23}\left(\omega_3 - \omega_3^0\right)\right] dx_1 + \\
& + \int_{-h}^{+h} dx_3 \int_{l_2'} \left(\sigma_{11}^0 u_1 + \sigma_{12}^0 u_2 + \sigma_{13}^0 u_3 + \mu_{11}^0 \omega_1 + \mu_{12}^0 \omega_2 + \mu_{13}^0 \omega_3\right) dx_2 + \\
& + \int_{-h}^{+h} dx_3 \int_{l_2''} \left[\sigma_{11}\left(u_1 - u_1^0\right) + \sigma_{12}\left(u_2 - u_2^0\right) + \sigma_{13}\left(u_3 - u_3^0\right) + \right. \\
& \left. + \mu_{11}\left(\omega_1 - \omega_1^0\right) + \mu_{12}\left(\omega_2 - \omega_2^0\right) + \mu_{13}\left(\omega_3 - \omega_3^0\right)\right] dx_2 \qquad (1.8)
\end{aligned}
$$

The functional (1.8) is called full functional of three-dimensional micropolar theory of thermoelasticity. On the basis of it variation equation $\delta I = 0$ can be obtained, accepting that virtual increments $\delta\gamma_{mn}, \delta\chi_{mn}, \delta u_n, \delta\omega_n, \delta\sigma_{mn}, \delta\mu_{mn}$ are mutually independent. Then all main equations (1.1) - (1.3) and natural boundary conditions of three dimensional problem of micropolar thermoelasticity will be obtained.

It is accepted that plate thickness is small compared with its other sizes. We?ll start from the following main concept: in static case general thermoelastic state of thin three-dimensional body consists of internal state, covering the plate, and of boundary layers, localizing near the plate edge Σ. The construction of the general

applied two-dimensional theory of thermoelasticity of micropolar elastic thin plates is closely connected with the construction of the internal problem.
Considering that the hypotheses method rather intensively and easily for engineering practice leads to final results, the model of thermoelasticity of micropolar isotropic thin plates will be constructed on the basis of hypotheses method. The hypotheses are formulated on the basis of the asymptotic analysis result of the stated three-dimensional boundary-value problem of micropolar theory of thermoelasticity in thin three-dimensional domain of the plate [6].

2 Initial hypotheses

On the basis of qualitative results [6] of asymptotic solution of the system of equations (1.1) - (1.4) with the above mentioned boundary conditions and asymptotic integration process of this boundary-value problem, following general hypotheses are stated for the construction of the model of micropolar thermoelasticity of isotropic thin plates with free fields of displacements and rotations [3] - [5]:
1)Assumption of linear distribution of components of vectors of displacement and free rotation by coordinate x_3 is accepted as kinematic hypothesis:

$$u_i = x_3\psi_i\left(x_1, x_2\right), u_3 = w\left(x_1, x_2\right) \qquad (i = 1, 2), \tag{2.1}$$

$$\omega_i = \Omega_i\left(x_1, x_2\right), \omega_3 = x_3\iota\left(x_1, x_2\right) \qquad (i = 1, 2), \tag{2.2}$$

where u_i, w are displacements of middle plane points along the x_i and x_3; ψ_i-full angels of rotation of the normal to the middle plane element around the axis x_i, Ω_i-free rotations of the three-dimensional plate points around the axis x_3. In papers [3] - [5] the kinematic hypothesis (2.1), (2.2) is called Timoshenko's generalized kinematic hypothesis of theory of micropolar plates and shells.
Following hypotheses are accepted as static ones:
2) In formulas for γ_{ii} of generalized Hook's law (1.2) force stress σ_{33} can be neglected in relation to force normal stresses, σ_{ii} and in formulas for $\chi_{i3}, (i = 1, 2)$ moment stresses μ_{3i} can be neglected in relation to moment stresses $\mu_{i3}, (i = 1, 2)$.
3) For determination of deformations, bending-torsions, force and moment stresses first we accept following relations for force stresses σ_{3i} and moment stress μ_{33}:

$$\sigma_{3i} = \sigma_{3i}^0\left(x_1, x_2\right), (i = 1, 2), \mu_{33} = \mu_{33}^0\left(x_1, x_2\right). \tag{2.3}$$

After determination of mentioned quantities values of σ_{3i} and μ_{33} will be determined as sum of (2.3) and result of integration of the first two and sixth equilibrium equations of (1.1), or which condition will be required that averaged along the plate thickness quantities are equal to zero.
4) Linear change along the plate thickness is accepted for temperature function T [7]:

$$T = \frac{x_3}{2h} T_0\left(x_1, x_2\right). \tag{2.4}$$

The accepted kinematic, static hypotheses and hypothesis on linear distribution of the temperature function let us reduce the problem of determination of spatial stress state of micropolar plate to two-dimensional problem.

3 Determination of components of deformation and bending-torsions tensors

On the basis of kinematic hypothesis (2.1), (2.2) following formulas will be obtained for components of deformation and bending-torsion tensors:

$$\begin{aligned}
&\gamma_{11} = x_3 K_{11}(x_1,x_2),\ \gamma_{12} = x_3 K_{12}(x_1,x_2),\ \gamma_{32} = \Gamma_{32}(x_1,x_2),\\
&\gamma_{22} = x_3 K_{22}(x_1,x_2),\ \gamma_{21} = x_3 K_{21}(x_1,x_2),\ \gamma_{23} = \Gamma_{23}(x_1,x_2),\\
&\gamma_{13} = \Gamma_{13}(x_1,x_2),\quad \gamma_{31} = \Gamma_{31}(x_1,x_2),\ \gamma_{33} = 0\\
&\chi_{11} = k_{11}(x_1,x_2),\quad \chi_{12} = k_{12}(x_1,x_2),\quad \chi_{31} = 0\\
&\chi_{22} = k_{22}(x_1,x_2),\quad \chi_{21} = k_{21}(x_1,x_2),\quad \chi_{32} = 0\\
&\chi_{33} = k_{33}(x_1,x_2),\quad \chi_{13} = x_3 l_{13}(x_1,x_2),\quad \chi_{23} = x_3 l_{23}(x_1,x_2)
\end{aligned} \tag{3.1}$$

where following notations are accepted:

$$\begin{aligned}
&K_{11} = \frac{\partial \psi_1}{\partial x_1},\ K_{22} = \frac{\partial \psi_2}{\partial x_2},\ K_{12} = \frac{\partial \psi_2}{\partial x_1} - \iota,\ K_{21} = \frac{\partial \psi_1}{\partial x_2} + \iota,\\
&\Gamma_{31} = \psi_1 - \Omega_2,\ \Gamma_{32} = \psi_2 + \Omega_1,\ \Gamma_{13} = \frac{\partial w}{\partial x_1} + \Omega_2,\ \Gamma_{23} = \frac{\partial w}{\partial x_2} - \Omega_1,\\
&k_{11} = \frac{\partial \Omega_1}{\partial x_1},\ k_{22} = \frac{\partial \Omega_2}{\partial x_2},\ k_{12} = \frac{\partial \Omega_2}{\partial x_1},\ k_{21} = \frac{\partial \Omega_1}{\partial x_2},\\
&k_{33} = \iota,\ l_{13} = \frac{\partial \iota}{\partial x_1},\ l_{23} = \frac{\partial \iota}{\partial x_2}.
\end{aligned} \tag{3.2}$$

4 Determination of components of force and moment stresses tensors

On the basis of physical relations (1.2), formulas for deformations, bending-torsions (3.1)-(3.2) and hypotheses 2)-4) following formulas will be obtained for force and moment stresses:

$$\begin{aligned}
&\sigma_{11} = x_3 \frac{E}{1-\nu^2}\left[K_{11} + \nu K_{22} - (1+\nu)\,\alpha_t \frac{T_0}{2h}\right],\\
&\sigma_{22} = x_3 \frac{E}{1-\nu^2}\left[\nu K_{11} + K_{22} - (1+\nu)\,\alpha_t \frac{T_0}{2h}\right],\\
&\sigma_{12} = x_3\left[(\mu+\alpha)K_{12} + (\mu-\alpha)K_{21}\right],\\
&\sigma_{21} = x_3\left[(\mu+\alpha)K_{21} + (\mu-\alpha)K_{12}\right],
\end{aligned} \tag{4.1}$$

$$\begin{aligned}
&\sigma_{13} = (\mu+\alpha)\Gamma_{13} + (\mu-\alpha)\Gamma_{31},\ \sigma_{23} = (\mu+\alpha)\Gamma_{23} + (\mu-\alpha)\Gamma_{32},\\
&\sigma^0_{31} = (\mu+\alpha)\Gamma_{31} + (\mu-\alpha)\Gamma_{13},\ \sigma^0_{32} = (\mu+\alpha)\Gamma_{32} + (\mu-\alpha)\Gamma_{23}.
\end{aligned} \tag{4.2}$$

$$\begin{aligned}
&\sigma_{31} = \sigma^0_{31}(x_1;x_2) + \left(\frac{h^2}{6} - \frac{x_3^2}{2}\right)\left(\frac{\partial \sigma^1_{11}}{\partial x_1} + \frac{\partial \sigma^1_{21}}{\partial x_2}\right)\\
&\sigma_{32} = \sigma^0_{32}(x_1;x_2) + \left(\frac{h^2}{6} - \frac{x_3^2}{2}\right)\left(\frac{\partial \sigma^1_{22}}{\partial x_2} + \frac{\partial \sigma^1_{12}}{\partial x_1}\right)
\end{aligned} \tag{4.3}$$

$$\sigma_{33} = -x_3\left(\frac{\partial\sigma_{13}}{\partial x_1} + \frac{\partial\sigma_{23}}{\partial x_2}\right) + \frac{p_3^+ - p_3^-}{2} = x_3\frac{\tilde{p_3}}{2h} + \sigma_{33}^0, \tag{4.4}$$

$$\begin{aligned}
&\mu_{11} = (\beta+2\gamma)k_{11} + \beta(k_{22}+k_{33}),\ \mu_{22} = (\beta+2\gamma)k_{22} + \beta(k_{11}+k_{33}),\\
&\mu_{33}^0 = (\beta+2\gamma)k_{33} + \beta(k_{11}+k_{22}),\\
&\mu_{12} = (\gamma+\varepsilon)k_{12} + (\gamma-\varepsilon)k_{21},\ \mu_{21} = (\gamma+\varepsilon)k_{21} + (\gamma-\varepsilon)k_{12},
\end{aligned} \tag{4.5}$$

$$\mu_{13} = x_3\frac{4\gamma\varepsilon}{\gamma+\varepsilon}l_{13},\ \mu_{23} = x_3\frac{4\gamma\varepsilon}{\gamma+\varepsilon}l_{23}. \tag{4.6}$$

$$\begin{aligned}
\mu_{31} &= -x_3\left(\frac{\partial\mu_{11}}{\partial x_1} + \frac{\partial\mu_{21}}{\partial x_2} + \sigma_{23} - \sigma_{32}\right) + \frac{m_1^+ - m_1^-}{2}\\
\mu_{32} &= -x_3\left(\frac{\partial\mu_{12}}{\partial x_1} + \frac{\partial\mu_{22}}{\partial x_2} + \sigma_{31} - \sigma_{13}\right) + \frac{m_2^+ - m_2^-}{2}.
\end{aligned} \tag{4.7}$$

$$\mu_{33} = \mu_{33}^0(x_1;x_2) + \left(\frac{h^2}{6} - \frac{x_3^2}{2}\right)\left(\frac{\partial\mu_{13}^1}{\partial x_1} + \frac{\partial\mu_{23}^1}{\partial x_2} + \sigma_{12}^1 - \sigma_{21}^1\right) \tag{4.8}$$

Here $\sigma_{11}^1, \sigma_{22}^1, \sigma_{12}^1, \sigma_{21}^1, \mu_{13}^1, \mu_{23}^1$ are coefficients of coordinate x_3 in relations (4.1) and (4.6).

5 Averaged forces, moments and hypermoments

In order to bring three-dimensional problem of micropolar thermoelasticity for thin plates to two-dimensional one, which is already done for deformations, bending-torsions, force and moment stresses, statically equivalent to them integral characteristics are introduced:

$$N_{13} = \int_{-h}^{h}\sigma_{13}dx_3,\ \ N_{23} = \int_{-h}^{h}\sigma_{23}dx_3,\ \ N_{31} = \int_{-h}^{h}\sigma_{31}dx_3,\ \ N_{32} = \int_{-h}^{h}\sigma_{32}dx_3 \tag{5.1}$$

$$\begin{aligned}
M_{11} &= \int_{-h}^{h}x_3\sigma_{11}dx_3,\quad M_{22} = \int_{-h}^{h}x_3\sigma_{22}dx_3,\\
M_{12} &= \int_{-h}^{h}x_3\sigma_{12}dx_3,\quad M_{21} = \int_{-h}^{h}x_3\sigma_{21}dx_3
\end{aligned} \tag{5.2}$$

$$\begin{aligned}
&L_{11} = \int_{-h}^{h}\mu_{11}dx_3,\quad L_{22} = \int_{-h}^{h}\mu_{22}dx_3,\quad L_{12} = \int_{-h}^{h}\mu_{12}dx_3,\\
&L_{21} = \int_{-h}^{h}\mu_{21}dx_3,\quad L_{33} = \int_{-h}^{h}\mu_{33}dx_3,
\end{aligned} \tag{5.3}$$

$$\Lambda_{13} = \int_{-h}^{h}x_3\mu_{13}dx_3,\quad \Lambda_{23} = \int_{-h}^{h}x_3\mu_{23}dx_3. \tag{5.4}$$

6 Main equations and boundary conditions of the applied theory of thermoelasticity of micropolar isotropic thin plates with free fields of displacements and rotations

Equilibrium equations for two-dimensional case can be obtained from the equations, defining force stresses $\sigma_{31}, \sigma_{32}, \sigma_{33}$ and moment stresses $\mu_{31}, \mu_{32}, \mu_{33}$, if we satisfy boundary conditions on plate planes $x_3 = \pm h$. It should be noted that the system of two-dimensional equations splits into two separate systems for the problems of bending and generalized plane stress state. The problem of bending is studied below.

Physical relations of thermoelasticity will be obtained on the basis of formulas (5.1) - (5.4) for averaged forces, moments and hypermoments using the corresponding formulas (4.1) - (4.6) or force and moment stresses.

Main system of equations of the problem of thermoelastic bending of micropolar thin plates with fee fields of displacements and rotations will be as follows:

Equilibrium equations:

$$\begin{gathered}
\frac{\partial N_{13}}{\partial x_1} + \frac{\partial N_{23}}{\partial x_2} = -\tilde{p_3}, \quad N_{3i} - \left(\frac{\partial M_{ii}}{\partial x_i} + \frac{\partial M_{ji}}{\partial x_j} \right) = h\tilde{p_i}, \\
\frac{\partial L_{ii}}{\partial x_i} + \frac{\partial L_{ji}}{\partial x_j} + (-1)^j (N_{j3} - N_{3j}) = -\tilde{m_i} \\
L_{33} - \left[\frac{\partial \Lambda_{13}}{\partial x_1} + \frac{\partial \Lambda_{23}}{\partial x_2} + (M_{12} - M_{21}) \right] = h\tilde{m_3}.
\end{gathered} \tag{6.1}$$

Physical relations of thermolasticity:

$$\begin{gathered}
N_{13} = 2h(\mu + \alpha)\Gamma_{13} + 2h(\mu - \alpha)\Gamma_{31}, \quad N_{23} = 2h(\mu + \alpha)\Gamma_{23} + 2h(\mu - \alpha)\Gamma_{32}, \\
N_{31} = 2h(\mu + \alpha)\Gamma_{31} + 2h(\mu - \alpha)\Gamma_{13}, \quad N_{32} = 2h(\mu + \alpha)\Gamma_{32} + 2h(\mu - \alpha)\Gamma_{23}, \\
M_{11} = \frac{2Eh^3}{3(1-\nu^2)} \left[K_{11} + \nu K_{22} - (1+\nu)\alpha_t \frac{T_0}{2h} \right], \\
M_{12} = \frac{2h^3}{3} \left[(\mu + \alpha)K_{12} + (\mu - \alpha)K_{21} \right], \\
M_{22} = \frac{2Eh^3}{3(1-\nu^2)} \left[K_{22} + \nu K_{11} - (1+\nu)\alpha_t \frac{T_0}{2h} \right], \\
M_{21} = \frac{2h^3}{3} \left[(\mu + \alpha)K_{21} + (\mu - \alpha)K_{12} \right], \\
L_{11} = 2h \left[(\beta + 2\gamma)k_{11} + \beta(k_{22} + k_{33}) \right], \; L_{22} = 2h \left[(\beta + 2\gamma)k_{22} + \beta(k_{11} + k_{33}) \right], \\
L_{12} = 2h \left[(\gamma + \varepsilon)k_{12} + (\gamma - \varepsilon)k_{21} \right], \; L_{21} = 2h \left[(\gamma + \varepsilon)k_{21} + (\gamma - \varepsilon)k_{12} \right], \\
L_{33} = 2h \left[(\beta + 2\gamma)k_{33} + \beta(k_{11} + k_{22}) \right], \\
\Lambda_{13} = \frac{2h^3}{3} \frac{4\gamma\varepsilon}{\gamma + \varepsilon} l_{13}, \quad \Lambda_{23} = \frac{2h^3}{3} \frac{4\gamma\varepsilon}{\gamma + \varepsilon} l_{23}.
\end{gathered} \tag{6.2}$$

Geometric relations ((3.2)):

$$K_{11}=\frac{\partial\psi_1}{\partial x_1},\ K_{22}=\frac{\partial\psi_2}{\partial x_2},\ K_{12}=\frac{\partial\psi_2}{\partial x_1}-\iota,\ K_{21}=\frac{\partial\psi_1}{\partial x_2}+\iota$$
$$\Gamma_{31}=\psi_1-\Omega_2,\ \Gamma_{32}=\psi_2+\Omega_1,\ \Gamma_{13}=\frac{\partial w}{\partial x_1}+\Omega_2,\ \Gamma_{23}=\frac{\partial w}{\partial x_2}-\Omega_1$$
$$k_{11}=\frac{\partial\Omega_1}{\partial x_1},\ k_{22}=\frac{\partial\Omega_2}{\partial x_2},\ k_{12}=\frac{\partial\Omega_2}{\partial x_1},\ k_{21}=\frac{\partial\Omega_1}{\partial x_2},$$
$$k_{33}=\iota,\ l_{13}=\frac{\partial\iota}{\partial x_1},\ l_{23}=\frac{\partial\iota}{\partial x_2}. \tag{6.3}$$

Following boundary conditions should be added to the system of equations (6.1) - (6.3) (on $x_1=const$) [3]:

$$M_{11}=M_{11}^*\ or\ K_{11}=K_{11}^*,\ M_{12}=M_{12}^*\ or\ K_{12}=K_{12}^*,\ N_{13}=N_{13}^*\ or\ w=w^*,$$
$$L_{11}=L_{11}^*\ or\ k_{11}=k_{11}^*,\ L_{12}=L_{12}^*\ or\ k_{12}=k_{12}^*,\ \Lambda_{13}=\Lambda_{13}^*\ or\ l_{13}=l_{13}^*, \tag{6.4}$$

Taking into consideration the formulas for stresses (4.1) - (4.8), formulas for forces, moments and hypermoments (5.1) - (5.4), formulas for deformations and bending-torsions (3.1) - (3.2), energy conservation law (1.4) for the applied theory of thermoelasticity of micropolar thin plates will be as follows:

$$\iint_S W_0 dx_1 dx_2 = A_0,$$

where density W_0 of the deformation potential energy is expressed by the following formula:

$$W_0=\frac{1}{2}(M_{11}K_{11}+M_{22}K_{22}+M_{12}K_{12}+M_{21}K_{21}+N_{13}\Gamma_{13}+N_{31}\Gamma_{31}+N_{23}\Gamma_{23}+$$
$$+N_{32}\Gamma_{32}+L_{11}k_{11}+L_{22}k_{22}+L_{33}k_{33}+L_{12}k_{12}+L_{21}k_{21}+\Lambda_{13}l_{13}+\Lambda_{23}l_{23})-$$
$$-\frac{\alpha_T}{2h}(M_1+M_2)T_0, \tag{6.5}$$

A_0 is the work of external forces, moments and hypermoments:

$$A_0=\frac{1}{2}\left\{\int_{l_1}(M_{21}^0\psi_1+M_{22}^0\psi_2+N_{23}^0w+L_{21}^0\Omega_1+L_{22}^0\Omega_2+\Lambda_{23}^0\iota)dx_1+\right.$$
$$+(M_{11}^0\psi_1+M_{12}^0\psi_2+N_{13}^0w+L_{11}^0\Omega_1+L_{12}^0\Omega_2+\Lambda_{13}^0\iota)dx_2+$$
$$+\iint_S\left[(p_1^+-p_1^-)h\psi_1+(p_2^+-p_2^-)h\psi_2+(p_3^++p_3^-)w+(m_1^++m_1^-)\Omega_1+\right.$$
$$\left.\left.+(m_2^++m_2^-)\Omega_2+(m_3^++m_3^-)h\iota\right]dx_1dx_2\right\}. \tag{6.6}$$

If physical relations of elasticity (6.2) are taken into account in relation (6.5), then following formulas will be obtained for density W_0 of the deformation potential

energy:

$$W_0 = \frac{1}{2}\left\langle \frac{2Eh^3}{3(1-\nu^2)}(K_{11}^2+K_{22}^2+2\nu K_{11}K_{22}) + \frac{2h^3}{3}\left[(\mu+\alpha)(K_{12}^2+K_{21}^2)+\right.\right.$$
$$+2(\mu-\alpha)K_{12}K_{31}] + 2h\left[(\mu+\alpha)(\Gamma_{13}^2+\Gamma_{31}^2+\Gamma_{23}^2+\Gamma_{32}^2)+\right.$$
$$+2(\mu-\alpha)(\Gamma_{13}\Gamma_{31}+\Gamma_{23}\Gamma_{32})] + 2h\left[(\beta+2\gamma)(k_{11}^2+k_{22}^2+k_{33}^2)^2+\right.$$
$$+2\beta(k_{11}k_{22}+k_{11}k_{33}+k_{22}k_{33})] + 2h\left[(\gamma+\varepsilon)(k_{12}^2+k_{21}^2)+2(\gamma-\varepsilon)k_{12}k_{21}\right]+$$
$$\left.\left.+\frac{2h^3}{3}\frac{4\gamma\varepsilon}{\gamma+\varepsilon}(l_{13}^2+l_{23}^2)\right\rangle - \frac{Eh^2}{3(1-\nu)}(K_{11}+K_{22})\alpha_T T_0. \tag{6.7}$$

Analoggicaly general variation functional of the applied theory of thermoelasticity of micropolar thin plates will be obtained from the variation functional (1.8) of the three-dimensional theory:

$$I_0 = \iint_S \left\langle W_0 - \left\{ M_{11}\left(K_{11}-\frac{\partial\psi_1}{\partial x_1}\right) + M_{22}\left(K_{22}-\frac{\partial\psi_2}{\partial x_2}\right) + \right.\right.$$
$$+N_{32}\left[\Gamma_{32}-(\psi_2+\Omega_1)\right] + N_{31}\left[\Gamma_{31}-(\psi_1+\Omega_2)\right] + M_{21}\left[K_{21}-\left(\frac{\partial\psi_1}{\partial x_2}+\iota\right)\right]+$$
$$+N_{13}\left[\Gamma_{13}-\left(\frac{\partial w}{\partial x_1}+\Omega_2\right)\right] + N_{23}\left[\Gamma_{23}-\left(\frac{\partial w}{\partial x_2}-\Omega_1\right)\right] + L_{11}\left(k_{11}-\frac{\partial\Omega_1}{\partial x_1}\right)+$$
$$+L_{22}\left(k_{22}-\frac{\partial\Omega_2}{\partial x_2}\right) + L_{33}(k_{33}-\iota) + L_{12}\left(k_{12}-\frac{\partial\Omega_2}{\partial x_1}\right) + L_{21}\left(k_{21}-\frac{\partial\Omega_1}{\partial x_2}\right)+$$
$$\left.\left.+\Lambda_{13}\left(l_{13}-\frac{\partial\iota}{\partial x_1}\right) + \Lambda_{23}\left(l_{23}-\frac{\partial\iota}{\partial x_1}\right) + M_{12}\left[K_{12}-\left(\frac{\partial\psi_2}{\partial x_1}-\iota\right)\right]\right\}\right\rangle ds-$$
$$-\iint_S \left[(p_1^+ h\psi_1 + p_2^+ h\psi_2 + p_3^+ w) + (m_1^+\Omega_1 + m_2^+\Omega_2 + m_3 h\iota)\right] ds+$$
$$+\iint_S \left[-p_1^- h\psi_1 - p_2^- h\psi_2 + p_3^- w + m_1^-\Omega_1 + m_2^-\Omega_2 + m_3^- h\iota)\right] ds+$$
$$+\int_{l_1'}(M_{21}^0\psi_1 + M_{22}^0\psi_2 + N_{23}^0 w + L_{21}^0\Omega_1 + L_{22}^0\Omega_2 + \Lambda_{23}^0\iota)dx_1+$$
$$+\int_{l_1''}\left[M_{21}(\psi_1-\psi_1^0) + M_{22}(\psi_2-\psi_2^0) + N_{23}(w-w^0) + L_{21}(\Omega_1-\Omega_1^0)+\right.$$
$$\left.+L_{22}(\Omega_2-\Omega_2^0) + \Lambda_{23}(\iota-\iota^0)\right] dx_1 + \int_{l_2'}(M_{11}^0\psi_1 + M_{12}^0\psi_2 + N_{13}^0 w+$$
$$+L_{11}^0\Omega_1 + L_{12}^0\Omega_2 + \Lambda_{13}^0\iota)dx_2 + \int_{l_2''}\left[M_{11}(\psi_1-\psi_1^0) + M_{12}(\psi_2-\psi_2^0)+\right.$$
$$\left.+N_{13}(w-w^0) + L_{11}(\Omega_1-\Omega_1^0) + L_{12}(\Omega_2-\Omega_2^0) + \Lambda_{13}(\iota-\iota^0)\right] dx_2 : \tag{6.8}$$

If we study variation equation $\delta I_0 = 0$, all main equations (6.1) - (6.3) of the applied theory of thermoelasticity of micropolar thin plates and boundary conditions will be obtained, when forces, moments and hypermoments are given or boundary conditions in displacements, rotations and hyperrotations or boundary conditions in mixed form.

7 Thermoelastic bending of micropolar rectangular plate

Problem is studied when the rectangular micropolar plate is hinged supported and is under the temperature field

$$T = x_3 \frac{T_0}{2h}, \quad where \;\; T_0 = const \tag{7.1}$$

Following boundary conditions take place in case of hinged support:

$$\begin{aligned} &w = 0, \psi_2 = 0, M_{11} = 0, L_{12} = 0, \Omega_1 = 0, \Lambda_{13} = 0, \;\; when \; x_1 = 0, x_1 = a \\ &w = 0, \psi_1 = 0, M_{22} = 0, L_{21} = 0, \Omega_2 = 0, \Lambda_{23} = 0, \;\; when \; x_1 = 0, x_1 = b \end{aligned} \tag{7.2}$$

System of equations for $w, \psi_1, \psi_2, \Omega_1, \Omega_2, \iota$ will be obtained if formulas (6.3) are substituted into (6.2), then into equilibrium equations (6.1).
If we take into consideration formulas for M_{11} and M_{12} from (6.2), it is easy to show, that temperature summands in these formulas give inhomogeneity in boundary conditions $M_{11} = 0$ when $x_1 = 0, x_1 = a$ and $M_{22} = 0$ when $x_2 = 0, x_2 = b$. In order to obtain homogeneous boundary conditions functions ψ_1 and ψ_2 must be replaced by the following formulas:

$$\begin{aligned} &\psi_1 = \tilde{\psi_1} + \frac{(1+\nu)\alpha_T T_0}{2\delta} \bar{x_1}, \quad \psi_2 = \tilde{\psi_2} + \frac{(1+\nu)\alpha_T T_0}{2\delta} \bar{x_2}, \\ &\bar{x_1} = \frac{x_1}{a}, \quad \bar{x_2} = \frac{x_2}{a}, \quad \bar{w} = \frac{w}{a}, \quad \bar{\iota} = \frac{\iota}{a}. \end{aligned} \tag{7.3}$$

As a result boundary conditions (7.2) will be homogeneous, and in this case method of separation of variables can be used for the solution of the problem (6.1) - (6.3) of rectangular plate. The solution of the mentioned system of equations will be introduced in double trigonometric Fourier series:

$$\begin{aligned} &\bar{w} = \sum_{m=1}^{\infty}\sum_{n=1}^{\infty} A_{mn} \sin m\pi\bar{x_1} \sin n\pi\bar{x_1}, \qquad \bar{\iota} = \sum_{m=1}^{\infty}\sum_{n=1}^{\infty} F_{mn} \cos m\pi\bar{x_1} \cos n\pi\bar{x_1}, \\ &\Omega_1 = \sum_{m=1}^{\infty}\sum_{n=1}^{\infty} B_{mn} \sin m\pi\bar{x_1} \cos n\pi\bar{x_1}, \quad \Omega_2 = \sum_{m=1}^{\infty}\sum_{n=1}^{\infty} C_{mn} \cos m\pi\bar{x_1} \sin n\pi\bar{x_1}, \\ &\tilde{\psi_1} = \sum_{m=1}^{\infty}\sum_{n=1}^{\infty} D_{mn} \cos m\pi\bar{x_1} \sin n\pi\bar{x_1}, \quad \tilde{\psi_2} = \sum_{m=1}^{\infty}\sum_{n=1}^{\infty} K_{mn} \sin m\pi\bar{x_1} \cos n\pi\bar{x_1}, \end{aligned} \tag{7.4}$$

which satisfy homogeneous boundary conditions (7.2). Functions $T_0 = const$, $T_0\bar{x_1}$ and $T_0\bar{x_2}$ should be also introduced in double trigonometric Fourier series:

$$\begin{aligned} &T_0 = \sum_{m=1}^{\infty}\sum_{n=1}^{\infty} T_{mn} \sin m\pi\bar{x_1} \sin n\pi\bar{x_1}, \quad T_0 x_1 = \sum_{m=1}^{\infty}\sum_{n=1}^{\infty} G_{mn} \cos m\pi\bar{x_1} \sin n\pi\bar{x_1}, \\ &T_0\bar{x_2} = \sum_{m=1}^{\infty}\sum_{n=1}^{\infty} M_{mn} \sin m\pi\bar{x_1} \cos n\pi\bar{x_1} \end{aligned} \tag{7.5}$$

where

$$T_{mn} = 4\int_0^1\int_0^1 T_0 \sin m\pi\bar{x}_1 \sin n\pi\bar{x}_1 d\bar{x}_1 d\bar{x}_2,$$
$$G_{mn} = 4\int_0^1\int_0^1 T_0 \cos m\pi\bar{x}_1 \sin n\pi\bar{x}_1 d\bar{x}_1 d\bar{x}_2,$$
$$M_{mn} = 4\int_0^1\int_0^1 T_0 \sin m\pi\bar{x}_1 \cos n\pi\bar{x}_1 d\bar{x}_1 d\bar{x}_2,$$

Further substituting (7.4) and (7.5) into the system of equations for coefficients $A_{mn}, B_{mn}, C_{mn}, D_{mn}, K_{mn}, F_{mn}$ system of inhomogeneous algebraic linear equations will be obtained. Solving this system and substituting the solution into (7.4) , the solution of the stated problem will be obtained. The result of the numerical calculations is introduced:

$$\delta = \frac{h}{a} = \frac{1}{40}, \nu = 0.33, \bar{\gamma} = \bar{\varepsilon} = 22{*}10^{-4}, \bar{\beta} = 11{*}10^{-2}, T_0 = 60^0 C, \alpha_T = 125{*}10^{-7}\ 1/g$$

Table 1: Rectangular micropolar and classical plate bending under the temperature influence, depending on $\frac{\alpha}{\mu}$.

$\frac{\alpha}{\mu}$	micropolar model $\bar{w}_{max} * 10^{-3}$	classical model $\bar{w}_{max} * 10^{-3}$	$\frac{w_{max}^{mik.}}{w_{max}^{cl.}}$
10^{-5}	3.266	3.277	0.99
10^{-4}	3.173	3.277	0.97
10^{-3}	2.494	3.277	0.76
10^{-2}	1.005	3.277	0.30
$4.2 * 10^{-2}$	0.569	3.277	0.17
10^{-1}	0.471	3.277	0.14

Numerical results, introduced in Table 1, state that the plate rigidity increases compared with the classical case, when the dimensionless quantity $\frac{\alpha}{\mu}$ increases.

8 Temperature bending of micropolar circular plate

Problem of temperature bending of micropolar circular plate is studied when the asymmetric stress state takes place and the temperature field is expressed by the formula (7.1).

It should be noted that the applied theory of thermoelasticity, introduced in the previous paragraphs, is related to the Cartesian coordinate system. Main equations of this theory can also be obtained in curvilinear orthogonal system of coordinates. Particularly, main equations of the applied theory of thermoelasticity of micropolar thin plates can be obtained in the polar system of coordinates. In axisymmetric case, when the bending deformation takes place, on the basis of the main system of equations of the applied theory of thermoelasticity of micropolar circular plates

and with the help of exception method the studied problem can be reduced to the solution of the following equation:

$$\tilde{\nabla}^2\tilde{\nabla}^2\tilde{\psi}_1 - k^2\tilde{\nabla}^2\tilde{\psi}_1 = -\frac{6\left(\frac{\alpha}{\mu}\right)^2(1-\nu)\alpha_T T_0}{\delta^3(\bar{\gamma}+\bar{\varepsilon})\left(1+\frac{\alpha}{\mu}\right)}\bar{r}, \tag{8.1}$$

where

$$\tilde{\psi}_1 = \psi_1 - \frac{\alpha_T T_0}{2\delta}\bar{r}, \quad \tilde{\nabla}^2\tilde{\psi}_1 = \frac{d^2\tilde{\psi}_1}{d\bar{r}^2} + \frac{1}{r}\frac{d\tilde{\psi}_1}{d\bar{r}} - \frac{1}{\bar{r}^2}\tilde{\psi}_1,$$

$$k^2 = \left(\bar{\gamma}+\bar{\varepsilon}+\frac{2\delta^2}{3(1-\nu)}\right)\frac{6\frac{\alpha}{\mu}(1-\nu)}{\delta^2(\bar{\gamma}+\bar{\varepsilon})\left(1+\frac{\alpha}{\mu}\right)}, \quad \bar{r} = \frac{r}{a},$$

a is the plate middle plane radii.
General solution of the inhomogeneous equation (8.1) can be obtained as follows:

$$\tilde{\psi}_1 = -\frac{C_1}{k^2}\bar{r} + C_2 I_1(k\bar{r}) + \frac{3\left(\frac{\alpha}{\mu}\right)^2(1-\nu)\alpha_T T_0}{4k^2\delta^3(\bar{\gamma}+\bar{\varepsilon})\left(1+\frac{\alpha}{\mu}\right)}\bar{r}^3 \tag{8.2}$$

where C_1 and C_2 are constants, $I_1(k\bar{r})$ is Bessel function.
Determining $\tilde{\psi}_1$, bending $\bar{w}$ and free rotation Ω_2 are determined by formulas:

$$\bar{w} = \frac{C_1}{2k^2}\bar{r}^2 + C_2 I_0(k\bar{r})\left[\frac{\delta^2 k}{3(1-\nu)} - \frac{1}{k}\right] - \frac{3\left(\frac{\alpha}{\mu}\right)^2(1-\nu)\alpha_T T_0}{16k^2\delta^3(\bar{\gamma}+\bar{\varepsilon})\left(1+\frac{\alpha}{\mu}\right)}\bar{r}^4 +$$

$$+\frac{\left(\frac{\alpha}{\mu}\right)^2\alpha_T T_0}{k^2\delta(\bar{\gamma}+\bar{\varepsilon})\left(1+\frac{\alpha}{\mu}\right)}\bar{r}^2 - \frac{\alpha_T T_0}{4\delta}\bar{r}^2 + C^*,$$

$$\Omega_2 = C_2 I_1(k\bar{r})\left[1 - \frac{\delta^2 k^2\left(1+\frac{\alpha}{\mu}\right)}{6\frac{\alpha}{\mu}(1-\nu)}\right] + \frac{3\left(\frac{\alpha}{\mu}\right)^2(1-\nu)\alpha_T T_0}{4k^2\delta^3(\bar{\gamma}+\bar{\varepsilon})\left(1+\frac{\alpha}{\mu}\right)}\bar{r}^3 +$$

$$+\left[-\frac{C_1}{k^2} - \frac{\frac{\alpha}{\mu}\alpha_T T_0}{k^2\delta(\bar{\gamma}+\bar{\varepsilon})} + \frac{\alpha_T T_0}{2\delta}\right]\bar{r}. \tag{8.3}$$

The case is studied, when the plate middle plane contour is hinged supported, i.e. following boundary conditions take place:

$$\bar{w} = 0, \ \frac{d\tilde{\psi}_1}{d\bar{r}} + \frac{\nu}{\bar{r}}\tilde{\psi}_1 = 0, \ \bar{L_{12}} = 0 \ \ when \ \ \bar{r} = 1. \tag{8.4}$$

Determining integral constants and substituting them into the corresponding formulas, the solution of the stated problem will be obtained, i.e. functions $\bar{w}(\bar{r}), \psi(\bar{r}), \Omega_2(\bar{r})$.
Results of numerical calculations are introduced below.

$$\delta = \frac{h}{a} = \frac{1}{40}, \nu = 0.33, \bar{\gamma} = \bar{\varepsilon} = 22 * 10^{-4}, T_0 = 60^0 C, \alpha_T = 125 * 10^{-7}\ 1/g$$

Table 2: Circular micropolar and classical plate bending under the temperature influence, depending on $\frac{\alpha}{\mu}$.

$\frac{\alpha}{\mu}$	micropolar model $\bar{w}_{max} * 10^{-3}$	classical model $\bar{w}_{max} * 10^{-3}$	$\frac{w_{max}^{mik.}}{w_{max}^{cl.}}$
$1.2 * 10^{-3}$	7.184	7.5	0.96
$1.4 * 10^{-3}$	6.451	7.5	0.86
$1.8 * 10^{-3}$	5.299	7.5	0.71
$2 * 10^{-3}$	4.825	7.5	0.64
$3 * 10^{-3}$	2.962	7.5	0.40
$4 * 10^{-3}$	1.521	7.5	0.20

As in case of rectangular plate, in case of circular plate it is stated that the plate rigidity increases compared with the classical case, when the dimensionless quantity $\frac{\alpha}{\mu}$ increases.

Conclusion

In the present paper applied theory and variation principle of thermoelasticity of bending deformation of micropolar thin plates are constructed. On the basis of the constructed applied theory of thermoelasticity of thin plates problems of thermoelastic bending of rectangular and circular plates are studied. Numerical results show that the plate rigidity increases in case of micropolar material.

Acknowledgements

The research is done by the financial support MoES SCS RA in the frame of scientific project No. SCS 15T-2C138.

References

[1] Nowacki W. Couple-Stresses in the Theory of Thermoelasticity// Irreversible Aspects of Continuum Mechanics and Transfer of Physical Characteristics in Moving Fluids. IUTAM Symposia. Vienna, 1966. P.260-278.

[2] Nowacki W. Theory of Asymmetric Elasticity. Pergamon Press. Oxford. New York. Toronto. Sydney. Paris. Frankfurt. 1986. P. 383.

[3] Sargsyan S. H. Mathematical model of micropolar elastic thin plates and their strength and stiffness characteristics//Journal of Applied Mechanics and Technical Physics. 2012.Vol.53. N 2.P.275-282.

[4] Sargsyan S. H.General theory of micropolar elastic thin shells// Journal of Physical Mezomechanics.2012.Vol.15. N 1-2.P.69-79.

[5] Sargsyan S. H. Mathematical Model of Micropolar Thermo-Elasticity of Thin Shells// Journal of Thermal Stresses.2013. Vol.36. N 11.P.1200-1216.

[6] Sargsyan S. H. Thermoelasticity of Thin Shells on the Basis of Asymmetrical Theory of Elasticity// Journal of Thermal Stresses. 2009. Vol 32. N8. P. 791-818.

[7] Bolie B., Weyner J. Theory of temperature stresses. M.: "Mir" 1964. 518p.

Aslanyan N.S., Shirak State University after M. Nalbandyan, Armenia
Sargsyan S.H., Shirak State University after M. Nalbandyan, Armenia

Hidden defects in covers of materials, faults in seismology and prevention of hazards

Vladimir A. Babeshko, Olga V. Evdokimova, Olga M. Babeshko, Aleksandr G. Fedorenko, Vladimir V. Lozovoi, Samir B. Uafa

babeshko49@mail.ru, babeshko49@mail.ru, afedorenko@mail.ru, niva_kgu@mail.ru, evdokimova.olga@mail.ru, uafa70@mail.ru

Abstract

The connection between the behavior of covered materials with defects such as cracks perpendicular to the boundaries of elastic bodies and lithospheric plates with faults in case of various external influences in layered bodies is explained. Such behavior of these mechanical structures is seen during different types of external influences. The block element method is applied, which allows to investigate arising boundary problems difficult to study with other approaches. The stress-strain state of block structures generated by the studied mechanical problems was investigated, and the conditions of stress concentration build-up in hazardous areas were found. It was established that there are parameters, the role of which is paramount in assessing the possibility of destruction of the structures under consideration. The conditions allowing to exclude the occurrence of damage because of defects and faults, or to reduce the level of destruction were formulated for a number of problems.

Keywords: packed block element, factorization, topology, integral and differential factorization methods, exterior forms, block structures, boundary problems, stress-strain state, deformable blocks, Kirchhoff plates, differential and integral equations

1 Introduction

The theory of blocked structures, designed in the South Research Center of RAS, has several various advantages discussed right below. It allows solvation of boundary value problems for the system of differential equations in particular derivatives in some systems in analytical form. The basis of this theory is differential method of factorization. This method has been overlooked by scientists involved in the development of factorizing approaches for a long time. The reason is that the method required involvement of modern mathematical methods. Being highly precise though still rather complex in application, the method was applied in various other areas. In the report there is an example of application of the method in the task of solidity

of bodies with plating. The possibility of an initial earthquake and the seismic rating in a restricted fault zone are being explored in this work with application of the method of block elements. Approximate integral equations are constructed for the cases of finite and semi-infinite faults, and the symbol structure of the kernel of integral equation is derived. The latter may be used not only for analyzing the singular features in boundary values, but also for studying wave processed in faults in dynamic tasks.

2 Stating The Aim

The starting data on initial earthquakes, research methods and the results are published in [1, 2, 3]. Let us consider the covering on the malformed base to represent Kirchoff's plate with three types of defects: infinite defect, which divides the plate into two semi-infinite plates; semi-infinite, when the defect is a semi-infinite fracture; and finite, when the defect is a finite fracture. Let us consider that, from a certain point, the edges of all three types of defects with parallel borders are remote from each other for 2θ and are on a linearly deformable base. Let us consider that the space between the edges of the defect is empty, and the butt ends of the plates are affected by outer forces directed according to the rule of external vectors. In the $x_1x_2x_3$ system of coordinates with the onset in the x_1x_2 plane, which is congruent with the median plane of the plate. the axis ox_3 directed up the normal to the plate, the axis ox_1 directed tangentially towards the border of the defect, the axis ox_2 – normally to the border. The area of the plate positioned to the left from the defect is marked λ and is described by the correlations $|x_1| \le \infty$, $x_2 \le -\theta$, and the one to the right – by the index r and coordinates $|x_1| \le \infty$, $\theta \le x_2$. Let us limit ourselves to the vertical influences on the plates only, considering that bending moments and shear forces different from zero can be assigned to the butt ends. Kirchoff's equation for the b fragments of the $b = \lambda, r$ covering which are situated in Ω_b areas with $\partial\Omega_b$ borders takes the following form with the determined vertical static influences with tension, t_{3b} up and g_{3b} down:

$$\mathbf{R}_b(\partial x_1, \partial x_2)u_{3b} + \varepsilon_{53b}(t_{3b} - g_{3b}) \equiv$$
$$\equiv \left(\frac{\partial^4}{\partial x_1^4} + 2\frac{\partial^2}{\partial x_1^2}\frac{\partial^2}{\partial x_2^2} + \frac{\partial^4}{\partial x_2^4}\right)u_{3b} + \varepsilon_{53b}(t_{3b} - g_{3b}) = 0 \quad (1)$$

$$\mathbf{R}_b(-i\alpha_1, -i\alpha_2)U_{3b} \equiv R_b(-i\alpha_1, -i\alpha_2)U_{3b} \equiv (\alpha_1^2 + \alpha_2^2)^2 U_{3b}$$

$$U_{3b} = \mathbf{F_2}u_{3b}, \quad G_{3b} = \mathbf{F_2}g_{3b}, \quad T_{3b} = \mathbf{F_2}t_{3b} \quad b = \lambda, r$$

$$M_b = -D_{b1}\left(\frac{\partial^2 u_{3b}}{\partial x_2^2} + \nu_b\frac{\partial^2 u_{3b}}{\partial x_1^2}\right), \quad D_{b1} = \frac{D_b}{2}, \quad D_{b2} = \frac{D_b}{3}$$

$$Q_b = -D_{b2}\left(\frac{\partial^3 u_{3b}}{\partial x_2^3} + (2 - \nu_b)\frac{\partial^3 u_{3b}}{\partial x_1^2 \partial x_2}\right) = f_{4b}(\partial\Omega_b)$$

$$u_{3b} = f_{1b}(\partial\Omega_b), \quad \frac{\partial u_{3b}}{\partial x_2} = f_{2b}(\partial\Omega_b)$$

$$D_b = \frac{E_b h_b^3}{12(1-\nu_b^2)}, \quad \varepsilon_{53b} = \frac{(1-\nu_b^2)12^4}{E_b h_b^3}, \quad \varepsilon_6^{-1} = \frac{(1-\nu)H}{\mu}$$

The connection between edge tensions and shifting on the surface of the elastic medium on which the plates are situated, takes the following form:

$$u_{3m}(x_1,x_2) = \varepsilon_6^{-1} \sum_{n=1}^{2} \iint\limits_{\Omega_n} k(x_1-\xi_1, x_2-\xi_2) g_{3n}(\xi_1,\xi_2) d\xi_1 d\xi_2,$$

$$x_1, x_2 \in \Omega_m, \quad m = \lambda, r, \theta,$$

$$\Omega_\lambda(|x_1| \le \infty;\ x_2 \le -\theta), \quad \Omega_r(|x_1| \le \infty;\ \theta \le x_2),$$

$$\Omega_\theta(|x_1| \le \infty;\ -\theta \le x_2 \le \theta), \quad n = \lambda, r$$

$$k(x_1,x_2) = \frac{1}{4\pi^2} \int\limits_{-\infty}^{\infty} \int K(\alpha_1,\alpha_2) e^{-i\langle\alpha,x\rangle} d\alpha_1 d\alpha_2$$

$$u_{3m}(x_1,x_2) = \frac{1}{\varepsilon_6 4\pi^2} \int\limits_{-\infty}^{\infty} \int K(\alpha_1,\alpha_2 G(\alpha_1,\alpha_2) e^{-i\langle\alpha,x\rangle} d\alpha_1 d\alpha_2$$

$K(\alpha_1,\alpha_2)$ is the analytical function of two complex variables α_k, particularly meromorphic, its various examples are presented in [4, 5], M_b and Q_b – bending moment and shear force in the $x_1 o x_2$ system of coordinates; h_b – thickness of the plates, H – dimensional parameter of substructure, for instance, the thickness of the layer. E_b – Young's moduli of the plates, ν_b – their Poisson ratios. The nomenclature is taken from [1], $\mathbf{F}_2 \equiv \mathbf{F}_2(\alpha_1,\alpha_2)$ and $\mathbf{F}_1 \equiv \mathbf{F}_1(\alpha_1)$, two- and one-dimensional Fourier-transform operators respectively.

3 The factorization method for block element

Above-mentioned academicians examine packed block elements in the blocked structure derived from a boundary-value problem for systems of linear differential equations in partial derivatives as topological objects. It is proved that they can be regarded as a manifold with brink edge in certain spaces representing the Cartesian product of topological spaces. This makes it possible to carry out the interference of packed block elements for block structure construction of varying degrees of complexity. The latter can be achieved by choosing the block elements with different properties and then can be obtained obtained the desired properties of the block structure. In the work [6] the notion of packed block elements was added. Packed block element – is locally represented accurate solution of a boundary-value problem in the chosen carrier. It derives from a regularized element of algebraic rings on ideal [7]. A regularization is being carried out by solving the pseudo-differential equations which being stated by external forms generated by boundary-value problem. With the aim of distancing from the "exterior algebra" which let to set up the external forms and which doesn't contribute to the transformations used in the regularization process in the block element theory which is called "external analysis" [8]. A block element can be called packed in case if the caused by regularization

pseudodifferential equations can be solved for it. Homeomorphisms in theory block elements are very effective and necessary as they allow by performing a constructional design in well-studied spaces from R^n to transfer them to a more complex structure.

Without an attempt to embrace a huge variety of boundary problems and geometric forms of packaged block elements carriers, let analyze the case of block elements obtained at the intersection of three-dimensional layer and an infinite prism which have a polygon in its intersection and which axis is perpendicular to the boundary layer. Let us approve that their conjunction can be built by two diverse neighboring packed blocks which have a common bound and in such a manner you can obtain a new packed block element which is ready to conjugate with adjacent element. After that this algorithm can be relatively easy applied to more difficult boundary problems and block elements. Let us denote one of the block elements b, its carrier – Ω_b and the second – d with carrier Ω_d. Flat contact borders of two block elements are signed as $\partial\Omega_{bd}$ for the side belonging to the block element b, $\partial\Omega_{db}$ – belonging to the element d and we consider that borders coincide on contact. Let us look firstly at a boundary problem of one linear partial differential equation in order $2r$ with boundary conditions of associated solutions, which include equality not only on the borders of solutions but also combinations of their derivate, on standards as well as on a tangent border, with the order of leading derivate r. Obviously, the borders are perpendicular to the stratum boundaries. Let us bring here Cartesian coordinate system $ox^1x^2x^3$, pointing the axis ox^3 perpendicular to the stratum boundary, axis ox^1 – perpendicular to the boundaries $\partial\Omega_{bd}$, $\partial\Omega_{db}$, and apply the right triple rule to the last axis. Let us denote as local solutions for the already discussed boundary problem for every block element in accordance. Added Cartesian coordinate system inducts in Euclidean space topology [9, 10, 11, 12]. Let us call open multitudes of block elements carriers opened spheres, which consist of inner points, and also sphere segments divided from the opened sphere with the border, which belongs to the block element. Every union of such opened spheres stays opened. Let us denote $P_b\left(x_b^1, x_b^2, x_b^3\right)$ and $P_d\left(x_d^1, x_d^2, x_d^3\right)$ as topological fields points of $\Omega_b\left(x_b^1, x_b^2, x_b^3\right)$ and $\Omega_d\left(x_d^1, x_d^2, x_d^3\right)$ carriers.

Thus, it is proved, packed block elements under coupling produce a packed block element with carrier, which unified initial ones. If initial block elements were single card manifolds, then a new block element is a manifold with double card atlas. This result increases opportunities of using of block elements for constructing of complex block constructions for different use.

In the another area of border of $\partial\Omega_{bdp}$ newly formed packed block elements $\Omega_{bd} = \Omega_b \cup \Omega_d$ there can be contact with another packed block element Ω_p. As above, borders have to be considered $\partial\Omega_{dbp}$ and $\partial\Omega_{pdb}$, further statements are analogous to given above ones. For the record, border conditions on the new border can differentiate from reviewed ones early it means, a boundary problem is set with mixed border conditions. This circumstance does not change stated constructions, as the problem of construction of packed block elements with mixed border conditions refers to the solution of pseudodifferential equations, which are supposed completed.

In the case of vectorial border problems, set in areas Ω_b and Ω_d, which are described by the system of differential equations in partial derivatives, solutions of which have

several components. First of all, each component of concerned border problems in the form of pack block element is formed by differential and integrated factorization methods with the using of function matrix factorization (external analysis [8]). Border conditions will be complicated by including a combination of different elements and variables. At that time, it is easy to understand, the topological characteristics of all components and variables remain and homeomorphisms of topological space carriers are under way. In the case, if packed block elements have carries with complicated shapes, multi-card atlas, then for the formation of homeomorphisms in the including topologies with the substitutions of variables areas can be demanded.

Thus, packed block elements allow forming block constructions, which in turn become packed block elements, which presenting the solution of border problem in the area of its carriers.

Considering the plates and base to be a block structure consisting of three deformable blocks, the block element method can be used to study it. This method, as described in [8], includes, as a first step, the immersion in the topological structure by means of exterior algebra of boundary value. The authors call the multistage algorithm of further research of the functional equation that have nothing to do with the means of exterior algebra peer evaluation in the block element theory [8]. It includes fluxional factorization of matrix functions with elements of several composite variables, the realization of automorphism consisting either of calculation of residue forms of Leray, or incomplete functional equations of Wiener-Hopf, building up of pseudodifferential equations, extraction from them integral equations, dictating by concrete boundary conditions of boundary value problem, solving integral equations and integral expression of the boundary value problem in every block in the form of the "packed" block element. Finally, "gluing together" solutions of every block, consisting of building of factor – the topology of some topological spaces, which are Cartesian products of topological spaces of carriers and solutions. Using the descriptive approach, the functional equation of the boundary value problem (1) has the following form

$$R_b(-i\alpha_1,-i\alpha_2)U_{3b} \equiv (\alpha_1^2+\alpha_2^2)^2 U_{3b} = -\int\limits_{\partial\Omega_b} \omega_b - \varepsilon_{53b} S_{3b}(\alpha_1,\alpha_2) \tag{2}$$

$$S_{3b}(\alpha_1,\alpha_2) = \mathbf{F}_2(\alpha_1,\alpha_2)(t_{3b}-g_{3b}), \quad b=\lambda,r$$

Here – participating in introduction exterior forms [1, 2, 3], which have, taking into account a choice of the coordinate system, the following view

$$\omega_b = e^{i\langle\alpha,x\rangle}\left\{-\left[\frac{\partial^3 u_{3b}}{\partial x_2^3} - i\alpha_2\frac{\partial^2 u_{3b}}{\partial x_2^2} - \alpha_2^2\frac{\partial u_{3b}}{\partial x_2} + i\alpha_2^3 u_{3b} + 2\frac{\partial^3 u_{3b}}{\partial x_1^2\partial x_2} - 2i\alpha_2\frac{\partial^2 u_{3b}}{\partial x_1^2}\right]dx_1 + \right.$$
$$\left. + \left[\frac{\partial^3 u_{3b}}{\partial x_1^3} - i\alpha_1\frac{\partial^2 u_{3b}}{\partial x_1^2} - \alpha_1^2\frac{\partial u_{3b}}{\partial x_1} + i\alpha_1^3 u_{3b}\right]dx_2\right\}, \quad b=\lambda,r$$

and in a special case of straight-line boundary there can be introduced by the fol-

lowing formulae

$$\omega_\lambda = e^{i\langle\alpha,x\rangle}\Bigg\{-\Bigg[i\alpha_2 M_\lambda D_\lambda^{-1} - Q_\lambda D_\lambda^{-1} - (\alpha_2^2+\nu_\lambda\alpha_1^2)\frac{\partial u_{3\lambda}}{\partial x_2}+ \\ + i\alpha_2\left[\alpha_2^2+(2-\nu_\lambda)\alpha_1^2\right]u_{3\lambda}\Bigg]\Bigg\}dx_1$$

$$\omega_r = -e^{i\langle\alpha,x\rangle}\Bigg\{-\Bigg[i\alpha_2 M_r D_r^{-1} - Q_r D_r^{-1} - (\alpha_2^2+\nu_r\alpha_1^2)\frac{\partial u_{3r}}{\partial x_2}+ \\ + i\alpha_2\left[\alpha_2^2+(2-\nu_r)\alpha_1^2\right]u_{3r}\Bigg]\Bigg\}dx_1 \quad (3)$$

In the formulas (2), (3) at the time of integration the boundary $\partial\Omega_b$ is represented by two butt-ends of right and left Kirchhoff plates, if defect is infinite and divides plates in half. As the area occupied with covering is treated as topological manifold with boundary, so local coordinates are set on the boundary, the orientation of which is coordinated with the orientation of the interior of manifold. If defect is semi-infinite or finite, the crack edges will be boundaries with the corresponding orientation. For implementation of the automorphism, calculated the residue forms of Leray [1, 2, 3], according to the parameter α_2, also in twofold poles, pseudodifferential equations of boundary value problem, taking into consideration agreed notations, we can represent in the following form

$$\mathbf{F}_1^{-1}(\xi_1^\lambda)\Bigg\langle -\int\limits_{\partial\Omega_\lambda}\Bigg\{i\alpha_{2-}D_{\lambda1}^{-1}M_\lambda - D_{\lambda2}^{-1}Q_\lambda - (\alpha_{2-}^2+\nu_\lambda\alpha_1^2)\frac{\partial u_{3\lambda}}{\partial x_2}+ \\ + i\alpha_{2-}\left[\alpha_{2-}^2+(2-\nu_\lambda)\alpha_1^2\right]u_{3\lambda}\Bigg\}e^{i\alpha_1x_1}dx_1 + \varepsilon_{53\lambda}S_{3\lambda}(\alpha_1,\alpha_{2-})\Bigg\rangle = 0$$

$$\alpha_{2-} = -i\sqrt{\alpha_1^2}, \quad \xi_1^\lambda \in \partial\Omega_\lambda$$

$$\mathbf{F}_1^{-1}(\xi_1^\lambda)\Bigg\langle -\int\limits_{\partial\Omega_\lambda}\left\{iD_{\lambda1}^{-1}M_\lambda - 2\alpha_{2-}\frac{\partial u_{3\lambda}}{\partial x_2} + i\left[\,3\alpha_{2-}^2+(2-\nu_\lambda)\alpha_1^2\,\right]u_{3\lambda}\right\}e^{i\alpha_1x_1}dx_1 + \\ + \varepsilon_{53\lambda}S'_{3\lambda}(\alpha_1,\alpha_{2-})\Bigg\rangle = 0$$

$$\xi_1^\lambda \in \partial\Omega_\lambda, \quad \partial\Omega_\lambda = \{-\infty \le x_1 \le \infty,\ x_2 = -\theta\}$$

The derivative is calculated according to the parameter α_2.
Using further on this method, we come to the system of functional equations of this sort

$$\left[\varepsilon_{53r}(\alpha_1^2+\alpha_2^2)^{-2} + \varepsilon_6^{-1}K_1(\alpha_1,\alpha_2)\right]G^+(\alpha_1,\alpha_2) = \\ = -\left[\varepsilon_{53\lambda}(\alpha_1^2+\alpha_2^2)^{-2} + \varepsilon_6^{-1}K_1(\alpha_1,\alpha_2)\right]G^-(\alpha_1,\alpha_2) + U_{3\theta}(\alpha_1,\alpha_2)+ \\ + (\alpha_1^2+\alpha_2^2)^{-2}[A_\lambda k_{1\lambda0} + B_\lambda k_{2\lambda0} + A_r k_{1r0} + B_r k_{2r0}+ \\ + \varepsilon_{53\lambda}T^+(\alpha_1,\alpha_2) + \varepsilon_{53r}T^-(\alpha_1,\alpha_2)], \quad \theta > 0$$

$$U_{3\theta}(\alpha_1,\alpha_2)=\int\limits_{-\infty}^{\infty}\int\limits_{-\theta}^{\theta}u_3(x_1,x_2)e^{i\langle\alpha,x\rangle}dx_1dx_2$$

$$\begin{aligned}&\left[\varepsilon_{53r}(\alpha_1^2+\alpha_2^2)^{-2}+\varepsilon_6^{-1}K_1(\alpha_1,\alpha_2)\right]G^+(\alpha_1,\alpha_2)=\\&=-\left[\varepsilon_{53\lambda}(\alpha_1^2+\alpha_2^2)^{-2}+\varepsilon_6^{-1}K_1(\alpha_1,\alpha_2)\right]G^-(\alpha_1,\alpha_2)+\\&+(\alpha_1^2+\alpha_2^2)^{-2}[A_\lambda k_{1\lambda0}+B_\lambda k_{2\lambda0}+A_r k_{1r0}+B_r k_{2r0}+\\&\qquad+\varepsilon_{53\lambda}T^+(\alpha_1,\alpha_2)+\varepsilon_{53r}T^-(\alpha_1,\alpha_2)],\quad\theta=0\end{aligned}$$

Here A_λ, B_λ, A_r, B_r – are the expressions of the composite species, for the sake of brevity, are omitted. It should be noticed, that the represented functional equations have as unknown variables not only functions $G^+(\alpha_1,\alpha_2)$, $G^-(\alpha_1,\alpha_2)$, but also the functionals $G^+(\alpha_1,\alpha_{2+})$, $G^-(\alpha_1,\alpha_{2-})$, $G^+(\alpha_1,\alpha_{2+})$, $G^{-\prime}(\alpha_1,\alpha_{2-})$, which enter linear $k_{1\lambda0}$, $k_{2\lambda0}$, k_{1r0}, k_{2r0} and which are in need of determination. We have obtained two different Wiener-Hopf's functional equations. The first one is the generalized Wiener-Hopf's functional equation, because of the presence of the function $U_{3\theta}(\alpha_1,\alpha_2)$. It can be solved as stated in [5], by the conversion of a system of two integral equations of the second kind with quite continuous functions in a certain space with weight, which has the form

$$X^+-\left\{-\frac{M_1^+}{M_2^-}Y^-e^{-i2\alpha_2\theta}\right\}^+=\left\{\frac{1}{M_2^-}\Phi e^{-i\alpha_2\theta}\right\}^+$$

$$Y^-+\left\{\frac{M_2^-}{M_1^+}X^+e^{i2\alpha_2\theta}\right\}^-=\left\{\frac{1}{M_1^+}\Phi e^{i\alpha_2\theta}\right\}^-$$

$$M_1=M_1^+M_1^-,\quad M_2=M_2^+M_2^-,$$

$$M_2^+G^+=X^+,\quad M_1^-G^-=Y^-$$

$$M_1=\left[\varepsilon_{53\lambda}(\alpha_1^2+\alpha_2^2)^{-2}+\varepsilon_6^{-1}K(\alpha_1,\alpha_2)\right]$$

$$M_2=\left[\varepsilon_{53r}(\alpha_1^2+\alpha_2^2)^{-2}+\varepsilon_6^{-1}K(\alpha_1,\alpha_2)\right]$$

Here the designations of the work [5] are accepted.
Having solved boundary problems and defined functions $G^+(\alpha_1,\alpha_2)$, $G^-(\alpha_1,\alpha_2)$ it is also required to find the values of the functionals $G^+(\alpha_1,\alpha_{2+})$ and $G^-(\alpha_1,\alpha_{2-})$, and also the functionals which are differentiated according to the second parameter of the form $G_+^{'}(\alpha_1,\alpha_{2+})$, $G_-^{'}(\alpha_1,\alpha_{2-})$. To find them, we use the fact that, the solutions that are constructed in this way have the following structure.

$$\begin{aligned}G_+(\alpha_1,\alpha_2)&=C_{1+}(\alpha_1,\alpha_2)G_+(\alpha_1,\alpha_{2+})+C_{2+}(\alpha_1,\alpha_2)G_-(\alpha_1,\alpha_{2-})+\\&+C_{3+}(\alpha_1,\alpha_2)G_+^{'}(\alpha_1,\alpha_{2+})+C_{4+}(\alpha_1,\alpha_2)G_-^{'}(\alpha_1,\alpha_{2-})+C_{5+}(\alpha_1,\alpha_2)\end{aligned}$$

$$\begin{aligned}G_-(\alpha_1,\alpha_2)&=C_{1-}(\alpha_1,\alpha_2)G_+(\alpha_1,\alpha_{2+})+C_{2-}(\alpha_1,\alpha_2)G_-(\alpha_1,\alpha_{2-})+\\&+C_{1-}(\alpha_1,\alpha_2)G_+^{'}(\alpha_1,\alpha_{2+})+C_{2-}(\alpha_1,\alpha_2)G_-^{'}(\alpha_1,\alpha_{2-})+C_{3-}(\alpha_1,\alpha_2)\end{aligned}$$

We differentiate the first and the second equations by means of.
Here functions $C_{n+}(\alpha_1, \alpha_2)$, $C_{n-}(\alpha_1, \alpha_2)$, $n = 1, 2, 3$ are known, they can be easy found from the given above expressions, and $G_+(\alpha_1, \alpha_{2-})$, $G_-(\alpha_1, \alpha_{2+})$, $G'_+(\alpha_1, \alpha_{2+})$, $G'_-(\alpha_1, \alpha_{2-})$, is required to be determined. For their determination, we put $\alpha_2 = \alpha_{2+}$ in the first equation and in the differentiated one, but $\alpha_2 = \alpha_{2-}$ in the second one and the differentiated equation. So we obtain an algebraic system for the determination of all the above unknowns, we find the required functions by solving it. The introduction of the found solutions into the relations with external forms, depending on the stated boundary problem, makes it possible to determine completely the stress-strain state of the covering with or without any defects which are under review.
The second functional equation is the Wiener-Hopf's equation. The methods of constructing its exact or approximate solutions can be found in [4, 5]. It is easy enough to prove that the solution of the first functional equation for leads to the following properties of contact stresses between the plates and a substrate at the edges

$$g_{3\lambda}(x_1, x_2) = \sigma_{1\lambda}(x_1, x_2)(-x_2 - \theta)^{-1/2}, \quad x_2 < -\theta$$

$$g_{3r}(x_1, x_2) = \sigma_{1r}(x_1, x_2)(x_2 - \theta)^{-1/2}, \quad x_2 > \theta$$

Here $\sigma_{1b}(x_1, x_2)$, $b = \lambda, r$ are the continuous on the both coordinates functions for sufficiently smooth t_{3b}, $b = \lambda, r$ [4, 5]. The conversion of the second equation $x_2 \to 0$ leads to the following properties of the solutions

$$g_{3\lambda}(x_1, x_2) \to \sigma_{2\lambda}(x_1, x_2)x_2^{-1}$$

$$g_{3r}(x_1, x_2) \to \sigma_{2r}(x_1, x_2)x_2^{-1}$$

Functions $\sigma_{nb}(x_1, x_2)$, $b = \lambda, r$; $n = 2, 3$ are continuous according to the both parameters.

4 Semi-limited and limited faults or defects

While further studying the main research result of the study has established: infinite and semi-infinite defects always have singular stress concentrations at the edges of the plates while approaching the defects banks which bearing the danger of destroying the coated structure. The degree of structure destruction decreases as the size reduces of the defect of the finite length. The destruction degree is determined by the combinations of some parameters. The latter is established by investigating the coefficients in the case of the characteristic features. The following approximate formulas for the solving the boundary value problem are taken place, which are represented structurally without specifying all the parameters in connection with the complexity, which allows one to estimate the possibility of solving integral equations

$$K_0(\alpha_1) = -D\left(1 + \frac{B_\lambda L_-(\alpha_{2\lambda-}) + B_r L_+(\alpha_{2r+})}{\left[(B_r L_+(\alpha_{2r+}) + B_\lambda L_-(\alpha_{2\lambda-})) - \varepsilon_6^{-1} k_\infty(\alpha_1)\right]}\right)$$

$$D = -A_\lambda Q_\lambda(\alpha_1, -\theta) + A_r Q_r(\alpha_1, \theta), \quad \theta \geq 0$$

$$G_-(\alpha_1, \alpha_2) = L_-(\alpha_2) \frac{1}{\varepsilon_6^{-1} k_\infty(\alpha_1)} K_0(\alpha_1, \alpha_2)$$

$$G_+(\alpha_1, \alpha_2) = L_+(\alpha_2) \frac{1}{\varepsilon_6^{-1} k_\infty(\alpha_1)} K_0(\alpha_1, \alpha_2)$$

$$A_\lambda(\alpha_1, \alpha_2) = -\frac{e^{-i\alpha_2\theta}}{\alpha_{2\lambda-}}, \quad B_\lambda(\alpha_1, \alpha_2) = \frac{e^{-i(\alpha_2 - \alpha_{2\lambda-})\theta}}{\alpha_{2\lambda-}}$$

$$A_r(\alpha_1, \alpha_2) = -\frac{e^{i\alpha_2\theta}}{\alpha_{2r+}}, \quad B_r(\alpha_1, \alpha_2) = \frac{e^{i(\alpha_2 - \alpha_{2r+})\theta}}{\alpha_{2r+}}$$

In the case of the faults limited by the length, the integral equation for the determination of the behavior of the shearing forces approximately has the form in the case of the plates with different properties

$$\int_{-\infty}^{\infty} k(y - \xi) s(\xi) d\xi = \sigma_2(y), \quad -\infty \leq y \leq \infty$$

$$\frac{1}{\varepsilon_6^{-1} k_\infty(\alpha_1)} K_0(\alpha_1) = K(\alpha_1), \quad k(x_1) = \mathbf{F}_1^{-1}(x_1) K(\alpha_1)$$

$$D(\alpha_1) = -A_\lambda Q_\lambda(\alpha_1, 0) + A_r Q_r(\alpha_1, 0), \quad s(x_1) = \mathbf{F}_1^{-1}(x_1) D(\alpha_1)$$

In the case of the equality of the properties of the left and the right half-plates, that is

$$k_\infty(\alpha_1) = \lim |\alpha_2|^{-1} K(\alpha_1, \alpha_2), \quad |\alpha_2| \to \infty$$

Then

$$D = \frac{1}{\alpha_{2\lambda-}(\alpha_1)} \left[Q_\lambda(\alpha_1, 0) + Q_r(\alpha_1,) \right]$$

$$s_0(x_1) = \mathbf{F}_1^{-1}(x_1) \left[Q_\lambda(\alpha_1, 0) + Q_r(\alpha_1,) \right] \quad c_1 \leq x_1 \leq c_2$$

$$\int_{c_1}^{c_2} k_1(y - \xi) s_0(\xi) d\xi = \sigma_2(y), \quad c_1 \leq y \leq c_2, \quad k_1(x_1) = \mathbf{F}_1^{-1}(x_1) \frac{K(\alpha_1)}{\alpha_{2\lambda-}(\alpha_1)}$$

In that case, if $c_2 = \infty$ then an integral equation for a semi-infinite fault is obtained.

$$\int_{c_1}^{\infty} k_1(y - \xi) s_0(\xi) d\xi = \sigma_2(y), \quad c_1 \leq y \leq \infty$$

By means of these integral equations it is possible to determine the degree of the impact on the bank of the fault in order to reduce or increase the coefficient of the singular term in the contact stresses.

5 CONCLUSION

In such a manner, it's shown that block structures of elastic materials are under-explored elastic objects which have incalculable properties. Among them there are singular particularities in contact voltage for approached lithosphere plates. The integral equation is built which describes behavior of the function being the index of singular particularity. This equation allows getting in boundary problem parameter points which reduce or increase the rate of the index under particularity.

ACKNOWLEDGMENTS

Separate fragments of the work were carried out as the part of the realization of the State project for the projects of 2017 (9.8753.2017/BC), (0256-2014-0006), the RAS Presidium program 1-33P, projects from (0256-2015-0088) to (0256-2015 -0093), and with the support of RFBR grants (15-01-01379), (15-08-01377), (16-41-230214), (16-41-230218), (16-48-230216), (17-08-00323).

References

[1] Babeshko V.A., Evdokimova O.V., Babeshko O.M. The problem of physical and mechanical precursors of earthquake: place, time, intensity. *Doklady Physics*, 2016, vol. 61, no. 2, pp. 92-97. doi: 10.1134/S1028335816020099

[2] Babeshko V.A., Evdokimova O.V., Babeshko O.M. Properties of "started" earthquake. *Doklady Physics*, 2016, vol. 61, no. 4, pp. 188-191. doi: 10.1134/S1028335816040054

[3] Babeshko V.A., Evdokimova O.V., Babeshko O.M. The theory of the starting earthquake. *Ekologicheskiy vestnik nauchnykh tsentrov Chernomorskogo ekonomicheskogo sotrudnichestva* [Ecological Bulletin of research centers of the Black Sea Economic Cooperation], 2016, no. 1, iss. 2, pp. 37-80.

[4] Vorovich I.I, Aleksandrov V.M., Babeshko V.A. *Nonclassical mixed problems in elasticity.* Moscow, Nauka Publ., 1974. 456 c. [In Russian]

[5] Vorovich I,I, Babeshko V.A. *Dynamic mixed problems from the elasticity for nonclassical domains.* Moscow, Nauka Publ., 1979, 320 p. [In Russian]

[6] Babeshko V.A., Evdokimova O.V., Babeshko O.M. Stages of transformation of block elements. *Doklady Physics*, 2016, vol. 61, no. 5, pp. 227-231. doi: 10.1134/S1028335816050049

[7] Naimark M.A. *Normed rings.* Moscow, Nauka Publ., 1956. 488 p. [In Russian]

[8] Babeshko V.A., Evdokimova O.V., Babeshko O.M. The external analysis in the problems of reserved defects and earthquake prognosis. *Ekologicheskiy vestnik*

nauchnykh tsentrov Chernomorskogo ekonomicheskogo sotrudnichestva [Ecological Bulletin of research centers of the Black Sea Economic Cooperation], 2016, no. 2, P. 19-28. [In Russian]

[9] Zorich V.A. *Mathematical analysis. The second part.* Moscow, Nauka Publ., 2002, 788 p. [In Russian]

[10] Kelly D. *General topology.* Moscow, Nauka Publ., 1968, 384 p. [In Russian]

[11] Mishchenko A.S., Fomenko A.T. *The short course of differential geometry and topology.* Moscow, Nauka Publ., 2004, 302 p. [In Russian]

[12] Golovanov N.N., Ilyutko D.P., Nosovskii G.V., Fomenko A.T. *Computational geometry.* Moscow, Academy Press, 2006, 512 p. [In Russian]

Vladimir A. Babeshko, Kuban State University, Krasnodar, 350040, Stavropolskaya st. 149, Russia & Southern Scientific Center RAS, Rostov-on-Don, 344006, Chekhov st, 41, Russia
Olga V. Evdokimova, Southern Scientific Center RAS, Rostov-on-Don, 344006, Chekhov st, 41, Russia
Olga M. Babeshko, Kuban State University, Krasnodar, 350040, Stavropolskaya st. 149, Russia
Aleksandr G. Fedorenko, Southern Scientific Center RAS, Rostov-on-Don, 344006, Chekhov st, 41, Russia
Vladimir V. Lozovoi, Southern Scientific Center RAS, Rostov-on-Don, 344006, Chekhov st, 41, Russia
Samir B. Uafa, Southern Scientific Center RAS, Rostov-on-Don, 344006, Chekhov st, 41, Russia

Numerical modelling of surface – reinforced rod tube structures

Anguel I. Baltov, Ana Ya. Yanakieva

aniyanakieva@imbm.bas.bg

Abstract

The study treats rod structures consisting of tubes whose external surfaces are reinforced by means of suitable reinforcing material (reinforced composites, special nanomaterials etc.). The technology of reinforcement deposition is assumed to be diffusive (i.e. painting, pulverization, some electrochemical methods of deposition). Thus a transition area of gradual penetration of the reinforcement into the basic material (substrate) emerges. The authors use in the transition area an approach, proposing a quadratic approximation of material elastic modulus, which varies within a range bounded by the elastic modulus of the reinforcement and that of the substrate. Loading is static (axial tension/compression) applied under normal temperature and humidity. The linear axial strains are constant within the core, but following a quadratic parabolic law within the transition area. Strain transition between both areas is also smooth. A rod under tension is separately considered and its strength is calculated. Moreover, a compressed rod is also analysed assuming a possibility of rod stability loss. The authors outline a possibility to homogenize the structural element using the stiffness values and employing FEM codes for complex rod tube structures.

1 Introduction

Consider rod structures composed of tubes fixed by two joints and reinforced by a high-strength material along their external surfaces. The reinforcing material can be a polymer composite reinforced by metal fibers or a special nanomaterial [1], [2]. Consider also some technologies of deposition of the reinforcing layer, which diffusively penetrates the substrate, for instance, painting, pulverization, concrete spraying, electrochemical deposition [3]. Some metal, concrete, steel fiber reinforced concrete etc. can be used as a basic material (substrate). Then, a transition area emerges within the tube, bounded by the tube surface and the basic material, where the concentration of the reinforcement varies from 100% to 0%. Thus, a combined structural element is formed, while the outline of the transition area and the assessment of the mechanical properties of the penetrated material can be performed by

solving the diffusion problem. Yet, this turns to be a complex task, since it is not possible to find exactly the specific coefficient of diffusion. To overcome that difficulty, we designed in previous studies an approximate calculation model (ACM), where the distribution of the elasticity modulus and that of the axial linear deformation of the compound material were approximated by means of quadratic relations [4], [5]. The approximation thus attained turned to be of the order of the approximation of FEM codes. Moreover, ACM yields simplified solutions to the problem of determining the stressed and strained state of surface-reinforced, i.e. combined, structural elements. Thus facilitating the calculation of structures composed of those elements. ACM enables also one to perform element homogenization by introducing combined stiffness. Finding the latter, one can use it in various FE commercial codes.

We use ACM in the present study. Rod loading is uniaxial and static, applied under normal temperature and humidity. Displacements and strains are small, and the linear geometrical theory of solid mechanics is assumed to hold [6]. Note also: (i) First-rate stresses and strains are uniformly distributed within the basic material, and they are identical along the rod; (ii) Shear stresses within the basic area are considered to be second-rate quantities, and they are found using known approximate relations of the AMC [6], [7]; (iii) When applying compression, one should check rod strength or find the condition of rod stability loss to be taken as criteria of rod strength calculation [8].

Rod reinforcement makes a structure lighter, since tube reinforcement increases material strength and tubes may be fabricated thinner thus reducing their weight and that of the overall structure. Thus, energy of structural production can be indirectly saved. The same energy-saving effect is attained when using recycled structural materials, which have lost to a certain extent their strength and deformability and are bound to rehabilitation, [5].

Regarding ACM, the distribution of the elasticity moduli follows a quadratic elliptic law in the transition area, while that of the axial strains follows a quadratic parabolic law.

The geometry parameters are as follows: R_1 – internal radius; R_2 – external radius; $h = R_1 - R_2$ – tube thickness; h_R – thickness of the transition area, $h_R = R_2 - z_L$, $h_L = h - h_R$, $R_L = R_1 + h_L$, $F = 2\pi R_M$ – cross section area; $R_M = 1/2(R_2 + R_2)$ – tube mean radius; $r_M = 1/2(R_1 + r_L)$ – core mean radius; $r_R = 1/2(R_2 + r_L)$ – mean radius of the transition area. The following additional geometry parameters are also accounted for:

$$K_F = \frac{F_L}{F}, F_L = 2\pi r_M h_L, K_R = \frac{h_R}{h}, K_M = \frac{r_M}{R_M}, K_R = \frac{r_R}{R_M}, K_L = \frac{h_L}{h} \tag{1}$$

Introduce a cylindrical coordinate system $Oxr\theta$. The cross section symmetry is entirely axial. Following the model, the mechanical characteristics do not depend on θ and x, but only on r.

2 Distribution of the elastic modulus in the transition area

Pursuant to ACM, the elastic modulus E depends on r, only, i.e. $E = E(r), r \in [0,1]$, while the distribution function has a quadratic elliptical form. Introduce a local coordinate $\rho = r - r_L/h_R, \rho \in [0,1]$. Then, the distribution function takes the form

$$E(\rho) = E_B + \Delta E_R \psi(\rho), \Delta E_R = E_R - E_B, \psi(\rho) = 1 - \sqrt{1-\rho^2} \tag{2}$$

The elastic modulus of the core material is constant, i.e. $E = E_B = const$ for $r \in [R_1, r_L]$.

3 Stiffness of an axially tensed combined rod

Consider an axially tensed combined rod $N = N^+$ and find its generalized tension stiffness. If a rod with dimensions (R_1, R_2) is not reinforced, its tension stiffness will be $K_I^0 = E_B J$, while the inertial moment is approximately expressed as $J \approx \pi R_M^3 h$, [8]. For a reinforced tube with a transition area, we express the generalized stiffness as follows:

$$K_I^+ = 2\pi \int_{R_1}^{R_2} E(r) r dr = K_{I1}^* + K_{I2}^* \tag{3}$$

where

$$K_{I1}^* = 2\pi \int_{R_1}^{r_L} E_B r dr = E_B F_L$$

$$K_{I2}^* = 2\pi \int_{r_L}^{R_1} E(r) r dr = 2\pi \int_0^1 E(\rho)(\rho h_R + r_L) h_R d\rho = F_I E_I + F_{II} E_0 \tag{4}$$

where

$$F_I = 2\pi h_R^2, F_{II} = 2\pi h_R r_L$$

We assume the following notation in rel. (4):

$$E_i = \int_0^1 E(\rho) \rho^i d\rho, (i = 0, 1 \cdots) \tag{5}$$

while

$$E_0 = E_B + 0,215 \Delta E_R, E_1 = 0,5 E_B + 0.167 \Delta E_R, E_2 = 0,5 E_B + 0,137 \Delta E_R, etc.$$

The degree of tube reinforcement is assessed pursuant to the ratio $\chi_I^* = K_I^*/K_I^0$, which reads:

$$\chi_I^* = Q_{I0} + Q_{I1} \Delta e_R, \Delta e_R = \frac{\Delta E_R}{E_B} \tag{6}$$

for

$$Q_{I0} = K_F + K_R(0,5K_M + K_L), Q_{I1} = K_R(0,167K_M + 0,215K_L) \quad (7)$$

Parameters K_F, K_R, K_L, K_M are found from rel. (1). If we introduce $\Delta e_R = (K_E - 1)$, then $K_E = E_R/E_B$ which sets forth the reinforcement. It is seen from expr. (6) that the generalized stiffness K_I^*, expressed by ratio χ_I^*, depends linearly on K_E. Considering the generalized stiffness K_I^* of each rod, we could calculate any combined rod tube structure (truss, frame etc.) via FEM. This procedure is additionally approximate. It can be treated as a homogenization of each combined structure, and it significantly facilitates the calculations.

4 Distribution of the axial linear strains within the cross section of a reinforced rod

We find the axial linear strains $\varepsilon(r)$ within the rod cross section using ACM. They are constant within the core and vary within the transition area following a parabolic quadratic function. Thus, we find:

$$for\ r \in [R_1, r_L], \varepsilon_x = \varepsilon_{x0} = const$$

$$for\ r \in [r_L, R_2], or\ \rho \in [0,1], \varepsilon_x = \varepsilon_x(\rho) = \varepsilon_{x0} + \Delta\varepsilon_{xR}\rho^2, \Delta\varepsilon_{xR} = \varepsilon_{xR} - \varepsilon_{x0} \quad (8)$$

where ε_{x0} is the constant linear strain within the core and ε_{xR} is the edge linear strain for $r = R_2$. Both strains, together with h_R, are to be found.

5 Distribution of the normal tension stress within the cross section of a reinforced rod tube

Knowing $\varepsilon_{x0}, \varepsilon_{xR}$ and h_R, we can find the normal tension stresses $\sigma_x(r)$ within the rod cross section. Following ACM, we consider an operating tube, which deforms linearly elastic. Hence, HookeвЃ™s law links the axial linear strains $\varepsilon_x(r)$ and the normal stresses $\sigma_x(r)$, i.e. $\sigma_x(r) = E(r)\varepsilon_x(r)$ or, accounting for the different areas

$$for\ r \in [R_1, r_L], \sigma_x = \sigma_{x0} = E_B\varepsilon_{x0} = const$$

$$for\ r \in [r_L, R_2], \rho \in [0,1], \sigma_x = \sigma_x(\rho) = E(\rho)\varepsilon_x(\rho) = E(\rho)\varepsilon_{x0} + E(\rho)\rho^2\Delta\varepsilon_{xR} \quad (9)$$

where $E(\rho)$ is given by expr. (2).

6 Determination of the linear axial strain in the basic core

To find the axial linear strain ε_{x0} in the basic core, we use a fictitious mean stress $\sigma_{xM} = N^+/F$ set forth in the problem statement. It is expressed as

$$\sigma_{xM} = \frac{1}{h}\int_{R_1}^{R_2} \sigma(r)dr = \sigma_{xM}(1) + \sigma_{xM}(2) \quad (10)$$

where

$$\sigma_{xM}(1) = \frac{1}{h}\int_{R_1}^{r_L} \sigma_{x0} dr = (1 - K_R) E_B \varepsilon_{x0}, \sigma_{xM}(2) = \frac{1}{h}\int_0^1 E(\rho)\varepsilon_x(\rho) h_R d\rho \quad (11)$$

Put $E(\rho)$ from expr. (2) and $\varepsilon(\rho)$ from expr. (8) in expr. (11) for $\sigma_{xM}(2)$. Then, after certain transformations, we find that

$$\varepsilon_{x0} = e_I - e_{II}\varepsilon_{xR} \quad (12)$$

where

$$e_I = \frac{\sigma_{xM}}{E_1}, E_1 = E_B(1 - K_R) + K_R \Delta E_{02}, \Delta E_{02} = E_0 - E_2, e_{II} = K_R \frac{E_2}{E_1} \quad (13)$$

7 Determination of the model parameters

Assume two methods of finding parameters h_R and ε_{xR}.
First method: Perform nanoindentation and a subsequent FEM numerical simulation [9] over a specific specimen to find h_R , assuming one and the same ratio K_R for the specimen and the tube. Then, we find ε_{xR} from the equilibrium condition

$$N^* = 2\pi \int_{R_1}^{R_2} \sigma_x(r) r dr = N_I^+ + N_{II}^+ \quad (14)$$

where

$$N_I^+ = 2\pi \int_{R_1}^{r_L} \sigma_{x0}(r) r dr = E_B F_L \sigma_{x0}$$

$$N_{II}^+ = 2\pi \int_{r_L}^{R_2} \sigma_x(r) r dr = 2\pi \int_0^1 E(\rho)\varepsilon_x(\rho)(h_R\rho + r_L) h_R d\rho \quad (15)$$

and

$$N_{II}^+ = \Delta P_{I,II}\varepsilon_{x0} + P_{II}\varepsilon_{xR}$$

$$\Delta P_{I,II} = P_I - P_{II}, P_I = F_I \Delta E_{13} + F_{II}\Delta E_{02}, P_{II} = F_I E_3 + F_{II} E_2 \quad (16)$$

where

$$\Delta E_{13} = E_1 - E_3, \Delta E_{02} = E_0 - E_2, E_3 = 0,250 E_B + 0,117 \Delta E_R \quad (17)$$

Unify expressions (14), (15), (16) and perform a subsequent revision. Then, we get

$$\varepsilon_{xR} = \frac{N^+ - P_{II} e_{II}}{P_{II} - P_{III} e_{II}}, P_{III} = E_B F_L + \Delta P_{I,II} \quad (18)$$

Secondt method: Perform tension of a reinforced rod tube specimen, applying load N^+, and measure ε_{xR} along its surface. Then, h_R can be found from eq. (18).

8 Strength check of a combined rod

Having found all characteristics of the stressed and strained state under a given load N^+, we can perform a strength check of the carrying capacity of a tensed rod, $N^+ \leq N_{per}$. N_{per} is found using an adopted strength criterion. If the reinforced combined rod undergoes compression $N = N^-$ we use formulas valid for tension considering the subsequent load signs and find the characteristics of the stressed and strained state. We perform a check of the rod carrying capacity, employing two criteria: *Strength check of a compressed combined rod*: We perform it similar to the strength check of a tensed rod presented above. *Check of the stability of a compressed combined rod fixed by joints*: We compare the compression load to the admissible value of the axial load avoiding stability loss N^-_{per}. It is found on the basis of the critical compression load N_{cr} for the reinforced rod, pursuant to Euler [8]. The basis of rod strength calculation is reliable. Pursuant to Euler, the critical force of a two-joint centrally compressed and reinforced rod reads [9].

$$N_{cr} = \frac{\pi_2 K^*_{II}}{L^2} \tag{19}$$

where K^*_{II} is the generalized bending stiffness of the combined rod and L is rod length. We find approximately the generalized bending stiffness of the reinforced rod, treating the tube as a two-layer body, consisting of a basic core with an elastic modulus E_B and a transition area with mean elastic modulus $E^* = 1/h_R \int_0^1 E(\rho) h_R d\rho$ for $r \in [r_L, R_2]$ or $\rho \in [0, 1]$. We assume that h_R is one and the same under tension and compression, since we consider a process of diffusion identical in both cases.

9 Test example. Parametric analysis

Consider a small frame structure shown in Fig. 1. It is subjected to a static vertical load P. The structural scheme is symmetrical. Its two-joint rods are aluminum tubes, being reinforced along their surfaces [10]. The static analysis yields the following loads acting on the rods: on Π_{01}, $N^-_{01} = -0,94P$; on Π_{02}, $N^+_{02} = 0,78P$; on Π_{12}, $N_{12} = 0$. For $P = 1,55x10^4[N]$ loads are $N^-_{01} = -1,46x10^4[N]$, $N^-_{02} = 1,21x10^4[N]$. The elastic modulus of the basic material is $E_B = 7x10^6[N/cm^2]$. The reinforcing material is a composite containing nanoparticles and its elastic modulus varies within limits $40 - 80[N/cm^2]$, [1]. Tube dimensions are $\Phi R_1 x1$ according to manufacturer data [10], with thickness $h = 1cm$. Consider data from nanoindentation [9] and assume $h = 0,1cm$. If the elasticity modulus of the reinforcing material is $E_R = 40x10^6[N/cm]$, we compare the calculation of the rods of the non-reinforced structure with that of the rods of the reinforced structure. The dimension of all rods of the non-reinforced structure is $\Phi 10x1$. The reinforced structure yields Π_{01} dimension $\Phi 18x1$, while the rest of the rods have a manufacturer dimension $\Phi 10x1$. This yield reduction of structure weight for reinforcement is 17%. A parametric analysis of the link between ε_{xR} and $K_E = E_R/E_B$ is performed for rod Π_{02}. The results are plotted in Fig. 2. The test example and the parametric analysis prove the efficiency of the reinforcement, thus contributing to the reduction of the structure weight and to the increase of its carrying capacity.

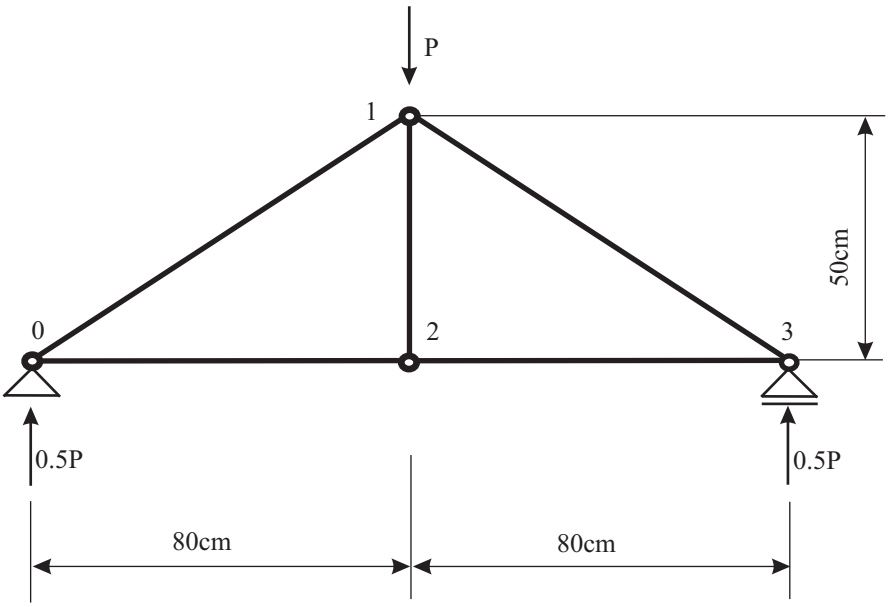

Figure 1: A test frame composed of reinforced aluminum rod tubes

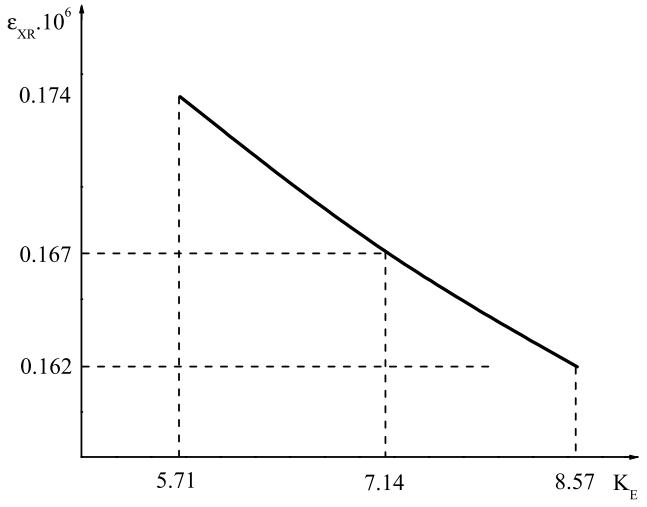

Figure 2: Link between ε_{xR} and K_E

Acknowledgements

The study has been supported by the National Science Fund, Project DFNI E02/10 121214.

References

[1] Mechanics of Nanomaterials and Nanotechnology (2012): Thematic Collection "Series in Applied Mathematics and Mechanics", Vol. 3. Publisher Institute of Mechanics, Bulgarian Academy of Sciences, Sofia.

[2] Hui-Shen Shen, J. G. Teng and J. Yang (2001): Interfacial Stresses in Beams and Slabs Bounded with Thin Plate. J. Eng. Mech. 127, pp. 399-406.

[3] Bakis, C. E., L. C. Bank, V. L. Brown, E. Cosenza, J. F. Davalos, J. J. Lesko, A. Machida, S. H. Rizkalla, and T. C. Triantafillou (2002): Fiber-Reinforced Polymer Composites for Construction, State of the Art-Review. J. of Comp. for Construction, 6, pp. 73-87.

[4] Baltov A., A. Yanakieva (2015): Local Deplanation of Double Reinforced Beam Cross Section Under Bending. J. of Theor. and Appl. Mech., 45(4), pp. 31-40.

[5] Baltov A., A. Yanakieva, G. Nikolova (2016) Modelling of the Bending Behaviour of a Double-Reinforced Beam from Recycled Materials for Application in NZEBs. Springer Proceedings in Energy (SPE), pp. 167-173.

[6] Timoshenko Stephen P. James M. Gere (1972): Mechanics of Material., Publisher: Van Nostrand Reinhold Company.

[7] Kazakov K (2012) Theory of Elastisity, Stability and Dynamics of Structures Common Problems. Trafford Publishing.

[8] Birger, I.A., Ya. G. Panovko (1969): Strength, Stability, Vibrations. Handbook 1. Mashinostroene, (in Russian).

[9] Datcheva M., S. Cherneva, M. Stoycheva, R. Iankov, D. Stoychev (2011): Determination of Anodized Aluminum Material Characteristics by Means of Nanoindentation Measurements. Materials Sciences and Applications. Scientific Research Publishing, USA, 2, pp.1452-1464.

[10] Internet information: Aluminium tubes.

Baltov A., G. Bonchev str.4, Institute of Mechanics, Bulgarian Academy of Sciences, 1113 Sofia, Bulgaria
Yanakieva A., G. Bonchev str.4, Institute of Mechanics, Bulgarian Academy of Sciences, 1113 Sofia, Bulgaria

Mechanics of penetration and structural protection in the frame of optimization game theory

Nikolay V. Banichuk, Svetlana Yu. Ivanova

banichuk@gmail.com

Abstract

The questions of the shape optimization of an axisymmetric rigid impactor and structure optimization of layered perforated plates are studied on the base of the Nash game approach [1], [2] for layered plates made on the given set of materials. As a criterion of the multipurpose optimization problem it is chosen the ballistic limit velocity under additional constraint on the layered shield mass. The process of penetration of the rigid body into an elastic-plastic medium is modelled by the application of the two parts representation for the resistance force [3]. It is proposed and realized the solution algorithm of the conflict game problem, namely, the optimal shape impactor against the optimal structure layered shield. It is considered the case when the impactor mass is given and does not depend on its volume. With the application of an evolution numerical method (genetic algorithm) the optimal shapes of penetrating bodies and corresponding optimal shield structures are found and analyzed for all cases.

1 Introduction

The study of processes of high-speed penetration of rigid strikers into deformed media and perforation of shield structures is actual and of theoretical and practical interest. Scientific investigations in this domain are very wide and include many experimental, analytical and numerical components. Also the optimal structural design plays the important role in this aspect. Many studies were devoted to the problem of optimal shape determination of rigid bodies penetrating with high speed into deformed (elastic-plastic, concrete, brittle) media. Also problems of shield structure optimization were investigated by many authors.

Now we propose the game approach to solve the problem of high-speed perforation of the layered slab by the axisymmetric striker (optimal shape striker against optimal shield structure).

2 Ballistic limit velocity (BLV) determinimg

The questions of shape optimization of rigid strikers perforating the layered slab are studied in game statement. As a criterion of multipurpose optimization problem it was taken the ballistic limit velocity, which is a very important characteristic of striker-medium interaction.

Dynamics of high-speed penetration of rigid axisymmetric striker (with velocities up to 10^3m/s) along the axis Ox is studied with application of relation connecting the resistance force $D(x)$ with strength characteristics $A_0(x)$, inertial property $A_2(x)$, striker shape $y(\eta)$ $(0 \le \eta \le L)$, its length L, and velocity $v(x)$ as

$$\begin{aligned} &D(x) = D_{nose}(x) + D_{lat}(x) = B_0(x) + B_2(x)v^2(x), \\ &B_0(x) = \pi r^2 A_0(x) - 2\pi \int_{x_*}^{x_{**}} A_0(\eta) y y_\eta d\eta, \\ &B_2(x) = \pi r^2 A_2(x) - 2\pi \int_{x_*}^{x_{**}} \left[A_2(\eta) y_\eta^3\right] \left(1 + y_\eta^2\right)^{-1} d\eta. \end{aligned} \tag{1}$$

Here $D_{nose}(x)$ is the resistance force applied to the truncated head part of striker, $D_{lat}(x)$ is the resistance force applied to the lateral area, r is the radius of truncation, $y_\eta = dy/d\eta$, x is the coordinate of striker nose, x_*, x_{**} are the values characterizing different stages of striker penetration into the medium (boundaries of contact region). If the entry (impact) velocity $v_0 = v_{imp}$ of striker penetration into the slab of thickness H is such that $v(x) > 0$ for $0 \le x < H + L$ and $v = 0$ for $x = H + L$, then, the impact velocity is called the ballistic limit velocity (BLV), i.e. $v_0 = v_{imp} = v_{BLV}$. Perforation of layered slab by the axisymmetric striker having ballistic limit velocity is shown in Fig.1.

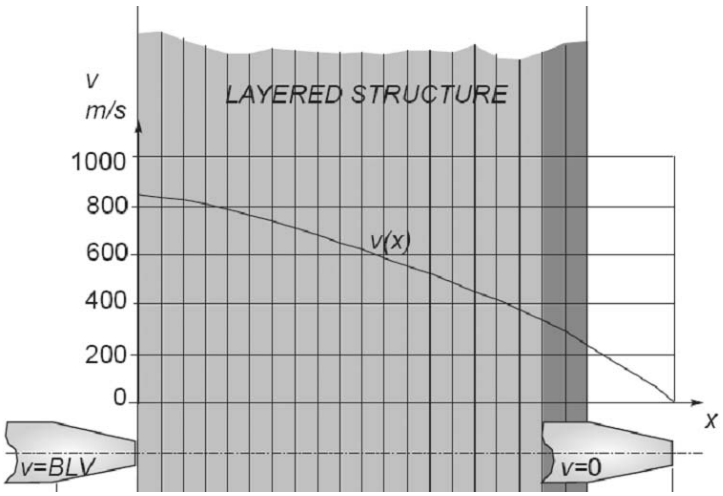

Figure 1: Perforating layered slab

We introduce for convenience the new independent variable

$$\xi = H + L - x, \quad d\xi = -dx$$

and formulate the problem of determining the velocity of striker in the medium as following Cauchy problem:

$$\frac{dv^2}{d\xi} = \beta\left(\alpha + v^2\right), \quad \left(v^2\right)_{\xi=0} = 0, \tag{2}$$

where $\alpha = B_0/B_2$, $\beta = 2B_2/m$ (m is the mass of striker).
For convenience, we assume that the perforated obstacle includes the slab and rear air region of length L, i.e. has total thickness $H+L$ and consists of n thin layers of equal thickness $h = (H+L)/n$. Each layer contains material with fixed properties. For such piece-wise constant structure, the problem (2) can be represented as

$$\begin{array}{l} \frac{dv^2}{d\xi} = \beta_{j+1}\left(\alpha_{j+1} + v^2\right), \\ v_0^2 = \left(v^2\right)_{\xi=0} = 0, \\ v_j = v(\xi_j), \quad \xi_{j+1} = \xi_j + h, \quad j = 0, 1, 2, ..., n-1, \\ \alpha_{j+1} = \left(\frac{B_0}{B_2}\right)_{j+1}, \quad \beta_{j+1} = \frac{2}{m}\left(B_2\right)_{j+1}, \\ v_n^2 = \left(v^2\right)_{\xi=H+L} = v_{BLV}^2. \end{array} \tag{3}$$

Layer-wise integration of the problem (3) results in algebraic relations

$$\begin{array}{l} \ln\left(\frac{\alpha_{j+1}+v_{j+1}^2}{\alpha_{j+1}+v_j^2}\right) = \mu_{j+1}, \quad \xi_j \le \xi \le \xi_{j+1}, \\ \mu_{j+1} = \beta_{j+1}h, \quad j = 0, 1, 2, ..., n-1, \end{array} \tag{4}$$

which determine the solution, i.e. the velocity distribution for each layer and, in particular, the value of ballistic limit velocity. We have

$$\begin{array}{l} \frac{v_{j+1}^2}{\alpha_{j+1}} = \exp\left(\mu_{j+1}\right) - 1 + \frac{v_j^2}{\alpha_{j+1}}\exp\left(\mu_{j+1}\right), \\ v_0 = 0, \quad v_n = v_{BLV}. \end{array} \tag{5}$$

3 Multipurpose optimization problem

Let us consider the ballistic limit velocity (BLV) as a quality criterion for multipurpose optimization problem according to game approach (with two gamers).
We formulate the problem A (for gamer 1) that consists in minimization of BLV by finding the optimal striker shape for given shield structure (given layered slab), i.e.

$$\begin{array}{l} J_1 = v_{BLV}(y(\eta), t(x)) \to \min_{y\in\Lambda_y}, \\ \Lambda_y = \left\{y: \ y_{con}(\eta) \le y(\eta) \le R, \ 0 < \eta \le L, \ y(0) = y_{con}(0) = R\right\}. \end{array} \tag{6}$$

Here $y_{con}(\eta)$ defines the conical shape of the striker, R is given base radius (midel) of the striker and we assume that the mass m is independent on the striker volume. The function $t(x)$, $x \in [0, H+L]$ is piece-wise constant and characterizes the layer-wise distribution of material characteristics. The number r_m of materials is assumed to be given, $s = 1, 2, ..., r_m$, where s is the material number.
The problem B (for gamer 2) consists in maximization of BLV by defining the optimal layered slab (plate) under the constraint on its mass M (on $1m^2$) as

$$\left\{\begin{array}{l} v_{BLV}(y(\eta), t(x)) \to \max_{t\in\Lambda_t}, \\ M(t(x)) \le M_0, \end{array}\right.$$
$$\Lambda_t = \left\{\begin{array}{l} t: \ t = t(x), \quad x \in [0, H+L], \quad t \in \{t_i = s\}, \\ i = 0, 1, 2, ..., n-1, \quad s = 1, 2, ..., r_m, \\ A_0(t(x)) = A_0^{i+1}, \quad A_2(t(x)) = A_2^{i+1}, \quad x \in [x_i, x_{i+1}), \\ \left(A_0^{i+1}, A_2^{i+1}\right) \in \left\{\left(A_0\right)_s, \left(A_2\right)_s\right\}. \end{array}\right\}. \tag{7}$$

Here the properties of material with number s filling the layer ($x_i \le x \le x_{i+1}$) with number $i+1$ are characterized by constants $\left(A_0^{i+1}\right)$ and $\left(A_2^{i+1}\right)$, M_0 is given constant. The problem B (7) can be rewritten by introducing the augmented Lagrange functional J^a as

$$J_2 = J^a(y(\eta), t(x)) \to \max_{t \in \Lambda_t}, \tag{8}$$

$$J^a = v_{BLV}(y(\eta), t(x)) - \lambda \left[M(t(x)) - M_0\right] \to \max_{t \in \Lambda_t},$$
$$\lambda = \begin{cases} 0, & if \quad M - M_0 \le 0, \\ \lambda_* > 0, & if \quad M - M_0 > 0. \end{cases}$$

The multipurpose optimization problem consists in defining the optimal (in the sense of the problem A) striker shape for optimal (in the sense of the problem B) layered structure. As a quality criterion, it is chosen the ballistic limit velocity (BLV).
Solving this multipurpose optimization problem is realized on the base of game iteration approach (Nash approach [1]) by performing the following steps.
Step 1. The initial distribution $t = t_1^*(x)$ of materials is realized for the layered structure.
Step 2. The problem A is solved (by the gamer 1) for given distribution $t_1^*(x)$ and the shape distribution $y_1^*(\eta)$ is defined as

$$y_1^*(\eta) = \arg\min_{y \in \Lambda_y} J_1\left(y(\eta), t_1^*(x)\right). \tag{9}$$

Step 3. The problem B is solved (by the gamer 2) for given distribution $y_1^*(\eta)$ and the improved distribution $t_2^*(x)$ of materials is found, i.e.

$$t_2^*(x) = \arg\max_{t \in \Lambda_t} J_2\left(y_1^*(\eta), t(x)\right). \tag{10}$$

Step 4. The iteration is completed and we will go to the Step 2 or terminate the optimization process.
For solving the optimization problems A and B, the numerical evolutionary method based on the genetic algorithm was realized. The considered set of admissible shapes (population) consists of thirty solutions (individuals) for each generation. Each individual of population consists of ten (the problem A) or fifty (the problem B) elements. The search of optimal shape was begun (initialization) using initial population consisted of arbitrary distributions $y(\eta)$ with given fixed R and performed up to 500 generations. The parameters of computational process included the probability of crossover $p_{CO} = 0.5$ and the mutation probability $p_m = 0.05$.
The computations were performed for the following values of the problem parameters, namely, $L = 0.02m$, $R = 0.005m$, $H = 0.1m$. Admissible values of material properties for slab layers were taken as [3]

$$s = 1 \quad (air) \quad (A_0)_1 = 0, \quad (A_2)_1 = 0;$$
$$s = 2 \quad (soft\ steel) \quad (A_0)_2 = 1850 \cdot 10^6 M/m^2, \quad (A_2)_2 = 7830 kg/m^3;$$
$$s = 3 \quad (copper) \quad (A_0)_3 = 910 \cdot 10^6 M/m^2, \quad (A_2)_3 = 8920 kg/m^3;$$
$$s = 4 \quad (duraluminum) \quad (A_0)_4 = 1330 \cdot 10^6 M/m^2, \quad (A_2)_4 = 2765 kg/m^3.$$

All optimal strikers have the shape with blunted (a little) nose part. The analysis of numerical results for all considered cases permits to make a conclusion (within the

framework of using model of high-speed interaction) that the optimal shape of striker is determined by its geometrical and inertial characteristics and do not depend on the mass of the slab, its thickness and layers ordering. Two optimal shape distribution are shown in Fig.2 by the curves with numbers 1 (thin solid line) and 2 (thick solid line). The curve 1 corresponds to optimal duraluminum slab of the thickness $0.056m$ and the values $m = 0.009kg$, $M_0 = 156.6kg/m^2$. The curve 2 corresponsd to optimal slab that consists of the frontal steel part (of thickness $0.006m$) and the rear duraluminum part (of thickness $0.094m$), and the values $m = 0.05kg$, $M_0 = 313.2kg/m^2$. Note that the optimal shapes shown in Fig.2 are practically the same, although they corresponds to different optimal layered structures and different striker mass values. This fact was noted for all considered cases including also the case where the mass of the striker was not fixed but satisfied the constraint imposed on its value.

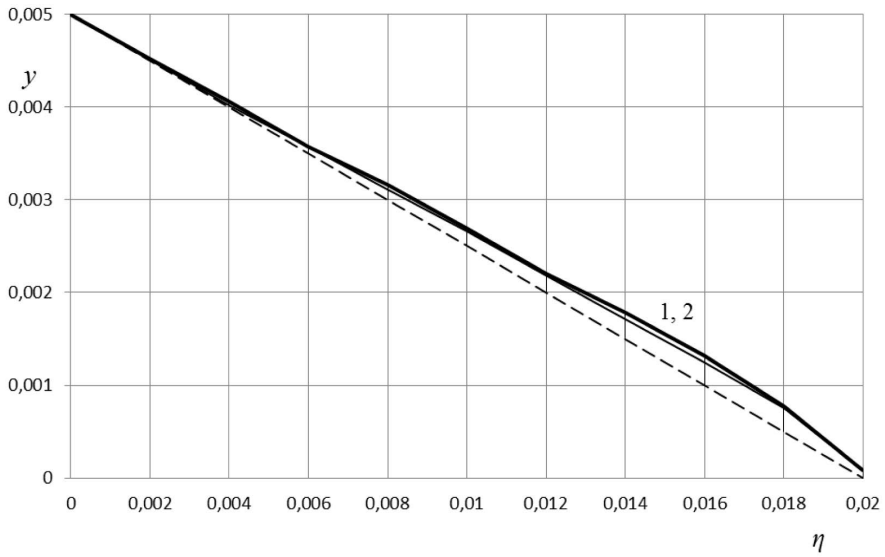

Figure 2: Optimal shapes of striker

Thus, it is sufficient to determine the optimal shape of the striker (minimizing the ballistic limit velocity) for some given layered structure and then use this solution for the shield optimization according to maximum of the ballistic limit velocity.

Acknowledgements

The work is performed under support of RFBR (grant 17-08-00775-a).

References

[1] Stadler W. Multicriteria optimization in mechanics (A survey). Applied mechanics review. 1984. Vol. 37, No 3. P. 227-296.

[2] Banichuk N.V., Ivanova S.Yu. The game approach to solution of an impactor shape and layered structure medium optimization problem for high speed perforation. Problems of Strength and Plasticity. 2016. 78(4). P. 426-435. (in Russian).

[3] Banichuk N.V., Ivanova S.Yu. Optimization: contact problem and high-speed penetration. 2016. M.: FIZMATLIT. 176p. (in Russian).

Nikolay V. Banichuk, Prospekt Vernadskogo, 101, bld.1, Moscow, Russia
Svetlana Yu. Ivanova, Prospekt Vernadskogo, 101, bld.1, Moscow, Russia

Stability assessment of a tibia fracture fixation in the case of thermal stresses

Elena Y. Belova

eyshukeylo@gmail.com

Abstract

Fractures of a tibial diaphysis constitute the largest percentage among all cases of fractures of long bones, namely 32-37%. Internal osteosynthesis is one of the modern operational treatment methods of these fracture types. Problems of determining thermal stresses and their further consideration when choosing a treatment method of a patient are resolved with regard to such the medicine section as the traumatology. However, temperature drop at a bone surface in an installation place of a plate and screws during surgery and temperature change of fixators after sealing of a wound are not taken in conducting similar studies for biotechnological systems (BTS) "bone–plate–screws". The aim of this study is determination of maximum values of thermal stresses in components of a BTS "tibia bone–plate TRKh–screws".

3D computer models of a tibia bone and a segmental fracture of this bone are created in the CAD SolidWorks. Fragment is localized to a middle third of a diaphysis, its size — 50 mm. Height of a diastase is 0.5 mm. Modelling of an internal osteosynthesis of the segmental tibia fracture are performed by a plate TRKh (named after the plate authors — Dr. S.Tkachenko, Dr. V.Rutsky and Dr. V.Khomutov) and 9 screws. An area, which is a contour projection of the plate TRKh, is built on the tibia bone surface.

3D computer finite element model of the BTS "tibia bone–plate TRKh–screws" is created in SolidWorks Simulation module. Diaphysis consists of cortical bone tissue, epiphyses and metaphyses — cancellous tissue, fixators — titanium alloy VT6. Temperature of the tibia bone is 37 °C, temperature of the area — 34.5 °C. Air temperature in an operating room is 21 °C.

Maximum values of thermal stresses occurring in components of the BTS "tibia–plate TRKh–screws", do not exceed values of dangerous stresses for materials of these components according to the results of this study. Stability fixation of the segmental fracture is not violated. Heating the area on the tibia surface and fixators to 37 °C occurs for 25 minutes.

1 Introduction

Fractures of a tibial diaphysis constitute the largest percentage among all cases of fractures of long bones, namely 32-37% [1]. The situation is compounded by the

fact that this type of fracture is most common in individuals of working age with the age category up to 40 years [2]. Internal osteosynthesis, which is based on a principle of connection of bone fragments by surgical way using various fixators inside a patient's body, is one of the modern operational treatment methods of the diaphyseal fracture.

Thermal stresses occur in living tissue due to uneven temperature distribution. Problems of determining thermal stresses and their further consideration when choosing a treatment method of a patient are resolved with regard to such the medicine section as the traumatology. Studies (in most cases) are performed for the purpose of rationale for an optimal choice of the fixator in a transverse fracture of femur, humerus, tibia bones [3, 4, 5, 6, 7, 8]. The authors suppose that bone temperature before installation of the metal construction is constant and equal to 37 °C. At that the change of temperature distribution that occurs in cortical and trabecular bone tissues in the process of operation, is not taken into account. In cases when a plate and screws are used to stabilization of the fragments, a surgeon makes an incision of soft tissues and exposes a part of the bone surface — an area. Temperature values of the area and air flowing around it are different, so convective heat transfer occurs and a cooling front starts to spread into the deep of the bone. Gradual heating of the bone tissue and metal construction occurs after installation of the fixators and wound closure. Therefore, change of temperature distribution in the BTS "bone–plate–screws" in the process of operation should be considered in determining of maximum values of the thermal stress.

Aim of this work is determining of maximum values of the thermal stress when occur in components of the BPS "tibia bone–TRKh plate–screws" after wound closure.

Main tasks of this study are listed below.

1. Create 3D computer model of the BTS "tibia bone–TRKh plate–screws" with the area, which is a projection of a contour line of the TRKh plate to a surface of the tibia bone.
2. Create 3D computer finite element model of this BTS.
3. Perform a biomechanical study of BTS "tibia bone–TRKh plate–screws" subject to the uneven temperature distribution in the bone tissues and fixators.

Temperature studies of the segmental tibia fracture model with the area and the BTS "tibia bone–TRKh plate–screws" are conducted by the author earlier.

2 Materials and methods

2.1 Modeling of the BPS "tibia bone–TRKh plate–screws"

3D computer model of the tibia bone is built in the SolidWorks CAD system. 50 cross-sectional (tomographic) images are used to create it: 9 for proximal, 11 for distal and 30 for diaphyseal aspects. The patient, whose cross-sectional images of the bone are used in this study, is considered average. This patient hasnвГЄt accompanying pathologies. His body mass is 70 kg, age — 40 years.

Building of the 3D computer model of segmental bone fracture is made using the created tibia bone model. Fragment is localized in the middle third of the diaphysis

and its size is 50 mm. Gap — diastasis — is formed at the moment of the fracture between fragments. Its height is taken equal to 0.5 mm [9].
Modeling internal osteosynthesis of segmental tibia fracture is made by TRKh plate, its length is 224 mm, and 9 screws. Four screws, their length are 40 mm and a diameter is 4.5 mm, are installed in order, starting with the top plate holes. Other five screws, their length are 35 mm and a diameter is 4.5 mm, are used to fastening of the lower plate part. Area, which is a projection of a contour line of the TRKh plate to a surface of the tibia bone, is created after the installation of the TRKh plate and screws in a predetermined position.
3D computer finite element model BTS "tibia bone–TRKh plate–screws" is built in the SolidWorks Simulation module. High quality mesh of parabolic tetrahedral solid elements is used in its creation. Average global element size is 6.10 mm, tolerance — 0.30 mm. Number of nodes is 49497, number of elements — 28736. Built 3D computer model of the BTS "tibia bone–TRKh plate–screws" and its finite element model are presented in figure 1, a,b, respectively.

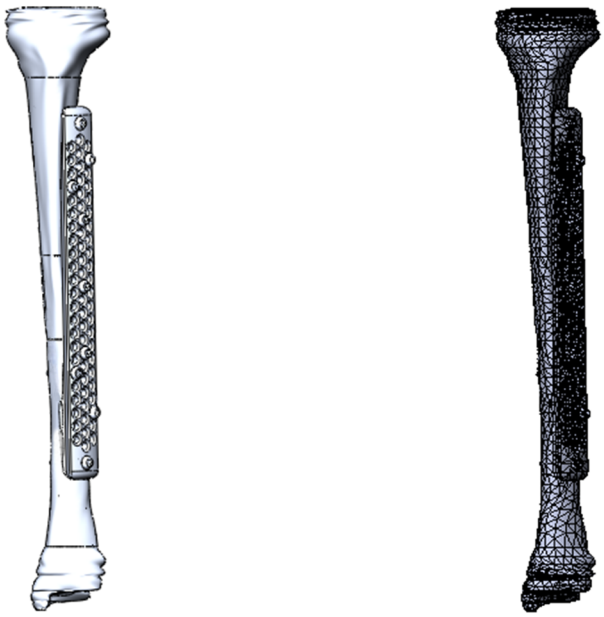

a b

Figure 1. BTS "tibia bone–TRKh plate–screws": a — 3D computer model, b — 3D computer finite element model

2.2 Physico–mechanical characteristics of the tibia bone materials

Epiphyses and metaphysi in the finite element model of the BTS "tibia bone–TRKh plate–screws" are modeled entirely from finite elements that have physical characteristics of trabecular bone tissue. Diaphysis is formed from cortical bone tissue excluding a bone marrow that fills an internal space [10]. Fixators — TRKh plate and screws — are made from VT6 titanium alloy. Elastic modulus of cortical bone

tissue, trabecular bone tissue, VT6 titanium alloy is 35,3 [11, 12], 0,40 [12], 115,00 GPa [13, 14], respectively. Poisson's ratio of these materials is 0.30 [15], 0.20 [15], 0.32 [14] respectively. Density — 1850 [16, 17], 300 [16, 17], 4430 [13] kg/m^3, dangerous stress — 129 [11, 12], 6 [18], 900 [13, 14] MPa. Linear temperature expansion coefficients of cortical bone tissue, trabecular bone tissue, VT6 titanium alloy is 32 [19], 10 [20], 8.4 [13] $°C^{-1}$, respectively.

2.3 External loads

Results of the temperature study of the considered BPS after installation of the fixators and wound closure obtained by the author earlier is used as the external load. Temperature distribution in the model in this study had determined at 10 different time stages — from 150 to 1500 seconds with a step of 150 seconds, — which allowed to trace a process of heating of the BPS components to a temperature of 37 °C. In addition, convective heat transfer, which occurs due to the difference of temperatures of the exposed area and air flowing around it, was taken into account.

3 Results

Biomechanical study of the BTS "tibia bone–TRKh plate–screws" subject to change of temperature distribution in a heating process of the BPS components after wound closure to a temperature of 37 °C is carried out in the SolidWorks Simulation module.

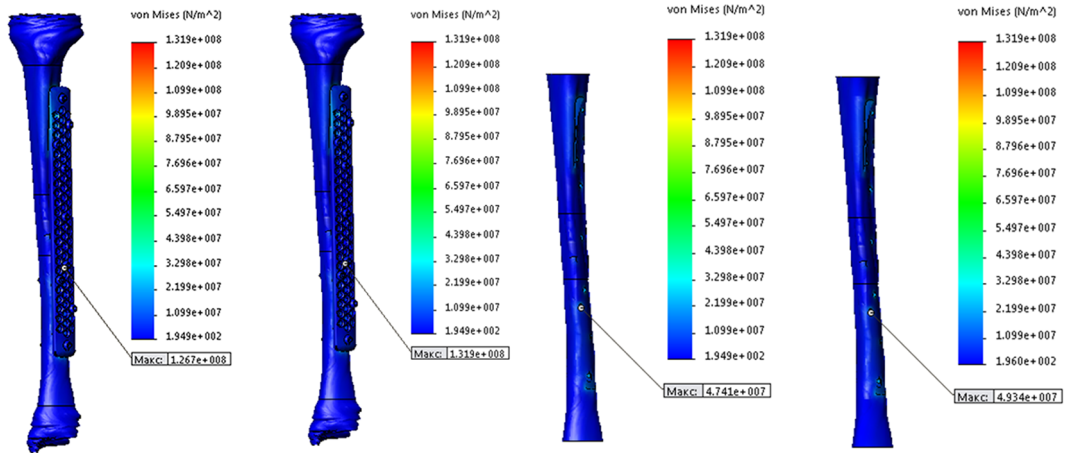

a b c d

Figure 2. Stress–strain state: a — BTS on the first stage, b — BTS on the tenth stage, c — tibia bone diaphysis on the first stage, d — tibia bone diaphysis on the tenth stage

Maximum values of equivalent stress (von Mises stress) in the diaphysis, epiphyses and fixators are defined for each of 10 considered stages. Criterion according to which maximum values of equivalent stress in the system components must not exceed corresponding values for dangerous stress in materials of these components which is numerically equal to yield stress, is used for evaluation of fixation stability

of the BTS. Stress–strain state of the BPS on the first (150 seconds) and tenth (1500 seconds) stages is shown in a figure 2, a, b respectively as an example. Note that contains of minimum value of equivalent stress in the model is shown on the figure. Stress–strain state of the tibia bone diaphysis on the first and tenth stages is shown in a figure 2, c, d.
Dependency graph of maximum values of equivalent stress in the considered BTS from time is presented in a figure 3.

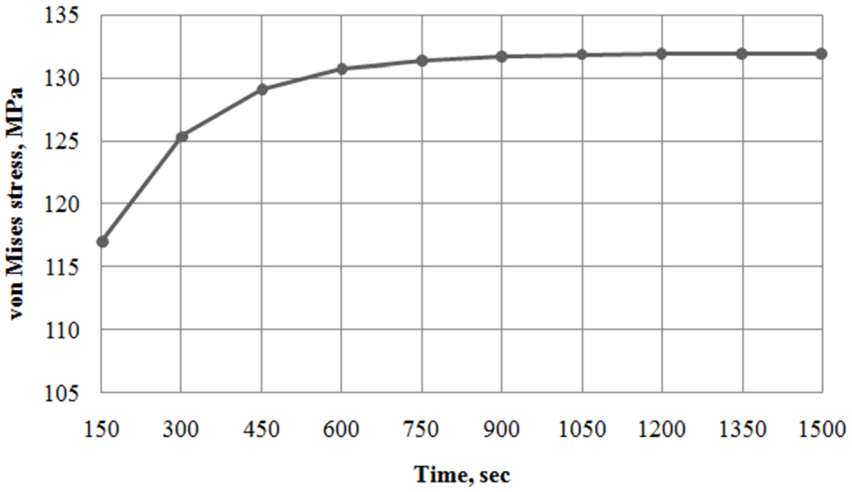

Figure 3. Dependency graph of maximum values of equivalent stress from time

4 Discussion

Conducted study is shown that occurrence of thermal stress in the BTS "tibia bone–TRKh plate–screws" after wound closure does not lead to violation of fixation stability of the considered BTS. Maximum value of equivalent stress on the first and tenth stages, which are shown in figures 2 a,b, differ by 5.19 MPa, which is insignificant. Maximum values of equivalent stress in the BPS grow with increasing time, as can be seen from the graph which presented in a figure 3. However, these values change slightly after the fifth stage.
Maximum value of equivalent stress in the fixators occurs in the fourth screw at the bottom and it doesnвГЄt exceed of dangerous stress for titanium alloy VT6, which is equal to 900 MPa. Maximum value of this stress in epiphyses on the same stage is 0.57 MPa, that is 10 times less of the value of dangerous stress for trabecular bone tissue. TRKh plate and screws are installed on the tibia diaphysis , therefore difference between maximum value of equivalent stress in this aspect and value of dangerous stress for cortical bone tissue isnвГЄt as great as in the previous cases. Values differ by 2.5 times.

5 Conclusion

Maximum values of equivalent stresses in the 3D computer finite element model of the BPS "tibia bone–TRKh plate–screws", subject to change of temperature

distribution after wound closure in 10 different stages are found in this study. Source data and described methodology of work realization is appropriate to use in carrying of biomechanical studies 3D computer finite element models of bone fracture, in which other types of plates are fixators.

References

[1] Shchukin V.M. Compression plate-dynamic osteosynthesis of diaphyseal fractures of shin bones in peacetime and in emergency situations: abs. dis... cand. med. sciences. — Moscow: I.M. Sechenov First Moscow State Medical University, 2005. — 25 p.

[2] Selitskii A.V., Kezlia O.P., Diatel S.V. Choice of optimal tactics of treatment of severe high-energy injury to the shin // Modern medical technologies in the context of regional health: collection of articles of the Republican scientific–practical conference. — Pinsk, 5th October 2012. — Pinsk: PolesSU, 2012. — P. 199–201.

[3] Nyashin Y.I., Kiryukhin, V.Y. Biological stresses in living tissues. Issues of modeling and management // Russian journal of biomechanics. — 2002. — V. 6. — N^o 3. — P. 13–32.

[4] Kiryukhin, V.Y., Nyashin Y.I. Management task of stress in actual problems of biomechanics // Russian journal of biomechanics. — 2005. — V. 9. — N^o 4. — P. 9–27.

[5] BayramoД§lu E. et al. Analysis of plate-screw fixation by finite element method in transverse fractures of the tibia diaphysis // Analysis. — 2016. — V. 55. — N^o 3. — P. 117–121.

[6] Tarnita D. et al. Modular adaptive bone plate for humerus bone osteosynthesis // Romanian Journal of Morphology and Embryology. — 2009. — V. 50. — N^o 3. — P. 447–452.

[7] Shukeilo Y.A. Influence of temperature deformations of the implant with shape memory on the stress state of bone tissue // Biomechanics–2006: 8th Russian conference on biomechanics, N. Novgorod, 22–26 may 2006: thesis of reports. — N. Novgorod, 2006. — P. 216–218.

[8] Shukeilo Y.A., Khomutov V.P., Samsonov S.Y. Influence of temperature effects on the system of plate osteosynthesis during rehabilitation of the patient // International conference on soft computing and measurements. — SPb. : Publishing house ETU "LETI", 2007. — V. 2. — P. 245–247.

[9] Lavrishcheva G.I., Onoprienko G.A. Morphological and clinical aspects reparative regeneration of supporting organs and tissues. — M.: Medicine, 1996. — 208 p.

[10] Maslov L.B. Resonance properties of the tibia in intact condition and with devices of external fixation // Russian journal of biomechanics. — 2003. — V. 7. — N^o 2. — P. 20–34.

[11] Nahum A.M., Melvin J.W. Accidental injury: biomechanics and prevention. — Springer Science and Business Media, 2012.

[12] Burstein A.H., Reilly D.T., Martens M. Aging of bone tissue: mechanical properties // The Journal of Bone and Joint Surgery. — 1976. — Рђ. 58. — N^o 1. — Рг. 82–86.

[13] Structural materials: reference book / B.N. Arzamasov [et al.].; ed. by B. N. Arzamesov. — M.: Mashinostroenie, 1990. — 688 p.

[14] Physical quantities: reference book / A.P. Babichev [et al.].; ed. by I.S. Grigoriev, I.S. Meilikhov. — M.: Energoatomizdat, 1991. — 1231 p.

[15] Wirtz D.C. et al. Critical evaluation of known bone material properties to realize anisotropic FE-simulation of the proximal femur // Journal of biomechanics. — 2000. — V. 33. — N^o 10. — P. 1325–1330.

[16] Marieb E.N., Hoehn K. Human anatomy and physiology. — Pearson Education, 2007.

[17] Gong J.K., Arnold J.S., Cohn S.H. Composition of trabecular and cortical bone // The Anatomical Record. — 1964. — V. 149. — N^o 3. — P. 325–331.

[18] Morgan E.F., Keaveny T.M. Dependence of yield strain of human trabecular bone on anatomic site // Journal of biomechanics. — 2001. — V. 34. — N^o 5. — P. 569–577.

[19] Pal S., Saha S. Coefficient of thermal expansion of bone // Biomechanics. — 1989. — P. 52.

[20] Magne P., Versluis A., Douglas W.H. Effect of luting composite shrinkage and thermal loads on the stress distribution in porcelain laminate veneers // The Journal of prosthetic dentistry. — 1999. — V. 81. — N^o 3. — P. 335–344.

Elena Y. Belova, Saint Petersburg, Russian Federation

Experimental study of stochastic processes for adaptive tilt correction of the signal beam at a long atmospheric path

Arkadiy V. Blank, Vitaliy V. Kapranov, Ruslan V. Mikhailov, Natalia A. Suhareva, Vjatcheslav Yu. Tugaenko

BlankArkadiy@physics.msu.ru

Abstract

The results of experimental study of adaptive correction dynamics for collimated coherence beam at the exit of 1350 meter atmospheric path are presented. The method of phase portraits and chaotic maps for processing the experimental series is used that allowing to visualize the transition phenomenon and the bistable system conditions. The system response to variations of a proportional algorithm parameters for adaptive correction, the frequency of sampling and a scale feedback factor are in details analyzed. Relations of the size of a beam spot on a recording device matrix and the stability of a correction algorithm are experimentally considered.

Introduction

The peculiarity of corrective procedures for laser beams propagating over near-the-ground tilt path is associated with the dynamic and statistical spatial inhomogeneity and non-stationarity of the refractive effects on the beam [1]. Usually available for actuators range of correction frequencies over such paths overlaps only the low-frequency part of the refraction modulation band of the beam displacement vector in the registration plane. Under this mode, effectiveness of the impact should increase when connecting a feedback loop output possessing a sufficient depth of memory.
The dynamical system evolution can be observed in the state space of the system, the modes available can be obtained from the phase portrait as a set of trajectories realized in phase space. Among the trajectories one can mark out a number of basic ones determining the qualitative properties of the system. These include the equilibrium points corresponding to stationary modes of the system and closed trajectories (limit cycles) corresponding to quasi-periodic modes. The stability of a particular mode manifests itself in the consistent behavior of neighboring trajectories, - stable equilibrium or limit cycle attracts all nearby trajectories, unstable ones repels at least some trajectories. The phase portrait, disassembled into groups of

trajectories, allows to describe all types of permissible movements arising under different initial conditions. Actually,the phase portraits apparatus for the description of the dynamics of complex non-stationary systems allows to visualize the solutions of differential or difference equations of a physical system motion [2].

1 The method of phase trajectories

For a system having N degrees of freedom one can map the feasible set of phase trajectories in the 2N вГЎ dimensional phase space. The unit vectors of phase space, in general, correspond to the function and its derivatives with respect to time. Due to uniqueness of differential equations solutions with the necessary set of initial conditions the phase trajectories in the space of correct dimension do not intersect [2]. Crossing of the paths on the reconstructions of phase portraits shows forced reduction of dimension, for example, when using the method of main components. Thus, based on the one-dimensional time sampling and its analysis, one can get a complete picture of a system behavior, combining the dynamic regularities and the statistical characteristics.

The reconstruction procedure of phase trajectories and attractors is based on TakensвГЄ theorem. It is formulated for the embeddings of compact and closed sets [3, 4, 5]. Let A be a compact subset of the G-dimensional space X. Define the embedding subset A in m-dimensional space Y as a transformation of X to Y .The coincidence of two images of the elements, belonging to A, is possible only in case of equality of these elements. According to TakensвГЄ theorem, any smooth transformation X into Y will set the embedding A to Y space on the condition:

$$m \geqslant 2D_A + 1, \tag{1}$$

here D_A вГЎ is a fractal dimension of a set A. For sufficiently large experimental samples the phase trajectories reconstructed from the time series will have the same dimension and mathematical properties as the original physical system.

The experimental 1350 m slant path with small tilt was arranged in the industrial area. [6, 7].A collimated single-mode Gaussian beam of continuous radiation was used. Its power does not exceed 4 Watt. Registration of the intensity distribution at the path output is carried out under the conditions of primary control of spacial beam modulation, at a frame rate of not less than 1 kHz, the sampling frame size is 128x128 pixels, 8-bit width and 1 pt/mm scale. The vector of the first space moments and the corresponding vector of the tilt angles for each video frame will be defined by the discrete intensity distribution:

$$r_x[k] = \frac{\sum_{c=1,128}\sum_{r=1,128} cI(c,r)[k]}{\sum_{c=1,128}\sum_{r=1,128} I(c,r)[k]},\ r_y[k] = \frac{\sum_{c=1,128}\sum_{r=1,128} rI(c,r)[k]}{\sum_{c=1,128}\sum_{r=1,128} I(c,r)[k]}, \tag{2}$$

here r, c - is the number of rows and columns of video selection elements, $I(c,r)[k]$ - is the intensity distribution matrix for the k-th frame of the video sample.

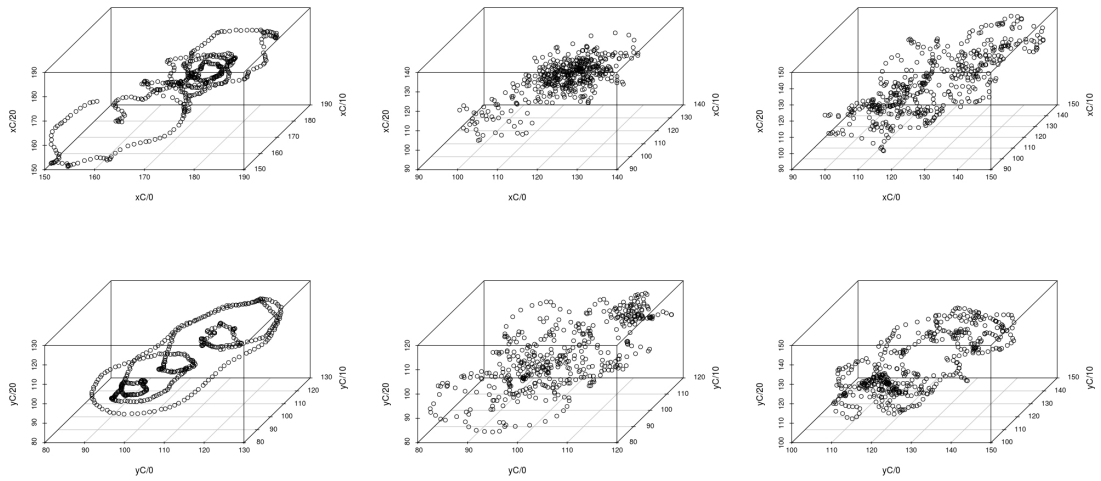

$\beta^2 = 0.3$ $\beta^2 = 1.0$ $\beta^2 = 2.6$

Figure 1: Phase trajectories for X (top) and Y (bottom) component of the first space moment.

The family of phase trajectories one can construct on the base of one dimensional equidistant in time sample by creating the two-dimensional and three-dimensional vectors with a variable time delay between the vector components:

$$(R[i], R[i-d])\,, \ \vec{R}^{(3)}[i] = (R[i], R[i-d], R[i-2d])\,. \tag{3}$$

The phase trajectory profile depends on the ratio of the analyzed system eigenfrequencies and the sampling step. If the ratio вГЎ $\tau s\omega_i = \pi/2$ (where τ вГЎ is a sampling step, ω_i вГЎ is one of the eigenfrequencies) is satisfied, the phase trajectory profile may be close to an ellipse. The optimum value of the delay interval one can select from additional conditions. For example, using the first minimum of the autocorrelation function of the analyzed time series or position of a local minimum of mutual information. According to a given length of the experimental sample N one can get $N - d(m-1)$ vectors, having the coordinates the set of which forms a phase trajectory [8, 9].
Examples of 3D phase portraits for three different turbulence modes characterized by three different values of Rytov parameter are shown in Fig.1. For all six reconstructions the time delay is equal to 10 ms, the coordinates of the vector components are given in millimeters. Note a significant topology difference for horizontal and vertical projections, well conspicuous eigenfrequency components for weakly developed turbulence, the beam characteristics transformation to dynamic chaos mode for moderate turbulence and the emergence of a coherent turbulence at the highest possible values of Rytov number (from those observed in the experiment). In a number of tasks the time scans of 2D phase trajectories can be informative, they allow to estimate the time spent by the system in a specified phase volume, to construct the movement approximations near the singular points of the phase trajectories.

2 Adaptive correction under random noise

Adaptive systems for the correcting of laser beams tilts are well developed for different applied problems, including the electromagnetic propagation through the atmospheric path of various lengths [10, 11]. The main criterion for the effectiveness of system performance leans on the statistics and the misalignment dynamics of the beam orientation and the working system axis. The elaboration of the adaptive correction algorithm, even in the simplest proportional version, demands the control of the beam profile, sample rate of the displacement sensors and the feedback coefficient in the process equation. At the first step of the experimental analysis let us replace the readings of a finite number of sensors of beam shift by a complete set of the meanings of intensity distribution matrix. Let's establish two variable parameter of the adaptive algorithm and one parameter for the beam size. The beam diameter will be varied in the range from 24 mm to 80 mm, by rearranging of the optical parameters of the collimating system.
The experimental results described were obtained under the conditions of a slightly perturbed atmosphere, Rytov parameter does not exceed 1.0 [7]. Sample rate of the displacements sensor varied in the range from 10 Hz to 100 Hz with steps 10 Hz, the feedback coefficient in the adaptive channel varied within $[0.1, 2]$. Here the unit coefficient corresponds to the total compensation of the recorded shift of the beam center for one positioning cycle. Let us represent the discrete equation for the vector projections $\vec{R} = (R_x, R_y)$ of the beam energetic center as follows:

$$\frac{R_i[n+1] - R_i[n]}{\Delta} = \frac{4}{S}(R_{0i} - R_i[n]) + N_i[n], \tag{4}$$

here Δ - is the sampling step, R_{0i} - are the coordinates of the target point on the registration plane, S вГУ is the pre-calibrated scale factor of an adaptive response, N_i вГУ is the anisotropic refractive component of the noise . The initial beam position for all video samples was located in the upper right corner of the working field, at the point with coordinates $(128, 1)$, the target coordinate corresponded to the value $(64, 64)$.

2.1 Variation of the scale correction coefficient

Let's analyze the change in structure of 2D phase trajectories for the fixed sampling rate of the displacements sensors equal to 30 Hz and the optimal beam grouping into a spot of 28 mm diameter. Fig.2 and Fig.3 demonstrate the results of experimental samples processing (scale factor is ranging from 2 -excessive response, to 28 - weak response). A significant difference in the phase portraits for horizontal and vertical correction directions was observed even for the simplest adaptive correction algorithm. For the chosen sampling rate and the compact beam grouping in the recording plane, the phase portraits for X-component demonstrate typical for the proportional algorithm self-oscillating mode under a small correction step and the static displacement in the case of large correction step [10, 11]. For the Y-component, the self-oscillatory mode for chosen sampling rate and the beam profile practically is not observed. The presented phase trajectories for the horizontal

component, show that the chosen range of the response step variations allows to investigate all three operating modes of the adaptive algorithm: self-oscillatory one in the range of the response step $S \subset [2, 8]$, quasiregular mode $S \subset [10, 20]$ and static displacement mode $S \subset [22, 28]$.

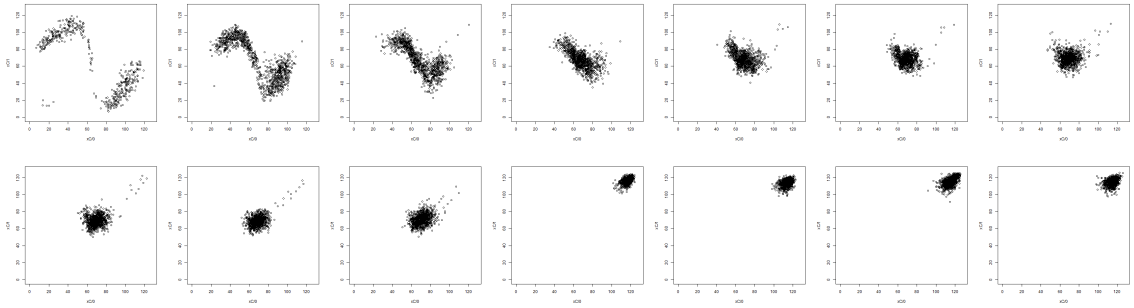

Figure 2: Phase trajectories for the horizontal direction of correction (a response step changes from 2 to 24)

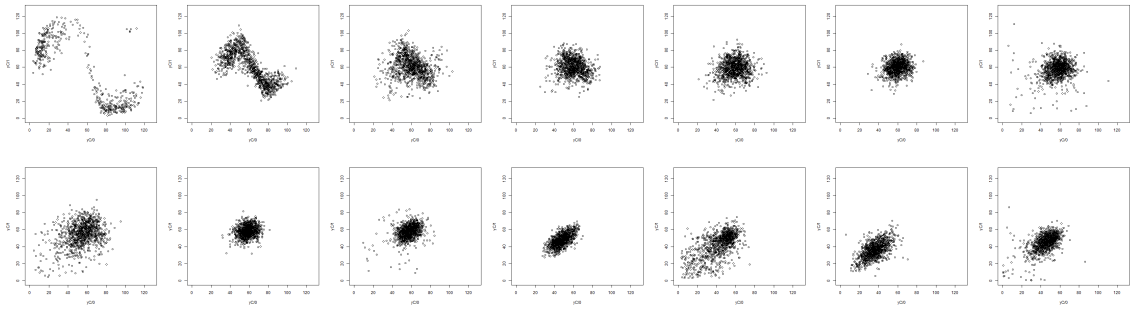

Figure 3: Phase trajectories for the vertical direction of correction (a response step changes from 2 to 24)

2.2 Variation of the sampling time

A random non stationary process in optical density variation of the atmosphere obtains a set of eigenfrequencies defined by both – the turbulent flows and acoustic industrial noise. Their interference spectrum can be determined using methods of nonlinear time-frequency analysis of one-dimensional time series for the components of the vector of the wave beam center, or deriving the spectrum of Poincare recurrence times for the beam phase trajectory (without adaptive correction).
Fig.4 and Fig.5 show the phase trajectories for the horizontal and vertical displacement components in the rate range from 10 Hz to 100 Hz with steps of 10 Hz. The beam grouping is chosen to be the same as for the analysis of the response to the variation of the scale correction coefficient - 28 mm in diameter, the correction scale is equal to 6. The frequency increases from left to right and from top to bottom. A characteristic feature of the observed phase portraits can be considered as the alternation of the regular auto-oscillatory and the unstable chaotic modes for the

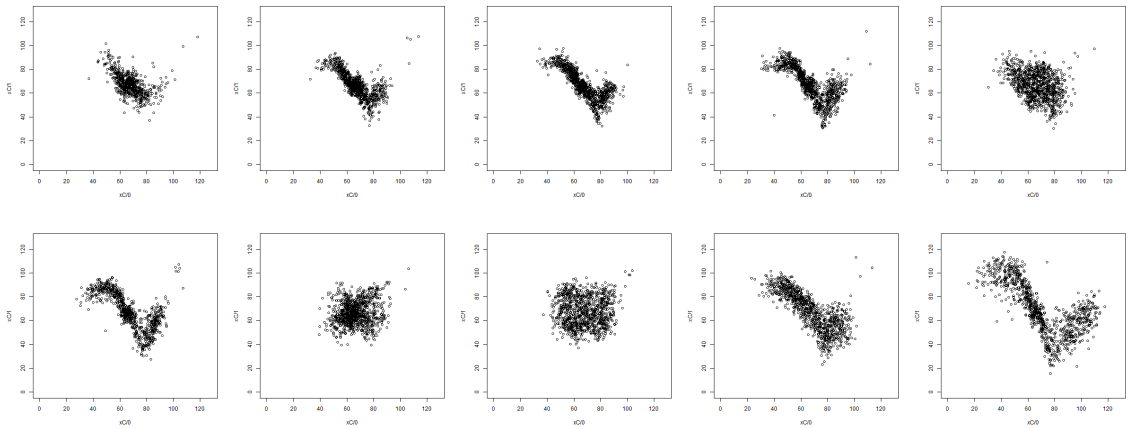

Figure 4: Phase trajectories for X with a frequency rate from 10 Hz to 100 Hz

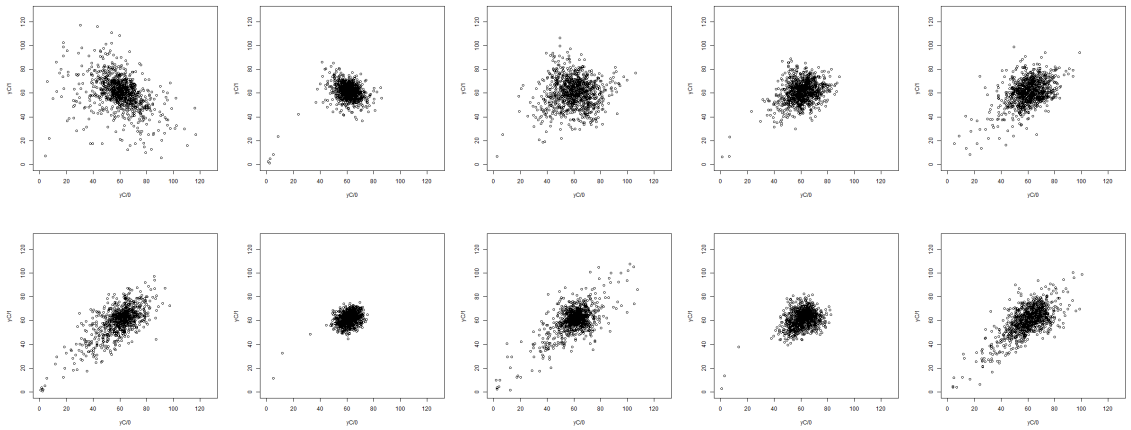

Figure 5: Phase trajectories for Y with a frequency rate from 10 Hz to 100 Hz

horizontal component and that of chaotic and regular stable quasi-stationary modes for the vertical component.

2.3 Variation of the linear beam dimension

On a number of occasions, the linear dimension of the beam can be a controlled parameter, just like the beam arriving angle. Used in the experiment targeting and focusing Gaussian wave beam allows to perform the similar transformation. It rearranges the positions of the lens group accurate within the wavelength of the radiation used [12]. Near the strangulation points of a wave beam in the observation plane it is possible to form the spots of different sizes. They can be both smaller then the size of the receiver or completely overlap its surface.

Spot sizes manipulation is reasonable under the conditions of relatively weak turbulence. The refractive diffusion in this case is relatively small. For the broadened beams propagating though an extended path even in a quiet atmosphere in their cross section there arises a local speckle structure generated by the stochastic distortions of the wave front [1]. Such a process can be observed in the two images

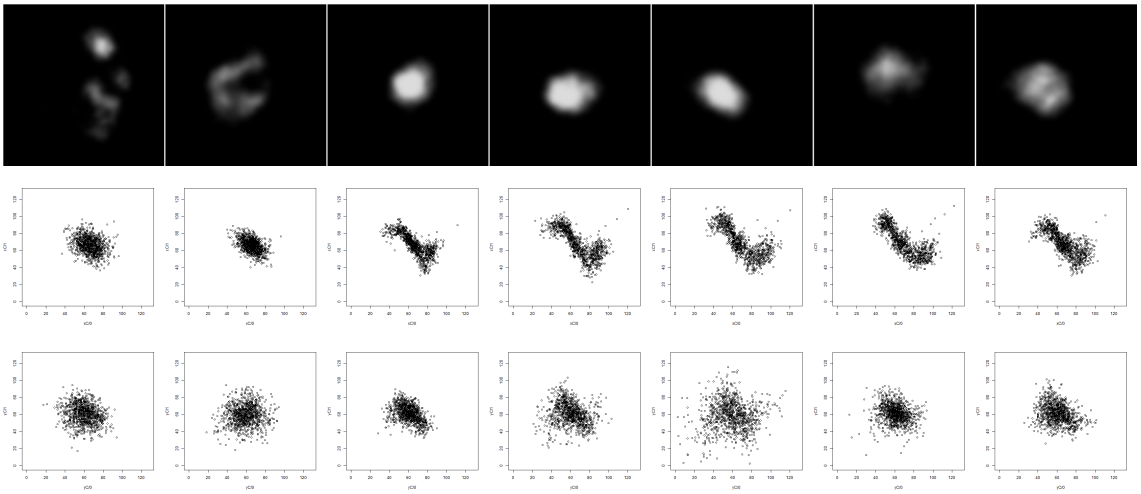

Figure 6: Video frames for the beams of different sizes (upper), phase portraits for the horizontal and vertical components of the beam center displacements (middle and bottom)

of the instantaneous intensity distributions shown in Fig.6 (left upper). Under the conditions of industrial interference the regular distortions of a characteristic spectrum in the range of low acoustic frequencies are often added. In this situation, it is reasonable to supplement the primary adaptive corrector with a frequency-selective stage, that cutting out the regular noise.

3 Geometry of the beam position detectors

The experimental results presented in the second part were obtained as an approximation of an "ideal" multichannel sensor that fixes the matrix of values of the instantaneous intensity distribution and transfers to the adaptive process the value of the beam center shift with a negligible time lag (not more than 1 millisecond). In reality one is not allowed to take the values from the entire operating field of the radiation detector. The most common options are those of the quadrant and peripheral or petal-shaped detectors. The number of parallel operating channels is limited by the decision time and the throughput of the feedback channel. In the experiment two geometric types of sensor position were tested, - a centered quadrant detector of various apertures and an eight-petaled peripheral detector with different spacing of a given petals size.
Let us define the quantitative evaluation of the time series correlations for coordinate and detector sweeps as the normalized values of the scalar multiplication of the corresponding sequences:

$$Corr_{X,Y}(\vec{D}\vec{R}) = \frac{\sum_{k=1}^{k=K} D_k R_k}{\sqrt{\left(\sum_{k=1}^{k=K} D_k^2\right)\left(\sum_{k=1}^{k=K} R_k^2\right)}} \tag{5}$$

here $\vec{D}, \vec{R}$ are the sequences of X or Y readings of the detector or the location of the

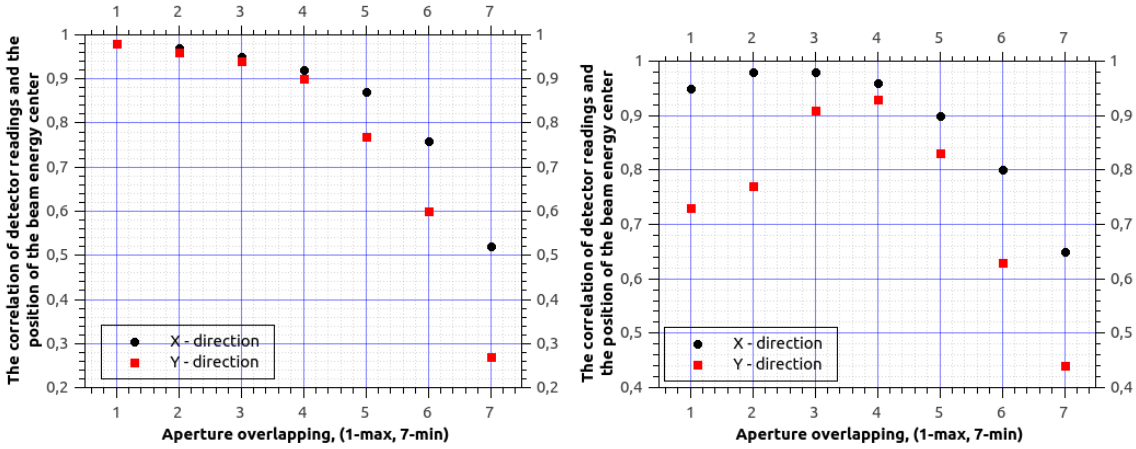

Figure 7: Correlation of the quadrant detector readings (left), the peripheral 8-lobe detector readings (right) and the position of the beam energy center for time sweeps

beam energy center. The length of the sequence corresponds to the video sample duration. The correlation value depends on the degree of the beam profile distortion, the beam splitting into fragments, absorption and scattering at the path. The typical dependencies of the detectors readings correlation on the size of the quadrant (for the quadrant detector) and the separation of the 10ptx10pt petal-sensors for the petal one are shown in Fig.7. The basic properties of the correlation characteristics for detectors of different geometries are retained in various realizations of the beam. Notably:

- a difference of the correlation value for the vertical and horizontal components of the beam displacements from the center of the operating platform,
- the existence of an optimal radius of the petals separation from the center for a particular turbulent state of the atmospheric path.

The adaptive correction process of the beam center position was compared for the quadrant and peripheral geometry of the sensor layout and the results are presented in Fig.8. The first and the third rows show the beam state sequences at the registration plane (a sampling rate is equal to 30 Hz, that corresponds to the sampling rate of the adaptive algorithm). The first and the second columns of the phase portraits correspond to the horizontal and vertical components of the center of the beam displacement, the third and the fourth columns depict the similar displacements for the proportional adapter (the readings of a square detector), the fifth and the sixth columns represent the results got for the eight-petaled peripheral detector.
As it is shown by comparative analysis of the adaptive corrector work under different sensor geometry in a wide range of the scale correction factor S, the sample intervals Δ and at various spot sizes, the peripheral detection has a low failure threshold in the cases of self-oscillatory and chaotic modes. The dispersion of the distribution function for the coordinates of the beam center in the case of quadrant positioning is much less, then that for the peripheral positioning. However, the peripheral detection practically exclude the static displacement of the beam center in a wide range of the adaptive corrector settings.

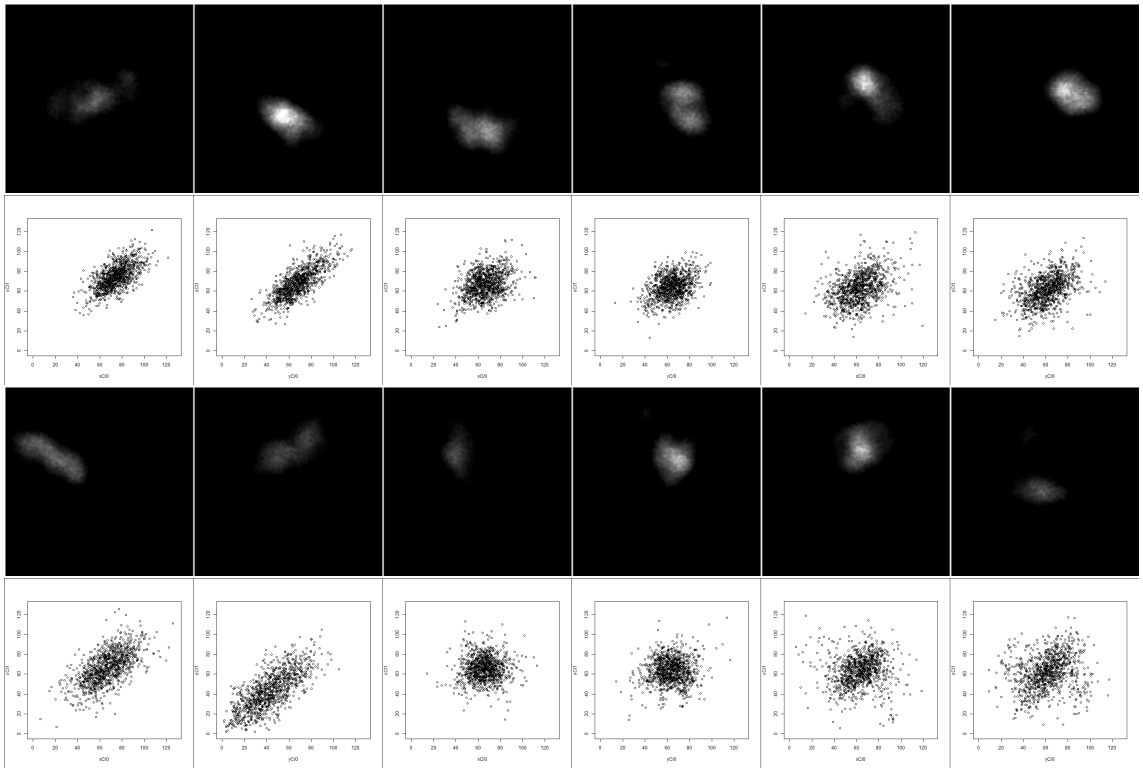

Figure 8: Examples of video frames sequences (the first and the third rows) and corresponding to them phase portraits (the second and the fourth rows)

Conclusion

The experimental study of the adaptive correction process for the first spatial moments of the beam intensity distribution at the output of a long atmospheric path was carried out. The results allow to formulate a number of statements about the stochastic and dynamic properties of the process:

- The dynamics and statistics of refraction distortions for the horizontal and vertical directions are significantly different. Accordingly the settings of the adaptive correction algorithms for orthogonal directions must be different.

- The scanning of the sampling rate for beam position detectors and the corrective procedures accomplishment reveals multiple changes of the beam movement modes for the beam center (localized near the center of the recorder, self-oscillatory, or stochastic one). They are related to the structure of the low-frequency component of the beam spot spectrum displacements in the range up to 100 Hz,

- Regular and spontaneous changes of the size of the registered beam spot under the influence of atmospheric refractive noise lead to changes in the modes of the beam center motion.

Acknowledgements

The work was supported by Russian Foundation for Basic Research. RFBR Project a-15-08-07484.

References

[1] Klyatskin V. I, *A statistical analysis of the coherent phenomena in stochastic dynamic systems*, Editorial of URSS, Moscow 2015.

[2] ArnolKed V. I., *Geometrical methods in the theory of ordinary differential equations*, Vol. 250, Springer Science and Business Media, 2012.

[3] Takens F., "Detecting Strange Attractors in Turbulence," *Lecture Notes in Math*, Vol. 898, Springer, New York, 1981.

[4] Kennel B., Brown R., Abarbanel H.D.I., "Determining embedding dimension for phase-space reconstruction using a geometrical constructions," *Phys. Rev. A* , Vol. 45, 3403, 1992.

[5] Hong-Guang, M. A., H. A. N. Chong-zhao, "Selection of Embedding Dimension and Delay Time in Phase Space Reconstruction," *JFrontiers of Electrical and Electronic Engineering in China*, No. 1, 111–114, 2006.

[6] Kapranov V. V., Matsak I. S., Tugaenko V. Yu, Blank A. V., Suhareva N. A., "Atmospheric turbulence effects on the performance of the laser wireless power transfer system," *Proc. SPIE 10096 Free-Space Laser Communication and Atmospheric Propagation XXIX* , 100961E (February 24, 2017); doi:10.1117/12.2252013

[7] Blank A. V., Kapranov V. V., Mikhailov R. V., Suhareva N. A., Tugaenko V. Yu, "Non-linear dynamics of positional parameters of the collimated coherent beam at the end of the long atmospheric path," *Proceedings of PIERS*, 2017 (in press)

[8] Noakes L., "The Takens embedding theorem," *International Journal of Bifurcation and Chaos*, Vol. 1, No. 4, 867–972, 1991.

[9] Sauer T., J. Yorke, V. Casdagli, "Embedology," *Journal of statistical Physics*, Vol. 65, No. 3, 579–616, 1991.

[10] Shanin O. I., *Adaptive optical systems of inclinations correction. Resonance adaptive optics*, Technospera, Moscow 2013.

[11] Kapranov M. B., Tomashevsky A. I., *The regular and chaotic dynamics of nonlinear systems with discrete time*, MEI publishing house, Moscow 2009.

[12] Kapranov V. V., Matsak I. S., Tugaenko V. Yu, Blank A. V., Suhareva N. A., "Super narrow beam shaping system for remote power supply at long atmospheric path," *Proc. SPIE 10090, Laser Resonators, Microresonators, and Beam Control XIX* , 100900U (February 20, 2017); doi:10.1117/12.2250752

Arkadiy V. Blank, S.P. Korolev Rocket and Space Corporation "Energia",Russia,Moscow
M.V. Lomonosov State University, Russia
Vitaliy V. Kapranov, S.P. Korolev Rocket and Space Corporation "Energia", Russia
Ruslan V. Mikhailov, Moscow M.V. Lomonosov State University, Russia
Natalia A. Suhareva, Moscow M.V. Lomonosov State University,Russia
Vjacheslav Yu. Tugaenko, S.P. Korolev Rocket and Space Corporation "Energia", Russia

Flow of viscoplastic suspensions in a hydraulic fracture: implications to overflush

Sergei S. Boronin, Andrei A. Osiptsov, and Jean Desroches

S.Boronin@skoltech.ru

Abstract

The study is devoted to modeling of multiphase flows of immiscible viscoplastic (or yield-stress) fluids in a hydraulic fracture. In the framework of the lubrication approximation, three-dimensional Navier-Stokes equations are reduced to hyperbolic transport equations for the fluid tracers and a quasi-linear elliptic equation in terms of the fluid pressure. The governing equations are solved numerically using the finite-difference approach. A parametric study of the displacement of Bingham fluids in a Hele-Shaw cell is carried out. It is found that fingers developed through the pillar of a yield-stress suspension trigger the development of unyielded zones. An increase in the Bingham number leads to an increase in the so-called finger shielding effect, which manifests itself via an increase in the overall finger penetration zone and a decrease in the total number of fingers. The effect of flow parameters on the displacement of hydraulic fracturing proppant-laden suspension by a clean fluid in the vicinity of the perforation zone is carried out. This particular case is considered in application to overflush at the end of a stimulation treatment, when a small portion of a thin clean fluid is injected to wash out the particles from the wellbore into the fracture. It is found that an increase in the yield stress and the viscosity contrast between the fracturing and the overflush fluids typically reduces the area of the cavity thus mitigating the risk of loosing the conductive path between the wellbore and the fracture after the fracture closure.

1 Introduction

Proppant transport models incorporated into existing hydraulic fracturing simulators describe the flow of particle-laden suspension inside a hydraulic fracture in the framework of the l;ubrication approximation using the power-law rheological model (see [7]). Hydraulic fracturing suspensions with large concentration of solids or fibers show a yield-stress behavior in rheological experiments ([8, 5], which is not taken into account in the proppant transport models implemented into commercial simulators of hydraulic fracturing.

A state of the art in the modeling of injection of particle-laden suspensions into hydraulic fractures is the family of 2D width-averaged models based on the lubrication

approximation to Navier-Stokes equations [8, 7, 7, 8]. In the regime of non-inertial settling, the momentum conservation equation for particles is reduced to an algebraic relation for the particle velocity slip in the vertical direction given by the Stokes formula with a correction for hindered-settling effects due to a finite particle volume fraction. In the case of Newtonian suspension rheology, the total momentum conservation equation for the suspension is reduced to the linear expression of the fluid (or mixture) velocity through the pressure gradient (similar to the Darcy law, hence a well-known analogy between filtration and a flow in a Hele-Shaw cell). The dependence of the width-averaged fluid velocity on the pressure gradient is nonlinear, if the rheology of the carrier fluid or the suspension as a whole is non-Newtonian (see, e.g., [11, 9, 10]).

A large number of papers deal with the Saffman-Taylor (S-T) instability accompanying displacement of fluids in a narrow plane channel or annulus, starting from the pioneering study by Muskat [13]. The instability at the interface between the fluids is triggered when a high-viscosity fluid is displaced by a low-viscosity one. Note that in the absence of a certain "cut-off" mechanism (molecular diffusion or surface tension), the growth rate of disturbances at the interface between the fluids increases unboundedly with a decrease in the wavelength. Review of studies on the S-T instability in Newtonian fluids is presented in [12].

In the present study, we continue to analyze the displacement of viscoplastic fluids in a Hele-Shaw cell approximating a hydraulic fracture. This work was started in [1]. A parametric study of different injection scenarios of yield-stress fluids is carried out. In particular, we analyzed the effect of flow parameters on the shape and dimensions of the particle-free zone developed during overflush at the end of a hydraulic fracturing treatment. It is the final stage of a hydraulic fracturing operation, when the proppant-laden slurry is displaced by a low-viscosity particle-free fluid in order to clean the well and perforations.

2 Problem Formulation

We consider the flow of immiscible incompressible fluids with the Bingham rheology in a narrow Hele-Shaw cell approximating a hydraulic fracture. A detailed derivation of 2D width-averaged governing equations is presented in [1], while here we present only the final system of equations in the non-dimensional form:

$$\frac{\partial wC_i}{\partial t} + \nabla \cdot (wC_i\mathbf{v}) = -2C_i v_l,\ i = 0,\ 1,\ 2 \tag{1}$$

$$\nabla \cdot \left(\frac{w^3}{12\mu_m} G(\phi) \left[\nabla p + \mathrm{Bu}\rho_m \mathbf{e}_y \right] \right) = \frac{\partial w}{\partial t} + 2v_l, \tag{2}$$

$$\mathbf{v} = -\frac{w^2}{12\mu_m} G(\phi)\nabla p,\ G(\phi) = 1 - 3\phi + 4\phi^3,\ \phi = \frac{\mathrm{Bn}\tau_m}{w|\nabla p|}, \tag{3}$$

$$\rho_m = C_0 + \zeta_1 C_1 + \zeta_2 C_2,\ \mu_m = C_0 + \xi_1 C_1 + \xi_2 C_2,$$

$$\zeta_i = \frac{\rho_i}{\rho_0},\ \xi_i = \frac{\mu_i}{\mu_0},\ \mathrm{Bu} = \frac{\rho_0 g d^2}{\mu_0 U},\ \mathrm{Bn} = \frac{\tau_0 d}{U\mu_0}$$

Here, Cartesian coordinate system Oxy is introduced in the cell plane, so that y-axis (with the basis vector $\mathbf{e}_y$) is vertical and origin O is located in the bottom left corner of the computational domain; C_i are the fluid tracer concentrations (with i being the number of fluid, so that $i = 0$ corresponds to the yield-stress fluid filling the slot initially); $w(x, y, t)$ is the width of the Hele-Shaw cell (currently it is a prescribed function of coordinates and time, while in the model describing the hydraulic fracture propagation, w is obtained via coupling the hydrodynamic equations describing the flow inside a hydraulic fracture with geomechanics equations describing the fracture growth [7]); $\mathbf{v}$ is the width-averaged fluid velocity; v_l is the velocity of fluid leak-off through the porous walls; G is the correction to fluid mobility due to the yield-stress rheology ($G = 1$ for Newtonian fluid); differential operator '∇' acts in the (x, y) plane as we applied the averaging procedure along the cell width. The flow scales are as follows: L is the cell length, U is the scale of the injection velocity, d is the cell width scale, ρ_0 is the fracturing fluid density, μ_0 and τ_0 are the fracturing fluid plastic viscosity and yield stress, respectively; g is the gravity acceleration. Non-dimensional parameters are as follows: Bu is the Buoyancy number, Bn is the Bingham number; ζ_i is the fluid density ratio; ξ_i is the fluid viscosity ratio. The flow domain according to the scaling introduced above is $(x, y) \in [0,\, 1] \times [0,\, H/L]$, where H is the height of the Hele-Shaw cell.
For hyperbolic equations (1), we impose initial distribution of fluid tracers and boundary conditions for fluid tracers and velocity at the inlet:

$$x = 0: \;\; C_i^{in} = C_i(y, t),\; i = 0,\, 1,\, 2; \tag{4}$$

$$t = 0: \;\; C = C_{i0}(x, y),\;\; i = 0,\, 1,\, 2 \tag{5}$$

The quasi-elliptic equation for pressure (2) requires either Neumann or Dirichlet boundary conditions to be specified at the boundaries of the flow domain. At the top and bottom boundaries, we impose the no-flow condition. There is a specified velocity at the inlet segment of the left vertical boundary. We assume that the flux at the right vertical boundary is horizontal (which is the variant of a "soft" non-reflecting outlet boundary condition). The corresponding boundary conditions for pressure are formulated as follows:

$$x = 0: \;\; \frac{\partial p}{\partial x} = -\frac{12\mu_m}{G(\phi)w^2}, \tag{6}$$

$$x = 1: \;\; \frac{\partial p}{\partial y} = -\mathrm{Bu}\rho_m(1, y) \Leftrightarrow p(1, y) = -\mathrm{Bu}\int\limits_0^y \rho_m(1, s)\mathrm{d}s \tag{7}$$

$$y = 0 \text{ and } y = h: \;\; \frac{\partial p}{\partial y} = 0. \tag{8}$$

Here, $h = H/L$ is the channel height-to-length ratio, and we assumed that the velocity at the inlet is constant, so that in a dimensionless form it is unity. Note that for a shorter notation, the boundary conditions (4–8) are formulated for the flow configuration when the inlet zone occupies the entire height of the fracture.

3 Numerical Implementation and Validation

The governing equations (1–3) coupled with the boundary and initial conditions (4–8) are solved numerically using the finite-difference method on a rectangular staggered grid. The advection equations are solved using the second-order TVD flux-limiting scheme, while the quasi-linear elliptic pressure equation is solved using the iterative process with the multigrid solver applied to the solution of a linearized equation. The details of numerical algorithm and thorough validation of the model (1–3) are presented in [1]. In particular, the model was validated against the following experiments made in Hele-Shaw cells: (i) gravitational slumping of a heavy oil in a confined cell; (ii) Saffman-Taylor instability during the displacement of a water-glycerin solution by water; (iii) set of experiments with the channeling of Newtonian and power-law fluids through the cell filled initially with a yield-stress fluid. The simulations presented below are carried out using the 513×513 mesh.

4 Results and Discussion

A parametric study of the interaction between viscoplastic and viscous fluids in a Hele-Shaw cell is conducted using the research code based on the model and its implementation described above. It is found that when a yield-stress fluid is displaced by a high-viscosity Newtonian fluid (so that there is no Saffman-Taylor instability at the interface), the viscoplastic fluid behaves very similar to the viscous fluid (Fig. 1*a,b*). The fingers of a low-viscosity fluid penetrating through the viscoplastic fluid trigger the development of unyielded zones (Fig. 1 *c,d*).

The effect of Bingham number on the Saffman-Taylor instability between the yield-stress fluid and the viscous fluid is studied (see Fig. 2). It is found that an increase in the Bingham number intensifies the finger shadowing effect: the growth rate of small fingers is damped, while the longer fingers grows faster and the total number of fingers is decreased. As a result, the finger penetration length is increased with an increase in the Bingham number.

A multistage hydraulic fracturing job in shales (typically in the U.S. Land) is usually followed by an injection of a small portion of particle-free low-viscosity fluid to clean up the well from the proppant. This stage is called an overflush. During this process, a portion of the clean fluid enters the hydraulic fracture and displaces the particle-laden suspension away from the perforations. Therefore, there is a risk of fracture closure in this proppant-free unsupported cavity, which would result in a dramatic decrease in the fracture conductivity. We carried out a sensitivity study of the shape and the area of the particle-free cavity developed during the displacement of a particle-laden suspension by a clean fluid in the vicinity of fracture inlet zone. We found that there are three qualitatively different displacement regimes, namely: (i) the slumping-dominated scenario Fig. 3 *a* ; (ii) an intermediate scenario Fig. 3 *b*; and (iii) the fingering-dominated scenario Fig. 3 *c*. The slumping-dominated regime provokes the development of a large particle-free zone at the lop of the hydraulic fracture, which would result in a significant decrease in the productive fracture area after closure. Among the other two regimes, the smallest area of the particle-free cavity is found in the case of a finger-dominated regime, which is achieved by an

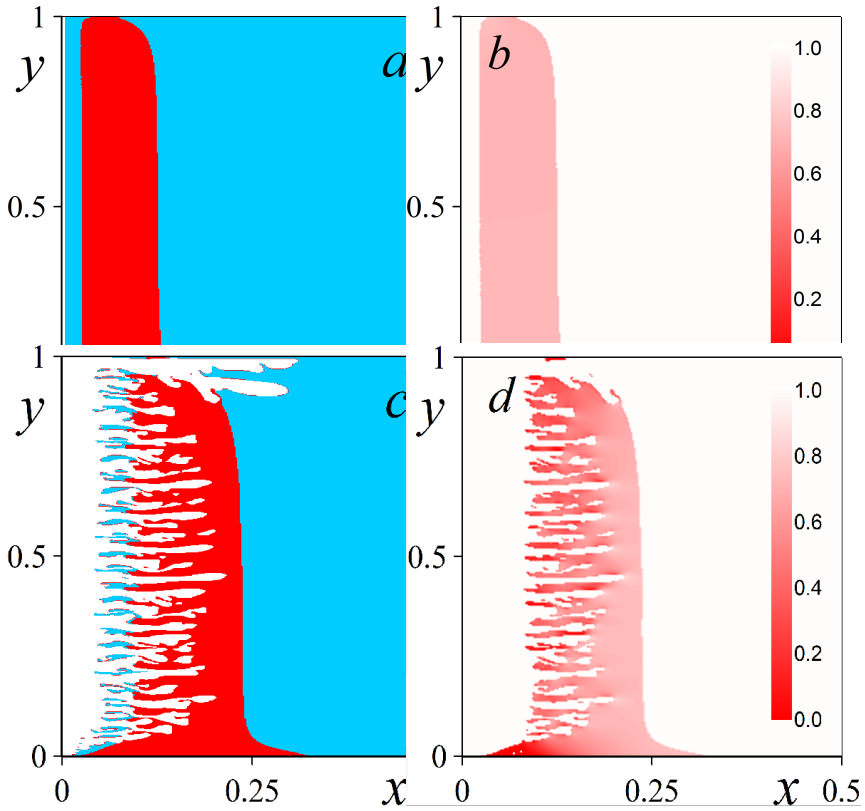

Figure 1: Distribution of fluids (a, c) and parameter G (3) describing the unyielding of the viscoplastic Fluid 0 (b, d) in a plane channel during a certain injection sequence. Viscoplastic Fluid 0 is red, high-viscosity Fluid 1 is blue and low-viscosity Fluid 2 is white. The inlet velocity is $4.76 \cdot 10^{-2} m/s$, $\xi_1 = 1.43$, $\xi_2 = 8.72 \cdot 10^{-4}$, $\zeta_1 = \zeta_2 = 0.5$, Bu $= 12.9$, Bn $= 1.43$, $t = 0.122$ (a, b) and $t = 0.235$(c, d).

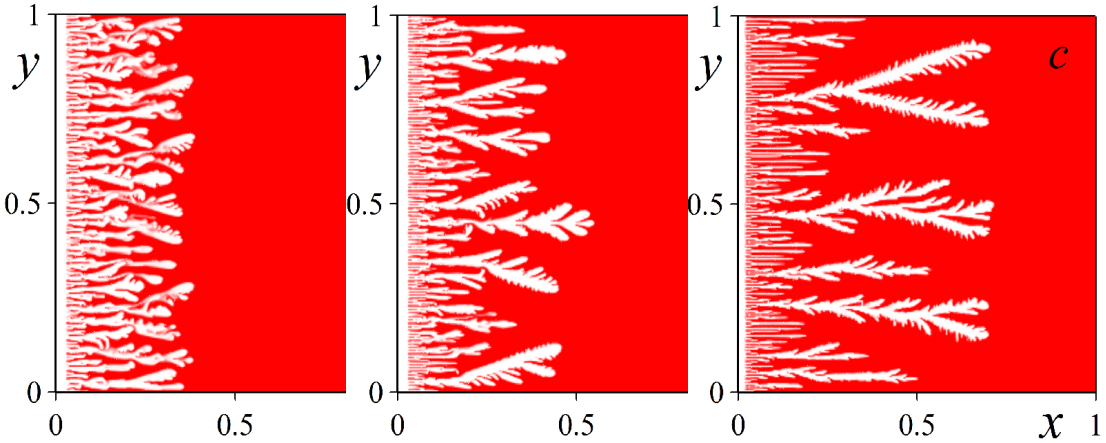

Figure 2: Effect of Bingham number on the fingering of a viscous fluid (white) through the viscoplastic fluid (red) for Bn $= 0.36$ (a), Bn $= 1.43$ (b) and Bn $= 5.72$ (c). The inlet velocity is $4.76 \cdot 10^{-2} m/s$, $\xi = 8.72 \cdot 10^{-4}$, $\zeta = 1$ and $t = 0.203$.

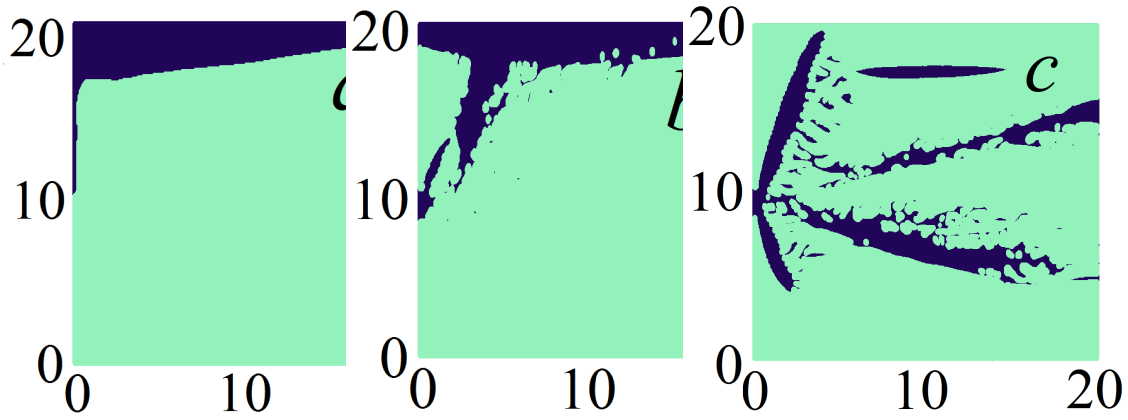

Figure 3: Typical regimes of displacement of a high-viscosity suspension by a low-viscosity fluid in the vicinity of perforations during hydraulic fracture overflush.

increase in the fluid viscosity ratio, injection rate or suspension yield stress.

5 Conclusions

In the framework of a lubrication approximation, the displacement of a viscoplastic fluid by viscous fluids in a Hele-Shaw cell is studied. It is found that the yield-stress rheology of the fluid results in a modification to the fluid mobility, which is the coefficient of proportionality between the pressure gradient and the width-averaged fluid velocity. In contrast to the flow of Newtonian fluids in narrow channels, the pressure equation describing the flow of viscoplastic fluid is strongly non-linear.

Based on the numerical simulations, we carried out the parametric study of interactions between viscous and viscoplastic fluids in a Hele-Shaw cell. It is found that when the yield-stress fluid is displaced by a viscous one and the interface is flat, the viscoplastic fluid behaves very similar to a viscous fluid. The instability triggered at the interface between the fluids leads to the development of unyielded zones in the viscoplastic fluid. During the displacement of a yield-stress fluid by a low-viscosity fluid, an increase in the Bingham number leads to an increase in the finger penetration length and a decrease in the total number of fingers.

The overflush stage at the end of a hydraulic fracturing treatment is studied with the aim to minimize the area of a particle-free zone in the vicinity of perforations inside a hydraulic fracture, which mitigates the risk of loosing well-to-fracture hydraulic connection. Numerical simulations of the displacement of a viscous or a viscoplastic fracturing fluid by a low-viscosity overflush fluid in the hydraulic fracture demonstrated that there are three qualitatively different overflush scenarios: (i) slumping-dominated; (ii) intermediate; (iii) fingering-dominated. The smallest area of particle-free zone in the vicinity of perforations is achieved in the fingering scenario, which occurs when either there is a large viscosity contrast between the fracturing and the overflush fluids, or the fracturing fluid shows a strong yield-stress behavior.

Acknowledgements

Startup funds of Skolkovo Institute of Science and Technology are gratefully acknowledged. The authors are thankful to Schlumberger for the permission to publish.

References

[1] Boronin, S. A., Osiptsov, A. A., Desroches, J. 2015 Displacement of yield-stress fluids in a fracture, Intl. J. Multiphase Flow **76**, 47–63.

[2] De Zeeuw, P. M. 1990 Matrix-dependent prolongation and restrictions in black-box multigrid solver, J. Comput. Appl. Math. **33**, 1–27.

[3] Adachi, J., Siebrits, E., Peirce, A., & J. Desroches, 2007 Computer simulation of hydraulic fractures. Int. J. of Rock Mech. and Mining Sci. **44**(1), 739–757.

[4] Economides, M.J., Nolte, K.G. 2000 Reservoir Stimulation. Third Edition. Wiley.

[5] Lecampion, B., Garagash, D. I. 2014 Confined flow of suspensions modelled by a frictional rheology. Journal of Fluid Mechanics **759**, 197–235.

[6] Pearson, J. R. A. 1994 On suspension transport in a fracture: framework for a global model. Non-Newtonian Fluid Mech. **54**, 503–513.

[7] Hammond, P. S. 1995 Settling and slumping in a Newtonian slurry, and implications for proppant placement during hydraulic fracturing of gas wells, Chem. Eng. Sci. **50**(20), 3247.

[8] Boronin, S. A., Osiptsov, A. A. 2010 Two Continua Model of Suspension Flow in a Hydraulic Fracture. Doklady Physics. **55**(4), 192–202.

[9] Frigaard, I. A., Howison, S. D., Sobey, I. J. 2010 On the stability of Poiseuille flow of a Bingham fluid. J. Fluid Mech. **263**, 133–150.

[10] Gorodtsov, V. A., Yentov, V. M. 1997 Instability of the displacement fronts of non-Newtonian fluids in a Hele-Shaw cell. J. Appl. Maths Mechs. **61**(1), 111–126.

[11] Bittleston, S. H., Hassager, O. 1992 Flow of viscoplastic fluids in a rotating concentric annulus. J. Non-Newtonian Fluid Mech. **42**, 19–36.

[12] Homsy, G. M. 1987 Viscous fingering in porous media. J. Non-Newtonian Fluid Mech. **19**, 271–311.

[13] Muskat, M. 1934 wo Fluid Systems in Porous Media. The Encroachment of Water into an Oil Sand Morris Muskat. Journal of Applied Physics. **5**, 250–264.

Sergei S. Boronin, Skolkovo Institute of Science and Technology, Nobel Street 3, 143026 Moscow, Russia
Andrei A. Osiptsov, Skolkovo Institute of Science and Technology, Nobel Street 3, 143026 Moscow, Russia

Jean Desroches, Services Petroliers Schlumberger, Le Palatin 1, 1 cours du Triangle, 92936 Paris La Défense Cedex, France

Pseudo 3D hydraulic fracturing model with account for vertical viscous dissipation

S. Budennyy, R. Nikitin, R. Sidtikov,
A. Bochkarev, A. Erofeev, D. Mitrushkin, V. Demo

budennyy.sa@cet-mipt.ru

Abstract

A great number of hydraulic fracturing (HF) models exists which are differentiated with complexity and physical accuracy. Most straightforward 2D models (PKN, KGD, radial models) are reasonable while express analysis or first estimations fulfilling only as they are restricted with geometrical shapes significantly and consequently are not of interest in HF design treatment. At the same time, fully 3D models or planar 3D models are most accurate ones from physical point of view but cause great times costs in numerical simulation.

Pseudo 3D (P3D) models play a role of compromise between two previously examined cases. Key results of P3D model fracture growth in multi-layered lithology with focus on proppant transport mechanism and tip-screen out are examined in [1] . To reduce the consequences of assumptions various efforts to enhance P3D models are made ([2], [3], [4], [5], [6]). In particular, pressure profile is assumed to be one-dimensional (along the fracture growth direction) within the P3D model. Consequently, the fluid flow in lateral direction is not examined, viscous dissipation is ignored in this direction and it turns into fracture height overestimating (toughness regime is observed only). To enhance the model authors in [5] account for viscous dissipation via so-called apparent fracture toughness that depends on propagation velocity on both lower and upper fracture tips. However, the case of symmetric three-layers lithology is investigated only.

The purpose in the present project is to generalize the concept of apparent fracture toughness for multi-layered lithology with arbitrary properties. Numerical results present significant difference in fracture width profile between classic P3D model and enhanced one (about 10 % of difference can be achieved). The enhancement is demonstrated in the frame of the problem of unwanted breakthrough layers that may lead to water or gas coning breakthrough.

1 Introduction

Enhanced pseudo-3D (EP3D) hydraulic fracture model is based on cell-based P3D model with non-equilibrium height growth. EP3D model aims to account for vis-

cous dissipation in vertical growth which is essential as break-through into high permeability layers takes place. Cell-based P3D model accounts for height growth mechanism in multi-layered lithology. Its enhanced modification represents the fracture as a series of connected cells with a plane strain and with account for excessive pressure inside each cell. The fracture opening profile and height are calculated analytically for the given piece-wise lithology (stress intensity, YoungвЂ™s modulus, PoissonвЂ™s ratio and fracture toughness). Initial growth state of each cell is examined via PKN model while its further growth takes place in accordance with P3D model.

2 Non-equilibrium height assessment

In the presence of significant vertical fluid flow within the fracture (accompanied with instant breakthrough into neighboring layers) the equilibrium height model is not reasonable. To bypass this problem the non-equilibrium growth model is applied: the excessive pressure is considered to depend on fracture tip velocity. The relation for this dependence is obtained at [7] and is given as follows

$$P_{net} = E' \frac{2\sqrt{2}(2+n)}{\pi(2-n)} \left[\frac{K}{nE'h^n} \left(\frac{cos[(1-\beta)\pi]}{sin(\beta\pi)} \right)^{n+1} \left(\frac{2n+1}{n(2+n)} \right)^{n} \right]^{1/(2+n)} v_{\pm}^{n/(2+n)}, \tag{1}$$

where u_{tip} - is a fluid velocity at the fracture tip, n and K are coefficients of power-law rheology, $\beta = 2/(2+n)$ is an auxiliary coefficient, h is a fracture height, $E' = E/(1-\nu^2)$, E is Young modulus, is Poisson coefficient.
The relationship governing net pressure P_{net} and stress intensity factor K_{Ic} is the following [8]

$$P_{net} = \frac{K_{Ic}}{\sqrt{\pi h/2}}. \tag{2}$$

The stress intensity coefficients at upper and lower fracture of tips $K_{I_{u/l}}$ are the following

$$K_{I_{u/l}} = \sqrt{\frac{\pi h}{2}}(p - \sigma_n + \rho_f g(h - \frac{h}{2} \pm \frac{h}{4})) + \sqrt{\frac{2}{\pi h}} \sum_{i=1}^{n-1} (\sigma_{i+1} - \sigma_i)(\frac{h}{2} \arccos(\frac{h-2h_i}{h}) \pm \sqrt{h_i(h-h_i)}) \tag{3}$$

where p is a pressure averaged along the fracture, h is a distance between lower fracture tip and its center, h_i is a distance between lower fracture tip and upper boundary if the i-th layer, σ_n and σ_i are stress at upper fracture tip and stress at i-th layer, respectively.
The workflow for non-equilibrium height assessment includes the following steps:

1. to estimate zero-order magnitude of both lower and upper fracture tip velocities for a given cell;

2. to find new positions of both lower and upper fracture tips for a given time step using received velocities;

3. using relations (3) to estimate stress intensity factors (SIF) at fracture tips with account for fracture toughness at those layers which are intersected with fracture tips;

4. using relations (1) and (2) to define such tip velocities that give us the values of SIF obtained at the previous step;

5. to accept received velocities and to repeat the whole workflow till the stability is respected.

As a result both lower and upper fracture tip velocities are estimated. Further new positions of grid nodes are estimated that define a new non-equilibrium height.
To get the fracture growth dynamics in addition t geo-mechanical relations one is to examine non-newtoninan liquid flow inside the fracture channel. The local conservation of fluid flow along the fracture channel with continuous cross section $A(x,t)$ is defined as follows

$$\frac{\partial A}{\partial t} + \frac{\partial Av}{\partial x} + q_l = 0,$$

where q_l is Carter's losses which is defined as follows [9]

$$q_l = \frac{2\widetilde{C}_l h}{\sqrt{t - \tau(x)}}$$

where τ is the time at which leak-off velocity was exposed, $\widetilde{C}_l$ is an effective leak-off coefficient, defined as weighted for all lithology layers

$$\widetilde{C}_l = \frac{1}{h_f} \int C_l dz.$$

The system is closed with following initial (initial zero opening profile) and boundary conditions (flow rate at the inlet and no flow condition at the fracture tip)

$$w(x, t = 0) = 0, \qquad q(x = 0, t) = q_0(t), \qquad q(x = L, t) = 0.$$

3 Numerical results

The system of equations is solved numerically using explicit gradient iteration scheme based on Newton's method. At each time step the hydraulics solution in iterative manner converges to the truth one by updating geo-mechanical parameters. This approach ensures the growth of numerical stability and reasonable linear convergence of numerical solution. Besides, the time step is adjusted in such a way the time cost of calculation keeps reasonable.
The strategy of space and time grid construction is chosen as follows. The number of grid points in vertical direction is fixed, its meshing is uniform. As for the lateral direction grid the idea is based on auto-growing calculation domain. At initial time the domain represents three sequential cells: well cell, fracture cell, tip cell. In the first and last cells the boundary conditions for slurry rate and zero flow rate are set, respectively. A new fracture cell is being added if the fracture opening at this cell width exceeds a certain level. Spatial grid cells are situated in the region where the fracture physically exists only while in most cases the calculation domain is predefined and consequently unwanted cells are involved. The time grid is non-uniform. The time derivative is approximated by the implicit first order Euler scheme while the fluxes at the cell faces are approximated with backward scheme. In addition, the fracture geometry changing is defined in accordance with criteria conditions for its growth.

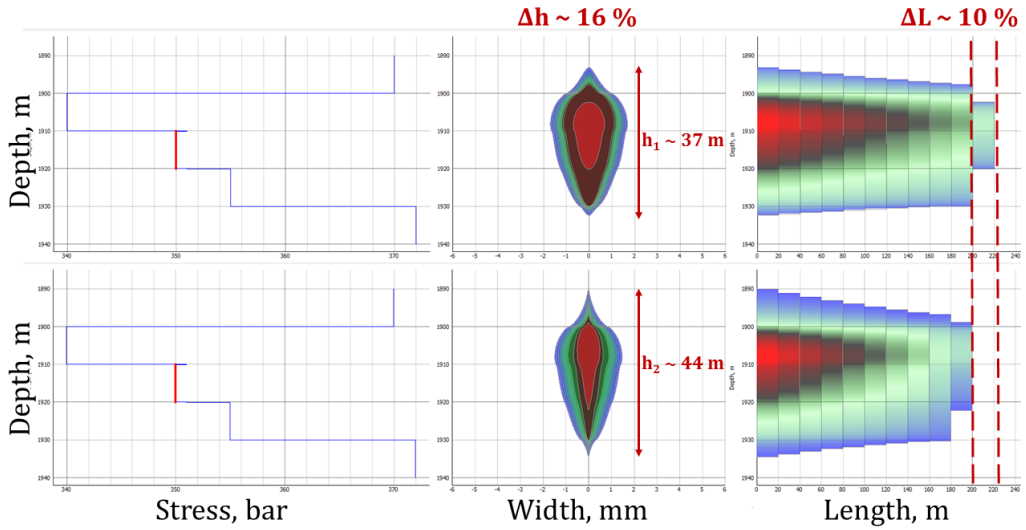

Figure 1: Lithology, fracture width profile, side view: upper picture - non-equilibrium height growth, lower picture - equilibrium height growth

On the picture above two cases are examined: equilibrium height growth and non-equilibrium one with the same inflow regime, liquid properties and lithology ($T = 10\ min.$ - pumping period, $q = 3.5m^3/min.-$ pump rate, K and n are 0.05 and 0.6, respectively). The set of parameters for the cases is $H = 10m$ for the height of reservoir layer, $\mu = 0.05Pa \cdot s$ for the fluid viscosity, $\nu = 0.3$ for the Poisson's ratio, $E = 30GPa$ for the value of Young's module and $K_{Ic} = 0.5MPa$ for the fracture toughness. The Carter's leak-off coefficient is the same for all layers, $C_l = 10^{-5}\ m \cdot s^{-0.5}$.

Neglecting viscous regime dissipation in vertical growth makes the height overestimated by 16 % while the fracture length is underestimated by 10 %. The account for viscous dissipation in lateral growth is vitally crucial in the context of breakthrough problems (in particular, water or gas coning).

4 Discussion

The solution for joint problem of fracture growth within multi-layered lithology and non-newtonian flow inside is developed. Enhanced cell-based pseudo-3D model is applied as it accounts for fracture height growth with viscous dissipation and represents relatively reasonable agreement between the complexity and accuracy.
Sequentially, we fulfilled benchmarking analysis: comparing equilibrium and non-equilibrium height growth models. As it turns out a significant deviation between two examined cases is observed (of order 10 %). Thereby, the risks of water or gas breakthrough may be over-estimated significanty if neglecting with viscous-dissipation in vertical growth.

References

[1] Bochkarev A., Budennyy S., Nikitin R., Mitrushkin D., Pseudo-3D Hydraulic Fracture Model with Complex Mechanism of Proppant Transport and Tip Screen Out // ECMOR XV - 15th European Conference on the Mathematics of Oil Recovery 2016;

[2] J. Adachi, E. Siebrits, A. Peirce, J. Desroches Computer simulation of hydraulic fractures // International Journal of Rock Mechanics and Mining Sciences 2007. V. 44. P. 739

[3] M. M. Rahman, M. K. Rahman A Review of Hydraulic Fracture Models and Development of an Improved Pseudo-3D Model for Stimulating Tight Oil/Gas Sand // Energy Sources, Part A: Recovery, Utilization, and Environmental Effects 2010. V.32

[4] JosГк I. Adachi, Emmanuel Detournay, Anthony P. Peirce Analysis of the classical pseudo-3D model for hydraulic fracture with equilibrium height growth across stress barriers // International Journal of Rock Mechanics and Mining Sciences 2010. V. 47. P. 625

[5] E.V. Dontsov, A.P. Peirce An enhanced pseudo-3D model for hydraulic fracturing accounting for viscous height growth, non-local elasticity, and lateral toughness // Engineering Fracture Mechanics 2015. V. 142. P. 116

[6] E.V. Dontsov, A.P. Peirce Proppant transport in hydraulic fracturing: Crack tip screen-out in KGD and P3D models // International Journal of Solids and Structures 2015. V. 63. P. 206

[7] Lenoach, B. Hydraulic Fracture Model Based on Analytical Near-Tip Solutions, Computer Methods and Advances in Geomechanics, 1994, 1597-1602 pp.

[8] Economides, M. J. Reservoir stimulation / M. J. Economides, K. G. Nolte. 3rd edition. Chichester: John Wiley and Sons Ltd, 2000. 856 p.

[9] Carter, R.D. Derivation of the General Equation for Estimating the Extent of the Fractured Area, Appendix I of Optimum Fluid Characteristics for Fracture Extension, Drilling and Production Practice, G.C. Howard and C.R. Fast, New York, NewYork, USA, American Petroleum Institute, 1957, 261-269 pp.

A posteriori error estimates for approximate solutions and adaptive algorithms for plane problems of elasticity theory

Maria A. Churilova, Maxim E. Frolov, Sergey I. Repin

frolov_me@spbstu.ru

Abstract

This work is devoted to functional approach [1],[2],[3] to a posteriori error control in classical [2] and Cosserat elasticity [4]-[5]. The approach yields reliable majorants that are valid for all conforming solutions of problems regardless of methods used for a numerical implementation of a solution process. Estimates include additional auxiliary fields and mesh-independent constants. It is shown that a reasonable and natural choice of conforming finite element approximations in the Hilbert space $H(div)$ for additional variables provides an efficient implementation of the error control. Efficiency of the above technique is shown on one set of numerical examples including consequent mesh adaptations with standard MATLAB tools as in [6].

1 Introduction

Nowadays, the theory of a posteriori error control is well-developed. The amount of the corresponding literature is vast and it is increasing continuously from the end of 1970-s (see, for instance, [3], [7], [8] for a review). Concerning error control for various problems of the elasticity theory, the first "geometrical" method appeared in [9] (much earlier than others, like [10], [11], [12]).

Fundamentals of the functional approach to a posteriori error control, including estimates for various problems of continuum mechanics, have been worked out in detail (see [13], [2], [3] for references). For example, functional a posteriori estimates for linear elasticity were obtained in [14] and [2] using different methodologies. Also in [14] some estimates for plane stress, plane strain and axisymmetric problems are considered.

Functional estimates for problems of Cosserat [15] elasticity have appeared during the last few years. Such media possess a wider range of properties as compared with classical continuous media. A mathematical description of Cosserat media can be found in [16] and [17]. In the last decades, methods for the numerical solution of problems related to the Cosserat continuum began to develop more intensively (see, for example, [18], [19], [20], [21], [22]). On the other hand, there are only few papers

addressed to a posteriori error control for computed approximations – [23], [24], [4], [5], and this work requires further developments related to the evolution of adaptive algorithms.

2 Statement

Majorants for both mathematical models (classical and Cosserat elasticity) have some important features in common. Estimates have the form

$$|||e|||\leq M := D(\tilde{u}, s^*) + R(s^*) + \text{penalty terms}, \qquad e := u - \tilde{u}, \tag{1}$$

where u contains all components of the exact solution, $\tilde{u}$ represents approximations of these components, e is the corresponding error formed by deviations from exact values, s^* is a set of auxiliary variables, and $|||...|||$ denotes the energy norm of the error. Term D represents errors in constitutive relations, R is a residual term including mesh-independent constants. The estimate (1) may contain optional penalty terms that violate the symmetry condition in a weak form. The right-hand side of (1) depends only on the known data – approximate solution, constants, positive parameters, additional variables, and it can be calculated explicitly. This estimate is exact in the sense that the equality is possible to be achieved with a proper setting of parameters and variables. For instance, estimates for problems in classical and Cosserat elasticity have the form (1) – see [2], [4] and [24] for details. All auxiliary fields can be constructed on a basis of finite elements suitable for space $H(div)$ – the Hilbert space of square summable vector-functions with square summable divergence.

A correct choice of one or more free variables in functional-type error estimates (majorants) allows obtaining accurate guaranteed upper error estimates. The functional approach does not impose significant additional restrictions (for example, satisfaction of equilibrium equations) on free variables. Any functional-type error estimate is universal – it is applicable to an arbitrary approximate solution from the corresponding energy space. It remains valid regardless of the approach used for calculating that solution, thus allows to take into account various error sources. Functional estimate (1) includes constants that depend only on domain geometry and not on the mesh for Finite Element Method (FEM). In addition to the global error estimation, the functional majorant can be used as an indicator of the local error distribution, considering the contributions to the global error on each finite element.

Modern adaptive algorithms for finite element methods consist of four main steps: solve, estimate, mark and refine. Concerning (1) the procedure can be specified as follows:

1. **solve** means *compute $\tilde{u}$ on a current finite element mesh*;
2. **estimate** means *compute* (1) *from individual loads to elements*;
3. **mark** means *mark elements of a mesh with large local errors by some marking strategy*;
4. **refine** means *divide marked elements and locally refine a mesh.*

3 Numerical results

One of the efficient ways to compute functional-type a posteriori error estimates for plane problems is to use mixed-FEM approximations. For example, these may be Raviart-Thomas [25] or Arnold-Boffi-Falk [26] approximations. For computation of approximate solutions, the commercial software can be used. Below, we present some recent results as an illustration.

Table 3: Comparison of results for uniform and adaptive mesh refinements, where the lowest-order Raviart-Thomas approximation is used for the implementation of the majorant M from (1)

Uniform refinement (classical elasticity)					
MESH	1	2	3	4	5
NODES	295	1147	4522	17956	71560
ELEMENTS	557	2228	8912	35648	142592
RELATIVE ERROR, %	10.1	6.6	4.2	2.6	1.6
Reference indicator (classical elasticity)					
MESH	1	2	3	7	20
NODES	295	353	423	765	2050
ELEMENTS	557	664	793	1428	3906
RELATIVE ERROR, %	10.1	6.9	4.9	2.6	1.6
Majorant-based indicator (classical elasticity)					
MESH	1	2	4	5	7
NODES	295	323	536	876	2955
ELEMENTS	557	606	1002	1648	5693
RELATIVE ERROR, %	10.1	7.1	3.7	2.7	1.4
$I_{eff} = M/\|\|\|e\|\|\|$	1.2	1.2	1.3	1.3	1.2
Reference indicator (Cosserat elasticity)					
MESH	1	2	3	7	22
NODES	295	348	410	720	2114
ELEMENTS	557	652	764	1334	3996
RELATIVE ERROR, %	12.0	9.8	8.0	5.1	3.0

Example (square domain with a hole). Let us consider one canonical example (see figure 1), where the results of adaptations and error estimation are compared for classical elasticity and Cosserat elasticity. Geometry and material properties for this example are taken from [19]: square side is 16.2 mm, hole radius is 0.216 mm, traditional elastic constants are λ= 0.11538e10 N/m^2 and μ= 0.76923e9 N/m^2, additional parameters of a microstructure are B= 0.31762e2 N and μ_c= 0.25638e11 N/m^2, size of particles is 0.2 mm (we note that the radius of the hole is close to the size of particles of a microstructure). The left edge of the square is clamped and a tensile loading is equal to 1 MPa (applied to the opposite edge).
Results collected in table 3 are mostly devoted to the classical elasticity. We start from the case where no adaptation is applied (uniform refinements). This part of

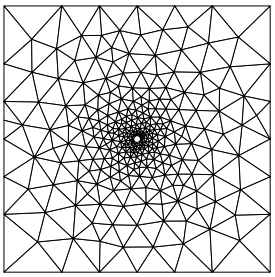

(a) 295 nodes

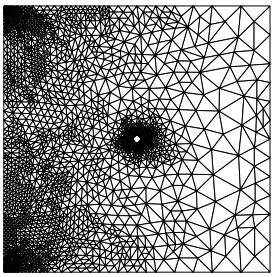

(b) 2955 nodes (majorant)

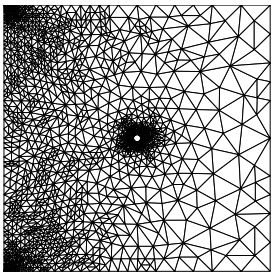

(c) 2050 nodes (reference 1)

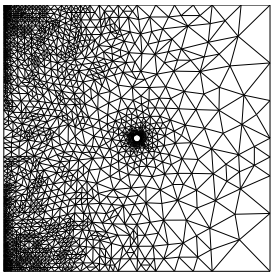

(d) 2114 nodes (reference 2)

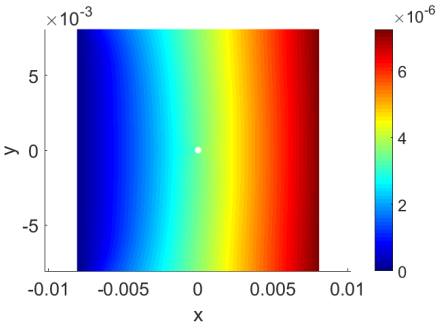

(e) u_x

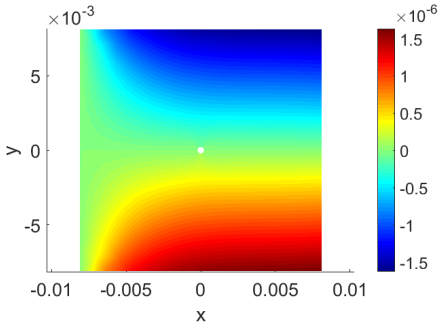

(f) u_y

Figure 1: (a) – initial mesh, (b) – result of adaptation by majorant-based indicator, (c) – result of adaptation by the reference indicator for classical elasticity, (d) – result of adaptation by the reference indicator for Cosserat elasticity, (e) and (f) – components of the solution u for classical elasticity (displacements)

the table shows how the solution process proceeds without any a posteriori error estimation. Values collected in lines of the table 3 are as follows: mesh numbers and the corresponding amounts of nodes and elements, and the relative error computed with the so-called *reference solution* – an approximate solution obtained on a fine mesh. Note that the reference solution is required only for numerical experiments on validation and comparison of different approaches. In engineering practise it is too time-consuming to compute it. For example, the reference mesh for the mesh 5 of the uniform refinement consists of 1141792 nodes and 2281472 elements. The

reference solution is also used for the construction of the reference indicator based on the energy norm of the difference between solutions on coarse and fine meshes. It is necessary for getting a final mesh (target) for comparisons, but this approach yields a large amount of steps of consequent mesh adaptations to achieve a good result.

The third block of the results is devoted to error estimation by the functional-type error majorant from [2]. The ratio between the error majorant M and the error $|||e|||$ is used as the main quality measure. This parameter is usually called *the efficiency index* – it is denoted by I_{eff}. In the last part of the table, results for similar reference indicator for the Cosserat elasticity are collected. Figure 1 includes following subplots: the initial mesh (a), the mesh 7 for the majorant-based indicator (b), the mesh 20 for the reference indicator for classical elasticity (c), the mesh 22 for the reference indicator for Cosserat elasticity (d), and the classical solution (e-f).

Results show that the functional approach provides reliable guaranteed upper bounds of the energy norm of the error with stable efficiency. Number of nodes required to reach the 98%-level of the accuracy with uniform refinements is 24-times larger than for the adaptive algorithm with the majorant M from (1). Thus, such approach saves a lot of computational resources to get an approximate solution of a good quality. After comparison of (b), (c) and (d), we make the conclusion that, for considered parameters, geometry and loading, both reference indicators and the majorant come to similar adaptive meshing.

In addition, table 4 illustrates the behavior of error estimation for several steps with uniform mesh refinements for the simplest Arnold-Boffi-Falk approximation. From these results for Cosserat elasticity we conclude that the efficiency index of estimates remains stable and overestimation of the true error is moderate and acceptable.

Table 4: Results for the lowest order Arnold-Boffi-Falk approximation for nested meshes [5]

MESH	1	2	3	4
D.O.F.[1]	504	1872	7200	28224
RELATIVE ERROR, %	15.8	11.1	7.3	4.0
I_{eff}	1.2	1.2	1.2	1.3

[1] number of degrees of freedom (111744 for the reference mesh)

Conclusions

The main conclusions are:

- The functional approach is reliable and estimates are guaranteed upper bounds of errors. This property is known from the theory and it is confirmed practically in the process of execution of adaptive algorithms.
- For the considered classes of problems, $H(div)$-conforming approximations as Raviart-Thomas or Arnold-Boffi-Falk yield good results from the viewpoint of a stability of the efficiency index and a moderate overestimation of the true error.

Acknowledgements

M.E. Frolov and M.A. Churilova are supported by the Grant of the President of the Russian Federation MD-1071.2017.1.

References

[1] Repin S. A posteriori error estimation for variational problems with uniformly convex functionals, Math. Comp. 69, 2000, P. 481-500.

[2] Repin S. A posteriori estimates for partial differential equations. Berlin: de Gruyter, 2008.

[3] Mali O., Neittaanmäki P., Repin S. Accuracy Verification Methods. Theory and algorithms. Computational Methods in Applied Sciences. Vol. 32. Springer, 2014.

[4] Frolov M. Functional a posteriori estimates of the error in the solutions of plane problems in Cosserat elasticity theory. Journal of Applied Mathematics and Mechanics. Vol. 78, Issue 4, 2014, P. 425-431.

[5] Frolov M. Reliable a posteriori error estimation for plane problems in Cosserat elasticity. Numerical Mathematics and Advanced Applications - ENUMATH 2013, Lecture Notes in Computational Science and Engineering 103, Springer: Switzerland, 2015, P. 225-232.

[6] Churilova M. The sensitivity of the adaptive algorithm with a posteriori error control to marking criteria. St. Petersburg State Polytechnical University Journal. Physics and mathematics. Vol. 4(230), 2015, P. 139-149.

[7] Verfürth R. A posteriori error estimation techniques for finite element methods. Oxford: Oxford University Press, 2013.

[8] Szabó B., Babuška I. Introduction to finite element analysis. Formulation, verification and validation, Hoboken, NJ: John Wiley & Sons, 2011.

[9] Prager W., Synge J.L. Approximations in elasticity based on the concept of function space. Q. Appl. Math. Vol. 5, 1947, P. 241-269.

[10] Ladevèze P., Leguillon D. Error estimate procedure in the finite element method and applications. SIAM J. Numer. Anal. Vol. 20, 1983, P. 485–509.

[11] Zienkiewicz O.C., Zhu J.Z. A simple error estimator and adaptive procedure for practical engineering analysis. Int. J. Numer. Methods Eng. Vol. 24, 1987, P. 337–357.

[12] Johnson C., Hansbo P. Adaptive finite element methods in computational mechanics. Comput. Methods Appl. Mech. Eng. Vol. 101, 1992, P. 143–181.

[13] Neittaanmäki P., Repin S. Reliable methods for computer simulation. Error control and a posteriori estimates. Amsterdam: Elsevier, 2004.

[14] Muzalevsky A., Repin S. On two-sided error estimates for approximate solutions of problems in the linear theory of elasticity. Russian Journal of Numerical Analysis and Mathematical Modelling. Vol. 18, Issue 1, 2003, P. 65-85.

[15] Cosserat E., Cosserat F. Théorie des corps déformables, Paris: Hermann, 1909.

[16] Nowacki W. Theory of elasticity [Russain transl.]. Moscow: Mir, M., 1975.

[17] Morozov N.F. Mathematical problems of crack theory [in Russian]. Moscow: Nauka, 1984.

[18] Providas E., Kattis M.A. Finite element method in plane Cosserat elasticity. Computers and Structures, Vol. 80, Issue 27-30, 2002, P. 2059-2069.

[19] Zhang H.W., Wang H., Wriggers P., Schrefler B.A. A finite element model for contact analysis of multiple Cosserat bodies. Computational Mechanics, Vol. 36, Issue 6, 2005, P. 444-458.

[20] Wheel M.A. A control volume-based finite element method for plane micropolar elasticity. International Journal for Numerical Methods in Engineering, Vol. 75, Issue 8, 2008, P. 992-1006.

[21] Hadjesfandiari A., Dargush G. Boundary element formulation for plane problems in couple stress elasticity. International Journal for Numerical Methods in Engineering. Vol. 89, Issue 5, 2012, P. 618-636.

[22] Sadovskaya O., Sadovskii V. Mathematical modeling in mechanics of granular materials. Advanced Structured Materials 21. Berlin: Springer, 2012.

[23] Perić D., Yu J., Owen D.R.J. On error estimates and adaptivity in elastoplastic solids: Applications to the numerical simulation of strain localization in classical and Cosserat continua. International Journal for Numerical Methods in Engineering, Vol. 37, Issue 8, 1994, P. 1351-1379.

[24] Repin S., Frolov M. Estimates for deviations from exact solutions to plane problems in the Cosserat theory of elasticity. Journal of Mathematical Sciences, Vol. 181, Issue 2, 2012, P. 281-291. (trans. from Problems of mathematical analysis, Vol. 62, 2011, P. 153-161.)

[25] Raviart P.A., Thomas J.M. A mixed finite element method for second order elliptic problems. Lecture Notes in Mathematics, Vol. 606, 1977, P. 292-315.

[26] Arnold D.N., Boffi D., Falk R.S. Quadrilateral $H(div)$ finite elements. SIAM Journal on Numerical Analysis, Vol. 42, Issue 6, 2005, P. 2429-2451.

Maria A. Churilova, Peter the Great St. Petersburg Polytechnic University, Polytechnicheskaya st. 29, Saint-Petersburg, 195251, Russia
Maxim E. Frolov, Peter the Great St. Petersburg Polytechnic University, Polytechnicheskaya st. 29, Saint-Petersburg, 195251, Russia
Sergey I. Repin, St. Petersburg Department of V.A. Steklov Institute of Mathematics of the Russian Academy of Sciences, Fontanka 27, Saint-Petersburg, 191023, Russia

The analysis of stress-strain state of a composite plane with interface crack for John's harmonic material

Domanskaya T.O., Malkov V.M., Malkova Yu.V.

tanyath57@gmail.com

Abstract

The analytical solutions of nonlinear problems for bi-material plane with an interface crack are obtained. The plane is made by joining of two half-planes from different materials. The plane is subjected to constant nominal (Piola) stresses at infinity. On the crack an external loading is applied. Mechanical properties of half-planes are described by the model of John's harmonic material. This model has allowed to use the methods of complex functions at solution of nonlinear plane-strain problems. The stresses and displacements are expressed through two analytic functions of a complex variable, defined from nonlinear boundary equations on an interface crack. Two problems are solved: a plane with a free interface crack and interface crack loaded uniform pressure. In the second problem the boundary conditions on a crack are depend from the deformation of its coasts. The exact analytical formulas for stresses and displacements are found. Using a global solutions the asymptotic expansions have been constructed for the stresses and displacements in vicinity of a crack tip.

In nonlinear problem of uniaxial extension of a plane with free crack it is established, that the formulas given the crack opening and the stress intensity factors (SIF) near the crack tips completely coincide with the similar formulas derived from the equations of a linear elasticity. The nominal stresses have the root singularity at the tips of a crack; the Cauchy stresses have no singularity.

It was found out, that in the problem of the crack under action of uniform pressure some critical pressures proportional to the shear module are exist and their excess leads to loss of a material stability and large stresses and strains.

1 General relations

In cartesian coordinates (x_1, x_2) the equations of equilibrium and compatibility of plane-strain problems in complex form are [1]

$$(s_{11} + is_{12})'_1 + i(s_{22} - is_{21})'_2 = 0, \tag{1}$$

$$(g_{22} - ig_{12})'_1 + i(g_{11} + ig_{21})'_2 = 0, \tag{2}$$

where s_{ij}, g_{ij} are components of nominal (Piola) stress tensor $\mathbf{S} = s_{\alpha\beta}\,\mathbf{e}_\alpha\mathbf{e}_\beta$ and deformation gradient $\mathbf{G} = g_{\alpha\beta}\,\mathbf{e}_\alpha\mathbf{e}_\beta$. The complex variables of initial and current configurations are $z = x_1 + ix_2$, $\zeta = \xi_1 + i\xi_2$ and the function of nominal stresses is σ. The equations (1), (2) are satisfied identically by substituting of expressions

$$s_{11} + is_{12} = \frac{\partial\sigma}{\partial z} - \frac{\partial\sigma}{\partial\overline{z}}, \quad s_{22} - is_{21} = \frac{\partial\sigma}{\partial z} + \frac{\partial\sigma}{\partial\overline{z}}, \tag{3}$$

$$g_{11} + ig_{21} = \frac{\partial\zeta}{\partial z} + \frac{\partial\zeta}{\partial\overline{z}}, \quad g_{22} - ig_{12} = \frac{\partial\zeta}{\partial z} - \frac{\partial\zeta}{\partial\overline{z}}. \tag{4}$$

Complex functions ζ and σ are defined from the law of elasticity and boundary conditions of the problem.

John's elastic potential (strain energy density) is considered [2]

$$\Phi = 2\mu[F(I) - J], \quad I = \lambda_1 + \lambda_2, \quad J = \lambda_1\lambda_2,$$

$$8\mu bF'(I) = I + \sqrt{I^2 - 16bc},$$

where λ_1, λ_2 are principal stretches; the factors b, c are defined by transition to Hookean law under small deformations: $4\mu b = 1 + \mu/(\lambda + 2\mu), c = 2\mu(1 - 2\mu b)$.

The law of elasticity for plane problem we shall write in complex form [1, 3]

$$\begin{aligned} s_{11} + is_{12} &= 2\mu\left[\frac{2}{I}F'(I)\frac{\partial\zeta}{\partial z} - \frac{\partial\zeta}{\partial z} + \frac{\partial\zeta}{\partial\overline{z}}\right], \\ s_{22} - is_{21} &= 2\mu\left[\frac{2}{I}F'(I)\frac{\partial\zeta}{\partial z} - \frac{\partial\zeta}{\partial z} - \frac{\partial\zeta}{\partial\overline{z}}\right]. \end{aligned} \tag{5}$$

Substituting (3), (4) into (5), we obtain the equations for functions $\sigma(z, \overline{z})$ and $\zeta(z, \overline{z})$

$$\begin{aligned} \frac{\partial\sigma}{\partial z} + 2\mu\frac{\partial\zeta}{\partial z} &= 4\mu\frac{1}{I}F'(I)\frac{\partial\zeta}{\partial z}, \\ \frac{\partial\sigma}{\partial\overline{z}} + 2\mu\frac{\partial\zeta}{\partial\overline{z}} &= 0. \end{aligned} \tag{6}$$

The solution of equations (6) is given by [4, 3]

$$\begin{aligned} \zeta &= b\varphi(z) + \overline{\psi(z)} + \frac{cz}{\overline{\varphi'(z)}}, \\ \sigma &= (1 - 2\mu b)\varphi(z) - 2\mu\overline{\psi(z)} - 2\mu\frac{cz}{\overline{\varphi'(z)}}, \end{aligned} \tag{7}$$

where $\varphi(z), \psi(z)$ are analytic functions of z. From (7) it follows $\sigma + 2\mu\zeta = \varphi(z)$.

For to simplify the boundary equations for functions $\varphi(z), \psi(z)$ we shall introduce an auxiliary function

$$\Omega(z) = \frac{c}{\overline{\varphi'(z)}} + \overline{\psi'}(z) - c\frac{\overline{\varphi''}(z)}{\overline{\varphi'^2}(z)}.$$

The formulas for nominal stresses becomes:

$$s_{11}+is_{12}=(1-2\mu b)\varphi'(z)-2\mu\left(\frac{2c}{\overline{\varphi'(z)}}-\Omega(\overline{z})+c\frac{(z-\overline{z})\overline{\varphi''(z)}}{\overline{\varphi'^2(z)}}\right),$$
$$s_{22}-is_{21}=(1-2\mu b)\varphi'(z)-2\mu\left(\Omega(\overline{z})-c\frac{(z-\overline{z})\overline{\varphi''(z)}}{\overline{\varphi'^2(z)}}\right), \tag{8}$$

In addition, the stresses and strains satisfy to the equalities

$$(s_{11}+is_{12})+2\mu(g_{22}-ig_{12})=\varphi'(z),$$
$$(s_{22}-is_{21})+2\mu(g_{11}+ig_{21})=\varphi'(z).$$

Consider the Cauchy's stress tensor $\mathbf{T}=t_{\alpha\beta}\,\mathbf{e}_\alpha\mathbf{e}_\beta$, from formula $\mathbf{S}=\mathbf{G}^{-1}\cdot J\mathbf{T}$ we obtain

$$\varkappa_1(t_{11}+it_{12})=s_{11}+is_{12},$$
$$\varkappa_2(t_{22}-it_{21})=s_{22}-is_{21}, \tag{9}$$

where $\varkappa_k=|\mathbf{e}_k\cdot J\mathbf{G}^{-1}|$ are the multiples of the areal change, $J=\det\mathbf{G}$.

2 The problem of the interface crack

A bi-material plane with an interface crack is considered. The crack is located in the interval $[-a,a]$ of interface line (Fig. 1). Nominal stresses are set at infinity $s_{ij}\to s_{ij}^{\infty}$ (for each half-plane). The surfaces of the crack are free from stresses

$$(s_{22}-is_{21})^{+}=0,\quad (s_{22}-is_{21})^{-}=0,\quad |x_1|<a. \tag{10}$$

The stresses (8) substitute in equations (10)

$$[(1-2\mu_2 b_2)\varphi'_2(z)-2\mu_2\Omega_2(\overline{z})]^{+}=0,$$
$$[(1-2\mu_1 b_1)\varphi'_1(z)-2\mu_1\Omega_1(\overline{z})]^{+}=0. \tag{11}$$

Here, we introduce the functions $h(z)$ and $r(z)$ which are analytic in all plane, excluding the interface. It allows to simplify the statement of the boundary problems and their solution. In upper half-plane S_2

$$h(z)=(1-2\mu_2 b_2)\varphi'_2(z)+2\mu_1\Omega_1(z),$$
$$r(z)=b_2\varphi'_2(z)-\Omega_1(z). \tag{12}$$

Complex potentials we shall express through functions (12)

$$\varphi'_2(z)=\frac{(h+2\mu_1 r)(z)}{1+2(\mu_1-\mu_2)b_2}, \tag{13}$$

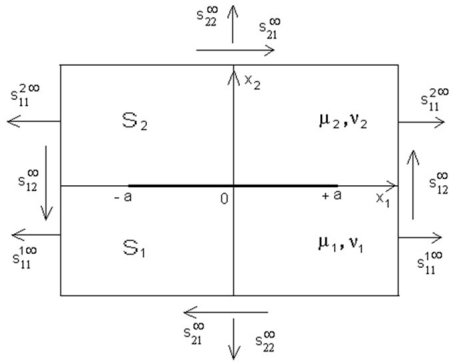

Figure 1: Bi-material plane with interface crack.

$$\Omega_1(z) = \frac{[b_2 h - (1 - 2\mu_2 b_2) r](z)}{1 + 2(\mu_1 - \mu_2) b_2}.$$

Formulas for the lower half-plane S_1 we obtain by cyclic changing of the indexes. The boundary conditions (11) in functions (12) take the form

$$h^+(x_1) - h^-(x_1) = 0, \quad r^+(x_1) + \delta r^-(x_1) = 0, \tag{14}$$

$$\delta = \frac{\mu_2(1 - 2\mu_1 b_1)}{\mu_1(1 - 2\mu_2 b_2)} \cdot \frac{1 + 2(\mu_1 - \mu_2) b_2}{1 + 2(\mu_2 - \mu_1) b_1}.$$

The solutions of equations (14) are

$$h(z) = h(\infty), \quad (r - Dh)(z) = AX(z)(z - 2ia\beta),$$

where

$$X(z) = \frac{1}{\sqrt{z^2 - a^2}} \left(\frac{z + a}{z - a} \right)^{i\beta}, \quad \beta = \frac{\ln \delta}{2\pi},$$

$$A = \frac{1}{2} \frac{(1 + 2b_2(\mu_1 - \mu_2))(1 + 2b_1(\mu_2 - \mu_1))}{\mu_1(1 - 2\mu_1 b_1) + \mu_2(1 - 2\mu_2 b_2)} (s_{22}^{\infty} - i s_{21}^{\infty}),$$

$$D = -\frac{1}{2} \frac{1 - 2\mu_1 b_1 - 2\mu_2 b_2}{\mu_1(1 - 2\mu_1 b_1) + \mu_2(1 - 2\mu_2 b_2)}.$$

The SIF of nominal stresses in vicinities of the crack ends are calculated under the formulas similar to that are used in linear elasticity [5]

$$K^{\pm} = \sqrt{2\pi} \lim_{r \to \pm 1 \pm 0} \left[(\pm\tau - 1)^{0.5 \pm i\beta} (s_{22} - i s_{21})(\tau) \right] = \tag{15}$$

$$= \pm\sqrt{\pi}(1 \mp 2i\beta) 2^{i\beta} (s_{22}^{\infty} - i s_{21}^{\infty}),$$

where $\tau = x_1/a$ is dimensionless variable on an interface. The same SIF are obtained in the linear problem of interface crack [5].
The displacements of the crack surfaces we shall find under the formula

$$g_{11} + i g_{21} = 1 + u_1' + i u_2' = \frac{1}{2\mu} \varphi'(t),$$

where u_1 and u_2 are the components of displacements. The disclosing of a crack for uniaxial extension of plane by the stresses s_{22}^{∞} is given by

$$\Delta u_2(z) = \frac{s_{22}^{\infty}}{2\mu_1\mu_2}\sqrt{(\mu_1+3\mu_2-4\nu_1\mu_2)(\mu_2+3\mu_1-4\nu_2\mu_1)}\sqrt{a^2-z^2}\left(\frac{a+z}{a-z}\right)^{i\beta}.$$

The similar formula is obtained in a linear problem [5].
Let's assume $z = a + re^{i\theta}$ and construct the asymptotic expansions of nominal stresses in a vicinity of a right tip of crack at $r \to 0$

$$s_{11} + is_{12} = A_1 + B_1(re^{-i\theta})^{-i\beta-0.5} + O(\sqrt{r}),$$

$$s_{22} - is_{21} = A_2 + B_2(re^{-i\theta})^{-i\beta-0.5} + O(\sqrt{r}),$$

where A, B are const. The nominal stresses have singularity $1/\sqrt{r}$.
The multiples of the areal change $\varkappa_1$ and $\varkappa_2$ have a singularity $1/\sqrt{r}$ at $r \to 0$, hence the Cauchy stresses (9) have no singularities on the ends of the crack

$$t_{11} + it_{12} = C_1 + D_1\sqrt{r} + O(r), \quad t_{22} - it_{21} = C_2 + D_2\sqrt{r} + O(r).$$

The calculations of displacements of crack surfaces are performed. The material parameters are considered: $\mu_1 = 1$ MPa, $\mu_2 = 5$ MPa, $\nu_1 = 0.48$, $\nu_2 = 0.45$. One-axis stretching along x_2-axis is taken as external loading: $s_{22}^{\infty} = 0.1$ MPa (a) and $s_{22}^{\infty} = 0.3$ MPa (b). The results of calculations are presented on Fig. 2.

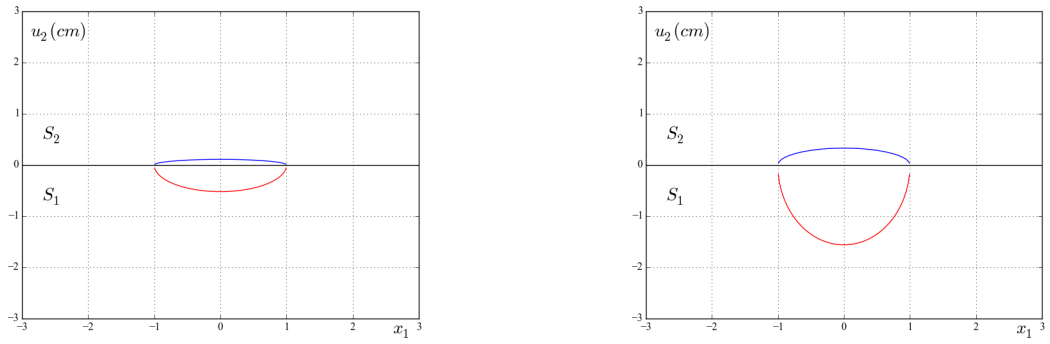

(a) (b)

Figure 2: The displacements of crack surfaces.

3 Interface crack loaded by pressure

The nonlinear plane-strain problem of a bi-material plane with an interface crack loading pressure is examined. Feature of a problem is dependence of boundary conditions on deformation of coasts. It was found out, that there are some critical pressures proportional to the shear module which excess conducts to the lost of stability material. The boundary conditions on a crack are reduced to [4]

$$s_{22} - is_{21} = -p\,(g_{11} + ig_{21}), \tag{16}$$

where $p > 0$ is value of pressure. Using formulas (8), (16) we obtain

$$s_{22} - is_{21} = -\frac{p}{2\mu - p}\varphi'(z), \quad g_{11} + ig_{21} = \frac{p}{2\mu - p}\varphi'(z). \tag{17}$$

It is visible in (17), that stresses and strains tends to ∞ when $p \to 2\mu$. Function $\varphi'(z) \neq 0$ if $p = 2\mu$. The boundary conditions for nominal stresses on the coats of crack are

$$[s_{22} - is_{21}]^+ = -\frac{p}{2\mu_2 - p}{\varphi'}_2(z), \quad [s_{22} - is_{21}]^- = \frac{p}{2\mu_1 - p}{\varphi'}_1(z). \tag{18}$$

The sum and the difference of the equations (18), written through functions h and r, gives us the equations

$$[h - pr]^+(t) - [h - pr]^- = 0,$$

$$r^+(t) + \delta(p)\, r^-(t) = f(p), \quad t \in (-a, a), \tag{19}$$

$$\delta(p) = \frac{2\mu_2 - p}{2\mu_1 - p}\,\frac{1 + 2(\mu_1 - \mu_2)b_2}{1 + 2(\mu_2 - \mu_1)b_1}\,\frac{1 - (2\mu_1 - p)b_1}{1 - (2\mu_2 - p)b_2},$$

$$f(p) = -\frac{1 - (2\mu_1 - p)b_1 - (2\mu_2 - p)b_2}{(2\mu_1 - p)[1 + 2(\mu_2 - \mu_1)b_1][1 - (2\mu_2 - p)b_2]}(h + pr)(\infty).$$

The factor $\delta(p)$ in equation (19) changes a sign depending on value of pressure p. If $\mu_1 \leq \mu_2$, then at $p < 2\mu_1$ and $p > 2\mu_2$ a factor δ will be positive, and at $2\mu_1 < p < 2\mu_2$ — negative. The form of the solution of the equation (19) depends on a sign on this parameter. Further we shall consider separately three cases. Cases $\delta = \infty$ and $\delta = 0$ to which correspond critical pressure $p_1 = 2\mu_1$ and $p_2 = 2\mu_2$, accordingly, we exclude from consideration.

At $p < 2\mu_1$ and $p > 2\mu_2$ we have $\delta > 0$, in this case the solution to equation (19) holomorphic at infinity is

$$r(z) = r(\infty) + B\,[1 - (z - 2i\beta a)\,X(z)], \tag{20}$$

$$B = -\frac{[1 + 2(\mu_2 - \mu_1)b_1 + 2(\mu_1 - \mu_2)b_2]\,p}{(2\mu_1 - p)[1 - (2\mu_1 - p)b_1] + (2\mu_2 - p)[1 - (2\mu_2 - p)b_2]}.$$

At segment $2\mu_1 < p < 2\mu_2$ factor $\delta < 0$. In this case the solution of equation (19) is given by the formula

$$r(z) = r(\infty) + B\,[1 - X_*(z)]. \tag{21}$$

$$X_*(z) = \left(\frac{z - a}{z + a}\right)^{i\,\beta}, \quad \beta = \frac{\ln|\,\delta|}{2\pi}.$$

The solution (21) remains limited near to the tips of a crack and anywhere does not zero. In the formula (21) it is supposed, that $\delta \neq -1$, the case $\delta = -1$ has been exclude. Value of parameter $\delta = -1$ is special, the solution (20) tends to infinity, corresponding critical pressure p is a root of the equation $1 + \delta = 0$.

Thus, during research and solution of the equation (19) are revealed three special values of parameter δ, namely, $\delta = \infty$, $\delta = 0$ and $\delta = -1$ to which there correspond critical values of pressure: $p_1 = 2\mu_1$, $p_2 = 2\mu_2$ and $p_* \in (2\mu_1, 2\mu_2)$. The

analysis shows, that at approach of pressure to these critical values the maximal displacements of coasts of a crack, and also stress intensity factors tends to infinity. The SIF for the right and left end of a crack we shall define under formulas (15). Let's consider a case when pressure on a crack satisfies to conditions $p < 2\mu_1$ or $p > 2\mu_2$. In the equation (19) parameter $\delta > 0$ and its solution is (20). The SIF are

$$K^+ = -A\sqrt{\pi}(1-2i\beta)2^{i\beta}, \quad K^- = +A\sqrt{\pi}(1+2i\beta)2^{-i\beta},$$

where

$$A = B\,\frac{(h+pr)(\infty)}{[1+2(\mu_1-\mu_2)b_2][1+2(\mu_2-\mu_1)b_1]}.$$

For negative values of parameter δ in the equation (19), when pressure varies within the limits of $2\mu_1 < p < 2\mu_2$, the SIF are calculated under formulas

$$K^+ = -A\sqrt{2\pi}\,2^{-i\beta}, \quad K^- = -A\sqrt{2\pi}\,2^{i\beta}.$$

The displacements of the coasts of crack it is convenient to define by the second formula (17)

$$g_{11} + ig_{21} = 1 + u_1' + iu_2' = \frac{1}{2\mu - p}\,\varphi'(t),$$

after replacement of complex functions with expressions (14). The displacements on normal to a crack are represented greatest interest

$$u_2^+ = -\frac{a\sqrt{\delta}(2\mu_1-p)\sqrt{1-\xi^2}}{(2\mu_2-p)[1+2(\mu_1-\mu_2)b_2]}B\cos\left[\beta\ln\frac{1+\xi}{1-\xi}\right], \quad \xi\in(-1,1),$$

$$u_2^- = \frac{a(2\mu_2-p)\sqrt{1-\xi^2}}{\sqrt{\delta}(2\mu_1-p)[1+2(\mu_2-\mu_1)b_1]}B\cos\left[\beta\ln\frac{1+\xi}{1-\xi}\right], \quad \xi\in(-1,1).$$

4 Conclusion

For model of John's harmonic material the problem of interface crack in bi-material plane is solved. The cases of a free crack and a crack loaded by uniform pressure are studied. The exact analytical formulas are found for the nominal (Piola) stresses, Cauchy stresses and the displacements. On the base of the common solution the asymptotic expansions of the listed functions are constructed in a vicinity of the ends of a crack. The nominal stresses have a root singularity, Cauchy stresses have no singularity. The stresses and displacements have an oscillation in the vicinity of the tips of the crack. The stress intensity factors for nominal stresses are received. Unlike a linear problem, where SIF have real physical sense, (the speed of liberated energy of deformation at development of a crack), here SIF are entered formally. The question about SIF in nonlinear problems is not studied and requires special research. The formulas of disclosing crack (jumps of displacements) are obtained. It is interesting, that formulas for SIF and disclosing of a free crack completely coincide with the results of similar linear problem.

5 Acknowledgements

This work is founded by Russian Foundation for Basic Research, No 16-31-00065.

References

[1] V. M. Malkov, *Introduction in non-linear elasticity*. St.Petersburg, Russia: St. Petersburg State University, 2010.

[2] C. Q. Ru, "On complex-variable formulation for finite plane elastostatics of harmonic materials," *Acta Mechanica*, vol. 156, pp. 219-234, 2002.

[3] V. M. Malkov, Yu. V. Malkova, T. O. Domanskaya, "Analysis of stresses of bi-material plane and half-plane at action of a point force for two models of harmonic materials," *Vestnic St. Petersburg State Univ. Ser. 10. Applied mathematics. Informatics. Control processes*, vol. 1, pp. 38-52, 2016.

[4] V. M. Malkov, Yu. V. Malkova, V. A. Stepanova, "Bi-material plane of John's material with interface crack loaded by pressure," *Vestnic St. Petersburg State Univ. Ser. 1. Mathematics. Mechanics. Astronomy*, vol. 3, pp. 113-125, 2013.

[5] Yu. V. Malkova, *Some problems for bi-material plane with curvilinear cracks*. St. Petersburg, Russia: St.Petersburg State University, 2008.

Domanskaya T.O., St.Petersburg, Russia
Malkov V.M., St.Petersburg, Russia
Malkova Yu.V., St.Petersburg, Russia

Elastic microslip in belt drive: influence of bending, shear and extension

Vladimir V. Eliseev, Evgenii A. Oborin

evgenii.oborin@jku.at

Abstract

We develop a model of elastic microslip with account for deformations of belt as a Cosserat rod. The general nonlinear problem with friction is divided into two stages: fitting the belt on the pulleys and then deforming the belt by the given pulley rotations. At the second stage we assume that friction forces act in the contact areas providing the displacements of the belt points equal to the displacement of pulley points. This problem is solved for small displacements and rotations using the superposition principle.

1 Introduction

The first study of the belt mechanics from the point of view of shear model was reported in [1]. An independent research of shear microslip concerning general friction modelling can be found in [2]. A combination of the belt shear and extension was presented in [3, 4], however the bending stiffness was neglected there.

In the present paper we address the mechanics of the belt drive taking into account the effect of elastic microslip. We formulate and solve the quasi-static nonlinear problem of the belt deformation and contact interaction of the belt with two equal non-smooth pulleys. The goal of the present study is in particular the analysis of influence of belt deformation and elastic microslip on the transmission ratio depending on the applied load.

The belt is modelled as elastic rod which initial configuration is a circle. In the geometrically nonlinear formulation we take into account bending, transverse shear and extension, and also friction on pulleys. The problem is solved in two stages.

At the first stage we model the fitting of the belt on the pulleys, determine the stress-strain state of the belt and calculate the contact pressure. We overcome difficulties of the nonlinear contact problem using computer mathematics. The arising boundary value problems are solved numerically by the shooting method and by the finite difference method.

At the second stage we consider the problem with prescribed rotations of pulleys and applied torques. We use the equations in variations superposed upon the stress state calculated at the first stage. We derive and solve the linear ODEs which variable

coefficients are determined at the first stage. The state of the belt on pulleys is described by the second-order ODEs, their solution allows determining the contact pressure and friction forces. For the free spans of belt we formulate and solve the sixth-order problems. As a result a general 16th-order system is combined and solved. We apply computer mathematics here as well.

2 Equations in variations

Before the varying we have the nonlinear static problem with tension and shear [5, 6]. (The simpler versions are possible, without shear or without tension, see [7].) We transform the obtained expressions for variables and constants using the coordinate $s \in [-s_1, s_4]$; $l = s_4 + s_1$ is the belt length (see Fig. 1). This coordinate is the arc coordinate in the reference undeformed configuration. The belt form in the reference configuration is circle [5, 6, 7]. The simplified model of elastic microslip in belt drive is presented in [8].
The equations in variations [9] read:

$$\tilde{\mathbf{Q}}' = -\tilde{\mathbf{q}}, \;\; \tilde{\mathbf{M}}' + \mathbf{u}' \times \mathbf{Q} + \mathbf{r} \times \tilde{\mathbf{Q}} = -\tilde{\mathbf{m}},$$
$$\tilde{\mathbf{M}} = \mathbf{A}^{-1} \cdot \boldsymbol{\theta}' + \boldsymbol{\theta} \times \mathbf{M}, \;\; \tilde{\mathbf{Q}} = \mathbf{B}^{-1} \cdot \boldsymbol{\gamma} + \boldsymbol{\theta} \times \mathbf{Q}, \;\; \boldsymbol{\gamma} \equiv \mathbf{u}' - \boldsymbol{\theta} \times \mathbf{r}'. \qquad (1)$$

Here we denote: $(...)'$ is the derivative with respect to coordinate s; $(\tilde{...})$ is the variation of a value; $\mathbf{r}$, $\mathbf{Q}$, $\mathbf{M}$ are the position vector of rod particles, force and moment in the rod before varying, respectively; $\mathbf{A}$, $\mathbf{B}$ are the compliance tensors of the rod (we take physically linear model); the vectors $\mathbf{u} \equiv \tilde{\mathbf{r}}$, $\boldsymbol{\theta}$ describe small displacements and rotations, respectively; and the vectors $\tilde{\mathbf{Q}}$, $\tilde{\mathbf{M}}$ are the force and moment variations, respectively. $\tilde{\mathbf{q}}$ and $\tilde{\mathbf{m}}$ are the variations of external load and moment distributed per unit length, respectively.
In the present paper we restrict ourselves to the plane problem. Therefore the vectors $\mathbf{r}$, $\mathbf{Q}$, $\mathbf{u}$, $\tilde{\mathbf{Q}}$, $\tilde{\mathbf{q}}$ lie in the drawing plane xy, and the vectors $\mathbf{M}$, $\tilde{\mathbf{M}}$, $\boldsymbol{\theta}$, $\tilde{\mathbf{m}}$ have just one component (for example, $\mathbf{M} = M\mathbf{k}$) directed along the z-axis. We take the following expressions for belt compliance tensors: the tensor $\mathbf{A} = A\mathbf{kk}$ determine the bending compliance, the tensor $\mathbf{B} = B_1\mathbf{e}_1\mathbf{e}_1 + B_2\mathbf{e}_2\mathbf{e}_2$ determine the tension and shear compliance. The unit vectors $\mathbf{e}_1$, $\mathbf{e}_2$ are rotated with respect to Cartesian axes x, y by an angle φ. The rules of differentiation are $\mathbf{e}_1' = \varphi'\mathbf{e}_2$, $\mathbf{e}_2' = -\varphi'\mathbf{e}_1$.

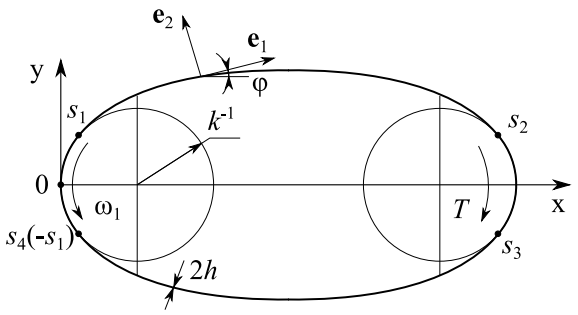

Figure 1: Scheme of belt drive

The term $\boldsymbol{\theta} \times \mathbf{M}$ vanishes for the plane deformation. We simplify and get the following system from (1):

$$\begin{aligned}
&\tilde{\mathbf{Q}}' = -\tilde{\mathbf{q}}, \;\; \tilde{M}' + \mathbf{k} \cdot \left(\mathbf{u} \times \mathbf{Q} + \mathbf{r}' \times \tilde{\mathbf{Q}} \right) = -\tilde{m}, \\
&\tilde{M} = A^{-1}\theta', \;\; \tilde{\mathbf{Q}} = \mathbf{B}^{-1} \cdot \boldsymbol{\gamma} + \theta \mathbf{k} \times \mathbf{Q}, \;\; \boldsymbol{\gamma} = \mathbf{u}' - D\theta\mathbf{n}, \\
&D \equiv |\mathbf{r}'| = \sqrt{(1 + B_1 Q_1)^2 + (B_2 Q_2)^2} = \sigma', \;\; \mathbf{n} = \mathbf{k} \times \mathbf{t}.
\end{aligned} \tag{2}$$

We shall write the systems in components specifically for the free segment and contact segment using different bases.

3 Contact segments

In the contact segment we decompose the vectors by the tangent and normal unit vectors. With the rotation of the pulley of radius k^{-1} by an angle ω_1 we have:

$$\begin{aligned}
&\mathbf{u} = u_t \mathbf{t} + u_n \mathbf{n} = -(k^{-1}\omega_1 + h\theta)\mathbf{t}, \\
&\mathbf{t} = D^{-1}\mathbf{r}' = t_1 \mathbf{e}_1 + t_2 \mathbf{e}_2; \;\; t_1 = D^{-1}(1 + B_1 Q_1), \;\; t_2 = D^{-1} B_2 Q_2.
\end{aligned} \tag{3}$$

The problem is linear, therefore we can take $\omega_1 = 1$. The formulae of differentiation are

$$\begin{aligned}
&\mathbf{t}'(s) = D\dot{\mathbf{t}}(\sigma) = -Dk\mathbf{n}, \;\; \mathbf{n}'(s) = Dk\mathbf{t}, \\
&\mathbf{u}' = (u_t' + Dku_n)\mathbf{t} + (u_n' - Dku_t)\mathbf{n} = -h\theta'\mathbf{t} + D(\omega_1 + kh\theta)\mathbf{n}.
\end{aligned} \tag{4}$$

Now we rewrite the system (2) for the plane deformation in components. The balance equations take the form:

$$\begin{aligned}
&\tilde{Q}_t' + Dk\tilde{Q}_n = -\tilde{q}_t, \;\; \tilde{Q}_n' - Dk\tilde{Q}_t = -\tilde{q}_n, \\
&\tilde{M}' + (u_t' + Dku_n)Q_n - (u_n' - Dku_t)Q_t + D\tilde{Q}_n = -\tilde{m}.
\end{aligned} \tag{5}$$

In the elasticity relations we express the stiffness tensor in the following form:

$$\begin{aligned}
&\mathbf{B}^{-1} = B_1^{-1}\mathbf{e}_1\mathbf{e}_1 + B_2^{-1}\mathbf{e}_2\mathbf{e}_2 = \mathbf{b} = b_t\mathbf{t}\mathbf{t} + b_n\mathbf{n}\mathbf{n} + b_{tn}(\mathbf{t}\mathbf{n} + \mathbf{n}\mathbf{t}), \\
&b_t = B_1^{-1}t_1^2 + B_2^{-1}t_2^2, \;\; b_n = B_1^{-1}t_2^2 + B_2^{-1}t_1^2, \;\; b_{tn} = t_2 t_1(-B_1^{-1} + B_2^{-1}).
\end{aligned} \tag{6}$$

We take into account the fact that $n_1 = -t_2, \; n_2 = t_1$. For the displacements, strains and forces we have

$$\begin{aligned}
&\mathbf{u} = -(k^{-1}\omega_1 + h\theta)\mathbf{t}, \;\; \boldsymbol{\gamma} = -h\theta'\mathbf{t} + D\mathbf{n}(\omega_1 - (1 - kh)\theta), \\
&\tilde{\mathbf{Q}} = \mathbf{b} \cdot \boldsymbol{\gamma} + \theta(Q_t\mathbf{n} - Q_n\mathbf{t}), \\
&\tilde{Q}_t = b_t\gamma_t + b_{tn}\gamma_n - \theta Q_n = -b_t h\theta' + b_{tn}D\omega_1 - (b_{tn}D(1 - kh) + Q_n)\theta, \\
&\tilde{Q}_n = b_{tn}\gamma_t + b_n\gamma_n + \theta Q_t = \\
&= -b_{tn}h\theta' + b_n D\omega_1 - (b_n D(1 - kh) - Q_t)\theta.
\end{aligned} \tag{7}$$

We write the relation between the force and moment loads in the form:

$$\tilde{m} = h\tilde{q}_t \Rightarrow \tilde{M}' - h\theta' Q_n - D(\omega_1 + kh\theta)Q_t + D\tilde{Q}_n = h\left(\tilde{Q}_t' + Dk\tilde{Q}_n\right). \tag{8}$$

Then we substitute the variations of the force factors and derive the ODE for $\theta(s)$. Let us rewrite this equation as follows:

$$\begin{aligned}
&L[\theta] \equiv c_0\theta'' + c_1\theta' + c_2\theta = c_\omega\omega_1,\\
&c_0 \equiv A^{-1} + h^2 b_t, \;\; c_1 \equiv h^2 b_t',\\
&c_2 \equiv -b_n D^2(1-kh)^2 + DQ_t(1-2kh) + h(1-kh)(b_{tn}D)' + hQ_n',\\
&c_\omega \equiv DQ_t - b_n D^2(1-kh) + h(b_{tn}D)'.
\end{aligned} \tag{9}$$

Here we have the second-order ODE with variable coefficients in the operator L. The solution is determined by the values at the ends $\theta(-s_1) \equiv \theta_4$, $\theta(s_1) \equiv \theta_1$, it depends on them linearly (according to the law of superposition):

$$\begin{aligned}
&\theta(s) = \omega_1\Theta_\omega(s) + \theta_q\Theta_1(s) + \theta_4\Theta_4(s);\\
&L[\Theta_\omega] = c_\omega, \;\; L[\Theta_1] = L[\Theta_4] = 0,\\
&s = -s_1: \;\; \Theta_\omega = \Theta_1 = 0, \;\; \Theta_4 = 1,\\
&s = s_1: \;\; \Theta_\omega = \Theta_4 = 0, \;\; \Theta_1 = 1.
\end{aligned} \tag{10}$$

However the values θ_1, θ_4 are yet unknown; they will depend linearly on the angles of pulley rotation ω_1, ω_2.
We solve this boundary value problem and find the bending moment. At the ends of the segment they are

$$\begin{aligned}
&M_4^+ = M_{4\omega}^+ + M_{44}^+\theta_4 + M_{41}^+\theta_1,\\
&M_1^- = M_{1\omega}^- + M_{14}^-\theta_4 + M_{11}^-\theta_1.
\end{aligned} \tag{11}$$

The superscripts $\pm$ denote the shift of the considered point; s_1^- is on the pulley, s_1^+ is on the free span.
We consider the second pulley with the segment $[s_2, s_3]$, unknowns θ_2, θ_3, and angle of rotation ω_2 in the same manner. However, the coefficients in the operator L are different. Therefore we distinguish the operators L^1, L^2. We make the change transiting to L^2:

$$Q_t^{(2)}(s) = -Q_t^{(1)}(l/2 - s), \;\; Q_n^{(2)}(s) = Q_n^{(1)}(l/2 - s). \tag{12}$$

Here we account for symmetry of the state before varying. Similar to (11) we find

$$\begin{aligned}
&M_2^+ = M_{2\omega}^+ + M_{22}^+\theta_2 + M_{23}^+\theta_3,\\
&M_3^- = M_{3\omega}^- + M_{32}^-\theta_2 + M_{33}^-\theta_3.
\end{aligned} \tag{13}$$

The coefficients of the expressions (11) and (13) will be present in the matrix of the resolving linear algebraic system of equations for four unknowns θ_i below.

4 Free segments (belt spans)

We have the following system in these segments with the absence of distributed loads

$$\begin{aligned}
&\tilde{\mathbf{Q}}' = 0, \;\; \tilde{\mathbf{M}}' + \mathbf{u}' \times \mathbf{Q} + \mathbf{r}' \times \tilde{\mathbf{Q}} = 0,\\
&\boldsymbol{\theta}' = \mathbf{A} \cdot (\tilde{\mathbf{M}} - \boldsymbol{\theta} \times \mathbf{M}), \;\; \mathbf{u}' = \mathbf{B} \cdot (\tilde{\mathbf{Q}} - \boldsymbol{\theta} \times \mathbf{Q}) + \boldsymbol{\theta} \times \mathbf{r}'.
\end{aligned} \tag{14}$$

Consider the projections onto Cartesian axes. We integrate the first two equations as follows:

$$\tilde{\mathbf{Q}} = \text{const}, \quad \tilde{M} + u'_x Q_y - u'_y Q_x + x\tilde{Q}_y - y\tilde{Q}_x = \tilde{M}_* = \text{const}. \tag{15}$$

The third and the fourth equations of (14) become

$$\begin{aligned} &\theta' = A\tilde{M}, \quad u'_x = B_x(\tilde{Q}_x + \theta Q_y) + B_{xy}(\tilde{Q}_y - \theta Q_x) - \theta y', \\ &u'_y = B_y(\tilde{Q}_y - \theta Q_x) + B_{xy}(\tilde{Q}_x + \theta Q_y) + \theta x'. \end{aligned} \tag{16}$$

For the six unknowns $\tilde{Q}_x,\ \tilde{Q}_y,\ \tilde{M}_*,\ \theta,\ u_x,\ u_y$ we derive the linear homogeneous system of ODE (the first three unknowns are constants, their derivatives equal zero):

$$Y' = F(s, Y), \quad Y \equiv \left(\tilde{Q}_x \ \ \tilde{Q}_y \ \ \tilde{M}_* \ \ \theta \ \ u_x \ \ u_y\right)^T. \tag{17}$$

The boundary conditions are the prescribed displacements and rotations:

$$\begin{aligned} &s = s_1: \quad \theta = \theta_1, \quad \mathbf{u} = -(k^{-1}\omega_1 + h\theta_1)\mathbf{t}_1, \\ &s = s_2: \quad \theta = \theta_2, \quad \mathbf{u} = -(k^{-1}\omega_2 + h\theta_2)\mathbf{t}_2, \\ &s = s_3: \quad \theta = \theta_3, \quad \mathbf{u} = -(k^{-1}\omega_2 + h\theta_3)\mathbf{t}_3, \\ &s = s_4: \quad \theta = \theta_4, \quad \mathbf{u} = -(k^{-1}\omega_1 + h\theta_4)\mathbf{t}_4. \end{aligned} \tag{18}$$

Here the tangent unit vectors $\mathbf{t}_1, ..., \mathbf{t}_4$ are determined by the formula (3). At the four contact area boundaries their projections onto the axes $x,\ y$ are equal by magnitude, but different by signs:

$$\begin{aligned} &t_{1x} = t_1 \cos\varphi_1 - t_2 \sin\varphi_1 = t_{2x} = -t_{3x} = -t_{4x}, \\ &t_{1y} = t_1 \cos\varphi_1 + t_2 \cos\varphi_1 = -t_{2y} = -t_{3y} = t_{4y}. \end{aligned} \tag{19}$$

We solve the boundary value problem for the ODE system (17) with the given values of θ at the ends (the displacements are given as well). We repeat this for both spans and determine the bending moments:

$$\begin{aligned} &M_1^+ = M_{1\omega}^+ + M_{11}^+\theta_1 + M_{12}^+\theta_2, \\ &M_2^- = M_{2\omega}^- + M_{21}^-\theta_1 + M_{22}^-\theta_2, \\ &M_3^+ = M_{3\omega}^+ + M_{33}^+\theta_3 + M_{34}^+\theta_4, \\ &M_4^- = M_{4\omega}^- + M_{43}^-\theta_3 + M_{44}^-\theta_4. \end{aligned} \tag{20}$$

5 Calculation of the whole belt

In the expressions (11), (13) and (20) we have the set of 16 coefficients and 8 free terms. Using this set we take into account the obvious condition of moment continuity at the points s_i and form the resolving fourth-order linear algebraic system for the unknowns θ_i:

$$\underline{\mathrm{M}\Theta = \Omega}, \Theta = (\theta_1 \ \ \theta_2 \ \ \theta_3 \ \ \theta_4)^T, \quad \Omega_i = M_{i\omega}^- - M_{i\omega}^+,$$

$$\mathrm{M} = \begin{pmatrix} M_{11}^+ - M_{11}^- & M_{12}^+ & 0 & -M_{14}^- \\ -M_{21}^- & M_{22}^+ - M_{22}^- & M_{23}^+ & 0 \\ 0 & -M_{32}^- & M_{33}^+ - M_{33}^- & M_{34}^+ \\ M_{41}^+ & 0 & -M_{43}^- & M_{44}^+ - M_{44}^- \end{pmatrix}. \tag{21}$$

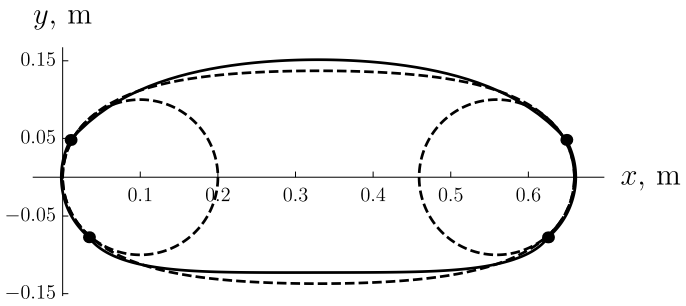

Figure 2: Form of belt. *Dashed line* denotes intermediate state and pulleys

To construct the matrix M it is sufficient to solve the problem for the whole belt four times, each time we take just one non-zero angle of rotation θ_i. For example, with $\theta_1 = 1$, $\theta_2 = \theta_3 = \theta_4 = 0$ we get the first column of the matrix. And to find Ω_i we need to compute the jumps of moments at the points s_i with $\Theta = 0$.
One of the main purposes of this paper is to calculate transmission ratio ω_2/ω_1. Due to the effect of elastic microslip it is not equal to the pulleys radii ratio (one in the case of equal radii as in the present work). Its value reduces with the increase of load - the resistance moment on the driven pulley:

$$T = -k^{-1} \int_{s_2}^{s_3} \tilde{q}_t ds. \tag{22}$$

The function under the integral $\tilde{q}_t$ is the friction force. It is determined from the first equation of (5) after $\tilde{Q}_t$, $\tilde{Q}_n$. It must not exceed (by absolute value) the dry friction limit.
The taken continuity of moment follows from the obvious impossibility of lumped moment reactions. If there exist no lumped contact forces, then the vector $\mathbf{Q}$ must be continuous too - it gives eight matching conditions. However we have no remaining values to satisfy these conditions. Even if we admit the translation of points $s_1, ..., s_4$, it gives just four additional unknowns whereas we need eight.
Therefore we conclude: the chosen problem formulation is hardly suitable for smooth belt without lumped contact forces. We can recommend the constructed solution only for the toothed belts where the lumped forces are possible (the concentration at the boundary teeth).

6 Numerical example

We consider a benchmark example with parameters: $k_0 = 4\,\mathrm{m}^{-1}$ is the initial curvature, $k_1 = 10\,\mathrm{m}^{-1}$ is the pulley circle curvature, $E = 10^9\,\mathrm{Pa}$ is the Young modulus, $\nu = 0.5$ is the Poisson coefficient, $2h \times b = 0.01 \times 0.01\,\mathrm{m}^2$ is the cross section. The loading parameters: $P = 200\,\mathrm{N}$ is the force taking the pulleys apart (first stage), $\omega_1 = 0.2$, $\omega_2 = -0.2$ are the pulley rotation (chosen for illustrative purpose).
The belt form is shown in Fig. 2. Points indicate the contact boundaries.
The variations of distributed contact reactions are presented in Fig. 3 for the first pulley, the picture for the second pulley is symmetrical. The resulting torques

Table 5: Lumped contact forces

	$\omega_1 = 0.2$, $\omega_2 = -0.2$		$\omega_1 = 0.2$, $\omega_2 = 0$	
	$[\![\tilde{Q}_t]\!]$, N	$[\![\tilde{Q}_n]\!]$, N	$[\![\tilde{Q}_t]\!]$, N	$[\![\tilde{Q}_n]\!]$, N
s_1	-2076	-11253	-802	-10562
s_2	-1256	-12001	-64	-1052
s_3	2076	11253	1274	692
s_4	1256	12001	1192	10949

equal $T_1 = -T_2 = 1912\,\mathrm{Nm}$ (in the case $\omega_1 = 0.2$, $\omega_2 = 0$ they equal $T_1 = 1666\,\mathrm{Nm}$, $T_2 = -246\,\mathrm{Nm}$). We calculate the variations of lumped contact forces as the jumps of the force components, their values are written in Table 5; $[\![...]\!] = ...|_{s=s_i+0} - ...|_{s=s_i-0}$.

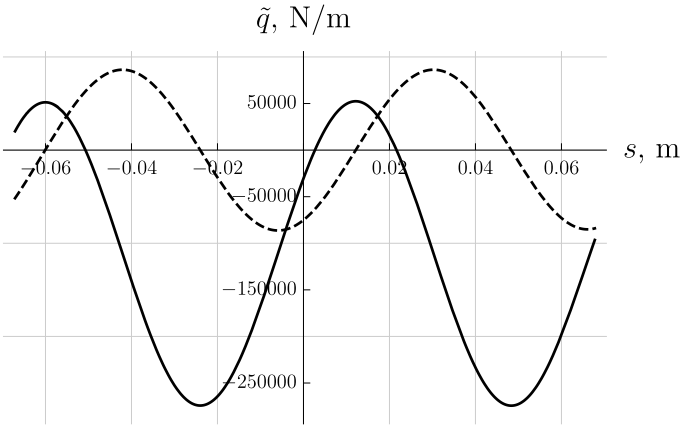

Figure 3: Variations of contact reactions. *Dashed line* denotes normal component, *full line* is tangent one

7 Conclusion

In the paper we presented the solution of the static problem for belt-pulley contact interaction taking into account stick and deformations caused by it. We derived the equations in variations superposed upon the stress state of fitting the belt on the pulleys. We assumed that the points of contact areas move along the pulley circles, hence the distributed contact reactions arise, both normal and tangential, and distributed moment as well. The proposed model is suitable only for the toothed belts, because the lumped contact reactions arise at the boundaries of contact zones.

Acknowledgements

This research is carried out in the framework of the joint project of the Russian Foundation for Basic Research (grant No. 14-51-15001) and the Austrian Science Fund (grant No. I 2093 International Project).

References

[1] T. Firbank. Mechanics of the belt drive. Int. J. Mech. Sci. 12 1970. P. 1053-1063 DOI 10.1016/0020-7403(70)90032-9

[2] C. Menq, J. Bielak, and J. Griffin. The influence of microslip on vibratory response, part i: a new microslip model. J. Sound Vib. 107(2) 1986. P. 279-293 DOI 10.1016/0022-460X(86)90238-5

[3] L. Kong, and R.G. Parker. Microslip friction in flat belt drives. J. Mech. Eng. Sci. 219 2005. P. 1097-1106 DOI 10.1243/095440605X31959

[4] D. Kim, M.J. Leamy, and A.A. Ferri. Dynamic modeling and stability analysis of flat belt drives using an elastic/perfectly plastic friction law. J. Dyn. Sys., Meas. & Contr. 133(4) 2011 DOI 10.1115/1.4003796

[5] A. Belyaev, V. Eliseev, H. Irschik, and E. Oborin. Contact of two equal rigid pulleys with a belt modelled as Cosserat nonlinear elastic rod. Acta Mechanica. 9 pp. (to appear in 2017)

[6] A. Belyaev, V. Eliseev, H. Irschik, and E. Oborin. On static contact of belt and different pulleys. IOP Conf. Ser.: Mater. Sci. & Eng. 8pp. (to appear in 2017)

[7] A. Belyaev, V. Eliseev, H. Irschik, and E. Oborin. Contact of flexible elastic belt with two pulleys, in: H. Irschik et al. (eds.) Dynamics & Control of Advanced Structures and Machines. Springer. 2017. P. 195-203 DOI 10.1007/978-3-319-43080-5_22

[8] A. Belyaev, V. Eliseev, and E. Oborin. About one-dimensional models for describing elastic microslip in belt drive. Int. Review Mech. Eng. 10(5) 2016. P. 333-338 DOI 10.15866/ireme.v10i5.8944

[9] V. Eliseev, Mechanics of deformable solid bodies. St.-Peterbg. State Polytech. Univ. Publ. House, St. Petersburg. 2006

Vladimir V. Eliseev, Polytechnicheskaya str. 29, 195251 St. Petersburg, Russia
Evgenii A. Oborin, Altenbergerstr. 69, 4040 Linz, Austria

Quasiclassics in Wigner-Moyal-von Neumann framework via Multiresolution

Antonina N. Fedorova, Michael G. Zeitlin

zeitlin@math.ipme.ru, anton@math.ipme.ru

Abstract

We present the application of our variational-multiscale approach to numerical/analytical calculations in the general quasi-classical set-up. The starting points are Wigner-Weyl-von Neumann framework as well as Moyal (naive) deformation quantization. Our technique allows to cover all complicated underlying features of compex quantum dynamics based on the proper choice of background functional spaces which determine dynamical properties together with the internal structure of pseudo-differential operators incorporated in the full hierarchy of Wigner-like equations describing the evolution of the quasiprobability beyond trivial gaussian-like area with pure postitive Wigner functions. The choice of hidden underlying symmetry and its representation on the orbits of proper actions provide us with the filtration of the background Hilbert space of states which implies the whole tower of internal hidden scales by using multiresolution decomposition. All that allows to consider maximally localized quantum states and most sparse representation for all set of observables. At the same time the orbit structure allows to consider basic nonlocal phenomena like entanglement with possible subsequent decoherence. Our main applications in this consideration are related with a description of quantum properties in nonlinear beam dynamics, both in accelerator and plasma physics but such general background provides all possibilities to describe the modeling of prototypes of any future quantum devices.

1 Introduction

In this paper we consider some starting points in the applications of a new numerical-analytical technique which is based on local nonlinear harmonic analysis (wavelet analysis, generalized coherent states analysis) to the quantum/quasiclassical (nonlinear) beam/accelerator physics calculations. The reason for this treatment is that recently a number of problems appeared in which one needs take into account quantum properties of particles/beams.Our starting point is the general point of view of deformation quantization approach at least on naive Moyal/Weyl/Wigner level (part 2). The main point is that the algebras of quantum observables are the deformations of commutative algebras of classical observables (functions) [1]. So, if we

have the Poisson manifold M (symplectic manifolds, Lie coalgebras, etc.) as a model for classical dynamics then for quantum calculations we need to find an associative (but non-commutative) star product $*$ on the space of formal power series in $\hbar$ with coefficients in the space of smooth functions on M such that

$$f * g = fg + \hbar\{f, g\} + \sum_{n\geq 2} \hbar^n B_n(f, g), \tag{1}$$

where $\{f, g\}$ is the Poisson brackets, B_n are bidifferential operators $C^\infty(X) \otimes C^\infty(X) \to C^\infty(X)$. There is also an infinite-dimensional gauge group on the set of star-products

$$f \mapsto f + \sum_{n\geq 2} \hbar^n D_n(f), \tag{2}$$

where D_n are differential operators. Kontsevich gave the solution to this deformation problem in terms of formal power series via sum over graphs [1]. He also proved that for every Poisson manifold M there is a canonically defined gauge equivalence class of star-products on M. Also there is the nonperturbative corrections to power series representation for $*$ [1]. In naive calculations we may use simple formal rules:

$$* \equiv \exp\Big(\frac{i\hbar}{2}(\overleftarrow{\partial}_x \overrightarrow{\partial}_p - \overleftarrow{\partial}_p \overrightarrow{\partial}_x)\Big) \tag{3}$$

$$f(x,p) * g(x,p) = f(x, p - \frac{i\hbar}{2}\overrightarrow{\partial}_x) \cdot g(x, p + \frac{i\hbar}{2}\overleftarrow{\partial}_x) \tag{4}$$

$$= f(x + \frac{i\hbar}{2}\overrightarrow{\partial}_p, p - \frac{i\hbar}{2}\overrightarrow{\partial}_x) g(x,p) \tag{5}$$

In this paper we consider calculations of Wigner functions (WF) as the solution of Wigner equations [2] (part 3):

$$i\hbar\frac{\partial}{\partial t} W(x,p,t) = H * W(x,p,t) - W(x,p,t) * H \tag{6}$$

and especially stationary Wigner equations:

$$H * W - W * H = Ef \tag{7}$$

Our approach is based on extension of our variational-wavelet approach [3]-[14]. Wavelet analysis is some set of mathematical methods, which gives us the possibility to work with well-localized bases (Fig. 1) in functional spaces and gives maximum sparse forms for the general type of operators (differential, integral, pseudodifferential) in such bases. These bases are natural generalization of standard coherent, squeezed, thermal squeezed states [2], which correspond to quadratical systems (pure linear dynamics) with Gaussian Wigner functions. So, we try to calculate quantum corrections to classical dynamics described by polynomial nonlinear Hamiltonians

such as orbital motion in storage rings, orbital dynamics in general multipolar fields etc. from papers [3]-[13]. The common point for classical/quantum calculations is that any solution which comes from full multiresolution expansion in all space/time (or phase space) scales represents expansion into a slow part and fast oscillating parts (part 4). So, we may move from the coarse scales of resolution to the finest one for obtaining more detailed information about our dynamical classical/quantum process. In this way we give contribution to our full solution from each scale of resolution. The same is correct for the contribution to power spectral density (energy spectrum): we can take into account contributions from each level/scale of resolution. Because affine group of translations and dilations (or more general group, which acts on the space of solutions) is inside the approach (in wavelet case), this method resembles the action of a microscope. We have contribution to final result from each scale of resolution from the whole underlying infinite scale of spaces. In part 5 we consider numerical modelling of Wigner functions which explicitly demonstrates quantum interference of the generalized "coherent" states.

2 Quasiclassical evolution

Let us consider classical and quantum dynamics in phase space $\Omega = R^{2m}$ with coordinates (x, ξ) and generated by Hamiltonian $\mathcal{H}(x, \xi) \in C^\infty(\Omega; R)$. If $\Phi_t^{\mathcal{H}} : \Omega \longrightarrow \Omega$ is (classical) flow then time evolution of any bounded classical observable or symbol $b(x, \xi) \in C^\infty(\Omega, R)$ is given by $b_t(x, \xi) = b(\Phi_t^{\mathcal{H}}(x, \xi))$. Let $H = Op^W(\mathcal{H})$ and $B = Op^W(b)$ are the self-adjoint operators or quantum observables in $L^2(R^n)$, representing the Weyl quantization of the symbols $\mathcal{H}, b$ [1]

$$(Bu)(x) = \frac{1}{(2\pi\hbar)^n} \int_{R^{2n}} b\left(\frac{x+y}{2}, \xi\right) \cdot e^{i<(x-y),\xi>/\hbar} u(y) \mathrm{d}y \mathrm{d}\xi, \tag{8}$$

where $u \in S(R^n)$ and $B_t = e^{iHt/\hbar} B e^{-iHt/\hbar}$ be the Heisenberg observable or quantum evolution of the observable B under unitary group generated by H. B_t solves the Heisenberg equation of motion $\dot{B}_t = (i/\hbar)[H, B_t]$. Let $b_t(x, \xi; \hbar)$ is a symbol of B_t then we have the following equation for it

$$\dot{b}_t = \{\mathcal{H}, b_t\}_M, \tag{9}$$

with the initial condition $b_0(x, \xi, \hbar) = b(x, \xi)$. Here $\{f, g\}_M(x, \xi)$ is the Moyal brackets of the observables $f, g \in C^\infty(R^{2n})$, $\{f, g\}_M(x, \xi) = f\sharp g - g\sharp f$, where $f\sharp g$ is the symbol of the operator product and is presented by the composition of the symbols f, g

$$(f\sharp g)(x, \xi) = \frac{1}{(2\pi\hbar)^{n/2}} \int_{R^{4n}} e^{-i<r,\rho>/\hbar + i<\omega,\tau>/\hbar} \cdot f(x+\omega, \rho+\xi) \cdot g(x+r, \tau+\xi) \mathrm{d}\rho \mathrm{d}\tau \mathrm{d}r \mathrm{d}\omega \tag{10}$$

For our problems it is useful that $\{f, g\}_M$ admits the formal expansion in powers of $\hbar$:

$$\{f, g\}_M(x, \xi) \sim \{f, g\} + 2^{-j} \cdot \sum_{|\alpha+\beta|=j\geq 1} (-1)^{|\beta|} \cdot (\partial_\xi^\alpha f D_x^\beta g) \cdot (\partial_\xi^\beta g D_x^\alpha f), \tag{11}$$

where $\alpha = (\alpha_1, \ldots, \alpha_n)$ is a multi-index, $|\alpha| = \alpha_1 + \cdots + \alpha_n$, $D_x = -i\hbar\partial_x$. So, evolution (9) for symbol $b_t(x, \xi; \hbar)$ is

$$\dot{b}_t = \{\mathcal{H}, b_t\} + \frac{1}{2^j} \sum_{|\alpha+\beta|=j\geq 1} (-1)^{|\beta|} \cdot \hbar^j (\partial_\xi^\alpha \mathcal{H} D_x^\beta b_t) \cdot (\partial_\xi^\beta b_t D_x^\alpha \mathcal{H}). \tag{12}$$

At $\hbar = 0$ this equation transforms to classical Liouville equation. Equation (12) plays the key role in many quantum (semiclassical) problems. We consider its particular case–Wigner equation–in the next section.

3 Wigner equations

According to Weyl transform quantum state (wave function or density operator) corresponds to Wigner function, which is analog of classical phase-space distribution [2]. We consider the following form of differential equations for time-dependent WF

$$\partial_t W(p, q, t) = \frac{2}{\hbar} \sin\Big[\frac{\hbar}{2}(\partial_q^H \partial_p^W - \partial_p^H \partial_q^W)\Big] \cdot H(p, q) W(p, q, t) \tag{13}$$

Let

$$\hat{\rho} = |\Psi_\epsilon >< \Psi_\epsilon| \tag{14}$$

be the density operator or projection operator corresponding to the energy eigenstate $|\Psi_\epsilon >$ with energy eigenvalue ϵ. Then time-independent Schroedinger equation corresponding to Hamiltonian

$$\hat{H}(\hat{p}, \hat{q}) = \frac{\hat{p}^2}{2m} + U(\hat{q}) \tag{15}$$

where $U(\hat{q}$ is arbitrary polynomial function (related beam dynamics models considered in [3]-[13]) on $\hat{q}$ is [2]:

$$\hat{H}\hat{\rho} = \epsilon\hat{\rho} \tag{16}$$

After Weyl-Wigner mapping we arrive at the following equation on WF in c-numbers:

$$H(p + \frac{\hbar}{2i}\frac{\partial}{\partial q}, q - \frac{\hbar}{2i}\frac{\partial}{\partial p}\Big) W(p, q) = \epsilon W(p, q) \tag{17}$$

or

$$\Big(\frac{p^2}{2m} + \frac{\hbar}{2i}\frac{p}{m}\frac{\partial}{\partial q} - \frac{\hbar^2}{8m}\frac{\partial^2}{\partial q^2}\Big) W(p, q) + U\Big(q - \frac{\hbar}{2i}\frac{\partial}{\partial p}\Big) W(p, q) = \epsilon W(p, q)$$

After expanding the potential U into the Taylor series we have two real partial differential equations

$$\Big(- \frac{p}{m}\frac{\partial}{\partial q} + \sum_{m=0}^{\infty} \frac{1}{(2m+1!)} \Big(\frac{i\hbar}{2}\Big)^{2m} \frac{\mathrm{d}^{2m+1} U}{\mathrm{d}q^{2m+1}} \frac{\partial^{2m+1}}{\partial p^{2m+1}}\Big) W(p, q) = 0 \tag{18}$$

$$\Big(\frac{p^2}{2m}+U(q)-\frac{\hbar^2}{8m}\frac{\partial^2}{\partial q^2}+\sum_{n=1}^{\infty}\frac{1}{(2n)!}\Big(\frac{i\hbar}{2}\Big)^{2n}\frac{\mathrm{d}^{2n}U}{\mathrm{d}q^{2n}}\frac{\partial^{2n}}{\partial p^{2n}}\Big)W(p,q)=$$
$$\epsilon W(p,q) \tag{19}$$

In the next section we consider variation-wavelet approach for the solution of these equations for the case of arbitrary polynomial $U(q)$, which corresponds to a finite number of terms in equations (18), (19) up to any order of $\hbar$.

4 Variational multiscale representation

Let L be arbitrary (non)linear differential operator with matrix dimension d, which acts on some set of functions $\Psi \equiv \Psi(x,y) = \Big(\Psi^1(x,y),...,\Psi^d(x,y)\Big), \quad x,y \in \Omega \subset \Re^2$ from $L^2(\Omega)$:

$$L\Psi \equiv L(Q,x,y)\Psi(x,y) = 0, \tag{20}$$

where

$$Q \equiv Q_{d_1,d_2,d_3,d_4}(x,y,\partial/\partial x,\partial/\partial y) = \sum_{i,j,k,\ell=1}^{d_1,d_2,d_3,d_4} a_{ijk\ell}x^i y^j\Big(\frac{\partial}{\partial x}\Big)^k\Big(\frac{\partial}{\partial y}\Big)^\ell \tag{21}$$

Let us consider now the N mode approximation for solution as the following ansatz (in the same way we may consider different ansatzes):

$$\Psi^N(x,y) = \sum_{r,s=1}^{N} a_{r,s}\Psi_r(x)\Phi_s(y) \tag{22}$$

We shall determine coefficients of expansion from the following Galerkin conditions (different related variational approaches are considered in [3]-[13]):

$$\ell^N_{k\ell} \equiv \int (L\Psi^N)\Psi_k(x)\Phi_\ell(y)\mathrm{d}x\mathrm{d}y = 0 \tag{23}$$

So, we have exactly dN^2 algebraical equations for dN^2 unknowns a_{rs}.
But in the case of equations for WF (18), (19) we have overdetermined system of equations: $2N^2$ equations for N^2 unknowns a_{rs} (in this case $d=1$). In this paper we consider non-standard method for resolving this problem, which is based on biorthogonal wavelet expansion. So, instead of expansion (22) we consider the following one:

$$\Psi^N(x,y) = \sum_{r,s=1}^{N} a_{r,s}\Psi_r(x)\Psi_s(y) + \sum_{i,j=1}^{N}\widetilde{a}_{ij}\widetilde{\Psi}_i(x)\widetilde{\Phi}_j(y), \tag{24}$$

where $\widetilde{\Psi}_i(x)\widetilde{\Phi}_j(y)$ are the bases dual to initial ones. Because wavelet functions are the generalization of coherent states we consider an expansion on this overcomplete set of bases wavelet functions as a generalization of standard coherent states expansion.
So, variational/Galerkin approach reduced the initial problem (20) to the problem of solution of functional equations at the first stage and some algebraical problems at the second stage. We consider now the multiresolution expansion as the second main part of our construction. Because affine group of translation and dilations is inside the approach, this method resembles the action of a microscope. We have contribution to final result from each scale of resolution from the whole infinite scale of increasing closed subspaces V_j:

$$...V_{-2} \subset V_{-1} \subset V_0 \subset V_1 \subset V_2 \subset ... \quad .$$

The solution is parametrized by solutions of two reduced algebraical problems, one is linear or nonlinear (23) (depends on the structure of operator L) and the second one is some linear problem related to computation of coefficients of algebraic equations (23). These coefficients can be found by the method of Connection Coefficients (CC) [15] or related method [16]. We use compactly supported wavelet basis functions for expansions (22), (24). We may consider different types of wavelets including general wavelet packets (section 5 below). These coefficients depend on the wavelet-Galerkin integrals. In general we need to find ($d_i \geq 0$)

$$\Lambda^{d_1 d_2 ... d_n}_{\ell_1 \ell_2 ... \ell_n} = \int\limits_{-\infty}^{\infty} \prod \varphi^{d_i}_{\ell_i}(x) dx \tag{25}$$

According to CC method [15] we use the next construction for quadratic case. When N in scaling equation is a finite even positive integer the function $\varphi(x)$ has compact support contained in $[0, N-1]$. For a fixed triple (d_1, d_2, d_3) only some $\Lambda^{d_1 d_2 d_3}_{\ell m}$ are nonzero: $2-N \leq \ell \leq N-2, \quad 2-N \leq m \leq N-2, \quad |\ell - m| \leq N-2$. There are $M = 3N^2 - 9N + 7$ such pairs (ℓ, m). Let $\Lambda^{d_1 d_2 d_3}$ be an M-vector, whose components are numbers $\Lambda^{d_1 d_2 d_3}_{\ell m}$. Then we have the following reduced algebraical system : Λ satisfy the system of equations ($d = d_1 + d_2 + d_3$)

$$A\Lambda^{d_1 d_2 d_3} = 2^{1-d}\Lambda^{d_1 d_2 d_3}, \quad A_{\ell,m;q,r} = \sum_p a_p a_{q-2\ell+p} a_{r-2m+p} \tag{26}$$

By moment equations we have created a system of $M + d + 1$ equations in M unknowns. It has rank M and we can obtain unique solution by combination of LU decomposition and QR algorithm. For nonquadratic case we have analogously additional linear problems for objects (25). Solving these linear problems we obtain the coefficients of reduced main linear/nonlinear algebraical system (23) and after its solution we obtain the coefficients of wavelet expansion (22), (24). As a result we obtained the explicit solution of our problem in the base of compactly supported wavelets (22).
Also in our case we need to consider the extension of this approach to the case of any type of variable coefficients (periodic, regular or singular). We can produce such approach if we add in our construction additional refinement equation, which

encoded all information about variable coefficients [16]. So, we need to compute only additional integrals of the form

$$\int_D b_{ij}(t)(\varphi_1)^{d_1}(2^m t - k_1)(\varphi_2)^{d_2}(2^m t - k_2)\mathrm{d}x, \tag{27}$$

where $b_{ij}(t)$ are arbitrary functions of time and trial functions φ_1, φ_2 satisfy the refinement equations:

$$\varphi_i(t) = \sum_{k \in \mathbf{Z}} a_{ik}\varphi_i(2t - k) \tag{28}$$

If we consider all computations in the class of compactly supported wavelets then only a finite number of coefficients do not vanish. To approximate the non-constant coefficients, we need choose a different refinable function φ_3 along with some local approximation scheme

$$(B_\ell f)(x) := \sum_{\alpha \in \mathbf{Z}} F_{\ell,k}(f)\varphi_3(2^\ell t - k), \tag{29}$$

where $F_{\ell,k}$ are suitable functionals supported in a small neighborhood of $2^{-\ell}k$ and then replace b_{ij} in (27) by $B_\ell b_{ij}(t)$. To guarantee sufficient accuracy of the resulting approximation to (27) it is important to have the flexibility of choosing φ_3 different from φ_1, φ_2. So, if we take $\varphi_4 = \chi_D$, where χ_D is characteristic function of D, which is again a refinable function, then the problem of computation of (27) is reduced to the problem of calculation of integral

$$H(k_1, k_2, k_3, k_4) = H(k) = \int_{\mathbf{R}^s} \varphi_4(2^j t - k_1) \cdot \varphi_3(2^\ell t - k_2)\varphi_1^{d_1}(2^r t - k_3)\varphi_2^{d_2}(2^s t - k_4)\mathrm{d}x \tag{30}$$

The key point is that these integrals also satisfy some sort of algebraical equation [16]:

$$2^{-|\mu|}H(k) = \sum_{\ell \in \mathbf{Z}} b_{2k-\ell}H(\ell), \qquad \mu = d_1 + d_2. \tag{31}$$

This equation can be interpreted as the problem of computing an eigenvector. Thus, the problem of extension of our approach to the case of variable coefficients is reduced to the same standard algebraical problem as in case of constant coefficients. So, the general scheme is the same one and we have only one more additional linear algebraic problem. After solution of these linear problems we can again compute coefficients of wavelet expansions (22), (24).

Now we concentrate on the last additional problem which comes from overdeterminity of equations (18), (19), which demands to consider expansion (24) instead of expansion (22). It leads to equal number of equations and unknowns in reduced algebraical system of equations (23). For this reason we consider biorthogonal wavelet analysis. We started with two hierarchical sequences of approximations spaces [16]:

$$\ldots V_{-2} \subset V_{-1} \subset V_0 \subset V_1 \subset V_2 \ldots,$$

$$\ldots \widetilde{V}_{-2} \subset \widetilde{V}_{-1} \subset \widetilde{V}_0 \subset \widetilde{V}_1 \subset \widetilde{V}_2 \ldots,$$

and as usually, W_0 is complement to V_0 in V_1, but now not necessarily orthogonal complement. New orthogonality conditions have now the following form:

$$\widetilde{W}_0 \perp V_0, \quad W_0 \perp \widetilde{V}_0, \quad V_j \perp \widetilde{W}_j, \quad \widetilde{V}_j \perp W_j,$$

translates of ψ span W_0, translates of $\tilde{\psi}$ span $\widetilde{W}_0$. Biorthogonality conditions are

$$< \psi_{jk}, \tilde{\psi}_{j'k'} >= \int_{-\infty}^{\infty} \psi_{jk}(x)\tilde{\psi}_{j'k'}(x)\mathrm{d}x = \delta_{kk'}\delta_{jj'},$$

where $\psi_{jk}(x) = 2^{j/2}\psi(2^j x - k)$. Functions $\varphi(x), \tilde{\varphi}(x-k)$ form dual pair:

$$< \varphi(x-k), \tilde{\varphi}(x-\ell) >= \delta_{kl}, \quad < \varphi(x-k), \tilde{\psi}(x-\ell) >= 0 \quad \text{for} \quad \forall k, \ \forall \ell.$$

Functions $\varphi, \tilde{\varphi}$ generate a multiresolution analysis. $\varphi(x-k)$, $\psi(x-k)$ are synthesis functions, $\tilde{\varphi}(x-\ell)$, $\tilde{\psi}(x-\ell)$ are analysis functions. Synthesis functions are biorthogonal to analysis functions. Scaling spaces are orthogonal to dual wavelet spaces. Two multiresolutions are intertwining

$$V_j + W_j = V_{j+1}, \quad \widetilde{V}_j + \widetilde{W}_j = \widetilde{V}_{j+1}.$$

These are direct sums but not orthogonal sums. So, our representation for solution has now the form

$$f(t) = \sum_{j,k} \tilde{b}_{jk}\psi_{jk}(t),$$

where synthesis wavelets are used to synthesize the function. But $\tilde{b}_{jk}$ come from inner products with analysis wavelets.

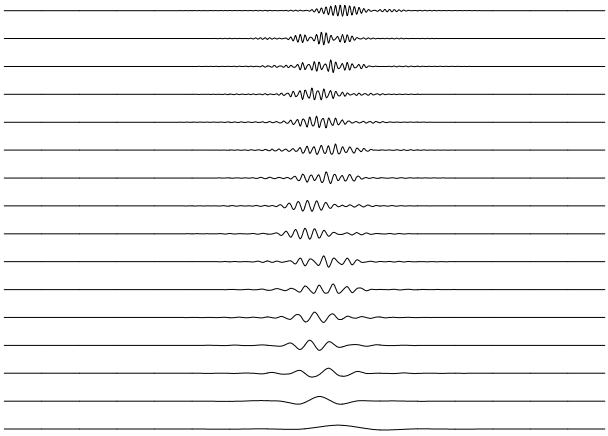

Figure 1: Localized contributions to beam motion.

Biorthogonal point of view is more flexible and stable under the action of large class of operators while orthogonal (one scale for multiresolution) is fragile, all computations are much more simple and we accelerate the rate of convergence of our expansions (24). By analogous anzatzes and approaches we may construct also the multiscale/multiresolution representations for solution of time dependent Wigner equation (13) [14].

5 Numerical Modelling

So, our constructions give us the following N-mode representation for solution of Wigner equations (18)-(19):

$$W^N(p,q) = \sum_{r,s=1}^{N} a_{rs}\Psi_r(p)\Phi_s(q), \tag{32}$$

where $\Psi_r(p)$, $\Phi_s(q)$ may be represented by some family of (nonlinear) eigenmodes with the corresponding multiresolution/multiscale representation in the high-localized wavelet bases (Fig. 1):

$$\Psi_k(p) = \Psi^{M_1}_{k,slow}(p) + \sum_{i\geq M_1} \Psi^i_k(\omega^1_i p), \quad \omega^1_i \sim 2^i, \tag{33}$$

$$\Phi_k(q) = \Phi^{M_2}_{k,slow}(q) + \sum_{j\geq M_2} \Phi^j_k(\omega^2_j q), \quad \omega^2_j \sim 2^j. \tag{34}$$

Our (nonlinear) eigenmodes are more realistic for the modelling of nonlinear classical/quantum dynamical process than the corresponding linear gaussian-like coherent states. Here we mention only the best convergence properties of expansions based on wavelet packets, which realize the so called minimal Shannon entropy property (Fig. 1). On Fig. 2 we present numerical modelling [17] of Wigner function for a simple model of beam motion, which explicitly demonstrates quantum interference property. On Fig. 3 we present the N-mode multiscale/multiresolution decomposition (32)-(34) for solution of Wigner equation. It demonstrates a variety of possible quantum states/patterns generated inside "deformed" Wigner-Moyal dynamics by means of action of internal hidden symmetry on the Hilbert space of states provided by a base set of fundamental localized (nonlinear) eingenmodes. The full zoo includes chaotic, entangled and decoherent states. Qualitative aspects will be considered elsewhere. Some novel approach to the description of quantum problems can be found in our recent papers [18] and at web pages below.

References

[1] D. Sternheimer, Los Alamos preprint: math.QA/9809056, M. Kontsevich, q-alg/9709040, V. Periwal, hep-th/0006001.

[2] T. Curtright, T. Uematsu, C. Zachos, hep-th/0011137, M.Huq, e.a., *Phys. Rev.*, **A 57**, 3188 (1998).

[3] A.N. Fedorova and M.G. Zeitlin, *Math. and Comp. in Simulation*, **46**, 527 (1998).

[4] A.N. Fedorova and M.G. Zeitlin, 'Wavelet Approach to Mechanical Problems. Symplectic Group, Symplectic Topology and Symplectic Scales', *New Applications of Nonlinear and Chaotic Dynamics in Mechanics*, 31, 101 (Kluwer, 1998).

[5] A.N. Fedorova and M.G. Zeitlin, **CP405**, 87 (American Institute of Physics, 1997). Los Alamos preprint, physics/9710035.

[6] A.N. Fedorova, M.G. Zeitlin and Z. Parsa, Proc. PAC97 **2**, 1502, 1505, 1508 (IEEE, 1998).

[7] A.N. Fedorova, M.G. Zeitlin and Z. Parsa, Proc. EPAC98, 930, 933 (Institute of Physics, 1998).

[8] A.N. Fedorova, M.G. Zeitlin and Z. Parsa, **CP468**, 48 (American Institute of Physics, 1999). Los Alamos preprint, physics/990262.

[9] A.N. Fedorova, M.G. Zeitlin and Z. Parsa, **CP468**, 69 (American Institute of Physics, 1999). Los Alamos preprint, physics/990263.

[10] A.N. Fedorova and M.G. Zeitlin, Proc. PAC99, 1614, 1617, 1620, 2900, 2903, 2906, 2909, 2912 (IEEE/APS, New York, 1999).
Los Alamos preprints: physics/9904039, 9904040, 9904041, 9904042, 9904043, 9904045, 9904046, 9904047.

[11] A.N. Fedorova and M.G. Zeitlin, Proc. UCLA ICFA Workshop, in press, Los Alamos preprint: physics/0003095.

[12] A.N. Fedorova and M.G. Zeitlin, Proc. EPAC00, 415, 872, 1101, 1190, 1339, 2325.
Los Alamos preprints: physics/0008045, 0008046, 0008047, 0008048, 0008049, 0008050.

[13] A.N. Fedorova, M.G. Zeitlin, Proc. LINAC00, 2 papers in press, Los Alamos preprints: physics/0008043, 0008200.

[14] A.N. Fedorova, M.G. Zeitlin, Localization and Pattern Formation in Quantum Physics. II. Waveletons in Quantum Ensembles, in The Nature of Light: What is a Photon? SPIE, vol. 5866, pp. 257-268, 2005; quant-ph/0505115; Localization and Pattern Formation in Quantum Physics. I. Phenomena of Localization, in The Nature of Light: What is a Photon? SPIE, vol. 5866, pp. 245-256, 2005; quant-ph/0505114.

[15] A. Latto, e.a. Aware Technical Report AD910708 (1991).

[16] W. Dahmen, C. Micchelli, *SIAM J. Numer. Anal.*, **30**, 507 (1993); Y. Meyer, *Wavelets and Operators*, Cambridge Univ. Press, 1990.

[17] F. Auger, e.a., Time-frequency Toolbox, CNRS/Rice Univ. (1996).

[18] A.N. Fedorova, M.G. Zeitlin, Quantum objects in a sheaf framework, Journal of Physics CS, vol. 490, 012224, 2014; Quantum multiresolution: tower of scales, Journal of Physics CS, vol. 490, 012216, 2014; arXiv:1703.09556; arXiv:1703.09546.

Antonina N. Fedorova, Michael G. Zeitlin
Mathematical Methods in Mechanics Group, IPME RAS, V.O. Bolshoj pr., 61, 199178, St. Petersburg, Russia
http://math.ipme.ru/zeitlin.html, http://mp.ipme.ru/zeitlin.html

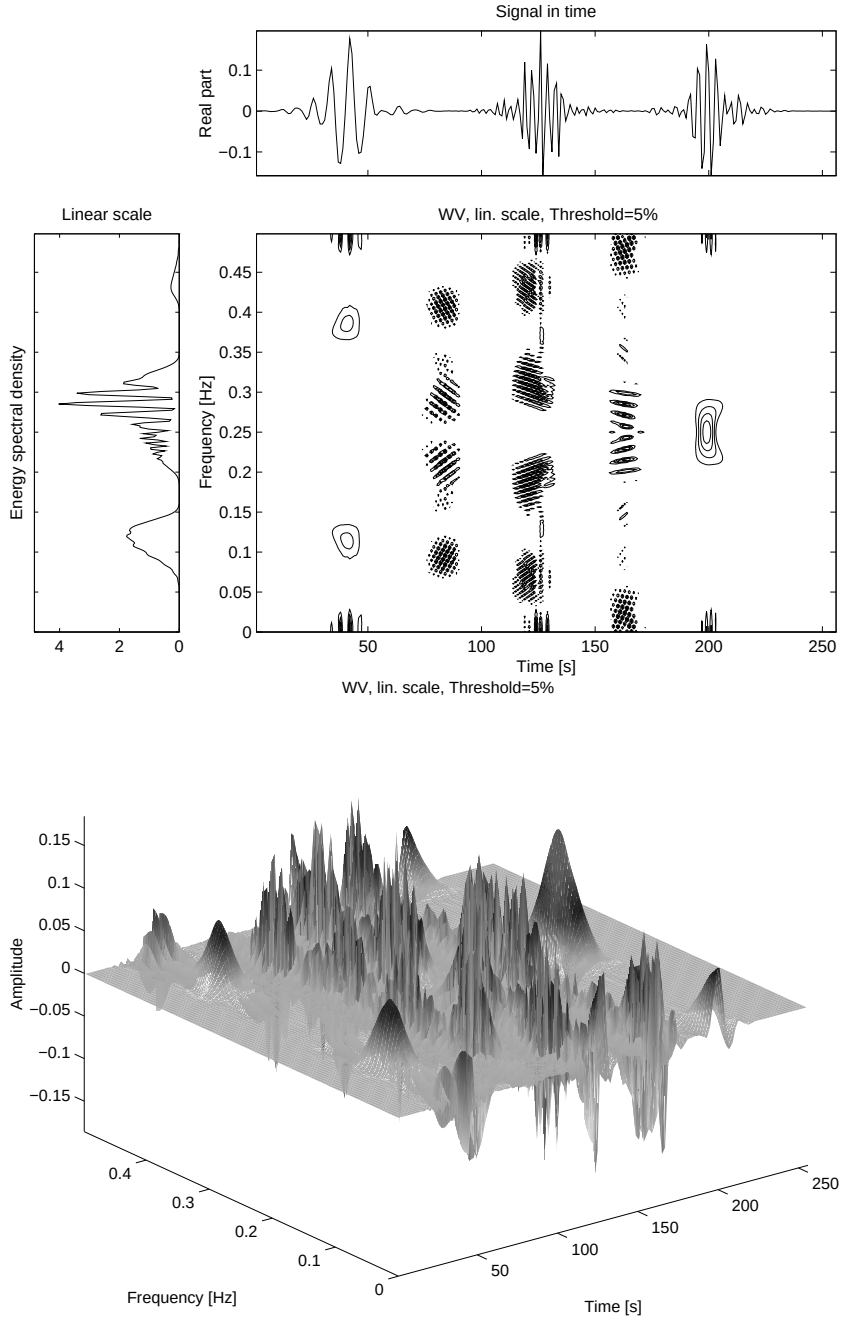

Figure 2: Wigner function for 3 wavelet packets.

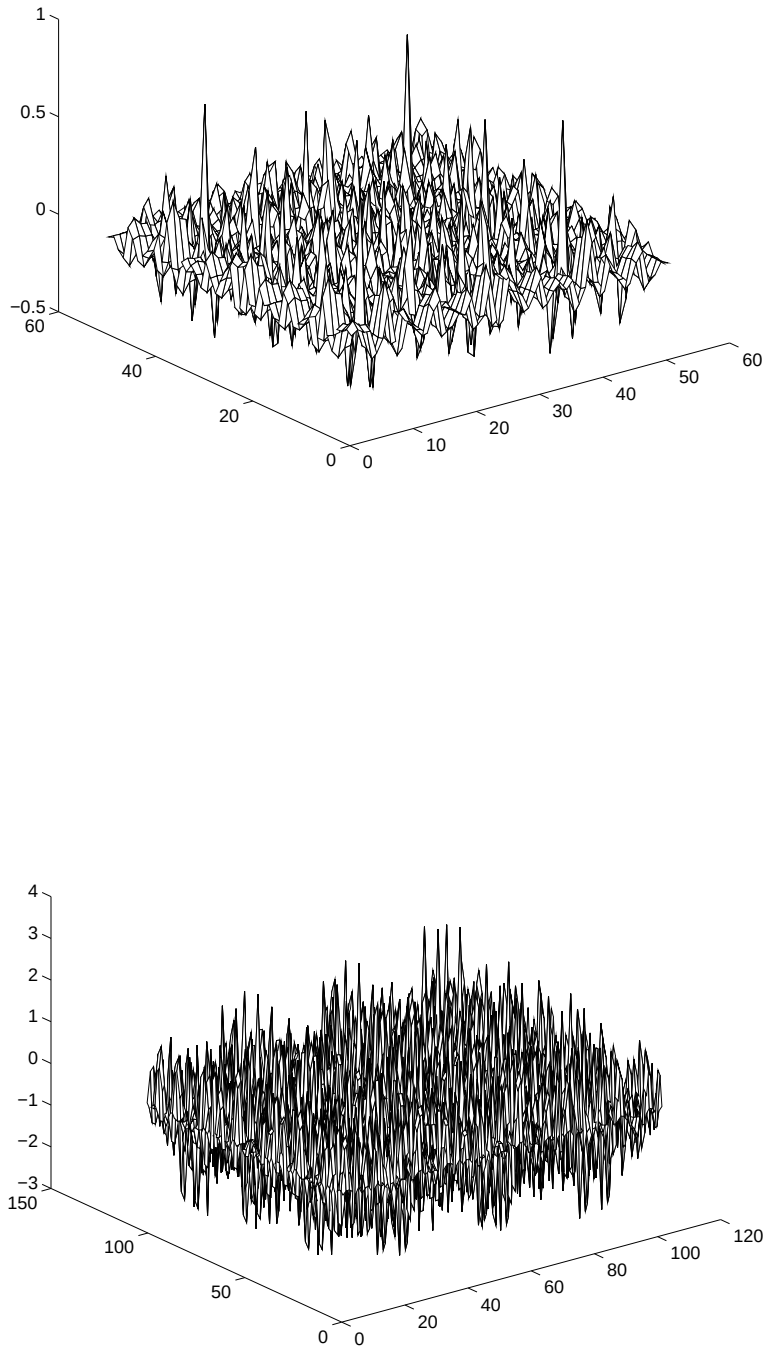

Figure 3: Multiresolution/multiscale representations for Wigner functions.

Multiscale structure of polynomial dynamics

Antonina N. Fedorova, Michael G. Zeitlin

zeitlin@math.ipme.ru, anton@math.ipme.ru

Abstract

We consider a wavelet based multiscale description for nonlinear optimal dynamics (energy minimization in a high power electromechanical system as a key example). In a particular case, we have the solution as a series on shifted Legendre polynomials parametrized by the solutions of the reduced algebraical systems of equations. In the general case, we represent the solution via multiscale decomposition in the base of various families of compactly supported wavelets. In this case the solution is parametrized by solutions of two reduced algebraic problems, one as in the first case and the second one is some linear problem obtained from the popular wavelet constructions: Fast Wavelet Transform, Stationary Subdivision Schemes, the method of Connection Coefficients. Such a machinery allows us to consider maximally localized bases in the underlying functional spaces together with most sparse representation for all type of operators involving in the initial set-up. All that provides the best possible convergence properties and as a result our numerical modeling is more flexible and saves CPU time. In addition, the final representation is parametrized by the reduced pure algebraic construction (the so-called general dispersion relations) and allows us to solve the dynamical or optimal control problems (energy minimizatin, e.g.)in a most effective way.

1 Introduction

Many important physical and mechanical problems are reduced to the solving of systems of nonlinear differential equations with the polynomial type of nonlinearities. In this paper and related paper in this volume, we consider applications of methods of nonlinear local harmonic analysis (a.k.a. wavelet analysis in a simple case of affine group) to such problems. Wavelet analysis is a relatively novel set of mathematical methods, which gives us the possibility to work with well-localized bases in functional spaces and with the general type of operators (including pseudodifferential) in such bases. Many examples may be found in papers [11]–[18]. Now we apply our approach to the case of a constrained variational problem: the problem of energy minimization in electromechanical systems. We consider a synchronous electrical machine and a mill as a load (in this approach we can consider instead of the mill any mechanical load with polynomial approximation for the mechanical moment).

We consider the problem of "electrical economizer" as an optimal control problem. As result of the first stage we give the explicit time description of optimal dynamics for that electromechanical system. As a result of the second stage we give the time dynamics of our system via a construction based on the set of switched type functions (Walsh functions), which can be realized on the modern thyristor technique. In this paper, using the method of analysis of dynamical process in the Park system [1], which we developed in ref. [9], [10], we consider the optimal control problem in that system. As in [9] and [10], our goal is to construct explicit time solutions, which can be used directly in microprocessor control systems. Our consideration is based on the Integral Variational Method, which was develo ped in [21]. As we shall see later, we can obtain explicit time dependence for all dynamical variables in our optimal control problem. It is based on the fact that optimal control dynamic in our case is given by some nonlinear system of equations which is the extension of initial Park system. Moreover, the equations of optimal dynamics also is the system of Riccati type (we use the quadratic dependence of the mechanical moment). It should be noted that this system of equations is not the pure differential system but it is the mixed differential-algebraic or functional system of equations [19].
In Section 2 we consider the description of our variational approach, which can be generalized in such a way that allows us to consider it in Hamiltonian (symplectic) approach [12].
In Section 3 we consider the explicit representation for solutions. Our initial dynamical problem (without control) is described by the system of nonlinear differential equations, which has the next Cauchy form (for definitions see [9], [10])

$$\frac{di_k}{dt} = \sum_{\ell} A_{\ell} i_{\ell} + \sum_{r,s} A_{rs} i_r i_s + A_k(t)$$

where $A_{\ell}, A_{rs} (\ell, r, s = \overline{1,6})$ are constants, $A_k(t), (k = \overline{1,5})$ are explicit functions of time, $A_6(i_6, t) = a + di_6 + bi_6^2$ is analytical approximation for the mechanical moment of the mill. At initial stage of the solution of optimal control problem in both methods we need to select from initial set of dynamical variables $i_1, \ldots, i_6$ the controlling and the controllable variables. In our case we consider i_1, i_2 as the controlling variables. Because we consider the energy optimization, we use the next general form of energy functional in our electromechanical system

$$Q = \int_{t_0}^{t} [K_1(i_1, i_2) + K_2(\dot{i}_1, \dot{i}_2)] dt,$$

where K_1, K_2 are quadratic forms. Thus, our functional is the quadratic functional on the variables i_1, i_2 and its derivatives. Moreover, we may consider the optimization problem with some constraints which are motivated by technical reasons [9], [10]. Then after standard manipulations from the theory of optimal control, we reduce the problem of energy minimization to some extended nonlinear system of equations. As a result, the solution of equations of optimal dynamics provides: 1). the explicit time dependence of the controlling variables $u(t) = \{i_1(t), i_2(t)\}$ which give 2). the optimum of corresponding functional of the energy and 3). explicit time dynamics of the controllable variables $\{i_3, i_4, i_5, i_6\}(t)$. The obtained solutions are

given in the following form:

$$i_k(t) = i_k(0) + \sum_{i=1}^{N} \lambda_k^i X_i(t),$$

where in our first case (Section 3), we have $X_i(t) = Q_i(t)$, where $Q_i(t)$ are shifted Legendre polynomials [21] and λ_k^i are the roots of reduced algebraic system of equations. In our second case, corresponding to the generic wavelet example, considered in Section 4, the base functions $X_i(t)$ are obtained from the multiresolution decomposition in the basis of compactly supported wavelets while λ_k^i are the roots of corresponding algebraic Riccati systems with coefficients, which are given by Fast Wavelet Transform (FWT) [2] or by Stationary Subdivision Schemes(SSS) [6] or by the method of Connection Coefficients (CC) [23].
Giving the controlling variables in the explicit form, we have optimal, according to energy, dynamics in our electromechanical systems. Obviously, the technical realization of controlling variables via the arbitrary continuous functions of time is impossible, but we can replace them by their re-expansions in the basis of switching type functions, which can be realized now on the modern thyristor technique. We considered this re-expansion in [9], [10], where we used Walsh and Haar functions [3] as a base set of switching type functions. This is a special case of general sequency analysis [20]. It should be noted that the best practical realization of the expansions described in Section 4 is based on the general wavelet packet basis [4].

2 Polynomial dynamics

Our problems may be formulated as the systems of ordinary differential equations:

$$dx_i/dt = f_i(x_j, t), \ (i, j = 1, ..., n)$$

with fixed initial conditions $x_i(0)$, where f_i are not more than polynomial functions of dynamical variables x_j and have arbitrary dependence of time. Because of time dilation we can consider only next time interval: $0 \leq t \leq 1$. Let us consider a set of functions:

$$\Phi_i(t) = x_i dy_i/dt + f_i y_i$$

and a set of the corresponding functionals:

$$F_i(x) = \int_0^1 \Phi_i(t)dt - x_i y_i \mid_0^1,$$

where $y_i(t)(y_i(0) = 0)$ are dual variables. It is obvious that the initial system and the system $F_i(x) = 0$ are equivalent. We mention here, that we can consider the symplectization of this approach (Hamiltonian version) [12] . Now we consider formal expansions for x_i, y_i:

$$x_i(t) = x_i(0) + \sum_k \lambda_i^k \varphi_k(t) \quad y_j(t) = \sum_r \eta_j^r \varphi_r(t), \tag{1}$$

where, because of initial conditions, we need only $\varphi_k(0) = 0$. Then we have the following reduced algebraical system of equations on the set of unknown coefficients λ_i^k of expansions (1):

$$\sum_k \mu_{kr}\lambda_i^k - \gamma_i^r(\lambda_j) = 0 \tag{2}$$

Its coefficients are

$$\mu_{kr} = \int_0^1 \varphi_k'(t)\varphi_r(t)dt, \quad \gamma_i^r = \int_0^1 f_i(x_j,t)\varphi_r(t)dt.$$

Now, when we solve system (2) and determine unknown coefficients for the formal expansion (1), we therefore obtain the solution of our initial problem.
It should be noted that in case when we consider only truncated expansion (1) with N terms then we have from (2) the system of $N \times n$ algebraical equations and the degree of this algebraical system coincides with degree of initial differential system. So, we have the solution of the initial value problem for nonlinear (polynomial) system in the form

$$x_i(t) = x_i(0) + \sum_{k=1}^{N} \lambda_i^k X_k(t), \tag{3}$$

where coefficients λ_i^k are roots of the corresponding reduced algebraical problem (2). Consequently, we have a parametrization of solution of initial value problem by solution of reduced algebraical problem (2). But in general case, when the problem of computation of coefficients of reduced algebraical system (2) cannot be solved explicitly as in the quadratic case, which we shall consider below, we also have parametrization of solution (1) by solution of some set of the corresponding problems, which appear during calculations of the coefficients of reduced algebraic system (2).
As we shall see below, these problems may be explicitly solved in general wavelet approach.

3 Solutions: simple case

Next we consider the construction of explicit time solution for our problem. The obtained solutions are given in the form (3), where in our first case we have $X_k(t) = Q_k(t)$, where $Q_k(t)$ are shifted Legendre polynomials and λ_k^i are roots of reduced quadratic system of equations. In wavelet case $X_k(t)$ correspond to multiresolution expansions in the base of compactly supported wavelets and λ_k^i are the roots of corresponding general polynomial system (2) with coefficients, which are given by FWT, SSS or CC constructions.
According to the variational approach, we provide the reduction from the initial system of differential equations to algebraical one by means of computation of the

objects γ_a^j and μ_{ji}, which are constructed from objects:

$$\begin{aligned}
\sigma_i &\equiv \int_0^1 X_i(\tau)d\tau = (-1)^{i+1}, \qquad (4)\\
\nu_{ij} &\equiv \int_0^1 X_i(\tau)X_j(\tau)d\tau = \sigma_i\sigma_j + \frac{\delta_{ij}}{(2j+1)},\\
\mu_{ji} &\equiv \int X_i'(\tau)X_j(\tau)d\tau = \sigma_j F_1(i,0) + F_1(i,j),\\
&\quad F_1(r,s) = [1-(-1)^{r+s}]\hat{s}(r-s-1), \quad \hat{s}(p) = \begin{cases} 1, & p \geq 0 \\ 0, & p < 0 \end{cases}
\end{aligned}$$

$$\begin{aligned}
\beta_{klj} &\equiv \int_0^1 X_k(\tau)X_l(\tau)X_j(\tau)d\tau = \sigma_k\sigma_l\sigma_j +\\
&\quad \alpha_{klj} + \frac{\sigma_k\delta_{jl}}{2j+1} + \frac{\sigma_l\delta_{kj}}{2k+1} + \frac{\sigma_j\delta_{kl}}{2l+1},\\
\alpha_{klj} &\equiv \int_0^1 X_k^* X_l^* X_j^* d\tau = \frac{1}{(j+k+l+1)R(1/2(i+j+k))} \times\\
&\quad R(1/2(j+k-l))R(1/2(j-k+l))R(1/2(-j+k+l)),
\end{aligned}$$

if $j+k+l = 2m, m \in Z$, and $\alpha_{klj} = 0$ if $j+k+l = 2m+1$; $R(i) = (2i)!/(2^i i!)^2$, $Q_i = \sigma_i + P_i^*$, where the second equality in the formulae for $\sigma, \nu, \mu, \beta, \alpha$ hold for the first case.

4 Wavelet computations

Now we give construction for computations of objects like (4) in the generic wavelet case. We use some constructions from multiresolution analysis [8]: a sequence of successive approximation closed subspaces V_j:

$$...V_2 \subset V_1 \subset V_0 \subset V_{-1} \subset V_{-2} \subset ...$$

satisfying the following properties:

$$\bigcap_{j\in\mathbf{Z}} V_j = 0, \overline{\bigcup_{j\in\mathbf{Z}} V_j} = L^2(\mathbf{R}), \qquad f(x) \in V_j <=> f(2x) \in V_{j+1}$$

There is a function $\varphi \in V_0$ such that $\{\varphi_{0,k}(x) = \varphi(x-k)_{k\in\mathbf{Z}}\}$ forms a Riesz basis for V_0. We use compactly supported wavelet basis: orthonormal basis for functions in $L^2(\mathbf{R})$. As usually $\varphi(x)$ is a scaling function, $\psi(x)$ is a wavelet function, where $\varphi_i(x) = \varphi(x-i)$. Scaling relation that defines φ, ψ are

$$\begin{aligned}
\varphi(x) &= \sum_{k=0}^{N-1} a_k\varphi(2x-k) = \sum_{k=0}^{N-1} a_k\varphi_k(2x),\\
\psi(x) &= \sum_{k=-1}^{N-2} (-1)^k a_{k+1}\varphi(2x+k)
\end{aligned}$$

Let be $f : \mathbf{R} \longrightarrow \mathbf{C}$ and the wavelet expansion is

$$f(x) = \sum_{\ell \in \mathbf{Z}} c_\ell \varphi_\ell(x) + \sum_{j=0}^{\infty} \sum_{k \in \mathbf{Z}} c_{jk} \psi_{jk}(x) \tag{5}$$

The indices k, ℓ and j represent translation and scaling, respectively:

$$\varphi_{jl}(x) = 2^{j/2} \varphi(2^j x - \ell), \qquad \psi_{jk}(x) = 2^{j/2} \psi(2^j x - k).$$

The set $\{\varphi_{j,k}\}_{k \in \mathbf{Z}}$ forms a Riesz basis for V_j. Let W_j be the orthonormal complement of V_j with respect to V_{j+1}. Just as V_j is spanned by dilation and translations of the scaling function, so are W_j spanned by translations and dilation of the mother wavelet $\psi_{jk}(x)$. If in formulae (5) $c_{jk} = 0$ for $j \geq J$, then $f(x)$ has an alternative expansion in terms of dilated scaling functions only

$$f(x) = \sum_{\ell \in \mathbf{Z}} c_{J\ell} \varphi_{J\ell}(x).$$

This is a finite wavelet expansion, it can be written solely in terms of translated scaling functions. We use wavelet $\psi(x)$, which has k vanishing moments

$$\int x^k \psi(x) dx = 0,$$

or equivalently

$$x^k = \sum c_\ell \varphi_\ell(x)$$

for each k, $0 \leq k \leq K$. Also we have the shortest possible support: scaling function DN (where N is even integer) will have support $[0, N-1]$ and $N/2$ vanishing moments. There exists $\lambda > 0$ such that DN has λN continuous derivatives; for small $N, \lambda \geq 0.55$. To solve our second associated linear problem we need to evaluate derivatives of $f(x)$ in terms of $\varphi(x)$. Let be $\varphi_\ell^n = d^n \varphi_\ell(x)/dx^n$. We derive the wavelet - Galerkin approximation of a differentiated $f(x)$ as:

$$f^d(x) = \sum_{\ell} c_l \varphi_\ell^d(x)$$

and values $\varphi_\ell^d(x)$ can be expanded in terms of $\varphi(x)$:

$$\phi_\ell^d(x) = \sum_m \lambda_m \varphi_m(x), \quad \lambda_m = \int_{-\infty}^{\infty} \varphi_\ell^d(x) \varphi_m(x) dx$$

The coefficients λ_m are 2-term connection coefficients. In general we need to find $(d_i \geq 0)$:

$$\Lambda_{\ell_1 \ell_2 \ldots \ell_n}^{d_1 d_2 \ldots d_n} = \int_{-\infty}^{\infty} \prod \varphi_{\ell_i}^{d_i}(x) dx \tag{6}$$

For Riccati case we need to evaluate two and three connection coefficients:

$$\Lambda_\ell^{d_1 d_2} = \int_{-\infty}^{\infty} \varphi^{d_1}(x)\varphi_\ell^{d_2}(x)dx, \quad \Lambda^{d_1 d_2 d_3} = \int_{-\infty}^{\infty} \varphi^{d_1}(x)\varphi_\ell^{d_2}(x)\varphi_m^{d_3}(x)dx.$$

According to CC method [23] we use the next construction. When N in scaling equation is a finite even positive integer, the function $\varphi(x)$ has compact support contained in $[0, N-1]$. For a fixed triple (d_1, d_2, d_3) only some $\Lambda_{\ell m}^{d_1 d_2 d_3}$ are nonzero: $2-N \le \ell \le N-2$, $2-N \le m \le N-2$, $|\ell - m| \le N-2$. There are $M = 3N^2 - 9N + 7$ such pairs (ℓ, m). Let $\Lambda^{d_1 d_2 d_3}$ be an M-vector, whose components are numbers $\Lambda_{\ell m}^{d_1 d_2 d_3}$. Then we have the first key result: Λ satisfy the system of equations ($d = d_1 + d_2 + d_3$):

$$A\Lambda^{d_1 d_2 d_3} = 2^{1-d}\Lambda^{d_1 d_2 d_3}, \quad A_{\ell,m;q,r} = \sum_p a_p a_{q-2\ell+p} a_{r-2m+p}.$$

By moment equations we have created a system of $M + d + 1$ equations in M unknowns. It has rank M and we can obtain unique solution by combination of LU decomposition and QR algorithm. The second key result gives us the 2-term connection coefficients:

$$A\Lambda^{d_1 d_2} = 2^{1-d}\Lambda^{d_1 d_2}, \quad d = d_1 + d_2, \quad A_{\ell,q} = \sum_p a_p a_{q-2\ell+p}.$$

For nonquadratic case we have analogously additional linear problems for objects (6). Also, we use FWT [2] and SSS [6] for computing coefficients of reduced algebraic systems. We use for modelling D6, D8, D10 functions and programs RADAU and DOPRI for testing [19].

As a result, we obtained the explicit time solution (3) for our problem in a basis of very effective high-localized functions, or nonlinear (in a sense of harmonic analysis) eigenmodes.

In addition to standard wavelet expansion on the whole real line which we used here, in calculation of the general Galerkin approximations, Melnikov function approach, etc. we need to use periodized wavelet expansion, i.e. wavelet expansion on finite interval [5]. Our approach works in such a case too.

Also, for the solution of perturbed system, we need to extend our approach to the important case of variable coefficients. For solving last problem we need to consider one more refinement equation for scaling function $\phi_2(x)$:

$$\phi_2(x) = \sum_{k=0}^{N-1} a_k^2 \phi_2(2x-k)$$

and corresponding wavelet expansion for variable coefficients:

$$b(t): \quad \sum_k B_k^j(b)\phi_2(2^j x - k),$$

where $B_k^j(b)$ are functionals supported in a small neighborhood of $2^{-j}k$ [7].

The solution of the first problem consists in periodizing. In this case we use expansion into periodized wavelets [5] defined by:

$$\phi^{per}_{-j,k}(x) = 2^{j/2} \sum_{Z} \phi(2^j x + 2^j \ell - k).$$

All these modifications lead to transformations of the coefficients of the reduced algebraic system only, but the general scheme described above remains the same. Extended versions and related results may be found in [11]–[18].

References

[1] Anderson P.M., Fouad A.A. (1977) *Power system control and stability*, Iowa State Univ. Press, USA.

[2] Beylkin G., Coifman R. and Rokhlin V. (1991) Fast wavelet transform, Comm. Pure Appl.Math., **44**, pp. 141–183.

[3] Blachman N.M. (1974) Sequentional analysis, Proc. IEEE, **62**, pp. 72–82.

[4] Coifman R.R., Wickerhauser M.V. (1993) Wavelets analysis and signal processing, in *Wavelets*, SIAM, pp. 153–178.

[5] Cohen A., Daubechies I., Vial P. (1993) Wavelets on the interval and fast wavelet transforms, preprint.

[6] Dahlke S., Weinreich I. (1993) Wavelet–Galerkin methods, Constructive approximation, **9**, pp 237–262.

[7] Dahmen, W., Micchelli C.A. (1993) Using the Refinement Equation for Evaluating Integrals of Wavelets, SIAM J. Numer.Anal., **30**, pp. 507–537.

[8] Daubechies I. (1988) Orthonomal bases of compactly supported wavelets, Comm. Pure Appl. Math., **41**, pp. 906–1003.

[9] A. N. Fedorova, M. G. Zeitlin (1993) Variational Analysis in Optimal Control of Synchronous Drive of Mill, Preprint IPME, **no. 96**.

[10] A. N. Fedorova, G. M. Rubashev, M. G. Zeitlin (1990) An algorithm of Solving of Equations of Synchronous Drive of Mill, Electrichestvo (Electricity), in Russian, **no. 6**, pp. 40–45.

[11] A. N. Fedorova, M. G. Zeitlin, 'Wavelets in Optimization and Approximations', *Math. and Comp. in Simulation*, **46**, 527-534 (1998).

[12] A. N. Fedorova, M. G. Zeitlin, 'Wavelet Approach to Mechanical Problems. Symplectic Group, Symplectic Topology and Symplectic Scales', New Applications of Nonlinear and Chaotic Dynamics in Mechanics, Kluwer, 31-40, 1998.

[13] A. N. Fedorova and M. G. Zeitlin, Quasiclassical Calculations for Wigner Functions via Multiresolution, Localized Coherent Structures and Patterns Formation in Collective Models of Beam Motion, in *Quantum Aspects of Beam Physics*, Ed. P. Chen (World Scientific, Singapore, 2002) pp. 527–538, 539–550; arXiv: physics/0101006; physics/0101007.

[14] A. N. Fedorova and M. G. Zeitlin, BBGKY Dynamics: from Localization to Pattern Formation, in *Progress in Nonequilibrium Green's Functions II*, Ed. M. Bonitz, (World Scientific, 2003) pp. 481–492; arXiv: physics/0212066.

[15] A. N. Fedorova and M. G. Zeitlin, Pattern Formation in Wigner-like Equations via Multiresolution, in *Quantum Aspects of Beam Physics*, Eds. Pisin Chen, K. Reil (World Scientific, 2004) pp. 22-35; Preprint SLAC-R-630; arXiv: quant-ph/0306197.

[16] A. N. Fedorova and M. G. Zeitlin, Localization and pattern formation in Wigner representation via multiresolution, *Nuclear Inst. and Methods in Physics Research, A*, **502A/2-3**, pp. 657 - 659, 2003; arXiv: quant-ph/0212166.

[17] A. N. Fedorova and M. G. Zeitlin, Fast Calculations in Nonlinear Collective Models of Beam/Plasma Physics, *Nuclear Inst. and Methods in Physics Research, A*, **502/2-3**, pp. 660 - 662, 2003; arXiv: physics/0212115.

[18] A. N. Fedorova and M. G. Zeitlin, Classical and quantum ensembles via multiresolution: I-BBGKY hierarchy; Classical and quantum ensembles via multiresolution. II. Wigner ensembles; *Nucl. Instr. Methods Physics Res.*, **534A** (2004)309-313; 314-318; arXiv: quant-ph/0406009; quant-ph/0406010.

[19] Hairer E., Lubich C., Roche M. (1989) *Lecture Notes in Mathematics*, **Vol. 1409**.

[20] Harmuth H.F. (1977) *Sequency theory*, Academic press.

[21] Hitzl D.L., Huynh T.V, Zele F. (1984) Integral Variational Method, Physics Letters, **104**, pp. 447–451.

[22] Hofer H., Zehnder E. (1994) *Symplectic Invariants and Hamiltonian Dynamics*, Birkhauser.

[23] Latto A., Resnikoff H.L. and Tenenbaum E. (1991) The Evaluation of Connection Coefficients, Aware Technical Report AD910708.

Antonina N. Fedorova, Michael G. Zeitlin
Mathematical Methods in Mechanics Group, IPME RAS, V.O. Bolshoj pr., 61, 199178, St. Petersburg, Russia
http://math.ipme.ru/zeitlin.html, http://mp.ipme.ru/zeitlin.html

Waves with the negative group velocity in cylindrical shell of Kirchhoff - Love type

George V. Filippenko

g.filippenko@gmail.com, g.filippenko@spbu.ru

Abstract

Cylindrical shells of different types are the often used models in modern engineering. It is the element of different line tubes, supports, oil rigs and so on. The problems of preventing from damaging of such the constructions, reducing the vibrations of them are the actual problems of modern technique. The exact calculation of such objects from one side needs great computational resources and from another side often mask some important effects. For example the effects of propagating of the waves with negative group velocity better to analyze on the simplest mechanical models which have the exact analytical solution. In report such the analysis is fulfilled on example of infinite thin cylindrical shell of Kirchhoff - Love type. The problem of free oscillations of such the shell is considered. The statement of the problem is considered in the rigorous statement. The dispersion equation is found on the base of exact analytical solution. The propagating waves are analyzed. The exploration of waves with negative group velocity in the neighborhood of bifurcation point of dispersion curves is fulfilled. The analysis of arising effects is fulfilled in terms of kinematic and dynamic variables, and in the terms of energy flux. The relative advantages and disadvantages of these approaches are discussed. The comparison of contributions in the integral energy flux of various mechanisms of energy transmission in the shell is fulfilled. The dependence of subzero energy flux, dynamic and kinematic variables on the relative thickness of the shell, the mode number and other parameters of system is discussed. The possible fields of applicability of the gained effects are established.

1 Statement of the problem

The problem of oscillations of the systems containing cylinder shells is one of the actual problems of modern techniques. It is important to estimate the parameters of vibrations and acoustical fields of such objects in order to provide the construction from damaging, but calculation of these complicated systems demands major computing resources. Therefore the consideration of simple model problems which have exact analytical solution ([1] - [5]) is actual. On these models it is possible

to analytically explore main effects and also to use them as the test problems for computing packages.
Let us start considering an infinite cylindrical shell of Kirchhoff–Love type in the cylindrical system of coordinates where the axis $0z$ coincides with axis of the cylinder. The source of an acoustic field in a wave guide is the vibrations of the cylinder shell, caused by the incident wave propagating from the infinite part of the shell. The frequency of this incident harmonic wave is equal to ω. All processes in the shell are supposed to be harmonic with this frequency. The factor $\mathrm{e}^{-i\omega t}$ describes the time-dependence and is omitted.
The balance of forces acting on the shell has a view [6]

$$\mathbf{L_w u} = (\mathbf{0}, \mathbf{0}, \mathbf{0})^{\mathbf{t}}. \tag{1}$$

Here following notations are introduced: $\mathbf{u}(\mathbf{'}, \mathbf{z}) = (\mathbf{u_t}, \mathbf{u_z}, \mathbf{u_n})^{\mathbf{t}}$ is the displacement vector of the shell (t is a badge of transposing), $\mathbf{L_w}$ is matrix differential operator of the cylindrical shell of Kirchhoff–Love type

$$\mathbf{L_w} \equiv [L_{ij}] = w^2\mathbf{I} + \mathbf{L}; \quad i, j = 1, 2, 3$$

$$\mathbf{L}= \begin{pmatrix} \alpha_1[\partial_\varphi + \nu_- \widetilde{\partial}_z^2] & \nu_+ \widetilde{\partial}_z \partial_\varphi & \partial_\varphi(1 + 2\alpha^2[1 - \partial_\varphi^2 - \widetilde{\partial}_z^2]) \\ L_{21} & \nu_- \partial_\varphi^2 + \widetilde{\partial}_z{}^2 & \nu \widetilde{\partial}_z \\ L_{31} & L_{32} & \alpha^2(2\partial_\varphi^2 - 2 + 2\nu\widetilde{\partial}_z{}^2 - [\partial_\varphi^2 + \widetilde{\partial}_z{}^2]^2) - 1 \end{pmatrix} \tag{2}$$

Here $L_{21} = L_{22}$, $L_{31} = -L_{13}$, $L_{32} = -L_{23}$, $\widetilde{\partial}_z = R\partial_z$, $\alpha_1 = 1 + 4\alpha^2$, $\nu_\pm = (1 \pm \nu)/2$, $\mathbf{I}$ is the unit matrix operator.
The following geometrical parameters of the shell are used: R — radius, h — thickness.
Properties of a material of the cylinder are characterized by E, ν and ρ_s - Joung's module, Poisson coefficient and volumetric density accordingly.
The surface density of the shell $\widetilde{\rho}$ ($\widetilde{\rho}$=$\rho_s h$) and the velocity of median surface deformation waves of the cylindrical shell c_s are introduced $c_s = \sqrt{E/((1-\nu^2)\rho_s)}$.
The following dimensionless parameters are put in: $\alpha^2 = \frac{1}{12}(\frac{h}{R})^2$ (the relative thickness of the cylindrical shell) and $w = \omega R/c_s$ (the dimensionless frequency).

2 Determination of the general representation of vibrational field

The solution of the equation (1) is searching in the form

$$\begin{pmatrix} u_t \\ u_z \\ u_n \end{pmatrix} = Ae^{i\lambda z} \begin{pmatrix} \zeta \sin(m\varphi) \\ \xi \cos(m\varphi) \\ \gamma \cos(m\varphi) \end{pmatrix}, \tag{3}$$

believing that $|\zeta|^2$+$|\xi|^2$+$|\gamma|^2$=1. Here following notations are introduced: A, ζ, ξ, γ are arbitrary constants, λ is the the wavenumber which we are looking for.

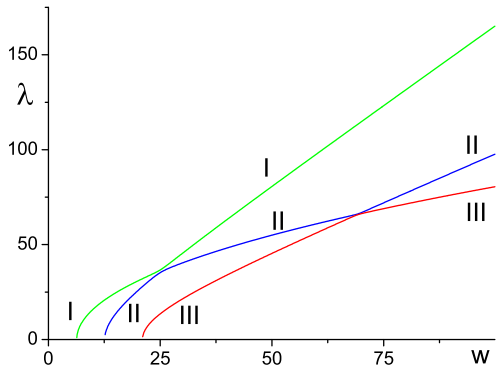

Figure 1: Dispersion curves ($m = 21$).

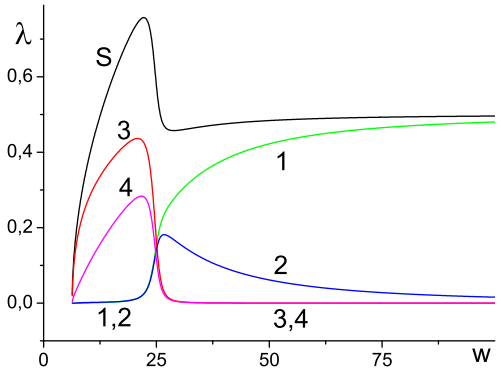

Figure 2: Energy fluxes for the waves from the first dispersion curve ($m = 21$).

After substituting (3) into (1) the following algebraic system is obtained

$$\widehat{\mathbf{L}}_w \mathbf{x} \equiv \left(w^2 \mathbf{I} + \widehat{\mathbf{L}} \right) \mathbf{x} = \mathbf{0}; \quad \mathbf{x} = (\zeta, \xi, \gamma)^t \tag{4}$$

Operator $\widehat{\mathbf{L}}_w$ is the Fourier image of operator $\mathbf{L}_w$. The dispersion equation is obtained from the condition of existence of nontrivial solution of this system

$$\det \widehat{\mathbf{L}}_w = 0. \tag{5}$$

We are looking for the real positive solutions of this equation [7] - [8]. If the corresponding set of wavenumbers is founded one can solve the equation (4) and define the previously unknown constants ζ, ξ, γ. After defining constants, the complete solution of the problem in terms of displacements of the shell $\mathbf{u}(', \mathbf{z})$ is determined. For the cylindrical shell of Kirchhoff–Love type this equation has three real positive roots $w_i^2 = w_i^2(\lambda^2)$, $i = 1, 2, 3$ which determine three dispersion curves $w_i(\lambda) := \sqrt{w_i^2(\lambda^2)} \geq 0$, (curves 1, 2, 3 in Fig. 1). When $\lambda = 0$ the points of these curves are designated as $w_i^0 = w_i(0)$, $i = 1, 2, 3$, $w_1^0 \leq w_2^0 < w_3^0$, where $w_2^0 = m\sqrt{\nu_-}$;
For certain combination of parameters points w_1^0 and w_2^0 can be coincided (in this case their abscises is equal to $w^0 \equiv m\sqrt{\nu_-}$) [5]. This point will be called the bifurcation point for convenience.

3 Energy streams in the shell

As it was mentioned above all processes in the shell are supposed to be harmonic with frequency ω. It is convenient to average the energy streams on period of oscillations $T = 2\pi/\omega$. The integral stream of the energy along axes z through the cross-section of the cylinder shell has a view

$$\Pi = \frac{\omega}{2} \int_0^{2\pi} \mathrm{Im} \left(\mathbf{u^4}, \mathbf{F u^4} \right)_{\mathbf{C}^4} R d\varphi = \Pi_t + \Pi_z + \Pi_n + \Pi_m, \tag{6}$$

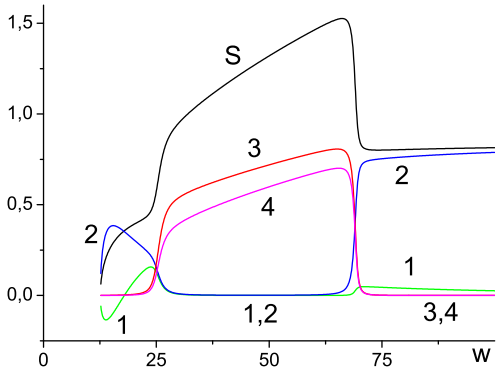

Figure 3: Energy fluxes for the waves from the second dispersion curve ($m = 21$).

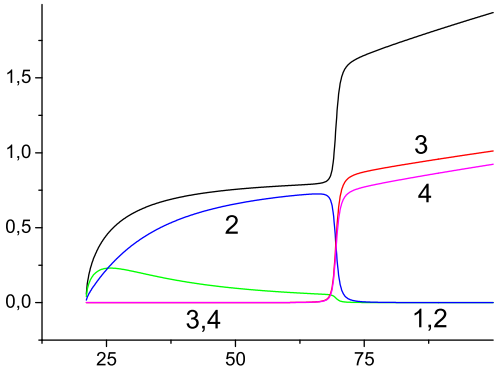

Figure 4: Energy fluxes for the waves from the third dispersion curve ($m = 21$).

$$\left\{\begin{array}{c}\Pi_t\\ \Pi_z\\ \Pi_n\\ \Pi_p\end{array}\right\} = \pi\rho c_s^2\frac{\omega}{2}\,\mathrm{Im}\left\{\begin{array}{c}(-\alpha_1\nu_-\widetilde{\partial}_z u_t - \nu_-\widetilde{\partial}_\varphi u_z + 2\alpha^2(1-\nu)\partial_\varphi\widetilde{\partial}_z u_n)\overline{u}_t\\ (-\nu\partial_\varphi u_t - \widetilde{\partial}_z u_z - \nu u_n)\overline{u}_z\\ \overline{u}_n\alpha^2(-2\partial_\varphi\widetilde{\partial}_z u_t + ((2-\nu)\partial_\varphi^2 - \nu + \widetilde{\partial}_z^2)\widetilde{\partial}_z u_n)\\ \alpha^2(-2\nu\partial_\varphi u_t + \nu(\partial_\varphi^2 - 1)u_z + \widetilde{\partial}_z^2 u_n)(-\widetilde{\partial}_z\overline{u}_n)\end{array}\right\}, \quad (7)$$

where $\mathbf{u^4} = (\mathbf{u_t}, \mathbf{u_z}, \mathbf{u_n}, -\mathbf{R}\partial_\mathbf{z}\mathbf{u_t})^\mathbf{t}$ is the vector of generalized displacements, $\mathbf{F}$ is the matrix differential operator 4×4 [5]. Here letters t, z, n, p marked tangential(rotating), longitudinal, normal and momentum components of energy flux Π and components of generalized vector $\mathbf{u^4}$.
In the particular case of axisymmetric rotating movements ($m = 0$) of the shell the integral energy flux Π^0 of it consists of unique component Π_t^0 and is equal to

$$\Pi^0 = \Pi_t^0 = 2\pi\rho c_s^2\frac{\omega}{2}|A|^2\beta; \quad \beta = w\sqrt{\alpha_1\nu_-} \quad (8)$$

4 Numerical calculations

Formulas (6)-(8) can be used for obtaining the normalized energy stream in the shell and it components

$$S = \Pi/\Pi^0, \qquad S_{t,z,n,m} = \Pi_{t,z,n,m}/\Pi^0. \quad (9)$$

The following values of parameters of the system are assumed for calculations ν=0.28, h/R=0.05 that corresponds to thin shell made of steel. Figures 1 - 4 are calculated for the mode $m = 21$, others for $m = 63$. Dimensionless frequency w is plotted along abscise axis on all figures.
The regular case (absence of bifurcation point) is considered at first. In Fig. 1 the dependence of dimensionless wavenumber $\lambda := \lambda R$ with respect to dimensionless

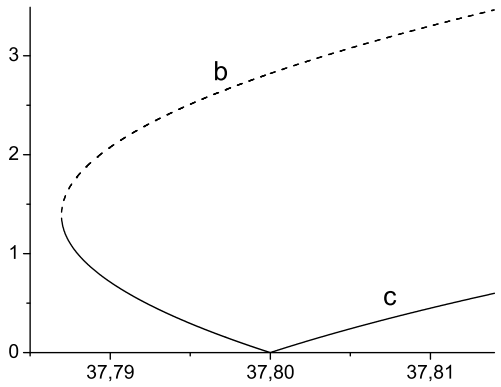

Figure 5: Dispersion curves ($m = 63$).

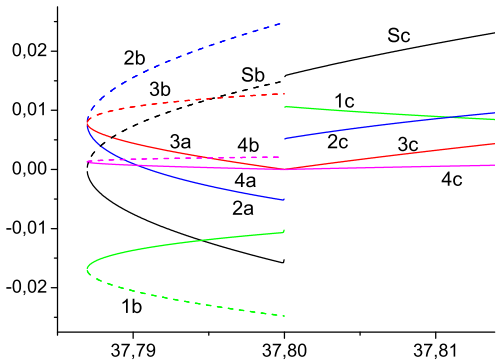

Figure 6: Integral energy fluxes and its components ($m = 63$).

frequency w is shown (these curves are marked by digits I, II, III). The veering (quasiintersection) of the curves I and II is well noted at $w \approx 25.0$. The veering is usual situation for the systems consisting of several subsystems. In our case it is caused by interaction of the different type of movements of the shell. It can be analyzed by energy fluxes components in Fig. 2 - Fig. 4.

The integral energy fluxes (curves S) and their components S_t, S_z, S_n, S_p (curves 1, 2, 3, 4) for the waves from dispersion curves in Fig. 1 are shown in Fig. 2 - Fig. 4 correspondingly according to formulas (9). The dominating of bending component in the wave from the first dispersion curve is changed to dominating of rotational component and dominating of longitudinal component in the wave from the second dispersion curve is changed to dominating of bending component. The interesting fact is that rotational component in the second dispersion curve is negative in the neighborhood of bearing point. There are no visible veering points for the third dispersion curve in Fig. 1 in the neighborhood of $w \approx 25.0$ but energy flux components "feel" the change of the wave character. The dominating of rotational component in Fig. 4 is changed to dominating of longitudinal component in this point.

It can be noticed that the veering of second and third dispersion curves is occurred at $w \approx 70$. The dominating of bending component in the wave from the second dispersion curve is changed to dominating of longitudinal component and dominating of longitudinal component in the wave from the third dispersion curve is changed to dominating of bending component.

In Fig. 5 the case of bifurcation point is considered. Two dispersion curves $w_1(\lambda)$ and $w_2(\lambda)$ (they will be called left and right brunches correspondingly) have the same bearing point $w = 37.80$. The behavior of the wave from the left dispersion curve differs from others significantly. This dispersion curve consists the section b with positive group velocity and smaller section a with negative group velocity. Right brunch consists of the singular section c with positive group velocity.

For these sections of the curves the integral energy fluxes (curve S) and their components S_t, S_z, S_n, S_p (curves 1, 2, 3, 4) are shown in Fig. 6. On these figures the curves with letters a, b, c in designations are corresponded to the sections of

dispersion curves in Fig. 5. For convenience the dependencies of the wave processes corresponding to the left dispersion curve are shown only for the frequencies less than bifurcation one.
Fig. 5 illustrates the fact that group velocity for the waves from both brunches in the neighborhood of bifurcation point is not equal to zero, have the opposite sign and equal module. It well corresponds with the fact that integral energy fluxes and their components have the opposite sign in this point (Fig. 6). Moreover the negative character of the integral energy flux is realized due to the negative character of the longitudinal and rotating components of it with dominating of rotating one. By contrast to this both integral fluxes (and its components) and group velocity are tending to zero if $\lambda \to 0$ in regular case. The exceptional case is when the dispersion curve is starting from the point $(w, \lambda) = (0, 0)$ $(m = 0)$ [5].
The numerical analysis shows that specific character of the waves with negative group velocity is their quick switching in the energy transmission process on the long waves (group velocity is not equal to zero at the point of their bearing).
The energy flux analysis [9] - [10] gives additional opportunities to investigate different components of vibrating and energy fields and their cross influence to each other [4] - [5].

Acknowledgements

The author is deeply grateful to Prof. D.P.Kouzov for the inspiration.

References

[1] Pavic G., 1990, Vibrational energy flow in elastic circular cylindrical shells, *J. Sound Vib.*, Vol. **142**(2), pp. 293-310.

[2] Pavic G., 1992, Vibroacoustical energy flow through straight pipes, *J. Sound Vib.*, Vol. **154**(3), pp. 411-429.

[3] Sorokin S.V., Nielsen J.B., Olhoff N., 2004, GreenŸs matrix and the boundaryintegral equation method for the analysis of vibration and energy flow in cylindrical shells with and without internal fluid loading, *Journal of Sound and Vibration*, 271, pp. 815–847

[4] Filippenko G. V. Energy aspects of axisymmetric wave propagation in an infinite cylindrical shell filled with the liquid. // Proceedings of the "XLIV Summer School Conference Advanced Problems in Mechanics APM 2016 St.Petersburg", pp. 119-125, http://apm-conf.spb.ru, http://apm-conf.spb.ru/proceedings-2016

[5] Filippenko G.V. Energy aspects of wave propagation in an infinite cylindrical shell fully submerged in liquid. Vycisl. meh. splos. sred - Computational Continuum Mechanics, 2014, vol. 7, no. 3, pp. 295-305, http://www.icmm.ru/journal/download/CCMv7n3a29.pdf; DOI: 10.7242/1999-6691/2014.7.3.29

[6] Yeliseev V.V., 2003, *Mechanics of elastic bodies*, SPb., SPbSPU, Russia, 336 p. (in Russian).

[7] Zinovieva T.V., 2007, Wave dispersion in cylindrical shell, *Acta of SPbSPU, Engineering*, SpbSPU press, St. Petersburg, Russia, No. 504, pp. 112–119.

[8] Yeliseyev V.V., Zinovieva, T.V., 2014, Two-dimensional (shell-type) and three-dimensional models for elastic thin-walled cylinder, *PNRPU Mechanics Bulletin*, No. 3., pp. 50–70

[9] Veshev V.A., Kouzov D.P., Mirolyubova N.A., 1999, Energy flows and dispersion of the normal bending waves in the X-shaped beam, *Acoustical Physics*, Vol. **45**(3), pp. 331–337.

[10] Kouzov D.P., Mirolubova N.A., 2012, Local energy fluxes of forced vibrations of a thin elastic band. *Vycisl. meh. splos. sred Ц Computational Continuum Mechanics*, Vol. **5**(4), pp. 397–404

Institute of Mechanical Engineering of RAS, Vasilievsky Ostrov, Bolshoy Prospect 61, St.Petersburg, 199178, Russia, g.filippenko@gmail.com
Saint Petersburg State University, 7-9, Universitetskaya nab., St.Petersburg, 199034, Russia, g.filippenko@spbu.ru

Experimental studies of rubbers filled by layered clay nanoparticles

Oleg K. Garishin, Vladimir V. Shadrin, Alexander L. Svistkov, Alexander K. Sokolov

gar@icmm.ru

Abstract

It is known that one of the main and most common fillers of rubbers based on natural and synthetic caoutchoucs are carbon black (black soot) and oxides of zinc (white soot). Putting into an elastomer such substances can significantly improve its mechanical properties (especially strength and deformability). To date, these effects are well understood and can be said that this method of modifying the properties of the rubber reached the ceiling. Further progress requires a search for new nonconventional types of fillers. One of perspective directions is the use of various clay minerals.

The paper presents the results of experimental studies of elastomeric nanocomposites containing a new (for elastomers) type of filler — montmorillonite (MMT). This material, in particular processing, is capable to be dispersed nanoparticles of ultrafine flakes with a minimum thickness of up to 1 nm, that may form individual packs of parallel plates — tactoids.

Experimental studies conducted by a special technique, based on cyclic deformation of the sample with a stepwise variable amplitude of the deformations. Tests of this kind are used in when it is necessary to receive in one experiment comprehensive data about the viscoelastic and elastic-plastic material properties. It was found that the addition of clay nanofiller rubber contributes to significant dissipative losses increase, indicating that the development of viscoelastic processes in the composite during its deformation. Also, the relative softening of material (compared with pure vulcanizate) occurred at large cyclic strains (more than 3–4 times). And these effects were stronger than for fillers with a larger basal spacing.

1 Introduction

It is known that the most common fillers of rubbers based on natural and synthetic caoutchoucs are carbon black (black soot) and oxides of zinc ZnO (fumed silica). The input of these substances in the elastomer can significantly improve its mechanical properties (particularly strength and deformability). To date, these effects are well understood and can be said that this method of rubber modifying reached

the ceiling. Further progress requires a search for new and innovative types of fillers. One promising area is the use of various clay minerals. This allows naturally vary the shape and size of the filler particles, depending on the task (for example, montmorillonite provides ultrathin plates, palygorskite — nanoneedles, shungit — nanoglobules).

Nanostructured materials are characterized by an extremely high total filler surface area (by orders of magnitude higher than in conventional composites with a filler of micron sizes). Therefore properties of nanomaterials significantly more dependent on structural effects generated by interphase boundaries ("linked" polymer layers formed on the nanoparticle surfaces, interfacial adhesion, etc.).

The thickness of the interfacial layers is measured in nanometers, which is comparable with the length of the polymer molecular chains, and the physical properties of the layers can be significantly different from the rest of the matrix (due to the orientation impact the of the particles surface). For example, these can explain the fact, the addition of even small portions (usually 3–5% by weight) of silica nanofiller in the polymer can significantly improve its operational properties. Meanwhile, to get a similar effect in conventional composite materials the filler concentration should be at least an order of magnitude higher [1, 2].

Historically, the first mineral-filled nanocomposites were polyolefins (polyethylene, polypropylene, etc.) with a filler of layered clay minerals (montmorillonite) [3, 4]. Their first commercial application were different auxiliary parts in cars (Toyota, General Motors, Mitsubishi, Honda), as well as packaging for liquids (Alco SCI, Nanocor). These materials are characterized by good thermal insulation properties, low diffusion permeability, high thermal stability and resistance to combustion. Currently, one of the most promising applications of elastomers with mineral nanofillers are the vehicle tires. Rubbers with this kind of filler are cheaper and differ the raised wear resistance [5, 6].

2 The object of study

The main object of study were elastomeric nanocomposites containing relatively new (for elastomers) type of filler — montmorillonite (MMT). This material refers to a class of swellable clay minerals and at certain treatments able to break up into ultrafine flakes with a minimum thickness of up to 1 nm and the characteristic size from 30 nm to several microns. These nanoparticles can form separate bundles — tactoids of parallel plates (up to tens). Natural montmorillonite consists of randomly oriented tactoids.

MMT is a hydrophilic material, which makes it difficult to wetting by organic substances (usually hydrophobic). Therefore, the particles of montmorillonite are modified to improve the thermodynamic compatibility with the matrix polymer, i.e. the organophilic surface layers with the desired level of interaction with the polymer matrix are created. Various surface active agents (surfactants) are used for this purpose, including those organic. Surfactant layer thickness on the surface nanoplates can reach 1–2 nanometers. Clay minerals treated with organic modifiers, are also called organoclays.

Montmorillonite nanoparticles treated as surfactants by distearil dimethylammonium chloride were used at carrying out of mechanical experiments [7, 8, 9]. The characteristic average particle (tactoids) size D_{MMT} was about 65–70 nm, the average distance between the layers in tactoids (basal) d_{MMT} = 2.9–3.0 nm. MMT density equaled 1.8 g/cm^3.
Materials for the study were provided by the Leibniz Institute of Polymer Research, Dresden, Germany (Leibniz-Institut fur Polymer for schung).
Vulcanizates of natural rubber (NR), containing carbon black (CB) of N330 brand were used as a matrix. Concentration of other additives (mineral oil, white carbon (ZnO), sulfur, a vulcanization accelerator TBBS (N-tert-butyl-2-benzothiazolylsulfenamide)) was the same for all samples. Accordingly, the matters of their effect on changes in mechanical properties of the composite in this study were not considered.
Thus, the following materials were studied in the experiment (ψ_{CB} — CB mass concentration, ψ_{MMT} — mass concentration of MMT filler):
1) NR: pure natural rubber without filler (NR) as a basis for comparison;
2) NR-CB30: natural rubber, filled with 30 phr of CB (ψ_{CB} = 21.2%-wt.);
3) NR-CB30-MMT5: natural rubber, filled with 30 phr of CB (ψ_{CB} = 21.2%-wt.) and 5 phr of MMT (ψ_{MMT} = 3.55 %-wt.).

3 Experiment

Experimental studies were carried out on the universal tensile testing machine Testometric FS100kN CT. The special technique was used, based on cyclic deformation of a sample with a variable step-by-step amplitude of deformations (and stops for relaxation when changing the direction of the load). Tests of this kind are usually used in the study of polymers, when it is required to obtain in one experiment complex data on the viscoelastic and elastoplastic properties of the material [10, 11, 12, 13, 14]. Speed of tensile machine grippers (in load increase and decrease) was 20 %/min. The time for each relaxation was 10 minutes. Samples were manufactured in accordance with the standard ISO 527-2-5A with working part 2 on 4 by 20 mm.

4 Results discussion

The dependences of the nominal stress σ^0 on extension ratio λ for 12 loading cycles of a pure elastomer (NR) are shown in Fig. 1. The maximum step values of λ ranged from 1.5 to 7, increasing by 50% on each subsequent cycle. Unloading in each case was carried out until the stresses in the sample completely disappeared. These curves were used as the reference basis for comparison with the filled elastomers.
It was found that the pure rubber behaved almost like an elastic material up to a extension ratio $\lambda < 3.5$ (first 5 cycles). At large values of λ, it softened and began to exhibit viscoelastic properties (a hysteresis loop appeared, the curve of each new stretching was below the previous stretching curve). The residual deformations were insignificant, that is, we can assume that there were no plastic flows in pure rubber.

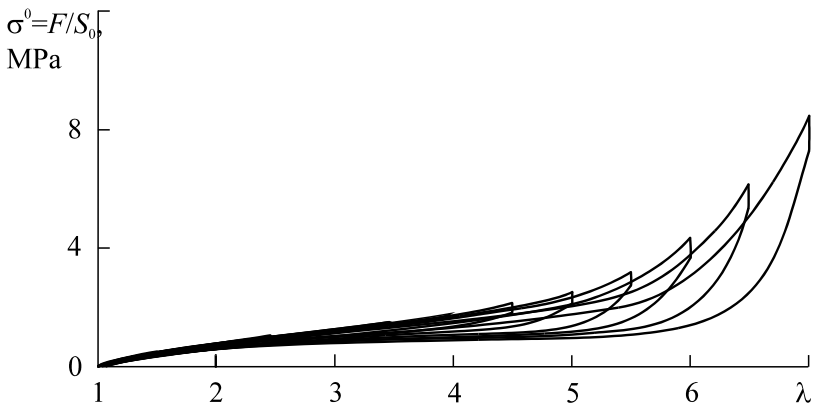

Figure 1: Cyclic stretching of pure natural rubber (NR): 12 cycles

The results of similar cyclic tests (12 cycles) for samples containing carbon black are shown in Figure 2. Adding 30 phr of CB significantly affected the mechanical properties of rubber:

First, the rigidity of the material has increased significantly. So, for example, in the samples filled with CB, maximum stresses on the second (maximum $\lambda = 2$), eighth ($\lambda = 5$) and twelfth ($\lambda = 7$) cycles increased approximately 3, 4 and 2 times, respectively, compared to the pure elastomer. At the same time, the differences between the unloading curves for filled and pure materials were significantly less.

Secondly, the dissipative losses increased significantly. The hysteresis of the load-unload curves was already observed on the second cycle, and, the larger the amplitude of the cycle tension, the stronger this effect was. The graphs show that there is also a significant softening of the material (Mullins effect [15, 16]) and it becomes viscoelastic.

Third, residual strains appeared in the filled samples.

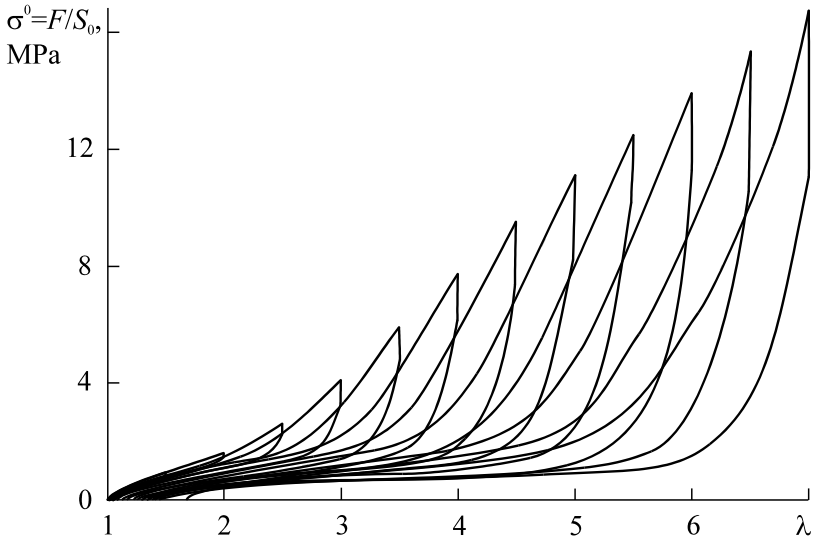

Figure 2: Curves of cyclic stretching of rubbers filled with carbon black (NR-CB30): 12 cycles

Therefore, the input of carbon black filler provokes the development of both reversible and irreversible rearrangements in the composite structure.

The following graphs show how the presence of clay filler affects the mechanical properties of rubber. Figure 3 demonstrates the results of cyclic loading (with stops at relaxation) samples NR-CB30 and NR-CB30-MMT5. Total twelve loading cycles are presented in Figure 3a, and only the first four (enlarged) in Figure 3b.

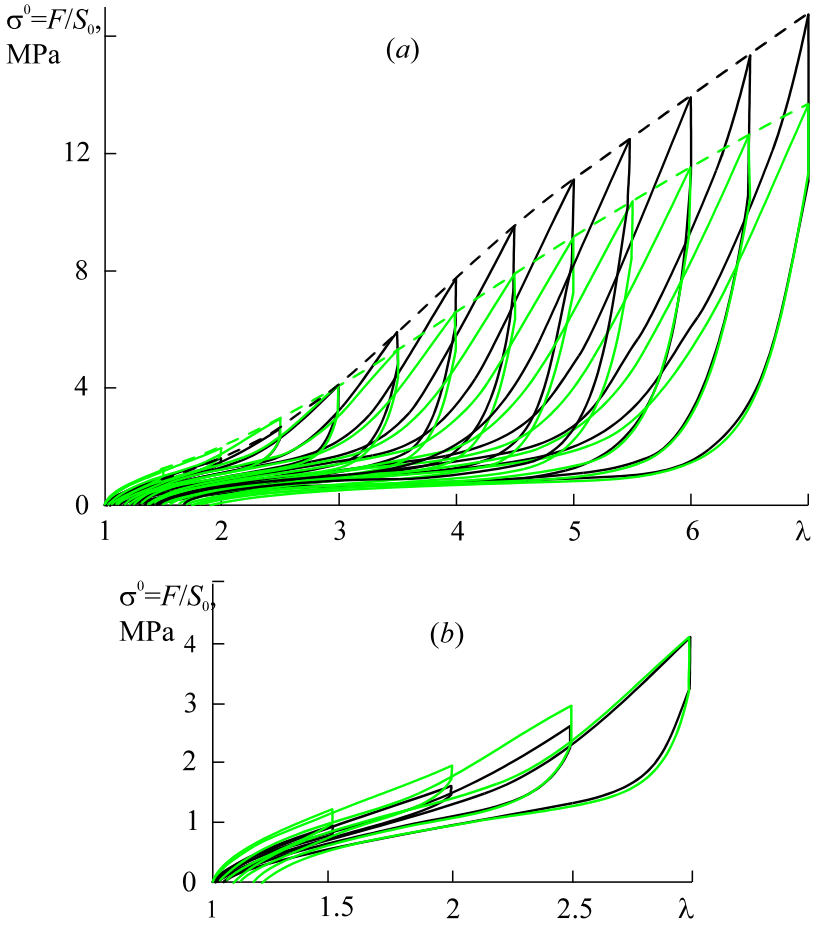

Figure 3: Curves of cyclic stretching of rubbers filled with СИ and ММТ. NR-CB30 — black lines, NR-CB30-MMT5 — green lines; (*a*) 12 cycles with full unloading on each of them; (*b*) 4 first cycles

At the initial stage of loading, the input of a clay nanofiller caused an increase in stresses compared to composites containing only CB. With further increase in the load, composites with clay nanoparticles became softer (compared to the systems "NR + CB"). For clarity, the dashed lines connecting the maximum stresses on the cycle for each material are plotted on the graphs.

In our opinion, this effect is due to the fact that at large extension ratios a reorientation of the montmorillonite particles along the extension axis occurs in the composite structure. The plates in the tactoids can slip relative to each other under the influence of external deformation, thereby unloading the overstressed places. Consequently, less energy is required to deform the system and the level of macrostresses is reduced.

It is interesting to note that the unloading curves and residual deformations for these materials turned out to be close, that is, the introduction of montmorillonite affects these stages of cyclic loading poorly.

As a result, we can conclude that the addition of relatively small amounts of montmorillonite to the rubber significantly affects its mechanical properties, contributing to the development of both reversible and dissipative processes (viscoelastic and elastic-plastic) during deformation of the material. This is due to the peculiarities of the structure of the filler particles, which are bundles of parallel arranged ultrathin silicate plates.
Reorientation and distortion of the shape of these filler particles occurs in the process of composite material loading. It leads to a decrease in stress concentration at the level of microstructure and energy dissipation.

Acknowledgements

This work is executed at a financial support of RFBR Grants: 16-08-00756 and 17-08-01118.

References

[1] Chvalun S.N. Polymeric nanocomposites // Nature, 2000, N 7, P. 22–30. (in Russian)

[2] Moshev V.V. Garishin O.K. Structural mechanics of dispersed filled elastomeric composites //Achievements in Mechanics, 2005, V. 4, N 2, P. 3–36. (in Russian)

[3] Fengge G. Clay/polymer composites: the story // Materials Today, 2004, N 11, P. 50–55.

[4] Theng B.K.G. Some Practical Applications of the Clay-Polymer Interaction // Developments in Clay Science, 2012, V. 4, P. 153–199 and P. 201–241.

[5] Kornev Yu.V., Chirkunova C.V. Boiko O.V., Simonova M.A., Shugaeva V.O., Yanovsky Yu.G. Investigation of the effect of dispersion of mineral shungite on the complex properties of elastomeric compositions based on rubber SKTN-A // Caoutchouc and rubber, 2012, N 6. P. 10–14. (in Russian)

[6] Kornev V., Yanovskiy G., Boiko V., Semenov N.A., Chirkunova S. Investigating the influence of the degree of dispersion of mineral shungite on the properties of elastomeric materials based on butadiene-styrene rubber // International Polymer Science and Technology, 2013, V. 40, N 3. P. 17–22.

[7] Rooj S., Das A., Stuckelhuber K.W., Reuter U., Heinrich G. Highly exfoliated natural rubber/clay composites by "propping-open procedure": the influence of fatty acid chain length on exfoliation // Macromol. Mater. Eng., 2012a, V. 297, P. 369–383.

[8] Rooj S., Das A., Stuckelhuber K.W., Mukhopadhyay N., Bhattacharyya A.R., Jehnichen D. Pre-intercalation of long chain fatty acid in the interlayer space of

layered silicates and preparation of montmorillonite/natural rubber nanocomposites // Appl. Clay. Sci., 2012, V. 67–68. P. 50–56.

[9] Rooj S., Das A., Morozov I.A., Stuckelhuber K.W., Stocek R., Heinrich G. Influence of "expanded clay" on the microstructure and fatigue crack growth behavior of carbon black filled NR composites // Composites Science and Technology, 2013, V. 76 P. 61–68.

[10] Meyer R.W. Pruitt L.A. The effect of cyclic true strain on the morphology, structure, and relaxation behavior of ultra high molecular weight polyethylene // Polymer, 2001, V. 42, P. 5293–5306.

[11] Bergstrom J.S., Rimnac C.M., Kurtz S.M. An augmented hybrid constitutive model for simulation of unloading and cyclic loading behavior of conventional and highly crosslinked UHMWPE // Biomaterials, 2004, V. 25, P. 2171–2178.

[12] Ayoub G., Zairi F., Nait-Abdelaziz M., Gloaguen J.M. Modelling large deformation behaviour under loading-unloading of semicrystalline polymers: application to a high density polyethylene // Int. J. Plasticity, 2010, V. 6, P. 329–347.

[13] Drozdov A.D., Klitkou R., Christiansen J.C. Cyclic viscoplasticity of semicrystalline polymers with finite deformations // Mechanics of Materials, 2013, V. 56, P. 53–64.

[14] Garishin O.K., Korlyakov A.S., Shadrin V.V. Investigation of the elastic-viscous-plastic behavior of thermoplastic materials. Experiment and simulation // XLII Summer School-Conference "Advanced problems in mechanics": Proceedings. St.-Petersburg, 2014, P. 547–553.

[15] Mullins L.J. Effect of stretching on the properties of rubbers // J. Rubber Res., 1947, V. 16. P. 275–89.

[16] Mullins L.J. Softening of rubber by deformation // Rub. Chem. Techn., 1969, V. 42, N 1, P. 165–185.

Oleg Konstantinovich Garishin, Institute of Continuous Media Mechanics UB RAS, Perm, Russia
Vladimir Vasilyevich Shadrin, Institute of Continuous Media Mechanics UB RAS, Perm, Russia, Perm State National Research University, Perm, Russia
Svistkov Alexander L'vovich, Institute of Continuous Media Mechanics UB RAS, Perm, Russia, Perm State National Research University, Russia
Sokolov Alexander Konstantinovich Institute of Continuous Media Mechanics UB RAS, Perm, Russia

Numerical study of hypersonic shock wave-boundary-layer interaction flow with ablation

Mingming Ge, Ming Zeng, Peng Jin, Xiaoliang Yang, Wei Liu

owen2024@sina.cn

Abstract

Through solving the Navier-Stokes equations of thermochemical nonequilibrium flow coupled with the ablating boundary condition, the hypersonic shock wave-boundary-layer interaction flows with ablation are numerically simulated. 16 species and 29 chemical reactions are adopted in the simulation. The oxidation and sublimation of C, as well as the recombination of O catalyzed by C are considered at the wall surface. Both the compression corner flow and the boundary-layer flow with incident shock wave are calculated. The compression corner angles are 15, 18, and 24 degree, and the angles of the wedge that produce the incident shock wave are 15, 21, and 27 degree. The free stream Mach number varies from 10 to 34 and the total enthalpy from 6 to 55 MJ/kg. Both ablating and non-ablating surface conditions are used to investigate the effects of ablation on the flow properties. The flow structure, the characteristics of shock wave-boundary-layer interaction, the separation properties, and the distribution of the thermochemical properties are analyzed. The results show that the possibility of flow separation or the separation range becomes larger as the corner angle (or the angle of the wedge which produce the incident shock) rises, while smaller as the free stream Mach number is increased. As compared with the cases with low-temperature wall, the flow separation zones are lager with ablating wall or with high-temperature wall in radiation equilibrium, and this leads to further effects on the flow properties of the downstream.

Key words: hypersonic nonequilibrium flow, ablation, compression corner flow, shock wave-boundary-layer interaction

1 Introduction

The hypersonic vehicle suffers from intense aerodynamic heating when it fly at a speed of more than 7 km/s in the atmosphere. The temperature of the surface in radiation equilibrium may reach 2000K under which the internal device cannot work normally. Ablative materials are often used to absorb heat through the phase change of the material and the surface reaction between the material and the high temperature gas, and keep the inner wall of the vehicle at a suitable temperature

[1]. The ablation products ejected into the boundary layer may affect the properties of the flow field around the vehicle, such as the distributions of the temperature, the heat flux, the species mass fraction, and the ionization or radiation properties. So the study of the reentry flow field with ablation is significant. A lot of work has been carried out on the the flow field over blunt nosed bodies [2∼8], and has achieved fruitful results. In this paper, the study of hypersonic flow with ablation is extended to bodies with other shape.
For the reentry vehicle and the airbreathing hypersonic vehicle, the flow in the region of control surface the engine inlet needs in-depth study because shock wave-boundary-layer interaction prevails in these regions, affecting the performance of control surface and the engine efficiency[9]. The compression corner flow and the plate boundary-layer flow with incident shock wave are typical representatives of the flow in these regions. In the compression corner flow, the boundary layer of flat plate develops gradually from the leading edge and may be interfered by the corner-generated shock. If the shock wave is strong enough, the boundary layer will be separated, and the recirculation zone will form in the corner region. The thicker boundary-layer compresses the incoming flow, resulting in a separation shock wave. The gas is compressed by the ramp near the reattachment point and a series of compression wave is produced, which coalesce into a shock wave that interact with the separation shock wave and affect the distribution of flow parameters along the compression surface. In the flow of an incident shock-generated interaction with a boundary layer, strong incident shock will lead to the separation of the boundary layer. New waves are induced, and the complex interactions will change the flow field distribution of pressure and heat flux, which may further affect the aerodynamic performance of the vehicle.
Under the condition of freestream with high-enthalpy, the wave structure and separation zone of the flowfield will be affected by the chemical reactions of the gas and the ablative wall material at high-temperature. Both the compression corner flow and the boundary-layer flow with incident shock wave corner are calculated. The compression corner angles are 15, 18, and 24 degrees, the angles of the wedge that produce the incident shock wave are 15, 21, and 27 degrees. The free stream Mach number varies from 10 to 30 and total enthalpy from 6 to 55 MJ/kg. Both ablating and non-ablating surface conditions are used to investigate the effects of ablation on the flow properties. The flow structure, the characteristics of shock-boundary-layer interaction, the separation properties, and the distribution of the thermochemical properties are analyzed.

2 Thermochemical Model

The high temperature air is composed of 10 species in the study: N2, O2, NO, N, O, NOђк, N2ђк, Oђк, Nђк, eђц. As graphite ablation occurs, the following species may also appear in the flow field: CO, CO2, C, C2, C3, CN. 29 chemical reactions are considered for these 16 species. [10, 11] The two-temperature (translational/rotational and vibrational temperature) model is used to describe thermal non-equilibrium and the coupling of vibration and chemical reactions. The thermodynamic and transport properties of the gas mixture are calculated with the

method described in [10]. The surface reactions take into account the process of thermo-chemical ablation due to both oxidation and sublimation [2, 3].

Table 1 Chemical reactions in the flowfield

Number	Reaction	Number	Reaction
1	$N_2+M_1 \rightleftarrows N+N+M_1$	16	$CO+C_2 \rightleftarrows C_3+O$
2	$O_2+M_2 \rightleftarrows O+O+M_2$	17	$C_3+N \rightleftarrows CN+C_2$
3	$C_2+M_3 \rightleftarrows C+C+M_3$	18	$C_3+C \rightleftarrows C_2+C_2$
4	$CN+M_4 \rightleftarrows C+N+M_4$	19	$O+N \rightleftarrows NO^+ + e^-$
5	$N_2+e^- \rightleftarrows N+N+e^-$	20	$N+N \rightleftarrows N_2{}^+ + e^-$
6	$O+e^- \rightleftarrows O^+ + e^- + e^-$	21	$CO_2+M_6 \rightleftarrows CO+O+M_6$
7	$N+e^- \rightleftarrows N^+ + e^- + e^-$	22	$CO_2+N \rightleftarrows CN+O_2$
8	$N_2+O \rightleftarrows NO+N$	23	$CO+NO \rightleftarrows CO_2+N$
9	$NO+O \rightleftarrows O_2+N$	24	$CO_2+O \rightleftarrows CO+O_2$
10	$CO+C \rightleftarrows C_2+O$	25	$2CO \rightleftarrows CO_2+C$
11	$CO+O \rightleftarrows O_2+C$	26	$N_2+CO_2 \rightleftarrows N+N+CO_2$
12	$CO+N \rightleftarrows CN+O$	27	$O_2+CO_2 \rightleftarrows O+O+CO_2$
13	$N_2+C \rightleftarrows CN+N$	28	$C_2+CO_2 \rightleftarrows C+C+CO_2$
14	$CN+O \rightleftarrows NO+C$	29	$CN+CO_2 \rightleftarrows C+N+CO_2$
15	$CN+C \rightleftarrows C_2+N$		

3 Governing Equations and Ablative Surface Boundary Conditions

3.1 Governing Equations and Numerical Methods

The governing equations for the flow field are the axisymmetric Navier-Stokes equations coupled with the vibrational and chemical kinetics, which are solved to obtain the steady state solution of the flow field. A finite difference method is used in the calculation. All inviscid terms are discretized with AUSMPW+ scheme [12]. The viscous terms are discretized with center difference scheme.The inviscid fluxes are discretized implicitly while the viscous terms explicitly. The implicit parts of the differential equations are disposed in two steps with the LU-SGS approach [13]. The details of the flow field governing equations are described in [14].

3.2 Ablative Surface Boundary Conditions and the Solution Method

To couple the flow field to the heat shield during ablation, mass balance and energy balance must be satisfied at the surface. The surface mass balance for each species is

$$-\left(æ D_s \nabla C_s \bullet \mathbf{n}\right)_w + \dot{m}_w C_{s,w} = \dot{m}_{s,w} \tag{1}$$

where the first term on the left side is the diffusion of species, $\mathbf{n}$ is the surface unit normal vector (away from the wall), $\dot{m}_w$is the total mass flux at the surface, and $\dot{m}_{s,w}$, the mass flux of species s per second, is determined from the surface thermochemistry [2]. There are 15 surface mass balance equations in this study with the assumption of quasi-neutral plasma.
The surface energy balance is expressed as

$$-q_w + q_{cond,w} - "æ T_w^4 + \sum_s \dot{m}_{s,w}\left(h_{solid,w} - H_w\right) = 0 \tag{2}$$

where q_w is the heat flux to the flow from the wall, which contains both the heat conduction and the diffusive chemical heat flux, $"\text{æ}T_w{}^4$ is the re-radiation of heat into the flow, $q_{cond,w}$ is the heat flux conducting energy to the surface from the heat shield (set as zero here for the quasi-steady-state ablation), the fourth term in (2) is the removal of energy from the surface due to mass removal. To set boundary conditions for the pressure and velocity, an assumption is made that blowing occurs only normal to the body. This allows the pressure and velocity to be related through the equation of state and the conservation of mass for one-dimension.

$$(\text{æ}\mathbf{V} \bullet \mathbf{n})_w = \dot{m}_w \tag{3}$$

The density of the gas in the above equation is determined from the equation of state. Moreover, the normal gradient of pressure at the surface is assumed to be zero. Then, from these surface boundary conditions (16 nonlinear equations), the surface temperature, pressure, species densities and injection velocities can be determined as part of the solution. Besides the ablative wall condition, three conditions without ablation, namely fully catalytic and non-catalytic wall at temperature of 300K, and non-catalytic wall in radiation equilibrium, are used in the flow simulation to analyze the effects of wall condition on flow properties. At full catalytic wall, the species mass fraction is set as the chemical equilibrium value at local temperature and pressure. At non-catalytic wall, the species mass fraction is determined by the zero gradient condition. The temperature of the wall in radiation equilibrium is determined by the energy balance relation $-q_w = "\text{æ}T_w^4$. The velocity at the wall is set as zero for the cases without ablation.

3.3 Validation of the In-house Code

The two-dimensional compression corner flow in Holdenrss Calspan 48-inch shock tunnel [15] is calculated with the present in-house code, which can be used as a validation of the code for simulating the hypersonic flow with shock wave-boundary-layer interactions. The freestream in the shock tunnel has a Mach number of 14.1, temperature of 89K, and density of 5.27×10^{-4} kg/m3. The calculated wall pressure and heat flux are consistent with the experimental results given by [16], which is described in detail in reference [17]. As a validation of the code for simulating the hypersonic flowfield with ablation, the flow over a sphere under the reentry conditions (at speed of 10km/s and altitude of 65km) is calculated. The numerical results are in good agreement with that of [3], and the details are given is in reference [8].

4 Simulation and Analysis of the Compression Corner Flow

4.1 Case Conditions and Computational Mesh

The total length of the compression corner model is 0.6096m, of which the length of the front plate is 0.3048m. The computational mesh (Figure 1) is 131×81 with 131

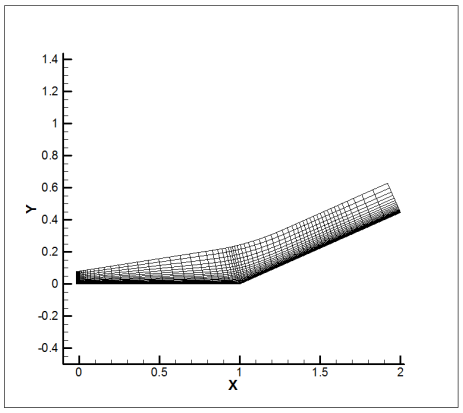

Figure 1: Computational mesh of compression corner flow

points along the surface and 81 points in the flowfield normal to the body, only half of the grid points in both directions are shown for clarity. Refined grids are used near the leading edge, the corner and the position of peak pressure. Exponential stretch is used from the wall. The first normal grid height at the wall is 6.096×10^{-5}m.

Three compression corner flows at 48 conditions are simulated. The corner angles are 15, 18, 24 degree respectively, the free stream Mach numbers are 10, 15, 20, 30, and the gas densities are those of atmosphere at altitude of 40km, 45km, 50km and 55km. The effects of the freestream conditions, the corner angle and the boundary conditions on the flow properties are analyzed. The free stream temperature is set as 300K.

4.2 Overview of the Flowfield Characteristics under Different Freestream and Wall Conditions

The calculation results show that the increase of the compression corner angle will promote the flow separation, and the increase of flow Mach number will suppress separation. The separation and reattachment point positions (SP and RP) for the corners with angle of 15 and 24 degree under 16 freestream conditions are listed In table 1 and table 2. The symbol $'\times'$ in the table represents the case without flow separation. The comparison of the flow separation characteristics under the four different wall conditions show that the results for fully catalytic and non-catalytic wall at low wall temperature are similar, while the results for the radiation equilibrium and ablative wall are similar. The flow separation zones are larger for the latter two wall conditions.

Table 1. Flow separation and reattachment position (s/L) of 15 degree compression corner

Freestream condition		300K fully catalytic		300K non-catalytic		Radiation equilibrium		Ablationm	
Altitude	Ma	SP	RP	SP	RP	SP	RP	SP	RP
40	10	0.8297	1.168	0.8297	1.168	0.7215	1.269	0.7215	1.269
	15	0.8904	1.153	0.8904	1.153	0.8056	1.251	0.8056	1.251
	20	0.9578	1.124	0.9578	1.124	0.9219	1.184	0.9219	1.200
	30	×	×	×	×	×	×	×	×
45	10	0.9353	1.124	0.9219	1.124	0.8297	1.234	0.8297	1.234
	15	0.9950	1.046	0.9950	1.046	0.9219	1.184	0.9219	1.200
	20,30	×	×	×	×	×	×	×	×
50	10	1.000	1.011	0.9950	1.011	0.9353	1.168	0.9353	1.168
	15,20,30	×	×	×	×	×	×	×	×
55	10	×	×	×	×	1.000	1.005	1.000	1.005
	15,20,30	×	×	×	×	×	×	×	×

Table 2. Flow separation and reattachment position (s/L) of 24 degree compression corner

Freestream condition		300K fully catalytic		300K non-catalytic		Radiation equilibrium		Ablationm	
Altitude	Ma	SP	RP	SP	RP	SP	RP	SP	RP
40	10	0.6287	1.167	0.6287	1.167	0.4870	1.267	0.4870	1.267
	15	0.7258	1.131	0.7258	1.131	0.6287	1.186	0.6287	1.186
	20	0.8084	1.115	0.8084	1.115	0.7551	1.149	0.7551	1.149
	30	0.8928	1.115	0.8744	1.115	0.8543	1.131	0.8543	1.149
45	10	0.5941	1.246	0.5941	1.246	0.3822	1.383	0.3822	1.415
	15	0.7551	1.167	0.7257	1.186	0.5587	1.288	0.5587	1.288
	20	0.8084	1.167	0.8084	1.167	0.7551	1.206	0.7551	1.206
	30	0.9095	1.149	0.8928	1.149	0.8543	1.186	0.8543	1.167
50	10	0.5587	1.328	0.5587	1.328	0.3822	1.493	0.3822	1.493
	15	0.6624	1.267	0.6624	1.267	0.5229	1.383	0.5229	1.383
	20	0.8323	1.206	0.8323	1.206	0.7258	1.288	0.7258	1.288
	30	0.9612	1.167	0.9246	1.186	0.8744	1.226	0.8928	1.226
55	10	0.6624	1.327	0.6624	1.327	0.5229	1.493	0.5229	1.493
	15	0.7551	1.288	0.7551	1.288	0.5587	1.288	0.5587	1.468
	20	0.8744	1.226	0.8744	1.226	0.7827	1.328	0.7827	1.328
	30	×	×	×	×	1.000	1.006	1.000	1.006

Figure 2 shows the wall pressure distribution of 24 deg compression corner at different Mach numbers and altitude of 40 km. As the Mach number increases, the flow separation zone decreases, and the peak value of the pressure on the ramp moves forward. The reason that the increase of Mach number suppresses separation has two points. On the one hand, as the Mach number increases, the shock angle of the main shock formed by the ramp decreases and the shock is closer to the surface, with the result of the decrease of the range of adverse pressure gradient. On the other hand, as the Mach number increases, the subsonic region range in the boundary layer decreases, which result in the decrease of the range for upstream propagation of the pressure gradient.

However, the influence of freestream gas density on flow separation at constant Mach number is relatively complicated. As can be seen from table 1, for 15deg compression corner flow, increasing the density will facilitate flow separation. At altitude of 40km, separation occurs at Mach number of 10, 15 and 20, only the case of Mach number of 30 is an exception; At altitude of 45km, there is separation at Mach number of 10 and 15 but not at Mach number of 20 and 30; At altitude of 50km, separation occurs only at Mach number of 10; At altitude of 55km, separation is observed only at Mach number of 10 and with wall in radiation equilibrium or with ablation. However, for 24deg compression corner flow, the effects of gas density on flow separation vary with Mach number. At high Mach number such as 30 and 20, the increase of density promotes separation; At Mach number of 15, the increase of density basically promotes separation at the low-temperature wall conditions, but postpones separation and decrease the separation zone at radiation equilibrium wall

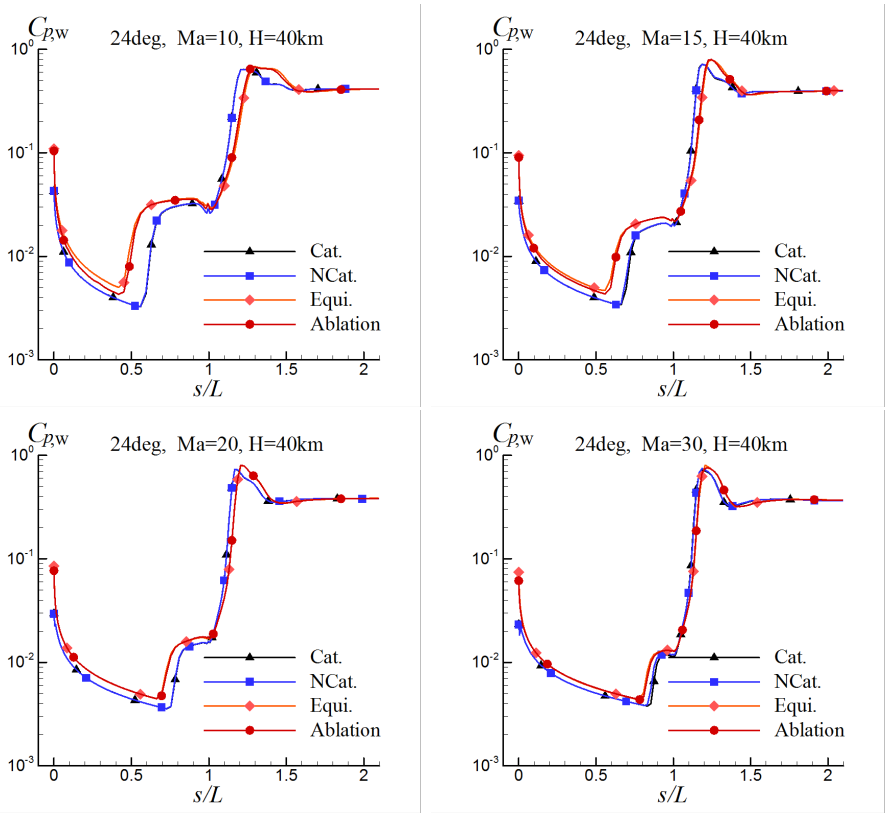

Figure 2: Surface pressure coefficient at different Mach numbers (24deg corner, H=40km)

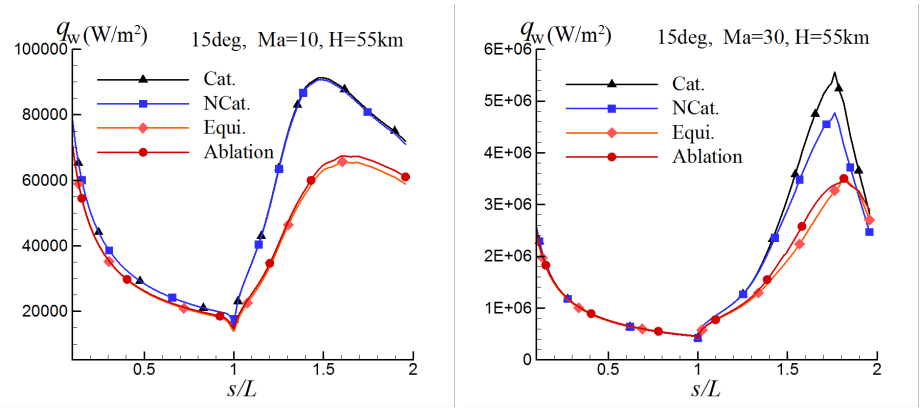

Figure 3: Surface heat flux at Mach number of 10 and 30 (15deg corner, H=40km)

and ablative wall; At lower Mach number (Ma=10), the increase of density mainly postpones separation.

4.3 Analysis of the Effects of Wall Conditions

When there is no flow separation, the wall condition mainly affects the wall heat flux, having little effects on the flowfield structure. Figure 3 shows the surface heat flux for 15deg corner at Mach number of 10 and 30 and altitude of 55 km. The heat flux values of the four different wall conditions are similar at the plate surface, but at the ramp surface, the value of radiation equilibrium wall and wall with ablation are much lower and the position of peak heat flux moves downward than that of the low temperature wall case.

As compared with the cases with low-temperature wall, the flow separation zones are lager with ablating wall or with wall in radiation equilibrium. This can be attributed to the increase of the of the boundary layer thickness induced by the increase in wall temperature. Moreover, the influence of wall conditions on the flow separation will further affect other flow properties. Take 24 deg compression corner at Mach number of 15 and altitude of 40 km and 55 km as examples, the flow field pressure distribution and the streamline in the recirculation zone for both the fully catalytic wall at 300 K and the ablative wall are given in Figure 4 and Figure 5 respectively. It can be seen that the size of the separation zone at low temperature wall is obviously smaller than that at ablative wall. This is due to the thickening of the boundary layer caused by the higher wall temperature, which affects the shape of the shock wave and its interaction with the boundary layer. With the same wall temperature, the wall catalytic properties have no significant effects on separation. The range of the separation zone under the ablative wall condition is close to that under the condition of radiation equilibrium wall without ablation.

Figure 6 shows the surface heat flux for 24 deg corner at Mach number of 15 and altitude of 40 km and 55 km. As compared with the low temperature wall case, the surface heat flux of radiation equilibrium wall and wall with ablation are fairly lower. However, the separation zone is enlarged by the higher wall temperature, and this cause the intersection of the separation shock, reattachment shock and the main shock move farther downstream, which leads to the positions of peak pressure

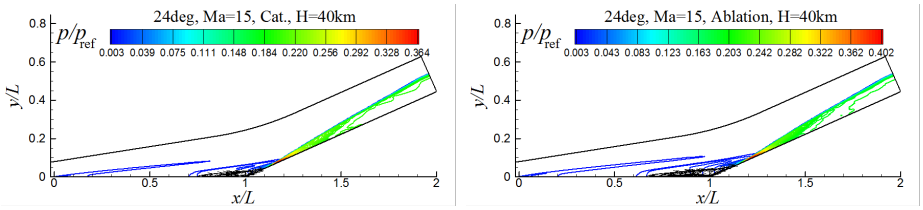

Figure 4: Pressure contour and separation zone streamline at H=40km (24deg corner, Ma=15)

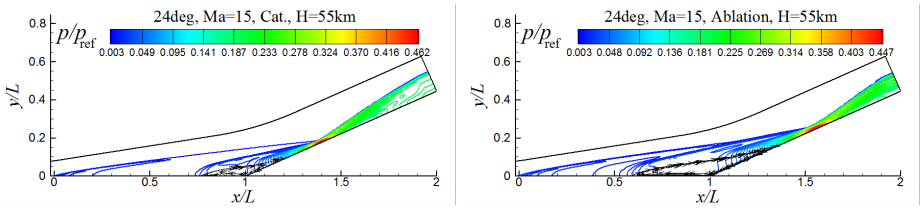

Figure 5: Pressure contour and separation zone streamline at H=55km (24deg corner, Ma=15)

and heat flux moving downstream.

Take the 24 deg corner flow at Mach number of 10 and altitude of 40 km, which has significant separation, as an example to investigate the influence of the wall conditions in detail. Figure 7 shows the normal distribution of pressure and temperature at three typical positions, namely, the start point of the ramp (x/L=1), the position of peak pressure and the point near the ramp end (x/L=1.9). The point x/L=1 is just near the separation chock. The thickness of the shock layer and the shock intensity under the condition of the radiation equilibrium wall and the ablative wall are obviously larger than that under the low wall temperature conditions. Moreover, the thickness for the case with radiation equilibrium wall is slightly larger than that with ablative wall. This phenomenon can be explained as follows. The increase of wall temperature leads to the thickening of the boundary layer, and therefore, enhances the leading edge shock and the separation shock, and at the same time pushes the shock away from the surface. The position of peak

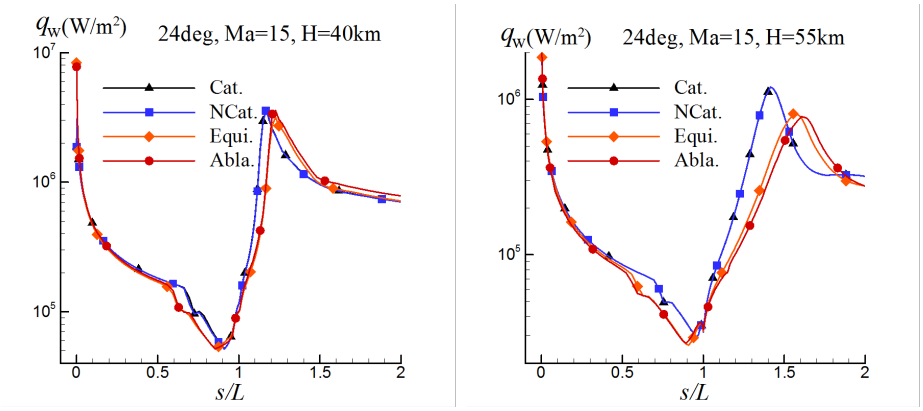

Figure 6: Surface heat flux at altitude of 40km and 55km (24deg corner, Ma=15)

pressure is just near the intersection of the main shock and the separation shock. The shock layer with high wall temperature is still thicker, and the peak values of pressure and temperature are also higher than those with low wall temperature.

4.4 Thermochemical Characteristics of the Flowfield

The 24deg compression corner flow at Mach number of 30 has the strongest shock wave, vibrational excitation, and chemical reaction. The extent of the flow nonequilibrium is enhanced with the raise of altitude and the resulting decrease of gas density. The 24 deg corner flow at Mach number of 30 and altitude of 55km is taken as an example here to analyze the thermochemical characteristics of the flowfield. The case with wall ablation is mainly discussed, and the results with other wall conditions are given only for comparison and analysis of the effects of wall condition. Figure 8 and Figure 9 show the pressure and temperature distribution of the flow field respectively, and one can see from Figure 9 that the high temperature region is near the front part of the compression surface, not coinciding with that of high pressure (Figure 8). The gas in this region has been heated first by the leading edge shock wave, then by the friction in the boundary layer, and last by the separation shock, so the temperature is even higher than the gas behind the main shock, which is heated only by the main shock from the low freestream temperature (300K).
Figure 10(a) and (b) gives the distribution of O, NO mass fraction, and Figure 10(c) gives that of the number density of electron. From comparison with Figure 9, one can see that the flow is in thermochemical non-equilibrium. The increase of the vibrational temperature and the chemical reaction lags behind the increase of translational temperature. The high translational temperature zone is located at the corner region for this case, and the translational temperature reaches its peak value at ħ„1.16, while the high vibrational temperature zone locates after the main shock, and the position of peak value is at ħ„1.4. The region of the high mass fraction of atoms is coincident with that of high vibrational temperature. There is a high temperature zone in the downstream of the main shock wave, and the vibrational excitation and chemical reaction in this high temperature zone are more significant than other regions. The peak value of mass fraction is 0.166 for O, 0.202 for NO, and up to 0.0812 for N. The peak value of NO+ mass fraction is 7.0×10^{-4}, slightly higher than that of N2+, which is 3.2×10^{-4}. The order of magnitude of mass fraction is $10^{-9}$for O+, and $10^{-10}$for N+. The peak value of electron number density reaches the order of 10^{14} [Figure 10(c)].
The shock layer of the case with radiation equilibrium wall and ablative wall are thicker than that with low wall temperature, which has been mentioned in 3.3, so there are also differences in the species mass fraction between the cases with high and low temperature wall. Further comparison is mainly on the species mass fraction between the cases of radiation equilibrium wall and the ablative wall. Figure 11 shows the normal distribution of the mass fraction of the main air species at the position of peak pressure and the end of the ramp under these two wall conditions. There is no significant difference in the shock layer thickness between the two conditions, and the effects of the ablation are limited to the boundary layer. The wall temperature and the surface heat flux under the ablative wall condition

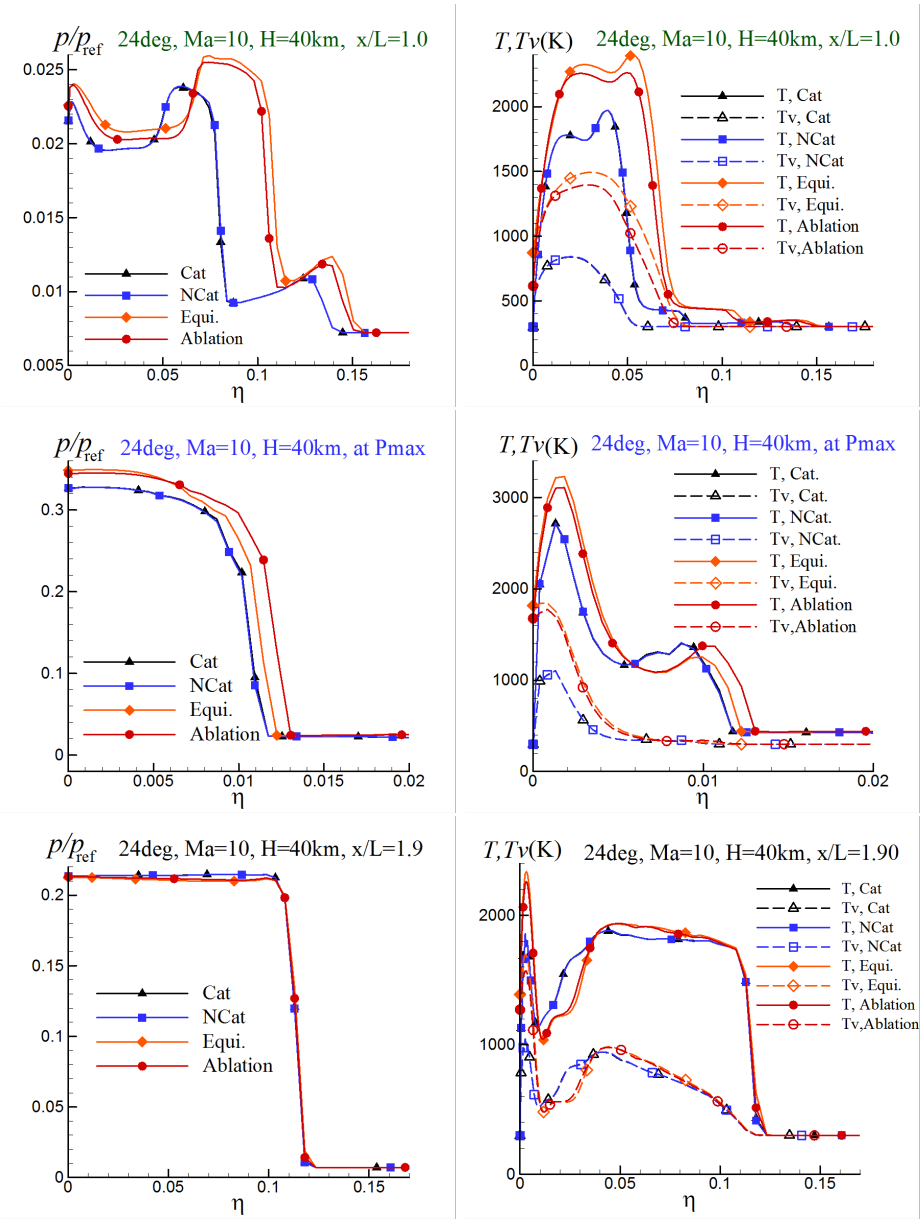

Figure 7: Normal distribution of pressure and temperature at 3 positions (24deg corner, Ma = 10, H = 40km)

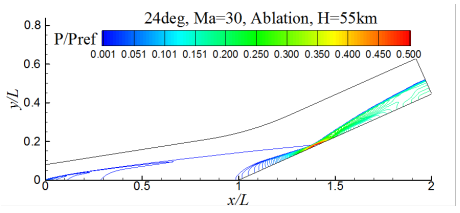

Figure 8: Pressure contour (24ocorner, Ma=30, H=55km)

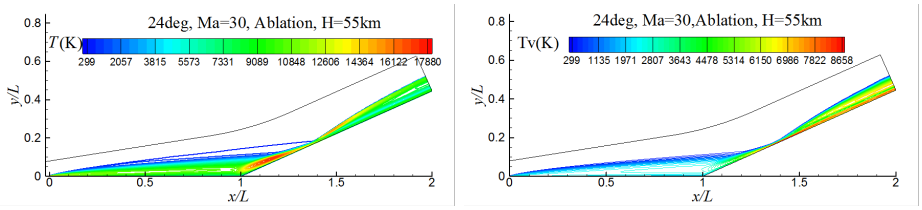

Figure 9: Temperature contours (24deg corner, Ma=30, H=55km)

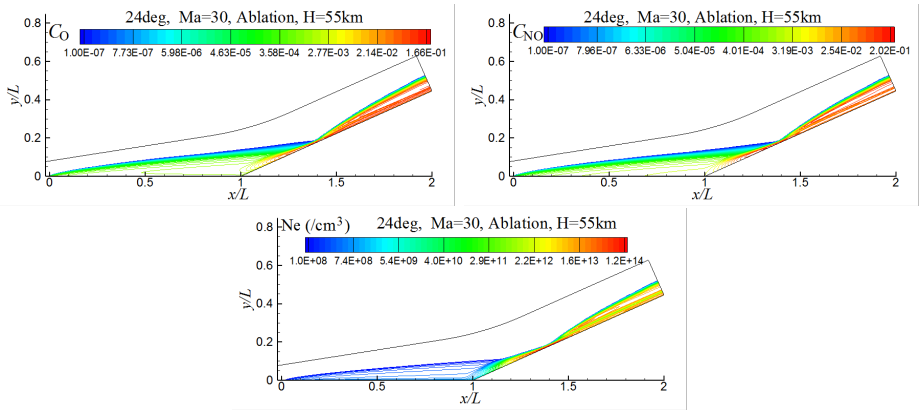

Figure 10: Contours of mass fraction of O and NO, number density of electron (24deg corner, Ma=30, H=55km)

are higher than that under radiation equilibrium wall condition. The chemical reaction and diffusion in the boundary layer are further affected by the diffusion of the ablation products into the boundary layer, which increases the mass fraction of neutral molecules (N_2 and O_2) and reduces those of the atoms (N, O) and the main ion species (NO+, N_2+).

The ablation products are mainly confined to the boundary layer, and ablative species with highest mass fraction is in turn CO, C_3, C_2, and CN. Figure 12 shows the mass fraction distribution of CO, C_3 and CN. In addition, the peak value of mass fraction is 0.0574 for C_2, 0.0211 for C, and in the order of $10^{-3}$for CO_2. Figure 13 shows the normal distribution of the mass fraction of the ablative species at the position of peak pressure and $x/L = 1.9$. The ablation in the plate region is rather small and the main ablation product is C3, which has a mass fraction of 0.01. The ablation becomes much stronger in the high pressure region after the intersection of the main shock and the reattachment shock, and the mass fraction of CO and C_3 attain the order of 0.1. The mass fraction of the ablative species continues rising downstream, and attaining their peak values near the end of the ramp.

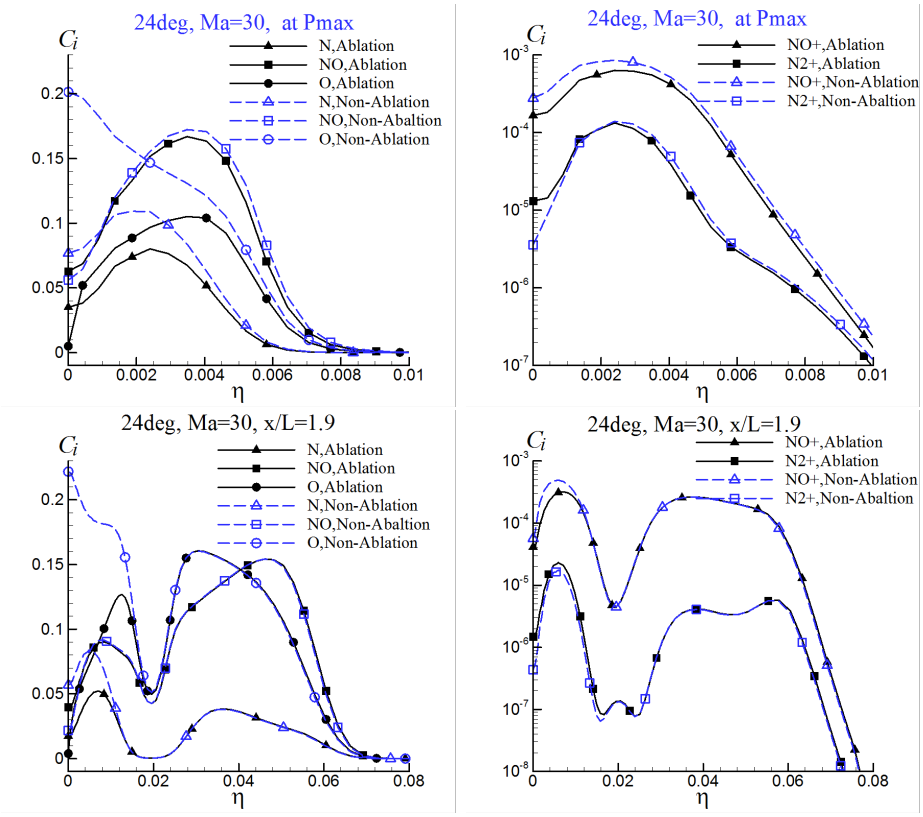

Figure 11: Normal distribution of species mass fraction at 2 positions (24deg corner, Ma=30, H=55km)

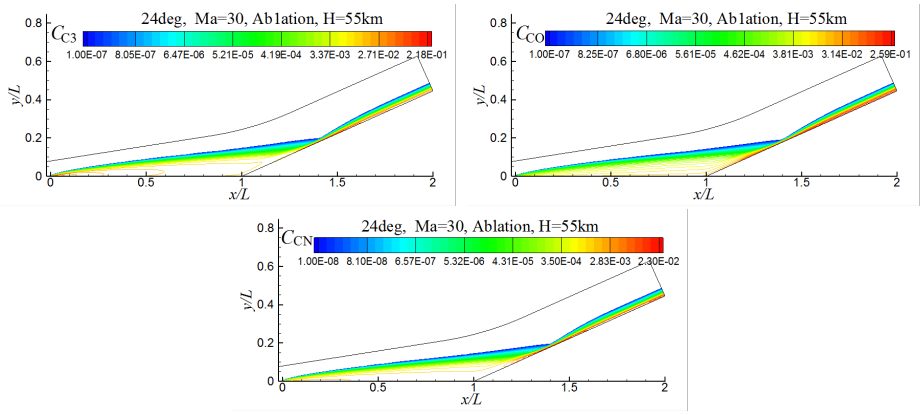

Figure 12: Mass fraction contours of the main ablation species (24deg corner, Ma = 30, H = 55km)

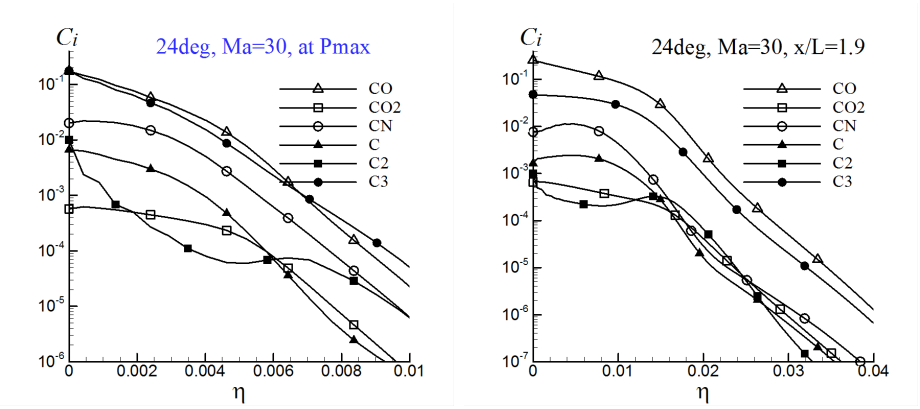

Figure 13: Normal distribution of ablation species at 2 positions (24deg corner, Ma=30, H=55km)

5 Simulation and Analysis of Boundary Layer Flow with Incident Shock

5.1 Case Conditions, Computational Boundary Conditions, and Mesh

Freestream density and temperature are set as those of the atmosphere at altitude of 60 km. Six freestream Mach number (14, 18, 22, 26, 30, 34) are selected, and the angles of the wedge which produces the incident shock are 15, 21, and 27 degree. The boundary layer flows with incident shock under a total of 18 case conditions are simulated numerically.

The computational boundary conditions of the plate flow field are set asa follows (Figure 14). The left boundary of the is supersonic freestream, and the right boundary is a supersonic exit. The "1" part of the lower boundary is the wall, and the "2" part is the flow in front of the plate and set as symmetric condition. The "3" part of the upper boundary is the supersonic freestream (also the flow before shock), the "4" part is the condition after the incident shock. The "5" part can be set as a non-reflective boundary condition. The incident shock parameters are determined through the numerical simulation of the nonequilibrium flow over a wedge. The freestream condition of the wedge flow is the same as that of the plate flow, and the intensity of the incident shock under the same freestream is controlled by changing the wedge angle. The intensity of the incident "oblique shock" increases with the increase of the wedge angle and the incoming Mach number. The method of extracting the incident shock parameters from the wedge flowfield is described in [17].

Fully catalytic wall at 300K condition is set for the calculation of wedge flow. Four different wall conditions (the same as those for the corner flow) are considered in the flow over the plate. The computational mesh for the wedge flow is 121×101. The plate length is 1m and the computational mesh is 121×101. The first normal grid height at the wall is 10^{-4} m. Refined grids are used near the leading edge and the wall.

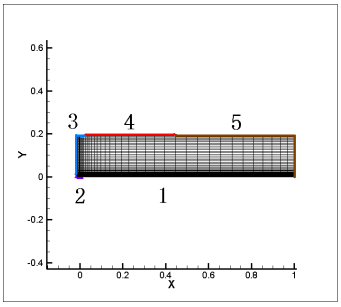

Figure 14: Boundary conditions of plate flowfield

5.2 Flowfield Characteristics under Different Freestream and Wall Conditions

Flow separations are observed for all 18 cases under the four different wall conditions. Table 3 to Table 5 give the locations of the separation and the reattachment location (x/L), in which L is the length of the plate, and x is the distance from the plate leading edge. The results show that the increase of the wedge angle promotes the separation while the increase of the Mach number delays the separation, which is similar to the case of compression corner flow. However, if the wedge angle and the wall condition keep unchanged, the reattachment location keeps stable as the Mach number changes. The separation characteristics under the fully catalytic and non-catalytic wall at low wall temperature are similar, and the results for the radiation equilibrium and ablative wall are similar. The flow separation zones are larger under the latter two wall conditions.

Table 3 Flow separation and reattachment position (x/L) for the case of 15 degree wedge

Ma	300 K fully catalytic		300K non-catalytic		Radiation equilibrium		Ablation	
	SP	RP	SP	RP	SP	RP	SP	RP
14	0.4273	0.5311	0.4273	0.5311	0.3478	0.5489	0.3478	0.5489
18	0.4611	0.5311	0.4611	0.5311	0.4108	0.5489	0.4108	0.5489
22	0.4783	0.5311	0.4783	0.5311	0.4273	0.5311	0.4273	0.5311
26	0.4783	0.5311	0.4783	0.5311	0.4611	0.5489	0.4611	0.5489
30	0.4958	0.5311	0.4958	0.5311	0.4783	0.5489	0.4783	0.5489
34	0.5134	0.5489	0.5134	0.5489	0.4958	0.5489	0.4958	0.5489

Table 4 Flow separation and reattachment position (x/L) for the case of 21 degree wedge

Ma	300 K fully catalytic		300K non-catalytic		Radiation equilibrium		Ablation	
	SP	RP	SP	RP	SP	RP	SP	RP
14	0.2394	0.3946	0.2277	0.3946	0.1657	0.4108	0.1657	0.4108
18	0.2905	0.3946	0.2905	0.3946	0.2394	0.3946	0.2394	0.3946
22	0.3184	0.3946	0.3329	0.3946	0.2771	0.3946	0.2771	0.3946
26	0.3478	0.3946	0.3478	0.3946	0.3042	0.4108	0.3042	0.4108
30	0.3478	0.3946	0.3478	0.3946	0.3184	0.3946	0.3329	0.3946
34	0.3631	0.3946	0.3631	0.3946	0.3478	0.3946	0.3478	0.3946

Table 5 Flow separation and reattachment position (x/L) for the case of 27 degree wedge

Ma	300 K fully catalytic		300K non-catalytic		Radiation equilibrium		Ablation	
	SP	RP	SP	RP	SP	RP	SP	RP
14	0.0361	0.3184	0.0361	0.3184	0.0230	0.3329	0.0230	0.3329
18	0.1173	0.3042	0.1173	0.3042	0.0859	0.3042	0.0916	0.3042
22	0.1848	0.3042	0.1750	0.3042	0.1399	0.3184	0.1567	0.3042
26	0.2164	0.3042	0.1949	0.3042	0.1657	0.3184	0.1848	0.3042
30	0.2054	0.3042	0.1847	0.3042	0.1750	0.3184	0.1848	0.3042
34	0.2277	0.3042	0.2164	0.3042	0.1949	0.3184	0.2054	0.3042

Figure 15 to Figure 17 show the flowfield pressure distribution and the streamline in the recirculation zone under different wall conditions. Figure 15 shows the results for the case of 15deg wedge and Figure 16 the 27deg wedge, both with Mach number of 14 and 34 and with ablative wall conditions. Figure 17 shows the results for the case of 27deg wedge under full catalytic wall at 300K conditions. Figure 18 shows the distribution of the wall pressure and that of the friction coefficient in the separation zone for the case of 28deg wedge and Mach number of 14.

When the freestream Mach number keeps constant, the incident shock intensity increases as the wedge angle increases. The impacts of the shock on the boundary layer flow increases, the possibility of separation and separation range becomes larger. Take the flow at Mach number of as an example, strong separation is observed for the case of 27deg wedge [see Figure 16 (a) (b)]. There are a large vortex and two small vortices in the recirculation zone. The separation for the case of 15deg wedge is much weaker, as can be seen in Figure 15 (a).

If the wedge angle keeps constant, the possibility and range of separation are reduced as the Mach number increases, which is obvious in Figure 15 and Figure 16. The reason why the increase of Mach number suppresses the separation is as follows. Although as the Mach number increases, the pressure after the incident shock rises and so does the adverse pressure gradient in the boundary layer, at the same time the kinetic energy of the gas in the boundary layer also increases. The post-shock pressure is proportional to the square of the product of the Mach number and the sine of the shock (the shock angle decreases with the increase of Mach number), but the kinetic energy of the gas in the boundary layer is proportional to the square of the freeatream Mach number. Therefore, the gas ability to withstand the adverse pressure gradient may increase more than the adverse pressure gradient as the Mach number rises, therefore possibility of flow separation decreases as the Mach number increases.

There is no significant difference in the flow separation characteristics between the fully catalytic and non-catalytic wall at low wall temperature (300K), but the separation zone under radiation equilibrium wall and ablative wall condition are larger than that under low temperature wall conditions. For example, under the fully catalytic wall at 300K condition, a big and a small vortex can be seen in the recirculation zone in Figure 17 (the case at Mach number of 14 with 27deg wedge), while under the fully catalytic wall. For the ablative wall condition [Figure 16(a) and (b)] another smaller vortex can be seen above the big and the small vortex, and the separation zone is larger than that in Figure 17. The friction coefficients at the separation point are all close to -0.004 under various wall conditions, and they attain the negative peak values before the reflected shock. The peak value is about -0.022 under low temperature wall conditions and are about -0.026 under radiation equilibrium wall and ablative wall conditions (see Figure 18). The reason of the enhancement of flow separation under radiation equilibrium wall and ablative wall conditions is mainly because the thickening of the boundary layer. Figure 19 shows the wall temperature distribution for the case at Mach number of 14 with 27deg wedge. The rise in wall temperature will obviously promote separation.

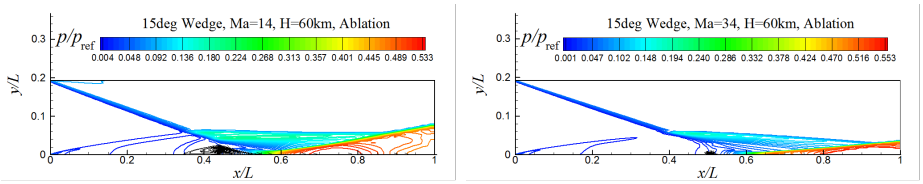

Figure 15: Pressure contour and separation zone streamline for the case of 15deg wedge (Ma= 14 and Ma=34, ablative wall)

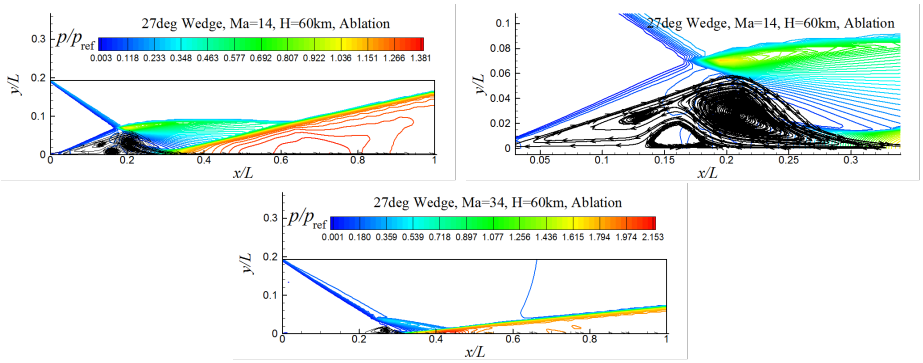

Figure 16: Pressure contour and separation zone streamline for the case of 27 deg wedge (Ma= 14 and Ma=34, ablative wall)

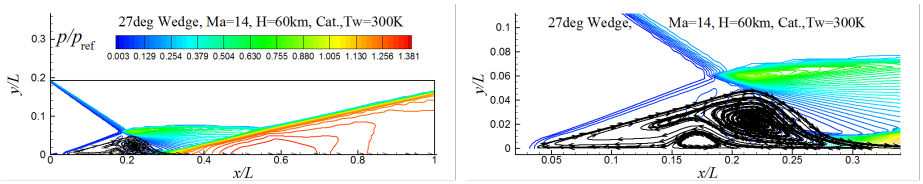

Figure 17: Pressure contour and separation zone streamline for the case of 27 deg wedge and fully catalytic wall (Ma= 14)

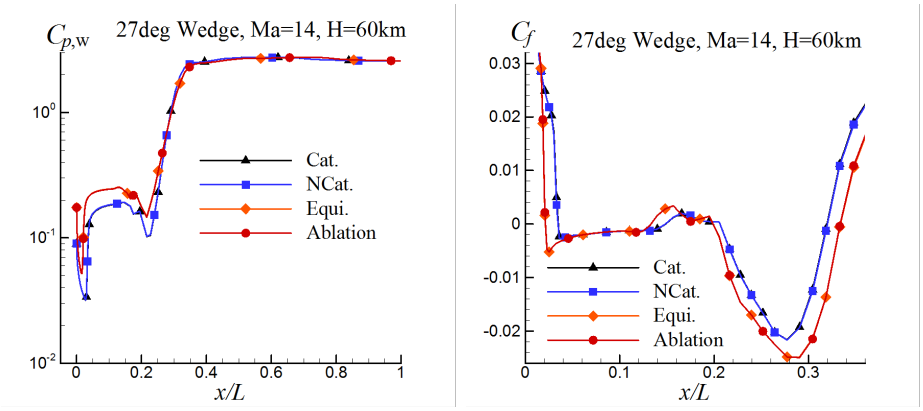

Figure 18: Surface pressure and friction coefficient (27deg wedge, Ma=14)

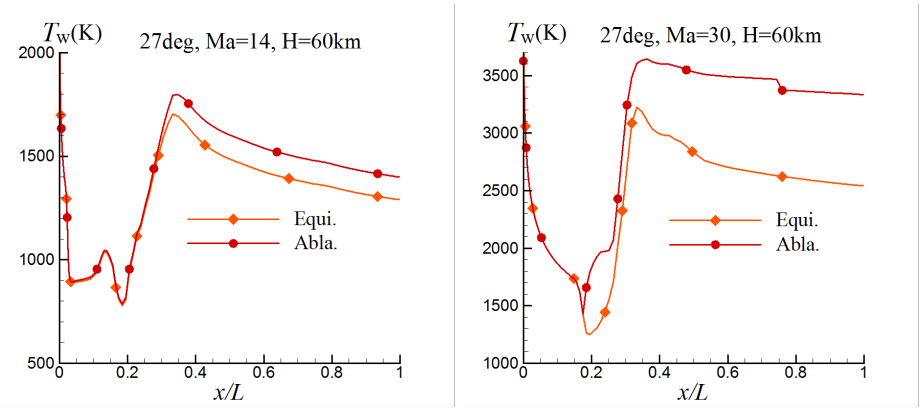

Figure 19: Surface temperature at Mach number of 14 and 30 (27deg wedge)

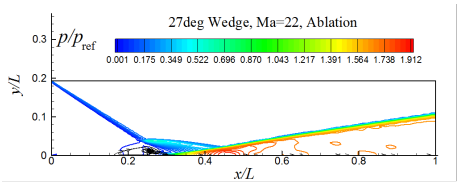

Figure 20: Pressure contour and separation zone streamline (27deg wedge, Ma= 22)

5.3 Thermochemical Characteristics of the Flowfield

The case at Mach number of 22 with 27deg wedge is taken as an example to investigate the thermochemical properties of the flowfield. Strong chemical reactions take place in the region after the incident shock (generated by the wedge), the separation and reattachment shock, and the reflected shock. Ablation at the wall is also evident. Considering that the effects of wall conditions are mainly confined to the vicinity of the wall besides the influence on the flow separation, only the results of ablation wall conditions is given here.

Figures 20 to 22 show the distributions of pressure, temperature, mass fraction of O and NO+ The flow is in thermohemical nonequilibrium, the increase of the vibrational temperature after the incident shock lags behind the increase of the translational temperature, and the chemical reaction lags more. The peak temperature appears in the vicinity of the reattachment and the reflected shock, and the peak mass fractions of atoms and ions appear near the end of the plate. This indicates that chemical reactions undergo a long relaxation distance. The vibrational temperature of the gas in the downstream of the incident shock is fairly high, and a certain amount of atoms and ions exist, which will increase further after the reflected shock.

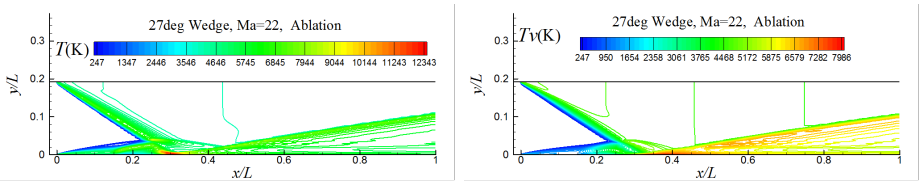

Figure 21: Temperature contours (27deg wedge, Ma= 22)

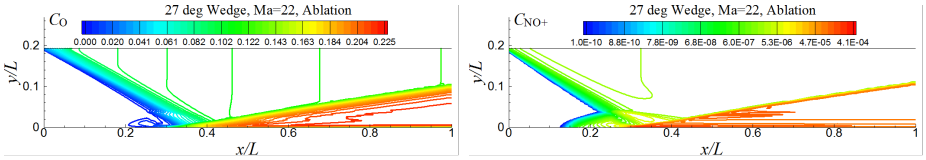

Figure 22: Mass fraction contours of O and NO+ (27deg wedge, Ma= 22)

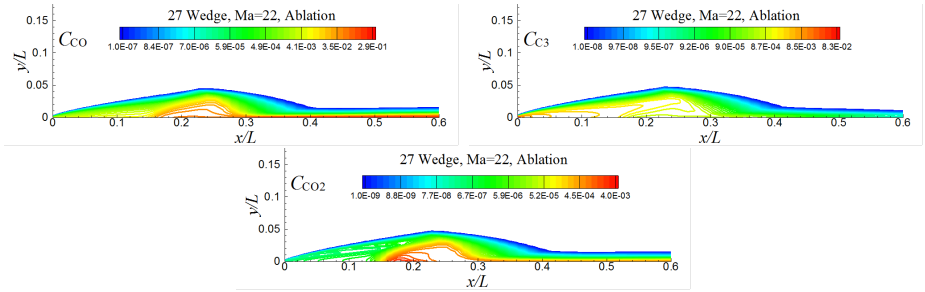

Figure 23: Mass fraction contours of main ablation species (27deg wedge, Ma= 22)

The lag of vibrational excitation and chemical reaction after the reflected shock is obviously weaker than that after the incident shock, which is closely related to the ?pre-heating? of the gas by the incident shock before the reflected shock.
The ablation products are basically confined to the recirculation zone and the boundary layer near the wall. The ablative species with highest mass fraction is in turn CO,C_3,C_2,CO_2, and CN. The peak mass fraction of CO and CN appears near the wall after the reflected shock, while that of CO_2 occurs in the recirculation zone, because the high temperature near the wall after the reflected shock leads to further decomposition of CO_2. The peak mass fractions of C_3 and C_2 appear after the leading edge shock in the vicinity of the leading edge, which originate from the sublimation of C. Then the amount of C_3 and C_2 decreases because of the reactions with O and N, resulting the formation of CO and CN. Figure 23 shows the mass fraction distribution of CO, C_3, and CO_2. Figure 24 shows the normal distribution of the mass fraction of the ablative species at the positions of peak pressure and peak temperature, and at the end of the plate. The range of the ablative species can be seen from the figure.

6 Conclusion

Taking the compression corner flow and the boundary-layer flow with incident shock wave as examples, the shock wave-boundary-layer interaction flows with ablation are numerically studied at free stream Mach number of 10 to 34 and total enthalpy from 6 to 55 MJ/kg. The compression corner angles are 15, 18, and 24 degree, and the angles of the wedge that produce the incident shock wave are 15, 21, and 27 degree. The results show:
(1) For the compression corner flow, the possibility of flow separation and the separation range become larger as the corner angle increases, while smaller as the free stream Mach number rises.
(2) For the boundary layer flow with incident shock wave produced by a wedge,

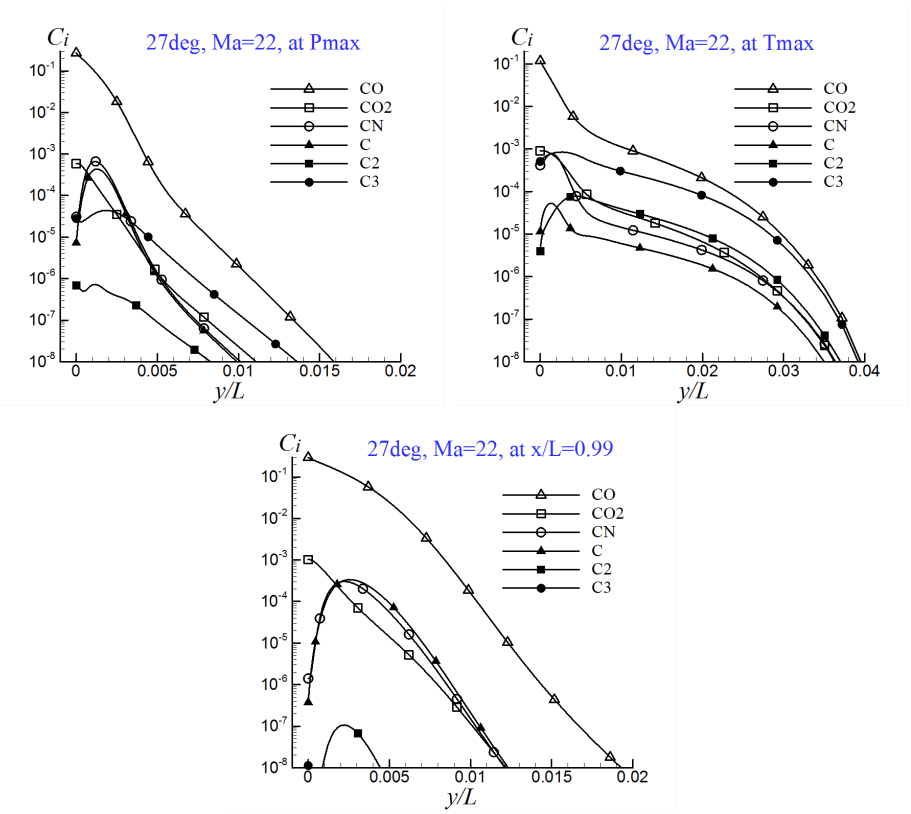

Figure 24: Normal distribution of mass fraction of main ablation species at 2 positions (27deg wedge, Ma =22)

the increase of the wedge angle and the decrease of the free stream Mach number increase the separation possibility and enlarge the separation zone.
(3) As compared with the cases with low-temperature wall, the flow separation zones are larger with ablating wall or with high-temperature wall in radiation equilibrium. For the compression corner flow, this make the positions for peak values of pressure, skin friction and heat flux move to downstream. For the boundary layer flow with incident shock wave, this also leads to further effects on the flow properties of the downstream. Therefore, the wall conditions have more evident effects on the flow properties for these shock wave-boundary-layer interaction flows than that for the flow over a sphere or a cone.
(4) As the ablation species are mainly limited to the boundary layer except for the circulation zone, the ablation effects are observed mainly in the boundary layer and the circulation zone. Out of these two regions, the flow properties for the radiation equilibrium wall condition are similar to that for the ablative wall.

Acknowledgements

The research is funded by the National Natural Science Foundation of China (11572348). and the Basic Research Foundation of National University of Defense Technology (No. ZDYYJCYJ20140101).

References

[1] LE JħæGAO TħæZENG X. Reentry Physics[M]. Beijing: National Defense Industry Press, 2005. (in Chinese)

[2] KEENAN J A, CANDLER G V. Simulation of ablation in Earth atmosphere entry[R]. AIAA 93-2789, 1993. DOI: 10.2514/6.1993-2789.

[3] KEENAN J A, CANDLER G V. Simulation of graphite sublimation and oxidation under re-entry conditions[R]. AIAA 94-2083, 1994. DOI: 10.2514/6.1994-2083.

[4] SUZUKI K, KUBOT H, FUJITA K, ABE T. Chemical nonequilibrium ablation analysis of MUSES-C super-orbital reentry capsule[R]. AIAA 97-2481, 1997. DOI: 10.2514/6.1997-2481.

[5] GAO T S, DONG W Z, ZHANG Q Y. The computation and analysis for the hypersonic flow over reentry vehicles with ablation[J]. Acta Aerodynamica Sinica, 2006, 24(1): 41-45. (in Chinese) . DOI:10.3969/j.issn.0258-1825.2006.01.008

[6] TISSERA S, TITAREV V, DRIKAKIS D. Chemically reacting flows around a double-cone including ablation effects[R]. AIAA 2010-1285, 2010. DOI: 10.2514/6.2010-1285.

[7] BIANCHI D, NASUTI F, ONOFRI M. Aerothermodynamic analysis of reentry flows with coupled ablation. AIAA 2011-2273, 2011. DOI: 10.2514/6.2011-2273.

[8] ZHANG W, ZENG M, XIAO L F, XU D. Numerical study for the effects of ablation and pyrolysis on the hypersonic reentry flow[J]. Journal of National University of Defense Technology, 2014,36(4): 41-48. (in Chinese) DOI: 10.11887/j.cn.20140400.

[9] MALLINSON S G, GAI S L, MUDFORD N R. High enthalpy, hypersonic compression corner flow[J]. AIAA Journal, 1996, 34(6):1130-1139. DOI: 10.2514/3.13202.

[10] PARK C, JAFFE R L, PARTRIDGE H. Chemical-kinetic parameters of hyperbolic Earth entry[J]. Journal of Thermophysics and Heat Transfer, 2001, 15(1):76-90. DOI: 10.2514/2.6582.

[11] BLOTTNER F G. Prediction of electron density in the boundary layer on entry vehicles with ablation[R]. N71-21113, 1971.

[12] KIM K H, KIM C, RHO O H. Accurate computations of hypersonic flows using AUSMPW+ scheme and shock-aligned grid technique[R]. AIAA 98-2442, 1998. DOI: 10.2514/6.1998-2442.

[13] STOLL P, GERLINGER P, BRUGGERMANN D. Domain decomposition for an implicit LU-SGS scheme using overlapping grids[R]. AIAA 97-0770, 1997. DOI: 10.2514/6.1997-0770.

[14] ZENG M. Numerical rebuilding of free-stream measurement and analysis of nonequilibrium effects in high-enthalpy tunnel. [Ph D Thesis]. Beijing: Institute of Mechanics, CAS. 2007. (in Chinese)

[15] HOLDEN M S, MOSELLE J. Theoretical and experimental studies of the shock wave-boundary layer Interaction on compression surfaces in hypersonic flow.[R]. ARL 70-0002, 1970.

[16] RUDY D H, THOMAS J L, KUMAR A. Computation of laminar viscous-inviscid interactions in high-speed internal flows[R]. N91-21087, 1991.

[17] WANG D F. Study of hypersonic viscous intereaction including high-temperature gas effects [Master of Enginerring Thesis]. Chasha: National University of Defense Technology. 2011. (in Chinese)

[18] BABINSKY H, HARVEY, J K. Shock Wave-Boundary-Layer Interactions[M].Cambridge University Press.2011

MingMing Ge, Changsha , China
Ming Zeng, Changsha , China
Ping Jing, Changsha , China
XiaoLiang Yang, Changsha , China
Wei Liu, Changsha , China

Micropolar media with structural transformations: Numerical treatment of a particle crusher

Sebastian Glane, Wilhelm Rickert, Wolfgang H. Müller, Elena Vilchevskaya
glane@tu-berlin.de

Abstract

In this work micropolar media capable of microinteria production are investigated. At the beginning a recently proposed kinetic equation for the moment of inertia tensor containing a production term is presented in order to extend the standard balances of continuum mechanics. The purpose of this paper is twofold: a brief introduction to extended micropolar theory studying resulting effects by means of a concise example and a discussion of the numerical approach to the presented example. For this purpose a continuous stream of matter through a crusher is considered so that the total number of particles will change and an EULERian approach is indispensable. This stream is characterized by a sharp front propagating through the domain. To resolve this sharp front, modern finite volume methods capable of shock capturing are discussed and applied to the problem.

1 Introduction

Recently, *Generalized Continuum Theories* (GCTs) have gained the attention of the materials science community. They are useful in context of high performance materials with an inner structure for large and small scale applications ranging from light-weight aerospace and automotive panels down to micromechanics and microelectronic gadgets. One of the GCTs is the so-called micropolar theory, which emphasizes the aspect of inner rotational degrees of freedom of a material, see [2], [3, Sec. 13] or [1]. This theory is particularly promising for applications in context with soils, polycrystalline and composite matter, granular and powder-like materials, and even with porous media and foams.

It should be noted that traditionally, the tensor of the moment of inertia of a discrete particle is a constant property in its co-moving reference frame—for a fixed observer, this tensor only changes due to rotation, *i.e.*, due to the angular velocity field $\boldsymbol{\omega}$. However, it has recently been emphasized by Ivanova and Vilchevskaya,

[5], that the moment of inertia tensor density in a micropolar continuum should be treated as an independent field variable just like the inertia linked to linear momentum, namely the field of mass density, ρ. They were the first to propose a balance equation for $\boldsymbol{J}$, which contains a production term, $\boldsymbol{\chi}_J$, of moment of inertia due to "structural transformations" as they called it. This is supposed to mean that the moment of inertia will change due to combination or fragmentation of particles during mechanical crushing or chemical reactions. In addition, a production may arise because of phase transitions or physical property changes, such as magnetization or polarization due to electromagnetic field.

We therefore need to extend the original goals of micropolar theory. In what follows we will initially formulate the corresponding equations in a rather general manner, ignoring a possible coupling between translational and rotational kinetic energy. After that we shall successively specialize to the needs of this paper. In this spirit, we state the theory as follows:

The determination of the primary fields of micropolar theory, *i.e.*, the mass density $\rho(\boldsymbol{x}, t)$, the linear velocity $\boldsymbol{v}(\boldsymbol{x}, t)$, the symmetric, second rank, and positive definite specific moment of inertia tensor $\boldsymbol{J}(\boldsymbol{x}, t)$ in units of m^2, and the spin $\boldsymbol{\omega}(\boldsymbol{x}, t)$ (a.k.a. angular velocity), relies on field equations for the primary fields. The field equations are based on balance laws and need to be complemented by suitable constitutive relations. In regular points the macroscopic balances read as follows:

- the balance of mass and balance of momentum:

$$\frac{\delta \rho}{\delta t} + \rho \nabla \cdot \boldsymbol{v} = 0\,, \quad \rho \frac{\delta \boldsymbol{v}}{\delta t} = \nabla \cdot \boldsymbol{\sigma} + \rho \boldsymbol{f}\,, \tag{1}$$

- the balance of the moment of inertia tensor:

$$\frac{\delta \boldsymbol{J}}{\delta t} + \boldsymbol{J} \times \boldsymbol{\omega} - \boldsymbol{\omega} \times \boldsymbol{J} = \boldsymbol{\chi}_J\,, \tag{2}$$

- and the balance of spin:

$$\rho \frac{\delta \boldsymbol{J} \cdot \boldsymbol{\omega}}{\delta t} = \nabla \cdot \boldsymbol{\mu} + \boldsymbol{\sigma}_\times + \rho \boldsymbol{m} + \rho \boldsymbol{\omega} \cdot \boldsymbol{\chi}_J\,. \tag{3}$$

We denote by

$$\frac{\delta(\bullet)}{\delta t} = \frac{\partial(\bullet)}{\partial t} + \boldsymbol{v} \cdot \nabla(\bullet) \tag{4}$$

the substantial (a.k.a. material) derivative of a field quantity. Moreover, $\boldsymbol{\sigma}$ is the (non-symmetric) Cauchy stress tensor, $\boldsymbol{f}$ is the specific body force, $\boldsymbol{\chi}_J$ (a second rank symmetric tensor) is the production related to the moment of inertia tensor $\boldsymbol{J}$; $\boldsymbol{\mu}$ is the couple stress tensor, $\boldsymbol{\sigma}_\times := \boldsymbol{\epsilon} \cdot\cdot \boldsymbol{\sigma}$ is the Gibbsian cross applied to the (non-symmetric) Cauchy stress tensor, $\boldsymbol{\epsilon}$ being the Levi-Civita tensor, and $\boldsymbol{m}$ are specific volume couples.

In context with Eqn. (2) several comments are in order. It has already been mentioned that in its present form this equation can only be found in a recent paper by one of the authors, [5]. There is a precedent to the equation for the inertia tensor, $\boldsymbol{J}$, namely what is called "conservation of microinertia" in [2, p. 15]. However, that

equation does not contain a production term, $\boldsymbol{\chi}_J$. On the macroscopic continuum level this new term must be interpreted as a constitutive quantity. One of the purposes of this paper is to investigate such a constitutive relation for the production of moment of inertia $\boldsymbol{\chi}_J$ (see below).

Due to the production of moment of inertia, we face another problem: Continuum mechanics of solids is typically formulated in the LAGRANGian form, a.k.a. material description, which is based on the concept of an indestructible "material particle." This particle is identifiable by its reference position vector, $\boldsymbol{X}$, which can then be used in a bijective mapping for describing uniquely the motion, $\boldsymbol{x} = \hat{\boldsymbol{x}}(\boldsymbol{X}, t)$, of the particle through three-dimensional space in time. If the LAGRANGian idea of a material particle is followed, the material particles must stay together during the motion and there should be no exchange of subunits between them. Particles are neither destroyed nor generated. In other words, this concept is not applicable to incorporate production. Also note that within the material description of a micropolar continuum, each material point is phenomenologically equivalent to a rigid body, such that its moments of inertia do not change.

However, as indicated, there is a catch: A granular medium (say) is frequently milled. This affects the material particle, because its subunits will be crushed. They will change their mass and their moment of inertia and, what is more, during the milling process there might even be an exchange of crushed subunits between neighboring material particles, which are then no longer material in the original sense. Consequently, on a macroscopic scale the moments of inertia will change as well and all of this gives rise to the production term, $\boldsymbol{\chi}_J$. This is why [5] have decided to depart from the LAGRANGian description and turned to the EULERian perspective (a.k.a. spatial description) instead.

Moreover, in this paper we are also not concerned with the determination of the angular velocity field $\boldsymbol{\omega}(\boldsymbol{x}, t)$. In fact, it is our intention to show that a balance for rotational inertia and hence the production term in Eqn. (2) are physical meaningful by themselves, independent of the angular velocity. In the following, problems are regarded where the angular velocity is equal to zero. Thus instead of Eqns. (1)–(3) we are left with the following simplified set of equations for ρ, $\boldsymbol{v}$, and $\boldsymbol{J}$:

$$\frac{\partial \rho}{\partial t} + \nabla \cdot (\rho \boldsymbol{v}) = 0\,, \quad \rho \frac{\partial \boldsymbol{v}}{\partial t} + \rho \boldsymbol{v} \cdot \nabla \boldsymbol{v} = \nabla \cdot \boldsymbol{\sigma} + \rho \boldsymbol{f}\,, \quad \frac{\partial \boldsymbol{J}}{\partial t} + \boldsymbol{v} \cdot \nabla \boldsymbol{J} = \boldsymbol{\chi}_J\,. \tag{5}$$

We now proceed and illustrate the theory with the example of a crusher and consider what happens if the number of particles does change. A production term in form of a linear population growth model has been proposed before in [5]. However, in that paper only the time dependence in a homogeneous medium was studied, whereas now an initial-boundary value problem is considered.

2 Analysis of a one-dimensional crusher

Consider the situation depicted in Fig. 1. We consider the following problem in infinite one-dimensional space, $-\infty < x < \infty$: A continuous flow of spherical particles is moving in from left to right at a constant prescribed speed, v_0. The flow passes a subregion $-\delta \leq 0 \leq \delta$. There, the entering particles of the flow are crushed

continuously to form smaller and smaller particles. As a simplification we assume that the momentum balance given in (5) is identically satisfied and the balance of mass and of moment of inertia read:

$$\frac{\partial \rho}{\partial t} + v_0 \frac{\partial \rho}{\partial x} = 0\,, \quad \frac{\partial J}{\partial t} + v_0 \frac{\partial J}{\partial x} = \chi_J. \tag{6}$$

For the production of moment of inertia we postulate the following relationship:

$$\chi_J\,(x,t) = \begin{cases} 0 & \text{if} \quad -\infty < x < -\delta\,, \\ -\alpha\,\langle \rho(x,t) \rangle^0\,\langle J(x,t) - J_* \rangle & \text{if} \quad -\delta \le x \le \delta\,, \\ 0 & \text{if} \quad \delta < x < \infty\,, \end{cases} \tag{7}$$

where α is a positive rate constant, J_* indicates the moment of inertia pertinent to the minimum crushing size of the particles, and $\langle \bullet \rangle$ denotes the Macaulay bracket[1]. The density field is corporated by a Heaviside function to ensure that the production vanishes if the density is zero.

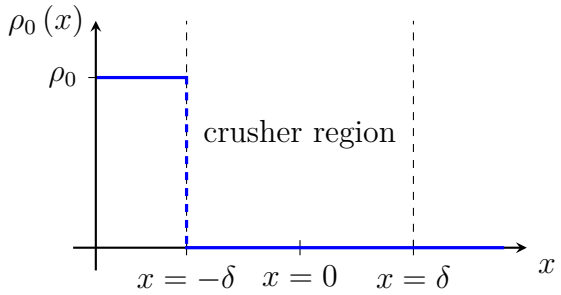

Figure 1: Sketch of the idealized one-dimensional crusher problem. The initial condition for the density is shown by the blue line.

The problem for the mass density can be solved in closed form by using the method of characteristics for initial value problems on the infinite domain (see [8]). We find:

$$\rho(x,t) = \rho_0(x - v_0 t)\,, \tag{8}$$

where ρ_0 is the initial mass density distribution, which, for simplicity, is assumed to be a piecewise constant function, see Fig 1, defined as follows:

$$\rho\,(x, t=0) = \rho_0\,(x) := \begin{cases} \rho_0 & \text{if} \quad -\infty < x < -\delta\,, \\ 0 & \text{if} \quad -\delta \le x \le \delta\,, \\ 0 & \text{if} \quad \delta < x < \infty\,. \end{cases} \tag{9}$$

In other words, the solution is a step function of height ρ_0 steadily and uniformly advancing from left to right with velocity v_0.

We will now find the solution for the moment of inertia, Eqn. $(6)_2$. Recall that we have to distinguish various cases in Eqn. (7), and therefore the infinite interval

[1] A representation for the Macaulay bracket is given by $\langle x \rangle = \frac{1}{2}\,(|x| + x)$.

$-\infty < x < +\infty$ is dissected into three regions, where the boundary value at $x = -\delta$ is known. Consequently, the method of characteristics as pertinent to a boundary value problem must be used. The solution process is also detailed in [8] and the final result with $J_0 = \text{const.}$ being the moment of inertia corresponding to the particles with density ρ_0 reads:

- at times $0 \leq t < \frac{2\delta}{v_0}$ with the position of the shock front $x_\mathrm{s} = -\delta + v_0 t < \delta$:

$$J(x,t) = \begin{cases} J_0 & \text{if} \quad -\infty < x < -\delta\,, \\ J_* + (J_0 - J_*) \exp\left(-\frac{\alpha}{v_0}(x+\delta)\right) & \text{if} \quad -\delta \leq x < x_\mathrm{s}\,, \\ 0 & \text{if} \quad x_\mathrm{s} \leq x < \infty\,. \end{cases} \tag{10}$$

- at times $\frac{2\delta}{v_0} \leq t < \infty$ with the position of the shock front $x_\mathrm{s} = -\delta + v_0 t \geq \delta$:

$$J(x,t) = \begin{cases} J_0 & \text{if} \quad -\infty < x < -\delta\,, \\ J_* + (J_0 - J_*) \exp\left(-\frac{\alpha}{v_0}(x+\delta)\right) & \text{if} \quad -\delta \leq x < \delta\,, \\ J_* + (J_0 - J_*) \exp\left(-\frac{2\alpha\delta}{v_0}\right) & \text{if} \quad \delta \leq x < x_\mathrm{s}\,, \\ 0 & \text{if} \quad x_\mathrm{s} \leq x < \infty\,. \end{cases} \tag{11}$$

In the following, numerical methods are assessed. It is analyzed which methods are able to reproduce satisfactory approximations for the problem of the particle crusher.

3 Numerical treatment of hyperbolic problems

The numerical treatment of Eqns. (5) or (6) (say) is performed using a finite volume approach. Problems in which transport phenomena are dominant are often solved using finite volume methods, since this method can resolve discontinuities more accurately than finite difference or finite element methods. The starting point of the finite volume approach is a partial differential equation of the form

$$\frac{\partial q}{\partial t} + \nabla \cdot \boldsymbol{f}(q) = p\,, \quad w_\perp [\![q]\!] + \boldsymbol{n} \cdot [\![\boldsymbol{f}(q)]\!] = p_I\,. \tag{12}$$

where the first equation describes the evolution of the state variable q in regular points, $\boldsymbol{f}$ is the flux density vector and p is a production density. The latter equation represents the balance equation on singular surfaces with unit normal vector $\boldsymbol{n}$ where jumps of the state variable occurs and the jump bracket $[\![\bullet]\!]$ is given by the difference of limits from both sides, *i.e.*, $[\![A]\!] = A^+ - A^-$. The quantity $w_\perp$ represent the discontinuity's velocity in surface normal direction, *i.e.*, $w_\perp = \boldsymbol{n} \cdot \boldsymbol{w}$ and p_I is a production density. Recall that if the productions vanish, *i.e.*, $p = 0$ and $p_I = 0$, Eqn. (12) is called a conservation law. Note that the argument of flux contains only the state variable itself and not its gradient. This form is chosen as this section considers purely hyperbolic equations without second order space derivatives, which may occur if, *e.g.*, the heat conduction equation employing FOURIER's law is considered. More precisely, the order of space and time derivatives in the considered PDE should be equal, because this allows to recast the PDE containing higher

derivatives such as elastodynamic's wave equation to a first order system describing the evolution of a state space vector.

In what follows, the basic principles of finite volume methods are introduced. The main idea is to divide the space into a number of finite EULERian cells $\mathcal{C}_i$, $i = 1, \ldots, N_{\text{cells}}$, and to take the volume average of Eqn. (12) on every cell. Hence, the averaged equation reads:

$$\frac{1}{\operatorname{vol}(\mathcal{C}_i)} \int_{\mathcal{C}_i} \frac{\partial q}{\partial t} \,\mathrm{d}V + \frac{1}{\operatorname{vol}(\mathcal{C}_i)} \oint_{\partial \mathcal{C}_i} \boldsymbol{n} \cdot \boldsymbol{f}(q) \,\mathrm{d}A = \frac{1}{\operatorname{vol}(\mathcal{C}_i)} \int_{\mathcal{C}_i} p \,\mathrm{d}V \,. \tag{13}$$

Through the application of the divergence theorem (GAUSS integral theorem) the term involving the flux was transformed to a surface integral. Note that the considered cells do not change in time and therefore the time derivative in the first term may be pull out of the integral. By introducing the average state and production in the ith cell through

$$\bar{q}_i(t) = \frac{1}{\operatorname{vol}(\mathcal{C}_i)} \int_{\mathcal{C}_i} q(x,t) \,\mathrm{d}V \,, \quad \bar{p}_i(t) = \frac{1}{\operatorname{vol}(\mathcal{C}_i)} \int_{\mathcal{C}_i} p(x,t) \,\mathrm{d}V \,, \tag{14}$$

the averaged equation reads:

$$\frac{\partial \bar{q}_i}{\partial t} + \frac{1}{\operatorname{vol}(\mathcal{C}_i)} \oint_{\partial \mathcal{C}_i} \boldsymbol{n} \cdot \boldsymbol{f}(q) \,\mathrm{d}A = \bar{p}_i \,. \tag{15a}$$

For the one-dimensional case, the previous equation specializes to read:

$$\frac{\partial \bar{q}_i}{\partial t} + \frac{1}{\Delta x_i} \left[f(q)|_{x_{i+\frac{1}{2}}} - f(q)|_{x_{i-\frac{1}{2}}} \right] = \bar{p}_i \,, \tag{15b}$$

where $\Delta x_i = x_{i+1/2} - x_{i-1/2}$ denotes the ith-cell's volume for the one-dimensional case and can be regarded as a measure for the grid spacing.

For the one-dimensional specialization further comments are in order. Regarding the discretization, consider Fig. 2. As before, the cells and also the cell centers, x_i, are numbered using integers. As common in literature on finite volume methods, the positions of the cell interfaces are numbered with half-integers. To each interface, a unique unit normal is attached, such that the ith-cell's normal vector coincides with it for $x_{i+1/2}$. For $x_{i-1/2}$ the ith-cell's normal vector is opposed to $\boldsymbol{n}$, *viz.*, it is given by $-\boldsymbol{n}$. Hence, the cell interface at $x_{i+1/2}$ may be called the "positive" interface Γ_i^+ and *vice versa* for the interface at $x_{i-1/2}$. This yields $\boldsymbol{n} \cdot \boldsymbol{f}(q) = f(q)$ for $x = x_{i+1/2}$ and $\boldsymbol{n} \cdot \boldsymbol{f}(q) = -f(q)$ for $x = x_{i-1/2}$.

Note that the flux term is evaluated on the two surfaces of every cell. This requires knowledge of the state variable q at $x_{i-1/2}$ and $x_{i+1/2}$. However, as indicated in Fig. 3 by solid red lines, the numerical scheme approximates the state variable $q(x,t)$ by means of cell averages $\bar{q}_i(x,t)$, which may be interpreted as the state variable's values at the cell centers. Hence, a piecewise constant function with jump at each interface results and these jumps can be regarded as RIEMANN problems occurring at each interface. In the view of these discontinuities, some methods for solving Eqn. (15b)

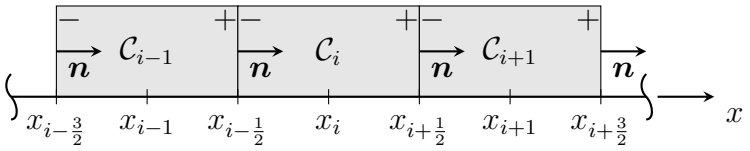

Figure 2: Discretization of a continuous domain into a finite number of cells, *i.e.*, finite volumes.

make explicit use of solutions to RIEMANN problems at each interface and are thus closely related to the method of characteristics. In general, the numerical schemes using RIEMANN solutions are characterized by the cyclic application of the following three steps:

1. Reconstruct the interface values from the cell averages, *viz.*, compute $q^+\left(x_{i+1/2}, t_i\right)$ and $q^-\left(x_{i+1/2}, t_i\right)$ for all $i = 1, \ldots, N_{\text{cells}} + 2$.
2. Evolve the averaged equation on the time interval $(t_i, t_i + \Delta t)$ by making use of exact RIEMANN solutions, *viz.*, one time integration step of Eqn. (15b) is performed.
3. Average the result to obtain updated cell averages.

This procedure is known as GODUNOV's scheme or the REA-algorithm (Reconstruct-Evolve-Average) and can be regarded as a starting point to develop numerical schemes for transport problems.

To summarize this very brief introduction to finite volume methods, time and space discretization does not naturally yield a discrete equation in context of finite volume methods, since the fluxes at the interfaces need to be approximated by the average cell values. This is in contrast to finite difference methods, whose so-called difference stencils are obtained by a straightforward application of a TAYLOR expansion. But this expansion requires that the solution is continuously differentiable, which is not the case in context of finite volume methods. The ability of finite volume methods to resolve discontinuities is due to abstract numerical schemes, which need to take the wave-like structure of the RIEMANN solution into account. To assess a numerical scheme for a conservation law, the following properties should be fulfilled: (a) low or vanishing numerical disspation, *i.e.*, the considered quantity is conserved, (b) high resolution of discontinuities, rarefactions and large gradients, (c) numerical stability, *i.e.*, absence of non-physical oscillatory.

3.1 High resolution methods

Recall that a reconstruction of the interface values is necessary in order to determine the flux at the interfaces $\Gamma_i^{\pm}$. As depicted in Fig. 3 by a red dashed line, a linear reconstruction of the former continuous function (solid blue line) yields a discontinuous representation with a jump at each interface, because the function's slope cannot be calculated exactly from a numerical approximation. Numerical schemes that reconstruct a numerical solution based on more than piecewise constant functions are usually termed as high resolution methods. This section presents two high resolution schemes: the VAN LEER and the KURGANOV-TADMOR scheme. The former one is available in the open-source python-based finite volume library FiPy, *cf.* [4]. The

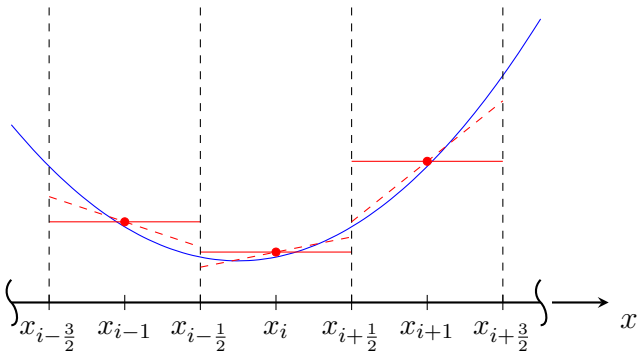

Figure 3: Approximation of continuous function (solid blue line) by cell average (solid red line). The dashed red lines represent the reconstruction of the function through piecewise linear polynomials.

two schemes are presented w.r.t. the following form of Eqn. (15b):

$$\frac{\partial \bar{q}_i}{\partial t} = -\frac{1}{\Delta x_i}\left[F_{i+\frac{1}{2}} - F_{i-\frac{1}{2}}\right] + \bar{p}_i\,. \tag{16}$$

Note that the flux f appearing in Eqn. (15b) was replaced by a numerical flux F in Eqn. (16), which is governed by the employed numerical scheme. This numerical flux in general depends on the limit values of the state variable at the cell interface, *i.e.*, $F = F\left(q^+, q^-\right)$. The discontinuities of the reconstructed state variable q at the cell interfaces are taken into account by denoting the limit values of the state variable q at $x_{i+1/2}$ through $q^+_{i+1/2}$ and $q^-_{i+1/2}$ respectively, where $q^+_{i+1/2}$ and $q^-_{i+1/2}$ denote the limit values of q from the cell $\mathcal{C}_i$ and $\mathcal{C}_{i+1}$, respectively. Likewise, $F_{i+1/2}$ is a short-hand notation for the numerical flux at $x_{i+1/2}$. Introducing the first space-derivative of the averaged state variable by $\bar{q}'_i$, the discussed linear reconstruction of the interface value yields the following interface values:

$$q^+_{i+\frac{1}{2}} = \bar{q}_i + \bar{q}'_i\frac{\Delta x_i}{2}\,, \quad q^-_{i+\frac{1}{2}} = \bar{q}_{i+1} - \bar{q}'_{i+1}\frac{\Delta x_{i+1}}{2}\,. \tag{17}$$

In the following, first the two high-order numerical schemes are presented and subsequently the determination of the slopes $\bar{q}'_i$ is discussed in Sect. 3.2.

3.1.1 van Leer scheme

The van Leer scheme is derived from Godunov's method by applying piecewise linear reconstruction for the linear flux $f\left(q\right) = qv$, where the convective speed v is known, *cf.* [10]. In doing so, an explicit time integration using a first-order Euler step is applied. Hence Eqn. (16) reads:

$$\frac{\bar{q}^{n+1}_i - \bar{q}^n_i}{\Delta t} = -\frac{1}{\Delta x_i}\left[F^n_{i+\frac{1}{2}} - F^n_{i-\frac{1}{2}}\right] + \bar{p}^n_i\,, \tag{18}$$

where the superscript n represents an index indicating the respective time-step. The convective flux for the piecewise linear construction reads, *cf.* [7, 10], as follows:

$$F^n_{i+\frac{1}{2}} = \begin{cases} v\bar{q}^n_i + \frac{1}{2}v\left(\Delta x_i - v\Delta t\right)\bar{q}'^n_i & \text{if} \quad v \geq 0\,, \\ v\bar{q}^n_{i+1} + \frac{1}{2}v\left(\Delta x_{i+1} + v\Delta t\right)\bar{q}'^n_{i+1} & \text{if} \quad v < 0\,. \end{cases} \tag{19}$$

A simple calculation shows how the interface value $q^+_{i+1/2}$ is comprised in the representation for $v \geq 0$

$$F^n_{i+\frac{1}{2}} = v\left(\bar{q}^n_i + \frac{\Delta x}{2}\bar{q}'^n_i\right) - v\frac{v\Delta t}{2}\bar{q}'^n_{i-1} = vq^+_{i+\frac{1}{2}} - v\frac{v\Delta t}{2}\bar{q}'^n_{i-1}\,, \quad v \geq 0\,. \tag{20}$$

The latter representation shows that the discussed flux is decomposed into the flux resulting from the interface value and an additional term that is governed by the slope. Note that the case discrimination stems from the fact that the transport velocity v determines the direction, in which the state variable q is transported.

For this flux to be numerical stable in the sense that non-physical oscillations are absent in the vicinity of shock fronts, the slope of the reconstructed solution needs to be limited. The technique of slope limiting is a consequence of the total variation property (TVD), for details the reader is referred to [7] among others. Hence, to obtain the VAN LEER scheme for the convection equation, the VAN LEER slope limiter is employed:

$$\bar{q}'_i = \text{minmod}\left(2\bar{q}'_{i,\text{bwd.}}, \bar{q}'_{i,\text{cnt.}}, 2\bar{q}'_{i,\text{fwd.}}\right)\,. \tag{21}$$

For approximations of the slope through backward, central and forward differences and the minmod-function see Sect. 3.2. Note that if such limiters are not used, the scheme presented is not fulfilling the TVD property. Furthermore, predecessors to the VAN LEER scheme were the LAX-WENDROFF and FROMM scheme, which do not use a slope limiter.

3.1.2 Kurganov-Tadmor scheme

The predecessor to the KURGANOV-TADMOR scheme (KT) is the NESSYAHU-TADMOR scheme (NT), see [9], which uses a staggered grid in space and is a RIEMANN-free solver using explicit time discretization. As outlined in [6], the main advantage of the NT-scheme is the fact that it is less dissipative compared to the non-staggered LAX-FRIEDRICHS scheme. In a loose sense, the KT-scheme extends the NT-scheme by incorporating local wave speed resulting from the discontinuities at the interfaces. Furthermore, the KT-scheme possesses a semi-discrete form, which allows to use explicit RUNGE-KUTTA methods for time integration. The numerical flux for the KT-scheme is given by, *cf.* [6],

$$F_{i+\frac{1}{2}} = \frac{f\left(q^+_{i+\frac{1}{2}}\right) + f\left(q^-_{i+\frac{1}{2}}\right)}{2} + \frac{a_{i+\frac{1}{2}}}{2}\left(q^+_{i+\frac{1}{2}} - q^-_{i+\frac{1}{2}}\right)\,, \tag{22}$$

where $a_{i+1/2}$ is the maximal local wave speed at $x_{i+1/2}$ which is given by

$$a_{i+\frac{1}{2}} = \max_{q\in\tilde{Q}} \varrho\left(\left.\frac{\partial f}{\partial q}\right|_q\right)\,, \quad \tilde{Q} = \{q^+_{i+\frac{1}{2}}, q^-_{i+\frac{1}{2}}\}\,. \tag{23}$$

Therein, $\varrho\,(\bullet)$ denotes the spectral radius, *i.e.*, the largest absolute value of the eigenvalues.

Obviously, the numerical flux used in the KT-scheme is composed of two parts: the average flux resulting from the two limit values and a local speed multiplied

by the jump at the interface. For this scheme to prevent non-physical oscillations close to shock fronts, the TVD property must hold as well, [6]. Likewise the slopes of the reconstructed piecewise linear functions need to be limited in a numerical implementation.

3.2 Flux and slope limiting

For a uniform spaced grid the backward, central and forward finite differences for the first derivative read

$$\bar{q}'_{i,\text{bwd.}} = \frac{\bar{q}_i - \bar{q}_{i-1}}{\Delta x}\,, \quad \bar{q}'_{i,\text{cnt.}} = \frac{\bar{q}_{i+1} - \bar{q}_{i-1}}{2\Delta x}\,, \quad \bar{q}'_{i,\text{fwd.}} = \frac{\bar{q}_{i-1} - \bar{q}_{i-1}}{\Delta x}\,. \tag{24}$$

As to which derivative should be used is determined by a so called "slope limiter." A slope limiter is a function that takes different approximations of derivatives as arguments and returns a derivative approximation limited to a realistic value. A simple limiter is the minmod-limiter[2] defined as:

$$\bar{q}'_i = \text{minmod}\left(\bar{q}'_{i,\text{bwd.}}, \bar{q}'_{i,\text{fwd.}}\right)\,.$$

It returns the smallest value if both arguments are of the same sign and zero otherwise. The idea behind the construction of this limiter is that if forward and backward finite differences have different sign, a vanishing slope might be a good approximation for a sharp front, *e.g.*, a sharp peak. It turns out that this limiter is a special case of a so called limiter family, *i.e.*, minmod-ϑ limiter, defined as:

$$\bar{q}'_i = \text{minmod}\left(\theta\bar{q}'_{i,\text{bwd.}}, \bar{q}'_{i,\text{cnt.}}, \theta\bar{q}'_{i,\text{fwd.}}\right)\,, \quad 1 \le \theta \le 2\,. \tag{25}$$

Alternatively, the "superbee"-limiter is used in this paper, which is defined as:

$$\bar{q}'_i = \text{maxmod}\left(\text{minmod}\left(2\bar{q}'_{i,\text{fwd.}}, \bar{q}'_{i,\text{bwd.}}\right), \text{minmod}\left(\bar{q}'_{i,\text{fwd.}}, 2\bar{q}'_{i,\text{bwd.}}\right)\right)\,, \tag{26}$$

where the maxmod-limiter returns the maximum value if both arguments are of the same sign and zero otherwise.

4 Numerical results

This section compares the numerical schemes introduced in Sect. 3. First a linear advection equation is investigated and then the crusher is considered. In doing so, the Kurganov-Tadmor scheme was implemented using the Python programming language using a fourth-order Runge-Kutta scheme for time integration. For comparison, the van Leer scheme from the FiPy package was used in junction with an explicit Euler time stepping[3], see [4].

[2] A representation for the minmod operation is given by $\text{minmod}(a,b) = \frac{1}{2}[\text{sign}(a) + \text{sign}(b)]\min\{a,b\}$.

[3] For all simulations using the KT scheme as well as the ones performed by FiPy the Courant number a.k.a. CFL number was chosen as 0.5.

4.1 Linear transport—comparison of numerical schemes

We consider the one-dimensional transport equation with constant velocity v_0 and piecewise constant initial conditions:

$$\frac{\partial q}{\partial t} + v_0 \frac{\partial q}{\partial x} = 0\,, \quad q(x, t=0) = q_0\,(x) = \begin{cases} 1 & x < x_0\,, \\ 0 & x \geq x_0\,. \end{cases}$$

As detailed in Sect. 2, the exact solution is the initial condition simply shifted in space, *i.e.*, $q_0\,(x - v_0 t)$. As a first step, the various limiter functions presented in Sect. 3.2 are compared. In order to do so, $v_0 = 0.1\,\mathrm{m/s}$, $x_0 = 0\,\mathrm{m}$ was chosen and the equation is solved on the interval $x \in (-1\,\mathrm{m}, 1\,\mathrm{m})$ applying an inlet-outlet boundary condition at both ends. The results for the superbee, minmod and minmod $-\theta$ limiter are depicted in Fig. 4 for two time steps. Note that $\vartheta = 2$ was applied, which corresponds the limiter function applied in the VAN LEER scheme.

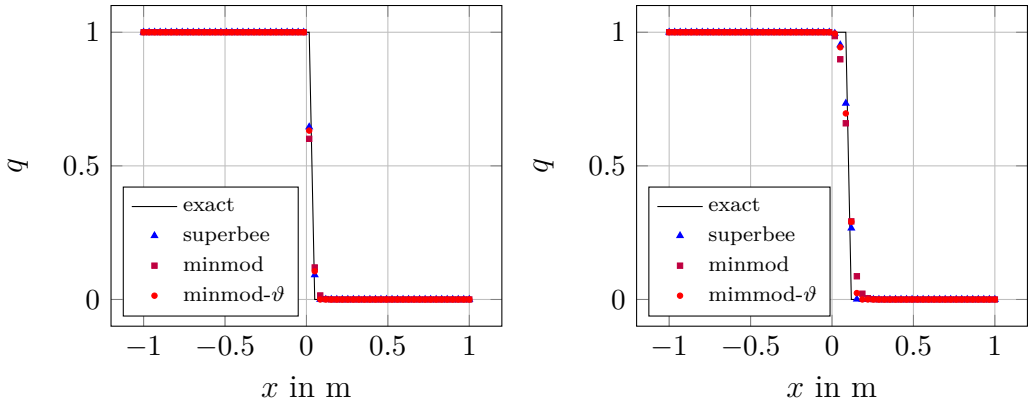

(a) t = 0.25 s (b) t = 1 s

Figure 4: Comparison of various limiters for the KURGANOV-TADMOR scheme w.r.t. the exact solution using 60 equidistant cells.

From Fig. 4 it can be seen that the analytic solution's sharp shock front is not retained by any of the limiters. However, non-physical oscillations do not occur and the shock is tracked sufficiently well. By closer inspection, it is evident that the front is resolved equally by all limiters at $t = 0.25\,\mathrm{s}$, *viz.*, the front is "smeared" or blurred over two cells. In contrast to this, the blur gets larger at $t = 1\,\mathrm{s}$. It is seen that the superbee and mindmod-θ limiter resolve the front within four cells, whereas the minmod limiter uses six cells. This trends continues for larger times and it turns out that the superbee limiter resolves the shock front the sharpest.

Next, the KURGANOV-TADMOR and the VAN LEER scheme implemented in FiPy are compared for the one-dimensional transport equation using the same initial and boundary conditions as well as $v_0 = 1\,\mathrm{m/s}$ and $x \in (-1\,\mathrm{m}, 5\,\mathrm{m})$. The simulations are performed on a coarse grid consisting of 100 equidistant cells and results are shown in Fig. 5. For the KT scheme, the superbee limiter was applied.

By comparing to the different numerical schemes shown Fig. 5, it can be see that both solutions approximate the solution with reasonable accuracy. But a close

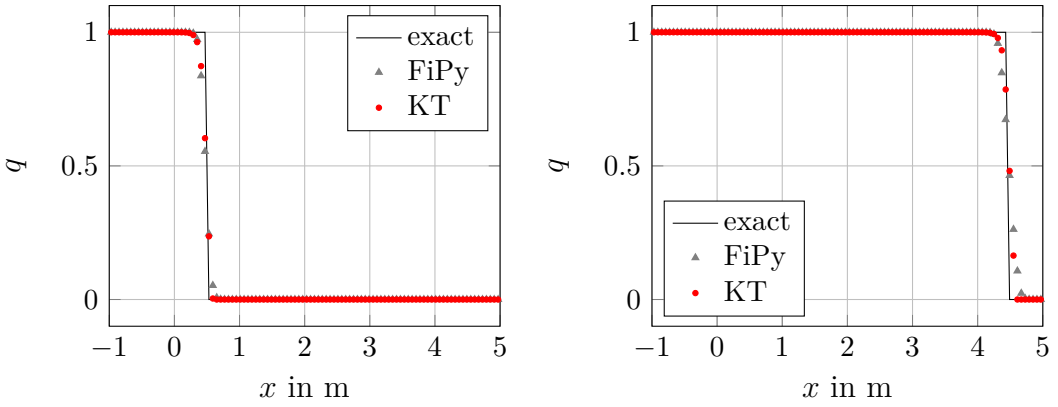

(a) t = 1 s (b) t = 5 s

Figure 5: Comparison of the Kurganov-Tadmor (KT) and the van Leer (FiPy) scheme w.r.t. the exact solution.

observation of the results for $t = 5\,\mathrm{s}$ shows that the shock front is blurred more by the scheme used in FiPy. The solution computed by FiPy uses seven cells in the shock region whereas the KT scheme resolves the shock within (say) 5 cells. This blur is more prominent if the space resolution, *i.e.*, the number of cells, is reduced. Therefore the KT scheme is regarded as preferable scheme for transport problems, since it not only provides a higher resolution for same discretization but it is also independent of the considered flux function.

4.2 Crusher problem

This section considers the crusher problem presented in Sect. 2 for $\delta = 0.25\,\mathrm{m}$, $v_0 = 1\,\mathrm{m/s}$, $J^* = 0.25\,\mathrm{m}^2$, and $\alpha = 2.75\,1/\mathrm{s}$. The problem is discretized using 200 cells on the interval $x \in (-1\,\mathrm{m}, 4\,\mathrm{m})$. As above the superbee limiter was applied for the KT scheme. The integral resulting from the additional production term is approximated by the midpoint rule for the KT scheme. In FiPy, this production term is incorporated through an internal function called `ImplicitSourceTerm`, [4]. Fig. 6 depicts the results for the shock front located inside the crusher, at the crusher's right boundary and very far away of the crusher.

As shown in Fig. 6, the solution is approximated well for $t = 0.25\,\mathrm{s}$ and $t = 0.5\,\mathrm{s}$ with exception of the blur of the shock front, which was already discussed in Sect. 4.1. If the results for $t = 5\,\mathrm{s}$ are considered, the numerical results in the vicinity of the crusher agree very well with the exact solution. However, the resolution of the shock front is poor. Also, the estimation of the shock's position from the numerical results is not in agreement with the exact solution. This effect is slightly more prominent in FiPy's numerical results than for those of the KT scheme. Regarding this, a spatial resolution of 25 cells per unit length was applied. In contrast to this, the spatial resolution used for the example in Fig. 5 is given by approx. 16.67 cells. Despite the lower spatial resolution, an estimation of the shock's position from the results depicted in Fig. 5 is better than the one from the results of the crusher problem depicted in Fig. 6. Hence, the additional production term influences the numerical propagation

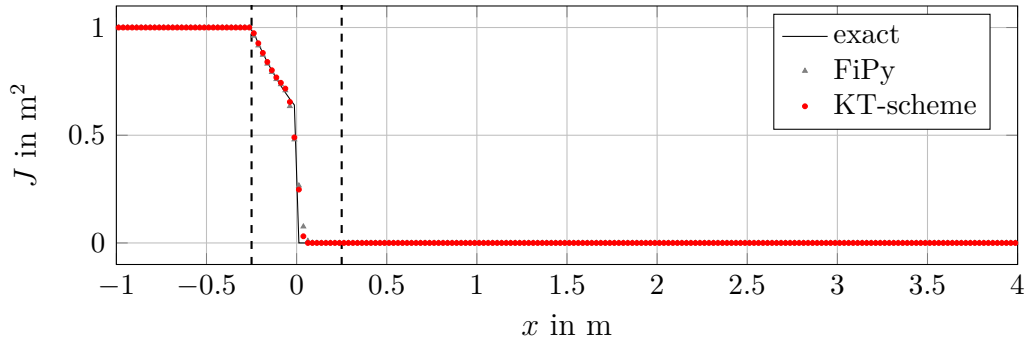

(a) $t = 0.25\,\mathrm{s}$

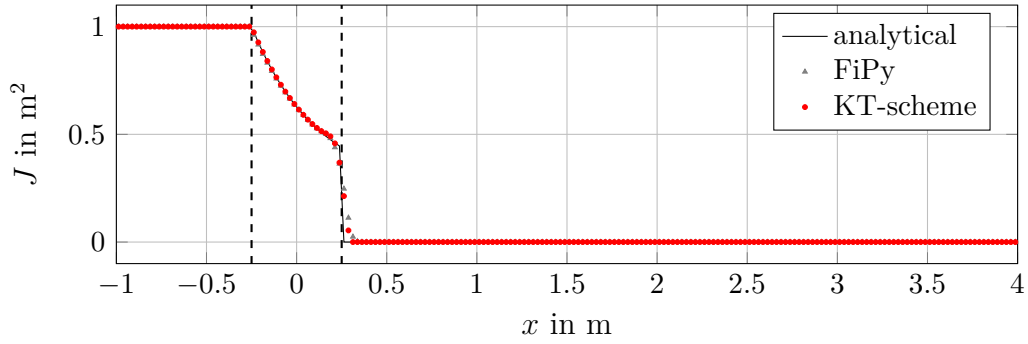

(b) $t = 0.5\,\mathrm{s}$

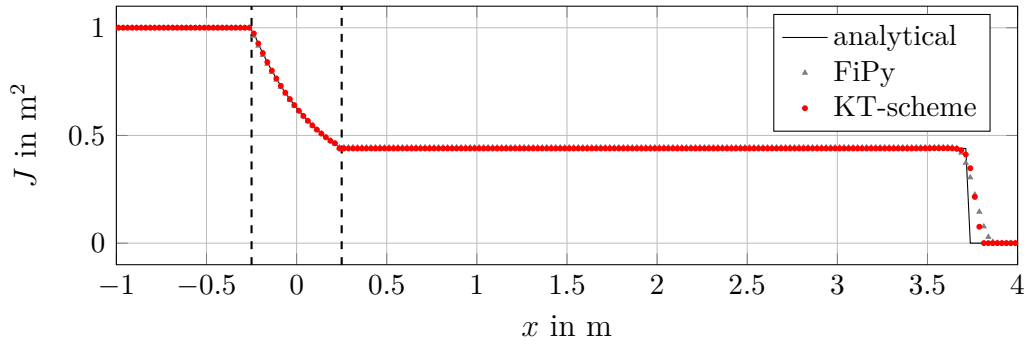

(c) $t = 5\,\mathrm{s}$

Figure 6: Comparison of the Kurganov-Tadmor (KT) and the van Leer (FiPy) scheme w.r.t. the exact solution for the crusher problem. The crusher region is indicated by bold dashed lines.

speed of the shock front. To overcome this problem, a piecewise reconstruction of integrand in the production term should applied as well.

5 Conclusions and outlook

This paper was dedicated to an investigation of micropolar theory in terms of rotational inertia production, which requires spatial (Eulerian) description of problems. In particular, the following tasks have been accomplished:

- Initially, the general balance equations of micropolar theory were stated. How-

ever, in contrast to classical micropolar theory an extension was made, which allows us to study the development of rotational inertial characteristics, namely the specific moment of inertia tensor, $\boldsymbol{J}$, in addition to the translational measure of inertia, the mass density, ρ. It is noteworthy that the balance for $\boldsymbol{J}$ contains a production term characteristic of structural transformations.

- As a consequence, the concept of an indestructible material particle became obsolete and required us to employ a spatial (EULERian) description when solving the resulting field equations. The whole formulation is EULERian based—this includes balances, field equations, and mathematical solution techniques.
- The set of general balance equations was then specialized to the case of the primary fields: mass density, ρ, specific moment of inertia tensor, $\boldsymbol{J}$, and translational velocity, $\boldsymbol{v}$. This was done in order to demonstrate that rotational inertia, $\boldsymbol{J}$, is a field of its own right and may develop without a present angular velocity, $\boldsymbol{\omega}$.
- An analytical solution to the corresponding field equations for non-homogeneous crushing of particles was found based on the method of characteristics.
- A brief introduction to the finite volume method was given and two numerical schemes were introduced—the KURGANOV-TADMOR and the VAN LEER scheme. In a first step, the schemes were compared and assessed regarding the linear transport of a shock front. Additionally, a comparison for the crusher problem was performed.
- Both schemes performed very well in regions where the solution is continuous. In case of linear transport, the shock resolution was good but the KT scheme is slightly preferable. For the crusher problem, the shock resolution was good if the distance traveled by the shock front remains relatively small. For large distances traveled, the prediction of the shock's position is not correct.
- As a last remark, it should be noted the KURGANOV-TADMOR scheme is in a sense more versatile than the VAN LEER scheme implemented in FiPy because it allows the use of non-linear flux functions. Future work therefore focuses on the application of the KT scheme to non-linear transport problems such as the EULER equation of gas dynamics incorporating micro-structural transformation as proposed in this paper.

References

[1] V. A. Eremeyev, L. P. Lebedev, and H. Altenbach. *Foundations of micropolar mechanics*. Springer Science & Business Media, 2012.

[2] A. C. Eringen and C. B. Kafadar. *Polar field theories. In: Continuum physics IV*. London: Academic Press, 1976.

[3] C. Eringen. *Nonlocal continuum field theories*. New York: Springer Science & Business Media, 2002.

[4] J. E. Guyer, D. Wheeler, and J. A. Warren. "FiPy: Partial Differential Equations with Python". In: *Computing in Science & Engineering* 11.3 (2009), pp. 6–15. DOI: 10.1109/MCSE.2009.52. URL: http://www.ctcms.nist.gov/fipy.

[5] E. A. Ivanova and E. N. Vilchevskaya. “Micropolar continuum in spatial description”. In: *Continuum Mechanics and Thermodynamics* 28.6 (2016), pp. 1759–1780.

[6] A. Kurganov and E. Tadmor. “New High-Resolution Central Schemes for Nonlinear Conservation Laws and Convection-Diffusion Equations”. In: *Journal of Computational Physics* 160.1 (2000), pp. 241 –282. ISSN: 0021-9991. DOI: http://dx.doi.org/10.1006/jcph.2000.6459.

[7] R. J. LeVeque. *Finite volume methods for hyperbolic problems*. Cambridge Texts in Applied Mathematics 31. Cambridge University Press, 2002.

[8] W. H. Müller, E. N. Vilchevskaya, and W. Weiss. “Micropolar theory with production of rotational inertia: A farewell to material description”. In: *Phys. Mesomech.* 20.3 (2017).

[9] H. Nessyahu and E. Tadmor. “Non-oscillatory central differencing for hyperbolic conservation laws”. In: *Journal of Computational Physics* 87.2 (1990), pp. 408 –463. ISSN: 0021-9991. DOI: http://dx.doi.org/10.1016/0021-9991(90)90260-8.

[10] B. van Leer. “Towards the ultimate conservative difference scheme. IV. A new approach to numerical convection”. In: *Journal of Computational Physics* 23.3 (1977), pp. 276 –299. DOI: http://dx.doi.org/10.1016/0021-9991(77)90095-X.

Sebastian Glane, Wilhelm Rickert, Wolfgang H. Müller, Technische Universität Berlin, Sek. MS 2, Einsteinufer 5, 10587 Berlin
Elena N. Vilchevskaya, Institute for Problems in Mechanical Engineering, Russian Academy of Sciences (IPME RAS), V.O., Bol’shoy Pr., 61, St.Petersburg 199178, Russia

Influence of the treatment parameters on the evolution the properties of the elasticity, plasticity and structural of polycrystalline alloy 43300

Ahmed Hakem, Amayas Hakem, Youcef Bouafia

Corresponding Author E-mail: a_hakem1951@yahoo.fr

Abstract

The purpose of this study is to determine the influence of the parameters of treatments on the evolution of the behavior and the damage in tension, the Brinell hardness, the microhardness, the resilience and the microstructure of the alloy of chemical designation AlSi10Mg and numerical 43300 considering three states of the material: crude of casting noted: F, tempered noted: T and matured followed by an artificial aging designated T46. The addition of 10% silicon which gives excellent casting ability and a percentage of magnesium ($\leq$ 1% Mg) to aluminum are the main agents for improving the mechanical properties in addition to specific thermal treatments which reveal precipitates of different kinds which hinder the movement of dislocations. We studied the influence of structural hardening, Mg addition and casting method: sand and shell metal on the elasticity and plasticity characteristics of the polycrystalline Al-10% alloy. This alloy supports mean mechanical stresses. Parts made from this alloy are part of the components and realizations of the SNVI (Unit Aluminum of Rouiba) and Electro-Industries (Unit Freha Motors in Tizi-Ouzou), Algeria.

keywords: Al - Si, sand, shell, tempered, tempering, mechanical properties..

1 Introduction

In this study we are interested in the mechanical properties of the alloy hypoeutectic Al - 10% mass. If for five different states (crude of casting noted: F, tempered condition noted: T, ripened noted: M12h). The three states are respectively matured each followed by tempering noted: T46. Measurements of the characteristics of strength and ductility were determined, respectively, at room temperature, using the traditional method of uniaxial tension. The analysis shows that maturation leads to changes in mechanical characteristics: rise and decline of the respective elastic and plastic characteristics. The observed variations are associated with the evolution of the microstructure: the presence of heterogeneities in the as-cast, removing the last during the homogenization and reduction of internal stress during

maturation of the material. The choice of this material was dictated by the fact that it is very much used in various mechanicalBŕapplications; while the addition of 10% silicon, $(0,17-0,40)\%$ Mg and ofBŕits heat treatment associated with the various industrial processes of molding of sandBŕand shell were selected following the considerable improvements of certain required properties of which silicon gives him excellent aptitudes forBŕcasting combined withBŕmagnesium which is the principal agent of improvement of the mechanical characteristics [112].

2 Studied material

BŕThe material used isBŕa nuance containing a littleBŕmagnesium added in small quantity $(0,17$ to $0,40)\%$ Mg toBŕalloyBŕto allow the hardening Bŕand for a rational use in applications toBŕhigh mechanical characteristics withBŕthe T46 state. This alloy contains silicon 10% which confers to him very good properties of implementation in foundry (average flow, weak volumetric contraction withBŕsolidification, reduction in the withdrawal inBŕa solid state and dilation coefficient.). It is used for complex piece, withBŕrequirements for average mechanical behaviors and of which the thicknesses are very low (≈ 5 mm).

3 Elaboration of the alloy studies

3.1 The casting

The fusion of metal is done in an oven with gas of production tipping the forward backward comprising a graphite crucible of capacity 350Kg of which charge is composed approximately $\approx 40\%$ of new bars in dimensions standard of composition and characteristics AlSi10Mg although determined., delivered by the French Pechiney company and a mixture of casting jets $\approx 60\%$ return (appendages of feeding, evacuation and regulation, parts defective and rejected). The parts can be respectively cast in the single metal shell or of the sand moulds prepared for this purpose, thus the test-tubes of reference are called crude of casting noted: F To seek to increase more the characteristics of resistances of the state F and to obtain essentially big constraints of elasticity, big modules of rigidity with low deformations, and the material of digital name 43300 is subjected to the noted specific treatments: T46.

3.2 Molding

1. Sand: this casting is composed of two half fingerprints left by the model in the packed sand.

2. Shell: in this method of casting, the mould is composed of two floor screeds (5% of chromium), which has the role to keep the fingerprints. These floor screeds, separated by a joint plan, must be eventually prepared and heated to a temperature (200div 300)° C After analysis, the test pieces cast in sand and metal shell by gravity have the following chemical composition.

Chemical elements	Si	Mg	Fe
% According to analysis	9,62	0,34	0,15

Results of the chemical analysis after control on test-pieces cast in sand and shell.

This alloy is manufactured by two different methods: casting sand and casting shell considering 03 States rated respectively; crude of casting: F, tempered: T and tempering: T46.

4 Experimental procedure

The physical characterization, chemical and mechanical in general especially crucial importance for the design of various metal parts subjected to external forces varied constituents various mechanisms in motion a mechanical component. The designer can therefore neither calculate nor size these parts without identifying and quantifying their characteristics. To determine them, we reproduce these loads using static or dynamic tests, usually performed on standard specimens. Four techniques are used, namely traction to identify the various constraints, the Brinell hardness HB for the stress field, Kcv resilience tells us about the mode of fracture, brittleness and impact resistance and metallographic shows the structures. We will describe in more detail and present in the main mechanical characteristics obtained from the chemical composition of material being AlSi10Mg purpose of this study

5 Results obtained and discussion

The average values вЃ Кв Ґ Кof tensile mechanical properties, resilience and hardness of the alloy AlSi10Mg are those given by averaging five identical specimens for each of the respective cases and are represented in Figures 1 to 3 below.
Influence of molding processes in the sand and in the shell for alloy AlSi10Mg on the characteristics in:

5.1 resistances

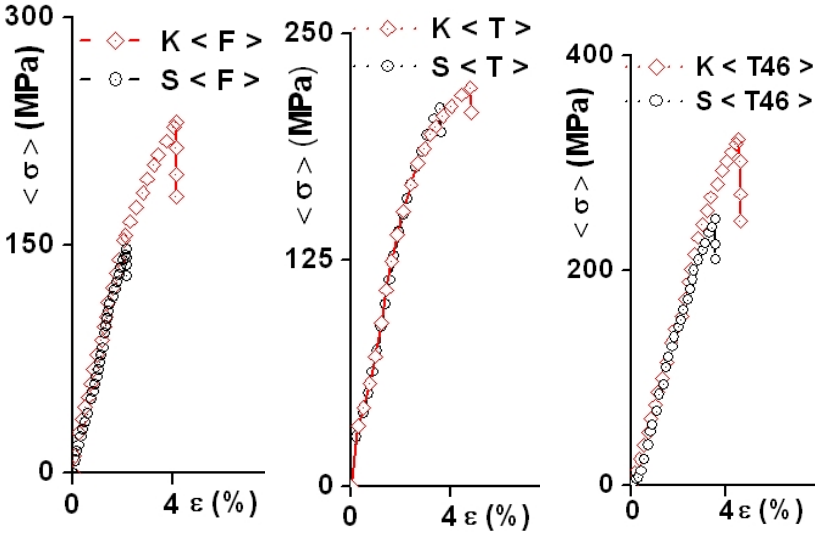

Figure.1 вГУ Grouping of the mean curves of comparison (mean stress - deformation) of the AlSi10Mg alloy casted in sand and in shell: $a - K < F > / S < F >, b - K < T > / S < T >$ and $c - K < T46 > / S < T46 >$.

Notation: F - Crude of casting, T - tempered, T46 - tempering, S вГУ sand, K - shell, Ox (%) - deformation (%) and $< \sigma >$ (MPa) - stress (Mega Pascal).

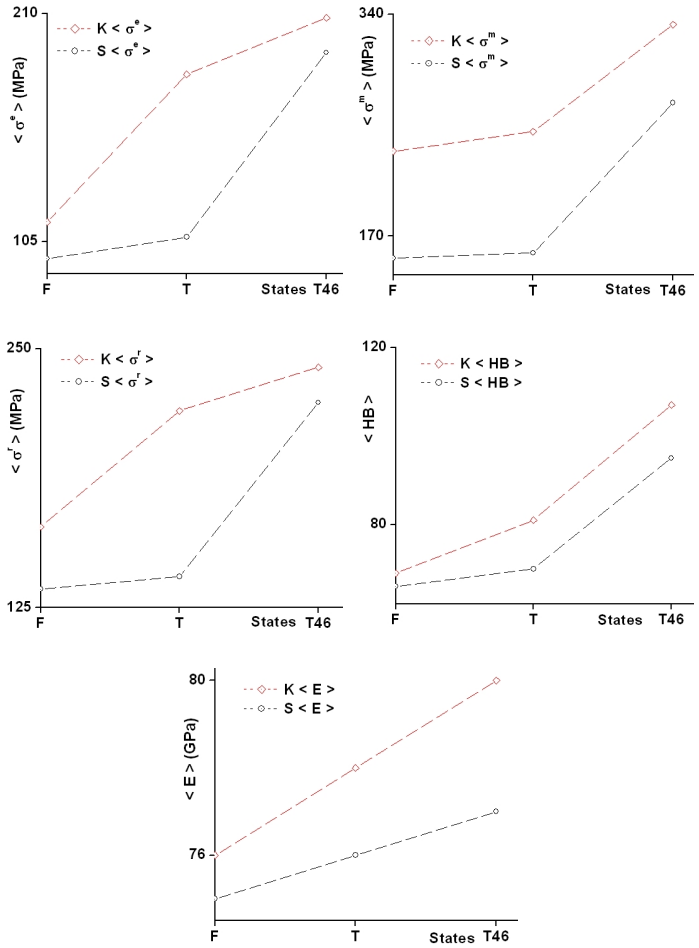

Figure.2 вГY Grouping of the mean Graphs of comparison (mean stress, mean hardness and mean Young's modulus - states) of the AlSi10Mg alloy casted in sand and in shell: $a-K<\sigma e>/S<\sigma e>, b-K<\sigma m>/S<\sigma m>, c-K<\sigma r>/S<\sigma r>, d-K<HB>/S<HB>$ and $e-K<E>/S<E>$.

Discussion. It is seen that all curves and all the graphs of the shell casting are above those of the sand casting whatever of the states considered. In addition to the increase in mean values вГКвГКof the characteristics of resistance is the state F to the T state, reaching its maximum value to the state T46 whatever the two modes of elaboration at the expense of ductility; This is probably due on the one hand, the mode for cooling the molds, on the other hand the addition of alloying elements combined with structural hardening treatment by precipitation.

5.2 Ductility

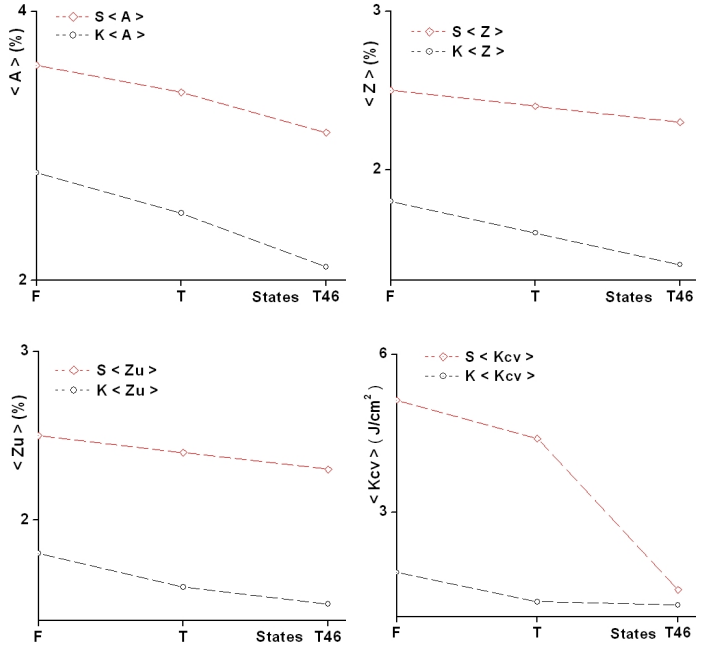

Figure.3 - Grouping of the mean Graphs of comparison (elongation, coefficient of necking, elongation of necking and resilience-states) of the AlSi10Mg alloy casted in sand and in shell: a-K $<A\%>/S<A\%>, bK<Z\%>/S<Z\%>, c-K<Zu\%>/S<Zu\%>$ and $d-K<Kcv>/S<Kcv>$.

Discussion We see that all curves of sand casting are above those of the shell casting whatever of the states considered. In addition to the increase in mean values of ductility characteristics is the state T46 that of T to reach its maximum value at state F regardless of the two modes of elaboration to the detriment of the characteristics of resistance.

Notation: $<\sigma m>$ (MPa) - mean maximum stress (Mega Pascal) ,$<\sigma e>$ (MPa) - mean elastic stress (Mega Pascal), $<\sigma r>$ (MPa) - mean breaking stress (Mega Pascal),$<HB>$ - mean hardness Brinell HB,$<E>$(GPa) - mean Young's modulus (Giga Pascal), $<A\%>$ - mean elongation (%), $<Z\%>$ - mean coefficient of

necking, $< Zu\% >$ - mean elongation of necking, F - crude of casting, T - Brtempered, T46 вГY tempering, - Sand and K-shell.

6 Influence of hardening on the evolution of mechanical properties of the alloy AlSi10Mg mode casting

Discussion in molding processes in the

6.1 Sand

The average curve of the sand casting to the S $< T46 >$ state is in top of the other curves i.e. those of the stateвГЄs S $< T >$ and S$< F >$. The constraints, hardness HB and the coefficient of rigidity means increase with a clear improvement of state S $< F >$ to the state S $< T >$ by reaching the maximum values with state S $< T46 >$ to the detriment of the characteristics of ductility which decrease in opposite direction. On the other hand the coefficient of consolidation and Poisson's ratios remain almost invariants for the sand casting.

6.2 Shell

In the same way the average curve of the shell casting to the K $< T46 >$ state is in top of the other curves i.e. those of the stateвГЄs K$< T >$ and K$< F >$. The constraints, hardness HB and the coefficient of rigidity means increase with a clear improvement of state K $< F >$ to the state K $< T >$ by reaching the maximum values with state K $< T46 >$ to the detriment of the characteristics of ductility which decrease in opposite direction. On the other hand the coefficient of consolidation and Poisson's ratios remain almost invariants for the shell casting.

References

[1] Jean Baralis, GГкrard Maeder, Handbook of Metallurgy: (elaboration, Structure-property, standardization), p.232, 1ere edition, AFNOR-Nathan, Paris (1997).

[2] Ahmed Hakem, doctoral thesis, Effects of elaboration mode and maturation on mechanical properties and microstructure of casting alloys Al-Si, 2014, Department of Engineering вГY Mechanical, Faculty of Engineering Construction, University Mouloud Mammeri Tizi вГY Ouzou , Algeria.

[3] Mr. Colombie and Coll, Industrial Materials: Metallic Materials, p.867, Wiley, Paris (2000).

[4] Pierre Guenin, Engineering Techniques: Metal alloys foundries - Treaty metallic materials M 3521, p.15, Dunod - AFNOR, Paris (2002).

[5] Roger Devaley, Techniques De l'ingГкnieur: Traitement thermique: Traitement de mise en solution-trempe-maturation et revenu M 1291, p.24, Dunod - Afnor, Paris (2002).

[6] H. Kamguo Kamga, Influence of Alloying Elements iron and silicon on mechanical properties of aluminum-copper alloys such B206, Ph.D. Thesis, University of Quebec at Chicoutimi, June 2010.

[7] Ahmed Hakem, Y. Bouafia, S. Naili, A. Bouhaci, Industrial Development of aluminum alloy casting AlSi7Mg, and AlSi10Mg AlSi13Mg, International Symposium - Characterization and Modeling of Materials and Structures 16, 17 and 18 November 2008 - Mr Mammeri University of Tizi-Ouzou, Algeria.

[8] Ahmed Hakem, memory magister, Microstructure and Mechanical Properties of the hypoeutectic alloy AlSi7Mg, 2005, Engineering Department - Mechanics, Faculty of Engineering Building, University Mouloud Mammeri Tizi - Ouzou.

[9] Jean GAUTHIER, effect of heat treatment on mechanical properties, microstructure and fractography for the alloy Al-Si-Cu-Mg. Master of Engineering University of Quebec at Chicoutimi in April 1994.

[10] Jean-Paul Baillon, Jean-Marie Dorlot, Materials, p.729, 3rd edition, Ecole Polytechnique de Montreal, Montreal (2000).

[11] Bruno Barlas, study of behavior and fatigue damage in aluminum alloy casting, thesis submitted and publicly defended the 5 'in February 2004, Ecole des Mines de Paris, p228.

[12] Asserin-Lebert Experimental study and prediction of failure mechanisms of plates and joints butt welded aluminum alloy 6056, and presented publicly defended February 18, 2005, Ecole des Mines de Paris, p190.

BELOW SHOULD BE YOUR ADDRESSES

A. HAKEM, Laboratory LaMoMS, Mouloud MAMMERI university of Tizi-Ouzou Hasnaoua II, 15000 Algeria

Y. BOUAFIA, Laboratory LaMoMS, Mouloud MAMMERI university of Tizi-Ouzou Hasnaoua II, 15000 Algeria

The Evolution of the System of Gravitating Bodies

Dmitry G. Kiryan and George V. Kiryan
diki.ipme@gmail.com

Abstract

A natural physical approach to the analysis of the structure of closed gravitating systems has been formulated in the scope of classical mechanics. The approach relies on the interrelation between densities of nested spheres inscribed in the circular orbits of the system bodies. An empirical law has been defined for the evolution of closed gravitating systems differing in mass, time scale and distance from the ground-based Observer. The gravitating systems undergo modifications and evolve from their initial state, namely, a gas-and-dust formation of almost constant density over the entire volume, to a certain terminal phase of the process when the system structure becomes similar to the planetary system (like the Solar system) where almost all the gravitating mass is concentrated in the vicinity of the system center of gravity. Using the proposed method of nested spheres, it is possible to reveal for the gravitating system the character of radial distribution of matter density in the system symmetry plane, quantitatively evaluate the density of medium containing the gravitating system under consideration, and assess the current phase of the system evolution. The research results have led us to a conclusion that introduction into the scientific practice of such an entity as "dark matter" has no physical background since it is based on a wrong interpretation of an "unordinary" distribution of star orbital velocities in galaxies.

1. Definition of the problem

Let us consider as the study object a galaxy that is a closed system of material bodies of various nature and size interacting purely by gravity. Assume that the system under consideration is dynamically quasi-stable. The galaxy time scale and distance from the Observer restrict significantly the methods and techniques for studying the dynamics and nature of these systems of gravitating bodies.

The visible galaxy structures allow us to suggest the existence of rotation motion about the dominant center of gravitational attraction since the straight-line motion is impossible in the system of gravitating bodies. The instrumentally observable

galaxy structures are nothing but manifestation of the current stage of gravitational compaction. This is only an instant at the time scale of evolution from a conditionally static gas-and-dust "cloud" to a quasi-stable rotating system of gravitating bodies.

The only available observation data are the Doppler[1] measurements of radial velocities[2] of some stars in the galaxy rotation plane. Hereinafter we assume that all the stars and other material objects move in the galaxy rotation plane along a circular trajectory about the dominant center of attraction.

Let us define the problem as follows: using linear velocities of a limited number of stars located in the galaxy rotation plane, construct the radial distribution of the matter density ignoring the star formation processes and non-gravitational interaction effects.

2. System of nested spheres

A galaxy is a quasi-stable cluster of material objects, such as stars, gas-and-dust formations, nearly invisible and absolutely invisible objects. The total galaxy matter as a whole participates in the complicated rotation about its dominant center of attraction. As known from classical mechanics, the very possibility of a material body motion in the gravity field along a circular orbit, i.e., with a constant radius and constant orbital velocity, is due to the total gravitating mass enveloped by a sphere inscribed in the circular orbit of the body under consideration.

Why it should be a sphere? Why not another rotary figure with the symmetry axis coinciding with the galaxy rotation axis? It is of note here that the probe mass[3] located in the galaxy rotation plane makes no difference (from the gravitational point of view) between the gravitating mass of a sphere and another rotary body inscribed in its orbit. We have chosen a sphere because parameters of other rotary figures can hardly be quantitatively described due to multiple conditionalities and uncertainties in the visible configuration of the galaxy.

Thus, the observed star belonging to the galaxy under consideration plays the role of a probe mass by observing which it is possible to assess the gravitating mass keeping it in the orbit (a circular orbit in our case).

Designate the dominant attraction center of the galaxy as O . Bring the xOy Cartesian system into coincidence with the galaxy rotation plane (Fig. 1).

Assume that all the A_i stars, as well as the remaining matter, move about the attraction center O in the xOy plane counterclockwise along circular orbits[4]. Based on the Doppler shift of star spectrum lines, Observers determine the stars' relative radial velocities which are further used to calculate star orbital velocities $\underline{v}_i$.

Let us write down an expression for the gravitating mass of matter located in a sphere whose radius is equal to that of the star A_i (a probe mass) circular orbit. Taking into account that any selected star A_i with gravitating mass m_i moves in

[1]The Doppler effect is the shift of spectral lines of a moving radiation source.

[2]The body velocity along the line connecting the Observer and radiation source.

[3]The "probe mass" is a material body (a research tool) that does not significantly distort the studied gravity field of the system of gravitating bodies.

[4]Generally, trajectories of stars and other bodies are continuously evolving open spatial curves.

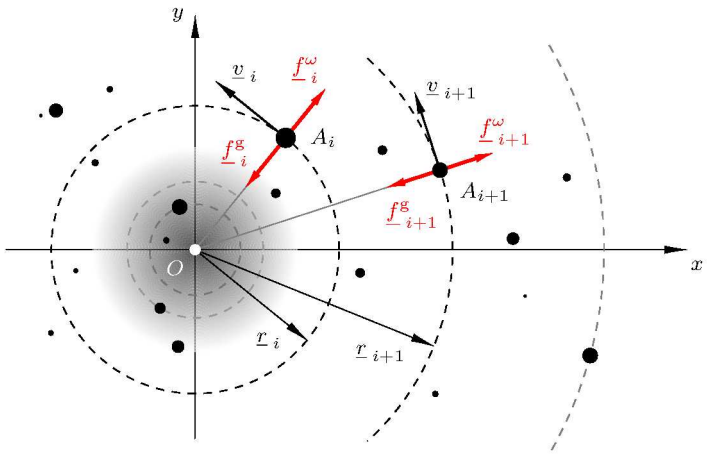

Figure 1: Galaxy rotation plane xOy.

the galaxy symmetry plane along a circular orbit of radius $\underline{r}$ (hereinafter we omit index i), the force balance equation for the gravity $\underline{f}^{\mathbf{g}}$ and centrifugal $\underline{f}^{\omega}$ forces may be written as:

$$\underline{f}^{\mathbf{g}} + \underline{f}^{\omega} = 0 \,, \tag{1}$$

where

$$|\underline{f}^{\mathbf{g}}| = \widetilde{m}\,\overbrace{\frac{\mathbf{G}\widetilde{M}}{r^2}}^{\mathbf{g}} \,, \qquad \widetilde{m} = m\left(1 - \frac{\rho_0}{\rho_{prob}}\right) \tag{2}$$

and

$$|\underline{f}^{\omega}| = m\, r\omega^2 \,, \qquad v = \omega r \,. \tag{3}$$

Here $\mathbf{G}$ is the gravitation constant; $\widetilde{M}$ is the gravitating mass of the sphere inscribed into the star orbit of radius r; m, $\widetilde{m}$ are the star inertia and gravitating masses[5]; ρ_0 is the density of medium containing the galaxy; ρ_{prob} is the probe mass (star A) density; $\mathbf{g}$ is the gravity field intensity at distance r from the attraction center O; ω is the angular velocity of the star rotating about attraction center O.

Therefore, based on the star A velocity and distance from the attraction center O, we can find gravitating mass $\widetilde{M}$ of the matter enclosed in the sphere inscribed in the star A orbit of radius r. Using the force balance equation (1) and taking into account (2) and (3), obtain the expression for gravitating mass $\widetilde{M}$

$$\widetilde{M}(r,v) = \frac{1}{\mathbf{G}k_\rho}\, rv^2 \,, \quad k_\rho = \left(1 - \frac{\rho_0}{\rho_{prob}}\right) \tag{4}$$

and density of the gravitating mass enclosed in the sphere of radius r

$$\rho(r,v) = \frac{\widetilde{M}(r,v)}{V(r)} = \frac{1}{\frac{4}{3}\pi\mathbf{G}k_\rho}\left(\frac{v}{r}\right)^2 \,, \tag{5}$$

[5]Interrelation between the inertial and gravitating masses is described in detail in paper [7, 8].

where $V(r)$ is the volume of the sphere inscribed into the star A circular orbit.

Here we should emphasize that the assumption on the star orbit circularity stipulates that the star is gravity-neutral to all the gravitating objects beyond the sphere inscribed into its orbit and interacts only with all the averaged gravitating matter located in the sphere. The orbit circularity also means that there is no friction with the material medium ρ_0 in density which is external to the star.

Now consider a group of n probe masses (stars) belonging to the galaxy under study and lying in its rotation plane xOy. In the scope of the defined task, our goal is to reveal how the gravitating matter is distributed in the galaxy rotation plane. Let us assign a gravitating sphere of radius r_i to each probe mass A_i moving along a circular orbit of radius r_i with velocity v_i. As a result, a sequence of n nested spheres with common symmetry center O was obtained. Designate the gravitating mass of the sphere inscribed in the star A_i orbit as $\widetilde{M}_i$. Assume that the matter is uniformly distributed over the sphere volumes. The sequence of uniform spheres nested in each other allows us to speak about a sequence of spherical layers, their masses and densities. Assume also that the spherical layer index is equal to the lesser of two orbit radii: $r_i < r_{i+1}$. Gravitating mass $\Delta\widetilde{M}_i$ of each i-th spherical layer $(r_{i+1} - r_i)$ in thickness is equal to the total gravitating mass of all the material bodies included in the considered spherical layer volume ΔV_i. Thus, we can define the volume and mass of the i-th spherical layer as

$$\Delta\widetilde{M}_i = \widetilde{M}_{i+1} - \widetilde{M}_i = \frac{1}{\mathbf{G}} \left(r_{i+1} v_{i+1}^2 - r_i v_i^2 \right) , \tag{6}$$

$$\Delta V_i = V_{i+1} - V_i = \frac{4}{3}\pi \left(r_{i+1}^3 - r_i^3 \right) , \tag{7}$$

and use the obtained spherical layer volume and mass to derive the expression for the density increment:

$$\Delta\rho_i = \Delta\widetilde{M}_i \,/\, \Delta V_i = \frac{1}{\frac{4}{3}\pi\mathbf{G}} \frac{r_{i+1} v_{i+1}^2 - r_i v_i^2}{r_{i+1}^3 - r_i^3} . \tag{8}$$

Thus we have obtained the radial distribution for mass increment $\Delta\widetilde{M}(r, v)$ and density increment $\Delta\rho(r, v)$ of a sequence of spherical layers for the galaxy which we regard as a system of nested spheres with respective gravitating masses that in the first approximation make the stars moving circularly with velocities known from observations.

In summary, we have defined in the scope of classical mechanics and based on the classical law of gravitational interaction between two point masses a method of nested spheres enabling deriving the radial mass (density) distribution from observations only of the star radial velocities and distances to the dominant galaxy attraction center O without refining the observed configuration of the galaxy. The method of nested spheres allows the transition from the real gravitating system characterized by a high extent of uncertainty in geometry and matter distribution to its centrosymmetric gravitational model.

Let us show that the approach suggested provides reliable and significant results in analyzing closed gravitating systems of various sizes and configurations. Let us test it by the example of such a relatively well studied system as the Solar System.

Solar system. Let us construct a gravitationally equivalent model of the Solar system in the form of a sequence of uniform nested spheres with the Sun as a dominant center of attraction.

Generally, all the planet trajectories are perturbed orbits, i.e., open spatial curves elliptic in the first approximation. We will rely upon the fact that we know only the planet velocities in the *pericenter* and *apocenter* and also the distances from these points of the elliptic orbit to the attraction center. Physical characteristics of the planets are listed in Table 3 (appendix A).

Assume that all the planets orbit in circular orbits with constant velocities, which *a priori* excludes from consideration their gravitational interactions. Each planet is associated with a sphere of a radius equal to that of its orbit. Let us take as the planet-to-Sun distance the elliptic orbit semiaxis and assume the planet velocity (Table 3) to be the arithmetic mean of velocities in the orbit *pericenter* and *apocenter*:

$$\bar{r} = {}^1\!/_2\,(r_{min} + r_{max})\,, \qquad \bar{v} = {}^1\!/_2\,(v_{min} + v_{max})\,. \tag{9}$$

The fact that we consider averaged velocities and orbit radii means that formally we have turned to circular orbits. However, in switching from elliptic orbits to circular ones, we should not lose the gravitational interconsistency of planet masses which breaks immediately after averaging the orbit radii and velocities. What does it mean? The planet gravitating masses should comply with the commonly accepted and many times verified values, namely, the spherical layer masses should be equal to the known planet masses. Gravitating mass of the sphere enclosing the Solar system matter should monotonically grow with its radius, while densities of the spheres inscribed in the planet orbits should form a decreasing sequence according to formula (5).

The sequence of spheres inscribed in the planet orbits makes it possible to estimate gravitating masses of these planets via the spherical layer masses (6). The order of the layer sequence depends on the planet distance from the Solar system attraction center. The mass of the sphere inscribed in the orbit of Mercury, the first planet, appears to be equal to the mass of the Sun and all the remaining matter of the near-Sun space inside the Mercury orbit. Then, the difference between the masses of spheres inscribed in the Mercury and Venus orbits is equal to the Mercury gravitating mass. Cycling through the orbits, we can calculate masses of all the planets except for Pluto since such calculation needs knowing orbital parameters of the next planet[6]

As the quantity to be corrected in order to ensure physical interconsistency of the system, the mean orbital velocity $\bar{v}$ of the planets was chosen; it is defined by (9). Designate the velocity $\bar{v}$ matching correction as Δv:

$$v = \bar{v} + \Delta v\,. \tag{10}$$

Strictly speaking, we might take as a corrected quantity the planet orbit radius and fix the velocity, but we have chosen the velocity as a quantity to be corrected.

[6]Probably, here planet **X** is meant, whose existence has been justified in paper [1].

Correction Δv was derived from the condition of constancy of the planet gravitating masses given in Table 3 (appendix A).

As a result, we have obtained a gravitationally balanced and centrally symmetric model for the Solar system whose characteristics are presented in Table 1.

	r, *min	v, km/s	ρ, kg/m^3	$m/M_\oplus$	$\widetilde{M}/M_\odot$
Sun	—	—	—	332937.079	1.000000000
Mercury	3.21945	47.87273 *2.14%*	0.0395751	0.055	1.000000166
Venus	6.01583	35.02123 *0.01%*	0.0113343	0.815	1.000002614
Earth	8.31659	29.78565 *0.02%*	0.0059305	1.012	1.000005654
Mars	12.67127	24.13072 *0.43%*	0.0025547	0.107	1.000005977
Jupiter	43.28383	13.05622 *0.18%*	0.0002189	317.901	1.000960814
Saturn	79.69541	9.62656 *0.09%*	0.0000646	95.184	1.001246705
Uranus	159.69159	6.80156 *0.02%*	0.0000161	14.536	1.001290364
Neptune	249.89844	5.43722 *0.04%*	0.0000065	17.152	1.001341881
Pluto	328.35911	4.74346 *3.29%*	0.0000038	0.002	1.001341888
X	583.75857	3.55757 *7.38%*	0.0000012	—	—

Table 1: Interconsistent parameters of the centrally symmetric gravitational model of the Solar system. Here m is the planet gravitating mass (including its satellites); r is the radius of the planet circular orbit expressed in light minutes; $\widetilde{M}$ is the gravitating mass of the sphere inscribed in the planet orbit; $M_\odot$ and $M_\oplus$ are the Sun and Earth masses (the values are taken from Table 3).

You can see that corrections Δv to circular velocity v are quite insignificant in percentage terms (see Table 1, the third column, italic type). However, just these minor corrections helped the centrally symmetric gravitational model of the Solar system to remain physically interconsistent with respect to the planet masses.

Fig. 2 represents the densities of nested spheres versus their radii, i.e., versus the planet distance from the dominant center of attraction (Sun).

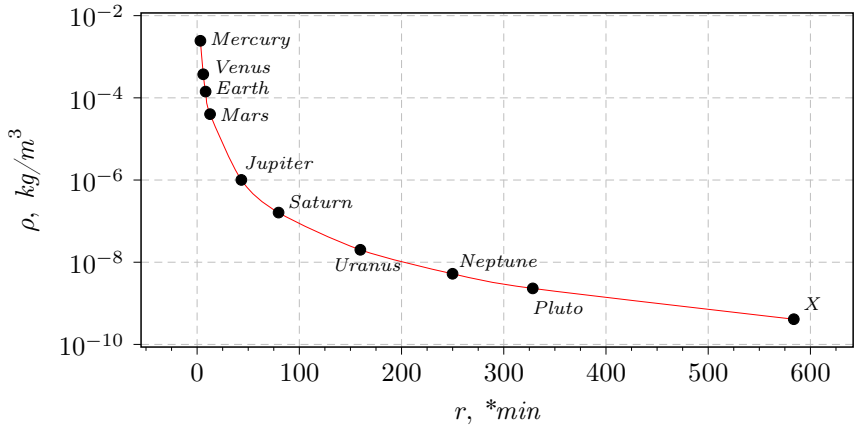

Figure 2: Distribution $\rho(r, v)$ of densities of nested spheres inscribed in respective circular orbits of the planets. The ordinate scale is logarithmic. Distance r is expressed in light minutes.

Analysis of the spheres' density ρ dependence on their radii r has shown that the

dependence is well fittable by an power function with the correlation of almost 1 :

$$\rho(r) = ar^{-3\beta} + \rho_0 \ , \quad \beta = 0.999999789 \ ^{*)} \tag{11}$$

where

$$\begin{array}{rcll} a & = & 4.7471194762 \cdot 10^{29} & [kg/m^{3(1-\beta)}] \ , \\ \rho_0 & = & 7.6646813633 \cdot 10^{-11} & [kg/m^3] \ . \end{array} \tag{12}$$

Hence, the density of gravitating spheres keeping the Solar system planets orbiting circularly with constant orbital velocities varies according to a power law with the power coefficient of -3β. Fig. 2 clearly demonstrates that any already known or yet unrevealed material body (e.g., planet **X**), its velocity and orbit radius should not contradict the power law of density distribution in the sequence of nested gravitating spheres. This means that, using formula (11) for the supposed average radius of the planet **X** circular orbit, it is possible to find the gravitating mass of the sphere inscribed in this orbit and then determine its circular velocity and respective period of revolution about the Sun.

Galaxies. After making sure that the above-described method of the nested sphere sequence is effective, let us apply this approach to spiral galaxies using their "rotation curves" obtained from measured Doppler shifts of star spectral lines. Let us consider the orbital velocity distribution for stars of the following galaxies: `NGC6503`, `NGC3198`, `NGC2403` [2]; `NGC598(M33)` [3]; `NGC7331`, `Milky Way` [4].

Assume that the observed stars of each galaxy move within the galaxy rotation planes along circular orbits about dominant centers of attraction with constant velocities. Fig. 3 represents "rotation curves" of the above-mentioned galaxies in one and the same scale.

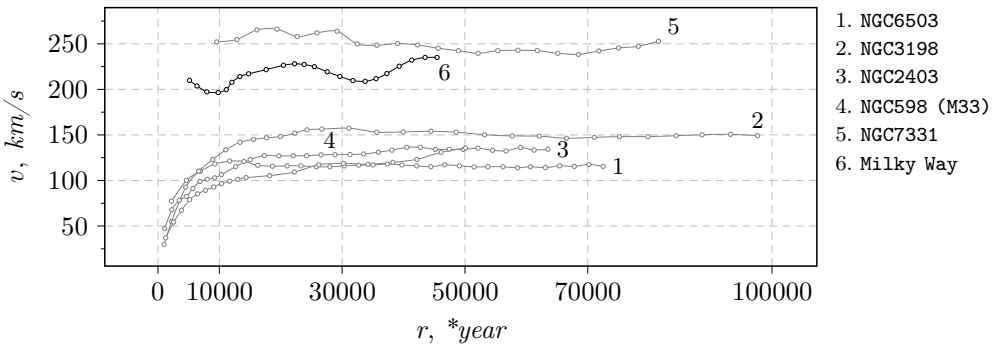

Figure 3: Galaxy "rotation curves".

These velocities were obtained from the measurements of spectral line Doppler shifts for stars lying predominantly in the galaxy rotation planes.

Substituting data on the radial distribution of orbital velocities (Fig. 3) into relations (4) and (5), construct for the sequence of nested spheres distributions of the gravitating masses (Fig. 4) and densities (Fig. 5).

The character of these plots lets us suggest mutual adequacy of kinematic and physical parameters of the galaxies as well as similarity of their evolution processes.

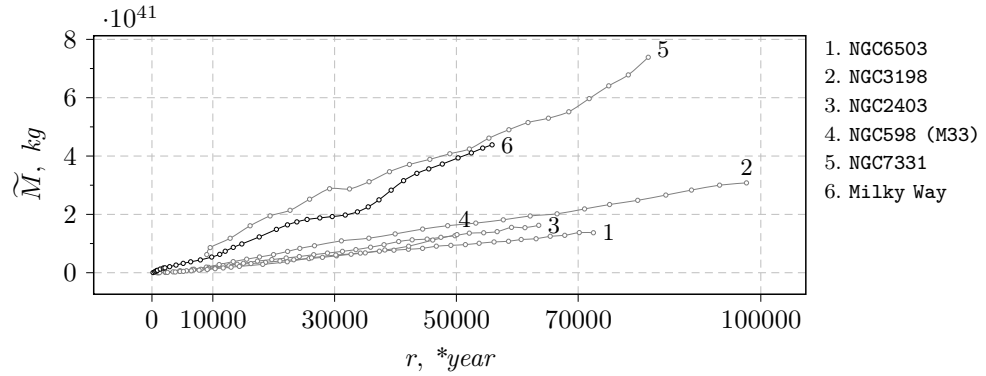

Figure 4: Increase in the sphere gravitating mass $\widetilde{M}$ with increasing radius of the sphere enclosing the galaxy matter.

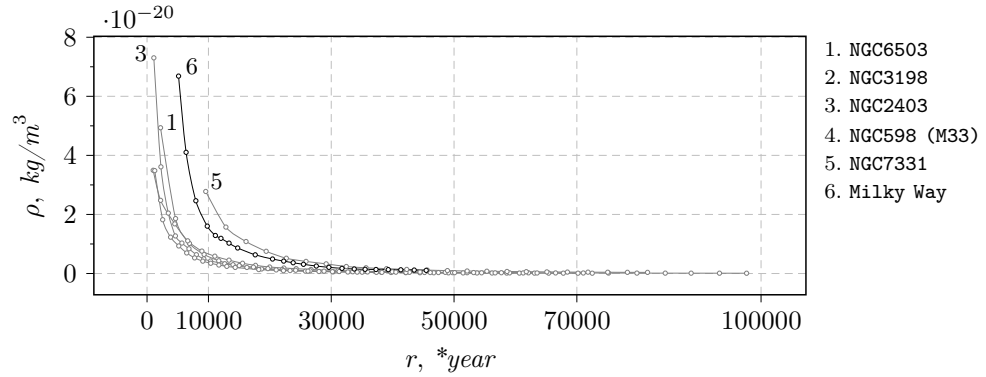

Figure 5: Radial distribution of the nested sphere densities.

Based on the velocity of the farthest star, we can quantitatively estimate the galaxy matter gravitating mass and calculate the galaxy mass. Hence, theoretically it is not difficult to estimate the galaxy mass; for this purpose one should merely select the galaxy star outermost from the galaxy center of attraction and measure the Doppler effect. However, here some technical difficulties arise, namely, the farther is the star, the lower is its angular and, hence, radial velocity, which manifests itself in the fact that the shift of the star spectral line is hardly detectable.

An important specific feature of falling sections of the plots representing a sequence of sphere densities shown in Fig. 5 is good fittability by a power function. Parameters of power function (11) approximating the falling sections of the sphere density plots are listed in Table 2. The results, including data on the Solar system, are arranged according to the increase in dimensionless coefficient β. One can see a regularity allowing an assumption that, as parameter β grows, the gravitation compaction intensity decreases, and the gravitating mass concentrates near the dominant center of attraction.

The obtained densities ρ_0 of the background medium (Table 2) do not contradict the estimates of densities of interstar space and Solar system interplanet matter.

Note. This concerns the comparison of two radial distributions of densities and their possible interchangeability. Here we mean the density expressions (5) and (8). For instance, Fig. 6 presents three curves constructed for galaxy `NGC3198`: the galaxy

	β	a	ρ_0 , kg/m^3	correlation
NGC598(M33)	0.5557725	$7.4682219 \cdot 10^{12}$	$1.9966367 \cdot 10^{-23}$	0.99973
NGC2403	0.6658555	$5.0648252 \cdot 10^{19}$	$3.4107570 \cdot 10^{-23}$	0.99969
NGC3198	0.7029228	$1.4582120 \cdot 10^{22}$	$4.6049746 \cdot 10^{-25}$	0.99972
NGC6503	0.7263460	$2.0268896 \cdot 10^{23}$	$3.3736620 \cdot 10^{-23}$	0.99976
NGC7331	0.7282799	$1.3999389 \cdot 10^{24}$	$2.0675915 \cdot 10^{-23}$	0.99938
Milky Way	0.7640299	$8.5863233 \cdot 10^{25}$	$1.2554146 \cdot 10^{-21}$	0.99996
Solar System	0.9999997	$4.7471194 \cdot 10^{29}$	$7.6646813 \cdot 10^{-11}$	1.00000

Table 2: Parameters of power function (11) fitting the falling sections of plots presenting densities of nested spheres.

"rotation curve", distribution of the spherical layer densities, and distribution of the nested sphere densities. The Fig. 6 curves show that it is quite possible to replace

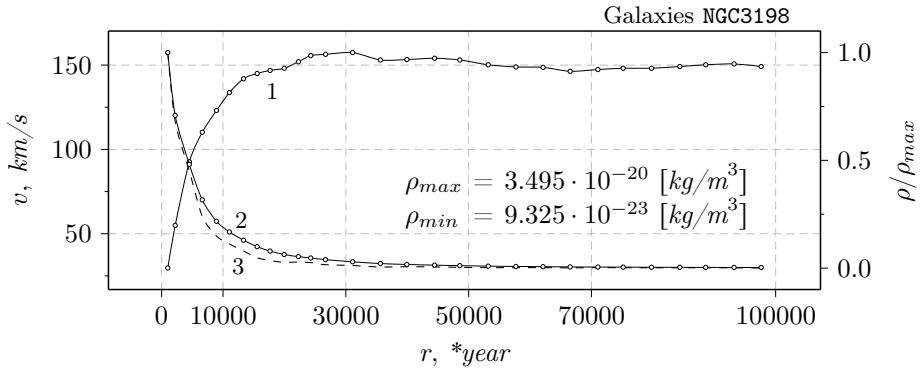

Figure 6: Comparison of density distributions for the sequence of nested spheres and spherical layers for galaxy NGC3198. 1 – the galaxy "rotation curve"; 2 – density distribution for the sequence of nested spheres, equation (5); 3 – density distribution for the sequence of spherical layers, equation (8).

the actual distribution of spherical layer densities with a smoother distribution of the nested sphere densities without losing physical sense. I.e., we may replace the sequence of nested spheres with only one sphere with the radial density distribution (5). We can assert that this sphere characterized by a nonlinear radial distribution of density is fully gravitationally consistent (via the probe mass) with the real galaxy, because orbital velocity of the probe mass (star) located at the preset distance from the center of attraction is consistent with observations.

3. Evolution of gravitating systems

The above-revealed power-like character of the nested sphere density distribution for the Solar system (Fig. 2) and family of galaxies (Fig. 5) allows generalization and makes it possible to formulate a law that functionally interrelates radius r of the sphere inscribed in the probe mass (star) circular orbit and density ρ of this sphere:

$$\boxed{\rho(r,\beta) = ar^{-3\beta} + \rho_0}\,, \qquad r > 0\,, \quad 0 < \beta < 1\,, \quad \rho_0 > 0\,. \tag{13}$$

Here β is the dimensionless coefficient characterizing the evolution stage of the gravitating bodies system, which may be interpreted as, e.g., the ratio between the current time and total time of existence of the system under study; ρ_0 is the density of medium containing the gravitating system. The dimension-matching factor a in (13) may be derived from boundary condition

$$\rho(r,\beta)\Big|_{r=r_{max}} = \rho_{min} \ . \tag{14}$$

Condition (14) is valid for any value from the $0 < \beta < 1$ range and may be regarded as the law of the gravitating mass constancy in the process of evolution of the closed gravitating system. Regardless of the way of the system gravitating matter redistribution with respect to the dominant center of attraction, the total gravitating mass remains constant at all the stages of the system gravitational compaction. All this also follows from the initial condition stating that the gravitating system is closed.

Substituting (14) into (13), define coefficient a as follows:

$$a = (\rho_{min} - \rho_0)\, r_{max}^{3\beta} \ , \qquad \rho_{min} > \rho_0 > 0 \ , \tag{15}$$

where ρ_{min} is the density of matter enclosed by the sphere inscribed in the orbit of the outermost observed object (probe mass) of the system under consideration; r_{max} is the radius of this outermost object (probe mass) orbit.

Thus, the densities of nested spheres inscribed in the probe mass circular orbits may be expressed as follows:

$$\rho(r,\beta) = \begin{cases} \rho(r_{min},\beta) & , \quad 0 < r \leqslant r_{min} \ , \\ \rho(r,\beta) & , \quad r_{min} < r \leqslant r_{max} \ . \end{cases} \tag{16}$$

Then, let us express the gravitating mass in terms of density and the circular velocity in terms of mass by using the empiric density distribution law:

$$\widetilde{M}(r,\beta) = \overbrace{\frac{4}{3}\pi r^3}^{\text{volume}}\ \rho(r,\beta) \ , \qquad v(r,\beta) = \sqrt{\frac{\mathbf{G}\widetilde{M}(r,\beta)}{r}\left(1 - \frac{\rho_0}{\rho_{prob}}\right)} \ , \tag{17}$$

where ρ_{prob} is the density of a probe mass that is a body moving with velocity v along a circular orbit of radius r about the center of attraction. The probe mass circular velocity depends only on the gravitating mass of the sphere inscribed in its orbit.

Choosing a few values of dimensionless parameter β successively growing from 0 to 1 and using (16) and (17), construct three curves for each fixed β: distributions of density $\rho(r)$, gravitating mass $\widetilde{M}(r)$, and orbital velocity $v(r)$. The obtained plots are presented in Fig. 7.

The Fig. 7 plots illustrate the unidirectional process of gravitational compaction at the constant total gravitating mass. What is meant here is the density redistribution within the system. This process is characterized by dimensionless parameter β from (13). Stating the empiric character of the inscribed spheres' density distribution and using the classical law of gravitational interaction between two point

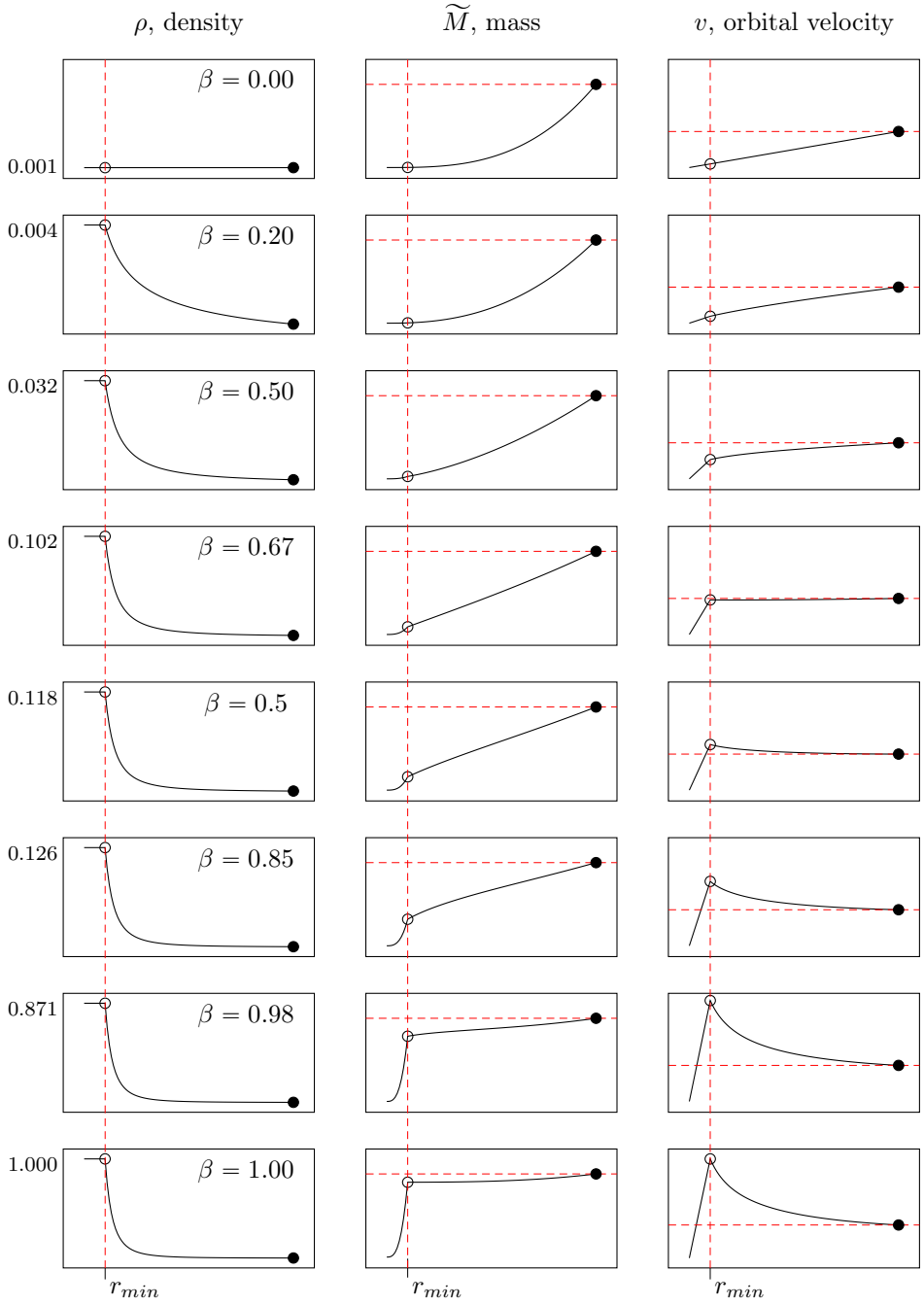

Figure 7: Here ρ is the density of a sphere from a sequence of nested spheres inscribed in the probe mass circular orbits; v is the probe-mass orbital velocity; $\widetilde{M}$ is the total gravitating mass. Black dots indicate the densities, masses and velocities at distance r_{max} from the center of attraction which remain invariant during the entire period of the system evolution.

masses (17), we have obtained a structured sequence of rotation curves (orbital velocity distribution). For instance, $\beta = 0.67$ relates to the orbital velocity distribution having a plateau-like section, which is characteristic of spiral galaxies, while $\beta = 0.98$ correspond to the velocity distribution in the Solar system.

Thus, dimensionless parameter β of the power function characterizes the current ratio between the densities of the nested spheres for a closed system of gravitating

bodies, which, in its turn, determines the "rotation curve" character.

Note that the range limits $\beta = 0$ and $\beta = 1$ should be regarded as singular points since they correspond to purely theoretical realizations of the physical systems. For instance, parameter $\beta = 0$ corresponds to the initial stage of evolution, namely, a motionless gas-and-dust "cloud" whose components then begin rotate regularly about the dominant center of attraction due to the internal gravitational interaction. The limiting but not accessible state will be that of total completion of gravitational compaction when all the gravitating mass concentrates in a finite volume with a complete absence of matter outside it. This phase is characterized by $\beta = 1$.

Actually, parameter β is a dimensionless time parameter characterizing the current state of natural gravitational self-compaction of a closed gravitating system. "Life times" of each closed gravitating system are different and depend on various initial conditions of the matter distribution and its characteristics, as well as, to a lower extent, on accompanying internal non-gravitational processes. The only feature common for all closed gravitating systems is the power-like character of the gravitational compaction (13).

"Dark matter". Based on the results of systematic observations of spiral galaxy 21 and empiric method for estimating the gravitating mass from star luminosity, Rubin V.C. [5] has concluded that characteristic radial distribution of the circular velocity with a plateau cannot be achieved in the absence of instrumentally observable material gravitating mass. The presence of the plateau in the "rotation curve" is out of the researchers' evident expectations. The dependence was assumed to be similar to the orbital velocity distribution in the Solar system since the planet orbital velocities decrease with increasing distance from the Sun. Therefore, in addition to the classical matter, a hypothetical invisible matter referred to as "dark matter" was introduced, its physical properties being very obscure.

For instance, Fig. 8 taken from the paper by Yang Y. and Yeung W.B. [2] presents a characteristic plot demonstrating, in their opinion, a qualitative discrepancy between the observed linear velocities of the spiral galaxy stars and those calculated in the scope of classical mechanics upon the condition that the main part of the galaxy gravitating mass is concentrated in the center of attraction. The anomalousness of the galaxies' "rotation curves" 3, namely, the presence of plateaus, disappears if the family of distributions of star angular velocities 9 in rotating about respective dominant attraction centers of the galaxies is constructed. These curves are quite ordinary. The angular velocities decrease towards the gravitating system periphery, the character of the decrease being consistent with that of the Solar system, i.e., everything remains in the frame of classical mechanic. This is just the base for further analysis. Everything located within the sphere inscribed in the star orbit, including objects instrumentally invisible at present, is material and has a gravitating mass dictating the star orbital velocity.

The existence of a plateau in the galaxy "rotation curve" can be explained only by the current matter distribution in the galaxy depending on its gravitational compaction. The rotation curve plateau is merely a reflection of the current distribution of the gravitating matter over the system, which corresponds to a certain stage of the gravitational compaction of matter in its classical sense. The example of the

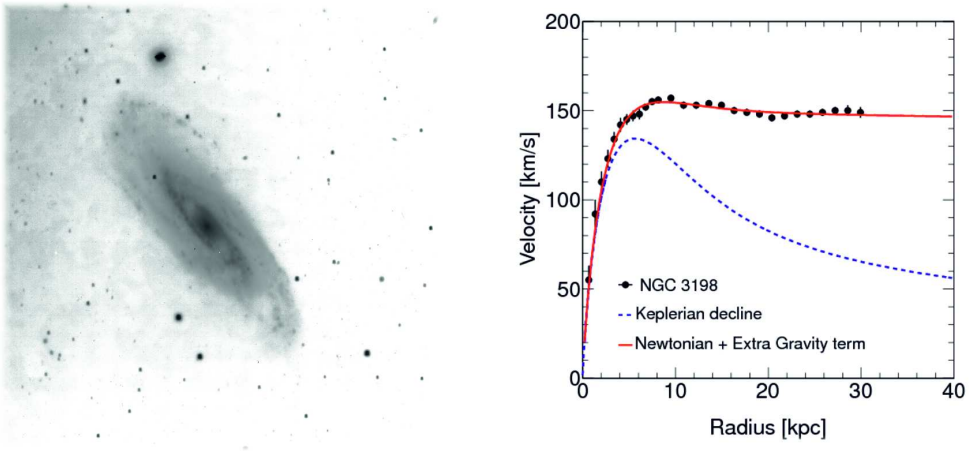

Figure 8: Characteristic distribution of the observed and calculated linear velocities of the stars over their distances from the Galaxy NGC3198 center [2].

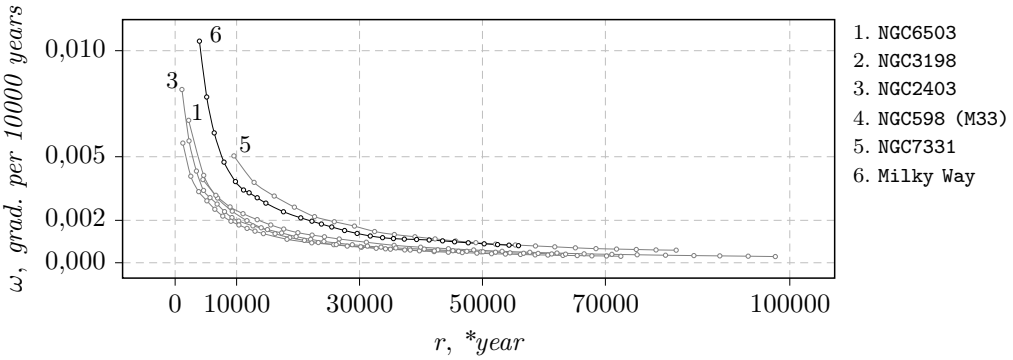

Figure 9: Angular velocities of rotation of stars about attraction centers of galaxies.

Solar system shows unambiguously that no additional gravitating mass with mystic properties is needed.

The revealed empiric dependence (13) valid both for the Solar system and galaxies leads to an unambiguous conclusion that the hypothetical "dark matter" does not physically exist as a gravitating substance.

4. Conclusions

Evolution of the gravitating system. The method of *a sequence of nested spheres* applied to real gravitating systems enabled us to reveal an empiric law describing the nonstationary process of gravitational compaction. A nonlinear mathematical model of the matter density distribution over a closed gravitating system has been created. Using the Doppler measurements of star velocities and the galaxy "rotation curve", it is possible to construct the density distribution of the gravitating matter and calculate the respective evolution parameter β. Dimensionless parameter β allows estimation of the system relative age and its comparison with that of other systems. Gravitating systems evolve from the initial state (a dust-and-gas formation with the initial density distribution) to a final state when almost all the system matter is concentrated in the vicinity of the dominant center of attrac-

tion of the system. Essentially, the obtained empiric law of natural gravitational self-compaction of the system is a variant of solution of the n -body gravitational interaction problem.

Universality of gravitational interaction. Due to the fact that the falling section of distribution of nested sphere densities in the Solar system and spiral galaxies can be described by a power function, we can speak about universality of the Gravity Law in its classical interpretation within the instrumentally observable Universe.

Vacuum density. Using the power function to describe the falling part of the nested sphere density distribution, we succeeded in quantitative estimation of the vacuum density, i.e., density of the inter-star and inter-galaxy medium containing the system of gravitating bodies. The results obtained do not contradict the currently known quantitative estimates of densities of different Universe regions.

"Dark matter". The analysis of "rotation curves" of galaxies belonging to the instrumentally observable Universe has shown unambiguously the sufficiency of existence of a sole gravitating mass perceived through classical physical experiments.

The horizontal section (plateau) of the distribution of star orbital velocities is merely a consequence of the current (by the moment of observation) distribution of the matter density in the evolving galaxy. The use of such an entity as "dark matter" for interpreting a "mystic" radial distribution of star orbital velocities in galaxies should be regarded as one of misconceptions that, unfortunately, sometimes occur in science[7] and always lead away from the truth.

In summary, we can recommend you the following:

> *Entering an unknown room and seeing nothing but darkness, do not hurry to create new entities — just switch on the light.*

Here words "switch on the light" mean improvement of the physical experiment technology and development of new physical principles and approaches to measuring the Doppler effect.

[7]It so happened that, in interpreting the observed time variations in the Polar Star altitude, astronomers have missed the fact that the star latitude variations are detected in the rotating frame of reference with a period equal to a solar day [6]. Theoretical physics has postulated the equality of the inertial and gravitating masses, however, time showed that this is valid only for a material medium with zero density which does not exist in our Universe [7, 8].

Appendix A. Solar System

planets	pericenter		apocenter		mass	radius
	r_p, *min	v_p, km/s	r_a, *min	v_a, km/s	$m_i/m_\oplus$	$r_i/r_\oplus$
☿ – Mercury	2.55732	58.98	3.88157	38.86	0.05526	0.38293
♀ – Venus	5.97524	35.26	6.05641	34.79	0.81498	0.94989
⊕ – Earth	8.17732	30.29	8.45584	29.29	1.00000	1.00000
♂ – Mars	11.48683	26.50	13.85569	21.97	0.10744	0.53202
♃ – Jupiter	41.16848	13.72	45.39918	12.44	317.83477	10.97331
♄ – Saturn	75.19368	10.18	84.19713	9.09	95.16123	9.14016
♅ – Uranus	152.39987	7.11	166.98329	6.49	14.53571	3.98085
♆ – Neptune	247.08482	5.50	252.71205	5.37	17.14831	3.86469
♇ – Pluto	246.66064	6.10	410.05756	3.71	0.00218	0.18631
– X	583.73716	3.84	583.77997	3.84	10.00000	

Table 3: Parameters of the Solar System planets[8]. The constants used are: $r_\oplus = 6371$ km is the Earth's average radius; $m_\oplus = 5.9726 \times 10^{24}$ kg is the Earth's mass. *min is the light minute (distance expressed in time units). During one minute, light covers a distance of 17987547.4 km.

[8] `http://nssdc.gsfc.nasa.gov/planetary/planetfact.html`.

References

[1] Batygin Konstantin, Brown Michael E. Evidence for a Distant Giant Planet in the Solar System // The Astronomical Journal. — 2016. — Vol. 151, no. 2. — P. 22.

[2] Yang Y., Yeung W. B. A New Approach to the Yang-Mills Gauge Theory of Gravity and its Applications // ArXiv e-prints. — 2013. — arXiv : physics.gen-ph/1312.4528.

[3] Corbelli E., Salucci P. The extended rotation curve and the dark matter halo of M33 // Monthly Notices of the Royal Astronomical Society. — 2000. — Jan. — Vol. 311, no. 2. — P. 441–447.

[4] Marr J. H. Galaxy rotation curves with lognormal density distribution // Monthly Notices of the Royal Astronomical Society. — 2015. — Mar. — Vol. 448, no. 4. — P. 3229–3241.

[5] Rubin V. C., Ford W. K. J., . Thonnard N. Rotational properties of 21 SC galaxies with a large range of luminosities and radii, from NGC 4605 /R = 4kpc/ to UGC 2885 /R = 122 kpc/ // The Astrophysical Journal. — 1980. — Jun. — Vol. 238. — P. 471–487.

[6] Kiryan Dmitry, Kiryan George. Moon's perigee mass as a missing component of the Earth's precession-nutation theory // PAMM. — 2014. — Dec. — Vol. 14, no. 1. — P. 49–60. — URL: http://dx.doi.org/10.1002/pamm.201410017.

[7] Кирьян Д. Г., Кирьян Г. В. Гравитационное взаимодействие в среде с ненулевой плотностью // e-prints viXra:1406.0128v1. — 2014. — Июнь. — P. 26. — URL: http://vixra.org/abs/1406.0128.

[8] Kiryan D. G., Kiryan G. V. Gravitational interaction in the medium of non-zero density // e-prints viXra:1406.0128v2. — 2014. — Jul. — P. 24. — URL: http://vixra.org/abs/1406.0128.

Dmitry G. Kiryan, Institute of Problems of Mechanical Engineering of RAS
61 Bolshoy Prospect V.O., 199178, Saint Petersburg, Russia

George V. Kiryan, Saint Petersburg, Russia

Adjustment for decrease of magnetic motor noise

Vitalij M. Kolykhalin

cap-007@mail.ru

Abstract

The electric motor inside volume formed by the winding stator and several rotor core elements is considered. Electromagnetic interaction between stator field winding and the rotor field winding, mechanical motor vibrations and air fluctuations from ventilation motor impeller excite the basic components of air noise in a wide frequency range. Magnetostrictive forces causing radial deformation of the stator core rings under alternate field action bring the special addition in motor noise. The dependence of the sound noise pressure from electromagnetic vibrations inside of the small volume chamber SVC is considered. The greatest linear size SVC less than half of wave length of the longest eighen frequency is installed. The construction of the stator core of the alternate bipolar commutator motor having two acoustic channels with determinate diameters in the center of each magnet poles is shown. Except of external surface stator core fluctuations there are two acoustic sources excited by internal surface stator core and influence through two channels in antiphrasis according external surface stator core fluctuations into SVC. The effective decrease of the carrying basic 100 Hz frequency magnetic motor noise is carried out. The method of the equivalent generator for symmetric parts in the electric analogue scheme is advanced. Equivalent generators as two sources of acoustic fluctuations switched on towards each other are described. The spectrograms illustrating of magnetic motor noise decrease are shown and the adjustment for decrease of magnetic motor noise is supported.

1 Formulation of the problem of the low frequency electric motor noise reducing

Perfection of acoustic measurement technique in low sound and infrasonic frequencies, development of person protection methods from detrimental of health are very importance as far as increasing functions of power transport and manufacture electronics.

Infrasonic fluctuations with long wavelength influence on all person surfaces by air, body and bone conductivity with loss of natural localization on a source.

Electromagnetic interaction between electric motor stator and electric motor rotor, mechanical external and internal vibrations and air rotation fluctuations excite the

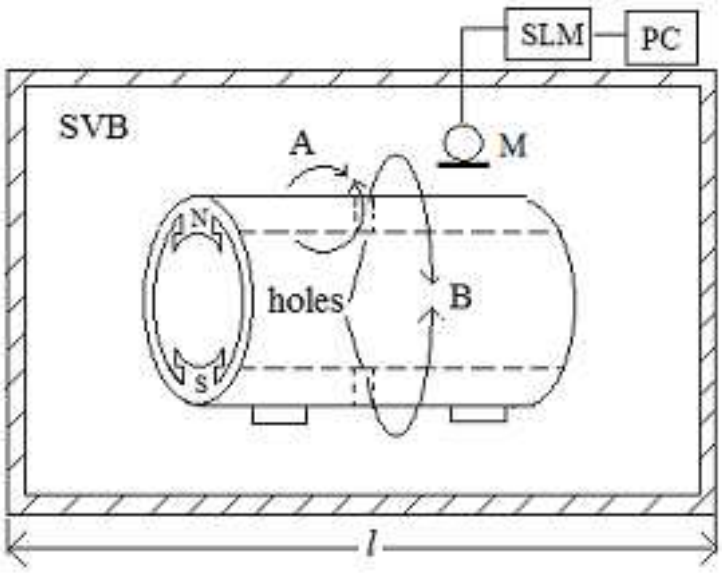

Figure 1

basic components of air noise in a wide frequency range [1]. It is essential the transition effects of motor slip and transformation of rotor core fluctuations bring appreciable spectral distortions in low sound and infrasonic frequencies.
The greatest distribution in power technical equipments with asynchronous motors and commutate alternating current motors with magnetic, mechanical and aerodynamic noise components have been received.
The magnetic motor noise components depending on stator core vibrations in the small volume box (SVB) with the maximal size no more than half of air wave length corresponded the double frequency network 100 Hz are investigated. Such SVB for graduation of measuring microphones, for estimation of sound insulation of small cabins and the casings damping noise by full or partial shielding of sources are applied.
The stator fluctuations by the electromagnetic forces are excited. During each half of a cycle of alternative electrical field the stator core as one compression - stretching cycle is deformed. The doubling network frequency corresponding of mechanical fluctuations 100 Hz is prevailed.
The sound pressure motornoise depended on motor force vibrationinto closed volume SVB from Poisson equation are found

$$p_m = \frac{\gamma P_0 Q_H}{V l_k} \int_0^{l_k} \xi_m \cos kx dx = \frac{p_m \sin k l_k}{k l_k}, \tag{1}$$

where $\gamma = 1{,}4$ is the adiabatic constant; P_0 is atmospheric pressure; x is the coordinate of SVB length l_k; k is the wave number, c is the sound speed in air, Q_H is the stator core external area.
Thus process as statistical is considered when the level of sound pressure is the same in all points of the SVB and does not depend on coordinates. It is exact restriction for infrasonic and low frequencies while eighen frequencies of the SVB considerably above frequencies investigated are excited [2].

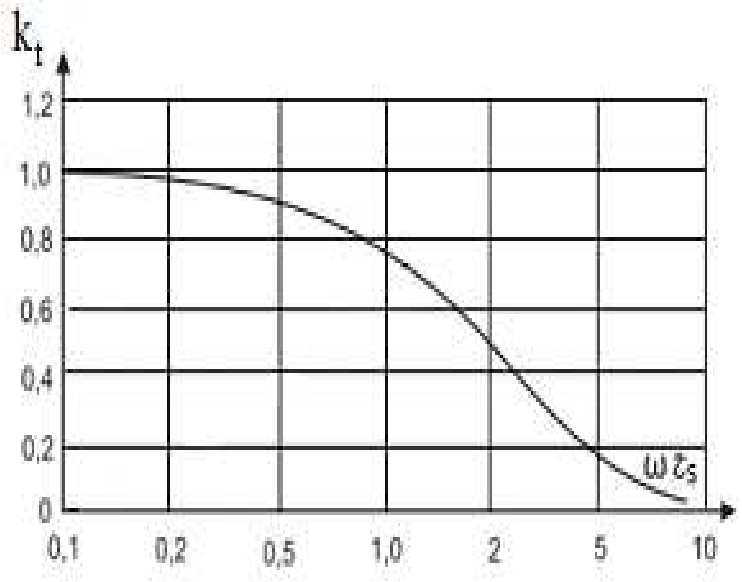

Figure 2: The SVB installation: N, S – the stator magnetic poles; SLM - the sound level meter; PC - the computer; M - the microphone; A - the acoustic short circuit effect; B - the negative correlation effect

An electric motor widely using in electric tools (for example drills), household appliances (washing machines) for research of motor noise was taken.
The installation for analysis of magnetic noise reduction including the SVB with the linear sizes 0,4m 0,5m 0,6m; the microphone with the amplifier; the sound level meter; the computer and the single-phase alternative current collector electric motor 800 Wt was developed (Fig.1).
All electric inputs into SVB and its cover during the measurements as much as possible were encapsulated and the electrical motor by the rubber damper was installed.

2 Effect of acoustic short circuit

The effect of acoustic short circuit for calculation of loudspeaker enclosure is well known. The alternative air compression and air stretch by opposite surfaces induction loudspeaker diaphragm are created. For example when sound pressure on the forward surface loudspeaker diaphragm is increased than one on the back surface is decreased. If loudspeaker acoustic baffle is absent the effect of acoustic short circuit on low frequencies is happened because of the diffraction of sound waves. The result sound pressure in surrounding space is decreased (Fig.1 curves A).
The similar acoustic effect to reduce of low frequency electric motor noise is applied. For study of the efficiency factor of motor noise reduction the basic magnetic noise component with carrying frequency 100 Hz in broadband spectrum of pressure is examined.
The air capacity inside of the electric motor in the form of volume formed by winding stator and rotor elements is considered. One hole with profile s through the stator core as the acoustic channel for passing internal sound fluctuations was drilled.

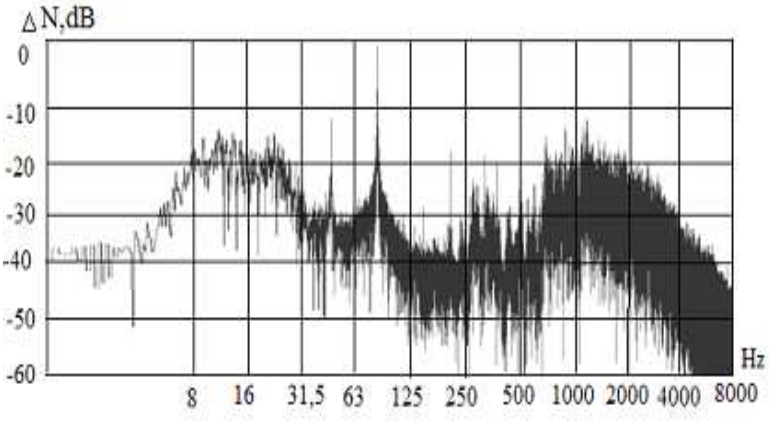

Figure 3: Frequency dependence between acoustic channel pressure and motor core external pressure

The passing internal sound fluctuations summarizing with antiphase stator external sound fluctuations are resulted. Then motor noise pressure into SVB as result of the interference of internal and external stator core fluctuations is decreased.
For example when motor internal air pressure by compression of stator core fluctuations is reduced then some air enters through the hole into motor. In the one hand the pressure work for this process as product of force on a way $uPs\Delta t$ is expressed. On the other hand the pressure into SVB is reduced and the work of the force for this process is $V\Delta P$. Then next equation is taken

$$uPs\Delta t = -V\Delta P, \tag{2}$$

were u is the speed of sound fluctuations, s is an area of hole, V is volume of SVB and P is acoustic pressure.
Passing to limit the equation (1) is presented

$$uPsdt = -VdP. \tag{3}$$

The common decision of the equation (3) after integration is shone

$$p = Ae^{-\frac{us}{V}t}, \tag{4}$$

were A is a constant of integration.
Other conditions being equal the noise pressure into SVB is summarized with external stator core pressure P_{ex} and some adding pressure of an acoustic channel

$$P_{SVB} = P_{ex} + Ae^{-\frac{us}{V}t} \tag{5}$$

The pressure into SVB changing under some law for example harmonious is considered

$$P_{SVB} = P_m \cos \omega t. \tag{6}$$

For simplification of the analysis the oscillating stator core as identity headphone diaphragm exciting flat sound waves is represented. Substituting (6) in (3) the

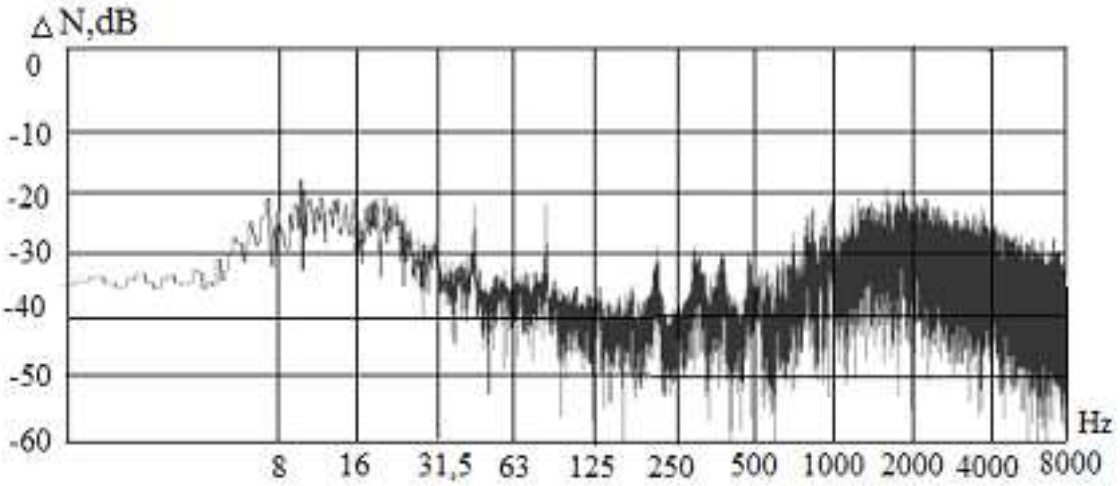

Figure 4: Noise pressure spectrogram for motor with a pier of stator core holes

differential equation having intensity in right part of the equation as the power characteristic of sound field is obtained:

$$usP_{SVB} + V\frac{dP_{SVB}}{dt} = uP_m \cos \omega t. \tag{7}$$

The decision in general view is represented in the form

$$P_{SVB} = p_m \cos(\omega t - \varphi) + Ae^{-\frac{us}{V}t}, \tag{8}$$

where A is a constant of integration, p_m is pressure in the acoustic channel, $PSVB$ - pressure into SVB.
The values of p_m and φ can be obtained as

$$p_m = P_m/\sqrt{1 + (\omega V/us)^2}, \varphi = arctg(\omega V/us). \tag{9}$$

If data about of the acoustic channel and the SVB is determined then preview equations can be found out finally but the product $\omega V/us$ especially if an equation for volumetric speed in the acoustic channel for laminar stream (the law Hagen-Poiseuille) is used in the form

$$u = \pi a_k^4 \Delta P/8\mu\lambda_k \tag{10}$$

and also ratio for active component of viscous friction in the channel reduced to area of diaphragm Sd is represented

$$r_c = 8\mu\lambda_k S_t/\pi a_k^4, \tag{11}$$

where a_k and λ_k are the radius and the length of the acoustic channel accordingly and μ is the air dynamic viscosity coefficient.
Then product $\omega V/us$ can be received in the form

$$\omega V/us = \omega c_f r_c = \omega \tau_s, \tag{12}$$

where cf is the air flexibility into SVB, ω is frequency of acoustic fluctuations and τs is a time constant of the system: channel - SVB or it is the acoustic low frequency filter.
The transfer coefficient of the acoustic channel kt into SVB can be found in the form

$$k_t = p_m/P_m = 1/\sqrt{1+(\omega\tau_s)^2}. \quad (13)$$

The frequency dependencies k_t in Fig.2 is shown.
The greatest effect of mutual antiphase compensation between the acoustic channel fluctuations and external motor core fluctuations at small $\omega\tau_k$ is shown in Fig. 2.

3 Negative correlation effect between two acoustic stator core channels

The construction with two opposite holes drilled through bipolar stator core as one in each magnetic pole has more effective result.
For discussion about effect of negative correlation method there are two motor noise pressure spectrograms into SVB: without stator core holes (Fig.3) and with a pier of stator core holes as two acoustic channels (Fig.4).
The frequency on abscissa (Hz) and the relative acoustic noise pressure (dB) on ordinate axis are constructed. The integrate level noise pressure 88 dB by the sound level meter $RFT0024$ was fixed. The maximum noise pressure value is corresponding of the basic magnetic motor noise frequency 100 Hz.
The frequency on abscissa (Hz) and the relative acoustic pressure (dB) on ordinate axis are constructed. The integrate level noise pressure 81 dB by the sound level meter $RFT0024$ was fixed. There are two effects of motor noise reduction in Fig.3: the acoustic short circuit (Fig.1 curves A) and the negative correlation effect for the frequency 100 Hz and first harmonics (Fig.1 curves B).

4 Analysis of the magnetic noise reduction effects

From comparison of spectrograms in Fig.2 and in Fig.3 the reducing motor noise pressure on 20 dB for the basic magnetic motor noise frequency 100 Hz is fixed. Integrate level pressure from 88 dB (without acoustic channels) to 81 dB (with acoustic channels) in wide strip is decreased.
As follows from stated the effective method developed making quieter electric motors for person protection in low sound and infrasonic frequencies and increasing functions of power electronics on transport is provided.

References

[1] Davydov V. V., Kolykhalin V. M. About compensation method of the electric motor noise.- B.: Vestnik BGTU named V.G. Shukhov, 2014.

[2] Kolykhalin V.M., Davydov V.V. Device of the electric motor noise compensation. Patent of the Russian Federation ϵ2528552, M. Federal serv., RU RU 2528552 C1, published 20.09.2014 Bul. 26

Kolykhalin V.M., St. Petersburg State Cinema and Television University, 191119, St. Petersburg, st. Pravdy, 13

A posteriori Error Bounds for numerical Solutions of Plate in Bending Problems

Vadim G. Korneev, Vladimir S. Kostylev

Vad.Korneev2011@yandex.ru

Abstract

For the efficient error control of numerical solutions of the solid mechanics problems, the two requirements are important: an a posteriori error bound has sufficient accuracy and computation of the bound is cheap in respect to the arithmetic work. The first requirement can be formulated in a more specific form of consistency of an a posteriori bound, assuming that it is not improvable in the order and, at least, coincides in the order with the a priori error estimate. Several new a posteriori error bounds are presented, which improve accuracy and reduce the computational cost. Also for the first time a new consistent guaranteed a posteriori error bound is suggested. The presented a posteriori bounds bear on the counter variational Lagrange and Castigliano principles which are valid for a wide class of problems.

Introduction

The use of adaptive algorithms can considerably reduce the cost of the stress and deformation states analysis of structures. The key module of such algorithms implements some a posteriori error bound or error indicator which allows adequate local thickening, *e.g.*, of the FEM (finite element method) mesh in consecutive steps. In the literature, illustrations of the efficiency of adaptive algorithms, arranged in this way, are numerous. Here only the references to [1, 2] are given, where several popular error indicators are compared when used for the adaptive FEM stress state analysis, and where many additional references can be found. There are also other strong incentives for the development of efficient APEB's (a posteriori error bounds), and nowdays many commercial computer codes like ANSYS, ABAQUS, FLUENT etc. contain modules allowing not only to solve the problem, but also to evaluate the majorant for the error.

For derivation of APEB's many techniques have been developed, which are well illuminated in the books of Verfurt [3] and Ainsworth & Oden [4], Neittaanmaki & Repin [5] and, *e.g.*, in recent papers of Ainsworth, Demkowicz & Kim [6] and Braess & Schoeberl [7]. Primarily they are related to the problems described by the 2^{nd} order partial differential equations with much less attention paid to the thin plate and shell bending problems, which are widely used in structures and

are discussed in this paper. We generalize upon thin plate bending problem the technique of Anufriev, Korneev & Kostylev [8, 9] based on the use of the *exactly equilibrated stress fields*. It allowed to suggest efficient a posteriori error bounds for the finite element solutions of the theory elasticity problems and other 2^{nd} order elliptic equations. In [8, 9] it was shown by many numerical experiments that these bounds are computationally cheap and provide very good effectiveness indices.

Classical formulations of thin plate and shell bending problems are described by the 4^{th} order elliptic partial differential equations and systems of equations. At present, numerical solutions of such equations are primarily obtained with the use of the mixed methods. However, at least sometimas, solution of the 4^{th} order elliptic equations is, for some reasons, preferable. This inspired development of the a posteriori estimators for the thin plate bending problem in classical formulations, including as conform [1, 10, 11] so different types of not conform and DG (discontinuous Galerkin) methods, see [12, 13, 14, 15]. A part of this paper concentrates on the conform finite element approximations and expand the technique of [8, 9], which in this case can be termed the *technique of the exactly equilibrated resultants*. Our main goals are to reduce the computational cost of the evaluation of the bounds and to make them sharper. For instance, in general the residuals, entering a posteriori bounds, contain second order derivatives of the approximate values of the moments. In the contrast, some bounds in this paper contain only first derivatives. More over, the norms in the right parts of the bounds contain not first derivatives of the moments, but one-dimensional integrals of them with variable upper limits. Clearly, both these features improve the accuracy of our a posteriori bounds. This is supported by the estimate of the order of convergence of the right part of the a posteriori bound, see Proposition 1. Finally, in Section 2, one of the most important a posteriori bounds of the paper is presented for the problem in an arbitrary sufficiently smooth domain. We term this bound *consistent* implying that the right part of it has the same order of smallness as predicted by the corresponding unimprovable a priori error bound.

To concentrate on the basic fatures of the exactly equilibrated resultants technique, the model problem of a thin plate in rectangle is considered Section 1. However, there is no principal difficulties visible for expansion of the bounds to the cases of more general domains and more general equations, e.g., of thin linearly elastic shells. For supporting the latter, we note that the equilibrated resultants and the spaces of the self-equilibrated resultants were defined for such problems in [16] and used there for construction of numerical algorithms.

The paper is arranged as follows. In Section 1 we consider approach based on direct of the equilibrated testing moments. In Subsection 1.1 the problem of thin linearly elastic plate bending is formulated. Also an example of a posteriori error bounds by means of exactly equilibrated moments of smooth approximate solutions are presented. Subsection 1.2 is allocated for a posteriory estimator of the type termed often functional error majorants. The use of smoothed moments, recovered from FEM, for the error estimation is considered in Subsection 1.3. The consistent a posteriori bound is given in Section 2.

The notation $\|\phi\|_{H^k(\mathcal{Q})}$ will stand for the norms in the Sobolev's spaces $H^k(\mathcal{Q})$ on a

domain $\mathcal{Q}$

$$\|\phi\|^2_{H^k(\mathcal{Q})} = \|\phi\|^2_{L_2(\mathcal{Q})} + \sum_{l=1}^{k} |\phi|^2_{H^l(\mathcal{Q})},\ |\phi|^2_{H^l(\mathcal{Q})} = \sum_{q_1+q_2=l} \int_{\mathcal{Q}} (\partial^l \phi / \partial x_1^{q_1} \partial x_2^{q_2})^2 dx,$$

where $\|\phi\|^2_{L_2(\mathcal{Q})} = \int_{\mathcal{Q}} \phi^2 dx_1 dx_2$. If $\mathcal{Q} = \Omega$, the simpler notations $\|\cdot\|_0$, $\|\cdot\|_k$ and $|\cdot|_k$ will be used for $\|\cdot\|_{L_2(\Omega)}$, $\|\cdot\|_{H^k(\Omega)}$ and $|\cdot|_{H^k(\Omega)}$, respectively. The finite element space is denoted as $V(\Omega)$ and it is always assumed that the finite element assemblage satisfies the generalized conditions of quasiuniformity with some mesh parameter $h > 0$, see [17].

1 A posteriori error bounds by means of exactly equilibrated moments

1.1 Problem and equilibrated bounds

For a model problem, it will be used the thin homogeneous linearly elastic plate in the square $\pi_1 = (0,1) \times (0,1)$ of the constant thickness h clamped at the boundary $\partial\pi_1$. Its deflection of the middle surface of the plate under the transverse load is described by the equation

$$D\Delta\Delta u = f(x),\ x = (x_1, x_2) \in \pi_1,\ u(y) = \frac{\partial u}{\partial n}(y) = 0,\ y = (y_1, y_2) \in \partial\pi_1 \quad (1)$$

where $D = Eh^3/(12(1-\nu^2))$ and n is the external normal to the boundary, E and ν are the elasticity module and Poisson coefficient. The vector $M = (M_{1,1}, M_{2,2}, M_{1,2})^{\mathrm{T}}$ of moments satisfy the equilibrium equation

$$L_M M \equiv \frac{\partial^2 M_{1,1}}{\partial x_1^2} + 2\frac{\partial^2 M_{1,2}}{\partial x_1 \partial x_2} + \frac{\partial^2 M_{2,2}}{\partial x_2^2} = f. \quad (2)$$

The *energy norms* are important characteristics of the error of approximate solutions of the problem, the squares of two norms can be written as

$$\begin{aligned} \lfloor v \rfloor^2_U &= \frac{D}{2} \int_{\pi_1} \left[(\frac{\partial^2 v}{\partial x_1^2})^2 + (\frac{\partial^2 v}{\partial x_2^2})^2 + 2\nu \frac{\partial^2 v}{\partial x_1^2} \frac{\partial^2 v}{\partial x_2^2} + 2(1-\nu)(\frac{\partial^2 v}{\partial x_1 \partial x_2})^2 \right] dx, \\ \lfloor M \rfloor^2_M &= \int_{\pi_1} M^{\mathrm{T}} \Xi M dx \\ &= \frac{1}{2D(1-\nu^2)} \int_{\pi_1} \left[M_{1,1}^2 + M_{2,2}^2 - 2\nu M_{1,1} M_{2,2} + 2(1+\nu) M_{1,2}^2 \right] dx \end{aligned} \quad (3)$$

where for the matrix Ξ stands

$$\Xi = \frac{1}{2D(1-\nu^2)} \begin{pmatrix} 1 & -\nu & 0 \\ -\nu & 1 & 0 \\ 0 & 0 & 2(1+\nu) \end{pmatrix}.$$

Suppose $\tilde{u}(x)$ is an approximation of the exact solution u, satisfying the boundary condition in (1), and $\Phi = (\Phi_{1,1}, \Phi_{2,2}, \Phi_{1,2})^{\mathrm{T}}$ is the corresponding vector of moments.

For the first step, the case of a smooth $\tilde{u}(x)$, *e.g.*, having 4^{th} bounded derivatives is considered.If $Z = (Z_{1,1}, Z_{2,2}, Z_{1,2})^{\mathrm{T}}$ is any vector of sufficiently smooth moments, which satisfy (2), then the bound

$$\lfloor u - \tilde{u} \rfloor_U^2 \leq \lfloor Z - \Phi \rfloor_M^2 \tag{4}$$

is the direct consequence Lagrange and Castigliano principles, see, *e.g.*, [18].
In order to get satisfactory bounds (4), the equilibrated vector of moments Z should be as close as possible to the exact one. Since as a rule the most reliable information about the exact solution is contained in the approximate solution $\tilde{u}$, it is natural to use it for definition of Z. The simplest way to take it into account is to adopt $Z_{k,l} = \Phi_{k,l}$ for two components of the vector Z and define the remaining one from the equilibrium equation (2). For instance, one can set $Z_{k,k} = \Phi_{k,k}$, $k = 1, 2$, and take into account that

$$\frac{\partial^2 Z_{1,2}}{\partial x_1 \partial x_2} = 0.5 \left[f - \frac{\partial^2 \Phi_{1,1}}{\partial x_1^2} - \frac{\partial^2 \Phi_{2.2}}{\partial x_2^2} \right] \text{ in } \pi_1. \tag{5}$$

Taking these facts, the boundary conditions and the notation $\mathbb{D} = 2D(1-\nu)$ into account, one comes to the bound (4) of the form

$$\lfloor u - \tilde{u} \rfloor_U^2 \leq \mathbb{D}^{-1} \int_{\pi_1} \left\{ 2\Phi_{1,2} - \int_0^{x_2} \int_0^{x_1} f(\eta) d\eta + \right.$$
$$\left. + \sum_{k=1,2} \int_0^{x_{3-k}} \left[\frac{\partial \Phi_{k,k}}{\partial x_k}(x_k, \eta_{3-k}) - \frac{\partial \Phi_{k,k}}{\partial x_k}(0, \eta_{3-k}) \right] d\eta_{3-k} \right\}^2 dx \tag{6}$$

Boundary conditions in (1) are *essential* and, at the numerical solution, e.g., by Galerkin and FE methods, can be satisfied exactly, i.e., $\Phi_{1,2} = 0$ on Γ_0. With the use of this the a posteriori error bound can be also transformed into

$$\lfloor u - \tilde{u} \rfloor_U^2 \leq \mathbb{D}^{-1} \int_{\pi_1} \left[\int_0^{x_2} \int_0^{x_1} \left[f(\eta) - L_M \Phi(\eta) \right] d\eta \right]^2 dx. \tag{7}$$

The bounds (6), (7) are more "symmetric" than the corresponding bounds at the choice, e.g., $Z_{1,1} = \Phi_{1,1}$, $Z_{1,2} = \Phi_{1,2}$ and computation of $Z_{2,2}$ from (2).
It should be underlined that in the contrast with a posteriori error bounds of many other types the evaluation of (6), (7) do not require any other computations (e.g., solution of global or local systems of algebraic equations for the rezidual minimization or local discrete equilibration etc.) except the evaluation of integrals.

1.2 Functional error majorants

For some purposes it is convenient to have an a posteriori bound with an arbitrary testing resultant vector, *i.e.*, not satisfying the equilibrium equations. This is the case, when the right part of the a posteriori bound is supposed to be minimized with the help of such vectors. Such bounds directly follow from the bounds of the previous section. Let $Y = (Y_{1,1}, Y_{2,2}, Y_{1,2})^{\mathrm{T}}$ be an arbitrary vector, sufficiently smooth on $\overline{\pi}_1$, and $Y^{Eq} = Y + \delta Y$ be the equilibrated vector. The latter can be defined by Y exactly, as it was suggested to define Z by Φ and, in particular, by

setting $Y^{Eq}_{k,k} = Y_{k,k}$, $k = 1, 2$, and defining $Y^{Eq}_{1,2}$ from (5), in which $\Phi_{k,k}$ are replaced by $Y_{k,k}$. At that, there is no difficulties to satisfy the boundary condition $Y_{1,2} = 0$ on $\partial\pi_1$. In this way, we come to the first one of the bounds

$$\lfloor u - \tilde{u} \rfloor_U \le \left\lfloor Y^{Eq} - \Phi \right\rfloor_M \le \lfloor Y - \Phi \rfloor_M + \lfloor \delta Y \rfloor_M \le \lfloor Y - \Phi \rfloor_M + \Xi(Y_{1,2}, f, Y^{[1,2]}), \quad (8)$$

in which $Y^{[1,2]} = (Y_{1,1}, Y_{2,2}, 0)$ and

$$\Xi^2(Y_{1,2}, f, Y^{[1,2]}) = \mathbb{D}^{-1} \int_{\pi_1} \left\{ 2Y_{1,2} - \int_0^{x_2} \int_0^{x_1} f(\eta) d\eta + \right.$$

$$\left. + \sum_{k=1,2} \int_0^{x_{3-k}} \left[\frac{\partial Y_{k,k}}{\partial x_k}(x_k, \eta_{3-k}) - \frac{\partial Y_{k,k}}{\partial x_k}(0, \eta_{3-k}) \right] d\eta_{3-k} \right\}^2 dx.$$

The second bound follows from the first one by the triangular inequality and can be rewritten in equivalent but simpler form

$$\lfloor u - \tilde{u} \rfloor_U \le \left\lfloor Y^{Eq} - \Phi \right\rfloor_M \le \left\lfloor Y^{[1,2]} - \Phi^{[1,2]} \right\rfloor_M + \Xi(\Phi_{1,2}, f, Y^{[1,2]}). \quad (9)$$

Clearly, the bound (7) turns into

$$\lfloor u - \tilde{u} \rfloor_U \le \lfloor Y - \Phi \rfloor_M + \left\{ \mathbb{D}^{-1} \int_{\pi_1} \left[\int_0^{x_2} \int_0^{x_1} [f(\eta) - L_M Y(\eta)] d\eta \right]^2 dx \right\}^{1/2}. \quad (10)$$

The drawback of this bound in comparison with (8), (9) is that it contains 2^{nd} derivatives of the components of Y instead first derivatives in (8), (9). For any smooth function $F(x)$ on rectangle $\Pi = (0, a) \times (0, b)$, vanishing on the intersections of $\partial\Pi$ with the axes, there is valid the inequality $\int_\Pi F^2 dx \le c \int_\Pi \left(\partial^2 F / \partial x_1 \partial x_2\right)^2 dx$ with $c \le 16a^2b^2/\pi^4$, from where and (10) it also follows that

$$\lfloor u - \tilde{u} \rfloor_U \le \lfloor Y - \Phi \rfloor_M + \left\{ \frac{c}{\mathbb{D}} \int_{\pi_1} [f(x) - L_M Y(x)]^2 dx \right\}^{1/2}. \quad (11)$$

The bound is only by the constant different from the popular bound, found in Neittaanmaki & Repin [5], in which $c = c_\Omega$ is the depending only on the domain constant from the Friedrichs type inequality. It is assumed, and it is often realized in practice, that the appropriate Y is found by minimization procedure applied to the right part of (11).

The bound (8), (9) has the advantages summarized as follows.

i) They do not contain constants beside one naturally entering the energy norm.

ii) The minimization of the right parts is done with respect only of two components of Y, and, therefore, the dimension of the system of algebraic equations to be solved is reduced by $\sim 1/3$.

iii) (8), (9) contain on the right only first derivatives of $Y_{k,k}$, $k = 1, 2$, implying that the finite elements of the class C can be used for definition of $Y_{k,k}$.

iv) Under the integral over π_1 we have the one-dimensional integrals of $\partial Y_{k,k}/\partial x_k$, which can additionally improve accuracy.

1.3 The use of smoothed finite element solutions

The minimization of the right parts can be circumvented if, before the equilibration, the FEM solution is subjected to some procedure of smoothing, as it is often done in many other approaches to the a posteriori error estimation, see [3, 4]. For instance, one can use the bound (6) with the equilibrated vector Z, in which $Z_{k,k} = \tilde{\Phi}_{k,k},\ k = 1, 2$, where $\tilde{\Phi}_{k,k}$ are smoothed fields $\Phi_{k,k}$, whereas $Z_{1,2}$ is defined from (5) with $\Phi_{k,k}$ replaced by $\tilde{\Phi}_{k,k}$. This transforms the estimate (9) into

$$\lfloor u - \tilde{u} \rfloor_U \le \Psi(h,u), \quad \Psi(h,u) = \text{where}$$
$$= \left\{ \int_{\pi_1} \left[(\Lambda_{1,1})^2 + (\Lambda_{2,2})^2 - 2\nu \Lambda_{1,1}\Lambda_{2,2} \right] dx \right\}^{1/2} + \Xi(\Phi_{k,k}, f, \tilde{\Phi}_{k,k}), \quad (12)$$

where $\Lambda_{k,k} = \Phi_{k,k} - \tilde{\Phi}_{k,k}$. One of the options is conveniently to define the components $\tilde{\Phi}_{k,k}$ as functions of a finite element space $V(\pi_1)$ of the class C^1 or even of the much simpler class C. In particular, it can be the same finite element space, which is used for solving the problem in (1). For each node $x^{(i)} \in \overline{\pi}_1$, the nodal parameters, *i.g.*, values of the moments and, if necessary, their derivatives, are evaluated by the averaging with weights of the corresponding values of $\Phi_{k,k}$ and their derivatives at $x^{(i)}$ over all finite elements having $x^{(i)}$ for the node. We will call the procedure of obtaining of smothed moment $\tilde{\Phi}_{k,l}$ consistent, if for $\tilde{\Phi}_{k,l}$ and $\Phi_{k,l}$ the same up to the constant estimates of convergence hold.

Proposition 1. *Suppose the FE mesh is a square mesh of size h, $u \in H^{p+1}(\Omega)$ and the convergence estimates (16) hold. Suppose also that the procedure of obtaining of smoothed moments $\tilde{\Phi}_{k,k}$ is consistent. Then $\Psi(h,u)$ satisfies the inequality $\Psi(h,u) \le c h^{p-5/2} |u|_{H^{p+1}(\Omega)}$ and can be calculated for $\mathcal{O}(N)$ arithmetic operations, where N is the dimension of the FE space.*

The proof is omitted, and it is worth mentioning that it is completed without use of the super-convergence property of finite element solutions, which under some additional conditions can take place and allows to improve the order of $h^{p-5/2}$ in the above estimate up to $h^{p-3/2}$. If the mesh is not rectangular, the computational cost of $Z_{1,2}$ can became super-linear with respect to N, even in the case of the quasiuniform mesh. Some procedures, which are not discussed in this paper, can be implemented to reduce the cost.

2 Consistent functional error majorant

The most desirable a posteriori error bound provides the exact order of accuracy, *i.e.*, not improvable for the particular numerical method, used for solution of the boundary value problem. In this section, it will be presented the a posteriori error bound, the order of which is the same with the approximation error for the finite element interpolation of the exact solution. We consider the problem

$$\Delta\Delta u = f(x), \quad x \in \Omega, \qquad u(y) = \frac{\partial u}{\partial n}(y) = 0, \quad y \in \partial\Omega, \quad (13)$$

under the assumptions that the domain Ω with the boundary $\partial\Omega$ are sufficiently smooth and $f \in L_2(\Omega)$. From these assumptions it follows that for any $f \in L_2(\Omega)$,

the solution u of the problem (13) satisfies the inequality

$$\|u\|_4 \leq c_\Omega \|f\|_0 , \quad c_\Omega = const. \tag{14}$$

We assume that $\tilde{u} \in H^2(\Omega)$ is the approximate solution of the problem by a compatible finite element method, *i.e.*, of the class C^1, which satisfies boundary conditions of (13) and that the finite element assemblage satisfies generalized conditions of quasiuniformity (see [17]) with the mesh parameter h.
To formulate our result we need to introduce the spaces $H^2(\Omega, \Delta\Delta) = \{v \in H^2(\Omega) : \Delta\Delta v \in L_2(\Omega)\}$ and $\mathbf{L}_2(\Omega, L_M) = \{Y \in (L_2(\Omega))^2 : L_M Y \in L_2(\Omega)\}$.
Theorem 1. *Let u be the solutin of the problem and above assumptions be fulfilled. Then the error of the finite element solution of the problem (13) satisfies the a posteriori bounds*

$$\begin{aligned} &|u - \tilde{u}|_2^2 \leq ch^4 \|f - \Delta\Delta w\|_0^2 + 2|w - \tilde{u}|_2^2 , \\ &|u - \tilde{u}|_2^2 \leq ch^4 \|f - L_M Y\|_0^2 + \left[\int_\Omega \sum_{k+l=2} (\tfrac{\partial^2 \tilde{u}}{\partial x_1^k \partial x_2^l} - Y_{k,l})^2\right]^{1/2} , \end{aligned} \tag{15}$$

where w and Y are arbitrary function and vector field from the spaces $H^2(\Omega, \Delta\Delta)$, and $\mathbf{L}_2(\Omega, L_M)$, respectively, and $c = 4c_{2,4}^2 c_\Omega^2$ is a constant with $c_{2,4}$ from (16).
The a posteriori bound (15) possesses several good properties. Suppose that $u \in H^{p+1}(\Omega)$, $p \geq 3$, and the a priori error estimates

$$\|(u - \tilde{u})\|_k \leq c_{k,p} h^{p-k+1} \|u\|_{p+1} , \quad k = 0, 1, 2, \quad c_{k,p} = \text{const}. \tag{16}$$

If to take for w a properly smoothed finite element solution, which is denoted as $\tilde{u}_{sm}$, then the right part of (15) has the same order h^{p-k+1} as the right part of the a priori error estimate (16), assuming $u \in H^{p+1}(\Omega)$, $p \geq 3$. Therefore, the bound (15) is consistent.
The outline of the proof is similar and it results in similar bounds as for FEM solutions of 2^{nd} order elliptic partial differential equations. For simplicity, the proof of a posteriori bound quite similar to (15) will be given below for the error of the finite element solution of the Poisson equation

$$Lu \;=\; -\Delta u = f(x), \; x \in \Omega, \qquad u\,|_{\partial\Omega} = 0. \tag{17}$$

With respect to the problem (17) and its finite element solution three assumptions will be used. i) The domain Ω is sufficiently smooth, $f \in L_2(\Omega)$ and, therefore, for each such f the inequality

$$\|u\|_2 \leq c_\Omega \|f\|_0 , \; c_\Omega = const, \tag{18}$$

holds. ii) The FEM mesh is a quasi-uniform mesh of size h and the conform FEM solutuion $\tilde{u}$ satisfies boundary condition $\tilde{u}|_{\partial\Omega} = 0$. iii) The solution u of the problem belongs $H^l(\Omega)$ with some integer l, $1 \leq l \leq p + 1$, and

$$\|(u - \tilde{u})\|_k \leq c_{k,p} h^{l-k} \|u\|_l , \; k = 0, 1,$$

where p characterizes the order of the polynomials from the space on the respective reference element.

According to the assumptions and the technique of Sea, see, *e.g.*, [19], the error in the $L_2(\Omega)$-norm satisfies also the inequality

$$\|(u-\tilde{u})\|_0 \le c_{1,2}c_\Omega h \|u-\tilde{u}\|_1 =: c_{1,2,\Omega}h \|u-\tilde{u}\|_1 , \ c_{1,2,\Omega} = \text{const}. \tag{19}$$

The subsidiary problem

$$Lu = -\Delta u + \sigma u = f_1(x), \ x \in \Omega, \ u\,|_{\partial\Omega} = 0, \tag{20}$$

with $f_1 = f + \sigma u$ and an arbitrary positive number σ, obviously, has the same solution with (17). According to (17), (18) and Theorem 22 of [19],

$$\|u-\tilde{u}\|_1^2 + \sigma \|u-\tilde{u}\|_0^2 \le \sigma^{-1} \|f_1 - \sigma\tilde{u} - \Delta w\|_0^2 + \|u-w\|_1^2 = \\ \sigma^{-1} \|f - \sigma(u-\tilde{u}) - \Delta w\|_0^2 + \|\tilde{u}-w\|_1^2 , \tag{21}$$

where,

$$\sigma^{-1} \|f - \sigma(u-\tilde{u}) - \Delta w\|_0^2 = \\ \sigma^{-1} \|f - \Delta w\|_0^2 + \sigma \|(u-\tilde{u})\|_0^2 + 2\int_\Omega (u-\tilde{u})(f-\Delta w)dx, \tag{22}$$

and, therefore, for any $\varepsilon>0$

$$2\int_\Omega (u-\tilde{u})(f-\Delta w)dx \le \varepsilon \|(u-\tilde{u})\|_0^2 + \frac{1}{\varepsilon}\|f-\Delta w\|_0^2 . \tag{23}$$

If to set $\varepsilon = 0.5 \ \|(u-\tilde{u})\|_1^2 / \|u-w\|_0^2$ and take into account (11), then one comes to the inequality $1/\varepsilon \le 2\ c_{1,2,\Omega}^2 h^2$, which when combined with (21) – (23) yields

$$0.5\|u-\tilde{u}\|_1^2 \le [\sigma^{-1} + 2c_{1,2,\Omega}^2 h^2] \|f-\Delta w\|_0^2 + \|\tilde{u}-w\|_1^2 \le ch^2 \|f-\Delta w\|_0^2 + \|\tilde{u}-w\|_1^2$$

Since σ can be any positive number, this inequality above approves the bound

$$\|u-\tilde{u}\|_1^2 \le ch^2 \|f-\Delta w\|_0^2 + 2\|\tilde{u}-w\|_1^2 , \ c = 4c_{1,2,\Omega}^2 . \tag{24}$$

The bound (24) is consistent. Together with (15) they greatly improve accuracy of the similar type posteriori bounds obtained for the approximate solutions of 2^{nd} and 4^{th} order elliptic equations earlier [4, 8, 10]. The difference is in the appearance of the multipliers h^2 and h^4 before the L_2-norns in (24), (15), respectively, instead of constants in the earlier bounds.

3 Concluding remarks

L_2-norms of the residual type terms multiplied by constants are a common place in the a posteriori error majorants of approximate solutions of the elliptic equations. In the case of the thin plate bending problem this term depends on the 2^{th}-order derivatives of the testing vector of moments. In the paper we obtained the majorant in which this term is replaced by the other one depending only on the firs derivatives. This considerably simplifies the numerical realization of the error majorant and at

the same time essentially improves accuracy. Additionally we obtained the majorant with the same as in the papers of other authors L_2-norm of the residual type term, but with the multiplier $\mathcal{O}(h^2)$ instead of a constant. This improves the accuracy of the majorant in the two orders of h making the majorant consistent with the a priori error bounds. At the derivation of these majorant, only general properties of solutions of the finite element method and elliptic boundary value problems were used. For this reason, there are no difficulties to generalize such error bounds to a wide range of finite element methods and elliptic equations. The generalization of the consistent a posteriori error majorants on the elliptic equations of the order $2n$ is considered in the forthcoming paper [20].

Research was supported by the grant from the Russian Fund of Basic Research, project N 15-01-08847 a.

References

[1] Gratsch Th., Bathe K.-J. A posteriori error estimation techniques in practical finite element analysis. Computers and Structures. 2005. No. 83. Pp. 235–265.

[2] Zienkiewicz O. C., Zhu J.Z. A simple error estimator and adaptive procedure for practical engineerng analysis. International Journal for Numerical Methods in Engineering. 1987. No. 24. Pp. 337-357.

[3] Verfurt R. A Review of a Posteriori Error Estimation and Adaptive Mesh-Refinement Techniques. Chichester: Wiley. 1996.

[4] Ainsworth M., Oden J.T. A posteriori estimation in finite element analysis New York John: Wiley & Sons, Inc. 2000. 243 p.

[5] Neittaanmaki P., Repin S.I. Reliable methods for computer simulation Error control and a posteriori esti-mates. New York: Elsevier. 2004. 305 p.

[6] Ainsworth M., Demkowicz L., & Kim C.-W. Analysis of the equilibrated residual method for a posterioti estimation on meshes with hanging nodes. Computer Meth. Appl. Math. Engrg. 2007, No. 196(37-40). Pp. 3493-3507.

[7] Braess D. & Schoberl J. Equilibrated residual error estimator for Maxswell's equations. Math. Comp. 2008. No. 77. Pp. 651-672.

[8] Anufriev I. E., Korneev V. G., Kostylev V. S. Exactly equilibrated fields, can they be efficiently used for a posteriori error estimation? //Uchenyye zapiski Kazanskogo gos. universiteta, Seriya: Fiziko-matematicheskiye nauki. Kazan: Kazanskiy gos. universitet. 2006. No. 148. Str. 94-143.

[9] Korneev V.G. Prostyye algoritmy vychisleniya aposteriornykh otsenok chislennykh resheniy ellipticheskikh uravneniy [Simple algorithms for computation of a posteriri bounds for numerical solutions of elliptic equations] // Uchenyye zapiski Kazanskogo universiteta, Seriya: Fiziko-matematicheskiye nauki. Kazan: Kazanskiy gos. universitet. 2011. No. 154. Str. 11-27. (rus)

[10] Neittaanmaki P., Repin S.I. A posteriori error estimates for boundary-value problems related to the biharmonic operator. East-West J. Numer. Math. 2001. No. 2. Pp. 157–178.

[11] Adjerid S. A posteriori error estimates for fourth-order elliptic problems. Comput. Methods Appl. Mech. Eng. 2002. No. 191. Pp. 2539–2559.

[12] Liu K. A Gradient Recovery-based a Posteriori Error Estimators for the Ciarlet - Raviart Formulation of the Second Biharmonic Equations. Applied Mathematical Sciences. 2007. No. 1. Pp. 997 – 1007.

[13] Beirao da Veiga, Niiranen J., Stenberg R. L. A posteriori error estimates for the Morley plate bending element. Numer. Math. 2007. No. 106. Pp. 165–179.

[14] Hansbo P., Larson M. G. A posteriori error estimates for continuous/discontinuous Galerkin approxima-tions of the Kirchhoff–Love plate. Preprint 2008:10. Geoteborg, Sweden. Chalmers University of Technology. 2008.

[15] Georgoulis E. H., Houston P., Virtanen J. An a posteriori error indicator for discontinuous Galerkin ap-proximations of fourth-order elliptic problems. IMA Journal of Numerical Analysis. 2011. No. 31. Pp. 281–298.

[16] Korneev V. G. Numerical solution in stresses of problems of shell theory using oblique-angled meshes. USSR Computational Mathematics and Mathemetical Physics. 1981. No. 21. Pp. 184-194.

[17] Korneev, V.G., & Langer, U. Dirichlet-Dirichlet Domain Decomposition Methods for Elliptic Problems, h and hp Finite Element Discretizations. New Jesey-London-Singapore-Beijing: World Scientific. 2015.

[18] Abovskiy N.P., Andreyev N.P., Deruga A.P. Variatsionnyye printsipy v teorii uprugosti i teorii odolochek [Variational principles in theory elasticity and shells theory]. Moskow. Nauka. 1978.

[19] Aubin J.-P. Approximation of elliptic boundary-value problems. New York-London-Sydney-Toronto. Wiley-Interscience. 1972.

[20] Korneev V.G. O tochnosti aposteriornyh funktsionalЎnyh mazhorant pogreshnosti priblizhennyh reshenii ellipticheskih uravnenii (On the accuracy of a posteriori functional error majorants for approximate solutions of elliptic equations), Doklady Academii Nauk. Matematika. (accepted for publication)

Vadim G. Korneev, St. Petersburg State University, Russia

In general, any smooth $w(\mathrm{x})$, $x \in \pi_1$, can be represented as

$$w(x) = \int_0^{x_2} \int_0^{x_1} \frac{\partial^2 w}{\partial x_1 \partial x_2}(\eta) d\eta + w(0, x_2) + w(x_1, 0) - w(0, 0). \tag{25}$$

and, therefore,

$$Z_{1,2} = \frac{1}{2} \int_0^{x_2} \int_0^{z_1} \left[f(\eta) d\eta - \sum_{k=1,2} \left(\frac{\partial^2 \Phi_{1,1}}{\partial \eta_1^2}(\eta) \right) \right] d\eta + \varphi_1(x_2) + \varphi_2(x_1) + c_\circ, \tag{26}$$

where $\varphi_k(x_{3-k})$ and $c_\circ$ are arbitrary functions and a number, respectively. However, from the boundary condition in (1), it follows that $M_{1,2} = 0$ on $\partial\pi_1$, and it can be accepted $Z_{1,2} = 0$ on the set Γ_0, which is the union of the left and the lower edges of π_1 and the point (0,0). As the result of this one can take $\varphi_k(x_{3-k}) \equiv 0$, $c_\circ = 0$ and set

$$Z_{1,2} = \frac{1}{2}\left\{\int_0^{x_2}\int_0^{z_1} f(\eta)d\eta - \int_0^{x_2}\left[\frac{\partial\Phi_{1,1}}{\partial x_1}(x_1,\eta_2) - \frac{\partial\Phi_{1,1}}{\partial x_1}(0,\eta_2)\right]d\eta_2 \right.$$
$$\left. - \int_0^{x_1}\left[\frac{\partial\Phi_{2,2}}{\partial x_2}(\eta_1,x_2) - \frac{\partial\Phi_{2,2}}{\partial x_2}(\eta_1,0)\right]d\eta_1\right\}. \quad (27)$$

The Comparison of Two Types of Boundary Conditions for the Active Electrode in Simulation of Ionic Wind

Kostin P.A., Poluektova K.D., Elagin I.A., Markovskii P.Y.
p.kostin@2014.spbu.ru

Abstract

The paper deals with computer simulation of ionic wind in the needle-plane electrode system with the positive polarity of the active electrode. Complicated processes in the corona sheath are substituted with two types of boundary conditions at the anode. The first method utilizes an approach, where the density of the flow of positive ions is set at the active electrode as the linear function of the electric field strength. Defining the function requires experimental values of ignition voltage of corona discharge measured for each electrode in the system under simulation. The second method uses a more complicated boundary condition for the ion flow, which bases on calculation of the number of ionization collisions near the anode surface. The advantage of the model is that it requires no experimental input data at a change of the electrode configuration. To verify the performance of the models, the structure of ionic wind in the needle-plate system was studied experimentally. The I-V curves of corona discharge were measured over a wide range of voltages. Air velocity distributions in the inter-electrode gap were obtained by the Particle Image Velocimetry method. Distributions of the electric field, charge density and integral value of the current were calculated for both models. Air velocity distributions in the ionic wind jet were obtained and analyzed. The simulation and experiment results agree within sufficient accuracy.

Keywords: Ionic wind, Electrohydrodynamics, Corona discharge, Needle-Plane, Computer Simulation, PIV method.

1 Introduction

Ionic wind is generated by the corona discharge due to the momentum transfer from ions moving into the inter-electrode gap to neutral molecules [1]. The phenomenon underlies a number of notable modern technologies, for example, it enables the creation of silent coolers for air ventilation [2] and efficient electrostatic precipitators [1]. The devices, based on corona discharge and ionic wind, demonstrate a number of advantages over earlier types: they can function in a wide range of temperatures, produce no noise, and have no moving parts, thus providing a higher reliability.

However, the actual development of such equipment pivots on a detailed insight into the physical processes that cause ionic wind. Computer simulation of the processes requires significant computational power; therefore, different simplified models are relevant. The work aims to compare two idealized models. Simplification consisted of substitution of complicated processes in the corona sheath with a boundary condition at the active electrode. The first method utilizes an approach, when the density of the flow of positive ions is set at the active electrode as the linear function of the electric field strength. Another way of setting a boundary condition was presented in [3]. In case of the negative polarity of the high voltage electrode, it represents a setting of the variation rate of electron flow from the electrode. Work [4] adopted this option for the positive polarity case.

2 Formulation of the problem

The calculation used the finite element method in the Comsol Multiphysics software for the needleвЃ“plane electrode system with axial symmetry S (Fig.1). The distance between the electrodes is fixed ($d = 20\ mm$). The region of interest (hashed on the figure) is bounded from below by ground electrode B. Another boundary Pz separates the region of interest and outer air and is formally open. A sharp tip of anode A (needle) is considered to be spherical. The sphere radius ($0.125\ mm$) was found by using photos of real needle that had been used in the experimental part of the research.

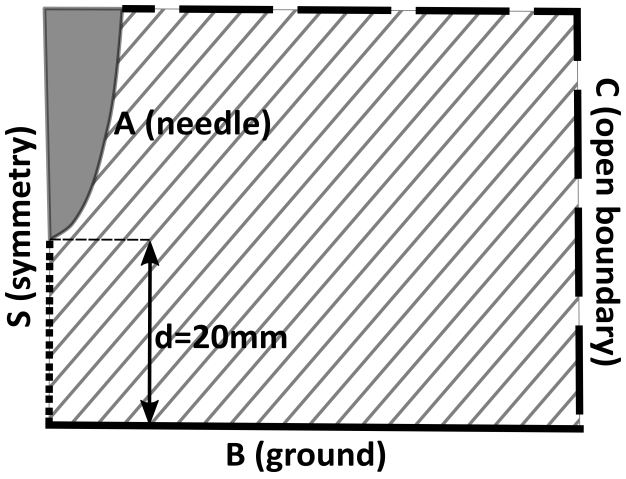

Figure 1: Schematic of the under study system

The electrohydrodynamics equation set (1) in general case describes the outer area of corona discharge, where ion-wind velocities are calculated [3]. The set includes the Poisson equation (1.1), the Nernst-вЃ“Planck equation (1.2) and NavierвЃ“Stokes equations (1.3)–(1.4), which are written in the incompressibility approximation. The interaction of ions and neutral air molecules, which sets the air in motion, is expressed by introducing the volume force $\mathbf{f} = en_i\mathbf{E}$ that appears in the right-hand part of the equation (1.3).

$$\begin{cases} \Delta\varphi = -\frac{e n_i}{\varepsilon}, \ (\mathbf{E} = -\nabla\varphi) & (1.1) \\ \frac{\partial n_i}{\partial t} + \operatorname{div}\left(n_i b\mathbf{E} - D\nabla n_i\right) = 0 & (1.2) \\ \rho\left(\frac{\partial \mathbf{V}}{\partial t} + (\mathbf{V}, \nabla)\,\mathbf{V}\right) = -\nabla p + \mu\Delta\mathbf{V} + e n_i \mathbf{E} & (1.3) \\ \operatorname{div}\mathbf{V} = 0 & (1.4) \end{cases} \tag{1}$$

Here φ is the electric potential, n_i is the ion concentration, $\mathbf{E}$ is the electric field, $\mathbf{V}$ is the air velocity, p is the pressure, e is the absolute value of the electron charge, ε is the absolute air permittivity, b is the ion mobility, D is the diffusion coefficient, ρ is the density of air, and μ is the dynamic viscosity of air. The ion mobility was chosen equal $1.9 \cdot 10^{-4}\, m^2/(V \cdot s)$, that is, within range given in [1]. The present research considers only the outer region of the corona discharge and the propagation of positive particles only (unipolar approximation). We can observe processes, which are specific to an actual corona sheath, as a result of defining the boundary condition at the active electrode. We consider two forms of the boundary condition.

In the case of first model, density of the flow of positive ions is set at the active electrode as the linear function of the electric field strength (2):

$$\mathbf{j}(E) = j_n \cdot \mathbf{e_n}, \quad j_n = \begin{cases} k \cdot (E - E_0), \ E \geq E_0 \\ 0, \ E < E_0 \end{cases}, \quad k \to \infty \tag{2}$$

In order to define this function we have to determine the value E_0, the electric field strength, at which the corona discharge ignites (the threshold field). To this end, the ignition voltage of corona discharge in the experimental electrode system was first determined by approximation of the current-voltage characteristics found experimentally. Then, computer simulation was used to tackle the auxiliary electrostatic problem (1.1) with the ignition voltage applied to the system, disregarding the space charge. The maximum value of the electric field strength that was observed at the needle was further used as E_0. Parameter k, which defines the slope of the function (2), has an evident effect on the solution of the problem. In this work, we hypothesized that the solution would attain a certain steady state with growing k. In this case, the electric field strength at the needle surface will be close to the threshold field strength E_0, at which the ionization processes start, in accordance with the general principles used in various simplified models of the corona discharge [5].

The second method that was examined in the work utilizes a more complicated boundary condition for the ion flux, which bases on calculating the number of ionization collisions near the electrode surface (3). The advantage of the model is that it requires no experimental input data at a change of the electrode configuration if the photoionization coefficient is known. If unknown, the coefficient can be measured for the electrode once in an experiment. As [2] shows, further variations of the geometrical parameters of the system require no additional experimental data for computer simulation.

$$\begin{cases} \dfrac{\partial}{\partial t} j = j \dfrac{\text{Ø} e^{M} - 1}{\text{ø}} & (3.1) \\ \text{ø} = \text{Ø} e^{M} \displaystyle\int_{0}^{b} \dfrac{ds}{\bar{}_{e} E\left(s\right)} & (3.2) \\ M = \displaystyle\int_{0}^{b} \text{ff}\left(E\left(s\right)\right) ds & (3.3) \end{cases} \tag{3}$$

Here j is the current density, the Ø is photoionization coefficient, $\bar{}_{e}$ is the mobility of electrons, M is the number of ionizing collisions. The variable of integration in (3.2)–(3.3) is the coordinate along electric-field line, and limits 0 and b correspond to electrode surface and the outer boundary of corona region, respectively. Function $\text{ff}(E)$ is the ionization coefficient. This research uses ff from [2]:

$$\text{ff}\left(E\right) = \begin{cases} 6.54e5\,[1/m] \cdot \bar{}_{e} E \cdot exp\left(-193e5\,[V/m]/E\right), E < 151.2e5\,[V/m] \\ 1.14e6\,[1/m] \cdot \bar{}_{e} E \cdot exp\left(-277e5\,[V/m]/E\right), E \geq 151.2e5\,[V/m] \end{cases} \tag{4}$$

Other boundary conditions are the same for both models. The full set is given in the table:

		High voltage electrode A	Symmetry axis S	Grounded electrode B	Open boundary C
both models	φ	$' = U$	$(\mathbf{E}, \mathbf{e_r}) = 0$	$' = 0$	$(\mathbf{E}, \mathbf{n}) = 0$
	$\mathbf{V}$	$\mathbf{V} = \mathbf{0}$	$(\mathbf{V}, \mathbf{e_r}) = 0$	$\mathbf{V} = \mathbf{0}$	$p=0$
model No2	M	–	–	$M=0$	–
model No1	n_i	$j = (E - E_0)$	$(\mathbf{j}, \mathbf{e_r}) = 0$	$(\nabla n_i, \mathbf{n}) = 0$	$(\mathbf{j}, \mathbf{n}) = 0$
model No2		$\frac{\partial}{\partial t} j = j \frac{\text{Ø} e^{M} - 1}{\text{ø}}$			

3 Experimental study

Verification of computer models is conducted as a comparison of calculated variable distributions to experimental data. Experimentally measured values are the electrode system current and the airflow velocity distribution. Current measurement is actually the voltage measurement on a known resistance using an ADC. The particle image velocimetry (PIV) method is used to visualize the flows in the presence of ionic wind: visualizing aerosol is sprayed in the air, its particles are illuminated with a laser beam, which goes through a cylindrical lens in order to form a lighted plane. The electrode system under study is placed in this plane in such a way that the plane is aligned with the region of interest and passes through the axis of the needle. Two shots are taken with a high-speed camera. The pair of frames show images of aerosol particle positions with a known time interval. Most probable displacements are determined using cross-correlation function. With displacements and time interval, velocity distribution is restored. In order to obtain reliable and authentic

results, multiple frame pairs are taken, and the velocities are averaged. The method reliability and absence of particles injection influence are proven in [7]. It should be noted that the laser plane is approximately *1 mm* thick, which is much greater than the radius of curvature for high-voltage electrodes used in the study. This should be taken into account, when comparing experiment and simulation results, especially if the region of the greatest velocity gradient is of the same scale.

4 Analysis of results

Below is the comparison of calculations (for both models) and experimental results. Additionally, some dependences and distributions are illustrated by the data obtained from the simulation.

The I-V curves (Fig.2 (left)) display a parabolic plot shape, typical for corona discharge. Besides, the fact follows from linearity of reduced I-V curves (current-voltage characteristics divided by voltage) shown on Fig.2 (right). The results of both models agree with the experimental curve within sufficient accuracy (about 5%). The first model describes the ignition voltage accurately, because the ignition voltage of corona discharge is a part of determined conditions for the model. But the second one predicts the threshold voltage with high accuracy also and requires no experimental I-V curve.

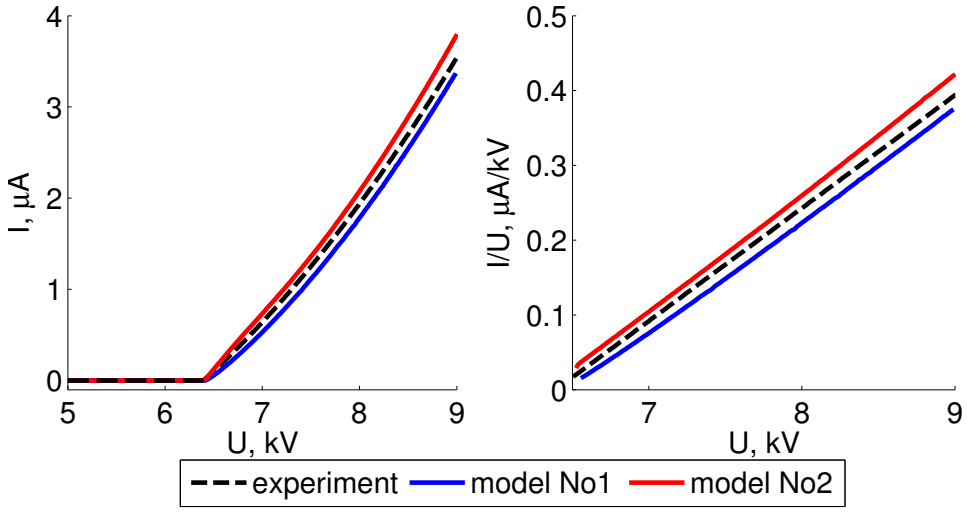

Figure 2: Current per voltage for the simulation and the experiment

The computer simulation allows finding many different quantities that we cannot measure experimentally. Fig.3 (left) shows distributions of electric field strength and ion concentration near the needle tip for voltage *8.8 kV* (the corona discharge has already ignited for the voltage). It is hard to see any visual difference in the distributions for two models, so the results only for first model are shown on the figure. The surface plots demonstrate the characteristic corona discharge distributions: the electric field attains the maximum on electrode surface and dramatically decreases with growing distance from the needle tip; the ion concentration Fig.3 (right) has

the same maximum point, but ions form a cloud that slowly spreads away from the needle tip.

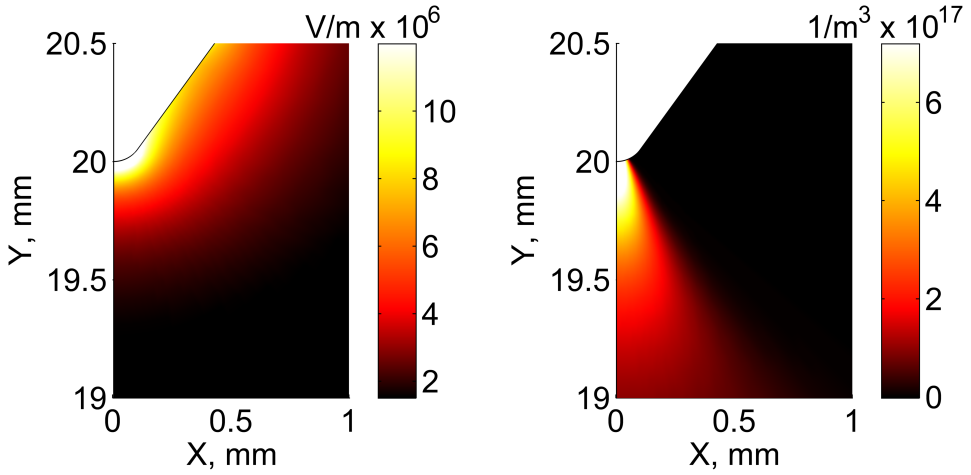

Figure 3: Distributions of electric field strength and ionic concentration in the region of needle tip

Let us consider the distribution of the electric field strength at the needle tip (Fig.4 (left), the zero point of arc length in the plot corresponds to the centerline of the system). Even though the surface field for the first method is stronger than for the second one, the total current from the electrode is higher for the second model (it is shown in I-V curve at Fig.2).The cause is that the first method uses the boundary condition, which leads to the current start only from the part of the electrode, where the electric field strength is higher than the threshold field (E_0). In the case of the second model, the produced current is independent of E_0 and is defined by the number of ionizing collisions (variable M in (3)). The needle tip distribution of M is shown on Fig.4 (right) and it is clear that the distribution shape follows that of the electric field. The relationship between these variables results from definition of M and form of function $ff(E)$ (4). Consequently, the current in the case of the second model depends also on electric field on the active electrode, but the dependence is more complicated than in the case of the first one.
The plot of axisymmetric distribution of electric field (Fig.5 (left)) illustrates the fact that the above-mentioned difference between models holds only for a small region near the needle tip. Both models yield the same values at distances more than $0.5\ mm$ from the needle (when the interelectrode gap is $20\ mm$).
The electric field maxima that correspond to different applied voltages are shown on Fig.5 (right). The plot illustrates that the difference between methods remains for every considered voltage that is higher than the ignition one. For small voltages, the plots are linear for both models, which is explained by space charge deficiency. After corona discharge ignition, electric field for both models tends to the stationary level and the second method allows predicting its value (E_0 in terms of the first one).
The velocity distributions were obtained from the simulation following the electric characteristics. Fig.6 shows the comparison between surface velocity plots for the experiment and the simulation near the symmetry axis for voltage $8.8\ kV$. It is hard to see any visual difference in the distributions for two models, so the figure

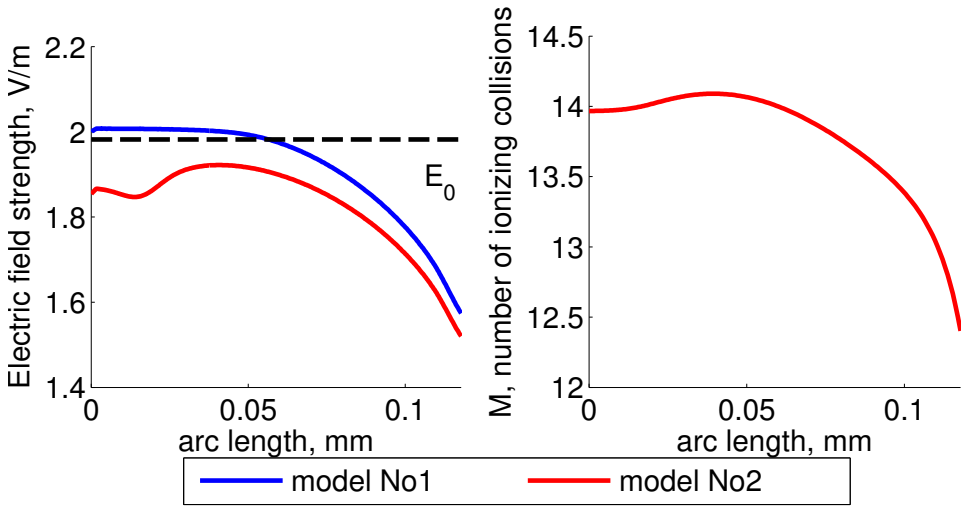

Figure 4: Electric field strength and number of ionizing collisions on the needle tip

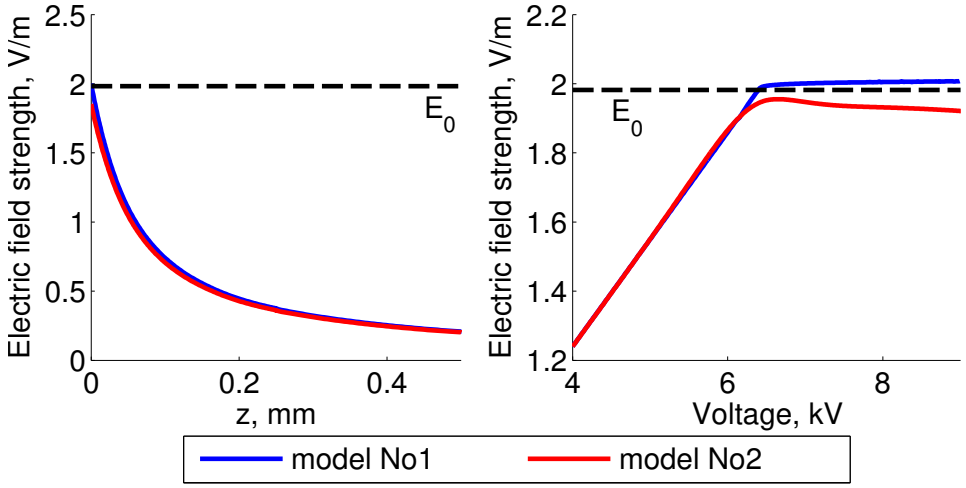

Figure 5: Axial distribution of electric field and electric field maximum from voltage

shows the results only for the first of them. Notice that the simulation gives us the structure of the jet similar to the experimental one (the scales are chosen identical and velocity maxima at right-hand plot are not shown). We can obtain more detailed information from the analysis of the line velocity plots.

The plot of radial velocity distribution for the distance of $5\ mm$ from the needle Fig.7 (left) illustrates a good agreement between models and the experiment in region $r > 0.8\ mm$. There is a singularity in the experimental research for the needle-plane system near the symmetry axis: the laser plane is about $1\ mm$ thick, and steep velocity gradient becomes smoothed. For this reason, we observe the average velocities in that region; additionally, a slight jet oscillation increases that effect. Therefore, it is not correct to compare results with the experiment for $r < 0.8\ mm$. Let us consider the vertical velocity distribution for $r = 0.8\ mm$ (Fig.7 (right)). It allows comparing the flow structures for the simulation and the experiment: they are agree within good accuracy. This means the simulation predicts the jet structure,

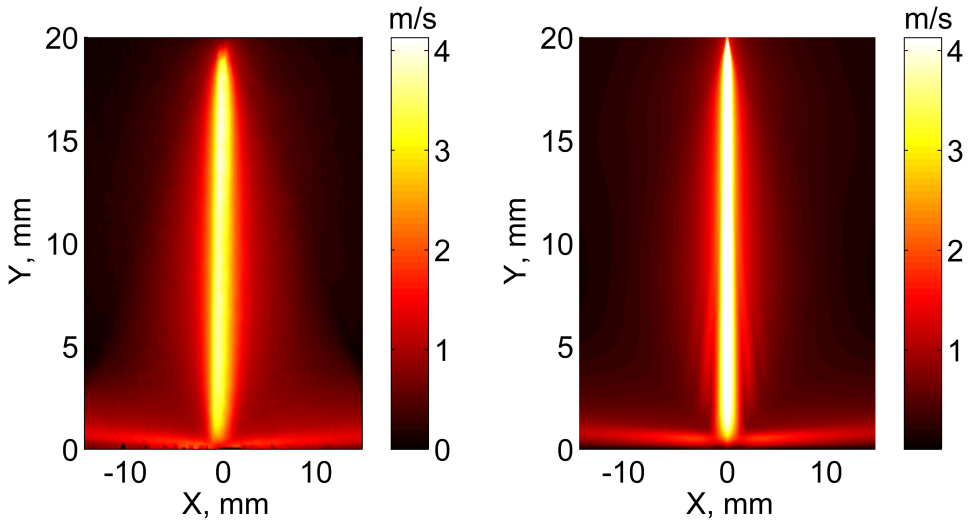

Figure 6: Velocity distributions experiment and simulation

typical for ionic wind: $0 - 3\ mm$ is the acceleration region, $3 - 17\ mm$ is the region of jet formation and $17 - 20\ mm$ is the deceleration region.

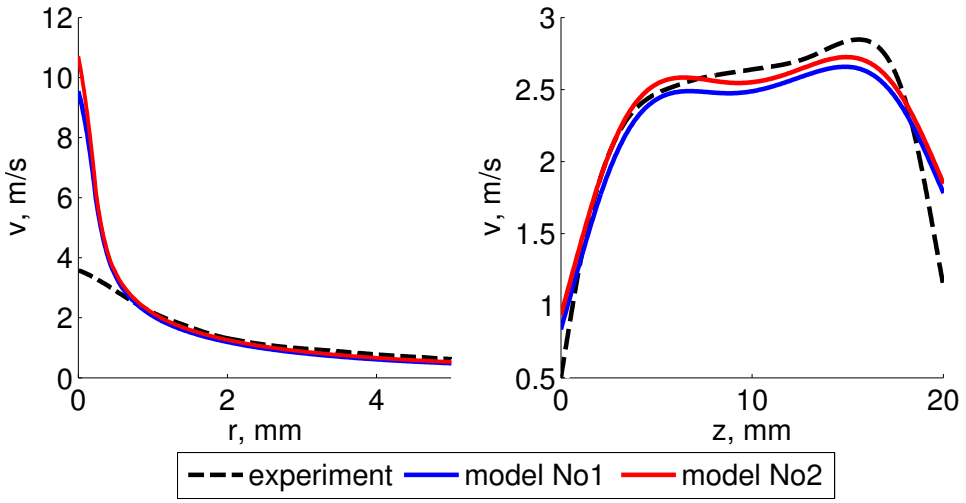

Figure 7: Radial ($5\ mm$ from needle tip) and vertical ($0.8\ mm$ from axis) velocity distributions

5 Conclusion

The computer simulation of a positive corona discharge in the needleвГYplane electrode system has been carried out. The results for ionic wind in unipolar approximation with the two types of boundary conditions on the ion flow were compared with those of experimental research. The analysis shows that the use of these types of boundary conditions allows describing the phenomenon of ionic wind within acceptable accuracy. Both methods describe special aspects of the phenomenon such as typical I-V curve and air velocity distribution.

Distributions of electric field strength, space charge density, and current on the active electrode surface demonstrate the coherence in investigated models. It should be noted that the second method is more flexible and comprehensive than the first one. This is grounded on a thorough understanding of corona discharge and generation of ionic wind. Thus, the model, based on calculation of the number of ionizing collisions, makes it possible to determine electric field strength associated with corona discharge ignition without experimental data. This fact is an advantage of the second model.
In addition, we were able to find hard-to-detect physical quantities by use of computer simulation because of similarities with the global experimental I-V curve. The knowledge of current distribution in corona discharge, distribution of electric field, ion concentration in the electrode gap, velocity of particles gives us an insight into ionic wind.

6 Acknowledgements

The study was supported financially by the Russian Foundation for Basic Research (project no. 15–08–07628a) and was performed using the equipment of resource centers вГЁGeomodelвГ№ and вГЁComputing centerвГ№ of the scientific park of the St. Petersburg State University.

References

[1] Vereshchagin I.P., Koronnyi razryad v apparatakh elektronno-ionnoi tekhnologii (Corona Discharge in Electron-Ion Devices), Moscow: Energoatomizdat, 1985.

[2] Yang F., Jewell-Larsen N.E., Brown D.L., Pendergrass K., et al., in Proc. Int. Symp. on High Voltage Engineering, Delft, Netherlands, August 25вГY-29, 2003, pp. 1вГY-4.

[3] Zhidkova P.S., Samusenko A.V., A computer model of the ionic wind in the unipolar approximation with the boundary condition on the ion flow variation rate, Surface Engineering and Applied Electrochemistry, 2016, 52(4), pp. 370-вГY379.

[4] Samusenko A.V., Safronova I.F.,Stishkov Yu.K., Unipolar model of the positive corona discharge, Surface Engineering and Applied Electrochemistry, 2016, 52(5), pp. 43-вГY50.

[5] Dordizadeh P., Adamiak K., Castle G.S.P., Parametric study of the characteristics of trichel pulses in the needle-plane negative corona discharge in atmospheric air, Journal of Electrostatics, 2016, 84, pp. 73–80.

[6] Raizer Yu.P., Fizika gazovogo razryada (Physics of Gas Discharge), Dolgoprudnyi: Intellekt, 2009.

[7] Hamdi M., Havet M., Rouaud O., Tarlet D., Comparison of different tracers for PIV measurements in EHD airflow, Experiments in Fluids, 2014, 55(4).

Kostin P.A., Poluektova K.D., Elagin I.A., Markovskii P.Y., St. Petersburg State University 7/9 Universitetskaya nab., St. Petersburg, 199034 Russia.

DNS of Turbulent Flows in Spherical Layer, Driven by Torsional Oscillations of Boundaries

Olga Krivonosova, Dmitry Zhilenko

olga@imec.msu.ru

Abstract

We have numerically studied the transition to turbulent flow in a layer of a viscous incompressible fluid confined between concentric spherical boundaries performing counter-rotational oscillations relative to the state of rest. The rotation speeds of both spheres were modulated at the same frequency and amplitude with the phase shift ПҐ. We used an algorithm of numerical solution based on a conservative finite difference scheme of the discretization of the NavierвҐYStokes equations in space and semi-implicit RungeвҐYKutta scheme of the third order integration accuracy in time. Discretization in space was performed on grids nonuniform in radial and meridional directions with concentration near the boundaries and equatorial plane. The transition to turbulence was caused by an increase in the amplitude of velocity modulation. Using the concept of instantaneous frequency/phase of flow (based on the building of the analytical signal of the velocity time series by means of Hilbert transform), it is established that the turbulence develops in a limited region of liquid layer, outside which the flow remains laminar. The turbulent region of flow exhibits intermittency of the chaosвҐYchaos type with random alternation of weak and strong turbulence.

1 Introduction

The transition of closed flows in a viscous incompressible fluid layer from laminar to turbulent regimes can take place under the action of temporally nonuniform rotation of boundaries [1]. In a flow of fluid confined between concentric spherical boundaries and driven by their rotation about a common axis, known as the spherical Couette flow (SCF), transitions to turbulence have been previously studied in the case of periodic variations in the velocity of one of the two boundaries. It was established that a change in the frequency of modulation of the rotation speed of the inner or outer sphere can lead to various turbulent flow regimes near the boundary of their formation [2, 3, 4].

Both the results of three-dimensional model calculations [2] and the measurements of flow velocity by laser Doppler anemometry [3] in combination with flow imaging showed that modulation of the rotation speed can lead to the development of

temporally non-uniform turbulence. The most frequently observed non-uniformity is intermittency of the cycleвГЎYchaos type, representing irregular alternation of the laminar and turbulent regions spreading over the entire spherical layer [2]. With increasing modulation frequency, intermittency of the chaosвГЎYchaos type (in the form of randomly alternating regions of weak and strong turbulence) [3] and cycleвГЎYchaosвГЎYchaos type [4] was observed. The further increase in the frequency leads to the development of temporally uniform turbulence. Our measurements [3, 4] were performed in the region of middle latitudes (i.e., between the equator and pole) close to the outer sphere, which did not allow us to assess whether nonuniform turbulence has been established in the entire spherical layer.
Previously, we have studied [2, 3, 4] the influence of modulation of the rotation speed on the initial periodic flow formed between counter-rotating spherical boundaries. It would be also of interest to consider the possible transition to turbulence directly from the state of rest. [5] investigated the flow around a torsionally oscillating sphere relative to the state of rest. Conclusions concerning the transition to turbulence were based on the data of flow imaging and the results of axisymmetric calculations. However, both these approaches do not allow a final judgment to be drawn on the establishment of a turbulent regime and its characteristics.
The present work aimed at numerically studying the possibility of turbulence formation and characterizing its properties during counterwise rotational oscillations of two spherical boundaries relative to the state of rest. We have considered the case of equal modulation frequencies and amplitudes for both spheres, the angular velocities of which vary with phase shift π.

2 Calculation method and field of study

The flow of a viscous incompressible fluid in a spherical layer is described by a set of the Navier-Stokes and continuity equations,

$$\frac{\partial U}{\partial t} = U \times rotU - grad\left(\frac{p}{\rho} + \frac{U^2}{2}\right) - \nu rotrotU, divU = 0 \qquad (1)$$

which are supplemented by the conditions of no slip and nonpercolation at the boundaries. In a spherical coordinate system with radial (r), polar (θ), and azimuthal (φ) directions, these conditions take the following form: $u_\varphi(r = r_k) = \Omega_k(t) r_k \sin(\theta), u_r(r = r_k) = 0, u_\theta(r = r_k) = 0, k = 1, 2$ where the subscripts 1 and 2 refer to the inner and outer sphere, respectively; U, p, and ρ are the fluid velocity, pressure, and density; u_φ, u_r, and u_θ are the azimuthal, radial, and polar components of the velocity; r_k and Ω_k are the radius and angular velocity of rotation of the corresponding sphere; and ν is the kinematic viscosity of fluid in the layer. The angular velocities of rotation of the spheres are periodically varied as $\Omega_1(t) = A\sin(2\pi ft + \psi_1), \Omega_2(t) = A\sin(2\pi ft + \psi_2), \psi_1 - \psi_2 = \pi$, where A and f are the amplitude and frequency of modulation, and ψ_1 and ψ_2 are the corresponding initial phases.
By analogy with [2], we have used the computation algorithm based on a conservative finite difference scheme of discretization for the Navier-Stokes equations and a semi-implicit third-order accurate RungeвГЎYKutta scheme for integration with respect

to the time [6]. The spatial discretization has been performed on non-uniform grids with decreasing cell size toward the boundaries and the equatorial plane. The ratio of the maximum to minimum cell size was 3, and the total number of nodes was $5.76 \cdot 10^5$.

Model calculations have been performed for the following set of dimensional parameters: $\nu = 5 \cdot 10^{-5} m^2/s, r_1 = 0.075m, r_2 = 0.15m$, and $f = 0.51Hz$. The character of flow depends on the values of A, f, r_1, r_2, and $\psi_1 - \psi_2$. By analogy with [5], the dimensionless parameters of similarity are introduced as Reynolds numbers for the inner and outer spheres, $Re_1 = 2Ar_1/2\pi f\delta$, and $Re_2 = 2Ar_2/2\pi f\delta$ (where $\delta = (2\nu/2\pi f))^{1/2}$ and relative thickness of layer $\beta = (r_2 - r_1)/r_1 = 1$. The dependence on the phase difference reduces to relation $\Omega_1(t) + \Omega_2(t) = 0$. For the parameters indicated above, we have $\delta = 5.64 \cdot 10^{-3} m$, which corresponds to seven nodes of the computational grid. Time series of the flow velocity were recorded at two points. Point 1 is situated near the inner sphere at the equator ($r = 3.55\delta, \theta = 1.586$), while point 2 is situated near the outer sphere at middle altitudes ($r = 2.84\delta, \theta = 1.033$)

3 Results

At $Re_1 \leq 55$, the flow is symmetric relative to the axis of rotation and equatorial plane and only the modulation frequency is present in the flow velocity spectrum. As Re_1 increases, the flow loses stability and becomes asymmetric relative to the rotation axis. Near the inner sphere, the secondary flow is asymmetric relative to the equatorial plane and its wave number in the azimuthal direction is $m = 1$. Near the outer plane, the flow is quasi-symmetric relative to the equatorial plane and $m = 2$. The velocity spectrum exhibits a second frequency, which is much smaller than the modulation frequency. With further growth in Re_1, the flow becomes turbulent and the level of the low-frequency ($0.01 - 0.1Hz$) region in the velocity spectrum increases by no less than two orders of magnitude. In a narrow region near the equator, the flow retains a spatial structure characteristic of secondary flow (Figure 1), while chaotization is observed at middle latitudes.

Let us quantitatively characterize the degree of flow chaotization in terms of correlation dimension D determined using the relation [7] $C(r) \sim r^D$, $C(r) = \lim_{m\to\infty} \frac{1}{m^2} \sum_{i,j=1}^{m} H(r^{(p)} - |x_i^{(p)} - x_j^{(p)}|)$, where H is the Heaviside function, $r^{(p)}$ is the distance in p - dimensional space, and $x(t_i), x(t_i + \tau), \ldots, x(t_i + (p-1)\tau)$ is a point in the p - dimensional space that characterizes the state of the system at time moment t_i. The $x(t_0 + kt)$ series represents a discrete record of the flow velocity at interval Δt. Thus, D is the slope of the plot of $logC(r) = f(log(r))$. Here, we calculate the values of dimensions D_1 and D_2 using time series of u_ϕ recorded at points 1 and 2, respectively, and the value of dimension D_A calculated for A_{3D} [6], which refers to the entire volume of flow:

$$A_{3D}^2 = (3/4\pi)(r_2^2 - r_1^2)^{-1} \int_0^{2\pi} d\varphi \int_0^{\pi} d\theta \int_{r_1}^{r_2} (U - U_{2D})^2 r^2 \sin(\theta) dr \qquad (2)$$

where U_{2D} is the axisymmetric velocity component defined as $U_{2D} = (2\pi)^{-1} \int_0^{2\pi} U d\varphi$ The length of records was no less than $5.9 \cdot 10^4$ points for $\tau = 300s$. The magnitude of D_A is plotted in Figure 2 (curve 1).

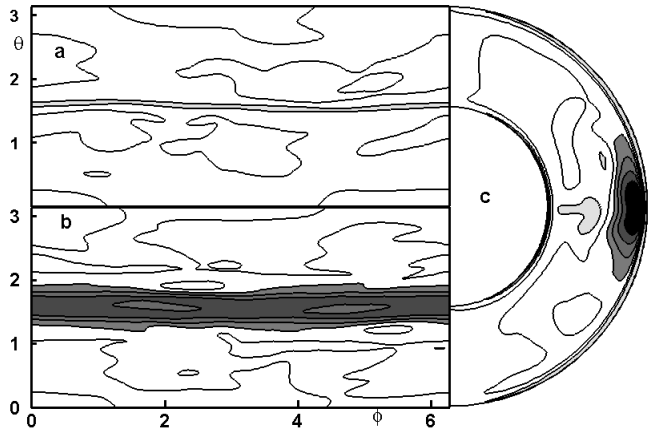

Figure 1: Equilevel lines $u_\varphi[m/s]$: (a) in the $\varphi - \theta$ plane near inner sphere (point 1), (b) in the $\varphi - \theta$ plane near outer sphere (point 2)), (c) in the meridional plane passing through the axis of rotation. $Re_1 = 72$, $u_{\varphi max} = 0.1, u_{\varphi min} = 0.4$, and $\triangle u_\varphi = 0.1$. White areas correspond to $u_\varphi \geq 0.1$; increasing intensity of background corresponds to decreasing u_φ. The moment of time corresponds to an increase in the rotation velocities of $0.2s$ upon passage through the zero level.

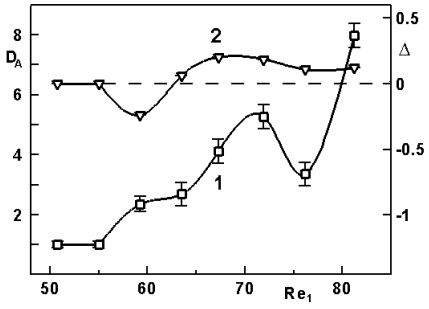

Figure 2: Plots of (1) D_A and (2) Δ vs. Re_1. Vertical bars indicate the possible spread of correlation dimensions for various τ.

Taking into account that, in spherical layers at constant speeds of rotation, the correlation dimension at a threshold of the chaotic flow regime formation falls in the interval $3.5 \leq D \leq 4$ [8, 9], we may conclude that transition to turbulence in the case under consideration takes place at $Re_1 \approx 65$ (Fig. 2, curve 1). At constant boundary conditions, the dimension is independent of their position of flow velocity recording [8, 10]. In order to check for this condition, let us consider the value of $\Delta = (D_1 - D_2)/D_A$. Maximum deviations of Δ from zero are observed in the transition region $55 \leq Re_1 \leq 65$ (Figure 2, curve 2). For all turbulent regimes, this value is $\Delta \geq 0$, which quantitatively characterizes a more pronounced stochasticity of flow at middle latitudes as compared to the near equatorial region, as is manifested by the flow structure (Figure 1). The dependence of the correlation dimensions on the point of determination suggests that the influence of rotational oscillations of the boundaries on the flow is differently manifested in various regions. This circumstance does not allow the flow upon transition to turbulence to be considered as a unified dynamical system.

In order to confirm this hypothesis, let us consider fragments of a record of the azimuthal velocity upon the transition to turbulence at $Re_1 = 72$ (Figure 3). As can be seen, the behavior of u_φ near the inner sphere at the equator (curve 1) is close to periodic with a weak irregular modulation of the amplitude, while flow near the outer sphere at middle altitudes (curve 2) becomes turbulent. Thus, the flow is spatially nonuniform so that the turbulence develops in a limited region and remains laminar outside this region. The degree of temporal nonuniformity can be determined from analysis of the behavior of instantaneous phase and frequency of the signal [11] by analogy with the procedure used in [4]. According to this, instantaneous phase $\Psi(t)$ of velocity $x(t)$ is defined as $\Psi(t) = \arctan(y(t)/x(t))$, where $y(t)$ is the orthogonal complement to $x(t)$, which is calculated as the Hilbert transform of the $x(t)$ series [11]. Derivative $\chi(t) = \partial\Psi(t)/\partial t$ is then the instantaneous frequency of modulation. Consider the difference of instantaneous phases and frequencies between the rotation speed of the inner surface and flow velocity at a given point of the flow. As can be seen, the phase difference at point 1 remains constant in time (Figure 3, curve 3) while the frequency difference exhibits regular variations (curve 6). Thus, the flow at point 1 is fully synchronized with rotation of the boundary. At the same time, these parameters at point 2 near the outer sphere vary with time. By analogy with [4], it is possible to reveal regions of weak turbulence, where strong synchronization also makes the phase difference constant and the frequency difference exhibits no jumps. In regions of strong turbulences and weak synchronization, the phase difference varies with the time and the frequency strongly deviates from average values. Regions with different character of turbulence are randomly alternating in the time, which leads to the conclusion that there is intermittency of the chaos-chaos type.

4 Conclusions

Thus, an increase in the amplitude of counterwise rotational oscillations of spherical boundaries leads to the formation of flow with random alternation of weakly and strongly turbulent regions in a part of the layer of fluid confined between these boundaries. At the same time, in other parts of the turbulent flow, the character of

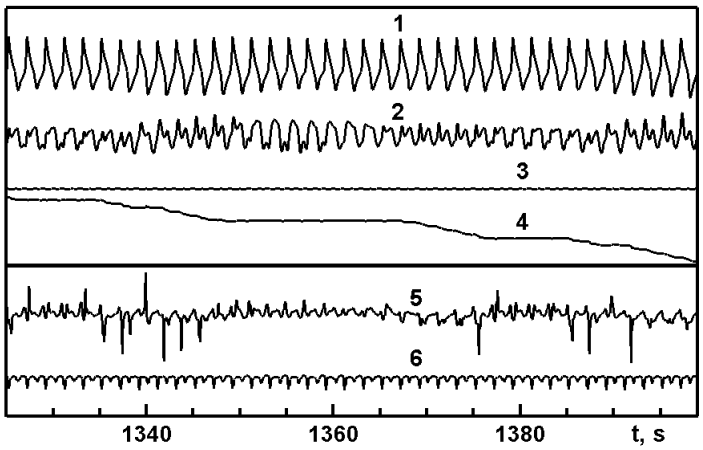

Figure 3: *1,2* time series of azimuthal flow velocity u_φ and differences of instantaneous *3,4* phases and *5,6* frequencies between the rotation speed of the inner sphere $\Omega_1(t)$ and flow velocity u_φ; *1,3,6* near the inner and *2,4,5* near the outer spheres vs. time t for $Re_1 = 72$. The dashed contours indicate regions of stronger turbulence.

flow can be different. It may be suggested that the approach described above, which is based on the concept of phase/frequency differences, can be used for determining boundaries both between the turbulent/nonturbulent regions of flow and between regions of temporally uniform/nonuniform turbulence.

Acknowledgements

This study was supported by the Russian Foundation for Basic Research, project no. 16-05-00004.

References

[1] D. Coles, J. Fluid Mech., 21, 385, 1965.

[2] D. Yu. Zhilenko and O.E. Krivonosova, Tech. Phys. Lett. 39 (1), 84, 2013.

[3] D. Yu. Zhilenko and O.E. Krivonosova, Fluid Dyn. 48 (4), 452, 2013.

[4] D. Yu. Zhilenko and O.E. Krivonosova, Dokl. Phys. 59 (1), 45, 2014.

[5] R. Hollerbach et al., Phys. Fluids 14 (12), 4192, 2002.

[6] N. Nikitin, J. Comput. Phys. 217 (2), 759, 2006.

[7] P. Grassberger and I. Procaccia, Phys. Rev. Lett. 50 (5), 346, 1983.

[8] Yu. N. Belyaev and I. M. Yavorskaya, Fluid Dyn. 26 (1), 7, 1991.

[9] K. Nakabayashi, W. Sha, and Y. Tsuchida, J. Fluid Mech. 534, 327, 2005.

[10] D. Yu. Zhilenko and O.E. Krivonosova, Tech. Phys. 55 (4), 449, 2010.

[11] V. Anishchenko et al., Nonlinear Dynamics of Chaotic and Stochastic Systems. Springer, Berlin, 2002.

Dmitry Y. Zhilenko, Krgiganovski str. 2/21, 51, Moscow, Russia
Olga E. Krivonosova, Krgiganovski str. 2/21, 51, Moscow, Russia

Destructive atmospheric vortices and the Earth's rotation around its axis

I.Yu. Krutova

IYKrutova@mephi.ru

Abstract

Interesting atmospheric phenomena are often found in nature. These are ascending swirling flows of air, such as whirlwinds, tornadoes, tornado.The results of theoretical and experimental studies of the ascending twisting flows encountered in nature in the form of tornadoes and tropical cyclones [1-3] are represented.

Theorems on the existence and the uniqueness of the solutions to specific initial-boundary value problems that, in particular, set the rotation direction of tornadoes, tropical cyclones and fire vortices are proved for the system of gas dynamics equations.

There are the constructed numerically the solutions of indicated systems of partial differential equations that model the gas flow from the simple planar spiral currents to the three-dimensional nonstationary flows in general. The calculation results are consistent with both the data of natural observations and the results of laboratory experiments.

The results of theoretical studies of the ascending twisting flows encountered in nature in the form of tornadoes and tropical cyclones [1-3] are proven in this research. We consider the system of gas dynamics equations in dimensionless variables under the action of gravity and Coriolis forses [3, 4]:

$$\begin{cases} c_t + uc_r + \frac{v}{r}c_\varphi + wc_z + \frac{(\gamma-1)}{2}c\left(u_r + \frac{u}{r} + \frac{v_\varphi}{r} + w_z\right) = 0, \\ u_t + uu_r + \frac{v}{r}u_\varphi - \frac{v^2}{r} + wu_z + \frac{2}{(\gamma-1)}cc_r = av - bw\cos\varphi, \\ v_t + uv_r + \frac{uv}{r} + \frac{v}{r}v_\varphi + wv_z + \frac{2}{(\gamma-1)}\frac{c}{r}c_\varphi = -au + bw\sin\varphi, \\ w_t + uw_r + \frac{v}{r}w_\varphi + ww_z + \frac{2}{(\gamma-1)}cc_z = bu\cos\varphi - bv\sin\varphi - g. \end{cases} \quad (1)$$

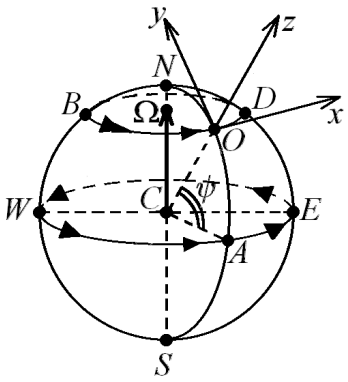

Fig. 1.

The symbols in system (1) are the following: ρ – is the density; u, v, w – are the projections of the velocity vector $\mathbf{V}$ on the axis of Cartesian coordinate system $Oxyz$ (see Fig.1) rotating together with the Earth and the beginning of which lies on the surface of the Earth at the point O on the parallels with the latitude ψ; $\mathbf{g}$ – is the acceleration vector of gravity; $a = 2\Omega \sin\psi$; $b = 2\Omega \cos\psi$; Ω – is the modulus of the angular velocity vector $\mathbf{\Omega}$ of the Earth's rotation.

The theorem on the smooth flow into the vertical cylinder. For the system of gas dynamics equations there are the specified conditions describing the initial time of the uniform, resting outside the cylinder $\sqrt{x^2+y^2} = r_0$, $r_0 > 0$ gas. Also the smooth radial flow into the cylinder are given. Then this problem has a unique solution in the neighbourhood of the given point $(t = 0, r = r_0, \varphi = \varphi_0, z = 0)$. Here r, φ – are the polar coordinates in the plane xOy.

The properties of the solution of this problem that since the time $t = 0$ in the gas flow occurs the twisting directed in the positive direction in the case of the Northern Hemisphere and the negative direction in the case of the Southern Hemisphere. This direction of rotation corresponds to the direction of air like tornadoes and tropical cyclones. If for the problem $\Omega = 0$, so the twisting does not arize.

The theorem on the smooth heating of the vertical cylinder. For the system of gas dynamics equations there are the specified conditions describing the initial time of the uniform, resting outside the cylinder $\sqrt{x^2+y^2} = r_0$, $r_0 > 0$ gas. Also the smooth heating of this cylinder are given. Then this problem has a unique solution in the neighbourhood of the given point $(t = 0, r = r_0, \varphi = \varphi_0, z = 0)$.

The properties of the solution of this problem that since the time $t = 0$ the twisting directed in the negative direction in the case of the Northern Hemisphere and the positive one in the case of the Southern Hemisphere appears in the gas flow. The air around the fire vortices has such direction of twisting. If for the problem $\Omega = 0$, the twisting in the flow is absent.

The paper provides examples of numerical construction of flows under the action of gravity and Coriolis forces for the system (1).

The geometric, speed and energy characteristics of stationary plane currents. The solution of problem (1) in the form convergent series, solves the corresponding characteristic Cauchy problem with data on an impenetrable plane $z = 0$. This solution describes a plane stationary spiral flow of gas when the Coriolis force is taken into account, which can be treated as a current in the bottom part of a tornado or a tropical cyclone. And, depending on the input data, such flows are obtained

with different geometric, speed and energy characteristics. The aim of the paper is to construct and analyze flat stationary flows in a tornado different intensities and in a tropical cyclone, consistent with the data of full-scale observations.Coordination with the data of field observations of tornadoes and tropical cyclones is achieved using the Fujita scale and data on tropical cyclones (Table 1).

Table 1

Classes tornado, cyclone	$F_{-0.5}$	$F0$	$F_{0.5}$	$F1$	$F2$	$F3$	$F4$	$F5$	Cyclone
$d = 2r_0$, m	2.0	5.0	10.0	16.0	51.0	161	547	1609	60000
Wind speed $V(r_0)$, m/s	15	19	25.5	33	51	71	93	117	51

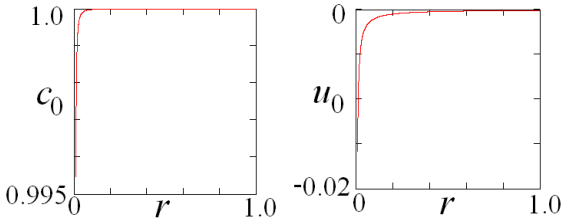

Fig. 2.

Based on the results of calculations on the left-hand side of Fig. 2 shows the graph of the function $c_0(r)$, and in right - the graph of the function $u_0(r)$ for a tornado of class $F3$

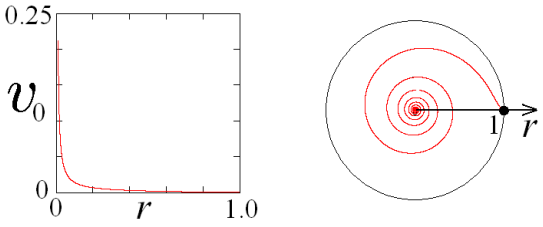

Fig. 3.

For this same tornado class on the left-hand side of Fig. 3 shows the graph of the function $v_0(r)$, and on the right an instantaneous streamline emerging from the point $(r = 1, \varphi = 0)$.

References

[1] Bautin S.P. Tornado i sila Koriolisa (Tornado and the Coriolis Force),Novosibirsk:Nauka, 2008.

[2] Bautin S.P. and Obukhov A.G. Matematicheskoe modelirovanie razrushitel'nykhatmosfernykh vikhrei (Mathematical Modeling of Destructive Atmospheric Vortices),Novosibirsk: Nauka, 2012.

[3] Bautin S.P., Krutova I.Yu., Obukhov A.G., Bautin K.V. Razrushitel'nye atmosfernyevikhri: Teoremy, raschety eksperimenty (Destructive Atmospheric Vortices: Theorems, Calculations, and Experiments), Novosibirsk: Nauka, 2013.

[4] Bautin S.P. Kharakteristicheskaya zadacha Koshi i ee prilozheniya v gasovoi dinamike(Characteristic Cauchy Problem and Its Applications to Gas Dynamics), Novosibirsk: Nauka, 2009.

[5] Bautin S.P., Deryabin S.L., Krutova I.Yu., Obukhov A.G. Razrushitelnye atmosfernye vixri i vrashhenie Zemli vokrug svoej osi(Destructive atmospheric vortices and the Earth's rotation around its axis), Ekaterinburg: USURT, 2017.

I.Yu. Krutova, National Research Nuclear University MEPhI, Moscow, Russia

Detonation control in a supersonic gas flow in a plane channel

Vladimir A. Levin, Tatiana A. Zhuravskaya

levin@imec.msu.ru, zhuravskaya@imec.msu.ru

Abstract

Using a detailed chemical kinetics, detonation combustion of a stoichiometrical hydrogen-air mixture flowing at a supersonic velocity into a plane symmetrical channel with a constriction was investigated with the purpose of both determination of conditions that provide detonation stabilization in the flow and study of methods of stabilized detonation location control.

In case of detonation initiation by energy input, the investigation of conditions of formation in the channel of a thrust developing flow with a stabilized detonation wave was carried out. The effect of variations of the inflow Mach number, the dustiness of the incoming gas mixture and the width of the outflow channel cross section on stabilized detonation location was examined. Some methods of controlling of detonation location in the flow that ensure of thrust increase have been proposed. The possibility of formation of the thrust developing flow with stabilized detonation in the channel under consideration without any energy input has been detected.

1 Introduction

One of the main areas of research of the process of detonation combustion is the investigation of detonation wave propagation in a supersonic gas flow [1], in particular, the determination of conditions that provide detonation stabilization in the flow. A detailed review of works devoted to this theme was presented in [2]. So, the conditions of stabilization of the formed detonation wave in a hydrogen-air mixture flowing at a supersonic velocity into a plane channel with constriction the outflow section of which is smaller than the inflow one were investigated in [3]. The stability of the formed gas flow with detonation to strong disturbances excited by an energy input has been examined in [4].

In the present research the study of conditions of formation of the thrust developing flow with the stabilized detonation wave in the channel with constriction is carried out, and some methods of control of stabilized detonation location are examined.

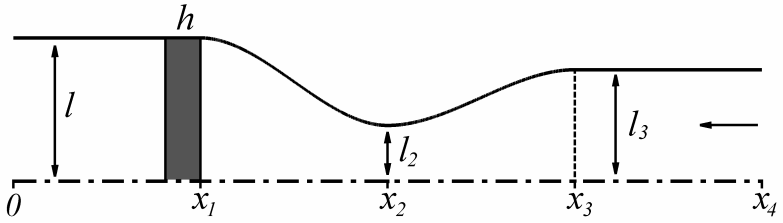

Figure 1: The schematic of the upper channel part (above the plane of symmetry). The arrow shows to flow direction

2 Mathematical Model

Similarly to [3], [4] detonation propagation in a premixed stoichiometrical hydrogen-air mixture flowing at a supersonic velocity into a plane symmetric channel with constriction is studied. The schematic of the upper part of the channel is shown in Fig. 1. The inflow boundary is $x = x_4$, the outflow boundary is $x = 0$. In contrast to the cited researches the gas flow in a channel with an output cross section size exceeding the input one is considered. The combustible gas mixture under the normal conditions (p_0=1atm, T_0=298K) is incoming into the channel parallel to its plane of symmetry at a supersonic velocity that exceeds a velocity of self-sustaining detonation propagation in the quiescent mixture with incoming flow parameters: that is $M_0 > M_{J0}$ (here M_0 is the incoming flow Mach number, M_{J0} is the Mach number of self-sustaining detonation). A stoichiometrical hydrogen-air mixture flowing into the channel is assumed to be a mixture of the H_2, O_2, N_2 and Ar gases in the volume ratio 42 : 21 : 78 : 1, respectively.
The set of gas dynamics equations describing a plain two-dimensional nonstationary flow of the inviscid reactive multi-component gas mixture is:

$$\frac{\partial \rho}{\partial t} + \frac{\partial(\rho u)}{\partial x} + \frac{\partial(\rho v)}{\partial y} = 0$$

$$\frac{\partial(\rho u)}{\partial t} + \frac{\partial(\rho u^2 + p)}{\partial x} + \frac{\partial(\rho uv)}{\partial y} = 0$$

$$\frac{\partial(\rho v)}{\partial t} + \frac{\partial(\rho vu)}{\partial x} + \frac{\partial(\rho v^2 + p)}{\partial y} = 0$$

$$\frac{\partial(\rho(u^2+v^2)/2 + \rho h - p)}{\partial t} + \frac{\partial(\rho u((u^2+v^2)/2 + h))}{\partial x} + \\ + \frac{\partial(\rho v((u^2+v^2)/2 + h))}{\partial y} = 0$$

$$\frac{\partial(\rho n_i)}{\partial t} + \frac{\partial(\rho u n_i)}{\partial x} + \frac{\partial(\rho v n_i)}{\partial y} = \rho\omega_i$$

where x and y are the Cartesian coordinates; u and v are the corresponding velocity components; t is the time; ρ, p and h are the density, the pressure and the specific enthalpy, respectively; n_i is the specific molar concentration of the ith species in the mixture; and ω_i is the specific rate of formation/depletion of the ith component.

The equations of state of the combustible mixture considered as a pefect gas are as follows

$$p = \rho R_0 T \sum_i n_i, \quad h = \sum_i n_i h_i(T).$$

Here T is the temperature, R_0 is the universal gas constant. The partial enthalpy $h_i(T)$ of the ith mixture component are determined from the reduced Gibbs energies of the corresponding mixture components [5].

The inflow boundary conditions are the incoming flow parameters, the outflow boundary condition is necessary only in the boundary points with the subsonic velocity of gas outflow (in this case, the boundary condition is $p_{out} = p_0$). Slip condition is imposed at the channel surface.

As the initial condition the steady plane channel flow of the gas mixture obtained by the marching to steady state method is used. As the zeroth approximation for determining the initial condition the incoming gas flow is taken. It should be noted that the geometric parameters of the channel were chosen so that the steady flow formed in the channel is supersonic everywhere. The initial instantaneous supercritical energy input E_0 (sufficient for direct initiation of detonation combustion) in a domain in the shape of a thin layer, h in thickness, located near the $x = x_1$ section (shaded region in Fig. 1) with the Gaussian dependence of the energy input density on the transverse coordinate is used for detonation initiation.

A set of Euler gas dynamics equations coupled with detailed chemical kinetics equations [6] has been solved using a finite-difference method based on the Godunov's scheme [7]. The size of mesh of a computational grid was selected so that the flow behind the detonation front (in particular, the flow in the induction zone) was represented correctly. Thus numerical investigations were carried out on the grid at step 0.02 mm – 0.04 mm.

In this research the plane channels with constriction the geometrical parameters of which differ from channel parameters of [4] by the value of l were considered, that is x_1=0.125 m, x_2=0.25 m, x_3=0.375 m, x_4=0.5 m, l_2=0.0175 m, l_3=0.035 m, and $l > l_3$.

3 Detonation stabilization in the supersonic flow

The initial supercritical energy input E_0 results in formation of two detonation waves: one of which propagates downstream and rapidly is carried away from the channel, whereas the other wave travels upstream. The conditions that provide stabilization of the second wave in the flow, so that the formed flow develops thrust, were studied. In the case under consideration thrust was defined as follows

$$T = 2 \int_0^{x_4} p(x, y(x), t) ctg\alpha(x)\, dx,$$

where $y(x)$ is the function defining the form of the upper wall of the channel, $\alpha(x)$ is the angle between the outer normal to this wall and the x axis.

It has been established that for some inflow Mach number M_0 the value of half-width l of the output cross section can be selected so that the thrust developing flow with detonation stabilized in the divergent channel part is formed. In particular, it was

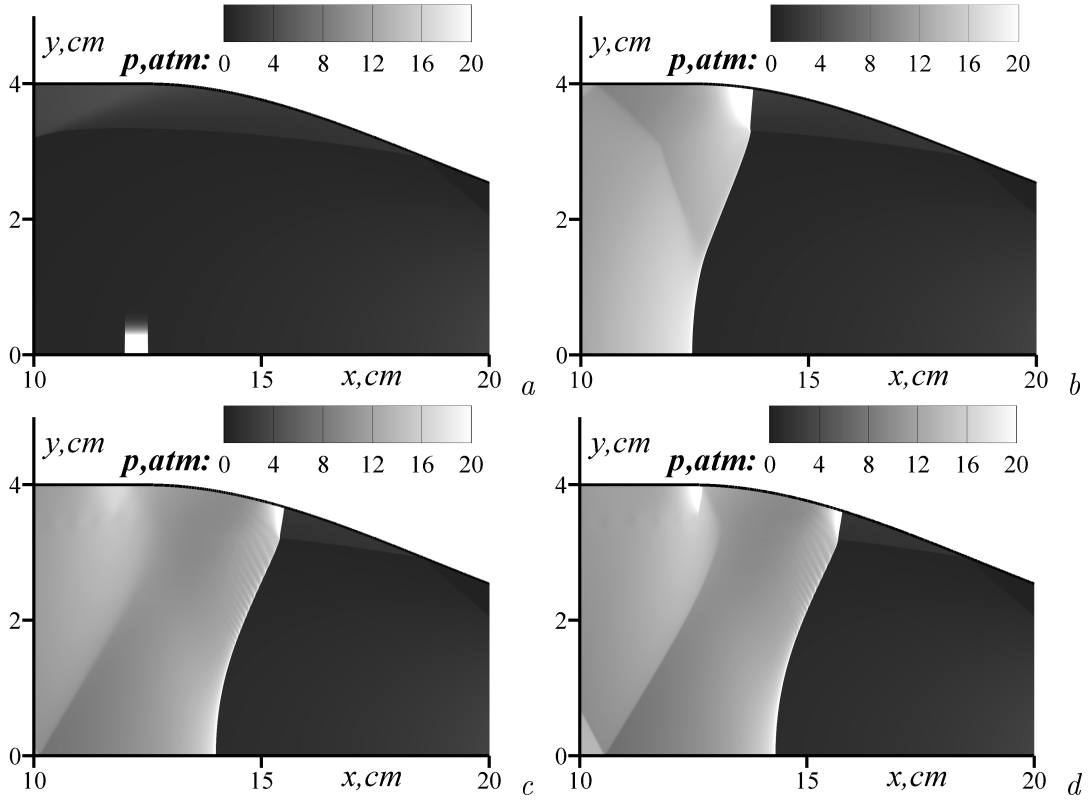

Figure 2: Formation of the flow with the stabilized detonation wave in the channel with constriction in case of M_0=5 and l=0.04 m: a – t=0.0 ms; b – t=0.2 ms; c – t=1.0 ms; d – t=3.1 ms

obtained that in the $M_0 = 5$ case the sufficient condition for effective stabilization of the detonation wave is the use of the channel with $l = 0.04$ m (Fig. 2). Note that, for the detailed representation of the flow in Fig. 2 (and in the figures that follow below) the pressure fields only in the channel part containing the detonation wave are plotted. In the case under consideration the detonation wave initiated by energy input near the x=0.125 m section moves upstream and is stabilized with time near x=0.143 m section (near to the symmetry plane). It forms a three-shock Mach configuration with the oblique shock wave of the stationary flow.

The control of stabilized detonation location in the gas mixture flow in the channel by means of variations of the inflow Mach number, the dustiness of the inflowing gas mixture and the width of the outflow channel section was studied with the purpose of increase in the efficiency of detonation combustion. The extended over multi-component mixtures [4] the one-velocity and one-temperature model [8], which describes the flow of gas with very small inert particles, was used for dusty-gas mixture flow simulation.

So, the decrease M_0 ($M_0 = 4.9$) leads to the situation in which the detonation wave moves through the throat and leaves the channel in counterflow direction (Fig. 3). It has been established that the addition of fine inert dust particles into the gas flow may be used for detonation stabilization. Thus, in case of dust density ρ_{s0}

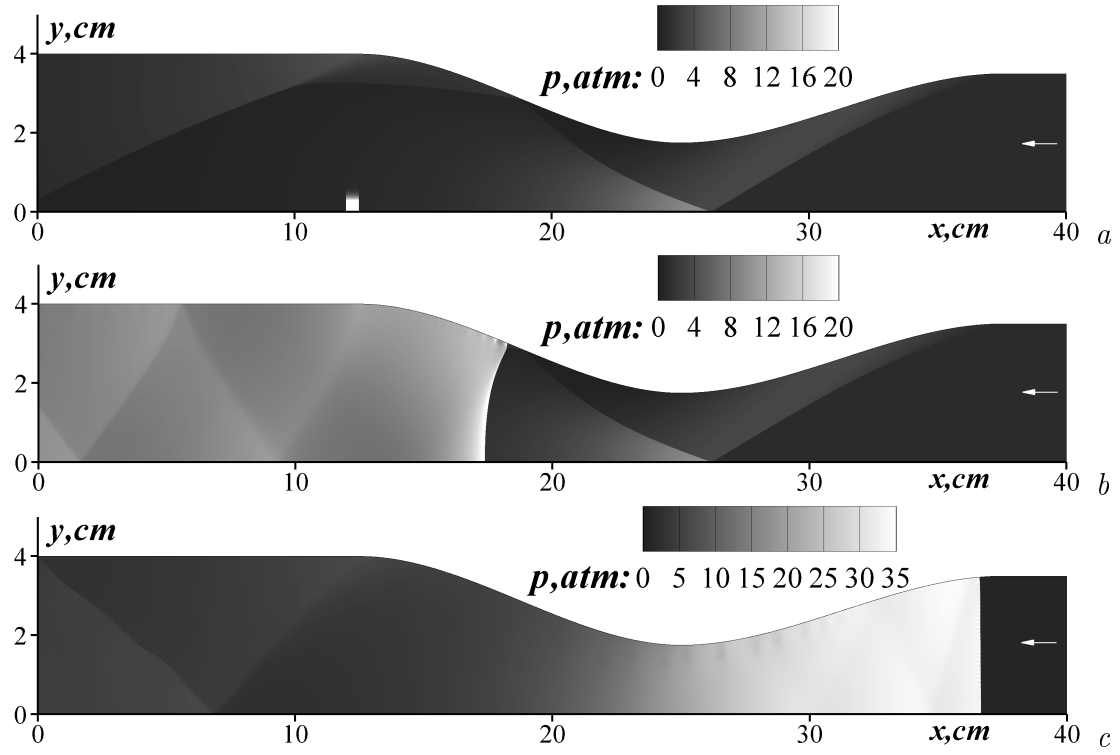

Figure 3: Propagation of the detonation wave in the channel in case of M_0=4.9 and l=0.04 m: a – t=0.0 ms; b – t=2.0 ms; c – t=3.0 ms

=0.1 kg/m^3 in the incoming flow of the dust-gas mixture (the flow Mach number $M_0 = 4.9$) the detonation wave is stabilized (Fig. 4) upstream of detonation location in the pure mixture in case of $M_0 = 5$ and thrust increases more than 3 times. Moreover, it was found that variation of a dust density in the incoming flow makes it possible to control the location of stabilized detonation.

Another mechanism of detonation location control is the variation of a width of the outflow channel section. So, in case of the pure combustible mixture flowing into the channel at a velocity corresponding to $M_0 = 4.9$, a width of the outflow channel section may be selected so that the formed in the channel flow with the detonation wave develops thrust that exceeds the one in the considered case of M_0=5. Thus, the small expansion of the output cross section (l = 0.045 m) in case of M_0=4.9 provides detonation stabilization in the divergent channel part and more than 2.5 times increase of thrust as compared to the considered case of M_0=5 (Fig. 5).

The possibility of detonation initiation and formation of the thrust developing flow with the stabilized detonation wave in the channel without any energy consumption has been detected. In these cases the obstacle (barrier) was used for detonation initiation. Thus, in the latter considered case of M_0=4.9 and l=0.045 m a detonation wave may be initiated by means of the barrier with height h=0.005 m located on the plane of symmetry near the x_b=0.1375 m section for period of time t=0.05 ms (Fig. 6). The detonation wave, formed in front of the barrier, is stabilized with time in that particular place where detonation initiated by initial energy input was stabilized. So, in this case the thrust developing flow with detonation is formed

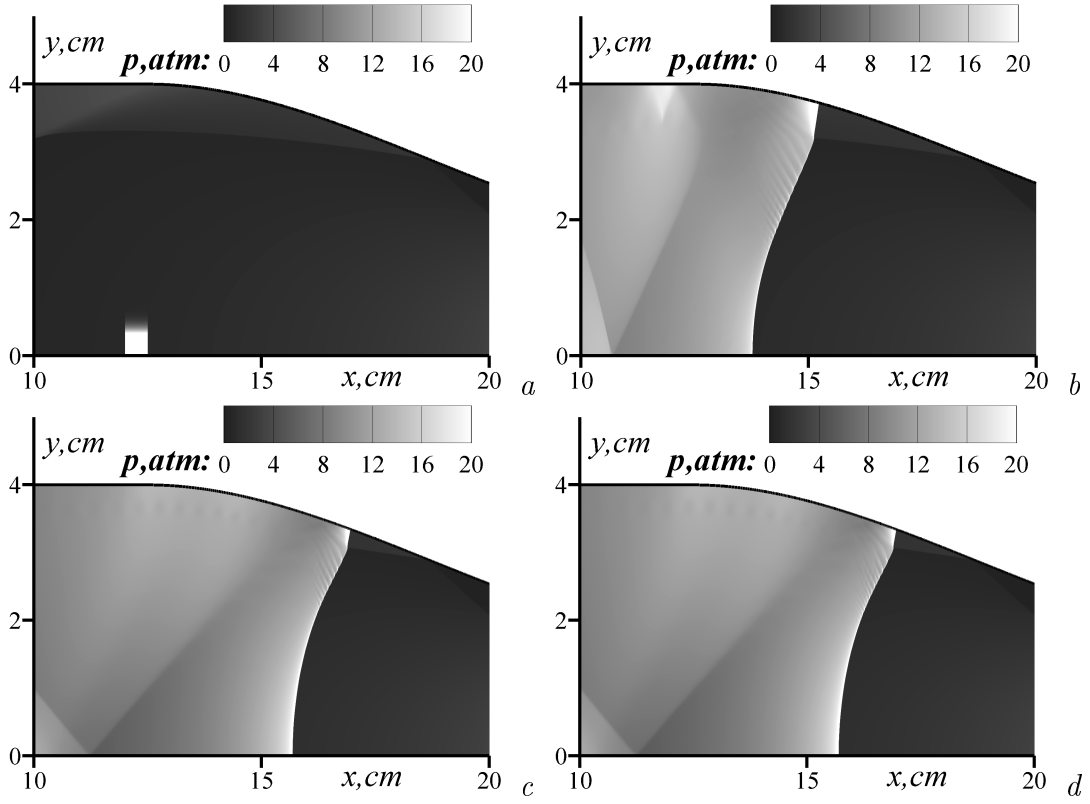

Figure 4: Formation of the flow with the stabilized detonation wave in the channel with constriction in case of M_0=4.9, l=0.04 m and dust density in the incoming flow ρ_{s0}=0.1 kg/m^3: a – t=0.0 ms; b – t=0.5 ms; c – t=3.5 ms; d – t=3.9 ms

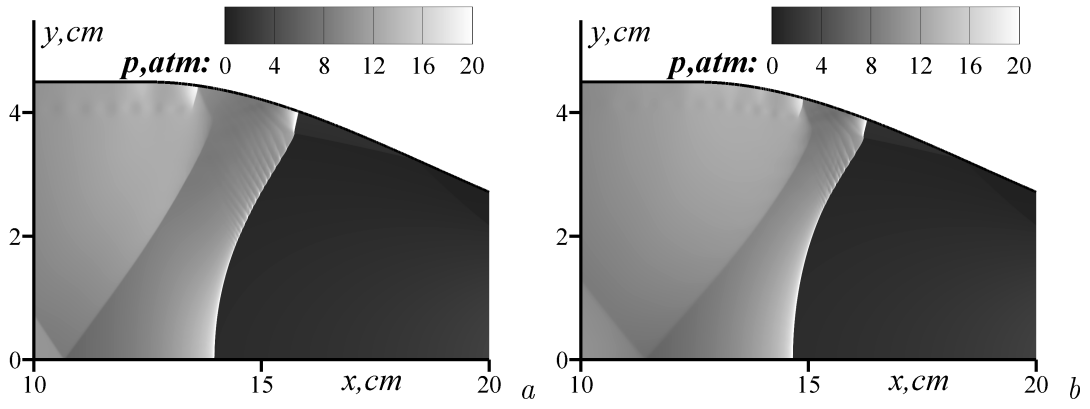

Figure 5: Formation of the flow with the stabilized detonation wave in the channel with constriction in case of M_0=4.9 and l=0.045 m: a – t=0.5 ms; b – t=2.0 ms

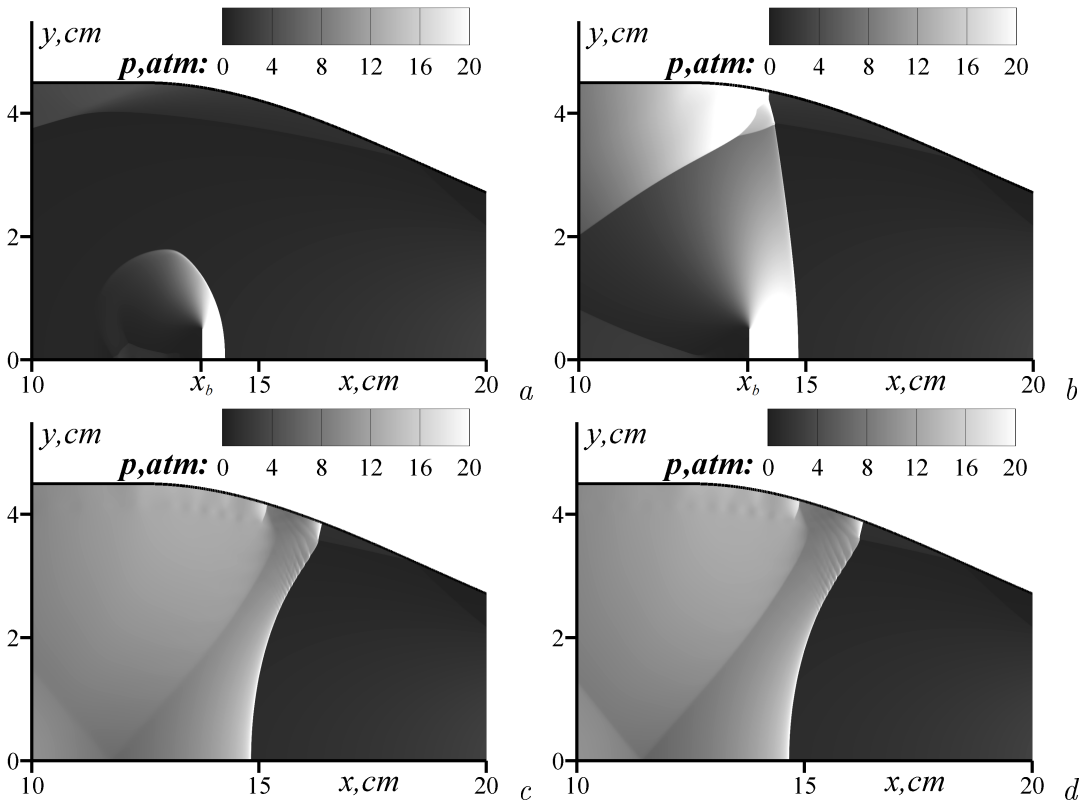

Figure 6: Formation of the flow with stabilized detonation in case of using the barrier for detonation initiation for M_0=4.9 and l=0.045 m: a – t=0.01 ms; b – t=0.05 ms; c – t=0.5 ms; d – t=2.5 ms

without any energy consumption.

4 Conclusions

Using a detailed kinetic model of chemical interaction, detonation stabilization in a stoichiometrical hydrogen-air mixture flowing at a supersonic velocity into a symmetric plane channel with constriction the outflow section of which exceeds the inflow one, and possibility of control of stabilized detonation location in the flow have been studied.

The possibility of formation of the thrust developing flow with a stabilized detonation wave in the channel has been established. The influence of variations of the inflow Mach number, the dustiness of the inflowing gas mixture and the width of the outflow channel cross section on the stabilized detonation location has been examined with the purpose of thrust increase. The methods of controlling of detonation location have been proposed. The possibility of detonation initiation and formation of the thrust developing flow with the stabilized detonation wave in the channel with constriction without energy consumption has been detected.

Acknowledgements

This research has been supported by the Russian Foundation for Basic Research (project No. 16-29-01092) and the Ministry of Education and Science of the Russian Federation (project NSh-8425.2016.1). This research has been supported by the Supercomputing Center of Lomonosov Moscow State University [9].

References

[1] Vasil'ev A.A., Zvegintsev V.I., Nalivaichenko D.G. Detonation waves in a reactive supersonic flow. Combustion, Explosion, and Shock Waves. 2006. 42(5). P. 85–100

[2] Zhuravskaya T.A., Levin V.A. Stabilization of detonation combustion of a high-velocity combustible gas mixture flow in a plane channel. Fluid Dynamics. 2015. 50(2). P. 283–293.

[3] Zhuravskaya T.A., Levin V.A. Investigation of certain techniques for stabilizing detonation waves in a supersonic flow. Fluid Dynamics. 2012. 47(6). P. 793–801.

[4] Zhuravskaya T.A., Levin V.A. Stability of Gas Mixture Flow with a Stabilized Detonation Wave in a Plane Channel with a Constriction. Fluid Dynamics. Fluid Dynamics. 2016. 51(4). P. 544–551.

[5] Glushko V.P. et al. (eds.) Thermodynamic properties of individual substances. Moscow: Nauka, 1978 [in Russia].

[6] Starik A.M., Titova N.S., Sharipov A.S., Kozlov V.E. Syngas Oxidation Mechanism. Combustion, Explosion, and Shock Waves. 2010. 46(5). P. 491–506.

[7] Godunov S.K., Zabrodin A.V., Ivanov M.Ya., Kraiko A.N., Prokopov G.P. Numerical Solution of Multidimensional Problems of Gasdynamics. Moscow: Nauka, 1976. 400 p. [in Russia].

[8] Sedov L.I. Similarity and dimensional methods in mechanics. 10th ed. Boca Raton: CRC Press, 1993. 493 p.

[9] Sadovnichy V., Tikhonravov A., Voevodin Vl., Opanasenko V. "Lomonosov": Supercomputing at Moscow State University. In Contemporary High Performance Computing: From Petascale toward Exascale (Chapman and Hall/CRC Computational Science). Boca Raton, USA: CRC Press, 2013. P .283–307.

Vladimir A. Levin, Michurinskiy av. 1, Institute of Mechanics M.V. Lomonosov Moscow State University, Moscow, Russia
Tatiana A. Zhuravskaya, Michurinskiy av. 1, Institute of Mechanics M.V. Lomonosov Moscow State University, Moscow, Russia

Strain rate effects at tensile loading of single crystal Cu nano-wires

Solveig Melin, Aylin Ahadi

solveig.melin@mek.lth.se

Abstract

It is well-known and experimentally confirmed that the mechanical response to loading of small enough structures differs from what applies to the macro-scale. This is valid for structures of linear measures at the nano-scale, typically below about 50nm. In addition to pure size effects also the crystallographic orientation becomes important at this scale. This study demonstrates the mechanical response to displacement controlled tensile loading of solid nano-sized fcc single-crystal Cu beams of square shaped cross sections. The investigation was performed through 3D molecular dynamic simulations using the free-ware LAMMPS. Two different crystal orientations and different loading rates were considered. Deformations and stress-strain curves were obtained and the necking behavior was studied in detail.

1 Introduction

Fragmentation of metals due to high strain rate loading is a well-recognized phenomenon at the global scale. The fragmentation pattern is affected by inertia as well as by stress waves traveling within the specimen. Also material properties, both the elastic and the plastic responses, are dependent on strain rate. This is true at the global scale but applies also at the nano scale. For nano-sized components further complications emerge because the material properties become size dependent for small enough components. This size effect is experimentally demonstrated; cf. e.g. [1, 2]. Further, from experiments Kraft and co-workers concluded that it is the relative number of surface atoms as compared to number of bulk atoms that influences the mechanical properties, cf. [3, 4, 5]. This is due to that surfaces imply the absence of atomic bonds, leaving surface atoms in energy states deviating from those of bulk atoms. The redistribution of the electron density close to a surface affects the inter-atomic bonding forces and, thereby, both the local load carrying capacity and the load distribution within the structure, cf. e.g. [6, 7, 8, 9]. Such an influence is not noticed, and thus not taken into account, at the macro-scale since the share of surface atom is small so that the mechanical response is ruled by the bulk atoms. Another aspect that has to be taken into account at the nano-scale

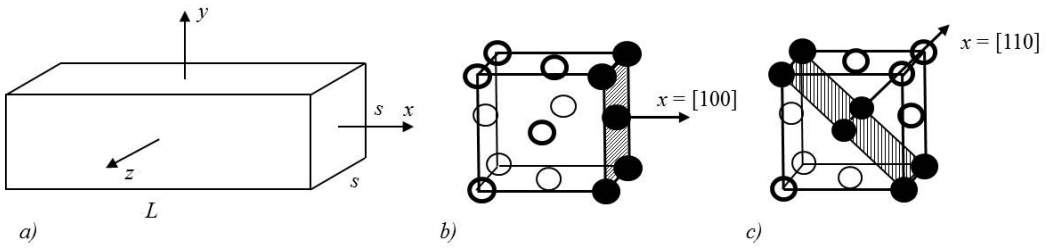

Figure 1: a) Beam configuration and coordinate system. b),c) Crystallographic orientations [100] and [110], respectively.

is the local crystallographic orientation, determining the elastic properties as well as defining pertinent slip plane directions determining the plastic response, cf. [7]. For components at the global scale normally there is an even spread of crystallographic orientations between the grains, eliminating directional dependence. In this paper the strain rate dependence at tensile loading of beams of single-crystal Cu of two different crystallographic orientations and three different cross section sizes is investigated. To accomplish this, 3D molecular dynamics simulations have been performed. As expected, both geometry and crystal orientation influences the mechanical response.

2 Statement of the problem

2.1 Model geometry

Beams of single crystal fcc Cu, of length L and quadratic cross section with side length s, are loaded under tension in their length direction x, cf. Fig. 1a) where a coordinate system (x, y, z) is introduced. The beam length is kept constant equal to $L = 300a_0$, with $a_0 = 3.615$ Å denoting the lattice constant for Cu. Three different cross section sizes are investigated, with $s = 6a_0$, $12a_0$ and $18a_0$.

Two different crystallographic orientations have been considered. For the first, referred to as the [100]-orientation, Fig. 1b), [100], [010] and [001] coincide with the $x-$, $y-$ and z-directions, respectively. For the second orientation, referred to as the [110]-orientation, Fig. 1c, [110], [-110] and [001] coincide with the $x-$, $y-$ and z-directions, respectively.

2.2 Molecular dynamics

The molecular dynamics free-ware LAMMPS, [10] has been used for the simulations and the atomic images are produced using OVITO developed by [11].

The beam is built from the repetition of Cu fcc unit cells and the interaction between the Cu atoms is described by an EAM-potential, giving the potential energy of an atom. This potential consists of one pair-wise repulsive part and one N-body attractive part, with a cut-off radii, cf. [12, 13]. The potential energy, of atom i of

type α is given by Eq. (1):

$$E_i^\alpha = f_\alpha \left(\sum_{i \neq j} \rho_\beta \left(r^{ij} \right) \right) + \frac{1}{2} \sum_{i \neq j} \varphi_{\alpha\beta} \left(r^{ij} \right) \tag{1}$$

where α and β are two types of atoms, r^{ij} is the distance between atoms i and j, $\varphi_{\alpha\beta}$ is a pair-wise potential function, ρ_β is the contribution to the electron charge density from atom j of type β at the location of atom i, and f_α is an embedding function that represents the energy required to place atom i of type α into the electron cloud. Here only one type of atoms is present so that α and β are the same. In this study the potential file named Cu-u3.eam, given in LAMMPS and developed by [14] have been used.
The per-atom stresses, σ_{kl}^i, $k, l = x, y, z$, of atom i are in LAMMPS calculated as

$$\sigma_{kl}^i = -\frac{1}{V^i} \left(m^i \nu_k^i \nu_l^i \; + \; \sum_j F_k^{ij} r_l^{ij} \right) \tag{2}$$

Here V^i is the atomic volume, assumed equal for all atoms and determined at the start of the simulation after an initial relaxation of the system to find the equilibrium state. Further, m^i is the atomic mass, ν_k^i and ν_l^i the velocities of atom i in the k- and l-directions, F_k^{ij} the force in the k-direction between atoms i and j, and the distance in the l-direction between atoms i and j.
A NVT-ensemble is generated and the temperature T is kept constant equal to $T = 0.01$K by a Nosé-Hoover thermostat according to [15]. Initially the atomic ensemble is relaxed to its equilibrium state for 5000 time steps, corresponding to 25ps. Thereafter an axial elongation is effectuated by applying a constant velocity v_{end} in the $+x$- and $-x$-directions to four unit cells at each end of the beam at the same time as the atoms of these cells are restricted from movements in the y- and z-directions. Thus clamped boundary conditions are mimicked. All atoms in between these end cells are free to move without constraints. The displacement controlled load is applied with time step $\Delta t = 5$fs and the end velocities investigated are $v_{end} = Mv_0$, with $v_0 = a_0/400/\text{ps}$ and $M = 1, 2, 4, 6, 8$. The results are evaluated using the centro-symmetry parameter CSP according to [16], as being a measure of the instantaneous lattice disorder. The centro-symmetry parameter for an atom is defined according to Eq. (3),

$$CSP = \sum_{i=1}^{N/2} |R_i + R_{i+N/2}|^2 \tag{3}$$

where the N is the number of nearest neighbors in the surrounding lattice, equal to 12 for a fcc lattice. R_i and $R_{i+N/2}$ are the vectors corresponding to pairs of opposite nearest-neighbors in the lattice. The value of the CSP signals whether an atom is part of a perfect lattice, a local defect (a vacancy, partial dislocation or a stacking fault), or part of a free surface. Commonly used CSP values for different situations in fcc lattices are shown in Table 6, cf. [17] for the values marked by $*$. However, for atoms situated along edges or at corners, the CSP values reach much higher values

than at a free surface. For the beam geometry with crystallographic orientations [100] and [110] as studied here, the pertinent CSP values for surface atoms together with edge- and corner-atoms are inserted in Table 6 and marked by Δ, cf. [18].

Lattice structure	CSP
$*$ Ideal fcc structure	$CSP < 3$
$*$ Partial dislocation	$3 < CSP < 5$
$*$ Stacking fault	$5 < CSP < 9$
$*$ Surface atoms	$9 < CSP < 20$
ΔSurface atoms [100]	$9 < CSP \leq 21$
ΔSurface atoms [110]	$9 < CSP \leq 25$
ΔEdge- and corner atoms [100]	$CSP > 21$
ΔEdge- and corner atoms [110]	$CSP > 25$

Table 6: CSP values for fcc lattices; $*$ after [17], Δ after [18].

3 Results and Discussion

3.1 Rate dependence of plasticity initiation and rupture

During loading of the beams, the deformations are monitored in detail. The initiation of plasticity, i.e. the time at the first slip event, is denoted t_i, and the strain at this event is denoted ε_i. At subsequent loading rupture of the beam eventually occurs at time t_{1f}, when the applied axial strain is ε_{1f}. In some cases rupture is found to occur more than once. The time at which this eventual second rupture occurs, resulting in three separate parts, is denoted t_{2f}. The times t_i, t_{1f} and t_{2f} are plotted in Fig. 2 for both orientations and all investigated velocities.
In Tables 7-9 the values of ε_i and ε_{1f} are found for cross section side lengths $s = 6a_0$, $12a_0$ and $18a_0$, respectively, for all investigated velocities and for both crystallographic orientations. The time delay to an eventual second rupture, $\Delta t = t_{2f} - t_{1f}$, is also given. The results are plotted in Fig. 3 for clarity.
As seen from the Tables 7-9 and Fig. 3, the plastic initiation strain ε_i is almost independent of size s. On the other hand, the dependence of ε_i on v_{end} is obvious. It seems that there is an overall tendency for ε_i to attend values at two different strain levels; very roughly $\varepsilon_i \approx 0.09$ for the lower end velocities and $\varepsilon_i \approx 0.03$ for the higher for the [100]-orientation. Similarly, $\varepsilon_i \approx 0.07$ at the lower end velocities and $\varepsilon_i \approx 0.02$ at the higher for the [110]-orientation. In both cases there is a drop of about a factor of 3, with the transition around $v_{end} = 4v_0$.
For the [100]-orientation the strain at first rupture, ε_{1f}, first increases with v_{end}, but beyond $v_{end} = 2v_0$ it decreases again. This coincides with the emergence of a second rupture at time t_{2f}, cf. Tables 8-10 and Fig. 2.

Orientation	[100]			[110]		
M	ε_i	ε_{1f}	Second rupture, Δt	ε_{1f}	ε_{1f}	Second rupture, Δt
1	0.0936	0.1291	no	0.0671	0.1326	no
2	0.0949	0.1479	0.525	0.0684	0.1300	0.425
4	0.0855	0.1300	0.100	0.0547	0.1146	0.100
6	0.0410	0.0975	0.150	0.0231	0.0949	0.075
8	0.0308	0.0752	0.050	0.0171	0.0821	0.125

Table 7: $s = 6a_0$; ε_i = strain at plastic initiation; ε_{1f} = strain at first rupture; Δt = time delay to second rupture (ps).

For the [110]-orientation, on the other hand, ε_{1f} shows no tendency for an initial increase followed by a decrease as for the [100]-orientation but instead a decrease with end velocity is at hand. Also here a second rupture occurs at high enough end velocities. Only one case differs from the rest, namely $s = 12a_0$ at end velocity $v_{end} = v_0$. Here a first rupture occurs after a substantial elongation of the beam, with $\varepsilon_{1f} \approx 0.53$ and the second after an additional 0.275ps.

For both orientations hold that, as v_{end} increases, decisive necking regions eventual

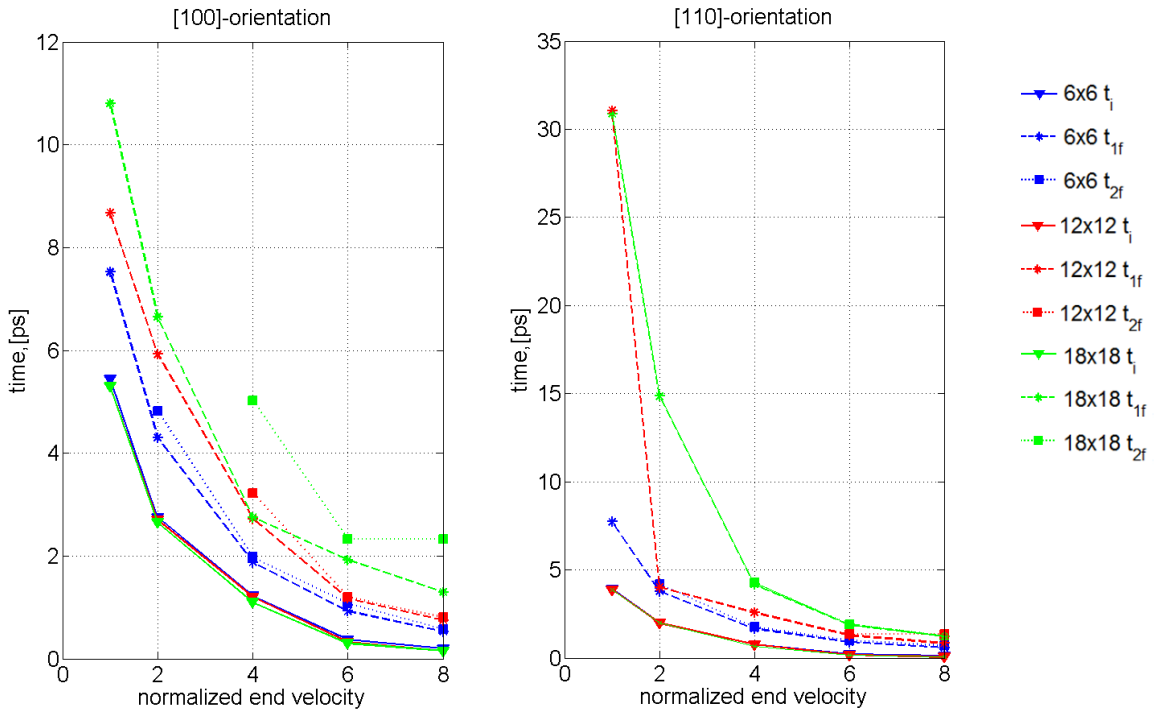

Figure 2: Time t_i, t_{1f} and t_{2f} versus normalized end velocity v_{end}/v_0.

Orientation	[100]			[110]		
M	ε_i	ε_{1f}	Second rupture, Δt	ε_{1f}	ε_{1f}	Second rupture, Δt
1	0.0911	0.1488	no	0.0667	0.5314	0.275
2	0.0932	0.2035	no	0.0684	0.1377	no
4	0.0838	0.1881	0.500	0.0547	0.1778	no
6	0.0359	0.1231	0.025	0.0205	0.1359	0.050
8	0.0239	0.1060	0.050	0.0103	0.1163	0.050

Table 8: $s = 12a_0$; ε_i = strain at plastic initiation; ε_{1f} = strain at first rupture; Δt = time delay to second rupture (ps).

Orientation	[100]			[110]		
M	ε_i	ε_{1f}	Second rupture, Δt	ε_{1f}	ε_{1f}	Second rupture, Δt
1	0.0911	0.1847	no	0.0667	0.5284	no
2	0.0915	0.2283	no	0.0684	0.5087	no
4	0.0770	0.1898	2.275	0.0479	0.2873	0.075
6	0.0334	0.2001	0.400	0.0180	0.1949	0.025
8	0.0239	0.1813	0.175	0.0137	0.1710	0.050

Table 9: $s = 18a_0$; ε_i = strain at plastic initiation; ε_{1f} = strain at first rupture; Δt = time delay to second rupture (ps).

leading to rupture develops closer to the clamped ends whereas rupture occurs more centrally for low end velocities. Thus the chosen region of end velocities in the present investigations cover the transition between these two behaviors.

3.2 Stress-Strain curves

Also the stress-strain relations were recorded for all cases. The axial stress $\sigma_{x[]}$, with [] holding the crystallographic orientation, was determined as the mean stress in the axial direction calculated over all atoms in the beam. It was found that the stresses $\sigma^0_{x[]}$ at $\varepsilon_x = 0$, directly after relaxation of the beams, were non-zero and decreasing with increasing beam size for both orientations. In Figs. 2-5 the stress-strain curves, compensated for $\sigma^0_{x[]}$ so that they all pass through the origin, are shown for cross section side lengths $s = 6a_0$, $12a_0$ and $18a_0$, respectively, for different end velocities v_{end} and for both crystallographic orientations. The stresses at the vertical axes in Figs. 4-6 thus equals the exceed stress $\sigma^{exceed}_{x[]} = (\sigma_{x[]} - \sigma^0_{x[]})$. The values of $\sigma^0_{x[]}$ are

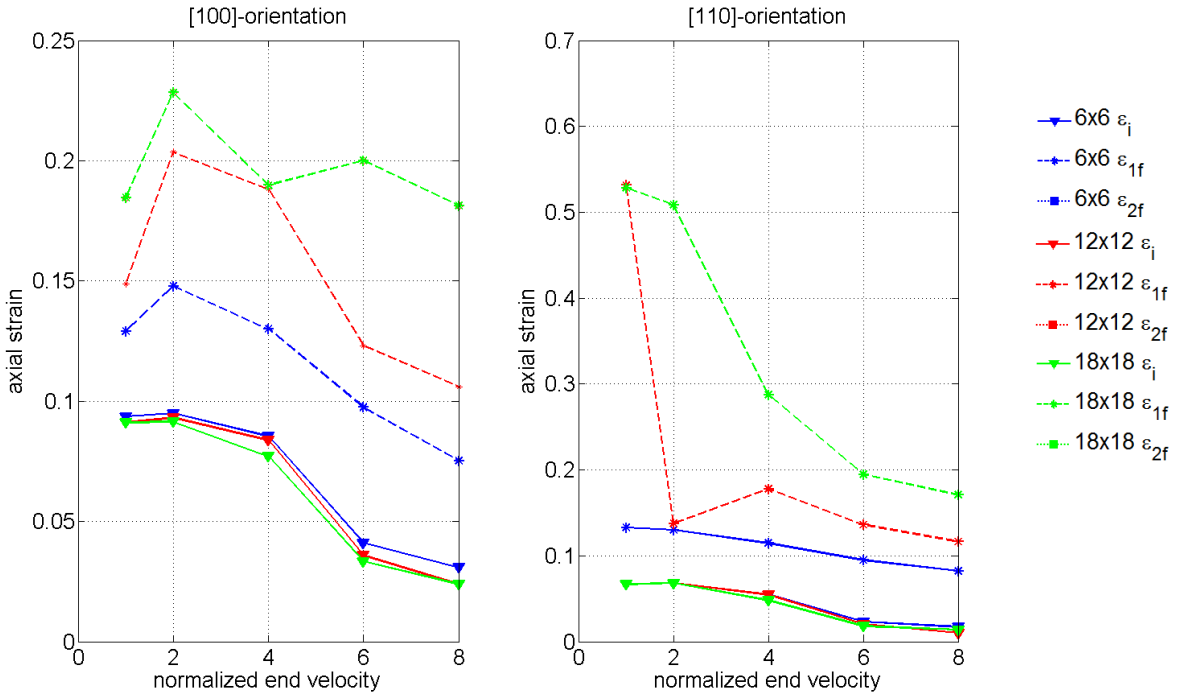

Figure 3: Applied axial strain ε_x versus normalized end velocity v_{end}/v_0. ε_i = strain at plastic initiation; ε_{1f} = strain at first rupture, versus normalized end velocity v_{end}/v_0.

given in Table 10. All curves in Figs. 4-6 are shown up to the point of first rupture strain ε_{1f}.

$s = 6a_0$	$s = 12a_0$	$s = 18a_0$
$\sigma^0_{x[100]} = 1.37$	$\sigma^0_{x[100]} = 0.679$	$\sigma^0_{x[100]} = 0.462$
$\sigma^0_{x[110]} = 1.28$	$\sigma^0_{x[110]} = 0.710$	$\sigma^0_{x[110]} = 0.521$

Table 10: Stress directly after relaxation (GPa).

As seen from the stress-strain curves the elastic behaviour is almost independent on end velocity for each orientation and for each size. Also, the elastic parts are nonlinear, most obvious for the [110]-orientation curves which are clearly convex. The [100]-orientation curves, on the other hand, are slightly concave. Thus the elastic behaviour is non-linear so that the modulus of elasticity varies with strain in addition to the well-known fact that it varies with size.
The first peek stress of each curve corresponds to the first dislocation formation, i.e. to plastic initiation, at strain ε_i. The yield stress is defines as the at which the material begins to deform plastically. Since the stresses $\sigma^0_{x[]}$ at $\varepsilon_x = 0$, directly after relaxation of the beams, were non-zero and decreasing with increasing beam size for both orientations, we introduce here the exceed yield stress, $\sigma^{exceed}_{Y[]}$, defined as

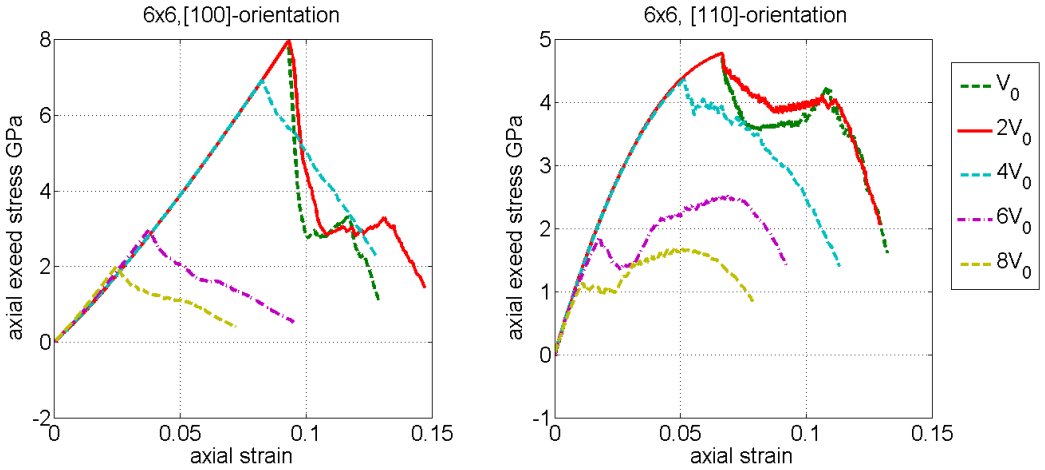

Figure 4: Axial exceed stress $\sigma_{x[]}^{exceed}$ versus applied axial strain ε_x, $s = 6a_0$.

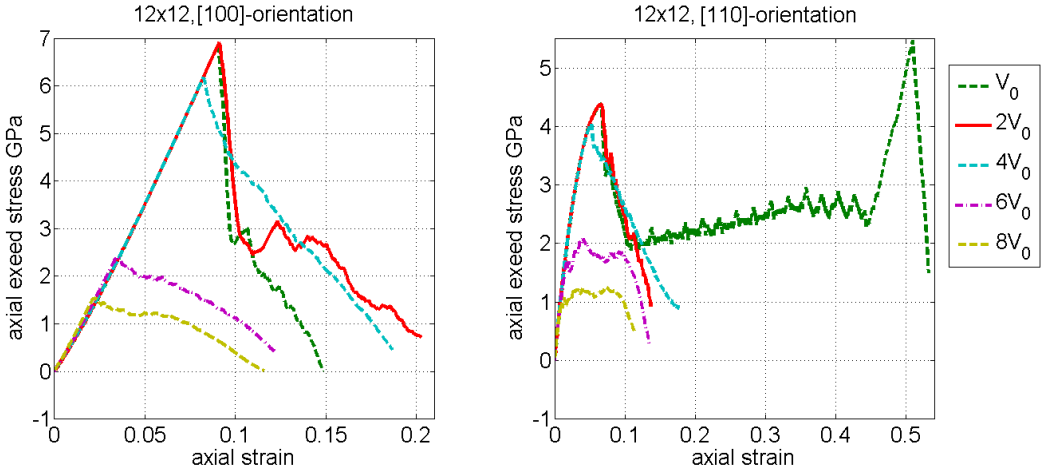

Figure 5: Axial exceed stress $\sigma_{x[]}^{exceed}$ versus applied axial strain ε_x, $s = 12a_0$.

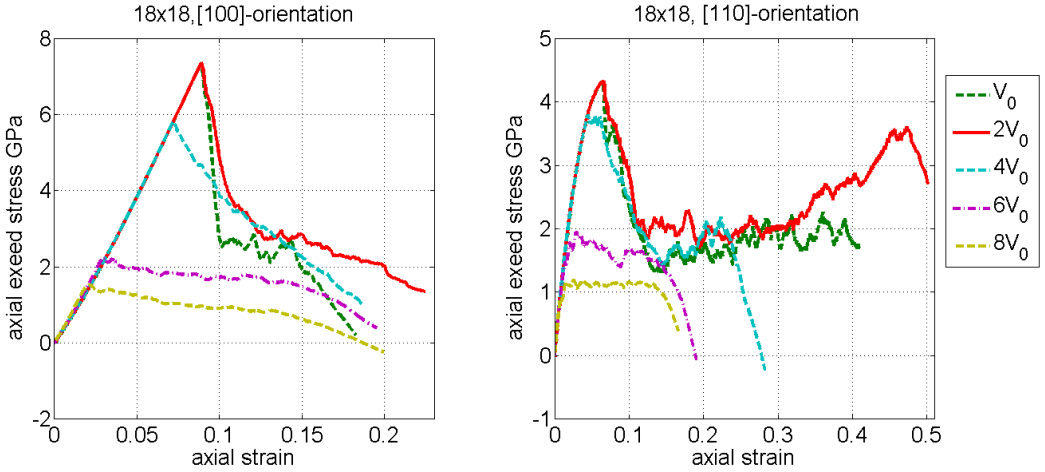

Figure 6: Axial exceed stress $\sigma_{x[]}^{exceed}$ versus applied axial strain ε_x, $s = 18a_0$.

$\sigma_{Y[]}^{exceed} = (\sigma_{x[]}(\varepsilon_i) - \sigma_{x[]}^0)$, is given in Table 11 and plotted in Fig. 7. As seen, $\sigma_{Y[]}^{exceed}$ does not vary much with size but, on the other hand, there is a drop in magnitude of $\sigma_{x[]}^{exceed}$ between low and high end velocities, a factor of $3-4$ for the velocity range investigated here. The shift starts as v_{end} exceeds $2v_0$. This holds for both orientations and all sizes.

M	1	2	4	6	8
$s = 6a_0$					
$\sigma_{Y[100]}^{exceed}$	7.95	7.98	6.98	3.14	2.13
$\sigma_{Y[110]}^{exceed}$	4.778	4.7794	4.43	1.96	1.31
$s = 12a_0$					
$\sigma_{Y[100]}^{exceed}$	7.95	7.98	6.98	3.14	2.13
$\sigma_{Y[110]}^{exceed}$	4.778	4.7794	4.43	1.96	1.31
$s = 18a_0$					
$\sigma_{Y[100]}^{exceed}$	7.95	7.98	6.98	3.14	2.13
$\sigma_{Y[110]}^{exceed}$	4.778	4.7794	4.43	1.96	1.31

Table 11: Stress directly after relaxation (GPa).

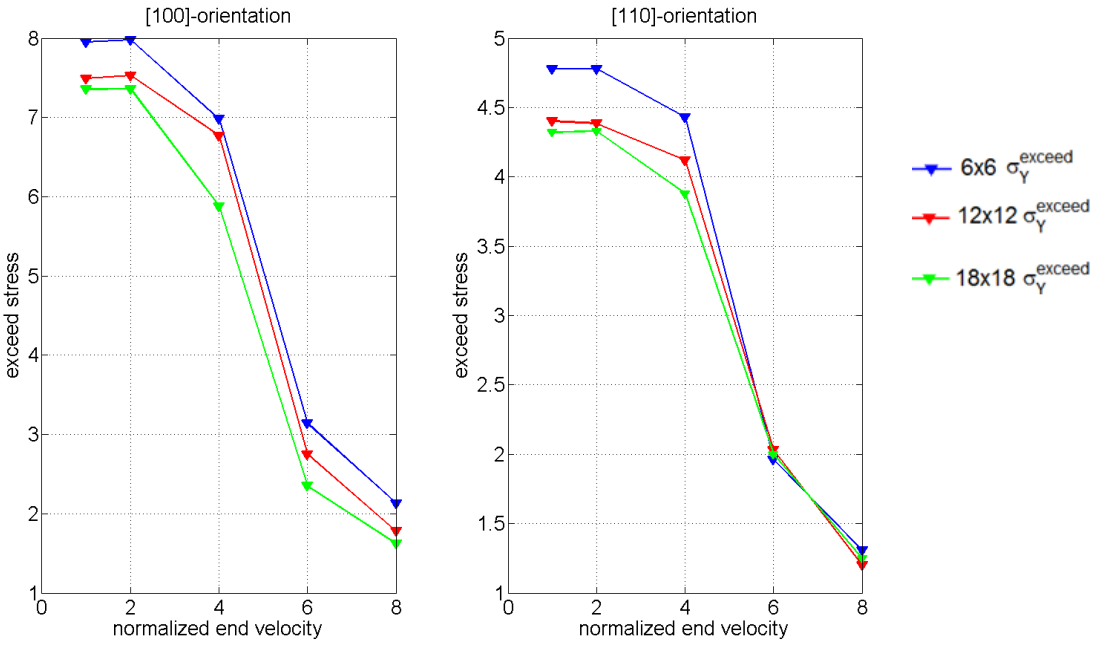

Figure 7: Exceed yield stress $\sigma_{Y[]}^{exceed}$ versus normalized end velocity v_{end}/v_0.

3.3 Deformation developments patterns

How the plasticity in the beam develops and spreads depends on end velocity. After plastic initiation the plasticity spreads from the initiation spots into the still elastic parts of the beam through slip along preferred slip planes. This spread ceases more or less as neck formation starts depending on the velocity; at this point most of the slip events localize to the dominant necking regions and areas that still are elastic after final rupture remain so. If necking starts early in the loading process, as is the case if v_{end} is high enough, the beam has not elongated very much and corresponding rupture strain is low.

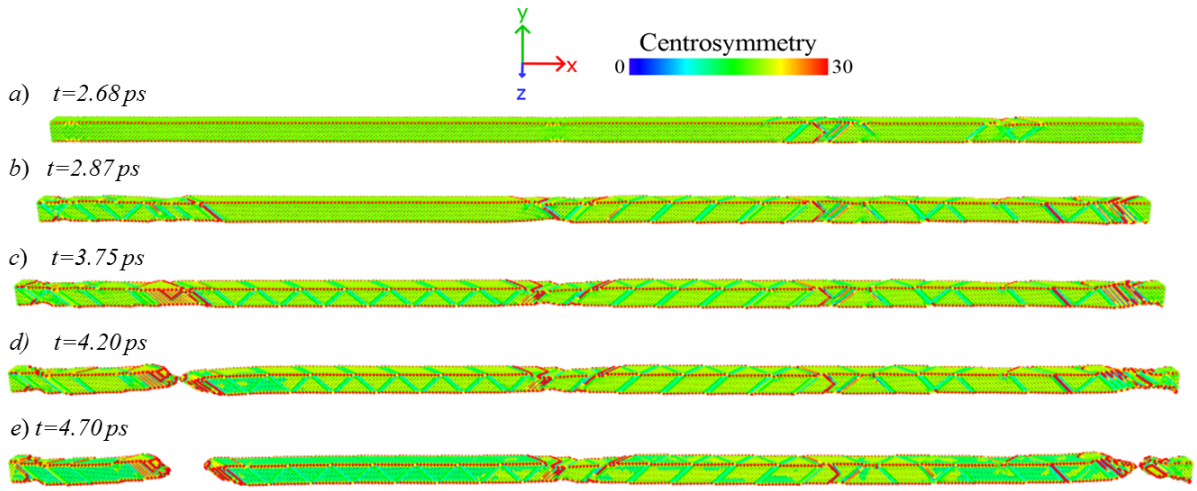

Figure 8: Snapshots of atomic arrangement along the curves in Fig. 4 for orientation [100] and velocity $2v_0$.

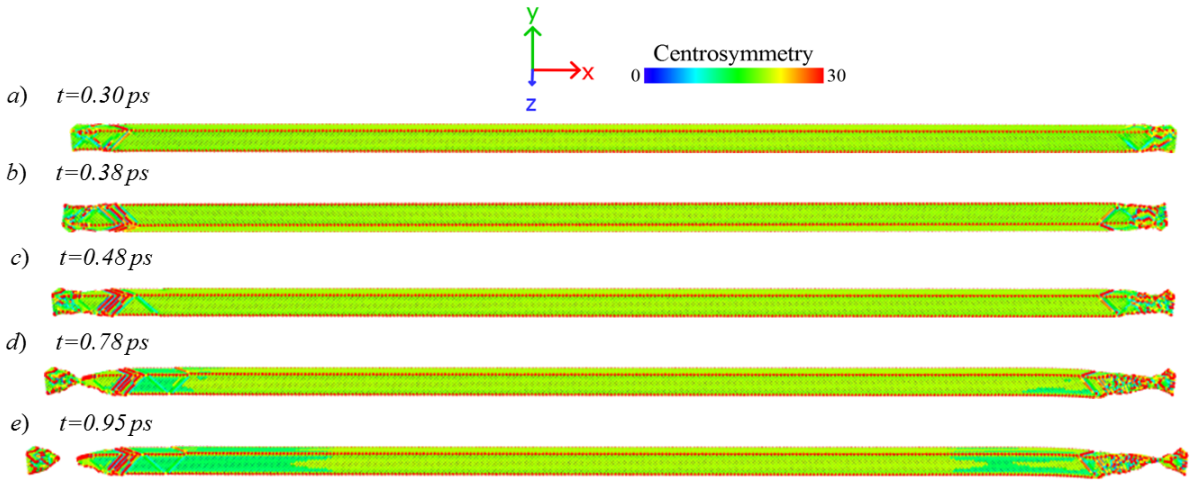

Figure 9: Snapshots of atomic arrangement along the curves in Fig. 4 for orientation [100] and velocity $6v_0$.

In Figs. 8-9 snapshots of the atomic arrangements for the [100]-orientation with end velocities $2v_0$ and $6v_0$, respectively, are shown, and in Figs. 10-11 the corresponding

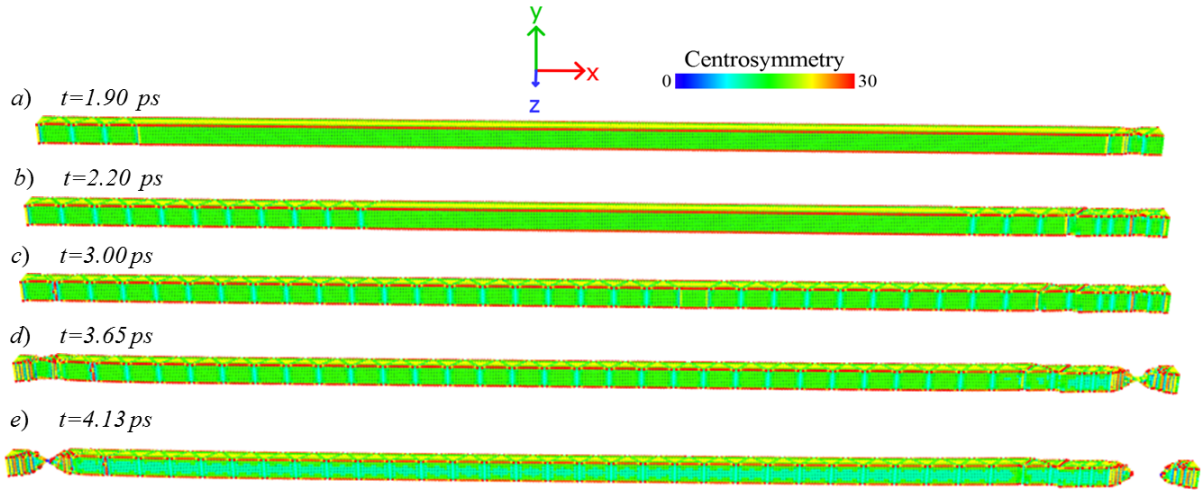

Figure 10: Snapshots of atomic arrangement along the curves in Fig. 4 for orientation [110] and velocity $2v_0$.

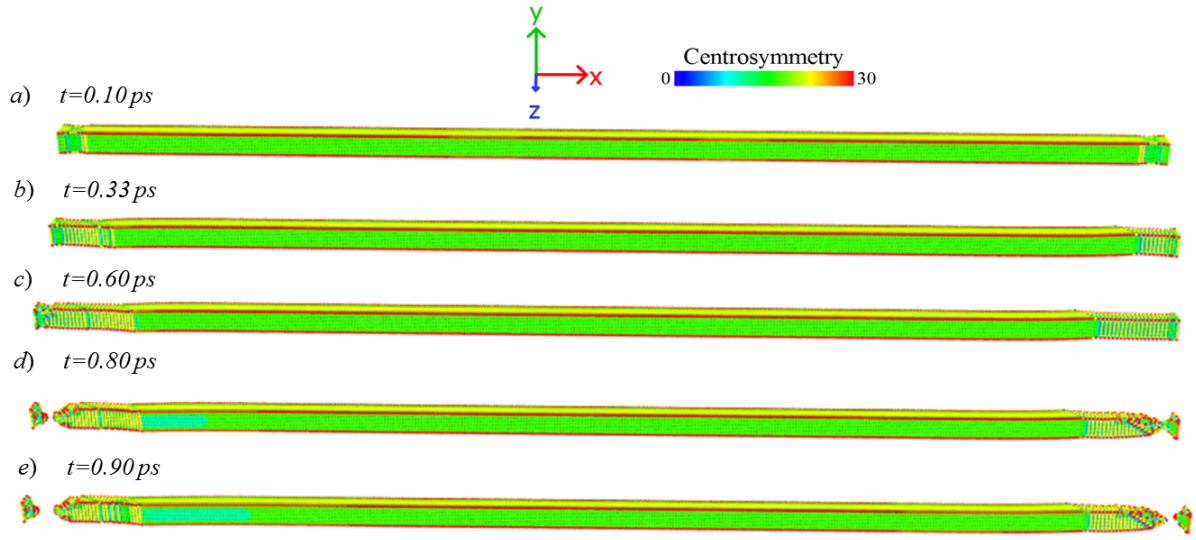

Figure 11: Snapshots of atomic arrangement along the curves in Fig. 4 for orientation [110] and velocity $6v_0$.

is shown for the [110]-orientation. Starting with [100]-orientation at low end velocity, $v_{end} = 2v_0$ shown in Fig. 8, it is seen that plasticity at time $t = 2.68$ps, Fig. 8a), has initiated over three parts of the beam, with the most intense development about 25% of the beam length from the right end, and the weakest close to the left end. Following the snapshots over time, slip is seen to spread from the initiation sites into the elastic areas and new spots of high plastic deformation emerge. Eventually, for $t = 4.20$ps as seen in Fig. 8d), rupture occurs at the distance of about 15% of the beam length from the left end, and this site is not one of the initial initiation sites from Fig. 8a). After this first rupture, relaxation of the beam starts from the rupture site but even so inertia causes a second rupture close to the right end at $t = 4.70$ps, Fig. 8e). For the higher end velocity, $v_{end} = 6v_0$ and with snapshots shown in Fig. 9, the development is different. Plasticity concentrates close to both

ends and accumulates there. When first and second ruptures have occurred, Fig. 9e) at time $t = 0.95$ps, the central part of the beam is still elastic and unaffected by the loading. As for the [110]-orientation the events are different as seen in Fig. 10 for $v_{end} = 2v_0$ and in Fig. 11 for $v_{end} = 6v_0$. Initiation always occurs close to the beam ends, Figs. 10a)-11a), and the plasticity spreads towards the center of the beam. Before rupture in the case of $v_{end} = 2v_0$ the entire beam is affected by slip before two subsequent ruptures take place. For the high loading velocity with $v_{end} = 6v_0$ as seen in Fig. 11 the plasticity spread from the ends is limited, leaving most of the center of the beam in an elastic state after the last rupture.

4 Conclusions

Through molecular dynamics simulations the influence of loading rate on the mechanical response of tensile single crystal fcc Cu nano beams have been investigated. The beams had a constant length of $300a_0$, with a_0 denoting the lattice constant for Cu, and quadratic cross section with side length $6a_0$, $12a_0$ or $18a_0$. Two different crystallographic orientations, with loading in the [100] or the [110] directions, were considered. The beams were loaded by applying a constant velocity $v_{end} = Mv_0$, with $v_0 = a_0/400/\text{ps}$ and $M = 1, 2, 4, 6, 8$, to each end of the beam and the deformation pattern was followed in detail and the stress-strain curves recorded. It was shown that the elastic behavior of the beams was non-linear and, in practice, independent of size for each orientation. On the other hand the strain rate dependence was obvious. The strain at plastic initiation was found to be about three times higher for the lowest end velocities as compared to the highest, with the swap around $M = 4$. Also the yield stress was heavily reduced, by a factor of around three or four, above $M = 4$. The hardening behavior differed between the orientations. It was substantial for the [110]-orientation but not very pronounced for the [100]-orientation. This is due to the difference in slip patterns between the orientations. The symmetrical atomic arrangement for the [100]-orientation provides equal deformations over beam height and beam width, which induces an hourglass shaped necking region and from this rupture. This deformation pattern is not at hand for the [110]-orientation since the Poisson ratio is differs between the height and the width directions. Slip in this case causes a deformation pattern similar to that of when tilting a deck of playing cards along the loading direction. The arrangement allows for substantial elongations before a neck weak enough to rupture has been formed.

References

[1] S. G. Nilsson and E. L. Sarwe and L. Montelius, Fabrication and mechanical characterization of ultrashort nanocantilevers, *Appl. Phys. Lett.*, **83**, 990–992, 2004.

[2] S. G. Nilsson and X. Borrisй and L. Montelius, Size effects on Youngұs modulus of thin chromium cantilevers, *Appl. Phys. Lett.*, **85**, 3555–3557, 2004.

[3] M. Hommel and O. Kraft, Deformation behavior of thin cupper films on deformable substrates,*Acta Mater.*, **49**, 3935–3947, 2001.

[4] R. Schweiger and G. Dehm and O. Kraft, Cyclic deformation of polychrystalline Cu films, *Phil. Mag.*, **83**, 693–710, 2003.

[5] R. Schweiger and O. Kraft, Size effects in the fatigue behavior in thin Ag films, *Acta Mater.*, **51**, 195–206, 2003.

[6] L. G. Zhou and H. C. Huang, Are surfaces elastically softer or stiffer?, *Appl. Phys. Lett.*, **84**, 1940, 2004.

[7] A. Ahadi and S. Melin, Size dependence of the Poisson's ration in single-crystal fcc copper nanobeams, *Comput. Mater. Sc.*, **11**, 322–327, 2016.

[8] P. A. T. Olsson, S. Melin and C. Persson, Atomistic simulations of tensile and bending properties of single-crystal BCC-Iron nanobeams,*Phys. Rev. B*, **76**, 1–15, 2007.

[9] P. A. T. Olsson and S. Melin., Atomistic studies of the elastic properties of metallic BCC nanowires and films,*Proc. IUTAM Symposium on Modelling Nanomaterials and Nanosystems*, **76**, 221–230, 2008.

[10] LAMMPS, http://lammps.sandia.gov.

[11] A. Stukowski, Visualization and analysis of atomistic simulation data with OVITO-the Open Visualization Tool,*Modelling Simul. Mater. Sci. Eng.*, **18**, 2010.

[12] B. L. Holian and A. F. Voter and N.J. Wagner and R.J. Ravelo and S. P. Chen and W. G. Hoover and C.G. Hoover and J. E. Hammerberg and T. D.Dontjie, Effects of pair-wise versus many-body forces on high-stress plastic deformation,*Phys. Rev. A*, **43**, 2655-2661, 1991.

[13] B. L. Holian and R. Ravelo, Fracture simulations using large-scale molecular-dynamics,*Phys. Rev. B*, **51**, 11275-11288, 1995.

[14] S. M. Foiles, M.I. Baskes and M.S. Daw, Embedded-atom-method functions for the fcc metals Cu, Ag, Au, Ni, Pd, Pt, and their alloys, *Phys. Rev. B*, **33**, 12–15, 1986.

[15] B. T. Ellad and R. E. Miller, Modeling Materials Continuum, Atomistic and Multiscale Techniques, Cambridge University Press, 2011.

[16] C. L. Kelchner and S. J. Plimpton and J. C. Hamilton, Dislocation nucleation and defect structure during surface indentation, *Phys. Rev. B*, **58**, 11085-8, 1998.

[17] H. Y. Liang and G. R. Liu and X. Han, Computational Methods, Cambridge University Press, 2011.

[18] P. Hansson, Influence of surface roughening on indentation behavior of thin copper coatings using a molecular dynamics approach, *Comput. Mater. Sc.*, **117**, 233–239, 2016.

Efficiency of ionocrafts: experimental investigation

Natalia Melnikova, Andrey Samusenko, Iulia Safronova

a.samusenko@spbu.ru

Abstract

Ionocraft is a flight facility which lifting force is created by means of ionic wind. Ionic wind is air flow caused by corona discharge. The flux of momentum which is whirled away by ionic wind jet may be used for propulsion. The ionocraft conception is known for decades but efficiency of the prototype models is still low. The main efficiency parameter for ionocraft is the relation of consumed electric energy and lifting force (вГЁthrust specific energy consumptionвГ№ Q — as an analogy to вГЁthrust specific fuel consumptionвГ№ which is a commonly used as a term in aviation). It is necessary to reach a certain level of thrust specific energy consumption for practical applications.

A classical construction of ionocraft segment вГY– wire-cylinder вГY– is considered. Presumable ways of efficiency improvement are discussed. Formally thrust specific energy consumption of ionocraft may be rather high especially for large interelectrode gaps. However, it usually leads to large air volume occupied by construction with significant total lifting force. Consequently, more sophisticated criteria should be used such as: thrust specific energy consumption level by fixed lifting force from unity volume.

1 Introduction

When high voltage is applied to interelectrode gap electrons accelerate in electric field and gain energy enough to ionize air molecules. So avalanche takes place increasing number of charged particles вГY– positive ions and electrons. If secondary processes of electrons production are intensive a new avalanche is caused by passing the first avalanche and self-maintained discharge process is formed which called corona discharge [2]. Charged particles appear in the air as a result of collision ionization in the corona layer. Coulomb force acts on charged particles in the interelectrode gap. In fact, electric force generates because of coupling electric field between electrodes and space charge. All kinds of ions (positive or negative –вГY it depends on the active electrode polarity) moving to the ground electrode gain the momentum in the electric field and transfer it to air molecules owing to collisions and the air starts to flow. And this process generates electrohydrodynamic flow which called ionic wind [2]. The reactive jet force of ionic wind can be used as a lifting force. So the lifting force is determined by the Coulomb force which

acts on ionocraft from ions. In such a case, ions quickly transfer momentum to air molecules.
There are many different ionocraft constructions –вГУ triangular, square, ring. These systems work as reactive engine and as a result they can levitate. The main issue in ionocraft designing is low specific thrust which is defined as the relation of the lifting force to consumed power.
In this paper lifting force results from current and voltage in the wire-cylinder are presented. The lifting force depends on the current I, interelectrode gap d and ions mobility μ in air gap [3]:

$$F = \frac{I}{\mu} d \tag{1}$$

Equation for specific thrust can be obtained from (1):

$$Q = \frac{F}{UI} = \frac{d}{\mu U} \tag{2}$$

As we can see from (2) thrust is lower when the voltage is higher. Consequently, thrust decreasing is caused by lifting force increasing (in specific geometry). So the main concern is searching a suitable configuration which solution will depend on applying technical restrictions (fixed voltage or fixed occupying volume). The next simplifying can be used for equations (1–2):

1. There are electrons only near active electrode. We neglect them in air gap.
2. Air friction force acting on electrodes is much smaller than lifting force.
3. Vertical projection of the ion path between electrons equals d.

2 Experimental setup

Wire-cylinder was studied when the interelectode gap varied. Active electrode is a wire with radius 0.042 mm and the ground electrode is cylinder with radius 0.93 mm. both electrodes was pulled in the wooden frame (Fig. 1). The construction length is 20 cm. Voltage and current are registered with the help dual-channel analog-digital converter (ADC) L-Card. Current was measured by voltage registration across the resistor 19.2 kΩ in series source-discharge gap. High voltage supply occurs with the help constant-voltage source. The setup allows to define corona inception voltage in wire-cylinder system and to analyze discharge current-voltage characteristic (CVC). Ionocraft segment hang up so that the thrust was directed upward vertically. Therefore, thrust value complements the ionocraft weight and the total value is measured by scales. The measurement is differ from usually applying ionocraft scaling [4]: decreasing lifting force is caused scaling the ionic wind jet which put pressure on scales. Due to our measurement the ionic wind jet encounters board which is stiffened (it is under the scales) and it doesnвГЄt influence on scales measurements.
Thus current and voltage oscillogramms and lifting force value can be analyzed.

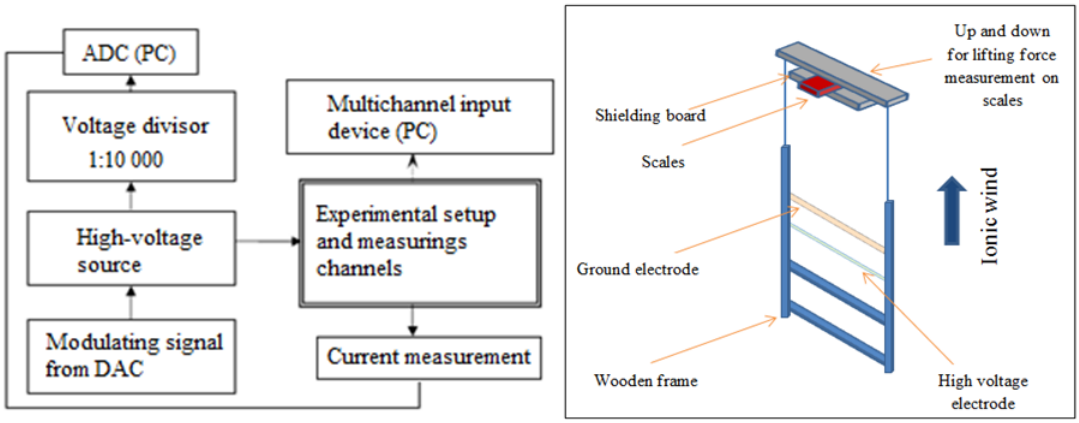

Figure 1: Experimental setup flow diagram (on the left) and lifting force measurement design (on the right).

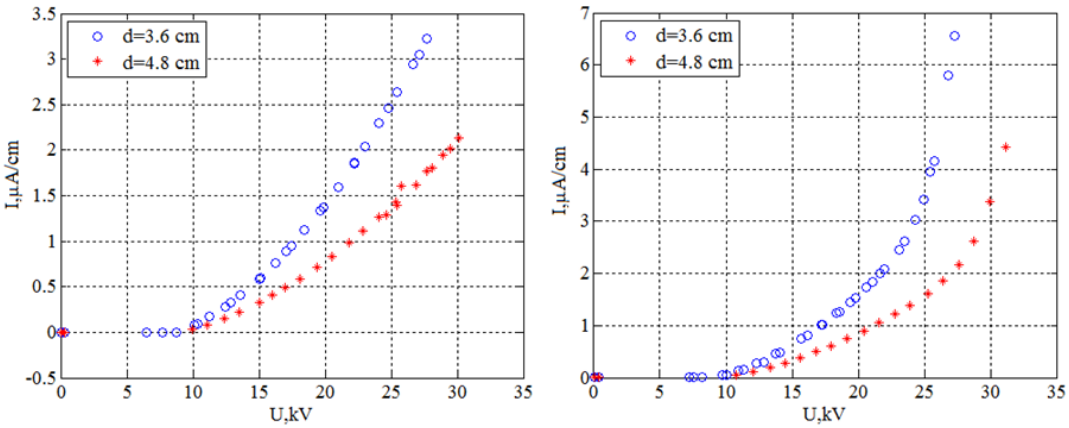

Figure 2: Current-voltage characteristics under positive (on the left) and negative (on the right) polarities. d вГ Y- electrode gap.

3 Results

In Fig. 2 CVCs are presented. On the one hand they are classical squared but it is incorrect for negative polarity. Analyzing the reduced CVC allows to state this fact (the relation U/I from U вГ Y linear function for classical discharge CVC) (Fig. 3). There is a deviation from linearity for reduced CVC with applying voltage over 20 kV under negative polarity.

In Fig. 4 lifting force dependence on current is shown. The linear dependence has to be seen due to (1). It is held under positive polarity. However, the lifting force isnвГЄt proportional to the current where the CVCs deviate from quadratic form under negative polarity. The structure of positive and negative corona discharge is significantly different. but it is thought to be the outer zone characteristic which structure less depends on polarity is more important for CVC and lifting force. We can add that special aspects outer zone have a streamer form of corona discharge in this case it is not seen the streamers in this system. At least there Is only one significant difference in positive or negative outer zone is electron existence in

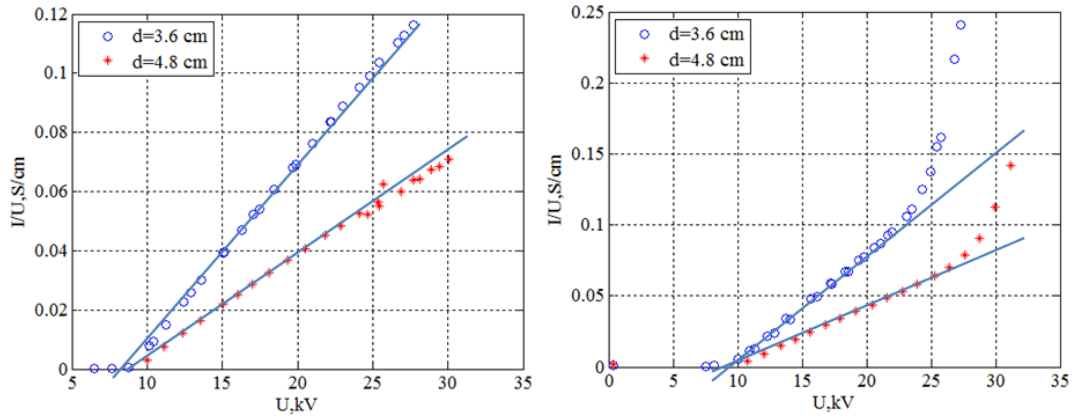

Figure 3: Reduced current-voltage characteristics under positive (on the left) and negative (on the right) polarities. d вГУ- electrode gap.

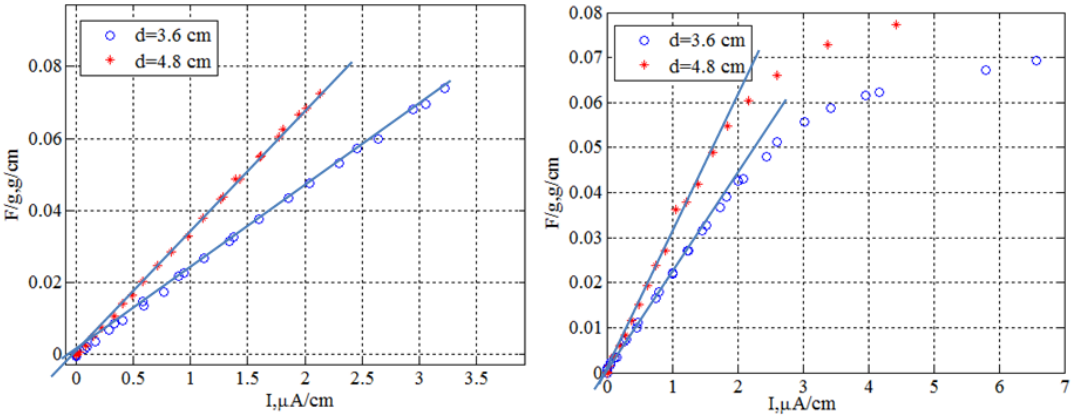

Figure 4: Lifting force dependence from current (per unit length) under positive (on the left) and negative (on the right) polarities. d вГУ- electrode gap.

outer zone. It is thought to be that there arenвГЄt electrons in outer zone under both polarities. But they can penetrate to the special distance which depends on velocity adhesion under negative polarity. The more is voltage the higher is electric field intensity and less velocity adhesion that is why by high voltage the length of electron propagation into outer zone [3] [6]. However, there are no electrons in outer zone under positive polarity because of the movement direction to the active electrode. They canвГЄt go out from the corona layer.

In such a way electrons locates in a wider space under negative polarity than under positive polarity. Moreover, the location space of electrons will expand with increasing voltage under negative polarity. That is why it is assumed that widening electron presence space in interelectrode gap with increasing voltage results in reduced CVC and lifting force deviation from linearity. Actually average charged particles mobility increasing in air gap is caused by the widening electron presence space and it leads to current increasing (at preset voltage) and lifting force decreasing (at preset current).

In Fig. 5 specific thrust dependence on lifting force are presented. According to (2)

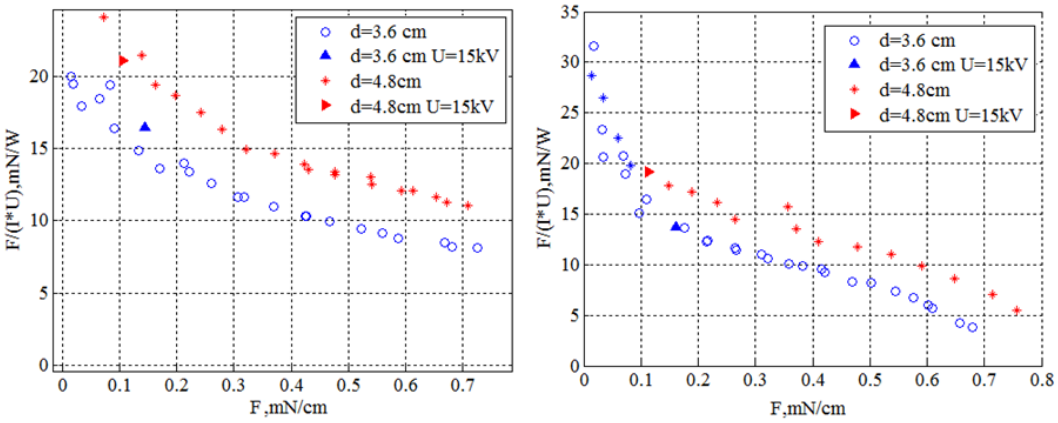

Figure 5: Specific thrust dependence from lifting force (per unit length) under positive (on the left) and negative (on the right) polarities. d вГУ- electrode gap.

specific thrust decreases with lifting force increasing besides electrode gap increasing for fixed lifting force leads to specific thrust increasing. Is it more profitable to use higher electrode gap in constructions? Consider this issue in detail.

In Fig. 5 there are points according to specific applying voltage (e.g. 15kV). Although the curve is higher with higher electrode gap but electrode gap increasing (at preset voltage) leads to specific thrust increasing and lifting force decreasing. Thus if one has a limitation on the operating voltage and the objective value of the lifting force then the optimal interelectrode gap distance may be evaluated. The voltage limitation may be linked to volume and isolation weight and also with size and increasing voltage electric transformer weight.

The question of ionocraft optimization may be as well turned round the other way. In a real construction one would rather have to use a set of parallel electrode systems to reach a valuable lifting force value. Neighbored electrodes of the same polarity influence against each other. It may be shown that wire-cylinder systems are possible to pull together only at the distance proportional to electrode gap. The next pulling together leads to quick growth the corona inception voltage. In this cast lifting force from N pairs of electrode will be more less than NF (F is lifting force from one pair of electrode). Therefore, occupying volume of one pair of electrodes can be evaluate as $2d3dL$, РУРУРХ L вГУ system length, d вГУ electrode gap. d increasing leads to quick volume increasing occupying the system of electrode.

Consider dependence of the thrust specific energy consumption from the unite volume (Fig. 6). As we can see the corresponding dependences come to an agreement with different electrode gap within the scatter accuracy. It would be possible to conclude that both electrode hap are equally profitable. But it has been seen that using less electrode gape at preset voltage we can reach more lifting force from unit of volume if we consider the points according to the same applying voltage. On the other hand the more electrode gap at preset voltage the more specific thrust.

These regularities may be useful in designing construction with a specific set of limitations (thrust specific energy consumption, total lifting force, operationg voatge, occupied volume).

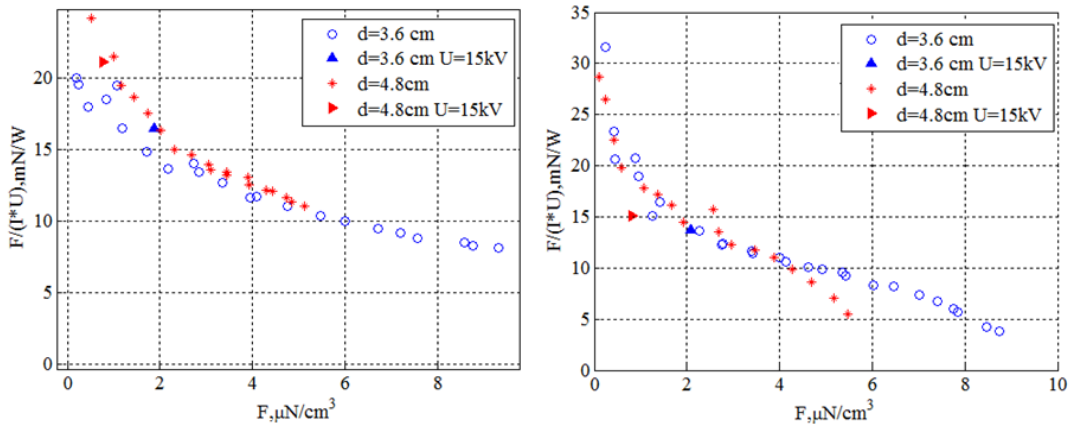

Figure 6: Specific thrust dependence from lifting force (per unit volume) under positive (on the left) and negative (on the right) polarities. d -вГУ electrode gap.

4 Conclusions

1. The reduced current-voltage characteristics and lifting force dependence on current deviation from linearity has been seen under negative polarity under a high applying voltage.

2. Using a system of electrode with higher electrode gap allows to gain more efficiency at preset lifting force from unit of distance but using a system with less electrode gap may prove to be more profitable in the case of the voltage and volume limitation.

References

[1] Yu. P. Raizer. Gas Discharge Physics. Springer, 1991. 449 p.

[2] Vereschagin I.P. Corona discharge in apparatus of electron-ion technology (in Russian). Russia: Energoatomizdat. 1985. 160 P.

[3] Eric Moreau, Nicolas Benard, Jean-Daniel Lan-Sun-Luk and Jean-Pierre Chabriat Electrohydrodynamic force produced by a wire-to-cylinder dc corona discharge in air at atmospheric pressure. J. Phys. D: Appl. Phys. 46 (2013) 475204 (14pp)

[4] Eric Moreau, Nicolas Benard, Frederic Alicalapa, Alexandre Douyere Electrohydrodynamic force produced by a corona discharge between a wire active electrode and several cylinder electrodes вГУ Application to electric propulsion. Journal of Electrostatics 76 (2015) 194-200

[5] Yu.K. Stishkov and A. V. Samusenko. Computer simulation of corona discharge in an inert gas. Surface engineering and applied electrochemistry. 2008. Vol. 44. No. 4. P. 271вГУ280.

[6] Zubkov, T.N., Samusenko, A.V., Stishkov, Y.K. Simulation of the seat form of a negative corona discharge in a point-plane electrode system. Surface Engineering and Applied Electrochemistry. 2013 49 (6) P. 474 - 479

Natalia Melnikova, St. Petersburg, Russia
Andrey Samusenko, St. Petersburg, Russia
Iulia Safronova, St. Petersburg, Russia

A Comprehensive Study of Water Transport Mechanisms through Carbon Nanotubes

Sritay Mistry, Kishore K. Kammara, Rakesh Kumar

kkkumar@iitk.ac.in

Abstract

Carbon nanotubes (CNT) are one of the most widely used and ideal nanofluidic devices. With an ever increasing field of applications, it becomes important to study novel mechanisms used to transport water molecules through carbon nanotubes and to compare the effectiveness and rate of fluid flow provided by them. In this study, we have considered three popular non-conventional mechanisms for pumping water through a CNT, namely, thermally driven flows, by rotating chiral CNT and by applying AC electric field to a carbon nanotube. Using molecular dynamics simulations these mechanisms are studied systematically to understand the flow behaviour inside carbon nanotubes and the pumping mechanism. Finally, a comprehensive analysis, of the efficiencies of flux obtained by the aforementioned mechanisms are presented in this work.

1 Introduction

Understanding of water transport through nanofluidic devices is of immense importance considering its potential applications in the fields of medical drug delivery systems, microbiological devices, nanorobotics, micro flow control and thermal management in MEMS/NEMS devices etc. To this front, carbon nanotubes (CNT) [1] are one of the most widely used and are also the ideal nanofluidic devices as they allow almost frictionless fluid flow through them [2]. The recent advances in the manufacturing of carbon nanotubes as well their hydrophobic properties have seen their widespread use in various industrial processes such as filtration, desalination[3] as well as in flow meter devices[4].

The transport of water molecules through the CNTs are stimulated through various mechanisms like hydrostatic pressure [5], rotation of a chiral CNT [6], AC electric fields [7], thermal flows with a temperature difference along the ends of the CNT [8] and passing Rayleigh waves along the surface of CNT [9]. The flow of water through CNT in all of the above-mentioned cases is governed through a multitude of factors, such as the nature and magnitude of the driving forces, the thermodynamic state of the system, the diameter, chirality and the length of the CNT. This clearly shows us

that there are a large number of factors involved in choosing a suitable CNT and an appropriate pumping mechanism to meet the needs of the user. Furthermore, there may possibly be more than one combination through which desired flow properties (thermodynamic state and the flow rate) can be obtained.

Three popular non-conventional mechanisms of pumping water through a CNT are, namely, thermally driven flows, rotation of chiral CNT and AC electric field driven flows. These mechanisms are explained in the following sections.

1.1 Thermally driven flows

The temperature of any system provides the thermal fluctuations associated in the molecules for the given value. Due to these thermal motions, the atoms move randomly in all the directions. When a passage for these random motions becomes restrictive than the atoms move only as the passage directs. This very nature of motions is been utilised in the transport of water molecules through carbon nanotubes. When a passage viz., CNT, is provided to water molecules present in two reservoirs at different temperatures, the asymmetric thermal fluctuations causes the water molecules to flow from one reservoir to another, as described by Zhao *et al.* [10]. They found a continuous flux of water being transported from the hot reservoir to the cold reservoir when the temperature difference is about 15-70 K, through a small (6,6) CNT. The flux obtained through this system is equivalent to that of the flux generated by a hydrostatic pressure difference which is of the orders of megapascals.

Zhao *et al.* [10] theorised that the forces working in the direction of the flow are neither the thermophoretic forces nor the thermal transpiration. This is because, as the water flows rapidly against the chemical potential barrier, the flow rate is independent of the length of the CNT, and hence, it is independent of the temperature gradient. The phenomenon that causes this flow of water from the hot reservoir to cold reservoir is not very clear and that forms one of the focuses of the current work and in order to understand the phenomenon, a number of simulations are carried out by varying the temperatures of the two reservoirs over a wide range.

1.2 AC electric field

When an electric field is applied to a CNT in the form of a travelling wave, it causes the water molecules to follow the gradients in the electric field due to their existence as dipoles. Klaus *et al.* [7] postulated an elaborate polarisation dragging theory to describe the effect of AC electric field on water molecules by simulating a system that uses discrete charged electrodes to simulate the travelling electric field wave. This travelling wave breaks the spatio-temporal symmetry of the water molecules and creates wave packets by periodically polarising the water in the direction of the local electric field. The resultant of this localised effect is that the packets of water molecules orient in opposite directions and are forced to travel along with a particular wave packet. As the wave itself travels along the CNT, this causes the water molecules to be dragged along with the wave packets and be pumped out of the tube. Dependence on the strength of electric field is studied in this work.

1.3 Rotation of CNT

Pumping water by rotating the chiral CNT is one of the unique concepts and it is possible because of the structure of CNT. The structure of a chiral CNT is such that there exists an asymmetry in one direction. This asymmetry interacts through mechanical impingement with water molecules. When a chiral CNT is rotated, this asymmetry of CNT produces the required axial force on the water molecules which moves them ahead along the length of CNT. Feng *et al.* [6] attempted to fit an empirical relation to the potential energy landscape to characterise the forces pushing the water out and came up with an empirical relation of the following form as given in Eq. 1 [6].

$$\begin{aligned} V(\theta,z,\omega,t) = {} & a\sin(n(\frac{5}{\sqrt{3}r}z+\theta-\omega t)) + b\cos(n(\frac{5}{\sqrt{3}r}z+\theta-\omega t)) \\ & + c\sin(2n(\frac{2}{\sqrt{3}r}z-\theta+\omega t)) + d\cos(2n(\frac{2}{\sqrt{3}r}z-\theta+\omega t)) \\ & + e\sin(3n(\frac{1}{3\sqrt{3}r}z+\theta-\omega t)) + f\cos(3n(\frac{1}{3\sqrt{3}r}z+\theta-\omega t)) + V_0 \end{aligned} \tag{1}$$

where, r denotes the radius of CNT, and a, b, c, d, e, f, V_0 are constants being obtained by fitting the function to the potential energy landscape.
The potential energy landscape depends on the parameters like radius and angular velocity of CNT, which can be readily changed, hence changing the flux of water being pumped through it. The flux is thought to increase with both radius and angular velocity, however Feng *et al.* [6] claim that increasing the angular velocity beyond a certain value decreases the pumping flux as the water molecules fail to adjust their structure to that of the fast rotating CNT. This is because as the time period of the oscillating potential energy landscape is faster than the relaxation time of water molecules. The interaction of the water molecules close to the wall to those near the centre transfers this axial force across the radial direction. A thick (16,32)CNT is used by [3] to ensure that the distribution of water molecules inside the CNT is unstructured and thus more efficient pumping of water is achieved.

This pumping efficiency can also be increased by decorating the CNT with any functional group. This functional group will induce a higher flow rate through physical means, such as that used in an Archimedes screw. Flow rates can also be increased with electrically charged particles, which would simulate a moving electric field on rotation of the CNT, similar to an AC electric field through the CNT. This can also be seen in the potential function proposed by Feng [6], the decoration increases the slope of the potential energy function, leading to larger forces.

In this study, we use molecular dynamics simulations to characterise various pumping mechanisms. A detailed study to estimate the flow rate of water molecules through CNT by using the above-mentioned mechanisms are attempted. In the remainder of the paper, computational details employed to describe each mechanism is provided in Sec. 2 followed by results and discussion where an elaborate description of flow rates obtained for each of the mechanisms are presented and finally concluding remarks are made in Sec. 4.

2 Computational Details

All the molecular dynamics simulations are carried out using the LAMMPS [11], an open source molecular dynamics package. Firstly, the common computational details that are been maintained constant in all the case studies that are carried out in this work are presented and later computational details that are relevant to particular mechanisms are explained. The system consists of a single carbon nanotube that connects the two reservoirs on either end of it as shown in the Fig. 1. The carbon atoms present in CNT are terminated using hydrogen at both ends. The TIP4P [12] model of water is used. The pppm style invokes a particle-particle particle-mesh solver [13] which maps atom charge to a 3d mesh, using 3d FFTs to solve PoissonвЂ™s equation on the mesh and then interpolates electric fields from the mesh points back to the atoms. The radial distribution function Fig. 2, plotted for this model shows that the potential predicts the behaviour of water molecules as obtained in literature [14]. CHARMM [15] force fields are used to model the interactions between carbon and water molecules. A time-step of 1 femtosecond is considered for all the cases studied in this work.

To statistically average the data obtained, the length of CNT is divided into 40 bins, each bin 0.4 nm in length, and the centre of mass velocities from each bin is calculated to determine the flow characteristics. The CNT was also divided into 4 concentric bins, each of thickness 0.1 nm, to find the variation of the flow characteristics between the CNT axis and walls. The system is first relaxed to a state of local minimum energy using the Polak-Ribiere [16] version of the conjugate gradient (CG) minimization algorithm. Nosé [17]-Hoover [18] thermostat is used to maintain the temperatures of water molecules. The time integration for the water molecules inside the CNT is performed by NVE integrator. Periodic boundary conditions were used in all directions. The system is allowed to simulate for 11 ns out of which the system is equilibrated for 1 ns and the next 10 ns of the simulation are considered to obtain the desired results.

Now, the computational details pertaining to the specific pumping mechanism are explained in following subsections.

2.1 Thermally driven flows

To generate a thermally driven flow a (15,14) CNT of 10 nm length is used to connect the two reservoirs that are placed on either side, each consisting of 5120 water molecules and are confined between two graphene sheets, with dimensions of 100 Å x 50 Å x 32 Å as shown in Fig. 1. This corresponds closely to a density of 1 g/cc of water at STP. At the initial timestep, there are no water molecules inside CNT. The CNT is held rigid and fixed in the same position. Various cases studies are considered by varying the temperature of the two reservoirs.

2.2 AC electric field

In this case, the system dimensions follow same as that used for thermally driven flow expect that one of the reservoirs is filled with water while the other is kept

empty. A number of cases studies were carried out by varying the magnitude of the electric field from 0 to 0.1 V/Å keeping the wave number and frequency constant.

2.3 Rotation of CNT

To pump water molecules through a rotating CNT, an asymmetric (chiral) CNT is required. Therefore, a chiral (16,32) CNT of length 10 nm is used. Each reservoir has the dimension of 100 Å x 50 Å x 63 Å and possesses 10240 water molecules, corresponding to the density of 1 g/cc of water. Case studies by varying the angular velocities of CNT are carried out and also the CNT is rotated both clockwise and counterclockwise direction to better understand the pumping mechanism. Fig. 3 shows the schematic of the simulation domain for this case.

3 Results and Discussion

In this section, we present and discuss the functioning of each mechanism used to pump water molecules through CNT. The focus of the present work is to understand the pumping mechanisms and calculate the flux rate for each mechanism. We have also calculated the number density of water molecules present across the CNT. This number density distribution across the CNT helps us to analyse where the water molecules are more concentrated. In the subsequent subsections, results and their analysis for each of the mechanism to pump water is presented.

3.1 Thermally driven flows

To study the thermally driven flow, several cases were considered in which the temperature of each of reservoirs are varied so as to have a temperature difference that would drive the molecules from one reservoir to another. As mentioned in the Sec. 2, the time integration for the water molecules in the reservoir were carried out by NVT ensemble while the time integration for water molecules inside CNT was performed by NVE ensemble.

Firstly, radial number density across the channel is calculated for various temperatures considered in this work. It is observed that the number of water molecules remained larger at the centre of CNT and gradually reduced when moved towards the walls. This clearly indicates that friction offered by the walls is very less, as the reduced number density near the walls indicate lesser fluid-surface interaction. The following Fig. 4, shows the distribution of number density radially across the CNT for various cases. Fig. 4, also clearly indicates that the radial distribution of number density does not vary much with the change in temperature.

Next, the flux of water molecules flowing through the CNT is presented in Table 12. As the temperature difference increases the flux rate also increases due to increased internal energy in the molecules. The sign of flux indicates the direction of flow and it is evident that the movement of water molecules is from the reservoir having the higher temperature to that of reservoir kept at lower temperature. Observing the direction of flow of water molecules we can say that due to increased internal

energy and confinement along a passage, the water molecules are forced to move in one particular direction.

Center of mass velocity (Z component) plotted along the CNT (aligned in Z direction) as shown in Fig. 5 indicates that the water molecules in the reservoir kept at higher temperature prefers to move towards the reservoir kept at lower temperature, while the molecules from the lower temperature reservoir move towards the higher temperature reservoir. However, due to their higher kinetic energies, the molecules of the high-temperature reservoir clearly dominate over the others, thus driving a net flow. Thus, it is the thermal motion of water molecules that drives the water molecules through CNT.

3.2 AC electric field

To study the pumping mechanism by using AC electric field, a travelling electric field is applied to the water molecules present in the CNT. This travelling wave drags the water molecules along it as it is explained in Sec. 1.2 By varying the strength of electric field from 0.1 V/Å to 1 V/Å, properties like radial number density distribution across the CNT and flux of water molecules are calculated.

The behaviour of radial number density across the channel is similar to that of the thermally driven case where the number of water molecules is higher at the centre of CNT than at the walls. For all the cases considered the behaviour remained similar without much difference indicating that the effect of electric field on the number density distribution negligible. The Fig. 6 show the distribution of number density radially across the CNT for various values of electric field.

Now, the flux of water molecules flowing through the CNT due to the presence of electric field are calculated and is presented in Table 14. With the increase in strength of electric field, the flux of water molecules also increased. This is because the moving travelling electric field has greater strength to pull the water molecules with it now. It is also observed that when the phase of this electric field is shifted by 180 degrees the results obtained remained same as that without phase shift.

3.3 Rotation of CNT

We now present the results for the case of rotating CNT obtained by our molecular dynamics simulations. The system consists of thick, chiral (16,32)-CNT, connecting two reservoirs, one of which is empty while the other is filled with water as mentioned in Sec. 2.3. The CNT is rotated at various angular speeds in both clockwise and anticlockwise directions.

Interestingly, the behavior of the radial number density distribution remained the same showing the consistency in the results obtained. As the CNT used for this case has a larger diameter than the other mechanisms, the graph appears different as can be seen in Fig. 7. Here the distribution remains constant for certain distance near the centre and distribution does not vary much with the variation in rotational speeds.

We then calculate the flux of water molecules that is being pumped out of CNT. We observe that the flux of water molecules shows a significant dependence on the angular speed of CNT. Table 14 shows the flux of water molecules that have been pumped out through CNT when CNT is rotated at various angular speeds in both clockwise and anticlockwise direction. It is observed that with an increase in angular speed, there is an increase in the number of water molecules that have been pumped out. It is found to be in qualitative agreement with the results from the works of Tu *et al.* [3] and of Feng *et al.* [6], who found a strong relationship between the rotation speed and cumulative flux of water molecules through CNT. It can also be observed that the there is negligible change in flux when the CNT is rotated either in the clockwise or anticlockwise direction as indicated in Table 14.

4 Concluison

In this study, molecular dynamics simulations were employed to study three nanoscale pumping mechanisms to transport water molecules through CNT. In the case of thermally driven flow case, the temperature difference maintained between two reservoirs enabled the transport of water molecules through the CNT. Due to high temperature, the thermal modes in water molecules have agitated and by confining the movement finite flow rates were achieved. In the case of AC electric field, the travelling wave drags the water molecules along with it and thus creating a finite flux.

Though with the increase in AC electric field the flux of water molecules increases, achieving very high electric field is difficult and at very high electric fields there is a possibility of breaking the water molecule. In the last mechanism, rotation of CNT, the transport of water molecules takes place due to structure (chirality) of CNT. Only a chiral CNT can transport water when rotated. It is also observed that as the rotational speed of CNT is increased, the flux of water molecules also increased. Flux is observed not to vary much with the direction of rotation. Thus, the above-mentioned nanoscale scale pumping mechanisms have crucial applications in various fields and to increase the pumping rates with higher efficiencies one can develop a hybrid mechanism combining the above-mentioned mechanisms.

Acknowledgements

The authors acknowledge the financial support provided by the Ministry of Human Resources and Development, Government of India to the graduate students. The high-performance computational facility at IITK, Computer Center, were used in simulating the case studies presented here and the same is acknowledged.
Sritay Mistry, Kishore K. Kammara and Rakesh Kumar, Aerospace Engineering Department, Indian Institute of Technology Kanpur, India

Table 12: Table showing flux of water molecules being pumped out of CNT for various temperatures of reservoirs

Temperature (K)		Flux of water molecules
Upper Reserviour	Lower Reserviour	
300	300	0.00510
400	300	-0.0700
500	300	-0.0515
500	400	-0.0650
600	500	-0.0340

Table 13: Table showing flux of water molecules being pumped out of CNT for various electric fields

Electric Field (eV)	Flux of water molecules
0	0.198
0.025	0.254
0.05	0.254
0.075	0.260
0.1	0.295

Table 14: Table showing flux of water molecules being pumped out of CNT for various rotational speeds in both clockwise and anticlockwise rotation

Rotational Speed (rad/ns)	Flux of water molecules	
	Clockwise	Anti-Clockwise
0	0.04	0.04
6.195	0.12	0.09
12.39	0.25	0.27
24.78	0.74	0.75

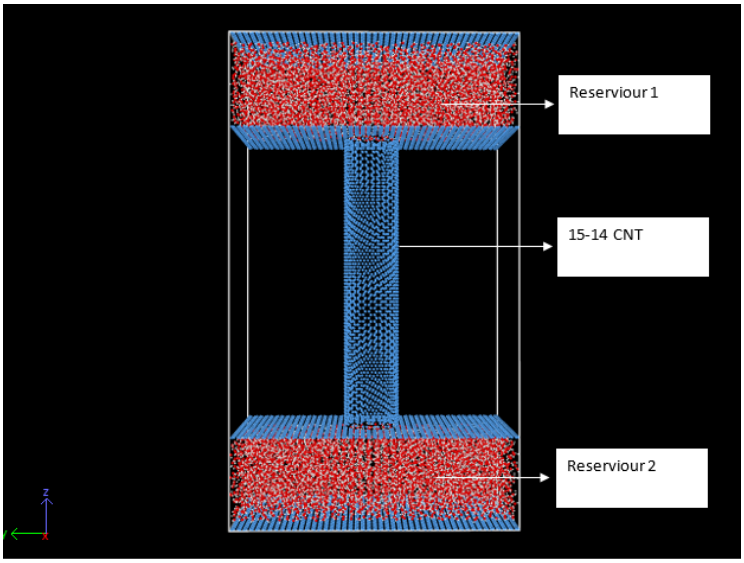

Figure 1: Schematic of simulation domain

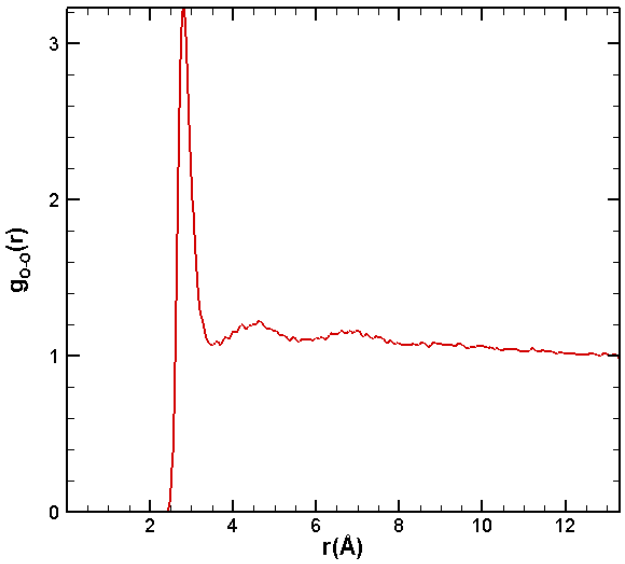

Figure 2: Radial distribution function of oxygen atoms in water molecule.

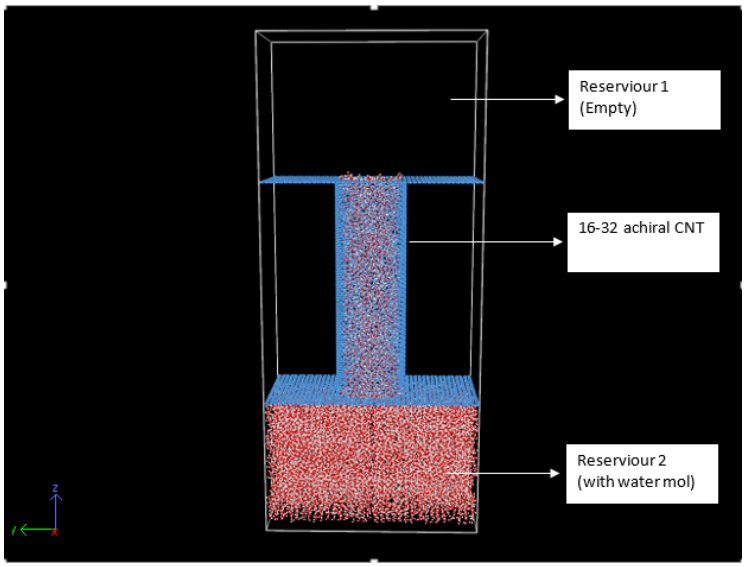

Figure 3: Schematic of simulation domain used to study rotation of CNT case

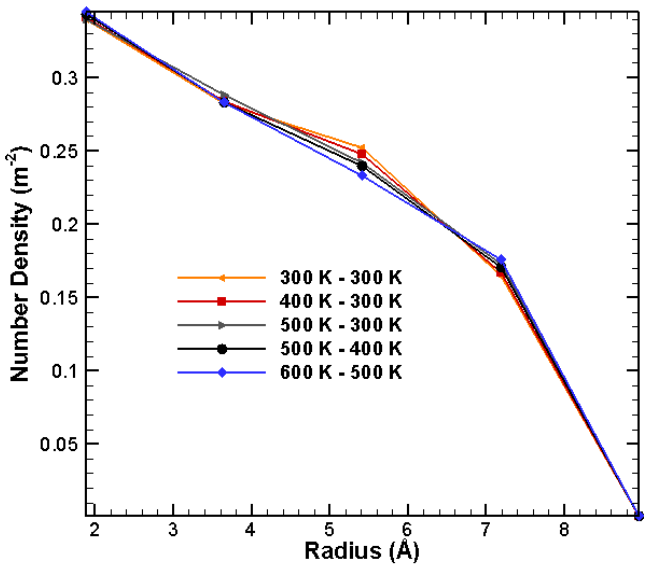

Figure 4: Cumulative radial number density of water molecules inside carbon nanotube in radial direction for various temperatures of reservoirs

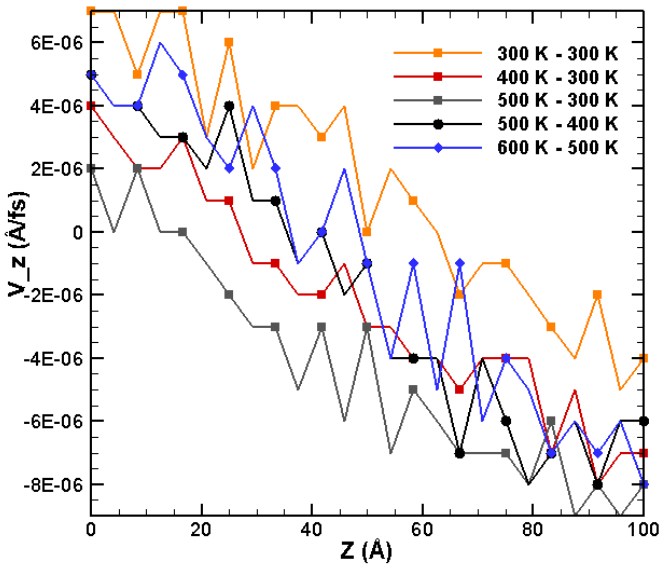

Figure 5: Center of mass velocity (Vz) of water molecules in each bin along the length of CNT

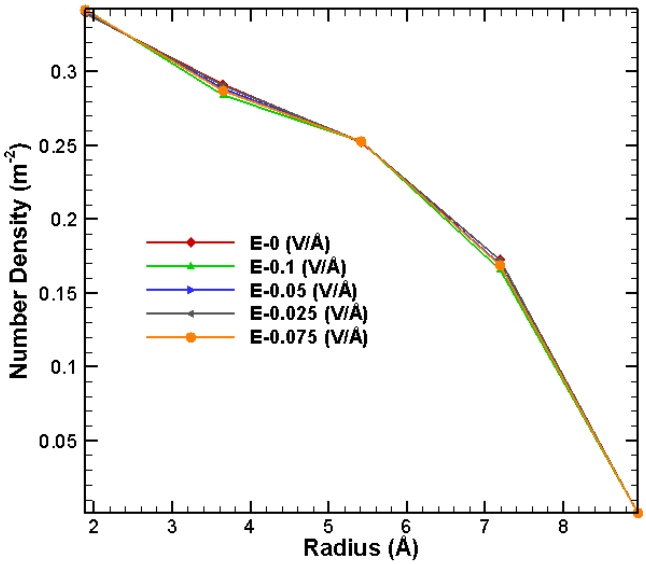

Figure 6: Cumulative radial number density of water molecules inside carbon nanotube in radial direction for various electric fields

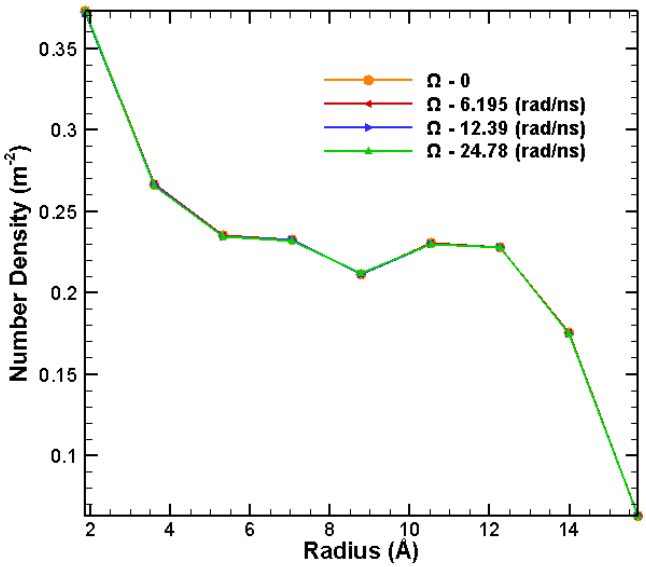

Figure 7: Cumulative radial number density of water molecules inside carbon nanotube in radial direction for various rotational speeds

References

[1] Iijima, S., "Helical microtubules of graphitic carbon," *Nature*, Vol. 354, No. 6348, 1991, pp. 56–58.

[2] Joseph, S. and Aluru, N. R., "Pumping of confined water in carbon nanotubes by rotation-translation coupling," *Phys. Rev. Lett.*, Vol. 101, 2008, pp. 064502–1 – 064502–4.

[3] Tu, Q., Yang, Q., Wang, H., and Li, S., "Rotating carbon nanotube membrane filter for water desalination," *Sci. Rep.*, Vol. 6, 2016, pp. 26183.

[4] Lina, Z., Yuliang, Z., and Ruhong, Z., "Novel Design of a Nanoflowmeter Based on Carbon Nanotubes," *J. Phys. Chem. C*, Vol. 116, 2012, pp. 13429–13434.

[5] Nicholls, W. D., Borg, M. K., Lockerby, D. A., and Reese, J. M., "Water transport through (7,7) carbon nanotubes of different lengths using molecular dynamics," *Microfluidics and Nanofluidics*, Vol. 12, No. 1, 2012, pp. 257–264.

[6] Feng, J., Ding, H., Ren, C., and Ma, Y., "Pumping of water by rotating chiral carbon nanotube," *Nanoscale*, Vol. 6, No. 22, 2014, pp. 13606–13612.

[7] Rinne, K. F., Gekle, S., Bonthuis, D. J., and Netz, R. R., "Nanoscale Pumping of Water by AC Electric Fields," *Nano Lett.*, Vol. 12, No. 4, 2012, pp. 1780–1783.

[8] Zhao, K. and Wu, H., "Fast Water Thermo-pumping Flow Across Nanotube Membranes for Desalination," *Nano Lett.*, Vol. 15, No. 6, 2015, pp. 3664–3668.

[9] Insepov, Z., Wolf, D., and Hassanein, A., "Nanopumping Using Carbon Nanotubes," *Nano Lett.*, Vol. 6, No. 9, 2006, pp. 1893–1895.

[10] Zhao, K. and Wu, H., "Fast Water Thermo-pumping Flow Across Nanotube Membranes for Desalination," *Nano Letters*, Vol. 15, No. 6, 2015, pp. 3664–3668.

[11] Plimpton, S., "Fast Parallel Algorithms for Short вГY Range Molecular Dynamics," *J. Comput. Phys.*, Vol. 117, No. June 1994, 1995, pp. 1–19.

[12] Abascal, J. L. and Vega, C., "A general purpose model for the condensed phases of water: TIP4P/2005." *J. Chem. Phys.*, Vol. 123, No. 23, 2005, pp. 234505.

[13] Hockney, R. and Eastwood, J., *Computer simulation using particles*, 1988.

[14] Soper, A. K., "The radial distribution functions of water and ice from 220 to 673 K and at pressures up to 400 MPa," *Chem. Phys.*, Vol. 258, No. 2-3, 2000, pp. 121–137.

[15] MacKerell, A. D., Bashford, D., Dunbrack Roland, L., J., Evanseck, J. D., Field, M. J., Fischer, S., Gao, J., Guo, H., Ha, S., Joseph-McCarthy, D., Kuchnir, L., Kuczera, K., Lau, F. T. K., Mattos, C., Michnick, S., Ngo, T., Nguyen,

D. T., Prodhom, B., Reiher, W. E., Roux, B., Schlenkrich, M., Smith, J. C., Stote, R. H., Straub, J., Watanabe, M., Wiórkiewicz-Kuczera, J., Yin, D., and Karplus, M., "All-Atom Empirical Potential for Molecular Modeling and Dynamics Studies of Proteins в Г r," *J. Phys. Chem. B*, Vol. 102, No. 18, 1998, pp. 3586–3616.

[16] Polak, E. and Ribière, G., "Note sur la convergence de directions conjuguB¥ee," *Rev. Fr. Informat Rech. Oper.*, Vol. 16, 1969, pp. 35–43.

[17] Nose, S., "A unified formulation of the constant temperature molecular dynamics methods," *J Chem Phys*, Vol. 81, 1984, pp. 511–519.

[18] Hoover, W., "Canonical dynamics: equilibrium phaseв Г Yspace distributions," *Phys Rev A*, Vol. 31, 1985, pp. 1695–1697.

Effect of interaction between ion drag and conduction on electrohydrodynamic pumping

Masahito Nishikawara, Kota Shomura, Hideki Yanada

nishikawara@me.tut.ac.jp

Abstract

Electrohydrodynamics (EHD) flow is induced by Coulomb force acting on excess charges in a dielectric fluid under a high electric field and can be applied to pumping. There are two types of EHD pump, ion drag pump and conduction pump that utilize excess charges caused by charge injection and electric field enhanced dissociation, respectively. This paper investigates numerically the interaction of the ion drag action and conduction action on EHD pump characteristics using three types of electrode configurations. It is found that when the ion drag and conduction act simultaneously, the developed pressure is augmented and is higher than the sum of the pressures developed separately by each action, and that the degree of pressure augmentation strongly depends on electrode configuration.

1 INTRODUCTION

Electrohydrodynamics (EHD) flow is induced by CoulombвЃ™s force acting on excess charges in a dielectric fluid under a high electric field and can be applied to pumping and heat transfer. Excess charges in the fluid are generated by charge injection from an electrode and/or a non-equilibrium state of dissociation-recombination of dissociative molecules. An EHD pump that utilizes the former phenomenon is called the ion drag pump and the one that utilizes the latter phenomenon is called the conduction pump. Both types of EHD pump have been widely investigated experimentally and numerically[1, 2, 3, 4]. However, the research on the interaction of the two charge generation phenomena is very limited[3]. This paper investigates numerically the effect of the interaction of the two charge generation phenomena on EHD pump characteristics.

2 NUMERICAL MODELING

The governing equations are the continuity equation (Eq. (1)), the NaviervЃ™YStokesvЃ™ equation (Eq.(2)) including Coulomb's force (Eq. (3)) as an external force, GaussvЃ™ law (Eq. (4)) and the charge conservation equations (Eqs. (6)-(10)).

$$\nabla \cdot \mathbf{v} = \mathbf{0} \tag{1}$$

$$(\mathbf{v} \cdot \nabla)\mathbf{v} = -\frac{\mathbf{1}}{\mathbf{æ}}\nabla \mathbf{p} + \mathbf{v}\nabla^{\mathbf{2}}\mathbf{v} + \mathbf{f} \tag{2}$$

$$\mathbf{f} = -\frac{\mathbf{q_{total}}}{\mathbf{æ}}\nabla \mathbf{Œ} \tag{3}$$

$$\nabla^2 \phi = -\frac{q_{total}}{\varepsilon} \tag{4}$$

$$q_{total} = q_{in} + q - w \tag{5}$$

In the equations, $\mathbf{v}$=(u, v) is the velocity,ρ is the density, p is the pressure, v is the kinematic viscosity, $\mathbf{f}$ is the Coulomb's force, q_{total} is the total charge density defined by Eq. (5), ϕ is the electric potential, ε is the permittivity, q_{in} is the positive charge density injected from a positive electrode, q and w are the densities of the positive and negative charges generated by dissociation, respectively. In this model, it is assumed that only positive charges are injected and that the injected positive charges are not combined with the negative charges generated by the dissociation. The charge conservation equations of the injected charges and dissociated ones are described separately as follows[2].

$$\nabla \cdot \mathbf{j}_{\mathrm{in}} = \mathbf{0} \tag{6}$$

$$\mathbf{j}_{\mathrm{in}} = {}^{-}{}_{\mathbf{in}}\mathbf{q}_{\mathbf{in}}\mathbf{E} + \mathbf{q}_{\mathbf{i}}\mathbf{n}\mathbf{v} - \mathbf{D}_{\mathbf{i}}\nabla \mathbf{q}_{\mathbf{i}}\mathbf{n} \tag{7}$$

$$\nabla \cdot \mathbf{j} = \mathbf{k}_{\mathbf{r}}\left(\mathbf{w}_{\mathbf{0}}^{\mathbf{2}}\mathbf{F}(\mathbf{E}) - \mathbf{q}\mathbf{w}\right) \tag{8}$$

$$\mathbf{j}_{+} = {}^{-}{}_{\mathbf{i}} + \mathbf{q}\mathbf{E} + \mathbf{q}\mathbf{v} - \mathbf{D}_{\mathbf{i}}\nabla \mathbf{q} \tag{9}$$

$$\mathbf{j}_{-} = {}^{-}{}_{\mathbf{i}} - \mathbf{w}\mathbf{E} + \mathbf{w}\mathbf{v} - \mathbf{D}_{\mathbf{i}}\nabla \mathbf{w} \tag{10}$$

j_{in} is the current density of the injected charge, μ_{in} is its mobility, E is the electric field strength, D_i is the charge diffusion constant, j_+ and j_- are the current densities of the dissociated positive and negative charges, respectively, k_r is the recombination rate constant, w_0 is the negative charge density at an equilibrium (=q_0), F(E) is a function representing the field enhanced dissociation, $\mathrm{Oë}_{i+}$ and $\mathrm{Oë}_{i-}$ are the mobilities of the positive and negative dissociated charges, respectively. It is assumed for simplicity that $\mathrm{Oë}_{in}$=$\mathrm{Oë}_{i+}$=$\mathrm{Oë}_{i-}$. To obtain F(E), an electric field dependence of the electric conductivity of dibutyl sebacate (DBS) was measured in laboratory using concentric cylinder electrodes [5]. Linear approximation was used to determine F(E).

$$F(E) = \frac{k_d}{k_{d0}} = \left(\frac{\sigma}{\sigma_0}\right)^2 \tag{11}$$

$$\frac{\sigma}{\sigma_0} = \gamma E + 1 \tag{12}$$

k_d is the dissociation constant, σ is the electric conductivity. The results is shown in Fig.1. It was found from the measurement that $\gamma = 2.46$ГЧ10^{-7} m/V for DBS. The field dependence of the electric conductivity was calculated from Onsager theory[6] and it was found that $\gamma =$1.31ГЧ10^{-7} m/V. The measurement result was larger than the value predicted from the theory. In this numerical simulation, the measured value was used.
The recombination rate constant k_r and the negative charge density at equilibrium, w_0 are expressed by

$$k_r = \frac{\mu_+ + \mu_-}{\varepsilon} \tag{13}$$

$$w_0 = \frac{\sigma_0}{\mu_+ + \mu_-} \tag{14}$$

The charge density, q_e, injected from an electrode can be given by Eq. (15)[4],

$$q_e = k(E_{static} - E_{thres}) \tag{15}$$

where k is the proportionality constant, E_{static} is a mean value of the electrostatic field strength at the charge injection region (see Fig. 2) and E_{thres} is the threshold value of E_{static} below which no charge injection takes place. The model detail is presented in Refs. [1, 2, 3].

3 ELECTRODE CONFIGURATION

Three EHD pumps with different electrode configurations in Fig. 2 are simulated. Plate-bar electrodes, two-plate electrodes mounted on the wall, and embedded two-plate electrodes are inserted in a two-dimensional flow channel. The geometries of the three types of electrodes are symmetrical about the centerline and, therefore, numerical simulations were conducted using half models in Fig. 1. The dimensions of the computational domain are 0.5 mm height and 8 mm length. The plate-bar electrodes consist of a plate 0.1 mm thickness and 0.5 mm length located in the center of the flow channel, and of two square bars with a cross-section of 0.3 ГЧ 0.3 mm2 mounted on the walls. The plate electrode is connected to a positive high voltage (HV) and the square bar electrodes are grounded. The two-plate electrodes on the wall consist of plate electrodes with different lengths of 0.15 mm and 0.5 mm and their thickness is 0.1 mm. The short electrode is connected to the positive high voltage and the long one is grounded. The two-plate electrodes embedded in the wall are basically the same as the two-plates electrodes mounted on the wall, except that the electrode surface is flush with the channel wall. The gap between the electrodes is 0.2 mm for the three types of electrodes. Numerical simulations were made for three cases: (1) only charge injection phenomenon (ion drag action), (2) only non-equilibrium phenomenon of dissociation-recombination (conduction action), and (3) both phenomena (ion drag + conduction actions) take place. Inlet flow rate is imposed as a boundary condition from zero to a maximum, at which the pressure

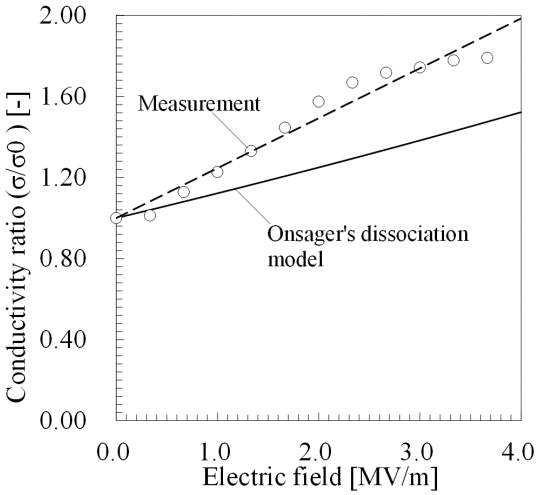

Figure 1: Electric field dependence of conductivity.

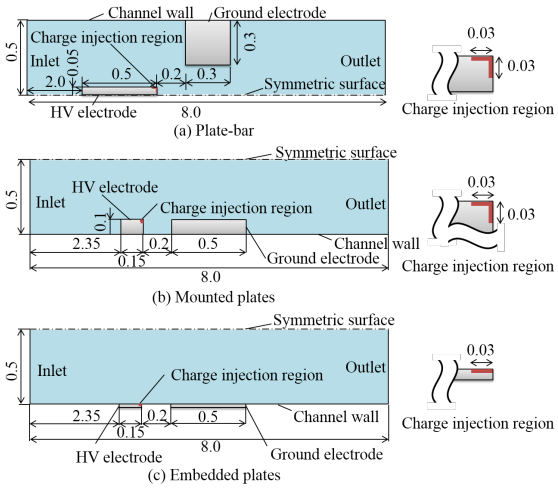

Figure 2: Electrode configuration (not to scale) (unit : mm).

difference between the outlet and inlet of the computational domain is zero, to obtain the pressure-flowrate characteristics. Charge injection region is imposed at a corner of each high voltage electrode, as shown in Fig. 2.
Table 1 Working fluid properties.

Table 15: Working fluid properties.

Fluid	Dibutyl sebacate (DBS)
Density [kg/m^3][7]	938
Relative permittivity [-]	4.5
Conductivity[S/m]	3.41×10^{-10}
Viscosity [Pa·s]	7.50×10^{-3}
Ionic mobility [m/V·s]	2.77×10^{-9}
k in Eq. (10) [C/V·m^3]	7.03×10^{-9}
E_{thres} in Eq. (10) [V/m]	0.245×10^{6}

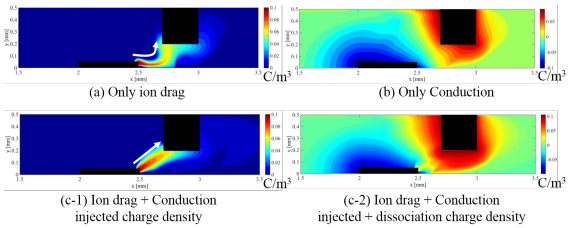

Figure 3: Charge density distribution (Ve=1.2 kV , Uin=0 m/s). Note that range of color bar of (a, c-1) and (b, c-2) is different.

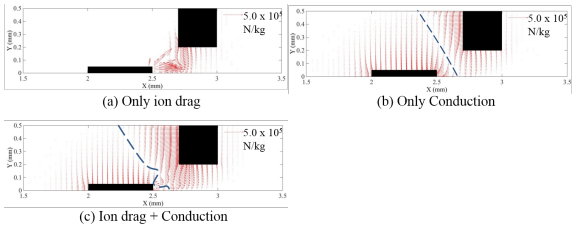

Figure 4: Coulomb's force distribution (Ve=1.2 kV , Uin=0 m/s). Dashed line is the boundary where the force is zero.

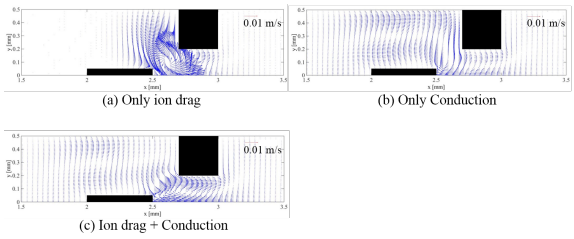

Figure 5: Flow velocity distribution (Ve=1.2 kV , Uin=0 m/s).

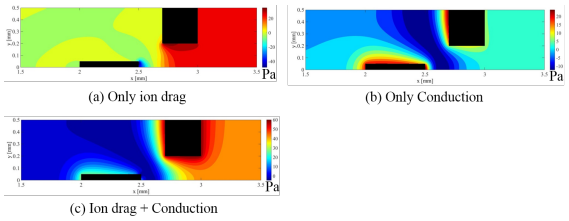

Figure 6: Pressure distribution (Ve=1.2 kV , Uin=0 m/s). Note that range of color bar is different.

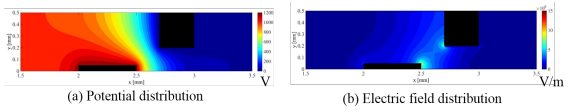

Figure 7: Distribution of potential and electric field (Ve=1.2 kV , Uin=0 m/s). Results of both ion drag and conduction actions.

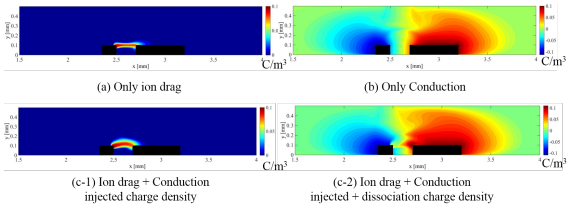

Figure 8: Charge density distribution (Ve=2.0 kV , Uin=0 m/s). Note that range of color bar of (a, c-1) and (b, c-2) is different.

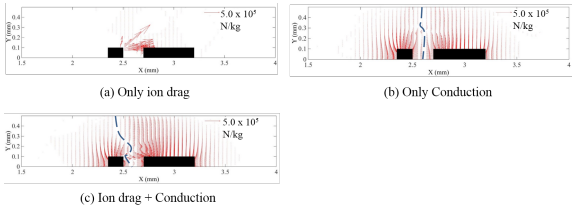

Figure 9: Coulomb's force distribution (Ve=2.0 kV , Uin=0 m/s). Dashed line is the boundary where the force is zero.

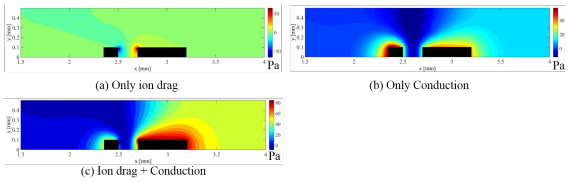

Figure 10: Pressure distribution (Ve=2.0 kV , Uin=0 m/s). Note that range of color bar is different.

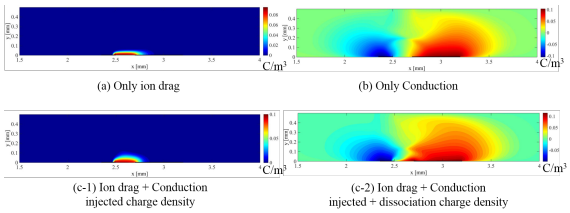

Figure 11: Charge density distribution (Ve=2.0 kV , Uin=0 m/s). Note that range of color bar of (a, c-1) and (b, c-2) is different.

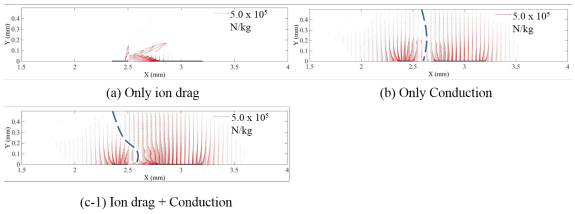

Figure 12: Coulomb's force distribution (Ve=2.0 kV , Uin=0 m/s). Dashed line is the boundary where the force is zero.

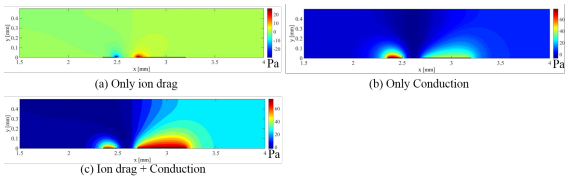

Figure 13: Pressure distribution (Ve=2.0 kV , Uin=0 m/s). Note that range of color bar is different.

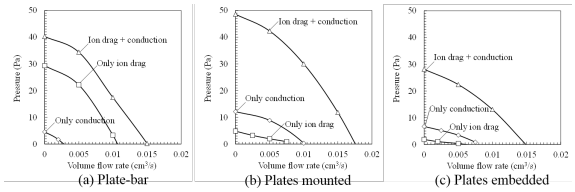

Figure 14: Pressure - flow rate characteristics (Ve=1.2 kV for (a) and 2.0 kV for (b) and (c)).The flow rate is calculated as the channel depth of 5mm.

In the simulation, physical properties of dibutyl sebacate (DBS, C18H34O4) as working fluid were used and are listed in Table 1. A cone-plate rotational viscometer (TOKI SANGYO RE80) was used for viscosity measurement. Relative permittivity was measured using a probe consisting of two concentric cylinders (RUFUTO Model 871). The proportionality constant k in Eq. (15) was determined by fitting the simulated pump pressure to the measured pressure when the flow rate is zero4. The ionic mobility was determined by the Walden's rule. Boundary conditions are listed in Table 2, where n stands for the unit normal vector.
Table 2 Boundary conditions.

Table 16: Boundary conditions.

Boundary location	Boundary conditions						Equation number
1. Inlet	$u = U_{in}(y)$	$v = 0$	$q = 0$	$w = 0$	$q_{in} = 0$	$\frac{\partial \phi}{\partial x} = 0$	(16)
2. Outlet	$\frac{\partial u}{\partial x} = 0$	$\frac{\partial v}{\partial x} = 0$	$\frac{\partial q}{\partial x} = 0$	$\frac{\partial w}{\partial x} = 0$	$\frac{\partial q_{in}}{\partial x} = 0$	$\frac{\partial \phi}{\partial x} = 0$	(17)
3. Channel wall	$u = 0$	$v = 0$				$\frac{\partial \phi}{\partial y} = 0$	(18)
4. Symmetrical surface	$\frac{\partial u}{\partial y} = 0$	$v = 0$	$\frac{\partial q}{\partial y} = 0$	$\frac{\partial w}{\partial y} = 0$	$\frac{\partial q_{in}}{\partial y} = 0$	$\frac{\partial \phi}{\partial y} = 0$	(19)
5. Surface of ground electrode	$u = 0$	$v = 0$	$\mathbf{n} \cdot \nabla q = 0$	$w = 0$		$\phi = 0$	(20)
6. Charge injection region	$u = 0$	$v = 0$	$q = 0$	$\mathbf{n} \cdot \nabla w = 0$	$q_{in} = q_e$	$\phi = V_e$	(21)
6'. Surface of HV electrode except for 6	$u = 0$	$v = 0$	$q = 0$	$\mathbf{n} \cdot \nabla w = 0$	$q_{in} = 0$	$\phi = V_e$	(22)

4 RESULTS AND DISCUSSION

Plate-bar electrodes

The distributions of charge density, Coulomb's force, flow velocity, pressure, potential and electric field are shown in Figs. 3-7. The cases for ion drag action,

conduction action, and ion drag and conduction actions are compared at the applied voltage of +1.2 kV and zero net flow rate.

Figure 3(a) shows the injected charge density distribution under no dissociation (no conduction action). For this case, the injected charges do not spread in y direction. Dissociation charges are generated more in higher electrode areas and surround the electrode with a sign opposite to the charges as shown in Fig. 3(b). When both charge injection (ion drag action) and dissociation (conduction action) take place, as can be seen by comparing Fig. 3(a) to Fig. 3(c-2), the injected charge density distribution changes to a straighter and thicker distribution from the HV electrode to the ground electrode. This change is caused by the conduction flow attracting to the HV electrode as shown in Fig. 5(b).

The maximum Coulomb's force in Fig. 4 is 5ГЧ105 N/m3 at the corner of the HV electrode for ion drag action. When conduction effect is added, the maximum Coulomb's force is weakened because negative charges are collected near the positive HV electrode. Although the maximum Coulomb's force is weakened, the developed pressure in Fig. 6 increases by 36

The maximum electric field strength in Fig. 7 is 15 MV/m on the charge injection region of the positive HV electrode. The electric field strength is not affected by conduction effect although not shown in the figure.

Two-plate electrodes mounted on wall

The distributions of charge density, Coulomb's force and pressure are shown in Figs. 8-10. The cases for only ion drag, only conduction and both actions are compared. The applied voltage is +2.0 kV and the flow rate is zero.

Comparison of Fig. 8(a) to Fig. 8(c-1) shows that the injected charge density distribution changes from a thin, flat shape to a thick, round shape. This change is caused by the conduction flow. In Fig. 8(b), dissociation charges are distributed more widely near the ground electrode than near the HV electrode. This is because the ground electrode is 3.3 times longer than the HV electrode. Such an asymmetric distribution of the charges may generate a net flow for the direction from narrow to wide electrode. This is the well-known working principal of conduction pump, which can be seen from the Coulomb's force distribution in Fig. 9(b). The area where the Coulomb's force acting to the right on and above the ground electrode is larger than that acting to the left on and above the HV electrode. When charge injection is added (Fig. 9(c)), the zero force boundary tilts toward the HV electrode, then Coulomb's force to the ground electrode is enhanced.

As shown in Fig. 10(c), high pressure appears at the left corner of ground electrode when both ion drag and conduction act. The pressure on and downstream the ground electrode for the case of both ion drag and conduction acting is higher than that for the case of only conduction.

Embedded two-plate electrodes

The distributions of charge density, Coulomb's force and pressure are shown in Figs. 11-13, respectively and are very similar to those for the two-plate electrodes mounted on the wall.

As with the mounted plates, dissociation charge occupies whole of the channel (Fig. 11(c-2)), so the Coulomb's force induced by the dissociation charge covers wide range of the channel (Fig. 12). In Fig. 13, high pressure area appears near the HV

electrode in case of only conduction flow, on the other hand, the area is near the ground electrode in case of the both ion drag and conduction flow. This change is because the charge injection from the HV electrode make pressure near the ground electrode high and weaken the Coulomb's force induced by the dissociation charge near the HV electrode.

Comparison of pressure - flow rate characteristics

Fig. 14 presents simulated pressure - flow rate characteristics for the three electrode configurations. The pressure difference between the outlet and inlet of the channel is plotted at different flow rates. The net flow direction is from left to right in Fig. 1. In Fig. 14(a), the pressure developed by the ion drag action is higher than that by conduction action, while the situation is reversed in Fig. 14(b) and (c). In all configurations, the pressure developed by both ion drag and conduction actions is the highest. At zero flow rate in Fig. 14(a), the developed pressure is 29 Pa for only ion drag action, is 5 Pa for only conduction action, and is 40 Pa for both actions. When the ion drag and conduction act simultaneously, the developed pressure is augmented and is higher than the sum of the pressures developed separately by each action. The augmentation effect in Fig. 14(b) is the largest of all. In Fig. 14(b), the developed pressure for ion drag action is 4.9 Pa. On the other hand, the conduction action develops 12 Pa. When the ion drag and conduction act simultaneously, the pressure increases to 49 Pa. This pressure augmentation may result from the variation of the CoulombвЃ™s force distribution in Fig. 9, which is caused by the variation of the dissociation charge distribution induced by the ion drag flow.

5 CONCLUSIONS

This paper investigates numerically the interaction between the ion drag and conduction actions using plateвЃ™Ybar, mounted plates and embedded plates electrodes in two-dimensional channel. It is found that when the ion drag and conduction act simultaneously, the developed pressure is augmented and is higher than the sum of the pressures developed separately by each action. It is also found that the pressure augmentation depends strongly on electrode configuration.

Acknowledgements

The authors would like to express their gratitude to Mr. Yuta OTSUKA for his help in the experiment. This research was partially supported by JSPS KAKENHI Grant number 16K06076.

References

[1] M. Nishikawara, M. Shimada, M. Saigo, and H. Yanada, Numerical investigation into characteristics of an ion drag pump, Journal of Electrostatics, Vol. 84, pp. 23-31, 2016.

[2] M. Yazdani, J. Seyed-Yagoobi, Effect of charge mobility on dielectric liquid flow driven by EHD conduction phenomenon, Journal of Electrostatics. Vol. 72, pp. 285вГ Y294, 2014.

[3] M. Yaszdani, J.Seyed-Yagoobi : The effect of uni/bipolar charge injection on EHD conduction pumping, Journal of Electrostatics, 75,43/48 (2015)

[4] H. Yanada, T. Yamada, Y. Asai, Y. Terashita, Measurement and numerical simulation of ion drag pump characteristics, Journal of Fluid Science and Technology. 5 (2010) 617вГ Y631.

[5] JIS C 2101, Testing Methods of Electrical Insulating Oils, 1999.

[6] J.K. Park, J.C. Ryu, W.K. Kim, K.H. Kang, Effect of Electric Field on Electrical Conductivity of Dielectric Liquids Mixed with Polar Additives: DC Conductivity, The Journal of Physical Chemistry B. 113 (2009) 12271вГ Y12276.

[7] Material Safety Data Sheet of DBS, available at: http://www.daihachi-chem.co.jp/msds/list.html, Daihachi Chemical Industry Co.,Ltd., last (accessed 08.07.16).

Masahito, Nishikawara, D2-202, Building D2, 1-1, Hibarigaoka, Tenpaku-cho, Toyohashi, Aichi, 441-8580, Japan

On the multi-fluid approach to multiphase flow modeling in hydraulic fracturing applications

Andrei A. Osiptsov

a.osiptsov@skoltech.ru

Abstract

In this review paper, we present a family of closely related models for multiphase flows at all stages of the technology of hydraulic fracturing, which is used for stimulation of production from oil and gas wells. The models are derived from conservation laws using asymptotic methods in the multi-fluid approach. Five separate problem formulations are distinguished: (i) suspension flow down the well, (ii) suspension flow and sedimentation in a hydraulic fracture, (iii) inertial migration of particles in the horizontal section of a vertical hydraulic fracture, (iv) filtration of fluid with fine particles through a random close pack of proppant in a closed hydraulic fracture, and, finally, (v) a gas-liquid flow in a well during cleanup and startup after the end of hydraulic fracturing. Advantages and drawbacks of the multi-fluid approach are discussed, in comparison to simplified semi-empirical effective-fluid and drift-flux models.

1 Introduction

The technology of hydraulic fracturing of a hydrocarbon bearing underground formation is based on injecting a fluid laden with rigid particles under a high pressure (up to several hundred bar) into the well to create fractures in the porous medium, which are filled with particles. After the end of pumping, fractures closed on packed granular material provide high-conductivity channels to transport hydrocarbons from reservoir to the well and all the way up to the surface. The well may be vertical (when a single bi-wing fracture is formed) or near-horizontal with several perforation clusters providing reservoir contact (the so-called multi-stage fracturing in low-permeability formations). The latter case gives rise to several transversal fractures.

With respect to different stages of the hydraulic fracturing technology, we consider four classes of multiphase flows that can be modelled within the multi-continua (or multi-fluid) approach [1]. In a more detail, we distinguish the following classes: (i) the flow of suspension of fluid with particles in a circular pipe at high Reynolds numbers during pumping, (ii) the flow of suspension in a narrow vertical hydraulic

fracture at moderate Re during pumping [2, 3], (iii) suspension filtration through a packed of proppant particles in a closed fracture during cleanup [4], and (iv) multiphase gas-liquid flow with admixture of rigid particles in a circular pipe during well start-up, cleanup and testing in a wide range of the Reynolds numbers [5]. We discuss the advantages and limitations of the multi-fluid approach based on the simulation examples from each of the four classes of multiphase flows, in comparison with simplified semi-empirical approaches, e.g. the drift-flux model for well flows, the effective-fluid model for suspension transport in fractures, and the deep-bed filtration model. The talk ends up with recommendations for future research on the topic. A detailed review of the state of the art in numerical modeling of hydraulic fracturing can be found in [7], and the most recent review with a specific focus on fluid mechanics of hydraulic fracturing is [6].

2 Two-fluid model for suspension transport in a fracture

In this section, we present in a lumped form the two-fluid model for suspension flow and sedimentation in a hydraulic fracture. This model was derived in the multi-continua approach [1] using asymptotic methods in the lubrication approximation. The key assumption is that the width-to-length ratio of the fracture is a small parameter: $\varepsilon = w/L \ll 1$. The cross-flow particle concentration profile is assumed uniform. In the width-averaged variables, the equations are as follows [2]:

$$\frac{\partial wC}{\partial t} + \nabla \left(wC\mathbf{V}_p \right) = 0 \quad (1)$$

$$\frac{\partial w}{\partial t} = \nabla \left[\frac{w^3}{12\mu(C)} \left(\nabla P + \mathrm{Bu} \left[1 + C(\eta - 1) \right] \mathbf{e}_2 \right) - wC\mathbf{V}_s \right] - 2v_l \quad (2)$$

$$\mathbf{V}_f = -\frac{w^2}{12\mu(C)} \left(\nabla P + \mathrm{Bu} \left[1 + C(\eta - 1) \right] \mathbf{e}_2 \right), \ \mathbf{V}_p = \mathbf{V}_f + \mathbf{V}_s \quad (3)$$

$$\mathbf{V}_s = -\frac{\mathrm{St}}{\mathrm{Fr}^2} \left(\frac{\eta - 1}{\eta} \right) f(C)\mathbf{e}_2, \ f(C) = \left(1 - \frac{C}{C_{max}} \right)^5, \ \mu(C) = \left(1 - \frac{C}{C_{max}} \right)^{-1.89}.$$

$$\mathrm{Bu} = \frac{\rho_f^0 g L^2}{\mu_0 U}, \quad \rho_p^0 / \rho_f^0.$$

Here, Cartesian coordinate system Oxy is introduced in the cell plane, so that y-axis (with the basis vector $\mathbf{e}_2$) is vertical and origin O is located in the bottom left corner of the computational domain; C is the particle volume fraction; $w(x, y, t)$ is the width of the fracture (in hydraulic fracturing simulators, the width is available from solving the geomechanics problem of fracture growth [7]); $\mathbf{V}_f$, $\mathbf{V}_p$, $\mathbf{V}_s$ are the width-averaged velocities of the fluid and the particles, and the settling velocity of particles relative to the fluid; v_l is the velocity of fluid leak-off through the porous walls; differential operator '∇' acts in the (x, y) plane as we applied the averaging procedure along the cell width. The flow scales are as follows: L is the cell length, U is the scale of the injection velocity, d is the cell width scale, ρ_0^f is the fracturing fluid density, μ_0 and τ_0 are the fracturing fluid plastic viscosity and yield stress, respectively; g is the gravity acceleration; Bu is the Buoyancy number.

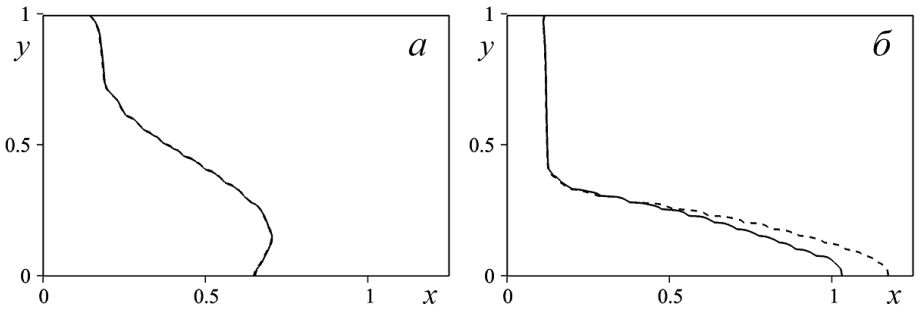

Figure 1: Particle concentration fronts in the fracture of elliptic cross-section at $t = 0.5$ for $Bu = 326$ (a) and $Bu = 3260$ (b). Result are obtained by the effective-fluid model (dashed line) and the two-fluid model (solid line).

Boundary and initial conditions for the hyperbolic equation for concentration (1) are given by:

$$t = 0 : C = 0, (x, y) \in [0, L/H] \times [0, 1]; \quad x = 0 : \; C = C_0, \, y \in [y_1, \, y_2]$$

Boundary conditions for the pressure equation (2) are as follows:

$$x = 0 : \; \frac{\partial p}{\partial x} = -\frac{12\mu\,(C)}{w^2}, \; y \in [y_1, \, y_2]; \; \frac{\partial p}{\partial x} = 0, y \in [0, \, y_1], [y_2, \, 1]$$

$$x = L/H : \; \frac{\partial p}{\partial y} = -\mathrm{Bu}; \quad y = 0, \; 1 : \; \frac{\partial p}{\partial y} = -\mathrm{Bu}(1 + C|_{y=0,1}(\eta - 1))$$

The particle settling velocity is given by an empirical formula, which is the generalization of the well-known Richardson-Zaki expression, taking into account the fact that particles slow down and stop completely when reaching the packed bed on the bottom. The existing effective-fluid models of suspension flows [8] contain an assumption that the *volume-averaged* suspension velocity is governed by the Poiseuille law, while in the present two-fluid model it is shown based on the derivation from the conservation laws that the Poiseuille law governs the *mass-averaged* velocity of the carrier fluid (3). Also, earlier models contained an assumption in the algebraic expression for the particle velocity (3) that the particles settle relative to the volume-averaged velocity of the suspension [8], and not relative to the fluid, as is the case on the two-fluid approach [2]. As a result, in contrast to the existing models the two-fluid model includes an additional term $-\nabla(wC\mathbf{V}_s)$ in the right-hand side of the pressure equation (2), which takes into account the two-speed effects.

3 Cross-flow inertial migration of particles in a fracture

Particle migration in fractures is essentially a multi-scale problem, spanning from the lift force on a single particle settling in a slot [9], through the inertial igration in a suspension flow in the horizotnal section of a fracture [10, 11] to the effects of cross-flow migration on the global transport and sedimentation in the entire fracture [12].

In thi seciton, we will consider in detail the inertial migration of particles in a dilute suspension flow through the entry region of a plane channel, which is important in application to modeling of proppant migration in the near-wellbore zone of the fracture. Within the two-fluid approach, an asymptotic one-way coupling model of the dilute suspension flow in the entry region of a channel is constructed in [10]. The carrier phase is a viscous incompressible Newtonian fluid, and the dispersed phase consists of identical non-colloidal rigid spheres. In the inter-phase momentum exchange, we take into account the drag force, the virtual mass force, the Archimedes force, and the inertial lift force with a correction factor due to the wall effect and an arbitrary particle slip velocity. The channel Reynolds number is high and the particle-to-fluid density ratio is of order unity or significantly larger unity. The solution is constructed using the matched asymptotic expansions method. The problem of finding the far-downstream cross-channel profile of particle number concentration is reduced to solving the equations of the two-phase boundary layer developing on the channel walls. The full Lagrangian approach is used to study the evolution of the cross-flow particle concentration profile.

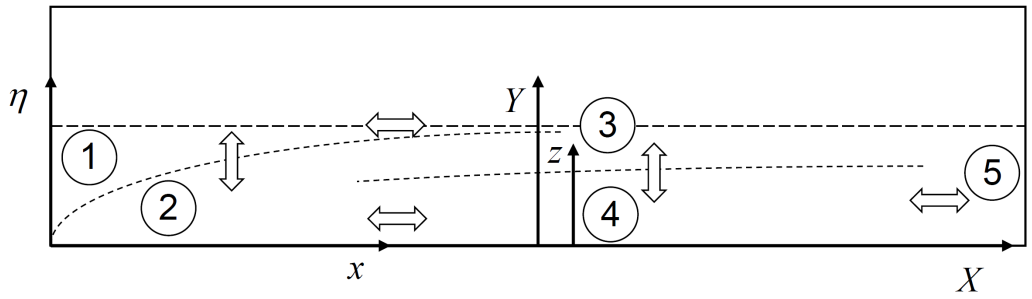

Figure 2: Asymptotic domains in the suspension flow in the horizontal section of an entry region of a fracture: *1* – the entry region, *2* – the boundary layer, *3* – the region of overlapping of the boundary layers, *4* – the lower sublayer, *5* – the far downstream region of the fully developed Poiseuille flow. Symbol ⇔ defines asymptotic matching of solutions in adjacent domains.

The system of equations of the two-phase boundary layer are as follows [10]:

$$\frac{\partial u}{\partial x}+\frac{\partial v}{\partial \eta}=0, \quad \frac{\partial \rho_s u_s}{\partial x}+\frac{\partial \rho_s v_s}{\partial \eta}=0, \qquad (4)$$
$$u\frac{\partial u}{\partial x}+v\frac{\partial u}{\partial \eta}=\frac{\partial^2 u}{\partial \eta^2}, \quad \frac{\partial p}{\partial \eta}=0,$$

$$u_s\frac{\partial u_s}{\partial x}+v_s\frac{\partial u_s}{\partial \eta}=F_{sx}=\frac{2\xi}{2\xi+1}D_0(u-u_s)+\frac{3}{2\xi+1}\left(u\frac{\partial u}{\partial x}+v\frac{\partial u}{\partial \eta}\right),$$
$$u_s\frac{\partial v_s}{\partial x}+v_s\frac{\partial v_s}{\partial \eta}=F_{s\eta},$$

$$F_{s\eta} = \frac{2\xi}{2\xi+1}\left[D_0(v-v_s) + \kappa_0 c_l\sqrt{\frac{\partial u}{\partial \eta}}(u-u_s)\right] + \frac{3}{2\xi+1}\left(u\frac{\partial v}{\partial x} + v\frac{\partial v}{\partial \eta}\right),$$

$$c_l(\chi, x, \eta) = c_l^{\infty}\left[1 - n\exp\left(-m_1(\chi)\frac{\eta}{x^{1/4}}\right)\right],$$

$$m_1 = m\frac{\sqrt{\varphi''(0)}}{(\varepsilon\lambda)^{1/4}}, \quad \chi = \frac{|u-u_s|}{(\varepsilon\lambda)^{1/4}}, \quad \xi = \rho_p^0/\rho_f^0$$

$$\kappa_0 = \frac{6.46}{12\sqrt[4]{18\pi}} Re_{s0}^{3/2}\left(\frac{\rho_s^0}{\rho}\right)^{1/4}, \quad D_0 = 1 + \frac{1}{6}Re_{s0}^{3/2}(u-u_s)^{3/2}, \quad \mathrm{Re}_{s0} = \frac{2aU\rho}{\mu}.$$

Here the latter terms in the right-hand side of the momentum conservation equations for the particulate phase correspond to the virtual mass force and the Archimedes force. Additionally, φ is the Blasius function from the well known solution of the boundary layer problem [13]. External flow is uniform, hence the longitudinal pressure gradient is zero. Boundary conditions take the form:

$$\begin{aligned} x = 0: \quad & u_s = \rho_s = 1, \quad v_s = 0; \\ \eta = 0: u = v = 0; \quad & \eta \to \infty: \quad u \to 1. \end{aligned} \tag{5}$$

The inertial migration in the entry region of a plane channel (a circular pipe) results in particle accumulation on two symmetric planes (an annulus) distanced from the walls, with a non-uniform concentration profile between the planes (inside the annulus) and particle-free layers near the walls. When the particle-to-fluid density ratio is of order unity, an additional local maximum of the particle concentration on inner planes (an inner annulus) is revealed. The inclusion of the corrected lift force makes it possible to resolve the non-integrable singularity in the concentration profile on the wall, which persisted in all previously published solutions for the dilute-suspension flow in a boundary layer [14]. The numerical results are compared with the tubular pinch effect observed in experiments, and a qualitative analogy is found.

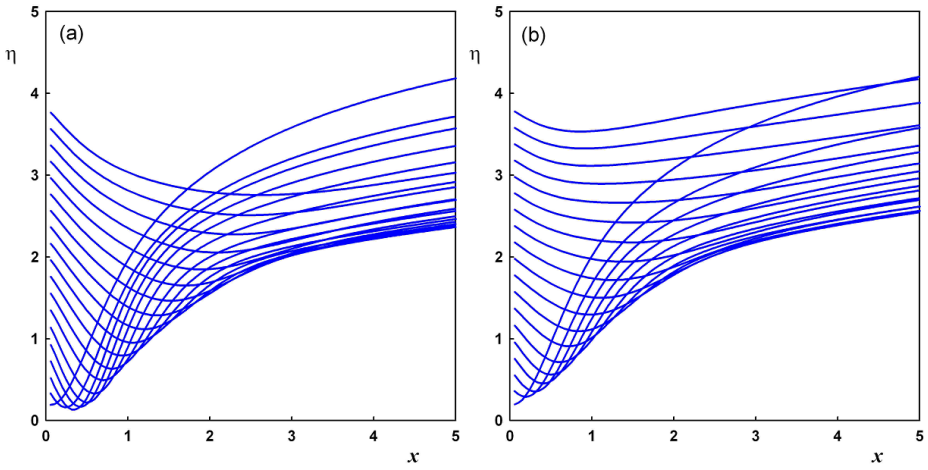

Figure 3: Trajectories of the particles in the boundary layer for the nondimensional intensity of the lift force $\kappa_0 = 20$, the particle-to-fluid density ratio $\xi = 3$ (a) and $\xi = 5$ (b).

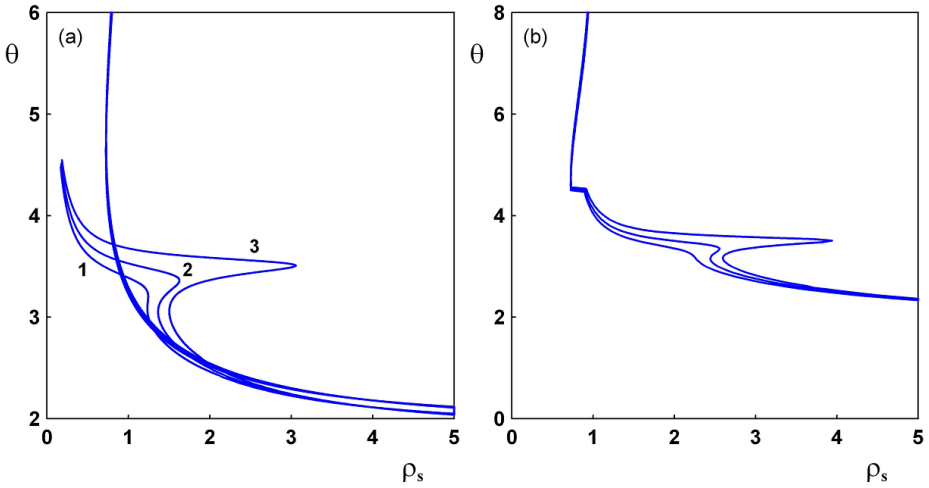

Figure 4: Far-downstream asymptotics of the cross-flow concentration profile ρ_s depending of the stream function θ in the boundary layer, $\kappa_0 = 20$ and $\xi = 5$, 4.5, Рч 4 – curves *1-3*. Profiles in each layer of the fold (a) and the total concentration profile (b).

In this case the trajectories shown in Fig. 3 are substantially different from the case of a dusty gas. The reason is that in the case of a suspension the particle-to-fluid density ratio is of order unity $\xi \sim 1$, and the terms due to the Archimedes force and the virtual mass force should be retained in the momentum conservation laws. These terms result in the formation of an additional local maximum in the cross-flow concentration profile (see Fig. 4,(a)).

4 Suspension filtration in proppant packings in a closed fracture

Suspension flow in the propped fracture is described within the three-continua approach: suspended partices (solid particles carried by the flow of a fluid within the porous space), trapped particles (solid particles, which are sedimented in pores), and carrier fluid (viscous incompressible Newtonian fluid). Suspended particles are characterised by the phase density ρ_p^{mob} and the mass-averaged velocity U_p^{mob}; the phase of trapped particles is characterized by the density ρ_p^{sed}; the carrier phase is characterised by the mass-averaged velocity U_f and density ρ_f. Particles have constant substance density ρ_p^0, and the fluid – a constant substance density ρ_f^0. Multi-continua modeling of suspension flows is applicable if the following hierarchy of scales exists: particle diamter is significantly smaller than the diameter of pore channels, while being significantly larger than the mean free path of the fluid molecules [1]. Large pore channels are the pore space excluding trapped particles and the void space between those. Small pore channels are pore space between trapped particles (Fig. 5, b).

Density of the particle phases are related to the porosity and the particle concen-

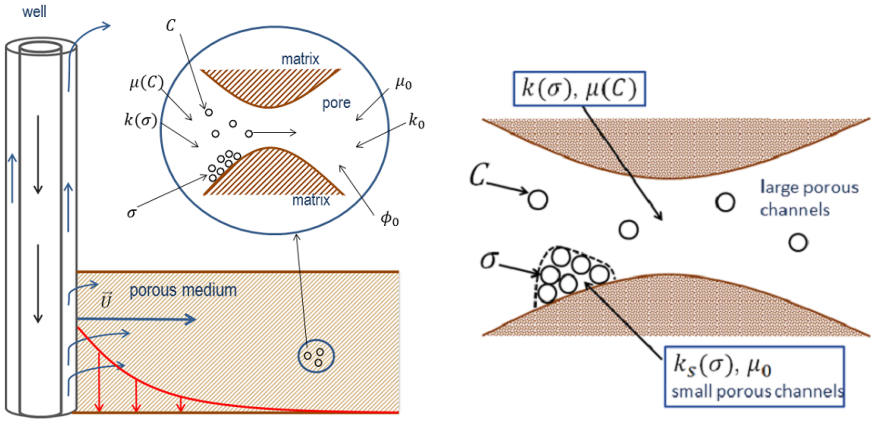

Figure 5: The sketch of suspension flow in a porous medium (a); a scheme of the porous space (b): large pore channels (1) and small pore channels (2).

tration by the following relations [15]:

$$\rho_p^{mob} = \rho_p^0 C\phi_c, \qquad \rho_p^{sed} = \sigma\rho_p^0, \qquad \rho_f = \rho_f^0(\phi_t - C\phi_c),$$

$$\phi_t = \phi_0 - \sigma, \qquad \phi_c = \phi_0 - \sigma/C_{max}, \tag{6}$$

where C is the particle volume fraction in the pore space available for the fluid to flow (in large pore channels), σ – the volume concentration of trapped particles in the entire volume of the porous medium, C_{max} is the maximum packing concentration (random close packing), ϕ_t – the porosity of the medium formed by the trapped particles and the matrix (large and small channels in total), ϕ_c – the porosity of the medium formed by the large pore channels; ϕ_0 – initial porosity of the medium.
The mass conservation equation for particles and fluid is written as [19]:

$$\frac{\partial\rho_p^{mob}}{\partial t} + \frac{1}{r^j}\frac{\partial(\rho_p^{mob}U_p^{mob}r^j)}{\partial r} = -q_s, \qquad \frac{\partial\rho_p^{sed}}{\partial t} + \frac{1}{r^j}\frac{\partial(\rho_p^{sed}U_p^{sed}r^j)}{\partial r} = q_s, \tag{7}$$

$$\frac{\partial\rho_f}{\partial t} + \frac{1}{r^j}\frac{\partial(\rho_f U_f r^j)}{\partial r} = 0.$$

Here $j = 0$ in a plane flow and $j = 1$ in a radial flow, q_s is the rate of trapping and mobilization of particles in the matrix, determined by the formulas [16]:

$$q_s = \rho_p^{mob}U_p^{mob}\lambda - \rho_p^0\alpha\sigma\delta(U_s - U_{crit}), \tag{8}$$

$$\delta(U_s - U_{crit}) = \begin{cases} U_s - U_{crit}, & U_s > U_{crit} \\ 0, & U_s < U_{crit} \end{cases}.$$

Here λ is the colmatation coefficient (intensity of particle trapping) [20], α – the coefficient of mobilization of trapped particle, U_s is the filtration velocity in large and small pore channels, U_{crit} is the critical suspension velocity, above which trapped particles are mobilized.

In large pore channels with the permeability $k(\sigma)$, the suspension is flowing with the viscosity $\mu(C)$. In small pore channels with the permeability $k_s(\sigma)$, only the clean fluid is flowing with the dynamic viscosity μ_0. The momentum conservation equations (Darcy laws) for the carrier phase, suspended particles and the suspension as a whole are obtained by volume-averaging in large and small pore channels:

$$U = -\frac{k(\sigma)}{\mu(C)}\frac{\partial p}{\partial r}, \qquad U_s = -\left[\frac{k(\sigma)}{\mu(C)} + \frac{k_s(\sigma)}{\mu_0}\right]\frac{\partial p}{\partial r}, \tag{9}$$

$$U_f^{filtr} = -\left[(1-C)\frac{k(\sigma)}{\mu(C)} + \frac{k_s(\sigma)}{\mu_0}\right]\frac{\partial p}{\partial r}, \qquad U_p = -C\frac{k(\sigma)}{\mu(C)}\frac{\partial p}{\partial r},$$

$$U_f^{filtr} = U_f(\phi_t - C\phi_c).$$

Here U is the suspension filtration velocity in large and small pores, U_f^{filtr} is the fluid filtration velocity in large and small pore channels, $U_p = U_p^{mob} C\phi_c$ is the volume-averaged velocity of suspended particles in large pore channels, p – pressure.
The work [3] suggests the following relation between the permeability in large pore channels and the volume fraction of trapped particles:

$$k(\sigma) = k_0\left(1 - \frac{\sigma}{\phi_0 C_{max}}\right)^3. \tag{10}$$

Permeability in small pore channels:

$$k_s = k_{s0}\left(\frac{\sigma}{\phi_0 C_{max}}\right)^3, \qquad k_{s0} = \frac{(1-C_{max})^3 d^2}{180 C_{max}^3}. \tag{11}$$

Here k_{s0} is the permeability of small pore channels during full packing of porous space ($\sigma = \phi_0 C_{max}$), determined from the Kozeny-Carman formula [21]; d is the diameter of particles in suspension.
Using the definitions introduced above, the conservation equations can be reformulated as:

$$\frac{\partial(C\phi_c)}{\partial t} + \frac{1}{r^j}\frac{\partial(CUr^j)}{\partial r} = -UC\lambda + \alpha\sigma\delta(U_s - U_{crit}), \tag{12}$$

$$\frac{\partial \sigma}{\partial t} = UC\lambda - \alpha\sigma\delta(U_s - U_{crit}),$$

$$\frac{\partial(U_s r^j)}{\partial r} = 0.$$

Classical deep-bed filtration models of suspension flow do not take into account the fact that the particles trapped in pores form a secondary porous medium (a random close packing of sedimented particles) with the permeability smaller than the permeability of the matrix. Filtration through the close packing of trapped particles is not considered in the classical models.

Below for comparison we present the classical model of deep-bed filtration in large pore channels without considering the flow in small pore channels in the packed bed of trapped particles ($\phi_c = \phi_t = \phi_0 - \sigma, U = U_s, k_s = 0$) [3, 5, 15, 24, 18]:

$$\frac{\partial(C\phi_c)}{\partial t} + \frac{1}{r^j}\frac{\partial(CUr^j)}{\partial r} = -CU\lambda(\sigma) + \alpha\sigma\delta(U - U_{crit}),$$
$$\frac{\partial\sigma}{\partial t} = CU\lambda(\sigma) - \alpha\sigma\delta(U - U_{crit}),$$
$$\frac{\partial(Ur^j)}{\partial r} = 0, \qquad U = -\frac{k(\sigma)}{\mu(C)}\frac{\partial p}{\partial r}. \tag{13}$$

Experiments on colmatation of core sample [23] have shown that the model (13) can be improved by introducing the following expression:$\lambda = \lambda_0(1+\beta\sigma)$. Here, λ_0 is the original colmatation coefficient. Thus, the classical model (13) contains two tuning parameters λ_0 Рч β.

Two versions of boundary conditions are considered: - (i) pressure is specified at the entry and at the outlet of the core sample (a): $r = r_0 : p = p_0, C = C_0; r = L : p = 0$. - (ii) the filtration velocity is specified at the inlet, and pressure – at the outlet (b): $r = r_0 : U_s = U_0, C = C_0; r = L : p = 0$.

Initial conditions: $t = t_0 : \phi = \phi_0, \sigma = 0$.

Closure relations for permeability of the random close packing of proppant in a hydraulic fracture can be found from direct numerical simulation supported by proper conductivity experiments (see, for example, LBM simulations in mixed packing of proppant particles of various shape in [25]).

5 Gas-liquid flows in a well during cleanup

In this section we will discuss the first-principles derivation of simplified drift-flux equations for gas-liquid flows in a well [26]. We consider a transient isothermal flow of a gas-liquid mixture in a long circular pipe with a variable inclination angle to the horizon. The flow is assumed to be axisymmetric and non-swirling. The liquid is a continuous carrier phase. The gas is a dispersed phase present in the form of monodisperse spherical bubbles suspended in the carrier fluid. The gas is compressible, and the liquid is incompressible. The cross-flow migration of the bubbles and their merging are not considered; however, we take into account the resulting nonuniform cross-flow profile of the gas volume fraction, which is formed as a result of the migration of the bubbles. The pressure difference in the bubbles and in the surrounding liquid due to surface tension is neglected. The bubble size is assumed to be much smaller than the spatial scales of variation of the fluid velocity, and the Reynolds numbers of the flow around individual bubbles are small.

The two-phase flow is considered within the approach of interpenetrating and interacting continua [1]. The problem is described by conservation laws in differential form, written for gas and liquid phases. The mass transfer between the phases is absent.

The balance laws of mass and momentum in the differential form for gas and liquid

take the form [1]:

$$\frac{\partial}{\partial t}(\alpha_i \rho_i) \; + \; \nabla(\alpha_i \rho_i \mathbf{v}_i) = 0 \tag{14}$$

$$\alpha_i \rho_i \frac{d_i \mathbf{v}_i}{dt} = -\nabla p_i \; + \; \nabla \cdot \boldsymbol{\phi}_i \; + \; \alpha_i \rho_i \mathbf{g} \; + \; n_b \mathbf{F}_{ij} \tag{15}$$

$$\frac{d_i}{dt} = \frac{\partial}{\partial t} \; + \; (\mathbf{v}_i \cdot \nabla).$$

Here, the indexes $i, j = g, l$ $(i \neq j)$ denote gas and liquid, respectively, α_i, ρ_i, and $\mathbf{v}_i$ are the volume fractions, densities and velocities of the phases, p_i and $\boldsymbol{\phi}_i$ are the pressures and viscous stress tensors in each phase, and $\mathbf{g}$ is the gravity force acceleration. The momentum exchange between the phases is described by the term $\pm n_b \mathbf{F}_{ij}$, where $\mathbf{F}_{gl} = \mathbf{F}$ is the force exerted on a single bubble by the fluid, $\mathbf{F}_{lg} = -\mathbf{F}_{lg}$, and n_b is the number concentration of the bubbles.

For simplicity, the following calculations are performed for a vertical pipe, although the results may be generalized to the case of an inclined pipe, excluding flows in near-horizontal pipes.

It is assumed that the chaotic motion of the bubbles can be neglected, and the deviation of the bubble velocity from the mass-averaged velocity of the dispersed phase $\mathbf{v}_g$ is small, hence the stress tensor in the dispersed phase can be neglected [2]. The presence of the dispersed phase affects the stress tensor of the carrier phase. On the other hand, the bubbles of a compressible gas travel with a velocity different from that of the fluid, and the bubble volume fraction varies. Accordingly, the condition $\nabla \mathbf{v}_l = 0$ is no longer true. In this sense, the averaged liquid phase is compressible, in contrast to the liquid as a material. Therefore, the stress tensor of the carrier phase is written as for a viscous compressible fluid, with the coefficients of shear viscosity μ and bulk viscosity ζ dependent on the gas volume fraction:

$$\boldsymbol{\phi}_l = 2\mu(\alpha_g)\left(\mathbf{e}_l \; - \; \frac{1}{3}\nabla \mathbf{v}_l \mathbf{I}\right) \; + \; \zeta(\alpha_g)\nabla \mathbf{v}_l \mathbf{I}.$$

Here, $\mathbf{e}_l$ is the strain rate tensor, and I is the unit tensor. To determine the dependences $\mu(\alpha_g)$ and $\zeta(\alpha_g)$ is a separate problem, which is usually solved for neutrally-buoyant particles, neglecting the phase slip. In what follows, we assume that $\mu(0) = \mu_0$, where μ_0 is the viscosity of the pure fluid, and $\zeta(\alpha_g)\nabla \mathbf{v}_l \to 0$ as $\alpha_g \to 0$.

The bubble radius is bounded by a limiting value R_c above which the bubble loses the spherical shape, becomes unstable, and is fragmented into smaller bubbles:

$$R \leq R_c \simeq \frac{1}{3}\left(\frac{\sigma}{\rho_l g}\right)^{\frac{1}{2}} \simeq 10^{-3}\text{m}.$$

Here, σ is the gas-liquid surface tension. Under the above assumptions, the total force exerted on a bubble by the fluid is a superposition of the Stokes $\mathbf{F}_s$, the Archimedes $\mathbf{F}_A$, the added mass $\mathbf{F}_{am}$, and the Basset-Boussinesq $\mathbf{F}_{BB}$ forces. Accordingly, the forces on a bubble can be written in the form:

$$\mathbf{F} = \mathbf{F}_{St} \; + \; \mathbf{F}_A \; + \; \mathbf{F}_{am} \; + \; \mathbf{F}_{BB}$$

$$\mathbf{F}_{St} = 6\pi\mu R(\mathbf{v}_l - \mathbf{v}_g), \quad \mathbf{F}_A = \frac{4}{3}\pi R^3\rho_l\left(\frac{d_l\mathbf{v}_l}{dt} - \mathbf{g}\right), \quad \mathbf{F}_{am} = \frac{2}{3}\pi R^3\rho_l\frac{d_g}{dt}(\mathbf{v}_l - \mathbf{v}_g)$$

For a transient flow in a well, the equations of the drift-flux model, known in the literature and implemented in the commercial reservoir simulator ECLIPSE (Schlumberger), take the form [27, 28]:

$$\frac{\partial}{\partial t}(A\alpha_i\rho_i) + \frac{\partial}{\partial z}(A\alpha_i\rho_i v_i) = 0 \tag{16}$$

$$\rho_m\left(\frac{\partial v_m}{\partial t} + v_m\frac{\partial v_m}{\partial z}\right) = -\frac{\partial p}{\partial z} + \rho_m g\cos\theta + \frac{2f\rho_m v_m|v_m|}{d} \tag{17}$$

$$v_g = C_0 v_m + v_d. \tag{18}$$

Here, A is the pipe cross-section, $v_m = \alpha_g v_g + \alpha_l v_l$ is the volume-averaged velocity of the mixture, $\rho_m = \alpha_g\rho_g + \alpha_l\rho_l$ is the mixture density, $f = f(\alpha_g, v_m, p)$ is the friction coefficient, d is the pipe diameter, and θ is the angle between the pipe axis and the vertical.

In the applications, a quasi–steady-state variant of the drift-flux model is widely used, in which the time-derivative in the momentum equation for the mixture is neglected and the total pressure difference is equal to the sum of the terms responsible for the gravity force, friction, and acceleration [27]. In the literature, this model is referred to as the no-pressure wave model, since it does not take into account the disturbance propagation with the transport velocity. In contrast to this quasi–steady-state formulation, we retain the time derivative of velocity in the momentum equation to take into account highly transient effects.

In the literature, formula (18) [1] (where $C_0 = C_0(\alpha_g, v_m, p)$ is the profile parameter which takes into account a non-uniform cross-flow profile of the bubble volume fraction and the carrier-phase velocity, and $v_d = v_d(\alpha_g, v_m, p)$ is the drift velocity) is called the drift-flux model relation.

There is also another known formulation of the drift-flux model [29], with the mixture momentum equation written as

$$\frac{\partial}{\partial t}(\alpha_g\rho_g v_g + \alpha_l\rho_l v_l) + \frac{\partial}{\partial z}(\alpha_g\rho_g v_g^2 + \alpha_l\rho_l v_l^2 + p) = Q_l + Q_g, \tag{19}$$

where Q_i are the source terms for each phase, and the drift-flux relation written as

$$v_g - v_l = \Phi(\alpha_g, v_g, p) \tag{20}$$

The asymptotic equations are derived in the long-channel approximation $\varepsilon \ll 1$, similar to the boundary-layer approximation, the narrow-channel approximation for fracturing flows [2], and the lubrication approximation for thin-film flows [30].

To come up with an algebraic relation between the phase velocities, additionally it is assumed that

$$\varepsilon\mathrm{St}\eta \ll 1, \quad \eta \gg 1, \quad \frac{\mathrm{St}}{\mathrm{Fr}^2}\eta \sim 1, \quad \varepsilon\mathrm{Re} \sim 1, \ \varepsilon\xi_0 \ll 1.$$

Thus, the drift-flux model in the form (16)-(18) can be derived from conservation laws only in the following three cases: (i) small volume fraction of the dispersed phase $\alpha \ll 1$; (ii) no phase velocity slip $|C_0 - 1| \ll 1$, $\eta \mathrm{St}/\mathrm{Fr}^2 \ll 1$; and (iii) inertialess flows $\varepsilon \mathrm{Re} \ll 1$.
Our analysis demonstrates that the drift-flux model [27, 28] in the form (16)-(18) for the present flow configuration strictly follows from the conservation laws in the limited number of cases (i)-(iii) and represents essentially the effective-fluid model. The closure relations published in open literature are obtained from a calibration against a large body of experimental data [27, 28] for the governing parameters satisfying at least one of conditions (i)-(iii). At the same time, our analysis indicates that the drift-flux model [29] in the form (16), (19), and (20) is more general because it follows from the balance laws without any additional assumptions, besides the requirement of noninertial slip $\varepsilon \mathrm{St} \ll 1$.

6 Conclusions

We review a family of closely-related multi-scale models derived by the author from conservation laws within the multi-fluid approach using perturbation methods to describe all stages of the technology of hydraulic fracturing. The models cover suspension injection into the well to create primary fractures, suspension transport and sedimentation in a fracture, cross-flow inertial migration of particles in a horizontal section of a hydraulic fracture, filtration of suspensions of non-colloidal particles in a random close packing of proppant particles in the closed fracture, and gas-liquid flows in a well during cleanup and startup. In particular, our review covers:
1. A novel two-fluid model of suspension transport in a hydraulic fracture. It is shown that the model is different from the existing effective-fluid model of suspension flow by additional terms due to two-speed effects. These terms are important at high buoyancy numbers Bu, which corresponds to the case of high-rate slick-water fracturing. In the case of conventional fracturing with high-viscosity cross-linked gels, the models match. This model is then generalized to the case of a Bingham fluid flow and validated against four different sets of experiments on slumping, Saffman-Taylor fingering in Newtonian fluids, fingering and channeling in yield-stress fluids, and suspension transport and sedimentation in a slot with formation of a packed bed of particles at the bottom.
2. A multi-scale model of particle migration in a dilute-suspension flow through the fracture is developed, including the expression for the lift force on a particle settling in a horizontal flow through a vertical slot, the model of particle migration in the entry region of a plane channel with account for the Saffman lift force on a particle with the correction due to the wall effect, the model of migration of settling particles in a fully developed Poiseuille flow in a channel. Using the full Lagrangian approach, the particle concentration profile with an integrable singularity is obtained as a solution to the problem of the two-phase boundary layer. This achievement marks the first time that a self-consistent solution is obtained for the two-phase boundary layer problem within the dilute-suspension approximation, as all earlier solutions contained a non-integrable singularity thus making the model of dilute suspension inapplicable. New 2D width-averaged equations of suspension transport in a fracture

are derived with account for the non-uniform cross-flow particle concentraiton profile formed as a result of the migration.
3. A three-continua model is constructed for the suspension flow in a porous medium with account for the effects of particle trapping and mobilization. The model takes into account the effect of trapped particles forming a secondary porous medium of random closed packing with smaller permeability. Fluid fluxe through packed trapped particles is taken into account. In order to close the model, for the first time in a wide range of porosity we derived a permeability-porosity correlation for the random close packing of non-spherical particles based on the 3D simulation of viscous flow using the lattice-Boltzmann method, validated against lab conductivity tests.
4. The derivation of asymptotic equations of the drift-flux model for a dilute gas-liquid disperse two-phase flow in a circular pipe is presented in the long-channel approximation. This asymptotic model is obtained as a limit of the full equations based on the balance laws, written for each phase in the multi-fluid approximation. The key assumptions are determined, which make it possible to derive the drift-flux model from the balance laws. This model contains an algebraic relation for the phase velocities and a single equation for the mixture momentum, written for the volume-averaged velocity of the mixture. To derive the drift-flux relation for the phase velocities, when one phase is continuous and the second dispersed, it is required to assume only that the characteristic length scale of the problem is significantly greater than the velocity relaxation length. To derive the single equation for mixture momentum, it is necessary to assume additionally that one of the following conditions is satisfied: (i) the dispersed-phase volume fraction is small, (ii) the phase velocity slip can be neglected, or (iii) the flow is inertialess, i.e. the mixture acceleration can be neglected. At the same time it is shown that the drift-flux model, in which a single mixture momentum conservation equation is obtained as the sum of two momentum conservation equations for the phases, follows from the conservation laws under one assumption that the characteristic length scale of the problem is significantly larger than the phase velocity relaxation length; hence, this model is more general.

Acknowledgements

Startup funds of Skolkovo Institute of Science and Technology are gratefully acknowledged.

References

[1] Nigmatulin, R.I., 1990. Dynamics of multiphase media (Vol. 1,2). CRC Press.

[2] Boronin, S.A. and Osiptsov, A.A., 2010. Two-continua model of suspension flow in a hydraulic fracture. Doklady Physics . 55(4), 199вГ˜202.

[3] Boronin, S. A., Osiptsov, A. A., Desroches, J. 2015 Displacement of yield-stress fluids in a fracture, Intl. J. Multiphase Flow **76**, 47–63.

[4] Boronin, S.A., Osiptsov, A.A. and Tolmacheva, K.I., 2015. Multi-fluid model of suspension filtration in a porous medium. Fluid Dynamics, 50(6), pp.759-768.

[5] Krasnopolsky, B., Starostin, A. and Osiptsov, A.A., 2016. Unified graph-based multi-fluid model for gasвГYliquid pipeline flows. Computers & Mathematics with Applications, 72(5), pp.1244-1262.

[6] Osiptsov, A.A. Fluid mechanics of hydraulic fracturing: a review // *Journal of Petroleum Science & Engineering*, 2017. (*under review*).

[7] Adachi, J., Siebrits, E., Peirce, A., & J. Desroches, 2007 Computer simulation of hydraulic fractures. Int. J. of Rock Mech. and Mining Sci. **44**(1), 739–757.

[8] Pearson, J. R. A. 1994 On suspension transport in a fracture: framework for a global model. Non-Newtonian Fluid Mech. **54**, 503–513.

[9] Asmolov, E.S. and Osiptsov, A.A., 2009. The inertial lift on a spherical particle settling in a horizontal viscous flow through a vertical slot. Physics of Fluids, 21(6), p.063301.

[10] Osiptsov, A.A., Asmolov, E.S. 2008 Asymptotic Model of the Inertial Migration of Particles in a Dilute Suspension Flow Through the Entry Region of a Channel. *Phys. Fluids* **20** (1вГY2), 123301.

[11] Asmolov, E.S., Lebedeva, N.A. and Osiptsov, A.A., 2009. Inertial migration of sedimenting particles in a suspension flow through a Hele-Shaw cell. Fluid Dynamics, 44(3), pp.405-418.

[12] Boronin, S.A. and Osiptsov, A.A., 2014. Effects of particle migration on suspension flow in a hydraulic fracture. Fluid Dynamics, 49(2), pp.208-221.

[13] Schlichting, H., 1960. Boundary-layer theory. New York: McGraw-hill. Vancouver.

[14] Foster M.R., Duck P.W., Hewitt R.E. Boundary layers in a dilute particle suspension // Proc. R. Soc. A. 2006. V. 462. P. 136 вГY 168.

[15] Gruesbeck C., Collins R.E. Entrainment and deposition of fine particles in porous media // SPE Journal. 1982. N 8430. P. 847-856.

[16] Bailey L., Boek E.S., Jaques S.D.M., Boassen T., Selle O.M., Argillier J.-F., Longeron D.G. Particulate Invasion From Drilling Fluids // SPE Journal. 2000. V. 5(4). P. 412-419.

[17] Boek E.S., Hall C., Tardy P. M. J. Deep bed filtration modelling of formation damage due to particulate invasion from drilling fluids // Transport in Porous Media. 2012. V. 91(2). P. 479-508.

[18] Guedes R.G., Al-Abduwani F., Bedrikovetsky P., Currie P.K. Deep-Bed Filtration Under Multiple Particle-Capture Mechanisms // SPE Journal. 2009. V. 14(3). P. 477-487.

[19] Sedov, L.I., 1972. A Course in Continuum Mechanics: Fluids, gases and the generation of thrust. Wolters-Noordhoff.

[20] Mikhailov N.N. Variation of physical properties of rocks in the near wellbore zone [in Russian]. Moscow. Nedra, 1987.

[21] Van Der Hoef M. A., Beetstra R., Kuipers J. A. M. Lattice-Boltzmann simulations of low-Reynolds-number flow past mono- and bidisperse arrays of spheres: results for the permeability and drag force // Journal of Fluid Mechanics. 2005. V. 528. P. 233- 254.

[22] Herzig J.P., Leclerc D.M., Le Goff P. Flow of Suspensions through Porous Media // Industrial and engineering chemistry. 1970. V. 62(5). P. 9-34.

[23] Heertjes P. M., Lerk C.F. The functioning of deep bed filters // Trans. Inst. Chem. Eng. 1967. V. 45. P. 124-145.

[24] Civan F. Reservoir Formation Damage. Gulf Professional Publishing. Elsevier Inc. 2007. 1135 CF.

[25] Osiptsov, A.A. Hydraulic fracture conductivity: effects of non-spherical proppant from lattice-Boltzmann simulations and lab tests // *Advances in Water Resources*, 2017. (*accepted*).

[26] Osiptsov, A.A., SinвГЄkov, K.F. and Spesivtsev, P.E., 2014. Justification of the drift-flux model for two-phase flow in a circular pipe. Fluid Dynamics, 49(5), pp.614-626.

[27] A.R. Hasan and C.S. Kabir, *Fluid Flow and Heat Transfer in Wellbores* (Society of Petroleum Engineers, Richardson, Texas, 2002).

[28] H. Shi, J.A. Holmes, L.J. Durlofsky, et al., “Drift-Flux Modeling of Two-Phase Flow in Wellbores," SPE J. **10**, 24–33 (2005).

[29] S. Evje and T. Flatten, “On the Wave Structure of Two-Phase Models," SIAM J. Appl. Math. **67**, 487–511 (2007).

[30] A.A. Osiptsov, Steady Film Flow of a Highly Viscous Heavy Fluid with Mass Supply, Fluid Dynamics **38** (6), 846-853 (2003).

[31] Zhibaedov, V.D., Lebedeva, N.A., Osiptsov, A.A. and SinвГЄkov, K.F., 2016. On the hyperbolicity of one-dimensional models for transient two-phase flow in a pipeline. Fluid Dynamics, 51(1), pp.56-69.

Andrei A. Osiptsov, Skolkovo Institute of Science and Technology, Nobel Street 3, 143026 Moscow, Russia

Stress-life criteria for fatigue assessment of structures: advantages and drawbacks

Sergey V. Petinov, Boris E. Melnikov

sergei.petinov@gmail.com

Abstract

Presently in rules for fatigue assessment of steel, and in particular, welded structures in different technologies subjected to intensive alternating service loading the Stress-Life (S-N) criteria are recommended in several versions of approaches. These are the Nominal stress approach based on typifying welded joints and representing fatigue resistance of the joints by classed S-N curves; the Hot-spot stress approach focused on evaluation of кstructuralь stress by the means of finite-element analysis (FEA) and the Notch-stress approach based on the FEA-based assessment of the local stress caused by the geometry of structural detail and the weld shape. The criteria and approaches provide assessment of fatigue properties of structures, however, accompanied with a series of approximations and uncertainties. The nature of drawbacks of the S-N criteria and approaches is commented and feasible means of improvement the fatigue criteria evaluation and applications in fatigue assessment procedures are proposed.

1 Introduction

The Stress-Life (S-N) criteria are recommended presently in rules for fatigue assessment of structures subjected to intensive alternating service loading in versions (approaches) differing mostly by the procedure of considering effects of stress concentration in critical locations. [1, 2, 6], etc. The approaches are supplemented with the linear damage summation rule to consider random character of service loading in fatigue analysis of structures. The criteria and approaches were derived aimed at a non-complicated application in practical problems; however, a series of drawbacks and inaccuracies of those was being noted. Firstly, the experimentally obtained data base Ц S-N curves - providing evaluation of fatigue properties of structures was collected by testing of кclassedнь (including typified welded joints, as in the case of the Nominal stress approach [6]) specimens under cyclic loading terminated at almost complete failure (кseparation in two partsнь). This was leading to uncertainties in considering fatigue properties of materials in welded joints, effects of residual welding stress, definition of the state of damage in structural components, crack size, corresponding exhaustion of fatigue life. Further, recommendations for

testing specimens comprising typified welded joints which were aimed at considering effects of materials of the joint (weld material, material of fusion zone, etc.), of residual welding stress, implemented in the data base did not provide identity of fatigue damage between specimens and structural details. Partly, it was because of diversity of geometry of structural details comprising ктypifiedњ joints, which was recognized decades ago. Development of the finite-element analysis (FEA) facilities allowed analyzing the stress field in actual structural details, in particular, stress at critical locations. These facilities [3] and experience of strain measurement in welded components [4] were used to derive the Hot-spot stress approach (HSS) [1, 2], etc. The approximate estimation of the local stress caused by the particulars of the stress flow at the welded joint in HSS, necessity to account for the effects of geometry of the weld itself, resulted lately in development of the Notch stress approach [5], etc. Assessment of local stress causing the damage process allowed reducing the range of the design S-N curves to those presenting properties of the base and weld material only. However, apart from solving the problem of effects of geometry of structural detail on the damage process, the mentioned above disadvantages were not corrected. The above criteria and approaches are commented in more details in the below focused on problems of practical application and certain remedial actions are proposed.

2 Introduction

The Stress-Life (S-N) criteria are recommended presently in rules for fatigue assessment of structures subjected to intensive alternating service loading in versions (approaches) differing mostly by the procedure of considering effects of stress concentration in critical locations. [1, 2, 6], etc. The approaches are supplemented with the linear damage summation rule to consider random character of service loading in fatigue analysis of structures. The criteria and approaches were derived aimed at a non-complicated application in practical problems; however, a series of drawbacks and inaccuracies of those was being noted. Firstly, the experimentally obtained data base Ц S-N curves - providing evaluation of fatigue properties of structures was collected by testing of кclassedњ (including typified welded joints, as in the case of the Nominal stress approach [6]) specimens under cyclic loading terminated at almost complete failure (кseparation in two partsњ). This was leading to uncertainties in considering fatigue properties of materials in welded joints, effects of residual welding stress, definition of the state of damage in structural components, crack size, corresponding exhaustion of fatigue life. Further, recommendations for testing specimens comprising typified welded joints which were aimed at considering effects of materials of the joint (weld material, material of fusion zone, etc.), of residual welding stress, implemented in the data base did not provide identity of fatigue damage between specimens and structural details. Partly, it was because of diversity of geometry of structural details comprising ктypifiedњ joints, which was recognized decades ago. Development of the finite-element analysis (FEA) facilities allowed analyzing the stress field in actual structural details, in particular, stress at critical locations. These facilities [3] and experience of strain measurement in welded components [4] were used to derive the Hot-spot stress approach (HSS)

[1, 2], etc. The approximate estimation of the local stress caused by the particulars of the stress flow at the welded joint in HSS, necessity to account for the effects of geometry of the weld itself, resulted lately in development of the Notch stress approach [5], etc. Assessment of local stress causing the damage process allowed reducing the range of the design S-N curves to those presenting properties of the base and weld material only. However, apart from solving the problem of effects of geometry of structural detail on the damage process, the mentioned above disadvantages were not corrected. The above criteria and approaches are commented in more details in the below focused on problems of practical application and certain remedial actions are proposed.

3 Stress-Life Approaches

The current S-N (Stress-Life) approaches to fatigue analysis and design of structures, e.g., [6], are based on assumption that material of structure nominally deforms elastically in service loading conditions. Respectively, in the range of fatigue lives between $10^4 \leq N(S) \leq (2 \ldots 5)10^6$ (the left-hand figure is related to the above statement, and the right-hand one corresponds to the long-established practice of assessment the fatigue limit stress in mechanical engineering) the **S-N** curve is usually approximated in logarithmic coordinates by the straight line, equation if which is given by the BasquinŸs formula (1910):

$$N(S) = C/S^m, \tag{1}$$

where S is the stress range, C and m are the кmaterial constantsњ, m is the S-N curve кslope parameterњ. The range of endurances of the design S-N curves is limited from the left side, as said, by the number of cycles prior to failure equal to , which approximately corresponds to the nominal stress amplitude around the yield stress.

Damaging effects of stress amplitudes below the conventional fatigue limit stress in service irregular loading histories is considered by the кtwo-slopeњ shape of S-N curves and by introducing the кcut-offњ fatigue limit stress, substantially lower than the conventional one, fig. 1 [6].

The mechanics of fatigue damage of welded joint materials is implied (not definitely specified) as built into the design S-N curves based on analysis of results of fatigue testing of specimens comprising the typified (classed) welded joints, e.g., shown in fig. 2.

The base and weld material mechanical properties are not specified, and the S-N curves uniquely represent fatigue properties of a range of structural steels supporting the so-called кNominal stress approachњ, as shown in fig. 1, whereas it is known that fatigue strength of steels is approximately proportional to the ultimate strength [7], although resistance of welded joints may depend substantially on the mechanical properties of the electrode material. The scheme of evaluation of the nominal stress in example of a bracket welded to the flange of stiffener in ship structure (fig. 2) is shown in fig. 3.

Specific of the testing specimensŸ procedure is automated termination of test when initiated and growing fatigue crack notably affects the specimen compliance preced-

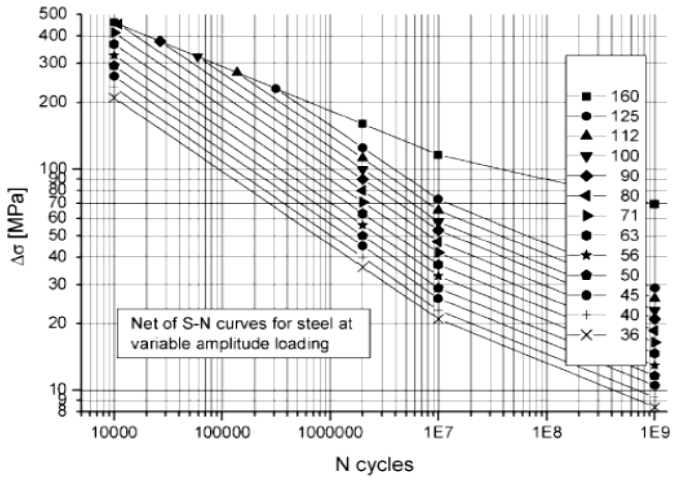

Figure 1: IIW classed design S-N curves for structural steels [6]

ing complete fracture in two parts. Therefore, the test result, the number of cycles by the test completion includes, roughly, a portion of life until the macroscopic crack origination and a part when crack propagates from the origination site. Respectively, when the approach is applied to assess fatigue resistance of a structural detail, the state of damage, corresponding crack size, occurs uncertain what attracted attention of experts (e.g., [5, 8, 9]). Fig. 2 shows a specimen with typified welded joint (one-side attachment) and a structural detail (in ship bottom structure) attributed to the same type of the joint. It may be seen a resemblance but not the identity between the specimen and detail, especially when the geometry and the crack extension particulars would be mentioned. Attempts were made to develop procedures which might have assisted in establishing the fatigue identity of welded joints in structural detail and respective test pieces and design S-N curves [8, 9]; however, the suggested procedures were substituted by implementing other approaches.

What is important, fatigue tests of typified welded joins at cyclic loading were being carried up with positive load ratio (ratio of the minimum to the maximum load in the cycle) to avoid buckling in the compressive part of the load cycle. This means the design S-N curves are related to the mentioned type of loading. Lately, attempts were made to consider in fatigue analysis of structural details effects of different loading conditions [10]. Meanwhile, loading asymmetry plays secondary role in the crack initiation phase which is controlled almost completely by the stress ranges, excursions causing slip processes in material microstructure [7, 12], etc. When the crack is initiated its further extensions substantially depend on the tensile part of alternating loading. Respectively, since a substantial portion of fatigue life of specimens represents the crack growth, it introduces additional uncertainty into the results of fatigue analysis of structural details.

The briefly mentioned disadvantages of the Nominal stress approach promoted development and application in practice of the Hot-spot stress (HSS) [1, 2], etc., and latterly, of the Notch-stress approach (NSA) [5], etc. These approaches are supported by respective Stress-life criteria, addressed to avoiding ambiguity in establishing the identity between classed welded joints and actual structural details, and providing considering effects of stress concentration in structural details by the finite-element

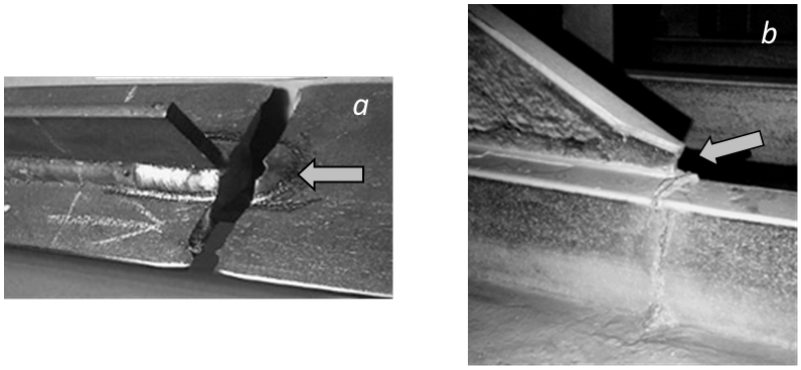

Figure 2: a) - Fractured specimen, FAT63 Class (Fig.1); b) - Crack in a ship structural detail identified as FAT63 (Courtesy B.Purtle, LloydŸs Register of Shipping, UK)

analysis. With regard to the principles of the HSS and the NS approaches the set of design S-N curves is reduced to those of the base material and material of welded joint (butt-welded joint), completed with the design curves for details in corrosive environment [10].

In HSS approach the stress at a critical location, typically at the weld toe, as show arrows in Fig.2, has to be found by extrapolating stress in element centroids towards the weld toe, fig. 3; by this the stress raise is assumed caused by the shape of structural detail and the role of the weld bead geometry is related to properties of the respective S-N curve (class D curve, butt-welded joint). Substantially fine meshing of the welded detail model in the NS approach allows obtaining local stress at the weld toe considering, both, effects of the detail and the weld bead geometry, as schematically shown in Fig.3; at the same time it is assumed that at the weld toe there is a smooth, radiused, transition from the parent to the weld material [5]. Such assumption is based on physics of liquid metal contact with the solid where meniscus appears.

So far, effects of stress concentration in critical locations of structure in the HSS and NS approaches are considered by multiplying the nominal stress range by the respective stress concentration factors or calculation local stress using, as said, the finite-element technique.

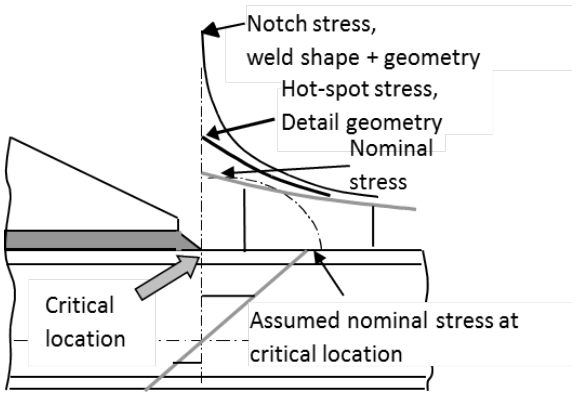

Figure 3: Assessment of characteristic stress for fatigue analysis of structural details

Fig. 4shows the types of meshing of the bracket ending in ship structure (fig. 2,b, fig. 3) designed for application of the mentioned approaches. The mesh type in fig. 4,a is attributed to the Hot-spot stress approach; its design follows the principle кt x tњ, t is the flange thickness and the size of finite elements at the bracket ending [9]. Another mesh, fig. 4,b, fits the requirements of the FE modeling when the Notch-stress has to be applied: the element size at the weld toe is 0.2 of the assumed weld toe radius [5].
It should be emphasized that assessment of the local stress in these approaches is based on assumed linear elastic material behavior in critical locations. Referring further the characteristic stress to the classed S-N curve makes rather an illusion of proper assessment of damage.

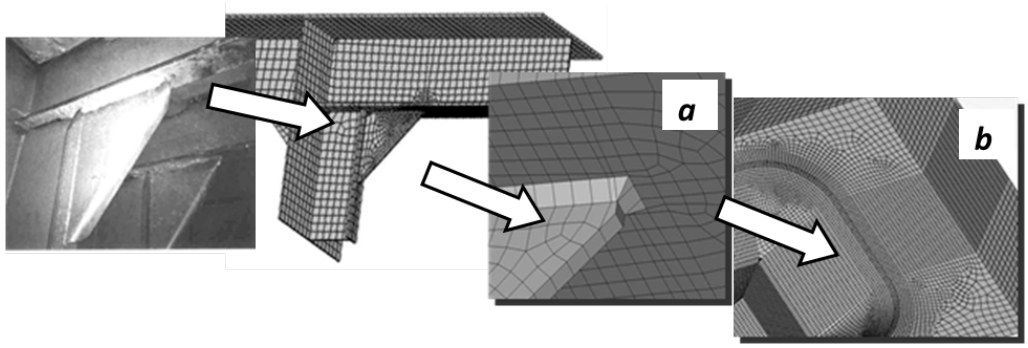

Figure 4: Structural detail and examples of FE meshes designed for application of the HSS (a) and the HSA (b) approaches [11]

In fact, it means evaluation of the damage with uncertainty, although somewhat on the conservative side. In the high-stress range of the service loading the input of this over-estimation of fatigue damage in the total sum might be regarded insignificant due to stochastic properties of excitation and relatively infrequent intensive loading of structures. Whereas at the moderate service loading, in the high-cycle regime, which provides the predominant damage, the above approaches neglecting the effects of material microplasticity at critical locations, may substantially over-estimate the damage.
Comparative analysis of fatigue properties of ship structural detail shown in fig. 4, кPost-Libertyњ dry cargo ship, non-specified wave climate, upper deck structure amidships [11], resulted in substantially differing values of fatigue damage related to 20 years of ship service: application of the HSS approach indicated D = 1.24, whereas the Notch-stress approach use shown the damage index as D = 0.54, and the Strain-life approach, where the inelastic behavior of material was accounted for, resulted in D = 0.35. The mentioned comparative study just illustrates the problem; perhaps, a comprehensive analysis might be needed. However, firstly, the apparent disadvantages of the current Stress-life methodologies should be corrected. First, the Hot-spot stress approach barely might be improved: the prospects of perfection of the technique of evaluation the hot-spot stress are not seen, receipts for design the FE model of welded detail barely allow for considering material inelastic behavior, the crack size, residual welding stress is accounted for fairly approximate.
The feasible means of improvement of the approaches and S-N criteria might be

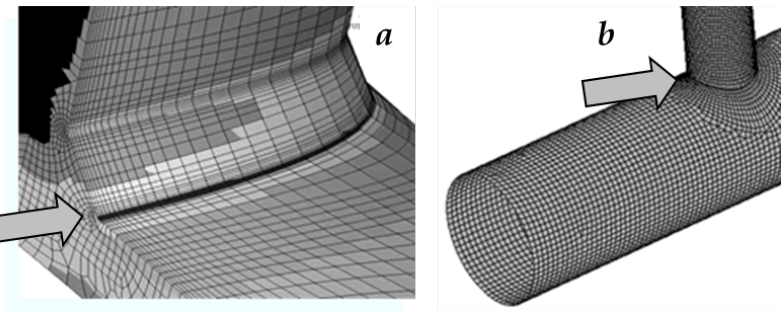

Figure 5: FE-models of tubular welded joints: a) Ц model developed for fatigue analysis with Strain-life approach [13]; b) Ц model of the joint for the HSS aided analysis [15]. Arrows indicate the critical locations

focused mostly on the Notch stress approach and be the following:

- In formulation of the S-N criteria fatigue testing of specimens has to be carried out until origination of macroscopic crack. It would need in application of the well developed methods and technique of crack detection and in respective improvement of the test procedure,
- Fatigue testing reasonably should be carried out at symmetrical loading, so that when necessary effects of mean stress on the damage might be reasonably accounted for,
- Approximate considering the inelastic cyclic behavior of the critical location material by correction of the local stress with the means of the notch factor value, e.g., formulated by Peterson [14]:

$$K_f = 1 + (K_t - 1)/(1 + g/r), \tag{2}$$

- where K_t is the theoretical stress concentration factor, g is "material structure" parameter, according to [14], this parameter for structural steels with the yield strength in the range of 235-390 MPa may be estimated by $g = 0.38(350/\sigma_u)$, where σ_u is the ultimate strength of material, r is the notch root radius,
- As to the effects of residual welding stress it may be assumed part stress relaxation at the very crack initiation phase due to the cyclic plasticity of material accentuated at the critical location.

The Notch stress approach may be completed by the procedure of evaluation of the crack initiation and extensions by further development of the damage accumulation principle suggested in [13, 16, 17], etc., complemented by designing the finite-element models of structural components with the necessary fineness of the mesh at critical locations and in the plane of expected crack growth, e.g. as shown in fig. 5,a. Material (finite) elements should be deigned small enough to neglect the stress and strain gradients through the element, but large enough to apply the continuum mechanics format.

Let the number of load cycles corresponding to crack initiation in themost stressed elements along the notch root (weld root as in fig. 4,b, 5,a) is ; then damage accumulated at this step in the surrounding elements:

$$d_{initial} = N_0/N_i \tag{3}$$

So far, $n_i = N_0$ is the initial part of the кfatigue processнь, N_i is the number of load cycles to failure in the successive stress range conditions, in every consecutive кmaterial elementнь where stress range prevailed the non-damaging level (cut-off fatigue limit stress) in the initial and sequential loadings, which develop due to кfailureнь of elements. The кfailureнь is defined by the condition:

$$d = d_{initial} + \sum(n_i/N_i) = 1 \tag{4}$$

Here $n_i = n_i(S_i)$ is the number of load cycles corresponding the stress range S_i, which completes the damage accumulation in a particular FE (кmaterial elementнь), d, at every кcrack extensionнь. - As said in above, effects of residual welding stress may be insignificant in the crack initiation phase and neglected; however, in analysis of the crack extensions the residual stress influence cannot be ignored and should be considered in dependence on the redundancy of structure.
I should be noted, the procedure would need in rearrangement of the mesh (automated procedure is presently provided by the FE software) and stress field assessment at every crack extension through successive finite elements (кmaterial elementsнь).
The approach would make feasible fatigue analysis of the damage process commencing from initiation of service loading through the crack initiation at a structural discontinuity and growth until onset of a critical condition, e.g., until the through crack in a pipe line (e.g., [13, 16], etc.).
What may be regarded promising, the damage accumulation model may be complemented by the crack growth model given by the Linear fracture mechanics (LFM) principles, e.g. [18], which would allow for predicting conditions for the instable fracture of a structural component. The approach was successfully tested in several examples where the crack extensions in fillet-welded joint were simulated [16], in analyses of crack growth in test specimens [17]; results of numerical simulation were in good agreement with the test data.

4 Conclusions

The Stress-Life (S-N) criteria applied in the Nominal stress approach, Hot-spot stress and Notch-stress approach provide assessment of fatigue properties of structures accompanied with a series of approximations and uncertainties. The most substantial drawbacks of the S-N criteria-based techniques of fatigue analysis are the problems of identity of damage between classed specimens and actual structures, considering effects of stress concentration in structural details, uncertainty of the crack size corresponding completion of estimated fatigue life of a structural component, etc. Several means of improvement of the Notch-stress approach and respective S-N criteria are suggested proved by results of a series of studies.

Acknowledgements

The report was prepared within the program supported by the Russian Fund for Fundamental Research (Grant 16-08-0845a)

References

[1] Paetzold, H., Fricke, W., Petershagen, H. Fatigue Assessment of Welded Ship Structures based on Hot-Spot Stresses. Seminar on Fatigue of Welded Structures. IPME RAS, St Petersburg, 25-27 Sept. 1992

[2] Niemi E., Fricke W., Maddox S.J. Structural Hot-spot Stress Approach to Fatigue Analysis of Welded Components. DesignersЎ Guide. Int. Institute of Welding, IIWЦIDoc. XIIIЦIWG3Ц31r1Ц14 Cambridge. Abington. 2015. P.49

[3] Marshall, P.W. Basic Considerations for Tubular Joint Design in Offshore Construction. WRC Bulletin 193. 1974. New York

[4] Haibach, E. Die Schwingfestigkeit von Schweib Verbindungen aus der Sicht einer Ortlichen Beanspruchungsmessung. Laboratorium fur Betriebsfestigkeit (LBF), Darmstadt, Report FB-77, 1968 (in German)

[5] Fricke, W. Guideline for the Fatigue Assessment by Notch Stress Analysis for Welded Structures, IIW-Doc. XIII-2240r1-08/XV-1289r1-08 Cambridge. Abington. 2008.

[6] EUROCODE 3: Design of Steel Structures. Part 1-9: Fatigue. BS EN 1993-1-9: 2009. P. 36

[7] Frost, N.E., Marsh, K.J., Pook, L.P. Metal Fatigue. Clarendon Press, Oxford. 1974

[8] Petinov, S.V., Thayamballi, A.K. The Application of S-N Curves Considering Mismatch of Stress Concentration between Test Specimen and Structure. Journal of Ship Research, Vol.42, No.1, 1998, p.68

[9] Petinov, S.V., Reemsnyder, H.S. and Thayamballi, A.K. The Similitude of Fatigue Damage Principle: Application in S-N Curves-based Fatigue Design. In: Fatigue Design and Reliability/ Ed. By G.Marquis and J.Solin. ESIS Publication 23. Elsevier Science Ltd., 1999, pp.219-228

[10] Det Norske Veritas. Fatigue Assessment of Ship Structures. Classification Notes є 30.7. 2010. Hovik, Norway

[11] Petinov, S.V., Afanasyeva, I.M. Fatigue Assessment of Structures in High-cycle Segment: Technique and Problems. Proc., The XXXVII Intern. Summer School - Conference кAdvanced Problems in Mechanicsњ APM-2010, SPb-Repino, 2010. pp. 519-525

[12] Petinov S.V. Fatigue Analysis of Ship Structures. Backbone Publishing, NJ. 2003. P. 262

[13] Petinov, S.V., Guchinsky, R.V. Fatigue Assessment of Tubular Structures // Magazine of Civil Engineering (Инженерно-строительный журнал) No1 (36), 2013, pp. 39 Ц 47. ISSN 2071-4726

[14] Peterson, RE Stress Concentration Factors. A Handbook. J.Wiley and Sons, New York. 1977, p.301

[15] Conti, F., Verney, L., Bignonnet. A. Fatigue assessment of tubular welded connections with the structural stress approach, кFatigue Design 2009нь. 25-26 November 2009. Senlis, France, pp.1-8

[16] Petinov, S.V., Guchinsky, R.V. Fatigue of a Fillet-welded Joint Assessment by the FEA Simulation of Damage Accumulation // Magazine of Civil Engineering (Инженерно-строительный журнал) No 4 (22), 2011, pp.5-9 ISSN 2071-4726

[17] Imran, M., Siddique, S., Guchinsky, R.V., Petinov, S.V. and Walther, F. Comparison of fatigue life assessment by analytical, experimental and damage accumulation modeling approach for steel SAE 1045. Fatigue and Fracture of Engineering Materials and Structures, 2016, pp.1-29.

[18] Guchinsky, R.V., Letova, T.I., Petinov, S.V. Modeling of Fatigue Process by Combining the Crack Initiation and Growth / Proc., The XLII Intern. Summer School - Conference кAdvanced Problems in Mechanicsнь APM-2014, SPb-Repino, SPb, IPME RAS, 2014, pp.128-134.

Sergey V. Petinov, SPbSPU, Politechnicheskaya 29; 195251, St. Petersburg, Russia
Boris E. Melnikov, SPbSPU, Politechnicheskaya 29; 195251, St. Petersburg, Russia

The structure of the interelectrode layers in low-conductive liquid flows in microchannels with a ion source affected by an applied field

Vitaly A. Polyanskiy, Irina L. Pankratyeva

ilpan@imec.msu.ru

Abstract

The interest in electrohydrodynamics of flows in micro- and nano-size channels, which has been observed in recent years in the literature, is caused by the need to manage the motion of ultrasmall portions of fluids in various devices employed in biological research, biotechnology, pharmacy, medicine, and other areas of science. This work is focused on the study of the influence of strong non-uniform electric fields on the ionization processes in partially ionized liquid mixtures as they flow through plane microchannels. The effects caused by the action of a non-uniform field on the bulk electrochemical kinetics in low-conductive liquids at moderate values of the Debye number are analyzed. In weakly conducting chemically reacting environments the applied electric field can affect the ionization process both indirectly, through redistribution of reactive charged components, and directly, by means of increasing the kinetic rate of ionization. In the last case, in the near-wall layers with a strong non-uniformity of the field, bipolar structures of uncompensated space charge are formed, which can be affected by the applied longitudinal field. The presence of the layers with the opposite Coulomb forces brings about inflection points in the velocity profile. This may cause instability of the flow and thereby induce the mixing of the liquid in the microchannel.

1 Description of the fluid model

We consider a two-dimensional nonstationary flow of a multicomponent liquid containing charged particles of two kinds: positively and negatively charged. Diffusion and drift of the particles of each kind of charge in the electric field, bulk reactions of ionization and recombination, and surface electrochemical processes that cause generation and absorption of charged particles are taken into account. The motion of the liquid as a whole is described by the conventional equations of conservation of momentum for viscous medium with due regard for the bulk Coulomb force, and the continuity equation for an incompressible fluid. The laws of conservation of mass

for the charged components and Poisson's equations for the field have the form [1]:

$$\begin{aligned} &\frac{\partial n_i}{\partial t} + \operatorname{div} n_i\vec{U}_i = w(E) - an_1n_2, \quad i = 1, 2, \\ &n_i\vec{U}_i = n_i\vec{u} + \operatorname{sign}(e_i)n_ib_i\vec{E} - D_i\nabla n_i, \quad e_1 > 0,\ e_2 < 0, \\ &\varepsilon \operatorname{div}\vec{E} = 4\pi q, \quad \vec{E} = -\nabla F. \end{aligned} \tag{1}$$

The boundary conditions for Equations (1) represent the balance between the ion fluxes from the bulk to the surface and the fluxes of the particles generated at the surface [2]:

$$n_i\vec{U}_i \cdot \vec{v} = A_i^k(E, n_m, \ldots) - K_i^k n_i. \tag{2}$$

Here v is the external normal to the interface, A_i^k, K_i^k are the effective parameters of the surface electrochemical processes, which depend on the properties of the kth surface of the channel walls, liquid content, etc. In formulae (1), (2) the quantities $\vec{u}$, n_i, U_i, D_i, b_i, e_i, q, E, F are, respectively, the velocity of the liquid as a whole, concentration, velocity, coefficients of diffusion and mobility, and the charge of the particles of ith kind, the volume charge density, the strength and the potential of the electric field, ε is the dielectric permeability, w is the bulk ionization rate (the rate of dissociation of the neutral molecules of the liquid into positive and negative ions), which may depend on the field strength, and a is the coefficient of the bulk recombination of ions.

2 Results

Let us consider the results of the calculation of a steady flow through a plane channel under the conditions that an electrical potential difference is applied to the channel walls from an external source and the channel walls exhibit different surface characteristics. Suppose that at one of the walls the surface reaction for the positive ions n_1 is in equilibrium with the corresponding value of their concentration, and for the negative ions n_2 this wall is chemically neutral (zero flux of this kind of ions to the wall). The potential of this wall (anode) is positive. The situation at the other wall is supposed to be the opposite: the equilibrium for the negative ions (for the sake of simplicity, with the same value of the equilibrium concentration), and zero flux of the positive ions to the wall. The potential of this wall (cathode) is equal to zero. The dependence of the bulk source of ions on the applied field was studied in [3], [4]. In the calculations presented in this work we use Frenkel's relation [3] (w_o is the rate of dissociation in the absence of the applied field):

$$w(E) = w_0(T, \ldots)\exp(2\gamma E^{0.5}), \quad \gamma = e^{1.5}/(\varepsilon^{0.5}kT). \tag{3}$$

Note that one of the first works devoted to the study of electrohydrodynamic flows through channels with regard to the effect caused by the applied field on the rate of the bulk dissociation within the framework of Onsager's model [4] was carried out by professor Antonio Castellanos [5].

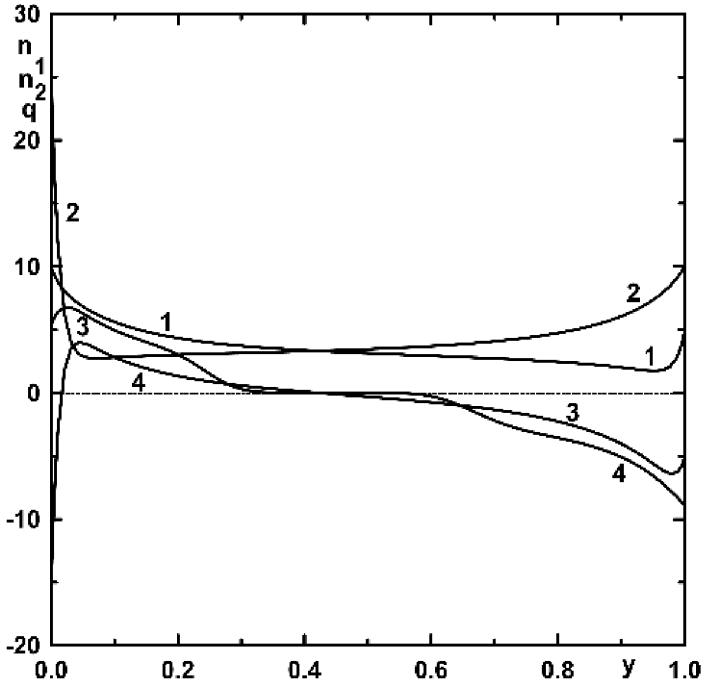

Figure 1: Distribution of the concentrations of ions n_1 (curve 1) and n_2 (curve 2), and density of the volume charge q with (curve 4) and without regard for the field dependence of the ionization rate ($\gamma = 0$, curve 3) in the channel cross-section.

The distributions of the dimensionless concentrations of ions n_1, n_2 and the space charge q in the cross-section of the channel for a given difference of the potentials between the walls are presented in Fig. 1. The concentrations are divided by the initial quasineutral concentration of ions, the coordinate is normalized by the channel width. The values of the equilibrium concentrations of ions specified in the calculations are presented in the figure.

It is seen that even in the case of a plane channel, when the applied uniform field is not distorted by the geometry and is constant across the channel, the presence of a field-dependent source of ions essentially changes the distribution of the space charge near the electrodes. In particular, in the vicinity of the anode ($y = 0$) a bipolar structure arises: the negatively charged near-wall layer is replaced with a layer of positive charge. This is due to the fact that the additional source of ions that arises in a strongly nonuniform field appreciably alters the distribution of their concentrations in the near-wall layers. The distribution of the dimensionless field and potential across the channel is presented in Fig. 2. The field and the potential are divided by the thermal potential and the corresponding field. It is seen that at moderate values of the Debye number, when the Debye length has the order of the characteristic size of the channel, the charged layers occupy a sufficiently large part of the channel cross-section and significantly alter the applied field. In particular, as the volume charge changes its sign in the bipolar layer near the anode, a local

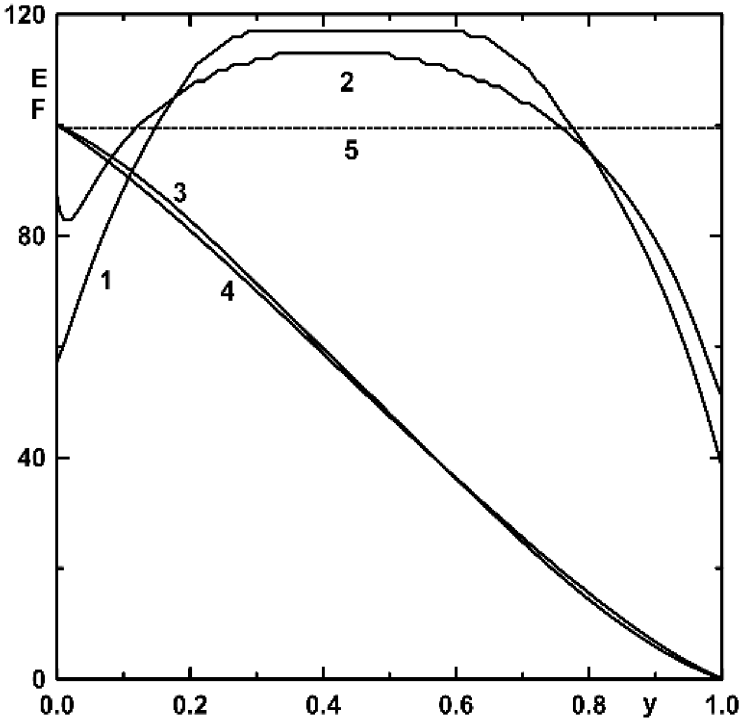

Figure 2: Distribution of the normal components of the field strength E (curves 1, 2) and potential F (curves 3, 4) in the channel cross-section. Curves 2, 4 — with regard for the field dependence of the ionizsation rate, curves 1, 3 — without regard ($\gamma = 0$). Curve 5 shows the applied external field.

extremum of the field strength occurs. Note that a local extremum of the field strength near the surface of the plane electrode caused by the bipolar structure of the near-wall layer was experimentally observed in [6]. In paper [7] in the framework of the tree-ion model a mechanism for the formation of the near-electrode bipolar layer with the field extremum was proposed. The key role was played by the bulk recombination processes which involve the ions injected by the wall. The effect caused by the field on the rate of ionization was disregarded. The results of this work suggest that the formation of the bipolar near-electrode structures may be governed by another mechanism.

Figure 3 shows the distribution of the bulk Coulomb forces $FK = qE$ affecting the fluid in the applied transverse field. It is seen that in most part of the charged domains the field repels the fluid from the walls. Such a configuration of forces directed towards each other is favourable for the rise of an instability analogous to the Rayleigh–Bénard thermogravitational instability in conventional hydrodynamics [8]. The fact that the bulk source depends on the field aggravates the matter.

As is shown in Fig. 1, under nonsymmetric boundary conditions for the ion concentrations, in the channel cross-section domains with positive and negative space charge are formed, which are adjacent to different walls. If an external electric field is applied along the channel, then the arising longitudinal component of the Coulomb

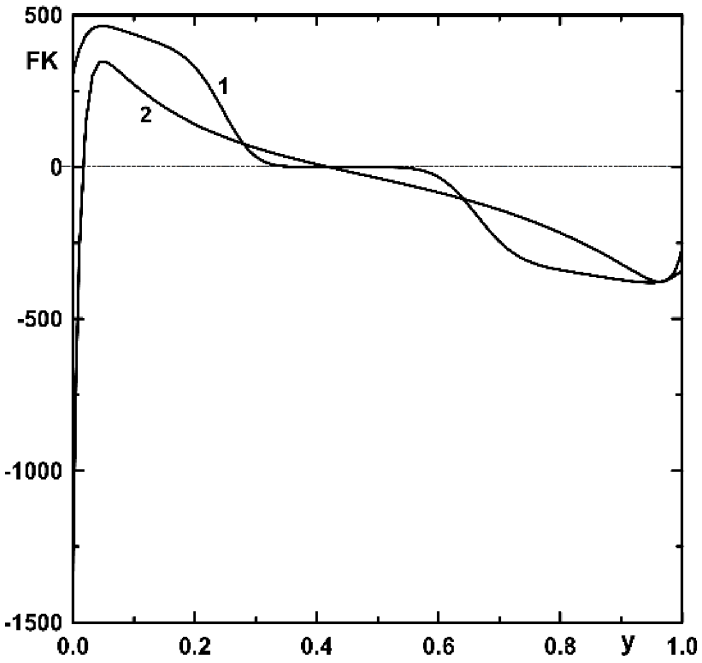

Figure 3: Distribution of the normal component of the Coulomb force $FK = qE$ affecting the fluid. Curve 2 — with regard for the field dependence of the ionization rate, curve 1 — without regard ($\gamma = 0$).

force is directed in the opposite ways near the opposite channel walls, thereby speeding up and slowing down the flow of the fluid. Figure 4 shows the cross profiles of the fluid velocity calculated with and without regard for these forces.

It is seen that in the domain of the negative space charge the Coulomb force, which slows down the flow, gives rise to a thin layer of the return flow and causes the appearance of inflection points in the velocity profile. This may cause the Kelvin–Helmholtz shear instability of the flow and thereby enhance the mixing of the fuild in the channel [8].

3 Conclusions

The study of the structure of the interelectrode space in a plane channel shows that the direct effect caused by the field on the rate of dissociation of the molecules of the fluid into positive and negative ions can significantly redistribute the concentration of these particles in the domains of the strong nonuniform field in the near-wall layers of the plane channel. If the channel walls have different surface electrochemical properties, then the external electric field applied along the channel may cause vigorous mixing of the fluid that flows along the micro-channel.

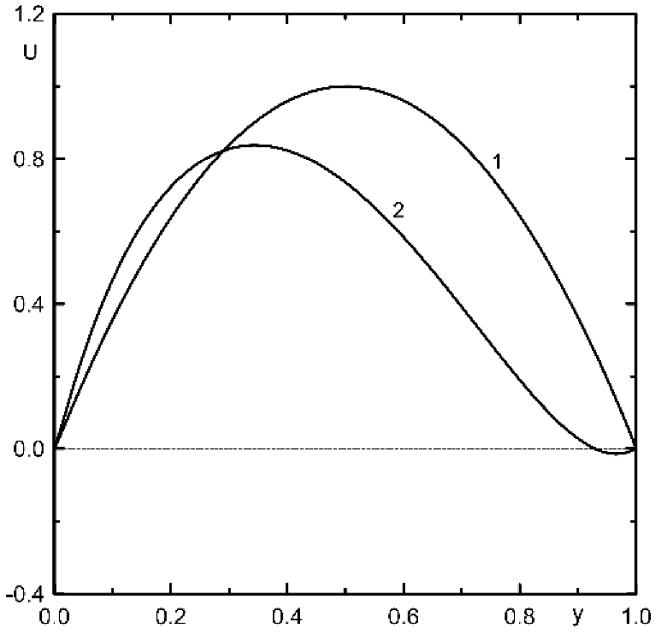

Figure 4: Velocity profiles of the liquid flow in the channel: the Poiseuille profile (curve 1) and the profile that has been transformed under the action of the longitudinal Coulomb forces in the applied longitudinal field (curve 2).

Acknowledgements

This work was supported by the Russian Foundation for Basic Research, project no. 16-01-00157.

References

[1] I. L. Pankrat'eva, V. A. Polyanskii, Modeling electrohydrodynamic flows in slightly conductive liquids , Journal of applied mechanics and technical physics, 36:4 (1995), 513–519; Translated from Prikladnaya Mekhanika i Tekhnicheskaya Fizika, 36:4 (July–August 1995), 36–44.

[2] V.V. Gogosov, K.V. Polyansky, V.A. Polyansky, G.A. Shaposhnikova, A.A. Vartanyan, Modeling of nonstationary processes in channels of EHD pump , Journal of Electrostatics, 34:2–3 (1995), 245–262.

[3] Ya. N. Frenkel, On the theory of electric breakdown in dielectrics and electronic semiconductors , Technical Physics of the USSR, 5:9 (1938), 685–695; Translated from Journal of Experimental and Theoretical Physics, 2:9 (1938), 1292–1301.

[4] L. Onsager, Deviations from Ohm's Law in Weak Electrolytes , The Journal of Chemical Physics, 2:9 (1934), 599–615.

[5] F. Pontiga, A. Castellanos, The effect of field-enhanced injection and dissociation on the conduction of highly-insulating liquids , IEEE Transactions on Dielectrics and Electrical Insulation, 3:6 (1996), 792–799.

[6] Yu. M. Rychkov, Yu. K. Stishkov, Electric field strength and space charge in technical liquid dielectrics , Colloid Journal, 41 (1978), 1204–1206; Translated from Kolloidnyi Zhurnal, 40:6 (1978), 1204–1206.

[7] V. A. Polyansky, I. L. Pankratieva, Multilayer Charged Structures in Nonpolar Dielectric Liquids , Journal of Colloid and Interface Science, 230:2 (2000), 306–311.

[8] I. L. Pankrat'eva, V. A. Polyanskii, Investigation of the mechanisms of the onset of instability in weakly conduction media in electric fields , Fluid Dyn., 50:6 (2015), 769–774; Translated from Izvestiya Rossiiskoi Akademii Nauk, Mekhanika Zhidkosti i Gaza, 50:6 (2015), 63–70.

Vitaly A. Polyanskiy, Lomonosov Moscow State University, Moscow, Russia
Irina L. Pankratyeva, Lomonosov Moscow State University, Moscow, Russia

Effects of dispersion and delay in mathematical models

Evelina V. Prozorova

e.prozorova@spbu.ru

Abstract

Analysis of the mathematical models that can write the influence of the angular momentum and delay in mechanics is suggested: under interaction of many particles, in continuous mechanics, in kinetic theory. Disturber of the ergotic is discussed for the classic equations of continuous environment. The new method of calculation pressure and energy for multicomponent environment was suggested. Non-symmetrical stress tensor is obtained as results of influence of angular momentum for continuous medium. The method for writing of interaction discretion and continuous mediums was suggested. Attention pays on delay for processes discrete mediums. Analytical results are obtained for cases of large gradient. The nucleus of the Navier-Stokes equations is obtained. Equations S.V. Vsallander were received from the kinetic equation.

Key words: Angular momentum, delay, conservation laws, non-symmetrical stress tensor, Boltzmann equations, Chapman-Enskog method, conjugate problem Navie-Stokes equations, equations S.V. Vsallander.

1 Introduction

An important area of current research is to study the effect of the angular momentum and the delay in the whole mechanics including quantum mechanics. The process is changing so it associated with the appearance of additional forces, which can play the role. These effects may affect at critical and near critical aircraft modes, rockets, various devices, building structures, as well as some natural processes. The value of the additional force is determined by the gradient of the value of physical quantities (density, velocity, momentum) and the structure of the object being studied. In the case of the dynamic formation of the structure, the position of the center of mass is changing, which entails a change of angular momentum of a small perturbation that affects the stability of the structure. In the static case, the angular momentum occurs at non-uniform distribution of parameters. For elementary volume is important that volume is rotated about its center of mass, and the involvement of volume in larger rotation. The definition of the velocity of divergence and the vortex velocity how the of decomposition with respect to an arbitrary point inside the elementary

volume is incorrect, as vortex part is the component of the velocity relative to the axis of inertia of the elementary volume. The mechanics is considering the Lagrange function for non-interacting and collectively interacting particles equally but this is questionable, especially in metallic and ionic bonds. In classical continuum mechanics had an opinion on the small contribution of the angular momentum force against surface forces, as their action has a volume character. In the classical mechanics of a continuous medium, there was an opinion about the small influence of the angular momentum with respect to the contribution of surface forces, since their action is of a bulk nature.

For long bodies and large gradients parameters contribution is significant and can be a cause of instability, leading to changes in the flow structure or destruction of the body. The second important effect-delay [1,2]. Delay in mechanics plays an important role under the relaxation in the case of the commensurability the time of relaxation and delay times. The new proposed option is to consider accounting delay between the time derivative as a limit and final value free path in a rarefied gas and time between collisions. This situation is typical for transition from discrete to continuous environment and is a key issue of mechanics and computational mathematics. For particles without structure is usually considered central of the interaction, i.e. variant, where the momentum cannot play a role in conditions close to equilibrium. For the remaining cases semi-empirical theory is included. In the classical approach, the law of conservation of angular momentum is not constructed. In view of these formulations actually postulated symmetry of any material system of reference and as a result, the symmetry of the angular momentum, the symmetry of the stress tensor and the violation of "continuity" of the medium, while for arbitrary perturbations of the motion of a material point is a non-inertial.

Selecting the conditions of equilibrium of momentums of forces leads to new formulations of equations [3-5]. Therefore, subject to the balance of power we come to a private classical formulation of continuum mechanics. The resulting formulation of conservation laws associates with the recording of the conservation laws for a system that is exchanging the components of physical quantities only by normal convection rate and ignoring all processes within an elementary volume, and the lack of rotation of the volume. Determination of physical quantities in the form of a sum of delta functions and terms of integrals by volume that tends to zero, leads to the same equations. This confirms what we said. Everything that is happening in the volume and with the volume are not considered. This has led to an incomplete accounting of the processes. The accumulated experimental facts led to the hypothesis of the importance of spatial gradients and time derivatives, which also contributed to the change of the momentum. The importance of these effects observed for fluid mechanics and gas plasma, and for the solid. It should be noted that in the kinetic theory (Boltzmann equation), the law of conservation of angular momentum is not executed. The existing representation likely linked to the consideration of an elementary volume as the closed. The effect of the angular momentum of the motion at the equations of the continuum mechanics in [7-9] was studied. The proposed theoretical method of accounting the angular momentum without new empirical constants equations, bases on the fact that in the angular momentum do not have new dimension. Another method was proposed in [10].

The order of given equations and boundary conditions requires a revision. The total consideration of the effects leads to a cumbersome system of equations, and therefore requires the allocation of the major effects in a particular situation. Examples were given showing the contribution of the no symmetric part of the stress tensor in the simplest problems of elasticity theory and boundary layer. Conclusion modified equations for gas based on the kinetic theory, for which it was suggested that the angular momentum need be included as an additional variable; to use a more precise asymptotic approach to Hilbert's paradox. As already mentioned, the elementary volume can itself rotate around the axis of inertia, or to be involved in a rotary motion. In both cases, the density of the flow across the border is changed to the $value\frac{d(\rho u)}{dr}\cdot(r'-r)+\cdots$ in rotation of the elementary volume. The contribution of other components is small, taking into consideration a little volume and the absence of rotation at the axis. In our opinion there is an inaccuracy in the calculation of the Lagrangian function as a sum mutually interacting particles. The position axis of inertia under equilibrium conditions and non-equilibrium conditions are different, and that leads to the existence of collective effects. Interestingly, the effects of the influence of the angular momentum and changing the position of the center of mass can be important in quantum mechanics when considering the particles decay into three or more particles; when writing potential in the Schrodinger equation.
As is known, the equation for the macro parameters can be derived from the Boltzmann equation by the Chapman-Enskog [11-15] method. We give qualitative and quantitative assessment of the impact of using a classic method of the Chapman-Enskog method of the calculation of local-equilibrium distribution function of the macro parameters (density, velocity and temperature), calculated from the zero approximation (of the Euler equations), without correction results using Navier-Stokes equations. The existence of the problem of coordination of macro parameters was pointed Gilbert on solution of the Boltzmann equation by a series expansion in the small parameter. We have proposed an algorithm for matching macro parameters locally equilibrium distribution function [3-5]. In the classical theory believe

$$\int\varphi(\xi)f^0d\xi=\int\varphi(\xi)fd\psi=\beta\ ,$$

п»„п»„п»„ β - macro parameters,

$$f\left(t,x,\xi\right)\equiv f_0\left(t,x,\xi\right)=n\left(\frac{m}{2\pi kT}\right)^{3/2}\exp\left\{-\frac{m}{2\pi kT}c^2\right\}\ ,$$

$$c^2=\left(c_1^2+c_2^2+c_3^2\right)=\left(\xi-u\right)^2\ ,$$

п»„ п»„п»„ п»„п»„п»„п»„п»„ п»„п»„п»„

$$f=f_0\left[1+\frac{p_{ij}m}{2pkT}c_ic_j-\frac{q_im}{pkT}c_i\left(1-\frac{mc^2}{5kT}\right)\right]$$

and the quantities are determined through the total distribution function
t - time, x_i - position, u_i - velocity, $\tilde{\nu}$ - viscosity, ρ - density, T- temperature, q - heat flux, P_{ij} - the tensor of viscous pressure, X - force. The Boltzmann equation is invariant with respect to the choice of macro parameters.

Consequently, the coincidence of Navier-Stokes equations and built equation has a formal character, order of approximation and the parameters in a locally equilibrium distribution function vary. Therefore, when constructing the first approximation in the Chapman-Enskog (Navier-Stokes equations), it seems necessary to clarify the values of density, velocity and temperature for matching orders of approximation. Therefore, in the equations of the first order terms will be responsible for clarification of macro parameters. Throw away they cannot be due to their definitions in the kinetic theory. However, after factoring formal kind of balance function does not change, but the macro parameters are responsible macro parameters Navier-Stokes equations. In the derivation of the first approximation in the Chapman-Enskog made implicitly significant approximation. Part of the terms discarded only after integration over the phase velocity, they differ in arbitrary locations. It does not take into account that in this case the integrals for $f\xi(\rho u)$ flow (ρu) and speed on the density of the product in the first approximation, differ from each other (analogue divergent and non-divergent difference schemes). In view of the difference obtained by the conservation equations S. V. Vallander [16, 17]. The paper summarizes the results of the study. For the multi-component gas and gas with rotational and vibrational degrees of freedom offered another form of calculation of the average values of pressure, temperature and energy. The effect of correlation of zero and first approximations of the Boltzmann equation for writing continuum mechanics equations.

2 Equations

The equations of motion, energy and angular momentum have been obtained earlier, but the use as force equilibrium condition does not require the calculation of the moment. Therefore, in the classical theory of equations conservation of angular momentum is not used explicitly. The modified equation

$$\frac{\partial \rho u_i}{\partial t} + \frac{\partial}{\partial x_i}\left(\rho u_j + P_{ij} + x_i \frac{\partial P_{ij}}{\partial x_i}\right) - \frac{X_i}{m}\rho = 0 \ .$$

$$\frac{\partial}{\partial t}\rho\left(\frac{3}{2}RT + \frac{1}{2}u^2\right) + \frac{\partial}{\partial x_i}\left[\rho u_j\left(\frac{3}{2}RT + u^2\right)\right] +$$

$$+\frac{\partial}{\partial x_i} x_i \frac{\partial}{\partial x_j}\left[\rho u_j\left(\frac{3}{2}RT + \frac{1}{2}u^2\right) + u_k P_{kj} + q_j\right] = 0$$

$$\frac{\partial \vec{r}}{\partial x} \times \vec{p_x} + \frac{\partial \vec{r}}{\partial y} \times \vec{p_y} + x_j \frac{\partial}{\partial x_j}\left(\vec{P_j}\right) = M_I$$

Where t - time, x, y, z - coordinates, ρ is the density, P_{ij} - stress tensor, u - velocity, q - heat flow, R - gas constant.

This equation is used to determine the degree of no symmetry of the stress tensor. The issue arose when writing the law of conservation of density. We will try to get it from the phenomenological principles. The modified equation for the density was obtained from the kinetic theory in the form of

$$\frac{\partial \rho}{\partial t} + \frac{\partial \rho u_i}{\partial x_i} + \frac{\partial}{\partial x_i}\left(x_i \frac{\partial \rho u_i}{\partial x_i}\right) = 0 \ ,$$

From Fig. we can see that velocity $u = \omega \times (r' - r)$ is the velocity with respect to the point M quasi solid movement around the axis r without forward speed. The point M may itself be in rotation around the axis of inertia. For elementary volume formula $u = \omega \times (r' - r)$ means that the rotation occurs around the axis of inertia, but the axis of rotation can lie outside the volume. Therefore, we obtain for elementary volume

$$\int_{(s)} \left(\nabla \rho u \left(r' - r_c\right)\right)_n ds = \int_{(s)} div \left(\nabla \rho u\right) \left(r' - r_c\right) dv \ .$$

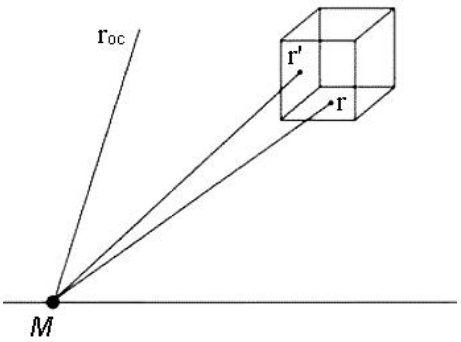

Figure 1: Elementary volume for the density

The degree of no symmetry of tensor derived from the law of conservation of momentum (in projections) ($\sigma = \tau$). Designations is standard.

$$y\left(\frac{\partial \sigma_{xz}}{\partial x} + \frac{\partial \sigma_{yz}}{\partial y} + \frac{\partial \sigma_{zz}}{\partial z}\right) - z\left(\frac{\partial \sigma_{xy}}{\partial x} + \frac{\partial \sigma_{yy}}{\partial y} + \frac{\partial \sigma_{zy}}{\partial z}\right) + \sigma_{zy} - \sigma_{yz} = 0 \ ,$$

$$x\left(\frac{\partial \sigma_{xz}}{\partial x} + \frac{\partial \sigma_{yz}}{\partial y} + \frac{\partial \sigma_{zz}}{\partial z}\right) - z\left(\frac{\partial \sigma_{xx}}{\partial x} + \frac{\partial \sigma_{yx}}{\partial y} + \frac{\partial \sigma_{zx}}{\partial z}\right) + \sigma_{zx} - \sigma_{xz} = 0 \ ,$$

$$x\left(\frac{\partial \sigma_{xy}}{\partial x} + \frac{\partial \sigma_{yy}}{\partial y} + \frac{\partial \sigma_{zy}}{\partial z}\right) - y\left(\frac{\partial \sigma_{xx}}{\partial x} + \frac{\partial \sigma_{yx}}{\partial y} + \frac{\partial \sigma_{zx}}{\partial z}\right) + \sigma_{yx} - \sigma_{xy} = 0 \ .$$

The procedure of calculation is to calculate the degree of no symmetry the stress tensor by the last equations and substitution of these values in the rest of the equations. The equation of state remain the same because as they are the higher-order corrections. Interestingly, some elasticity theory provisions lп»„ses force in case no symmetric stress tensor. For example, we have for two opposite sides of an elementary volume of its direction of principal stressestg $tg2\theta_1 = \frac{2\tau_{xy}}{\sigma_x - \sigma_y}$, $tg2\theta_2 = \frac{2\tau_{yx}}{\sigma_x - \sigma_y}$ and since $\tau_{xy} \neq \tau_{yx}$ we get different results. Thus, at each point we have main its direction of stresses.

3 Delay Effects

In the kinetic theory when considering the role of delay should deal with the question of what measures the experiment: the instantaneous values or averaged. If the

experiment was dealing with averages, it is important to choose the time and scope of averaging. At the agreed time, in this case to take into account the delay is not necessary, except in cases of commensurable of relaxation times and delay, otherwise it is necessary to bear in mind the following:
The mean free path of molecules of the i-th group relative to the molecules of the j-th group is equal in classical mechanics

$$\lambda_{ij} = \frac{\xi_i}{\sigma_{ij} n_j g_{ij}} \ .$$

The mean free path of molecules

$$\overline{\lambda} = \frac{\sum_i^k \xi_i n_i}{\frac{1}{2}\sum_{i,j=1}^k \sigma_{ij} n_i n_j g_{ij}} \ .$$

The mean velocity of molecules

$$\overline{g} = \frac{1}{2n^2} \sum_{i,j=1}^{k} n_i n_j g_{ij} \ .$$

The mean time

$$\overline{\tau} = \frac{\overline{\lambda}}{\overline{g}} \ .$$

Taking this into account, the Boltzmann equation can be written in the form

$$\frac{df}{dt} = \frac{\partial f}{\partial t} + c_i \cdot \frac{\partial f}{\partial r_i} + c_i \cdot \frac{\partial}{\partial r_i} r_i \frac{\partial f}{\partial r_i} - \frac{F}{m}\frac{\partial f}{\partial c_i} = I$$

$$\frac{df}{dt} = \frac{\partial f}{\partial t} + \overline{\tau}\frac{\partial^2 f}{\partial^2 t} + c_i \cdot \frac{\partial f}{\partial r_i} + c_i \cdot \frac{\partial}{\partial r_i} r_j \frac{\partial f}{\partial r_j} - \frac{F}{m}\frac{\partial f}{\partial c_i} = I'$$

$$\Delta^- = dt\ d\vec{x}\ \ d\vec{\xi}\ f\left(t, \vec{x}, \vec{\xi}\right) \int \left[f_1\left(t, \vec{x}, \vec{\xi}\right) + O\left(\Delta t\ \vec{\xi}\ \frac{\partial f_1}{\partial x}\right)\right] gb\ db\ d\epsilon\ d\vec{\xi}_1$$

$$\Delta^+ = dt\ d\vec{x}\ \ d\vec{\xi'} \int \left[f\left(t, \vec{x}, \vec{\xi'}\right) f\left(t, \vec{x}, \vec{\xi'}_1\right) + O\left(\Delta t\ \vec{\xi}\ \frac{\partial f}{\partial x}\right)\right] g'b'\ d\epsilon'\ d\vec{\xi}_1$$

$$I = \Delta^- - \Delta^+$$

$$\frac{df}{dt} \leftrightarrow \frac{df}{dt} + \overline{\tau}\frac{\partial^2 f}{\partial^2 t}$$

$$f'\left(t, x, \xi'\right) \leftrightarrow f'\left(t, x, \xi'\right)$$

$$f\left(t, x, \xi\right) \leftrightarrow f\left(t + \overline{\tau}, x + \overline{\lambda}, \xi\right) \leftrightarrow f\left(t, x, \xi\right) + \overline{\tau}\frac{\partial f}{\partial t} + \overline{\lambda}\frac{\partial f}{\partial x} + \cdots$$

$$f_1\left(t, x, \xi_1\right) \leftrightarrow f_1\left(t + \overline{\tau}, x + \overline{\lambda}, \xi_1\right) \leftrightarrow f_1\left(t, x, \xi_1\right) + \overline{\tau}\frac{\partial f_1}{\partial t} + \overline{\lambda}\frac{\partial f_1}{\partial x} + \cdots$$

In general, this formula is necessary to write in this form, but for small gradients for simple gas can be limited to one time and one length of path. However, for structural gas, for example, at heights of more than 120 km of the mean for three

Mach numbers the lag time 10^{-8} c. and can be more that can be comparable with the relaxation time. In fact, the expression can be simplified, if given the orders of magnitude. Then

$$ff_1 - f'f'_1 \leftrightarrow ff_1 - f'f'_1 + \tau\frac{\partial f^0}{\partial t}f_1^0 + \tau_1 f^0\frac{\partial f_1^0}{\partial t} + \lambda\frac{\partial f^0}{\partial x}f_1^0 +$$

$$+\lambda\frac{\partial f_1}{\partial x}f^0 + \cdots - \tau'\frac{\partial f'^0}{\partial t}f'^{0_1} - \tau'_1 f^0\frac{\partial f'^0_1}{\partial t} - \cdots - \lambda'\frac{\partial f'^0}{\partial x}f'^0_1 - \lambda'_1\frac{\partial f'^0_1}{\partial x}f' - \cdots$$

The integrals can be calculated, and you can find the appropriate kernel of Navier-Stokes equations. Thus, for small and medium gradients mean free time is one and the mean free path for a single-component gas is one. Significant differences will be in the interaction of gases with very different properties. So for some organic molecules the relaxation and time of the delay time with the mean free path is comparable (about $10^{-9} - 10^{-8}$ c.)

It should be noted that, in general, ergodicity is not observed, which is very important, especially for turbulent flows. This analysis was made by T.G. Elizarova [18]. Averaging is performed for the space but is no for time. This is if we use the integral method for the construction of continuum mechanics equations. Perhaps more appropriate for the theory is the formulation of an integral equations with the average in the space and in the time that should be the average time between collisions of molecules. Otherwise, to record the derivative in a case of finite length of middle-free path of molecules (rarefied gas), we take into account only the molecules at high speed as slow collisions do not have the time to collision. One of the ways using in the kinetic theory, the replacement of discrete distribution on the smooth distribution function. However, even for the uniform distribution of function this way to replace it was not study in the transient case. A new wording of the definition of pressure, temperature and energy are suggested. The conventional formulation [11-16]

$$\frac{3}{2}kT=\frac{1}{n}\sum_k\int\frac{m_k c^{k2}}{2}f_k\,d\xi_k\ , \quad \left(n=\sum_{k=1}^{N}n^k\right)\ ,$$

here k - number of components, the T is the temperature, $c^k = \xi^k - u$, its own rate ξ^k - molecule speed. Another definition

$$\frac{3}{2}kT=\frac{\int\left(\sum_k\frac{n_k}{n}m_k\right)\left(\sum_k\frac{n_k}{n}c_k\right)^2}{2}f\,d\xi\ .$$

In this case, one term, the traditional second-connected with a second viscosity. For the pressure tensor

$$P_{ij}=\int\left(\sum_k\frac{n_k}{n}m_k c_k\right)_i\left(\sum_k\frac{n_k}{n}m_k c_k\right)_j f d\xi\ .$$

Heat flux

$$q_j=\frac{\int\left(\sum_k\frac{n_k}{n}m_k\right)\left(\sum_k\frac{n_k}{n}c_k\right)_j\left(\sum_k\frac{n_k}{n}c_k\right)^2}{2}f d\xi\ .$$

The question is what is measured in the experiment!

$$f_{\nu}^{(0)}{=}n^{\nu}\left(\frac{m}{2\pi kT}\right)^{3/2}\exp\left(-\frac{m}{2kT}c^{\nu 2}\right)$$

or temperature

$$f_{\nu}^{(0)}{=}n^{\nu}\left(\frac{m}{2\pi kT^{\nu}}\right)^{3/2}\exp\left(-\frac{m}{2kT^{\nu}}c^{\nu 2}\right)$$

We may have the wrong result for average temperature.
Old formulas remain for internal energy, but the definition of temperature varies. The results allow one to obtain Maxwell's equation for temperature.

4 The S.V. Vallander equations and the Chapman -Enmskog method for the Boltzmann equation

A known solution of the Chapman-Enskog obtained using many approximations [15]. On the other hand, the classical laws of conservation, that we study in this part, the normal velocity component [19] is enters.

$$\frac{\partial}{\partial t}\int_{\tau}\rho\delta\tau+\int_{\sigma}\rho V_n\delta\sigma=\int_{\tau}M\delta\tau\ .\ Consequently,$$

$$f\left(t+dt,x+(\xi\cdot n)dt,x+(\xi\cdot\tau)dt,\xi_i+\frac{x_{0i}}{m}dt\right)dx\ d\xi=$$

$$=f(t,x,\xi_i)dx\ d\xi+\left(\Delta^{+}-\Delta^{-}\right)dx\ d\xi\ dt\ .$$

As a result, we need to get the conservation law in the form of

$$\frac{\partial\rho}{t}+\frac{\partial\left[(\rho u)\cdot n+(\rho u)\cdot\tau\right]}{\partial x_i}=0\ .$$

Where n, τ - the unit vectors along the normal and tangential to the surface. If the Boltzmann equation is written out in the projections, more properly, all the same in the arbitrariness of the volume should be considered normal and tangential velocities. The velocity projections on the coordinate axes are used in the numerical analysis. Therefore, the error values are of the order of self-diffusion and thermal diffusion, which will be determined by the tangential components. To understand the process of self-diffusion and thermal turn to the equilibrium distribution function and investigate the effect of small additions to the values of macroscopic parameters on its value. The equilibrium function

$$f_0=n^0\left(\frac{m}{2\pi kT^0}\right)^{3/2}e^{-\frac{m(\xi-u)^2}{2kT^0}}\ .$$

Let Δ is a small correction. The behavior of the function we are interested in the effect of calculating the Hilbert hypothesis macro parameters through the equilibrium distribution function.

For $\rho \cdot u$

$$\frac{1}{(n+\Delta n)} \int (n+\Delta n+\cdots) \left(\frac{m}{2\pi k(T+\Delta T)}\right)^{\frac{3}{2}} e^{-\frac{m(\xi-u-\Delta u)^2}{2k(T+\Delta T)}} d\xi \ .$$

$$\int (n+\Delta n+\cdots)\, \xi \left(\frac{m}{2\pi k(T+\Delta T)}\right)^{\frac{3}{2}} e^{-\frac{m(\xi-u-\Delta u)^2}{2k(T+\Delta T)}} d\xi \ .$$

We are using the formula in the series expansion given that in both cases one of the formulas for $\rho \cdot u$ u and (ρu) matches. The difference between the approximations defined with first-degree order and has a structure of the solution of the Chapman-Enskog.

$$\frac{1}{n}\left(1-\frac{\Delta n}{n}+\cdots\right) \int n \left(1+\frac{\Delta n}{n}+\cdots\right) \left(\frac{m}{2\pi kT}\right)^{\frac{3}{2}} \left(1-\frac{3}{2}\frac{\Delta T}{T}\cdots\right) e^{-\frac{m(\xi-u-\Delta u)^2}{2k(T+\Delta T)}} d\xi =$$

$$\frac{1}{n}\left(1-\frac{\Delta n}{n}+\frac{\Delta n}{n}+\cdots\right)\left(1-\frac{3}{2}\frac{\Delta T}{T}\cdots\right) \int n \left(\frac{m}{2\pi kT}\right)^{\frac{3}{2}}$$

$$e^{-\frac{m(\xi-u)^2}{2kT^0}} e^{-\frac{m(\xi-u)^2}{2kT^0}\left(-2(\xi-u)\Delta u-\cdots\frac{\Delta T}{T}\right)} d\xi =$$

$$\frac{1}{n}\left(1+\cdots\right)\left(1-\frac{3}{2}\frac{\Delta T}{T}\cdots\right) \int n \left(\frac{m}{2\pi kT}\right)^{\frac{3}{2}} e^{-\frac{m(\xi-u)^2}{2kT^0}}$$

$$\left(1-\frac{m(\xi-u)^2}{2kT^0}\left(-2(\xi-u)\Delta u-\cdots\frac{\Delta T}{T}\right)\right) d\xi$$

$$\frac{m(\xi-u-\Delta u)^2}{2k(T+\Delta T)} = \frac{m(\xi-u)^2}{2kT}\left(1+2(\xi-u)\Delta u+\cdots\right)\left(1-\frac{\Delta T}{T}\right) =$$

$$\frac{m(\xi-u)^2}{2kT}\left(1+2(\xi-u)\Delta u+\cdots-\frac{\Delta T}{T}\right)$$

For large values of the number of particles of both formulas coincide. In general, we obtain values of various functions. Functionally-Boltzmann equation is invariant with respect to the selection of macro-distribution function. You must compare equilibrium distribution function with macro parameters that taken from the Euler and from the Navier-Stokes equations.

The difference will give us a small increment functions. We find that for the Euler equations (zero approximation of the Chapman-Enskog) the difference is zero. There are differences to the first approximation. The first approximation is responsible for the tangential component (p_{ij} - tensor of viscous stresses). Euler equations are obtained with the use of locally-equilibrium distribution function. Consequently, they are responsible for the normal component of the velocity values. In case p_{ij} of receipt of the first order correction of the parameters included in the final decision of the Chapman-Enskog we leave only part of terms after integration over the phase velocity ξ. The integrals are taken from $f\xi$ functions, i.e. for (ρu). Consider regardless of macro parameters.

$$\frac{Df_0}{dt} = \frac{1}{n} f_0 \frac{\partial n}{\partial t} + \frac{3}{2}\frac{1}{T} f_0 \frac{\partial T}{\partial t} + \frac{mc^2}{2kT^2} f_0 \frac{\partial T}{\partial t} + f_0 \left(\frac{m}{kT}(\xi-u)\frac{\partial u}{\partial t}\right) +$$

$$\xi \cdot \left\{ \frac{1}{n} f_0 \frac{\partial n}{\partial x} + \left(-\frac{3}{2} \right) \frac{1}{T} f_0 \frac{\partial T}{\partial x} + \frac{mc^2}{2kT^2} f_0 \frac{\partial T}{\partial x} + f_0 \left(\frac{m}{kT} (\xi - u) \frac{\partial u}{\partial t} \right) \right\} =$$

$$= 2J\left(f_0, f_0\varphi^k\right) = \int f_0 f_1^0 \left(\varphi_1^{(k)'} + \varphi^{(k)'} - \varphi_1^{(k)} - \varphi^{(k)} \right) g \; b \; db \; d\epsilon \; d\xi_1 \; \xi = 0 \; .$$

In classical case

$$\left. \frac{\partial f_0}{dt} \right|_{t=0} = f_0 \left\{ \frac{m}{kT} \left(c_i c_j - \frac{1}{3} c^2 \delta_{ij} \right) \frac{\partial u_i}{\partial t} + \frac{1}{2T} \frac{\partial T}{\partial t} c_i \left[\left(\frac{m}{kT} \right) c^2 - 5 \right] \right\} \; .$$

The Boltzmann equation is written relative to the total distribution function and consists of locally-equilibrium functions and additional term.
The tangential component of the velocity, which is obtained due to the arbitrary direction of the velocity relative to the position of the coordinate axes, is equal to

$$\int n \cdot (\tau \cdot f\xi) \, ds \; d\xi = \int div \, (\tau \cdot f\xi) \, dx \; d\xi$$

τf gives us additional term. In addition to locally equilibrium function has a term

$$f_0 \left[\frac{p_{ij}}{2p} \left(\frac{m}{2T} \right) c_i c_j - \frac{q_i}{p} \left(\frac{m}{kT} \right) \left(1 - \frac{c^2}{5} \frac{m}{kT} \right) c_i \right]$$

The main contribution to the integral will give the derivatives of locally equilibrium distribution function, which determines the self-diffusion equations and termodiffusion S.V. Vallander. The second derivative appears due term $c_i \cdot \frac{\partial f}{\partial r_i}$.

5 Conclusion

The paper proposes a refinement of the equations of a continuous environment and the Boltzmann equation with allowance for the angular momentum and delay, as well as the position of the center of inertia of the elementary volume. The possibility of describing discrete media in the framework of continuum mechanics is analysed. Set the role of dispersion and delays in physical and chemical processes of relaxation type. Equations by S.V. Vallander theory were obtained from the kinetic results.

References

[1] D.N. Zubarev, Nonequilibrium statistical thermodynamics . Moscow: Nauka, 1971. 414 p.

[2] B.V.Alekseev. Mathematical kinetics reacting gases. Nauka. 1982. 420.

[3] E.V. Prozorova. About models of continuum mechanics. International Scientific IFNA-ANS Journal "Problems of nonlinear analysis in engineering systems",п»„1(39), v.19, 2013, 45-57.

[4] E. V. Prozorova The Influence of the Dispersion of Non-equilibrium Continuum Mechanics.// Problems Environment. Moscow State University Electronic Journal: Physical and Chemical Kinetics in Gas Dynamics 13: 30. URL: http://www.chemphys.edu.ru/pdf/2012-10-30-001.pdf.

[5] Evelina V. Prozorova. Influence of the Delay and Dispersion In mechanics. Journal of Modern Physics, 2014, 5, 1796-1805

[6] Eugene P. Wigner. Symmetries and reflections. Bloomigston-London. 1970. 318p.

[7] V.A.Kononenko, E.V. Prozorova, A.V. Shishkin. Influence dispersion for gas mechanics with great gradients. 27-th international symposium on Shock waves. St. Peterburg. 2009, pp. 406-407.

[8] Oleg Galaev, Evelina Prozorova. Dispersion effects in the Falkner-Skan problem and in the kinetic theory. Proceeding the 13th International Conference on Heat Transfer, Thermal Engineering and Environment (HTE15) to be held in Salerno, Italy, June 27-29, 2015,

[9] Oleg Galaev, Evelina Prozorova. Dispersion Effects in the Falkner-Skan Problem in the Kinetic Theory. Journal of Applied Mathematics and Physics, 2017, 5, 522-537

[10] E. A. Bulanov. 2012."The momentum tension on mechanics of solid, free flowing and liquid medium". M.:College book. 2012,130p.

[11] Cercignani, Mathematical methods in kinetic theory Macmillan. 1969

[12] J.H. Ferziger, H.G. Kaper, Mathematical theory of transport processes in gases./ Amsterdam-London.1972.J.O. Hirschfelder, C.F. Curtiss, R.B. Bird, The molecular theory of gases and liquids. New-York, 1954.

[13] N.N. Bogolubov. Problems of dynamical theory on statistical physics. Gostexizdat, 1946. 146 p. (in Russian)

[14] K.P. Gurov. Basis of the kinetic theory. M.: Nauka. 1966. 351 (in Russian)

[15] M.N. Kogan. The Dynamics of the Rarefied Gases. // M.: Nauka, 1967.440 (in Russian).

[16] S. V. Vallander. The equations for movement viscosity gas.// DAN SSSR .1951. V. LXX п»„п»„п»„ , N 1

[17] S.V.Vallander, M.P. Elovskih. Theoretical dependence of the heat conductivity of gases on temperature. Reports of the USSR Academy of Sciences, 1951, v. 79 (1). 37-40.

[18] T.G. Elizarova. Quasigasdynamic equations and methods for calculating viscous flows. M: The scientific world.2007, 352 p.

Evelina V. Prozorova, Mathematics & Mechanics Faculty, St. Peterburg State University, University av. 28, Peterhof, 198504, Russia.

Charge accumulation and dissipation in micrometer sized powders.

Quintanilla, M.A.S., Pérez-Vaquero, J.

quintani@us.es

Abstract

When moving, dry particles tend to acquire electric charge due to collisions between themselves and other solid surfaces, in a process called tribocharging. Provided there is enough number of collisions in a short amount of time, the charge accumulated can be high enough to constitute and electrostatic hazard. However, when the particles finally come at rest, the electric charge tends to dissipate, even if the particles are made of insulating material. In fact, in general the time it takes for the charge to dissipate is much shorter than what it would be expected from the electrical conductivity of the material of the particles. In this work, we present a model that describes the discharge of a powder layer formed by the settling of charged particles based on the assumption that the settled powder has an effective conductivity. We compare the model with the results of an experiment in which particles are charged and collected in a Faraday cage. The value of the conductivity that the model requires to match the experimental results is compared with the electrical conductivity of the bulk powder measured directly.

1 Introduction

Dry powder handling operations are usually accompanied by electric charge built-up due to triboelectrification. Pneumatic transport is specially prone to triboelectrification as the particles carried by the gas experience many collisions with other solid surfaces, each collission contributing to the built up of charge in the particles. Once the particles settle to form a packed powder, the concentration of charge can create electric fields large enough to trigger electrical discharges. The likehood of electrical discharges depends on the charge accumulated in the settled powder at any given time, which depends on the balance between the electric charge accreted by the incoming particles in the heap and the dissipation of electric charge to the surroundings. In this work, we study the temporal evolution of charged particles dispersed in a gas stream, ressembling pneumatic transport which, after being charged, are allowed to settle by gravity.

Material	d_p (μm)	Material	d_p (μm)
Sipernat D10	3.4	5-50 glass beads	33.9
TiO_2	3.7	70-110 glass beads	92.0
Sand	4.0	90-150 glass beads	125.4
Sipernat 320DS	6.6	Pmma beads	200
Cornstarch	7.3	sugar	720
Coated cornstarch	7.3	semoline	796
Regolith	9.7		

Table 17: Materials used in the experiments presented in this report. With the exception of PMMA beads, whose size is provided by the manufacturer, their mean particle size d_p (surface-mean diameter) was measured in a Mastersizer 2000 using the Sirocco 2000 air dispersion unit (air dispersing pressure 1 bar).

2 Materials

The materials used in the experiments are listed in Table 17 in ascending average particle diameter. Different samples of the same material were stored at different controlled relative humidities in chambers with 10%, 30% and 60% R.H. Samples were contained in these chambers for months and were taken out only to perform experiments, after which they were placed again in the controlled ambients.

3 Experimental set-up

We have built two experimental set-ups. In one of them a sample powder is dispersed in a gas stream, charged by collisions against solid surfaces and the charge acquired by the particles is measured. In the second set-up, we have measured the electrical conductivity of a powder layer. The set-up used to charge powder samples is composed of three units: the disperser, the tribocharger and the collection unit. A picture of the set-up showing the tribocharger and collection unit is shown in Fig. 1. The disperser makes use of a venturi device which entrains powder particles in a gas stream prior to the injection in the tribocharger system. The sample is fed into the venturi through a low pressure port, with a mass rate that should be as constant as possible, and with total masses of tens of grams at least.
We have made experimental runs with two tribochargers: a nylon cyclone tribocharger with a cone shape on its bottom part (350 mm in length, 74 mm internal diameter) and a steel pipe (length 540 mm and internal diameter 21 mm). Collisions of particles against the tribocharger inner walls generate the electrical charge build up on the particles surfaces. In the experiments with steel pipe as the tribocharger, a programmable electrometer (Keithley 6512) working in the ammeter mode connects ground to the tribocharger, thus measuring the electric current involved in the charge transfer process between powder and steel pipe. The electric charge Q_d transferred to the particles while they are dispersed into the gas stream is obtained by numerical integration of the registered current.
After exiting the tribocharger, charged powders fall by gravity into a cylindrical

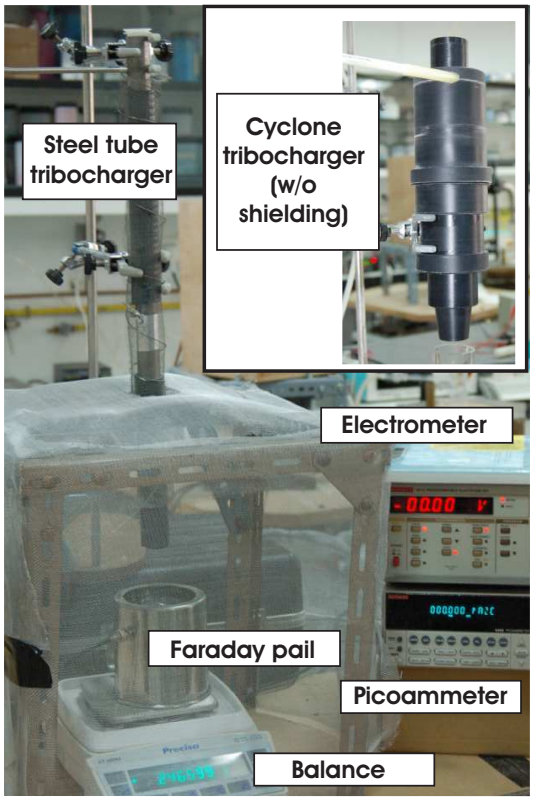

Figure 1: The experimental setup for measuring triboelectrification levels, with the steel tube tribocharger in place and the nylon cyclone tribocharger in the inset, shown without electric shielding. The Faraday pail resting on the balance collects the powder coming from the tribocharger. The electric current flowing into the Faraday pail is measured by the picoammeter and recorded by a PC. When the steel pipe is used as tribocharger, the electrometer depicted in the figure is connected to it and its data is also registered by the PC. The metallic mesh around all the setup is grounded to reduce electric noise from the rest of the lab. The dispersion units do not appear in the figure.

cell made of insulating material (a methacrylate tube), closed at its bottom with a metallic filter to help separate the particles from the gas. The filter inside cell is electrically insulated to the outside of the cell. The cell is located inside a Faraday pail consisting of an inner and an outer cage made of conductive material, the former being connected to ground through a picoammeter (Keithley 6485). The picoammeter measures the current flowing from ground to the inner cage of the Faraday pail as the collecting cell is filled by the material exiting the tribocharger. Integration of this current yields the charge $Q_s(t)$ in the settled powder as a function of time. The Faraday pail system rests on a mass balance that measures the collected powder mass $m(t)$ as a function of time. More details of this experimental set up are given in ref. [1].

The experimental set-up to measure the effective electrical conductivity of bulk powders σ consists on a cell of rectangular cross section (internal dimensions 48×24 mm) in which a layer of powder rests on a porous metallic plate (5μm pore size).

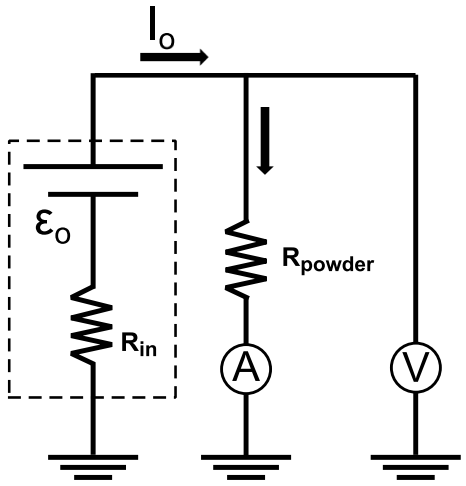

Figure 2: Electric diagram of the experimental arrangement to measure powder electrical conductivity. The granular material in the cell has an electric resistance R_{powder}. The HV source is enclosed in dotted line. Ammeter and voltage probe are pictured as A and V.

The cell has transparent methacrylate walls. The sample of powder in the cell is compressed by a punch of rectangular cross-section (dimensions 10% smaller than the inner dimensions of the cell), also made of transparent methacrylate walls, except for the face of the punch pressing the powder, which is made of the same porous metallic plate as the cell filter. With this arrangement, a flow of gas can be set to pass through the powder and exit the layer of powder through the filter on the punch. The reason to allow gas to pass through the powder is that other authors working in similar experiments [2, 3] have found that the humidity of the gas changes the electrical conductivity of the powders. For each of the materials used in the experiments, we have tested one sample with a flow of dry nitrogen and another with a flow of humid air that had passed bubbling through a beaker holding hot water. In both cases, the flow of gas is maintained during 60 minutes before inserting the punch to start the measurement of the powder conductivity. Before inserting the punch, the relative humidity inside the cell was measured with a hygrometer. When using dry nitrogen, the relative humidity inside the cell was found to be 14% RH, while when using humid air it was 80 % RH. Since the consolidation stress acting on the powder can also affect the powder conductivity, the punch can be loaded using weights. Two weights have been used in each experiment: for the smaller weight, the combined weight of the punch and the weight is 218 g, while for the larger weight is 3218 g. The resulting consolidation stresses acting on the layer of powder in the cell are 1.9 and 27.3 kPa, respectively.

Both filters also serve as electrodes: the filter on the cell is connected to a high DC voltage source (Spellman RHR20) while the filter on the punch is connected to ground through a picoammeter (Keithley 6485) to measure the current intensity through the sample. A multimeter equipped with a high voltage probe measured the voltage drop between the live electrode in the cell and ground. With minor modifications undergone through the several experiments, the equivalent circuit of

the set-up is shown in Figure 2. Powder conductivity is tested measuring the current through the powder I as a function of the voltage drop V across the cell, ideally lying on a straight line. Readings from the ammeter are taken as soon as a voltage V is set adjusting the high the voltage source, since the number of mobile charge carriers within the powder normally decreases with time, and so it does the current passing through the cell [3].
The slope of the best fit straight line throught the $I - V$ plot is the electrical conductance G of the cell loaded with powder, which is the sum of the electrical conductance due to the powder G_p and the electrical conductance due to the walls of the cell G_w ($G = G_p + G_w$). Only if $G_p \gg G_w$ are the results meaningful. This fact makes it necessary to measure the conductance of the empty cell at the two relative humidities used in our experiments. The results for a gap of 9 mm between the electrodes for 14% RH and a gap between the electrodes of 15 mm for 80 % RH are 4.1×10^{-4} nS/m and 1.6×10^{-3} nS/m, respectively. Both the conductance of the powder G_p and the conductance of the empty cell G_w depend on the gap h between the electrodes, because this gap represents the distance the charge carriers must travel between the two electrodes. The electrical conductance of the cell is assumed to be inversely proportional to the gap h between the electrodes.
From the powder conductance $G_p = G - G_w$, the powder conductivity is determined as:

$$\sigma = G_p \frac{h}{wd} \tag{1}$$

where w and d are the dimensions of the cross section of the cell. In practice, the current that flows through the cell walls limits our measurement of the conductivity of a powder to values larger than about 3×10^{-3} nS/m at 14 %RH and about 2×10^{-2} nS/m at 80 %RH

4 Results.

The charge acquired by the particles in the tribocharger while they are dispersed in the gas stream q_d can only be evaluated for the steel tube tribocharger, for which the total charge Q_d given to the powder can be measured. Assuming the sample is monodisperse and that all particles have the same charge to mass ratio, the individual particle charge is $q_d = Q_d(m_p/m)$ where m_p is the particle mass. Fig. 3 shows the value of q_d as a function of the particle radius r_p (half the surface mean diameter listed in Table 17) for the experiments using the steel tribocharger. Since there is always some powder that remains stuck to the inner walls of the tribocharger, using the collected mass m somewhat overestimates the value of q_d. The typical mass loss ranges from 19% to 69% of the total mass of dispersed powder for 5-50 μm glass beads and 1% to 20% in 90-150 μm. In general, the mass loss decreases with larger particles and higher storage humidity. Such overestimation in charged mass contributes to the experimental error in q_d in figures 3. In this figure a grey coloured bar by each group of symbols indicate the uncertainty in q_d, when mass losses between 19% and 69% are considered for the 5-50 μm glass beads, and

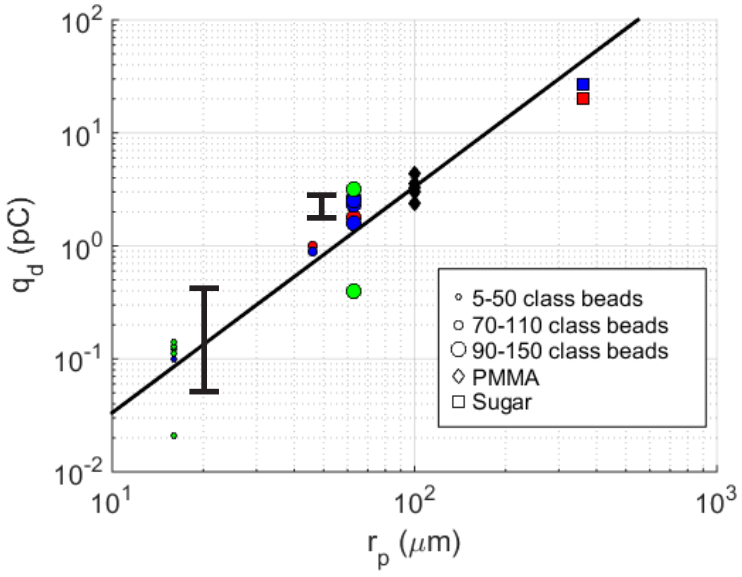

Figure 3: Results of absolute values of transferred charge q_d from the steel pipe tribocharger to particles of different materials. The line marks the theoretical values for maximum charge of particles limited by planar corona discharge.The dispersing gas and storage conditions of the material at each experimental point are given according to the following color code: Black: storage RH not controlled, dispersed in compressed air. Blue: stored at 56% RH, dispersed in compressed air. Red: stored at 30% RH, dispersed in compressed air. Green: stored in dry N2, dispersed in dry N2. Error bars indicate the typical uncertainty for each size range. For the larger particles particles, error bar and symbol are aprox. the same size.

20% for the 90-150 μm glass beads. The bar corresponding to a mass loss of 1% is neglected since its effect is not visually noticeable.
In Fig. 3 we have drawn a line for the maximum particle charge $q_{d,max}$, assuming the value of $q_{d,max}$ is given by the condition that the electric field on the particle surface equals the breakdown field for corona discharge as suggested in Ref. [4], that is:

$$q_{d,max} = 4\pi\epsilon_o r_p^2 E_c\,, \tag{2}$$

where we assume the breakdown field is equal to $E_c = 3 \times 10^6$ V/m irrespective of particle size and ϵ_o is the electric permittivity of the gas surrounding the particle, which we assume is equal to the permittivity of vacuum ($\epsilon_o = 8.85 \times 10^{-12} F/m$). All the experimental data lie very close to the corona discharge line, which means that, when dispersed, particles charge up to their maximum attainable value.
If the powder particles did not discharge during collection of the sample into a settled powder, the charge Q_s in a settled sample would equal the total charge Q_d transferred to its particles in the steel tube tribocharger. However, this is not so: in experimental runs $Q_s < Q_d$. The average electric charge per particle in the collected sample can be calculated from $q_s = Q_s m_p/m$. For the experiments with the steel tube tribocharger q_s can be compared with the electric charge per particle when the sample was dispersed in the gas stream q_d to evaluate the amount of

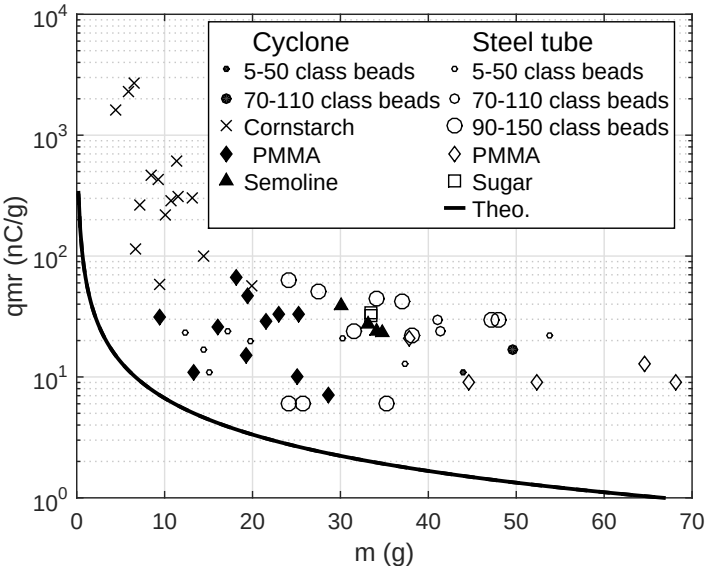

Figure 4: Specific charge qmr (charge to mass ratio) of the collected sample as a function of the collected mass m. Data for all the experimental runs are included. The void symbols represent data from experiments using the steel tube tribocharger. Data with filled symbols represent data from the experiments using the nylon cyclone tribocharger. The solid line represents the result of the model presented in discussion for 5-50 μm glass beads.

charge lost during settling: in most cases q_s is between 1/100 to 1/10 of the charge q_d acquired from the tribocharger. Fig. 4 illustrates the specific charge qmr of the collected powder against the collected mass m for all the available experiments, that is, using the steel tube and the nylon cyclone tribochargers. For a given material, the specific charge qmr tends to decrease when more mass is collected. Although the data points presented in Fig.4 have a large scatter, there is a visible tendency of decreasing specific charge qmr with sample mass m. More details of the results obtained with this set up are given in ref. [1].

Some of the missing charge may be in the layer of powder that remains stuck on the inner walls of the tribocharger. However, this layer forms in the initial seconds of each experimental run which lasts for a few minutes. Once the layer of stuck powder is formed, all the electric charge flowing to the tribocharger has no option but to be carried away by the particles, so this argument does not explain the decreasing trend of specific charge qmr with collected mass m.

The remain option is that the charge in the collected bulk powder is somehow lost while the powder is being collected. As the particles settle to form a bulk powder, there is a increase in the spatial concentration of the electric charge and we must expect the electric field on the bulk powder to increase to very high levels, high enough to cause ionization of the surrounding air. Ions of opposite polarity of the charge in the bulk powder would be attracted to the powder surface, neutralizing its charge with time. The charge inside the bulk powder must also have some mobility, to be able to reach the powder heap surface and be neutralized. So a model the

of charge accumulation and dissipation must account for: (1) Charge accumulation due to the inflow of charged settling particles; (2) charge dissipation on the bulk powder surface due to attraction of ions of opposite polarity from the surrounding air and possible transfer to the conductive surfaces of the Faraday pail, and (3) charge redistribution inside the powder, which can be represented as an effective conductivity.
Regarding the conductivity of powders, we have tested four materials: 70-100 μm glass beads, 5-50 μm glass beads, sipernat 320DS (a hydrophilic micron-sized silica) a sipernat D10 (a hydrophobic micron-sized silica). The conductivity of these powders is represented in Fig. 5 and its accompanying Table. The electrical conductivity of Sipernat D10 was so small that their $I-V$ plot did not differ significantly from that of an empty cell in the same conditions of relative humidity and electrode gap and therefore no value is quoted.
While the consolidation stress acting on the powder has little effect on the conductivity, the relative humidity has a very large effect, changing the conductivity by one to two orders of magnitude. Although three data is too little a sample to judge trends, the electrical conductivity decreases as the particles gets smaller when the interstitial gas is dry, but increases as the particles get smaller for wet air. Both trends can be explained if the mobility of the electrical charge in a bulk powder is caused by the presence of physisorbed water layers on the surface of the particles. The electrical conductivity raises with the humidity because the thickness of the physisorbed water layer increases with increasing relative humidity. And the increase may be more marked for smaller particles because the pores between the particles are smaller and capillary condensation favors the growth of the water layer. Besides, this mechanism would explain why the Sipernat D10, which is hydrophobic, is much less conductive than the hydrophilic Sipernat 320DS. The decrease of the conductivity for smaller particles for 14% RH would be explained if, at this level of humidity, charge carriers had to pass from one particle to the other at existing particle contacts. Powders with smaller particle sizes have lower solid fractions and lower average number of contacts between particles than larger sized powders.

5 Discussion.

To make a model we assume that as particles settle there is a corona discharge from the surface of the settled sample to the surrounding air and that the remaining charge is determined by the condition that the electric field at the surface of the sample must equal the electric field for corona discharge in air, which we take for simplicity as $E_c = 3 \times 10^6$ V/m. Since the calculation of the electric field created by a cylindrical heap of powder is not straightforward, the sample is assumed to be an infinite layer in the XY plane that grows in the positive Z direction by uniform addition of particles to its surface. The layer rests on a conductive plate representing the metallic filter of the collecting cell. The mass flow rate of new particles per unit area is F_m, so if the mass density of the powder layer is ρ_m, the height H of the powder layer grows as:

$$H = \frac{F_m}{\rho_m} t \tag{3}$$

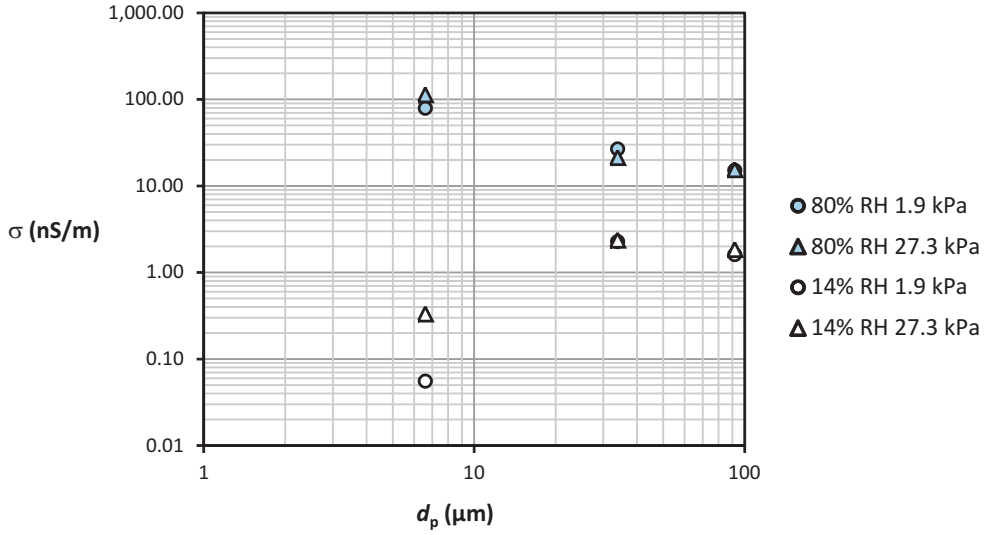

Material	Effective conductivity σ (nS/m)			
	14% RH		80% RH	
	1.9 kPa	27.3 kPa	1.9 kPa	27.3 kPa
7-70 μm glass beads	1.61 ± 0.06	1.85 ± 0.06	15.1 ± 1.0	15.4 ± 1.1
5-50 μm glass beads	2.28 ± 0.14	2.37 ± 0.13	26.7± 0.7	21 ± 12
Sipernat 320DS	0.056 ± 0.022	0.33 ± 0.02	79.0 ± 2.5	113 ± 12

Figure 5: Effective electrical conductivities of glass beads 70-110 μm and 5-50 μm and hydrophylic sipernat 320 DS as a function of consolidation pressure and relative humidity of the gas flowing through the cell.

until at $t = t_o$ the sample collection stops and the powder layer attains its final depth H_f. The powder layer has an electrical conductivity σ that represents the ability of the electric charge inside the powder layer to move. The temporal evolution of the charge per unit volume $\rho(z,t)$, the electric displacement $D(\vec{z},t)$ inside the layer as well as the surface charge density on the conductive plate $\sigma_p(t)$ are given by the solution of the set of equations:

$$\begin{aligned} \nabla \cdot \vec{D} &= \rho + \sigma_p \delta(z) \\ \frac{\partial \rho}{\partial t} + \nabla \cdot \vec{j} &= \rho_o \delta(t - z\frac{\rho_m}{F_m}) \\ \frac{d\sigma_p}{dt} &= -j_z(0,t) = -\frac{\sigma}{\epsilon} D_z(0,t) \end{aligned} \tag{4}$$

where $\delta(t - z\rho_m/F_m)$ is the Dirac's delta function and ρ_o represents the charge per unit volume on a newly deposited layer of powder. Due to the geometry of the problem, spatial derivatives are given by $\nabla = \vec{u}_z \partial/(\partial z)$, the electric displacement by $\vec{D} = D_z \vec{u}_z$ and the current density by $\vec{j} = \sigma D_z/\epsilon \vec{u}_z$. As the powder losses its charge, the charge per unit volume $\rho(z,t)$ decreases from the value ρ_o: part of the charge is lost to the surrounding air by corona discharge and part migrates to the metallic filter. As initial conditions we take that the initial height of the powder layer is zero and that the plate representing the filter is discharged.

The solution of Eq. 4 for $t \leq t_o$ is:

$$\begin{aligned} \rho(z,t) &= \rho_o \exp\left[-\frac{\sigma}{\epsilon}\left(t - \frac{\rho_m}{F_m}z\right)\right]\Theta\left(t - \frac{\rho_m}{F_m}z\right) \\ D_z(z,t) &= \rho_o \frac{\epsilon}{\sigma}\frac{F_m}{\rho_m}\left\{\exp\left[-\frac{\sigma}{\epsilon}\left(t - \frac{\rho_m}{F_m}z\right)\right] - \exp(-\frac{\sigma}{2\epsilon}t)\right\} \\ \sigma_p(t) &= \rho_o \frac{\epsilon}{\sigma}\frac{F_m}{\rho_m}\left[1 + \exp(-\frac{\sigma}{\epsilon}t) - 2\exp(-\frac{\sigma}{2\epsilon}t)\right] \end{aligned} \tag{5}$$

The total charge per unit area in the layer of powder for $t \leq t_o$ is given by:

$$\frac{Q}{A} = \int_o^{H(t)} dz\rho(z,t) \Rightarrow \frac{Q}{A} = \rho_o \frac{\epsilon}{\sigma}\frac{F_m}{\rho_m}\left[1 - \exp\left(-\frac{\sigma}{\epsilon}t\right)\right] \tag{6}$$

While the powder layer is growing $t \gg \epsilon/\sigma$ the electric displacement on the surface of the powder layer tends to the value:

$$D_z(H,t) \rightarrow \rho_o \frac{\epsilon}{\sigma}\frac{F_m}{\rho_m} = D_{z,lim} \tag{7}$$

The electric field outside the powder layer is given by $E_z = D_z(H,t)/\epsilon_o$. If we identify the value of the electric field obtained from Eq. 7 with the electric field $E_c = 30$ kV/cm for corona discharge on air, we get:

$$E_c = \rho_0 \frac{\epsilon}{\epsilon_o}\frac{1}{\sigma}\frac{F_m}{\rho_m} \tag{8}$$

From this equation we can also evaluate the effective conductivity of the powder σ if we assume that the charge per unit volume of a newly deposited layer ρ_o is formed by particles charged up to the limit set by Eq. 2. In this case:

$$\rho_o = \frac{3\epsilon_o E_c}{r_p} \rightarrow \sigma = \frac{3\epsilon F_m}{r_p \rho_m} \tag{9}$$

In our experiments, the mass flow rate into the collecting cell was 0.2 g/s, while the diameter of the collecting cell was 4 cm. In total, the mass flow rate per unit area is 0.16 kg/(m^{2}s). In using Eq.9, we assume the solid fraction of the settled material is $\phi = 0.6$, the density of bulk glass is 2.5 g/cm^3, $r_p = 17.0$ μm for the 5-50 μm glass beads and $r_p = 46.0$ μm for the 70-110 μm glass beads. The dielectric permittivity of both powders is $\epsilon = 2.95\epsilon_o$ assuming the dielectric constant of bulk glass is 5 and that the dielectric constant of glass powder can be found using Bruggeman mixing rule [5]. Under these assumptions Eq. 9 predicts an effective conductivity of $\sigma = 0.29$ nS/m for 5-50 μm glass beads and $\sigma = 0.10$ nS/m for 70-110 glass beads, one order of magnitude less than the value measured directly (see Fig. 5).
The theoretical model outlined here predicts that the total charge per unit area in the collected layer of powder layer is given by:

$$\frac{Q}{A} + \sigma_p = 2\rho_o \frac{\epsilon}{\sigma}\frac{F_m}{\rho_m}\left[1 - \exp\left(-\frac{\sigma}{2\epsilon}t\right)\right] \tag{10}$$

If the values obtained for ρ_o, σ and ϵ are substituted in Eq. 10 we can obtain a prediction of the specific charge qmr as a function of the collected mass $m(t)$. The resulting curve for 5-50 μm glass beads is plotted in Fig. 4, where it can be compared with the experimental data. The model seems to give the correct trend in the data of specific charge against collected mass, although the values of the specific charge are about an order of magnitude smaller than the experimental values if a value of $\sigma = 0.29$ nS/m is used. Larger values of the effective conductivity increase the discrepancy between the predictions of the model and the experimental results.

6 Conclusions.

From the experiments presented in this manuscript it can be concluded that the rate of charge dissipation in a settled bulk powder would depend on the effective conductivity of the powder. Large accumulations of electric charge would appear in those situations in which the charge on the bulk powder is replenished by the arrival of charged particles at a rate faster than the rate of charge dissipation. If the uncharged particles leave the bulk powder for some reason, there would be an equilibrium between inflow of charge and its dissipation leading to a stable value of the charge to mass ratio. If the uncharged particles remain in the bulk powder, as it is the case for example of heap formation, the charge to mass ratio of the powder will decrease with time even as new charged particles are constantly arriving. However, although as a whole the powder discharges, those regions of the bulk powder formed by newly arrived particles would still hold large concentrations of electric charge, giving rise to localized regions of high electric fields.

Acknowledgements

This work has been funded by the Spanish Ministerio de Economía y Competitividad (project no. FIS2014-54539-P) and by the International Fine Particle Research Institute (IFPRI). We would like to dedicate this manuscript to the memory of Antonio Castellanos, who led this research until he passed away in January 2016.

References

[1] J. Pérez-Vaquero, M. A. S. Quintanilla and A. Castellanos. Electric charge limits on settled powders. Journal of Applied Physics 119(22) 223302 (2016).

[2] K.J. McLean, R.M. Huey. Influence of electric field on the resistivity of a particulate layer. Proceedings of the Institution of Electrical Engineers, 121(1) pp. 76-80 (1974).

[3] Y. Aleksin, A. Vora, U. Riebel. A new understanding of electric conduction in highly resistive dusts and bulk powders. Powder Technology, 294 pp. 353-364 (2016).

[4] Tatsushi Matsuyama, Hideo Yamamoto. Impact charging of particulate materials. Chemical Engineering Science 61(7), pp. 2230-2238 (2006).

[5] Kimmo Karkkainen, Ari Sihvola, Keijo Nikoskinen. Analysis of a three-dimensional dielectric mixture with finite difference method. IEEE Transactions on Geoscience and Remote Sensing. 39(5), pp. 1013-1018 (2001).

Miguel Ángel Sánchez Quintanilla, Universidad de Sevilla, Faculty of Physics, Dept. of Electronics and Electromagnetism, Avenida Reina Mercedes s/n 41012, Sevilla, Spain.
Javier Pérez Vaquero, Universidad de Sevilla, Faculty of Physics, Dept. of Electronics and Electromagnetism, Avenida Reina Mercedes s/n 41012, Sevilla, Spain.

Drag reduction on a circular cylinder by corona discharge

Renev M.E., Safronova I.F.
m.renev@2014.spbu.ru

Abstract

The paper considers the capability of ion wind, caused by corona discharge, of changing the wake structure behind a circular cylinder, the maximum Reynolds number being 3600. Computer simulation of positive corona discharge uses the unipolar model. The electrode system consists of a grounded circular cylinder and a high-voltage wire placed behind the cylinder. The corona discharge has been shown to be capable of changing the wake structure of Karman vortex street significantly. Frequencies of the vortices decrease 2.5 times with applications of 30 kV voltage, sizes and rotation speeds of the vortices increasing notably as well. The drag force is mostly defined by the pressure distribution on the cylinder surface and displays quasi-periodic behavior. The average value of the force is a linear function for studied voltages. The value decreases markedly with increasing voltage.

1 Introduction

The control of aerodynamic characteristics of bodies is an important applied problem of mechanics. When a body is bluff, the viscosity component of the drag force is less then pressure one, so the problem of lowering the drag force in the case reduces to that of making the pressure difference on the surface of the bluff body smaller. The pressure drag force emerges because of the boundary layer separation. There are many ways of changing the separation angle, both active and passive. The former require additional power and include blowing out the separated layer, acoustic perturbation, vibrating walls. The latter comprise regulating surface roughness and placing wake structure separators. When the Reynolds number is 50-10^5, the Karman vortex street behind bluff bodies appears [1]. It is a periodic motion with vortices, which detach alternately from the top and the bottom of the body. Mechanical oscillations, caused by vortices, might bring about vibrations, noise and even the system destruction.

Despite many studies in the field of physics, of interest today is controlling the wake structures by ion wind, caused by a corona discharge. The manner of control has many advantages: it is simple, robust, cost-effective, and has no moving parts.

A corona discharge occurs in electrode systems with small curvature radius; this is needed to establish strong and localized electric field near the sharp electrode. The

field makes charged particles collide and thus ionize, so the number of ions in the air grows exponentially. The region, where the electric field is strong enough to ensure the collisions, is called the corona sheath and is typically rather small (near 0.1 mm in radius). Outside the corona sheath, the ions drift under the action of the electric field and share their momenta with neutral particles in collisions; the air is set in motion in the direction from the sharp electrode to the grounded one. This phenomenon is called the ion wind.

The paper presents the computer simulation of the positive corona discharge and the ion wind. In case of the positive corona discharge, electrons appear near corona sheath because of photoionization [2], are drawn into the sheath, forming an avalanche, and disappear on the surface of the sharp electrode. The flux of the positive ions moves outwards. The simulation uses an original unipolar model of the positive corona discharge, which replaces the ionization processes in the sheath with a boundary condition on the sharp electrode [3, 6]. The input parameters include physical quantities, which can be measured independent, such as ionization rate, ions mobility, diffusion coefficient, critical value of ionization collisions. The authors of the current paper sought to demonstrate the capability of controlling the wake structures of the airflow near a circular cylinder by means of a corona discharge. The drag force was calculated, the Karman vortex street was analyzed in great detail, and it was shown how these characteristics change when a voltage is applied.

2 Simulation

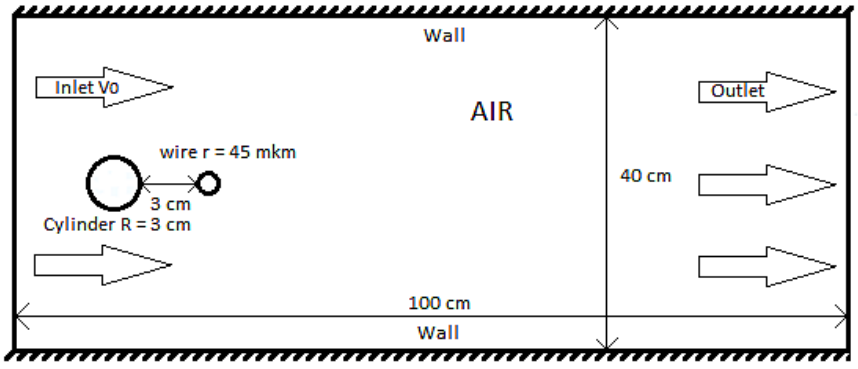

Figure 1: Geometry for the computer simulation (wire is not in scale).

The wire-cylinder electrode system is placed into an aerodynamic tunnel with airflow velocity V_0. The wire has radius r = 45 μm and is at a high voltage, the cylinder has a radius R = 3 cm and is grounded. The wire is placed behind the cylinder, and the electrodes are spaced at 3 cm. Figure 1 shows the geometry of computer model. Simulation used the plane geometry with width L = 28 cm. Inflow velocities V_0 were 0.6 m/s and 0.8 m/s; the Reynolds numbers for the velocities in case of the circular cylinder and no applied pressure are 2700 and 3600, respectively. The applied voltage was in range 16.2kV-30kV. The experiments [4] show that, when the

voltage is more than 30 kV, an electric breakdown occurs in such electrode systems.

$$\Delta\varphi = -\frac{|e|n_+}{\varepsilon_0} \tag{1}$$

$$\overrightarrow{E} = -\nabla\varphi \tag{2}$$

$$\frac{\partial n_+}{\partial t} + div\left[-D\nabla n_+ + bn_+\overrightarrow{E}\right] = 0 \tag{3}$$

$$\rho\frac{d\overrightarrow{v}}{dt} = -\nabla p + \eta\Delta\overrightarrow{v} + |e|\, n_+\overrightarrow{E} \tag{4}$$

$$div\,\overrightarrow{v} = 0 \tag{5}$$

$$\frac{\partial j_s}{\partial t} = j_s\frac{e^{-M_{cr}}e^M - 1}{\tau} \tag{6}$$

$$M = \int_0^s \alpha_{eff}\left(E\left(s\right)\right)ds \tag{7}$$

The mathematical model of ion wind includes Poisson equation (1) for the electric potential φ, the equation linking the electric field $\overrightarrow{E}$ and the potential (2), the Nernst-ВГУPlanck equation (3) for the concentration of positive ions n_+, the Navie-Stokes equation for the air velocity $\overrightarrow{v}$ and the pressure p (4) with external volume force, the continuity equation (5) for uncompressible air. The unipolar model [3, 6] includes boundary condition (6) for the partial time derivative of positive ions flux density j_s from the sheath of corona discharge to exterior. The $e^{-M_{cr}}$ coefficient is an photoionization coefficient, M is the collision number (7) along the electric field line in the corona sheath, which depends on effective ionization coefficient α_{eff}, s is the coordinate along the electric field line, $\tau = 10^{-3}$s is the characteristic time. M_{cr} is the value of ionization collisions needed for the discharge ignition. Boundary conditions are shown in the table 18 ($\overrightarrow{n}$ is the normal vector of surface, $\overrightarrow{e_x}$ is the x-axis vector, U is the applied voltage).

Table 18: Boundary conditions for the simulation

	air flow	electrostatics	transporting of ions
wall	$\overrightarrow{v} = \overrightarrow{0}$	$\overrightarrow{n} * \overrightarrow{E} = 0$	$\overrightarrow{n} * (-D\nabla n_+ - bn_+\overrightarrow{E}) = 0$
inlet	$\overrightarrow{v} = V_0 * \overrightarrow{e_x}$	$\overrightarrow{n} * \overrightarrow{E} = 0$	$\overrightarrow{n} * (-D\nabla n_+ - bn_+\overrightarrow{E}) = 0$
outlet	$\sum_{j=1}^{3}\left[-p\delta_{ij} + \eta\sigma_{ij}\right]n_j = -p^*n_i; p^* \leq 0$ $\sigma_{ij} = \frac{\partial v_i}{\partial x_j} + \frac{\partial v_j}{\partial x_i}$ (zero relative pressure)	$\overrightarrow{n} * \overrightarrow{E} = 0$	$\overrightarrow{n} * (-D\nabla n_+ - bn_+\overrightarrow{E}) = 0$
wire	$\overrightarrow{v} = \overrightarrow{0}$	$\varphi = U$	j_s (5)
cylinder	$\overrightarrow{v} = \overrightarrow{0}$	$\varphi = 0$	$\mathrm{j}_\tau = 0$

η is the air viscosity (16 μPa*s), ρ is the air density (1.2 kg/m^3), e is the electron charge (1.6*10^{-19} C), D is the effective diffusion coefficient of positive ions (10 mm^2/s), b is the effective mobility of positive ions (2.14*10^{-4} m^2/(V*s)), ε_0 is the vacuum dielectric permittivity (8.85^{-12} F/m). The simulation was carried out with COMSOL Multiphysics.

3 Results

The calculated current-voltage curve (I-V curve) of the corona discharge agrees quite well with the experimental one [4] for given electrode system Figure **??**. The I-V curve is the quadratic function and equation (**??**) is suitable for it:

$$I = KU(U - U_0) \tag{8}$$

K - is the coefficient of I-V curve growth and depends on geometry of electrodes and the positive ion mobility. b was taken equal $2.1{*}10^{-4}$ $m^2/(\mathrm{V}{*}\mathrm{s})$, it conform with data from different literature [2, 5]. U_0 - is the treshold voltage, which depends on M_{cr}. For this study $M_{cr} = 11$, so treshold voltage is nearly 7 kV. This value of M_{cr} also was used in studies [3, 5] and match with experiments. Figure (**??**) shows, that the experimental treshold voltage is nearly 10 kV. If M_{cr} increases, the treshold voltage does so, too. The treshold voltages may be made equal, but M_{cr} =18-20 is the value of streamer ignition. Such difference between current at low voltages less than 10 kV might be caused by currents too low for registration.

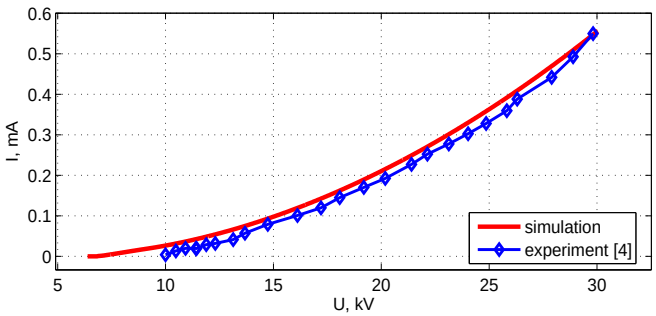

Figure 2: The I-V curve of the corona discharge: the simulation and the experiment [4].

When U and V_0 attain steady-state, the airflow is considered quasi-periodic. Figure **??**a shows Karman vortex street without the corona discharge at V_0= 0.6m/s, and Figure **??**b shows the street with the applied voltage 21.2 kV at V_0= 0.6m/s. The ion wind moves from the wire to the cylinder and it pushes vortexes to the cylinder and enhance them. This phenomenon could be called "ion wind enhancement of vortexes". Figure **??**b shows the vortexes that much bigger than common ones. The maximal vortex radius in this paper is nearly 2 times bigger than the cylinder radius and the maximal rotation speed increases in 3 times.
In addition, there is a region between the vortex and the cylinder, where small vortices may occur and cause small and fast oscillations of the drag force (Figure 4).
Figure 4 shows the time-dependent drag force F(t) at V_0 = 0.6 m/s and U = 0 kV; 21.2 kV. There are quasi-periodic oscillations. If a voltage is applied, the main period becomes longer, the amplitude rises, the mean value decreases. The shape of oscillations becomes non-harmonic.
Figure 5 shows one period of the drag force for some parameters V_0, U. The part, where F(t) is decreasing, is considered the part of the vortex accumulation, the

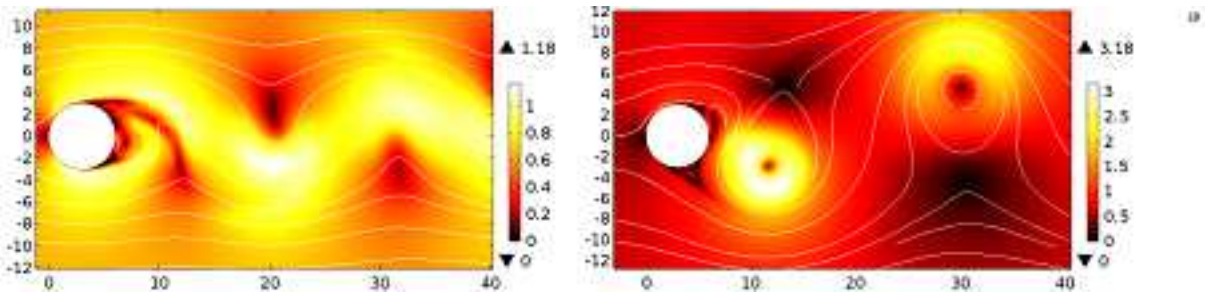

a) b)

Figure 3: Contour plots of air velocity with streamlines. 3a: $V_0 = 0.6$ m/s $U = 0$ kV; 3b: $V_0 = 0.6$ m/s, $U = 21.2$ kV.

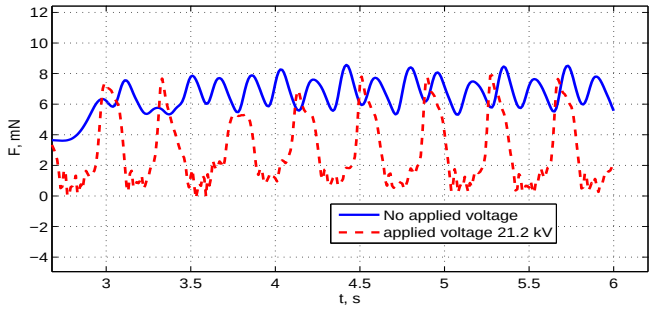

Figure 4: The drag force vs. time for cases: no applied voltage and $U = 21.2$ kV; $V_0 = 0.6$ m/s.

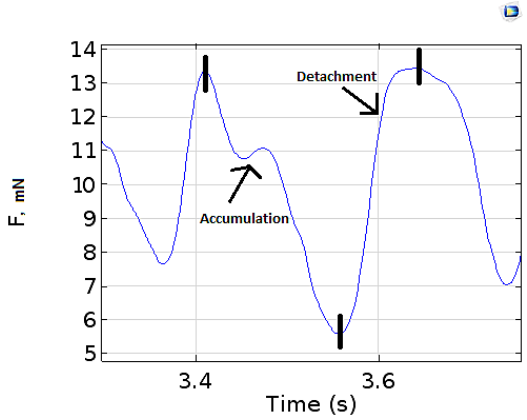

Figure 5: The accumulation and the detachment parts of a period of drag force.

second part is the vortex detachment. While the voltage is increasing, the accumulation part becomes longer. So, it has to be considered that the vortices plays the main role in the drag reduction. If the accumulation time grows, the mean value of the drag force decreases. Below, some relative dimensionless quantities will be calculated. The equation for them is number (9): a ratio of the value of a quantity at some applied voltage to its value without applied voltage.

$$relative\ variable = \frac{variable(U)}{variable(U=0)} \tag{9}$$

Figure 6 shows the relative variable of the vortex frequencies. Freq($U = 0$, $V_0 = 0.8$ m/s) = 8.13 Hz, Freq($U = 0$, $V_0 = 0.6$ m/s) = 5.48 Hz.

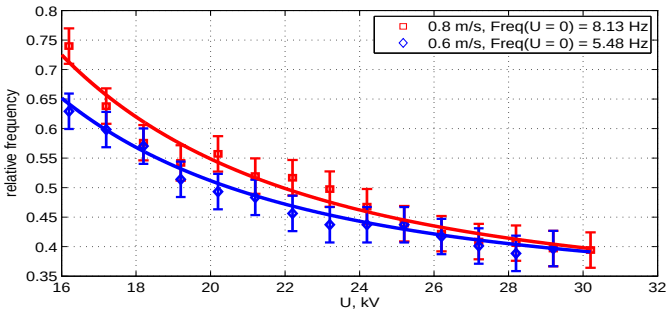

Figure 6: Relative frequency of vortexes vs applied voltage for different velocities of inflow.

As it was expected, when V_0 rises, the frequency rises, too, because higher velocities make vortices move away faster. At $U = 30$ kV, the relative frequency decreased 2.5 times. It happens because of the stronger ion wind push on vortices; the accumulation time and sizes of vortices increase.

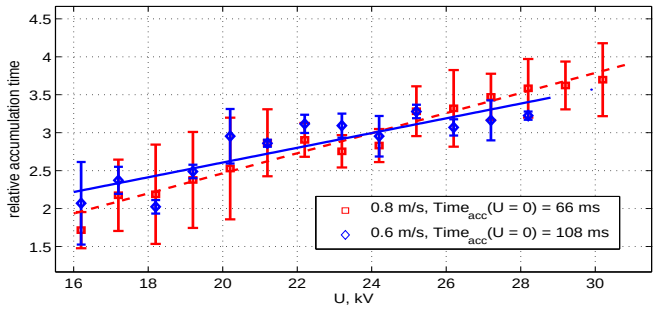

Figure 7: The accumulation time vs applied voltage for different inflow velocities.

Figure 7 shows dependence between the relative accumulation time and the applied voltage for different inflow velocities. $Time_{acc}(U = 0,\ V_0 = 0.8$ m/s) = 66 ms, $Time_{acc}(U = 0,\ V_0 = 0.6$ m/s) = 108 ms. The accumulation time rises along with the voltage. In addition, the time plays the main role in the frequency decreasing. Figure 8 shows the relative detachment angle vs applied voltage at different inflow velocities. The angles are reckoned counter-clockwise and the starting point is the most right point of the cylinder (Figure 1). There are voltages, where angles are nearly constant. Afterwards, the visible rise occurs, which starts earlier at smaller inflow velocities. It is related with the phenomenon of the wind enhancement of vortices. The enhanced vortices significantly change the wake structure and might be considered as obstacles so the angle increases. The plot can be used to evaluate the voltage, at which small oscillations of the drag force occur.

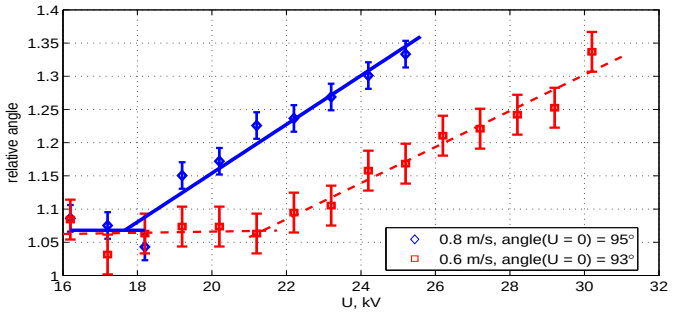

Figure 8: The relative detachment angle vs the applied voltage for different inflow velocities.

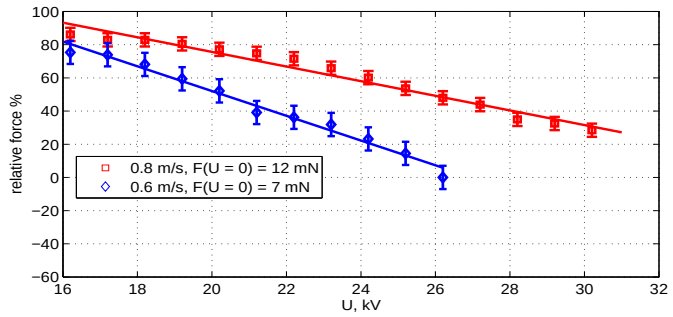

Figure 9: The relative mean value of drag force vs. the applied voltage for different inflow velocities.

Figure 9 shows the relative mean value of drag force vs. the applied voltage at different inflow velocities. The mean value is a decreasing linear function of the applied voltage. For higher inflow velocities, the mean value decreases slower. For V_0=0.6 m/s, $U = 26$ kV is the voltage, at which the drag force is zero. At this voltage, the ion wind effect balances the one of the external flow.

4 Conclusion

The simulation has shown the corona discharge to significantly change the periodic behavior of Karman vortex street. The maximal drop of the vortex frequencies is 2.5 for $U = 30$ kV as compared with $U = 0$ kV. At high voltages, the vortices can accumulate more momentum, because the corona discharge pushes them stronger. Increasing the accumulation time by corona discharge can reduce the mean value of the drag force. The pressure distribution plays a major part in the drag force. The mean value of drag force is a linear function of the applied voltage. The drag force is quasi-periodical. There is a voltage, at which the drag force is zero. For higher velocities, all considered effects are less noticeable, because the vortices move away faster.

5 Acknowledgements

Research was carried out using computer resources provided by Resource Center "Computer Center of SPbU" (http://cc.spbu.ru).

References

[1] Milton van Dyke. An album of fluid motion. Parabolic Press, 1982, 176 p.

[2] Yu. P. Raizer. Gas Discharge Physics. Springer, Berlin, New York, 1991, 450 p.

[3] A.V. Samusenko, I.F. Safronova, Yu.K. Stishkov. Unipolar model of the positive corona discharge.Surface Engineering and Applied Electrochemistry, 2016, 52(5), pp.43-вГY50.(in russian)

[4] K.T. Hyun, C.H. Chun. The wake flow control behind a circular cylinder using ion wind. Experiments in Fluids, 2003, 35, pp. 541–552 DOI 10.1007/s00348-003-0668-z.

[5] Yu. K. Stishkov, A.V. Samusenko. Electrophysical processes in gases in strong electric field. 2011, 567 p.

[6] P. S. Zhidkova, A. V. Samusenko. A computer model of the ionic wind in the unipolar approximation with the boundary condition on the ion flow variation rate. Surface Engineering and Applied Electrochemistry, 2016, 52(4), pp. 370-вГY379. doi: 10.3103/S106837551604013X.

Renev M. E., Safronova I. F, St. Petersburg State University 7/9 Universitetskaya nab., St. Petersburg, 199034 Russia.

The opposite mode of streamer-to-leader transition

Andrey Samusenko, Yury Stishkov

a.samusenko@spbu.ru

Abstract

Streamer discharge propagates in air by impulse voltage impact. It is not dangerous for high voltage devices itself. However if streamer channel closes a pair of electrodes –вГ´Y breakdown may occur. Barrier insulation may be used to increase breakdown voltage вГ´Y– solid dielectric elements are placed on the supposed path of the streamer. Elongation the shortest path through air between electrodes ("arcing length") leads to proportional increase of breakdown voltage in a first approximation. In this regard the following question occurs вГ´Y– what is a limitation on this method of breakdown voltage increasing.

1 Rounding breakdown mode in system with dielectric barrier

In systems of electrodes with a highly inhomogeneous distribution of electric field both without barriers and with a barrier, a streamer discharge arises from a certain voltage level [1]–[4]. If the voltage is large enough, the streamers reach the surface of the barrier and change the direction of their propagation to a tangent to the surface of the barrier. In this case they propagate first along the surface of the barrier, and then, reaching the edge of the barrier, they germinate towards the counter electrode. From a certain voltage level the length of the streamers becomes sufficient to go around the edge of the barrier and then reach the counter electrode. When streamers reach an opposite (grounded) electrode and close the interelectrode gap, a spark breakdown is possible. The spark channel in this case is located above the surface of the barrier ("envelopes" the barrier), passing mainly through air, at some distance from the surface of the solid dielectric (Fig. 1–2). Such a situation is analogous to the classical breakdown mode at small interelectrode distances without a solid dielectric: the barrier only extends the trajectory of the closing streamers and the subsequent leader, forcing them to walk through the air in order to bypass the obstacle. We will call such a breakdown mode as an "enveloping leader" or вГ´Ёenveloping mode of breakdownвГ´№.

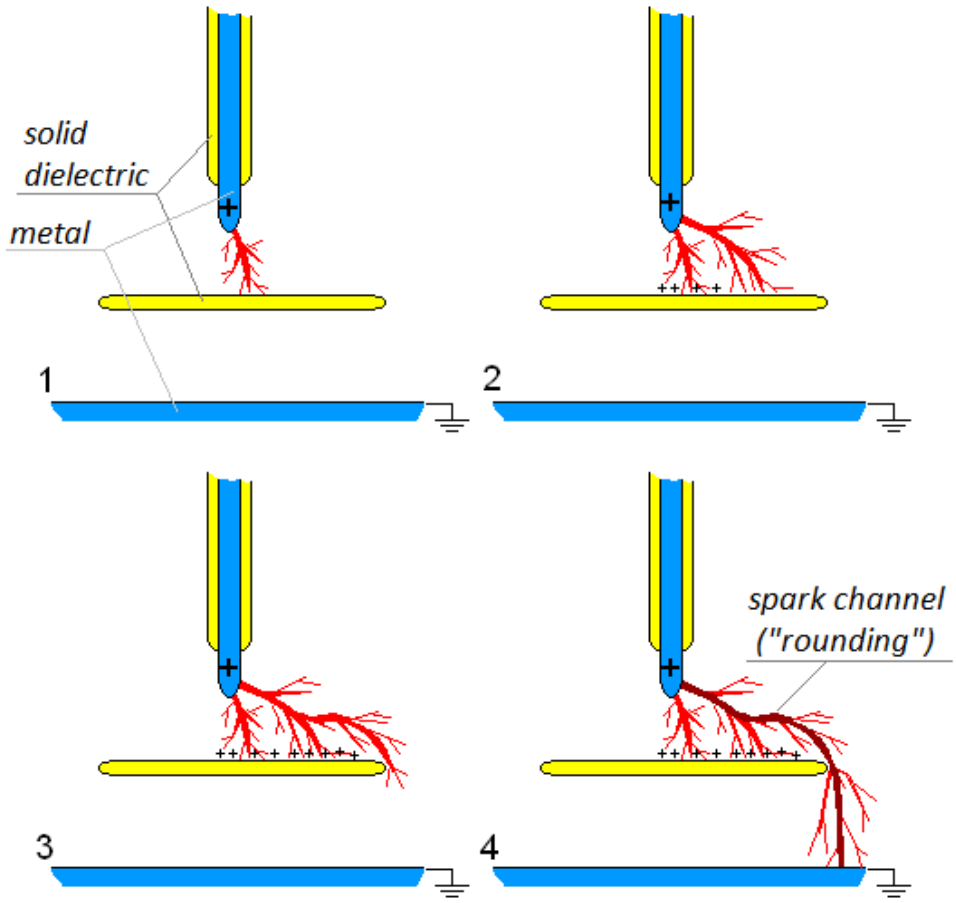

Figure 1: "Enveloping" breakdown mode outline.

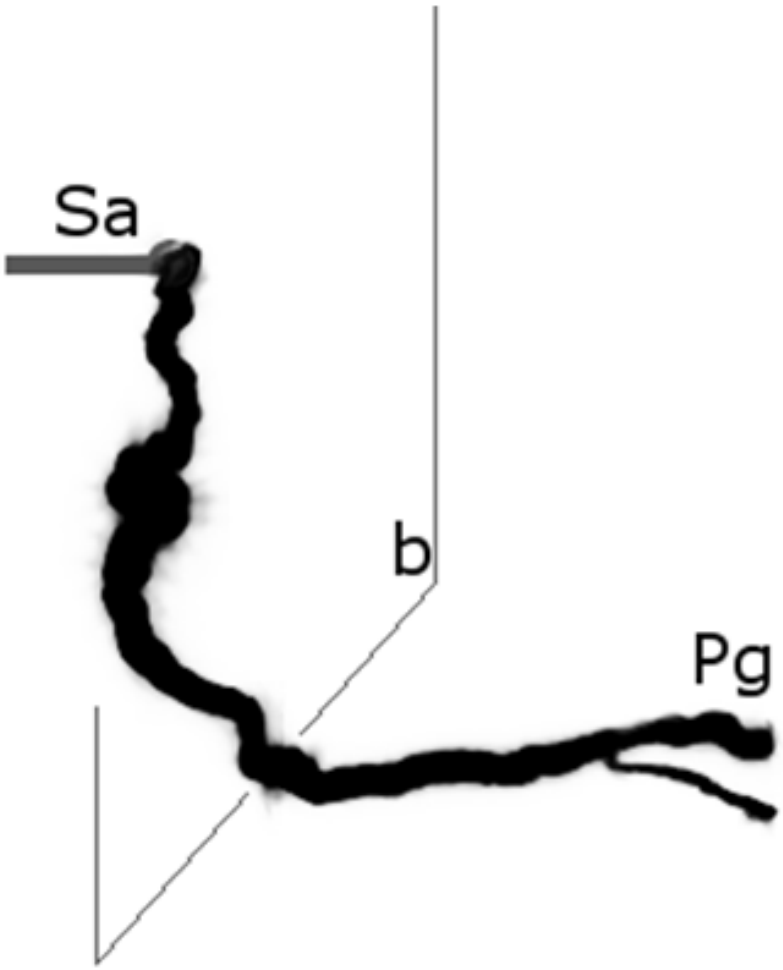

Figure 2: Negative of a photograph of spark breakdown in the sphere-plane system. "Sa" вЃY– high voltage spherical electrode, "Pg" вЃY– plane spherical electrode, "b" вЃY– dielectric barrier. The leader has an "enveloping" shape — spreads over the barrier surface and envelops the dielectric barrier through air.

2 Opposite streamers

The source of standard lightning voltage pulses is used (the duration of the leading edge is 1.5 μs, the trailing edge is 50 μs). The stand is equipped with a highly sensitive camera, which provides receiving photos of leaders and streamers. Exposure time exceeds the duration of the applied voltage pulse, therefore the resulting photographs are not instantaneous images of the glow of the discharge, but integral pictures. Visualization of the surface charge at the barriers is accomplished by applying an electrically conductive powder.

If the barrier diameter is sufficiently large, one can observe the formation of streamers on the either side of the barrier (Fig. 3). A similar situation arises both in "symmetric" systems such as sphere-sphere, cylinder-cylinder, and in systems with a flat counter electrode. Why is the formation of streamers possible not only near the high-voltage electrode, but also near the grounded one, where the field strength is lower? The reason is the distortion of electric field by the "primary streamers" (propagating between the high-voltage electrode and the barrier). The occurrence of conductive channels between the high-voltage electrode and the barrier leads to the fact that the field strength in this air gap decreases, and, in contrast, increases between the barrier and the counter electrode (potential difference between the electrodes is fixed and equals to the voltage).

Experimental evidence of electric field redistribution by streamers development is the accumulation of surface charge at the barrier. Since the barrier material has electrically insulating properties, a significant portion of electric charge remains on it after exposure to a voltage pulse, its distribution can be visualized, and the charge density can be measured.

Fig. 4 shows the distribution of the surface charge at the upper and lower sides of the barrier. As can be seen, a wider spot is observed from the side of the high-voltage electrode — this is the "imprint" of the "primary" streamers, which provide redistribution of electric field in favor of the gap between the barrier and the counter electrode. The trace of the "secondary" streamers is more concentrated — these streamers propagate directly to the center of the barrier.

Thus, streamers develop on both sides of the barrier at a sufficiently high voltage. The structure of streamers from the positive and negative electrodes corresponds to the previously described structure of positive and negative streamers in the air gap [1].

Both the "primary" and "secondary" streamers deposit surface charge on the barrier (Fig. 4). The polarity of charge on the opposite sides of the barrier differs. Thus, an electric capacitor appears on the barrier, the "plates" of which are two spots of surface charge.

3 Opposite leader formation and breakdown

Consider breakdown in systems with a large barrier size (Fig. 5). The spark channel has a complex shape. A common feature of spark channels in such systems is the pair sections of channels that run along the barrier surface on its both sides opposite each other ("2" and "3" in Fig. 4). Sometimes spark channels branching is

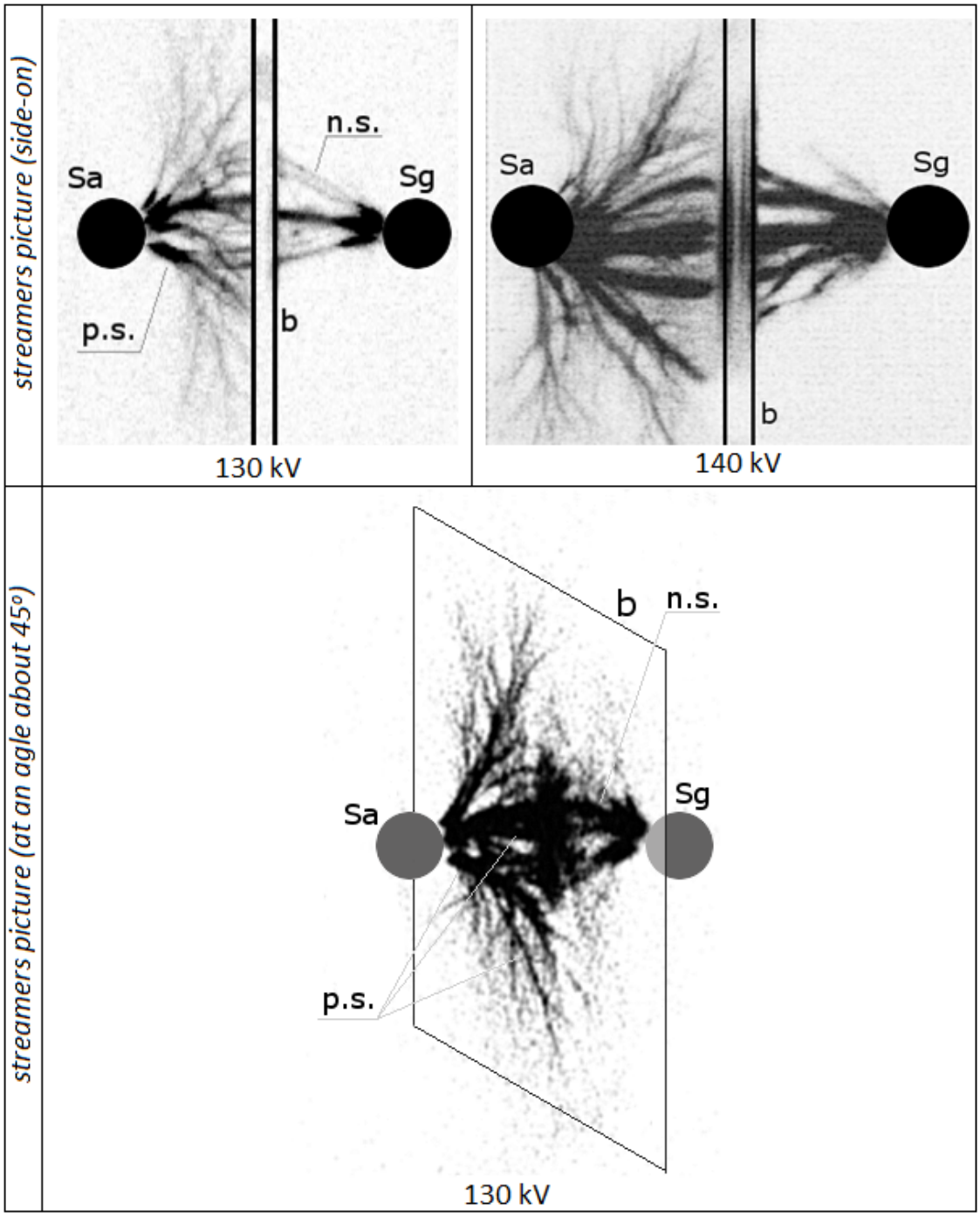

Figure 3: Photos of streamers from different angles. Negatives of photographs. "Sa" –вГ΄Y high voltage spherical electrode, "Sg" –вГ΄Y grounded spherical electrode, "b" –вГ΄Y dielectric barrier. "p.s." — positive streamers, growing from the active electrode, "n.s." — negative (вГ΄ËoppositevГ№) streamers, growing from the grounded electrode. Images of electrodes and a barrier on a photo are put artificially during processing of the data.

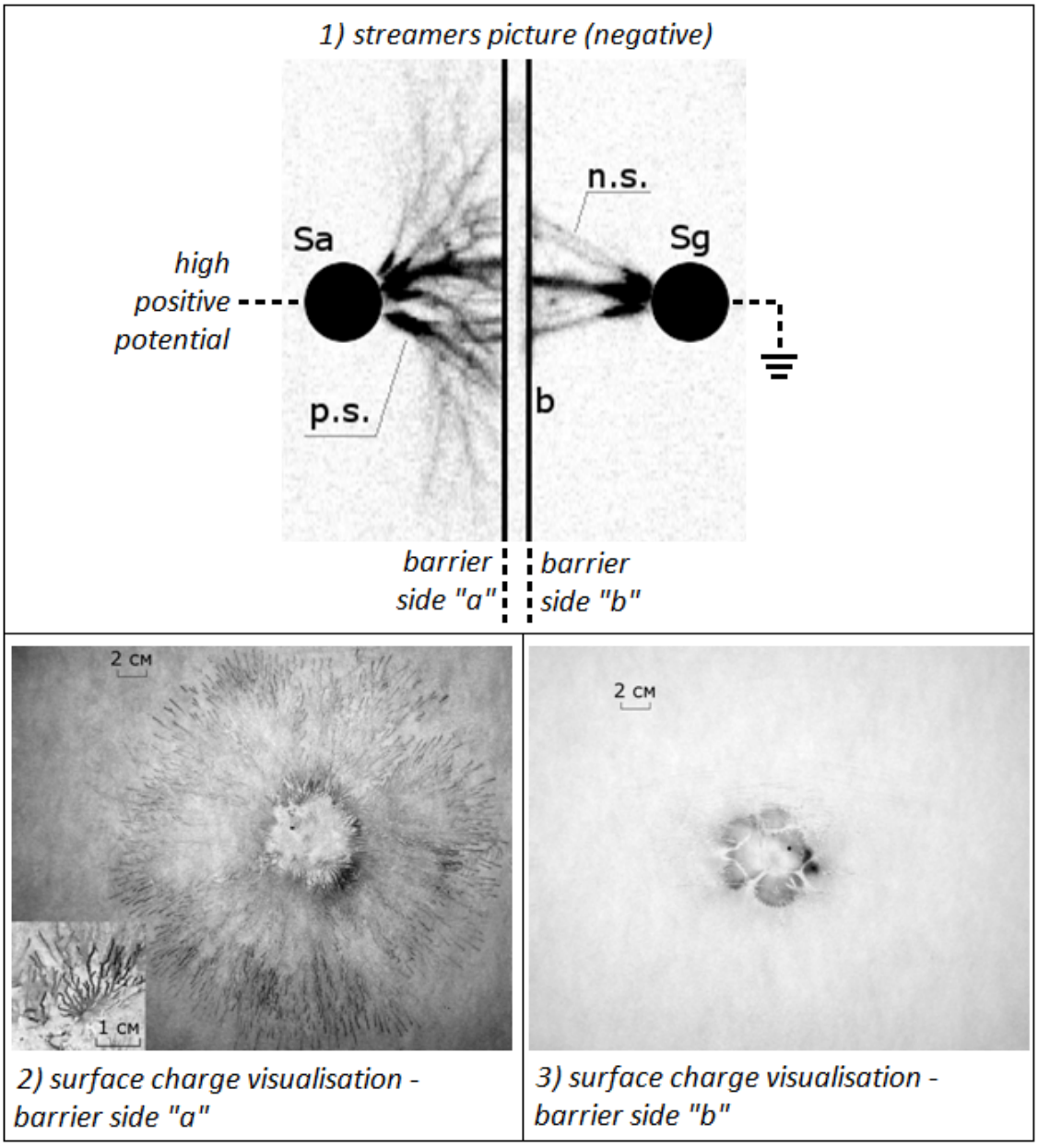

Figure 4: 1) Negative of a photograph of spark breakdown in the sphere-sphere system. "Sa" –вГУ high voltage spherical electrode, "Sg" –вГУ grounded spherical electrode, "b" –вГУ dielectric barrier. 2-3) surface charge visualization on the opposite barrier sides.

observed, which is reproduced on the other side of the barrier. It is interesting that in this situation the spark channel does not go along the shortest path between the electrodes: at the photo (Figure 5b) the spark channel does not close from the end of the barrier directly to the grounded plane — instead the channel goes along the opposite side of the barrier and closes on the plane opposite the active electrode. This property can be explained by assuming that regions "1" and "5" are first formed (in Fig. 5a) — connecting electrodes with a barrier (resulting in two unclosed leader areas), and then the resulting pair of leaders propagate along the barrier ("2" and "3" in Figure 5a), and only when they close at the edge of the barrier, there is a single spark A channel that closes the electrodes and provides a breakdown.
The described mechanism is shown schematically in Fig. 6. This scheme also explains why the breakdown of gaps in the case of a large-diameter barrier occurs with a small length of streamers, which is not enough to bend the barrier. Indeed, the leader channels originate from short streamers connecting the electrodes to a barrier, and further propagation of the discharge occurs already in the leader stage. However, it is generally assumed that at moderate voltages (up to about 400 kV [3]), the formation of a leader is possible only when the pair of electrodes close up the streamers. Otherwise, the heating of the streamer channels with Joule heat is not enough to transfer the plasma in the channels from the low-temperature (nonequilibrium) to the high-temperature (equilibrium) state. As in this case, the necessary heating is achieved, if the streamer channels do not explicitly close the air gap (Fig. 4), they are separated by a solid dielectric barrier.
The necessary heat is released as a result of the capacitance presence described above, which arises between the charge spots on the barrier. Due to the large area of the spots and the small thickness of the barrier, the capacity can be quite large. Consider in the first approximation the situation after the emergence of primary and secondary streamers as charging the RC circuit from the voltage source U, in which C is the capacity of the pair of charge spots on the barrier, R is the resistance of the streamer channels. In such a system, the energy stored in the capacitor ($CU^2/2$) is equal to the energy of Joule losses scattered by the resistance. This implies the presence of a link –вЃY increasing the capacitance C entails an increase in the thermal energy released in the streamer channels. It is due to the large capacity between the charge spots on the barrier that it becomes possible to form a pair of leaders ("opposite leaders") from unclosed streamer channels.

4 Consequences for high-voltage insulation

Since the threshold for the formation of opposite leaders in the described scheme is determined by the capacitive electric energy accumulated in the barrier between the charge spots, the breakdown voltage in such a situation does not depend on the diameter of the barrier. Indeed, experiments show that while the diameter of the barrier is small, the breakdown voltage depends linearly on the diameter. However at some point the curve suffers a break and reaches a constant (within the inaccuracy) level (Fig. 7). Analysis of the photographs of spark channels shows that in the first section of this dependence the channels have an "enveloping" shape, and on the second one — the channels stick along the surface in pair, which is characteristic for

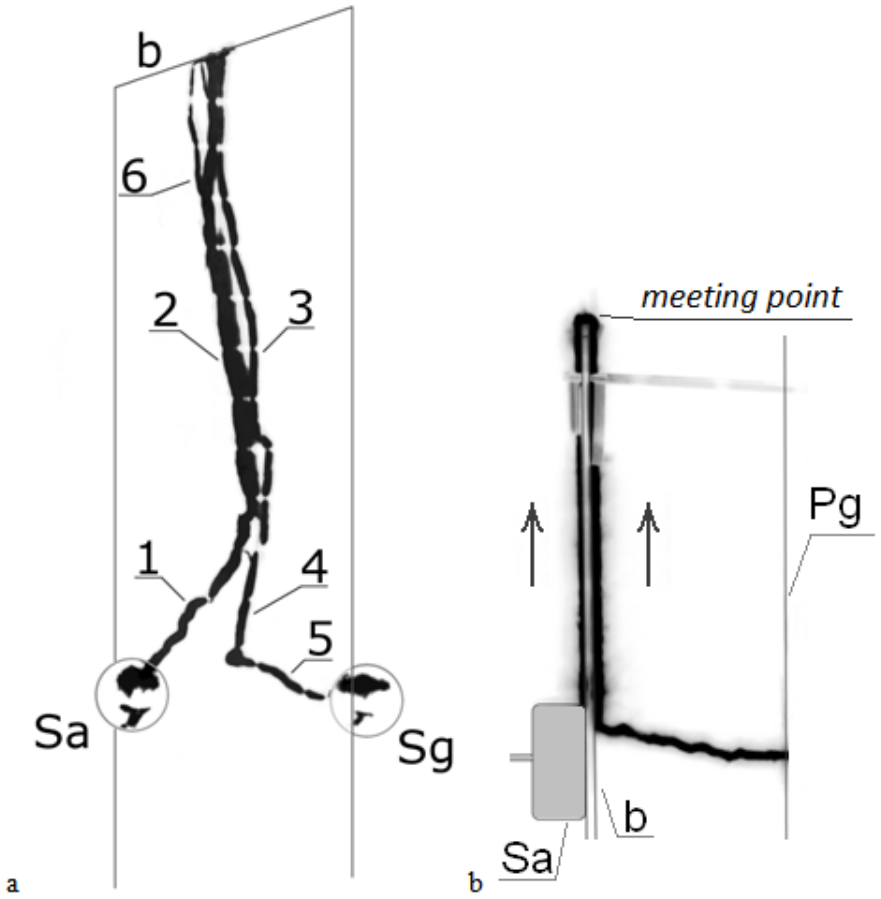

Figure 5: Breakdown by opposite leaders in the sphere-sphere electrode system (a) and in the cylinder-plane electrode system (b). Pictures negatives. "Sa" — high-voltage electrode, "Sg" вЃ Y grounded spherical electrode, "Pg" –вЃ Y grounded plane electrode, "b" вЃ Y dielectric barrier. "1" — the section of the positive leader channel from the active electrode to the barrier, "2", "3" — a pair of positive and negative leader channels spread along the upper and lower surfaces of the barrier: on the side of the active ("2") and grounded ("3") electrodes , "4" — the section of the negative leader channel spreads over the surface of the barrier from the side of the grounded electrode, "5" — the negative leader channel section from the grounded electrode to the barrier, "6" –вЃ Y the branch point of the positive leader channel. The images of the electrodes and the barrier are artificially imprinted to the photograph during the processing of the data.

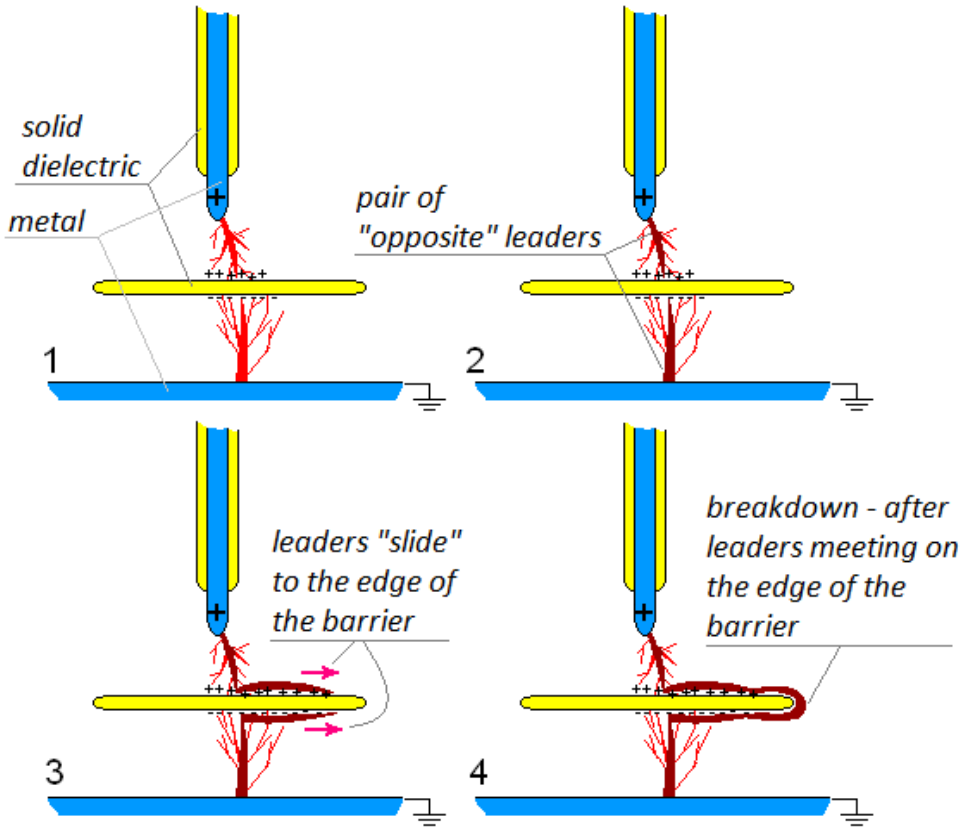

Figure 6: "Opposite leaders" formation outline.

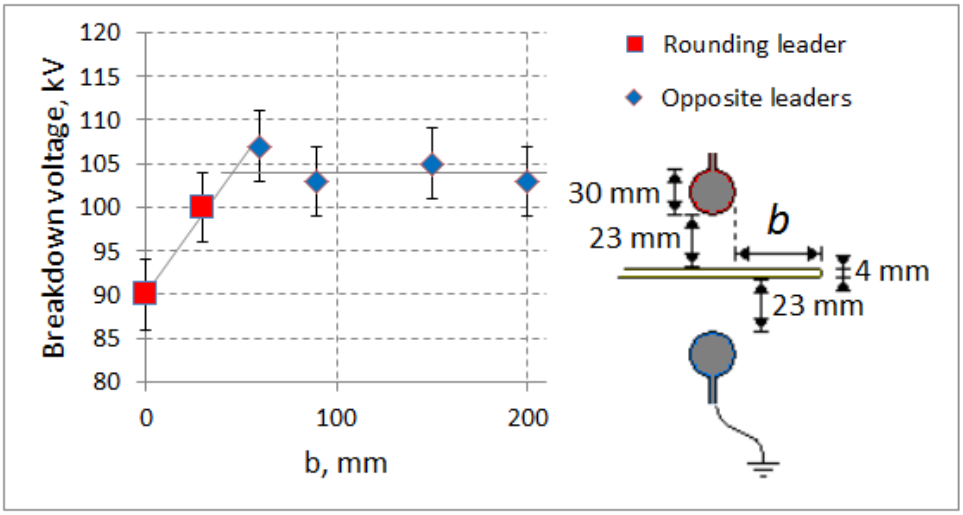

Figure 7: Dependence of breakdown voltage on the "offset" b.

opposite leaders.

5 Conclusions

1. A new mechanism for leadersвЃЄ formation in systems with solid dielectric barriers is identified and described — "opposite leaders". The feature of the mechanism is the formation of different polarity leaders pair, extending to the barrier from different sides.

2. In вЃЁopposite leadersвЃ№ mode the heating in streamers channels (which is necessary for streamer-to-leader transform) is due to the passage of significant charge deposited on the barrier. The accumulation of significant charge on the barrier becomes possible due to the fact that charge accumulates in the form of two large unipolar spots spaced a short distance (the thickness of the barrier). Thus, an effective large capacity is formed in which charge is accumulated.

3. The mechanism of "opposite leaders" limits the breakdown strength of systems with large-diameter dielectric barriers, in which breakdown along the trajectory "bypassing" the barrier is obstructed

References

[1] Stishkov Yu.K., Samusenko A.V., Subbotskii A.S., Kovalev A. N. Experimental study of pulsed corona discharge in air. Technical physics. 2010. Vol. 55. вЊЏ 11. P. 1569вЃY1576.

[2] Raizer Yu. P.. Gas Discharge Physics. Springer, 1991. 449 p.

[3] Bazelyan E. M., Raizer Yu. P. Spark Discharge. CRC–Press. 1998. 400 P.

[4] Bazelyan E. M., Raizer Yu. P. Lightning Physics and Lightning Protection Taylor & Francis 2001. 320 P.

Andrey Samusenko, St. Petersburg, Russia
Yury Stishkov, St. Petersburg, Russia

Cases of integrability corresponding to the motion of a pendulum in the four-dimensional space

Maxim V. Shamolin

shamolin@rambler.ru, shamolin@imec.msu.ru

Abstract

In this activity, we systematize some results on the study of the equations of a motion of dynamically symmetric four-dimensional fixed rigid bodies-pendulums located in a nonconservative force fields. The form of these equations is taken from the dynamics of real fixed rigid bodies placed in a homogeneous flow of a medium. In parallel, we study the problem of a motion of a free four-dimensional rigid body also located in a similar force fields. Herewith, this free rigid body is influenced by a nonconservative tracing force; under action of this force, either the magnitude of the velocity of some characteristic point of the body remains constant, which means that the system possesses a nonintegrable servo constraint, or the center of mass of the body moves rectilinearly and uniformly; this means that there exists a nonconservative couple of forces in the system.

1 Introduction

Earlier (see [1, 2]), the author already proved the complete integrability of the equations of a plane-parallel motion of a fixed rigid body–pendulum in a homogeneous flow of a medium under the jet flow conditions when the system of dynamical equations possesses a first integral, which is a transcendental (in the sense of the theory of functions of a complex variable, i.e., it has essential singularities) function of quasi-velocities. It was assumed that the interaction of the medium with the body is concentrated on a part of the surface of the body that has the form of a (one-dimensional) plate. In [2, 3], the planar problem was generalized to the spatial (three-dimensional) case, where the system of dynamical equations has a complete set of transcendental first integrals. It was assumed that the interaction of the homogeneous medium flow with the fixed body (the spherical pendulum) is concentrated on a part of the body surface that has the form of a planar (two-dimensional) disk. Later on (see [4, 5]), the equations of motion of the fixed dynamically symmetric four-dimensional rigid bodies, where the force field is concentrated on a part of the body surface that has the form of a (three-dimensional) disk.

In this activity, the results relate to the case where all interaction of the homogeneous flow of a medium with the fixed body is concentrated on that part of the surface

of the body, which has the form of a three-dimensional disk, and the action of the force is concentrated in a direction perpendicular to this disk. These results are systematized and are presented in invariant form.

2 Model assumptions

Let consider the homogeneous three-dimensional disk $\mathcal{D}^3$ (with the center in the point D), the hyperplane of which perpendicular to the holder OD in the four-dimensional Euclidean space $\mathbf{E}^4$. The disk is rigidly fixed perpendicular to the tool holder OD located on the (generalized) spherical hinge O, and it flows about homogeneous fluid flow. In this case, the body is a physical (generalized spherical) pendulum. The medium flow moves from infinity with constant velocity $\mathbf{v} = \mathbf{v}_\infty \neq \mathbf{0}$. Assume that the holder does not create a resistance.

We suppose that the total force $\mathbf{S}$ of medium flow interaction perpendicular to the disk $\mathcal{D}^3$, and point N of application of this force is determined by at least the angle of attack α, which is made by the velocity vector $\mathbf{v}_D$ of the point D with respect to the flow and the holder OD; the total force is also determined by the angles β_1, β_2, which are made in the hyperplane of the disk $\mathcal{D}^3$ (thus, $(v, \alpha, \beta_1, \beta_2)$ are the (generalized) spherical coordinates of the tip of the vector $\mathbf{v}_D$), and also the reduced angular velocity tensor $\tilde{\omega} \cong l\tilde{\Omega}/v_D,\ v_D = |\mathbf{v}_D|$ (l is the length of the holder, $\tilde{\Omega}$ is the angular velocity tensor of the pendulum). Such conditions generalize the model of streamline flow around spatial bodies [3, 5, 6].

The vector $\mathbf{e} = \mathbf{OD}/l$ determines the orientation of the holder. Then $\mathbf{S} = s(\alpha)v_D^2\mathbf{e}$, where $s(\alpha) = s_1(\alpha)\operatorname{sign}\cos\alpha$, and the resistance coefficient $s_1 \geq 0$ depends only on the angle of attack α. By the axe-symmetry properties of the body–pendulum with respect to the point D, the function $s(\alpha)$ is even.

Let $Dx_1x_2x_3x_4$ be the coordinate system rigidly attached to the body, herewith, the axis Dx_1 has a direction vector $\mathbf{e}$, and the axes Dx_2, Dx_3 and Dx_4 lie in the hyperplane of the disk $\mathcal{D}^3$.

By the angles (ξ, η_1, η_2), we define the position of the holder OD in the four-dimensional space $\mathbf{E}^4$. In this case, the angle ξ is made by the holder and the direction of the over-running medium flow. In other words, the angles introduced are the (generalized) spherical coordinates of the point D of the center of a disk $\mathcal{D}^3$ on the three-dimensional sphere of the constant radius OD.

The space of positions of this (generalized) spherical (physical) pendulum is the three-dimensional sphere

$$\mathbf{S}^3\{(\xi, \eta_1, \eta_2) \in \mathbf{R}^3 :\ 0 \leq \xi, \eta_1 \leq \pi,\ \eta_2 \bmod 2\pi\}, \tag{1}$$

and its phase space is the tangent bundle of the three-dimensional sphere

$$T_*\mathbf{S}^3\{(\dot{\xi}, \dot{\eta_1}, \dot{\eta_2}; \xi, \eta_1, \eta_2) \in \mathbf{R}^6 :\ 0 \leq \xi, \eta_1 \leq \pi,\ \eta_2 \bmod 2\pi\}. \tag{2}$$

The tensor (of the second-rank) $\tilde{\Omega}$ of the angular velocity in the coordinate system

$Dx_1x_2x_3x_4$, we define through the skew-symmetric matrix

$$\tilde{\Omega} = \begin{pmatrix} 0 & -\omega_6 & \omega_5 & -\omega_3 \\ \omega_6 & 0 & -\omega_4 & \omega_2 \\ -\omega_5 & \omega_4 & 0 & -\omega_1 \\ \omega_3 & -\omega_2 & \omega_1 & 0 \end{pmatrix}, \ \tilde{\Omega} \in \mathrm{so}(4). \tag{3}$$

The distance from the center D of the disk $\mathcal{D}^3$ to the center of pressure (the point N) has the form $|\mathbf{r}_N| = r_N = DN\,(\alpha, \beta_1, \beta_2, l\Omega/v_D)$, where $\mathbf{r}_N = \{0, x_{2N}, x_{3N}, x_{4N}\}$ in system $Dx_1x_2x_3x_4$ (we omit the wave over Ω).

3 Set of dynamical equations in Lie algebra so(4)

Let a four-dimensional rigid body Θ of mass m with smooth three-dimensional boundary $\partial\Theta$ be under the influence of a nonconservative force field; this can be interpreted as a motion of the body in a resisting medium that fills up the four-dimensional domain of Euclidean space $\mathbf{E}^4$. We assume that the body is dynamically symmetric. In this case, there are two logical possibilities of the representation of its inertia tensor in the case of existence of *two* independent equations on the principal moments of inertia; i.e., either in some coordinate system $Dx_1x_2x_3x_4$ attached to the body, the operator of inertia has the form

$$\mathrm{diag}\{I_1, I_2, I_2, I_2\}, \tag{4}$$

or the form $\mathrm{diag}\{I_1, I_1, I_3, I_3\}$. In the first case, the body is dynamically symmetric in the hyperplane $Dx_2x_3x_4$ and in the second case, the two-dimensional planes Dx_1x_2 and Dx_3x_4 are planes of dynamical symmetry of the body.

The configuration space of a free, n-dimensional rigid body is the direct product $\mathbf{R}^n \times \mathrm{SO}(n)$ of the space $\mathbf{R}^n$, which defines the coordinates of the center of mass of the body, and the rotation group $\mathrm{SO}(n)$, which defines the rotations of the body about its center of mass and has dimension $n + n(n-1)/2 = n(n+1)/2$.

Respectively, the dimension of the phase space is equal to $n(n+1)$.

In particular, if Ω is the tensor of angular velocity of a four-dimensional rigid body (it is a second-rank tensor, see [3, 6, 7, 8]), $\Omega \in \mathrm{so}(4)$, then *the part of the dynamical equations of motion corresponding to the Lie algebra* so(4) has the following form (see [9, 10, 11, 12]):

$$\dot{\Omega}\Lambda + \Lambda\dot{\Omega} + [\Omega,\ \Omega\Lambda + \Lambda\Omega] = M, \tag{5}$$

$$\Lambda = \mathrm{diag}\{\lambda_1, \lambda_2, \lambda_3, \lambda_4\},\ \lambda_1 = \frac{-I_1 + I_2 + I_3 + I_4}{2},$$

$$\lambda_2 = \frac{I_1 - I_2 + I_3 + I_4}{2},\ \lambda_3 = \frac{I_1 + I_2 - I_3 + I_4}{2},\ \lambda_4 = \frac{I_1 + I_2 + I_3 - I_4}{2},$$

$M = M_F$ is the natural projection of the moment of external forces $\mathbf{F}$ acting on the body in $\mathbf{R}^4$ on the natural coordinates of the Lie algebra so(4) and $[.,.]$ is the commutator in so(4). The skew-symmetric matrix corresponding to this second-rank tensor $\Omega \in \mathrm{so}(4)$ we represent in the form (3), where ω_1, ω_2, ω_3, ω_4, ω_5, ω_6 are

the components of the tensor of angular velocity corresponding to the projections on the coordinates of the Lie algebra so(4).
In this case, obviously, the following relations hold: $\lambda_i - \lambda_j = I_j - I_i$ for any $i, j = 1, \ldots, 4$.
For the calculation of the moment of an external force acting on the body, we need to construct the mapping $\mathbf{R}^4 \times \mathbf{R}^4 \longrightarrow$ so(4), than maps a pair of vectors $(\mathbf{DN}, \mathbf{F}) \in \mathbf{R}^4 \times \mathbf{R}^4$ from $\mathbf{R}^4 \times \mathbf{R}^4$ to an element of the Lie algebra so(4), where $\mathbf{DN} = \{0, x_{2N}, x_{3N}, x_{4N}\}$, $\mathbf{F} = \{F_1, F_2, F_3, F_4\}$, and $\mathbf{F}$ is an external force acting on the body. For this end, we construct the following auxiliary matrix

$$\begin{pmatrix} 0 & x_{2N} & x_{3N} & x_{4N} \\ F_1 & F_2 & F_3 & F_4 \end{pmatrix}.$$

Then the right-hand side of system (5) takes the form

$$M = \{M_1, M_2, M_3, M_4, M_5, M_6\} =$$

$$= \{x_{3N}F_4 - x_{4N}F_3, x_{4N}F_2 - x_{2N}F_4, -x_{4N}F_1, x_{2N}F_3 - x_{3N}F_2, x_{3N}F_1, -x_{2N}F_1\},$$

where M_1, M_2, M_3, M_4, M_5, M_6 are the components of tensor of the moment of external forces in the projections on the coordinates in the Lie algebra so(4),

$$M = \begin{pmatrix} 0 & -M_6 & M_5 & -M_3 \\ M_6 & 0 & -M_4 & M_2 \\ -M_5 & M_4 & 0 & -M_1 \\ M_3 & -M_2 & M_1 & 0 \end{pmatrix}.$$

In our case of a fixed pendulum, the case (4) is realized. Then the dynamical part of the equations of its motion has the following form:

$$\begin{aligned} &(I_1 + I_2)\dot{\omega}_1 = 0, \ (I_1 + I_2)\dot{\omega}_2 = 0, \\ &2I_2\dot{\omega}_3 + (I_1 - I_2)(\omega_2\omega_6 + \omega_1\omega_5) = x_{4N}\left(\alpha, \beta_1, \beta_2, \frac{\Omega}{v}\right) s(\alpha)v^2, \\ &(I_1 + I_2)\dot{\omega}_4 = 0, \\ &2I_2\dot{\omega}_5 + (I_1 - I_2)(\omega_4\omega_6 - \omega_1\omega_3) = -x_{3N}\left(\alpha, \beta_1, \beta_2, \frac{\Omega}{v}\right) s(\alpha)v^2, \\ &2I_2\dot{\omega}_6 + (I_2 - I_1)(\omega_4\omega_5 + \omega_2\omega_3) = x_{2N}\left(\alpha, \beta_1, \beta_2, \frac{\Omega}{v}\right) s(\alpha)v^2, \end{aligned} \tag{6}$$

since the moment of the medium interaction force is determined by the following auxiliary matrix:

$$\begin{pmatrix} 0 & x_{2N} & x_{3N} & x_{4N} \\ -s(\alpha)v_D^2 & 0 & 0 & 0 \end{pmatrix},$$

where $\{-s(\alpha)v_D^2, 0, 0, 0\}$ is the decomposition of the force $\mathbf{S}$ of medium interaction in the coordinate system $Dx_1x_2x_3x_4$.
Since the dimension of the Lie algebra so(4) is equal to 6, the system of equations (6) is a group of dynamical equations on so(4), and, simply speaking, the motion equations.

We see, that in the right-hand side of Eq. (6), first of all, it includes the angles α, β_1, β_2, therefore, this system of equations is not closed. In order to obtain a complete system of equations of motion of the pendulum, it is necessary to attach several sets of kinematic equations to the dynamic equations on the Lie algebra so(4).

3.1 Cyclic first integrals

We immediately note that the system (6), by the existing dynamic symmetry

$$I_2 = I_3 = I_4, \tag{7}$$

possesses three cyclic first integrals

$$\omega_1 \equiv \omega_1^0 = \text{const}, \ \omega_2 \equiv \omega_2^0 = \text{const}, \ \omega_4 \equiv \omega_4^0 = \text{const}. \tag{8}$$

In this case, further, we consider the dynamics of our system at zero levels:

$$\omega_1^0 = \omega_2^0 = \omega_4^0 = 0. \tag{9}$$

Under conditions (7)–(9) the system (6) has the form of unclosed system of three equations:

$$\begin{gathered} 2I_2\dot{\omega}_3 = x_{4N}\left(\alpha, \beta_1, \beta_2, \frac{\Omega}{v}\right) s(\alpha)v^2, \ 2I_2\dot{\omega}_5 = -x_{3N}\left(\alpha, \beta_1, \beta_2, \frac{\Omega}{v}\right) s(\alpha)v^2, \\ 2I_2\dot{\omega}_6 = x_{2N}\left(\alpha, \beta_1, \beta_2, \frac{\Omega}{v}\right) s(\alpha)v^2. \end{gathered} \tag{10}$$

4 First set of kinematic equations

In order to obtain a complete system of equations of motion, it needs the set of kinematic equations which relate the velocities of the point D (i.e., the center of the disk $\mathcal{D}^3$) and the over-running medium flow:

$$\mathbf{v}_D = v_D \cdot \mathbf{i}_v(\alpha, \beta_1, \beta_2) = \tilde{\Omega}\mathbf{l} + (-v_\infty)\mathbf{i}_v(-\xi, \eta_1, \eta_2), \ \mathbf{l} = \{l, 0, 0, 0\}, \tag{11}$$

$$\mathbf{i}_v(\alpha, \beta_1, \beta_2) = \begin{pmatrix} \cos\alpha \\ \sin\alpha\cos\beta_1 \\ \sin\alpha\sin\beta_1\cos\beta_2 \\ \sin\alpha\sin\beta_1\sin\beta_2 \end{pmatrix}. \tag{12}$$

The equation (11) expresses the theorem of addition of velocities in projections on the related coordinate system $Dx_1x_2x_3x_4$.
Indeed, the left-hand side of Eq. (11) is the velocity of the point D of the pendulum with respect to the flow in the projections on the related with the pendulum coordinate system $Dx_1x_2x_3x_4$. Herewith, the vector $\mathbf{i}_v(\alpha, \beta_1, \beta_2)$ is the unit vector along the axis of the vector $\mathbf{v}_D$. The vector $\mathbf{i}_v(\alpha, \beta_1, \beta_2)$ has the spherical coordinates $(1, \alpha, \beta_1, \beta_2)$ which determines the decomposition (12).

The right-hand side of the Eq. (11) is the sum of the velocities of the point D when you rotate the pendulum (the first term), and the motion of the flow (the second term). In this case, in the first term, we have the coordinates of the vector вектора $\mathbf{OD} = \{l, 0, 0, 0\}$ in the coordinate system $Dx_1x_2x_3x_4$.
We explain the second term of the right-hand side of Eq. (11) in more detail. We have in it the coordinates of the vector $(-\mathbf{v}_\infty) = \{-v_\infty, 0, 0, 0\}$ in the immovable space. In order to describe it in the projections on the related coordinate system $Dx_1x_2x_3x_4$, we need to make a (reverse) rotation of the pendulum at the angle $(-\xi)$ that is algebraically equivalent to multiplying the value $(-v_\infty)$ on the vector $\mathbf{i}_v(-\xi, \eta_1, \eta_2)$.
Thus, the first set of kinematic equations (11) has the following form in our case:

$$\begin{aligned} &v_D \cos\alpha = -v_\infty \cos\xi,\ v_D \sin\alpha \cos\beta_1 = l\omega_6 + v_\infty \sin\xi \cos\eta_1, \\ &v_D \sin\alpha \sin\beta_1 \cos\beta_2 = -l\omega_5 + v_\infty \sin\xi \sin\eta_1 \cos\eta_2, \\ &v_D \sin\alpha \sin\beta_1 \sin\beta_2 = l\omega_3 + v_\infty \sin\xi \sin\eta_1 \sin\eta_2. \end{aligned} \tag{13}$$

5 Second set of kinematic equations

We also need a set of kinematic equations which relate the angular velocity tensor $\tilde{\Omega}$ and coordinates $\dot{\xi}, \dot{\eta_1}, \dot{\eta_2}, \xi, \eta_1, \eta_2$ of the phase space (2) of pendulum studied, i.e., the tangent bundle $T_*\mathbf{S}^3\{\dot{\xi}, \dot{\eta_1}, \dot{\eta_2}; \xi, \eta_1, \eta_2\}$.
We draw the reasoning style allowing arbitrary dimension. The desired equations are obtained from the following two sets of relations. Since the motion of the body takes place in a Euclidean space $\mathbf{E}^n, n = 4$ formally, at the beginning, we express the tuple consisting of a phase variables $\omega_3, \omega_5, \omega_6$, through new variable z_1, z_2, z_3 (from the tuple z). For this, we draw the following turn by the angle η_1, η_2:

$$\begin{pmatrix} \omega_3 \\ \omega_5 \\ \omega_6 \end{pmatrix} = T_{1,2}(\eta_2) \circ T_{2,3}(\eta_1) \begin{pmatrix} z_1 \\ z_2 \\ z_3 \end{pmatrix}, \tag{14}$$

$$T_{2,3}(\eta_1) = \begin{pmatrix} 1 & 0 & 0 \\ 0 & \cos\eta_1 & -\sin\eta_1 \\ 0 & \sin\eta_1 & \cos\eta_1 \end{pmatrix},\ T_{1,2}(\eta_2) = \begin{pmatrix} \cos\eta_2 & -\sin\eta_2 & 0 \\ \sin\eta_2 & \cos\eta_2 & 0 \\ 0 & 0 & 1 \end{pmatrix}.$$

In other words, the relations

$$\begin{pmatrix} z_1 \\ z_2 \\ z_3 \end{pmatrix} = T_{2,3}(-\eta_1) \circ T_{1,2}(-\eta_2) \begin{pmatrix} \omega_3 \\ \omega_5 \\ \omega_6 \end{pmatrix}$$

hold, i.e.,

$$\begin{aligned} z_1 &= \omega_3 \cos\eta_1 + \omega_5 \sin\eta_2, \\ z_2 &= -\omega_3 \cos\eta_1 \sin\eta_2 + \omega_5 \cos\eta_1 \cos\eta_2 + \omega_6 \sin\eta_1, \\ z_3 &= \omega_3 \sin\eta_1 \sin\eta_2 - \omega_5 \sin\eta_1 \cos\eta_2 + \omega_6 \cos\eta_1. \end{aligned}$$

Then we substitute the following relationship instead of the variable z:

$$z_3 = \dot{\xi},\ z_2 = -\dot{\eta_1}\frac{\sin\xi}{\cos\xi},\ z_1 = \dot{\eta_2}\frac{\sin\xi}{\cos\xi}\sin\eta_1. \tag{15}$$

Thus, two sets of Eqs. (14) and (15) give the second set of kinematic equations:

$$\begin{aligned}
\omega_3 &= \dot{\xi}\sin\eta_1\sin\eta_2 + \dot{\eta_1}\frac{\sin\xi}{\cos\xi}\cos\eta_1\sin\eta_2 + \dot{\eta_2}\frac{\sin\xi}{\cos\xi}\sin\eta_1\cos\eta_2,\\
\omega_5 &= -\dot{\xi}\sin\eta_1\cos\eta_2 - \dot{\eta_1}\frac{\sin\xi}{\cos\xi}\cos\eta_1\cos\eta_2 + \dot{\eta_2}\frac{\sin\xi}{\cos\xi}\sin\eta_1\sin\eta_2,\\
\omega_6 &= \dot{\xi}\cos\eta_1 - \dot{\eta_1}\frac{\sin\xi}{\cos\xi}\sin\eta_1.
\end{aligned} \tag{16}$$

We see that three sets of the relations (10), (13), and (16) form the closed system of equations.
These three sets of equations include the following functions:

$$x_{2N}\left(\alpha,\beta_1,\beta_2,\frac{\Omega}{v_D}\right),\ x_{3N}\left(\alpha,\beta_1,\beta_2,\frac{\Omega}{v_D}\right),\ x_{4N}\left(\alpha,\beta_1,\beta_2,\frac{\Omega}{v_D}\right),\ s(\alpha).$$

In this case, the function s is considered to be dependent only on α, and the functions x_{2N}, x_{3N}, x_{4N} may depend on, along with the angles α, β_1, β_2, generally speaking, the reduced angular velocity tensor $l\tilde{\Omega}/v_D$.

6 Case where the moment of nonconservative forces depends on the angular velocity

6.1 Dependence on the angular velocity

This section is devoted to dynamics of the four-dimensional rigid body in the four-dimensional space. Since this subsection is devoted to the study of the case of the motion where the moment of forces depends on the angular velocity tensor, we introduce this dependence in the general case; this will allow us to generalize this dependence to multi-dimensional bodies.
Let $x = (x_{1N}, x_{2N}, x_{3N}, x_{4N})$ be the coordinates of the point N of application of a nonconservative force (interaction with a medium) on the three-dimensional disk $\mathcal{D}^3$, and $Q = (Q_1, Q_2, Q_3, Q_4)$ be the components independent of the angular velocity. We introduce only the linear dependence of the functions $(x_{1N}, x_{2N}, x_{3N}, x_{4N})$ on the angular velocity tensor Ω since the introduction of this dependence itself is not a priori obvious (see [1, 3, 5]).
Thus, we accept the following dependence: $x = Q + R$, where $R = (R_1, R_2, R_3, R_4)$ is a vector-valued function containing the angular velocity tensor Ω. Here, the dependence of the function R on the angular velocity is gyroscopic:

$$R = \begin{pmatrix} R_1\\ R_2\\ R_3\\ R_4 \end{pmatrix} = -\frac{1}{v_D}\begin{pmatrix} 0 & -\omega_6 & \omega_5 & -\omega_3\\ \omega_6 & 0 & -\omega_4 & \omega_2\\ -\omega_5 & \omega_4 & 0 & -\omega_1\\ \omega_3 & -\omega_2 & \omega_1 & 0 \end{pmatrix}\begin{pmatrix} h_1\\ h_2\\ h_3\\ h_4 \end{pmatrix},$$

where (h_1, h_2, h_3, h_4) are certain positive parameters (comp. with [2, 4]).

Now, for our problem, since $x_{1N} = x_N \equiv 0$, we have

$$x_{2N} = Q_2 - h_1\frac{\omega_6}{v_D},\ x_{3N} = Q_3 + h_1\frac{\omega_5}{v_D},\ x_{4N} = Q_4 - h_1\frac{\omega_3}{v}.$$

Thus, the function $\mathbf{r}_N$ is selected in the following form (the disk $\mathcal{D}^3$ is defined by the equation $x_{1N} \equiv 0$):

$$\mathbf{r}_N = \begin{pmatrix} 0 \\ x_{2N} \\ x_{3N} \\ x_{4N} \end{pmatrix} = R(\alpha)\mathbf{i}_N - \frac{1}{v_D}\tilde{\Omega}h, \tag{17}$$

$$\mathbf{i}_N = \mathbf{i}_v\left(\frac{\pi}{2}, \beta_1, \beta_2\right),\ h = \begin{pmatrix} h_1 \\ h_2 \\ h_3 \\ h_4 \end{pmatrix},\ \tilde{\Omega} = \begin{pmatrix} 0 & -\omega_6 & \omega_5 & -\omega_3 \\ \omega_6 & 0 & -\omega_4 & \omega_2 \\ -\omega_5 & \omega_4 & 0 & -\omega_1 \\ \omega_3 & -\omega_2 & \omega_1 & 0 \end{pmatrix}$$

(see (3), (12)).
Thus, the following relations

$$x_{2N} = R(\alpha)\cos\beta_1 - h_1\omega_6/v_D,\ x_{3N} = R(\alpha)\sin\beta_1\cos\beta_2 + h_1\omega_5/v_D,$$

$$x_{4N} = R(\alpha)\sin\beta_1\sin\beta_2 - h_1\omega_3/v_D,$$

hold, which show that an additional dependence of the damping (or accelerating in some domains of the phase space) moment of the nonconservative forces is also present in the system considered (i.e., the moment depends on the angular velocity tensor).
And so, for the construction of the force field, we use the pair of dynamical functions $R(\alpha), s(\alpha)$; the information about them is of a qualitative nature. Similarly to the choice of the Chaplygin analytical functions (see [1, 2]), we take the dynamical functions s and R as follows:

$$R(\alpha) = A\sin\alpha,\ s(\alpha) = B\cos\alpha,\ A, B > 0. \tag{18}$$

6.2 Reduced systems

Theorem 6.1. *The simultaneous equations (6), (13), (16) under conditions (7)–(9), (17), (18) can be reduced to the dynamical system on the tangent bundle (2) of the three-dimensional sphere (1).*

Indeed, if we introduce the dimensionless parameters and the differentiation by the formulas

$$b_* = ln_0,\ n_0^2 = \frac{AB}{2I_2},\ H_{1*} = \frac{h_1 B}{2I_2 n_0},\ < \cdot >= n_0 v_\infty <'>, \tag{19}$$

then the obtained equations have the following form ($b_* > 0,\ H_{1*} > 0$):

$$\begin{aligned}
&\xi'' + (b_* - H_{1*})\xi' \cos\xi + \sin\xi\cos\xi - [\eta_1'^2 + \eta_2'^2 \sin^2\eta_1]\frac{\sin\xi}{\cos\xi} = 0,\\
&\eta_1'' + (b_* - H_{1*})\eta_1' \cos\xi + \xi'\eta_1' \frac{1+\cos^2\xi}{\cos\xi\sin\xi} - \eta_2'^2 \sin\eta_1\cos\eta_1 = 0,\\
&\eta_2'' + (b_* - H_{1*})\eta_2' \cos\xi + \xi'\eta_2' \frac{1+\cos^2\xi}{\cos\xi\sin\xi} + 2\eta_1'\eta_2' \frac{\cos\eta_1}{\cos\eta_1} = 0.
\end{aligned} \tag{20}$$

After the transition from the variables z (about the variables z see (15)) to the intermediate dimensionless variables w

$$z_k = n_0 v_\infty (1 + b_* H_{1*}) Z_k,\ k = 1, 2,\ z_3 = n_0 v_\infty (1 + b_* H_{1*}) Z_3 - n_0 v_\infty b_* \sin\xi,$$

system (20) is equivalent to the system

$$\xi' = (1 + b_* H_{1*}) Z_3 - b_* \sin\xi, \tag{21}$$

$$Z_3' = -\sin\xi\cos\xi + (1 + b_* H_{1*})(Z_1^2 + Z_2^2)\frac{\cos\xi}{\sin\xi} + H_{1*} Z_3 \cos\xi, \tag{22}$$

$$Z_2' = -(1 + b_* H_{1*}) Z_2 Z_3 \frac{\cos\xi}{\sin\xi} - (1 + b_* H_{1*}) Z_1^2 \frac{\cos\xi}{\sin\xi}\frac{\cos\eta_1}{\sin\eta_1} + H_{1*} Z_2 \cos\xi, \tag{23}$$

$$Z_1' = -(1 + b_* H_{1*}) Z_1 Z_3 \frac{\cos\xi}{\sin\xi} + (1 + b_* H_{1*}) Z_1 Z_2 \frac{\cos\xi}{\sin\xi}\frac{\cos\eta_1}{\sin\eta_1} + H_{1*} Z_1 \cos\xi, \tag{24}$$

$$\eta_1' = -(1 + b_* H_{1*}) Z_2 \frac{\cos\xi}{\sin\xi}, \tag{25}$$

$$\eta_2' = (1 + b_* H_{1*}) Z_1 \frac{\cos\xi}{\sin\xi\sin\eta_1}, \tag{26}$$

on the tangent bundle $T_*\mathbf{S}^3\{(Z_3, Z_2, Z_1; \xi, \eta_1, \eta_2) \in \mathbf{R}^6 :\ 0 \le \xi, \eta_1 \le \pi,\ \eta_2 \bmod 2\pi\}$ of the three-dimensional sphere $\mathbf{S}^3\{(\xi, \eta_1, \eta_2) \in \mathbf{R}^3 :\ 0 \le \xi, \eta_1 \le \pi,\ \eta_2 \bmod 2\pi\}$.
We see that the independent fifth-order subsystem (21)–(25) (due to cyclicity of the variable η_2) can be substituted into the sixth-order system (21)–(26) and can be considered separately on its own five-dimensional manifold.

6.3 Complete list of the first integrals

We turn now to the integration of the desired sixth-order system (21)–(26) (without any simplifications, i.e., in the presence of all coefficients).
Similarly, for the complete integration of sixth-order system (21)–(26), in general, we need five independent first integrals. However, after the change of variables

$$w_3 = -Z_3,\ w_2 = \sqrt{Z_2^2 + Z_1^2},\ w_1 = \frac{Z_2}{Z_1}, \tag{27}$$

the system (21)–(26) splits as follows:

$$\left.\begin{aligned} \xi' &= -(1+b_*H_{1*})w_3 - b_*\sin\xi, \\ w_3' &= \sin\xi\cos\xi - (1+b_*H_{1*})w_2^2\frac{\cos\xi}{\sin\xi} + H_{1*}w_3\cos\xi, \\ w_2' &= (1+b_*H_{1*})w_2w_3\frac{\cos\xi}{\sin\xi} + H_{1*}w_2\cos\xi, \end{aligned}\right\} \tag{28}$$

$$\left.\begin{aligned} w_1' &= d_1(w_3,w_2,w_1;\xi,\eta_1,\eta_2)\frac{1+w_1^2}{w_1}\frac{\cos\eta_1}{\sin\eta_1}, \\ \eta_1' &= d_1(w_3,w_2,w_1;\xi,\eta_1,\eta_2), \end{aligned}\right\} \tag{29}$$

$$\eta_2' = d_2(w_3,w_2,w_1;\xi,\eta_1,\eta_2), \tag{30}$$

$$\begin{aligned} &d_1(w_3,w_2,w_1;\xi,\eta_1,\eta_2) = \\ &= -(1+b_*H_{1*})Z_2(w_3,w_2,w_1)\frac{\cos\xi}{\sin\xi} = \mp\frac{w_1w_2}{\sqrt{1+w_1^2}}\frac{\cos\xi}{\sin\xi}, \\ &d_2(w_3,w_2,w_1;\xi,\eta_1,\eta_2) = \\ &= (1+b_*H_{1*})Z_1(w_3,w_2,w_1)\frac{\cos\xi}{\sin\xi\sin\eta_1} = \pm\frac{w_2}{\sqrt{1+w_1^2}}\frac{\cos\xi}{\sin\xi\sin\eta_1}, \end{aligned}$$

in this case $Z_k = Z_k(w_3,w_2,w_1)$, $k=1,2,3$, are the functions by virtue of change (27).

We see that the independent third-order subsystem (28) (which can be considered separately on its own three-dimensional manifold), the independent second-order subsystem (29) (after the change of independent variable) can be substituted into the sixth-order system (28)–(30), and also Eq. (30) on η_2 is separated (due to cyclicity of the variable η_2).

Thus, for the complete integration of the system (28)–(30), it suffices to specify two independent first integrals of system (28), one first integral of system (29), and an additional first integral that "attaches" Eq. (30) (*i.e., only four*).

First, we compare the third-order system (28) with the nonautonomous second-order system

$$\begin{aligned} \frac{dw_3}{d\xi} &= \frac{\sin\xi\cos\xi - (1+b_*H_{1*})w_2^2\cos\xi/\sin\xi + H_{1*}w_3\cos\xi}{-(1+b_*H_{1*})w_3 - b_*\sin\xi}, \\ \frac{dw_2}{d\xi} &= \frac{(1+b_*H_{1*})w_2w_3\cos\xi/\sin\xi + H_{1*}w_2\cos\xi}{-(1+b_*H_{1*})w_3 - b_*\sin\xi}. \end{aligned} \tag{31}$$

Using the substitution $\tau = \sin\xi$, we rewrite system (31) in the algebraic form:

$$\begin{aligned} \frac{dw_3}{d\tau} &= \frac{\tau - (1+b_*H_{1*})w_2^2/\tau + H_{1*}w_3}{-(1+b_*H_{1*})w_3 - b_*\tau}, \\ \frac{dw_2}{d\tau} &= \frac{(1+b_*H_{1*})w_2w_3/\tau + H_{1*}w_2}{-(1+b_*H_{1*})w_3 - b_*\tau}. \end{aligned} \tag{32}$$

Further, if we introduce the uniform variables by the formulas $w_3 = u_2\tau,\ w_2 = u_1\tau$, we reduce system (32) to the following form:

$$\begin{aligned}\tau\frac{du_2}{d\tau} &= \frac{(1+b_*H_{1*})(u_2^2-u_1^2)+(b_*+H_{1*})u_2+1}{-(1+b_*H_{1*})u_2-b_*},\\ \tau\frac{du_1}{d\tau} &= \frac{2(1+b_*H_{1*})u_1u_2+(b_*+H_{1*})u_1}{-(1+b_*H_{1*})u_2-b_*}.\end{aligned} \tag{33}$$

We compare the second-order system (33) with the nonautonomous first-order equation

$$\frac{du_2}{du_1} = \frac{1-(1+b_*H_{1*})(u_1^2-u_2^2)+(b_*+H_{1*})u_2}{2(1+b_*H_{1*})u_1u_2+(b_*+H_{1*})u_1}, \tag{34}$$

which can be easily reduced to the exact differential equation

$$d\left(\frac{(1+b_*H_{1*})(u_2^2+u_1^2)+(b_*+H_{1*})u_2+1}{u_1}\right)=0.$$

Therefore, Eq. (34) has the following first integral:

$$\frac{(1+b_*H_{1*})(u_2^2+u_1^2)+(b_*+H_{1*})u_2+1}{u_1} = C_1 = \text{const}, \tag{35}$$

which in the old variables has the form

$$\Theta_1(w_3,w_2;\xi) =$$

$$= \frac{(1+b_*H_{1*})(w_3^2+w_2^2)+(b_*+H_{1*})w_3\sin\xi+\sin^2\xi}{w_2\sin\xi} = C_1 = \text{const}. \tag{36}$$

Then the additional first integral has the following structure:

$$\Theta_2(w_3,w_2;\xi) = G\left(\sin\xi,\frac{w_3}{\sin\xi},\frac{w_2}{\sin\xi}\right) = C_2 = \text{const}. \tag{37}$$

Thus, we have found two first integrals (36), (37) of the independent third-order system (28). For its complete integrability, it suffices to find one first integral for the system (29), and an additional first integral that "attaches" Eq. (30).
Indeed, the desired first integrals have the following forms:

$$\Theta_3(w_1;\eta_1) = \frac{\sqrt{1+w_1^2}}{\sin\eta_1} = C_3 = \text{const}, \tag{38}$$

$$\Theta_4(w_1;\eta_1,\eta_2) = \eta_2 \pm \operatorname{arctg}\frac{\cos\eta_1}{\sqrt{C_3^2\sin^2\eta_1-1}} = C_4 = \text{const}, \tag{39}$$

in this case, in the left-hand side of Eq. (39), we must substitute instead of C_3 the first integral (38).

Theorem 6.2. *The sixth-order system (28)–(30) possesses the sufficient number (four) of the independent first integrals (36), (37), (38), (39).*

Theorem 6.3. *Three sets of relations (6), (13), (16) under conditions (7)–(9), (17), (18) possess four the first integrals (the complete set), which are the transcendental function (in the sense of complex analysis) and are expressed as a finite combination of elementary functions.*

6.4 Topological analogies

We can present two groups of analogies, which describes the motion of a free body in the presence of a tracking force [1, 10, 11]. Thus, we have the following topological and mechanical analogies in the sense explained above.
(1) A motion of a fixed physical pendulum on a (generalized) spherical hinge in a flowing medium (nonconservative force fields under assumption of additional dependence of the moment of the forces on the angular velocity).
(2) A spatial free motion of a four-dimensional rigid body in a nonconservative force field under a tracing force (in the presence of a nonintegrable constraint under assumption of additional dependence of the moment of the forces on the angular velocity).
(3) A composite motion of a four-dimensional rigid body rotating about its center of mass, which moves rectilinearly and uniformly, in a nonconservative force field under assumption of additional dependence of the moment of the forces on the angular velocity.

Acknowledgements

This work was supported by the Russian Foundation for Basic Research, project no. 15-01-00848-a.

References

[1] M. V. Shamolin, “Comparison of complete integrability cases in Dynamics of a two-, three-, and four-dimensional rigid body in a nonconservative field”, Journal of Mathematical Sciences, 187:3 (2012), 346–359.

[2] M. V. Shamolin, “Some questions of qualitative theory in dynamics of systems with the variable dissipation”, Journal of Mathematical Sciences, 189:2 (2013), 314–323.

[3] M. V. Shamolin, “Variety of Integrable Cases in Dynamics of Low- and Multi-Dimensional Rigid Bodies in Nonconservative Force Fields”, Journal of Mathematical Sciences, 204:4 (2015), 379–530.

[4] M. V. Shamolin, “Classification of Integrable Cases in the Dynamics of a Four-Dimensional Rigid Body in a Nonconservative Field in the Presence of a Tracking Force”, Journal of Mathematical Sciences, 204:6 (2015), 808–870.

[5] M. V. Shamolin, “Some Classes of Integrable Problems in Spatial Dynamics of a Rigid Body in a Nonconservative Force Field”, Journal of Mathematical Sciences, 210:3 (2015), 292–330.

[6] M. V. Shamolin, “Integrable Cases in the Dynamics of a Multi-dimensional Rigid Body in a Nonconservative Force Field in the Presence of a Tracking Force”, Journal of Mathematical Sciences, 214:6 (2016), 865–891.

[7] M. V. Shamolin, “Integrable Systems with Variable Dissipation on the Tangent Bundle of a Sphere”, Journal of Mathematical Sciences, 219:2 (2016), 321–335.

[8] M. V. Shamolin, “New Cases of Integrability of Equations of Motion of a Rigid Body in the n-Dimensional Space”, Journal of Mathematical Sciences, 221:2 (2017), 205–259.

[9] M. V. Shamolin, “Some Problems of Qualitative Analysis in the Modeling of the Motion of Rigid Bodies in Resistive Media”, Journal of Mathematical Sciences, 221:2 (2017), 260–296.

[10] V. V. Trofimov, “Euler equations on Borel subalgebras of semisimple Lie algebras,” *Izv. Akad. Nauk SSSR, Ser. Mat.,* **43**, No. 3 (1979), 714–732.

[11] V. V. Trofimov, “Finite-dimensional representations of Lie algebras and completely integrable systems,” *Mat. Sb.,* **111**, No. 4 (1980), 610–621.

[12] V. V. Trofimov and M. V. Shamolin, “Geometric and dynamical invariants of integrable Hamiltonian and dissipative systems”, Journal of Mathematical Sciences, 180:4 (2012), 365–530.

Maxim V. Shamolin, Lomonosov Moscow State University, Russian Federation

Structural modeling of nanostrands formation in dispersedly filled elastomers

Alexander K. Sokolov, Oleg K. Garishin, Alexander L. Svistkov

Sokolov-ak@icmm.ru

Abstract

It is well known that filling carbon black to rubbers significantly improves their strength and deformation properties. One possible explanation for this phenomenon is that the nanofiller creates a huge amount of uniformly distributed micro-breaks to facilitate transfer of the rubber matrix from complex stress state into the system of many uniaxially loaded fibers (strands). Therefore, rupture efforts for them to be much higher than the corresponding values for the same elastomer in an undirected condition.

Appropriate structural model of an elastomeric composite was developed to verify this hypothesis. It is based on a new criterion of deformation strength, taking into account the possibility of an anisotropic hardening of the elastomer under the stretching.

The results of computer simulation showed that in case of a new strength criterion using matrix breaks occurred not in the gap between the inclusions, but on some removal from it. Thus, the formation of a weakened zone in the form of a "hollow ring" occurred around the gap between the particles, that is quite be interpreted as a possible appearance of the elastic strand between the particles.

1 The object of study

Rubbers are one of the most important and common industrial polymers. These materials belong to the class of dispersed-filled elastomeric composites, the specific feature of which lies in the fact that their basis is a continuous low-modulus, highly elastic rubber phase (matrix) with solid granular filler particles (dispersed phase) embedded.

A lot of practical experience has been accumulated in the creation of rubbers for various purposes by now. However, the progress in this area of material science is still hampered by insufficient knowledge of structural mechanisms for formation of mechanical behavior of filled elastomers. Some mechanical properties of rubbers still remain the subject of discussions among materials scientists.

One such issue is the effect of rubber hardening when carbon black dispersed particles are embedded into it [1, 2, 3, 4]. It is known since the beginning of the XX

century, that filling rubber by carbon black (20-30 % by volume) greatly improves its operational properties: enhances the stiffness, rupture force increases 5–15 times, the limiting deformation in 2–4 times, and the smaller size of the filler particles, the stronger is reinforced material [5].

To explain these changes in terms of classical mechanics to date have not succeeded. This problem is one of the most important in modern mechanics of elastomers, because true understanding of hardening mechanisms will reduce the time and costs for experimental development of composite materials with predetermined properties and move to the calculation methods of design[6].

Most researchers agree that when the filled elastomer is deformed, structural changes occur in it, for the description of which additional hypotheses and assumptions are required. This work is devoted to the verification of one of these hypotheses. Its essence lies in the fact that nanoparticles have a huge surface of interphase contacts, which turns a significant portion of matrix into a bounded, that is, more durable state. At the same time the granular nanofiller composite creates a huge amount of uniformly distributed micro-breaks to facilitate transfer of the rubber matrix from complex stress state into the system of many uniaxially loaded fibers —nanostrands. Therefore, rupture efforts for them to be much higher than the corresponding values for the same elastomer in an undirected condition.

The presence of such formations is confirmed experimentally [7]. Studies of the nano-structure of the filled natural rubbers in the extended (up to the prebreaking) state using atomic-force microscopy methods, which were being carried out in ICMM UB RAS [8, 9], experimentally also confirmed this fact. Fig. 1 shows nanoscans of pre-stretched rubber containing carbon black particles. It is easy to see both the strands and the aggregates of soot particles they connect.

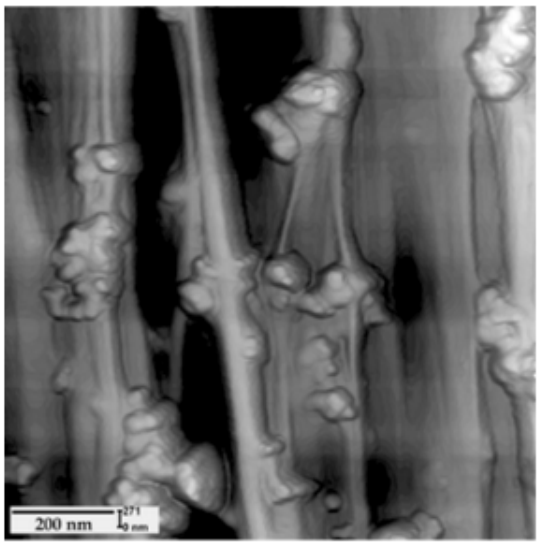

Figure 1: Stretched high-strength bonds between aggregates of carbon black particles obtained by atomic force microscopy

2 Methods

The structural model of the dispersed filled elastomeric composite was developed for description and analysis of the effect of nanostrands appearance under deformation. It is based on new deformation criterion of strength (1), considering the possibility of anisotropic strengthening of elastomer (due to the reorientation of the molecular chains in the direction of the load application).

$$f(\lambda_1, \lambda_2, \lambda_3) = \frac{\lambda_e}{\beta \sum_{i=1}^{3} \exp(-\alpha \lambda_i^2) - 1} < A, \tag{1}$$

$$\lambda_e = \sqrt{(\lambda_1 - \lambda_2)^2 + (\lambda_2 - \lambda_3)^2 + (\lambda_1 - \lambda_3)^2},$$

$$\boldsymbol{V} = \sum_{i=1}^{3} \lambda_i \boldsymbol{n_i} \otimes \boldsymbol{n_i},$$

where λ_e the invariant of left tensor of tension $\boldsymbol{V}$ (analog of the intensity of deformations), $\boldsymbol{n_i}$ - the orthonormalized three of its eigenvectors (in the current configuration),λ_i corresponding main extension ratios, α and β are constants chosen from experiments (biaxial loading of the elastomer);A - tensile strength of the destruction. The main feature of the criterion that a tensile or compression biaxial its value will be higher than when a uniaxial deformation (this is at the same strain intensity). That is, when the uniaxial loading material collapses later than in the case of two or triaxial deformation.$\lambda_1 = \lambda, \lambda_2 = 1/\lambda^x, \lambda_3 = 1/\lambda_1\lambda_2$
Fig. 2 represents the dependences of deformation criterion f for various for various relations between $\lambda_1, \lambda_2, \lambda_3$, illustrating this property (assuming that the medium is incompressible). It was accepted that x is varied from -1 to $1/2$. Constants α, β are taken by the equal 0.5. It is evident on the graph that the curve l ($x = 0.5$), corresponding to uniaxial stretching, lies below all.

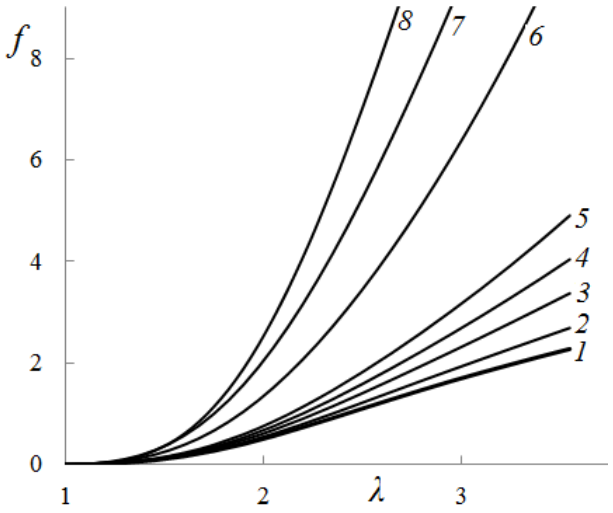

Figure 2: Dependence of the strength criterion f on the main extension ratios on different axes: (1) x= 0.5; (2) 0.25; (3) 0.1; (4) 0; (5) -0.1; (6) -0.5; (7) -0.75; (8) -1.

3 Results discussion

The main load during the deformation of elastomeric composites with a rigid granular filler occurs in the matrix interlayers between the inclusions (gaps). The rest of the elastomer is loaded much weaker. Accordingly, structural damage occurs, as a rule, near the gaps between the particles [10] these are the most dangerous zones. The appearance of strands in the composite structure occurs precisely there. Therefore, in modeling the development of internal damage in a composite, its structure was represented as a cell of incompressible nonlinear elastic matrix and two rigid spherical inclusions of radius R located at a distance δ from each other along the vertical. The mechanical properties of the matrix were described by neo-Hookean potential (2)

$$w = C(tr\boldsymbol{V}^2 - 3), \tag{2}$$

where C is the elastic constant, which according to its physical sense is equal 1/6 from initial Young's modulus E (for the incompressible medium). E was taken equal to 10 MPa in the calculations. The values of model constants were taken as follows: α=0.5; β=0.5; A=1. The choice was made for reasons of clarity of demonstration of process of the strand formation.

The initial gap between the inclusions was 40% of their radius. Inclusions were moving apart step-by-step apart vertically. The problem was solved by the finite element method. At each step, the stress-strain state in the cell was calculated and the fracture zones of the material were determined using deformation strength criterion. At the following loading steps, these areas were replaced by pores (i.e., the corresponding elements were excluded from the finite element mesh).

In Fig. 3 shows distribution maps of deformation strength parameter f at cell elongation (ratio of current and initial distances between centers of spheres) 160%, 200% and 250%. Fig. 4 depicts maps of deformation intensity λ_e at the same elongations.

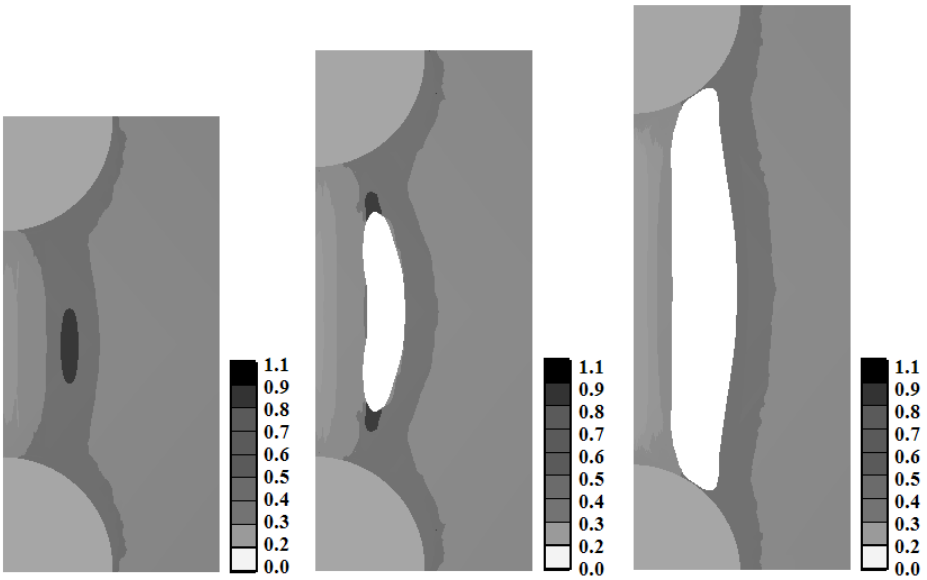

a *b* *c*

Figure 3: Distribution maps f, elongation: *a* - 160%; *b* - 200%; *c* - 250%

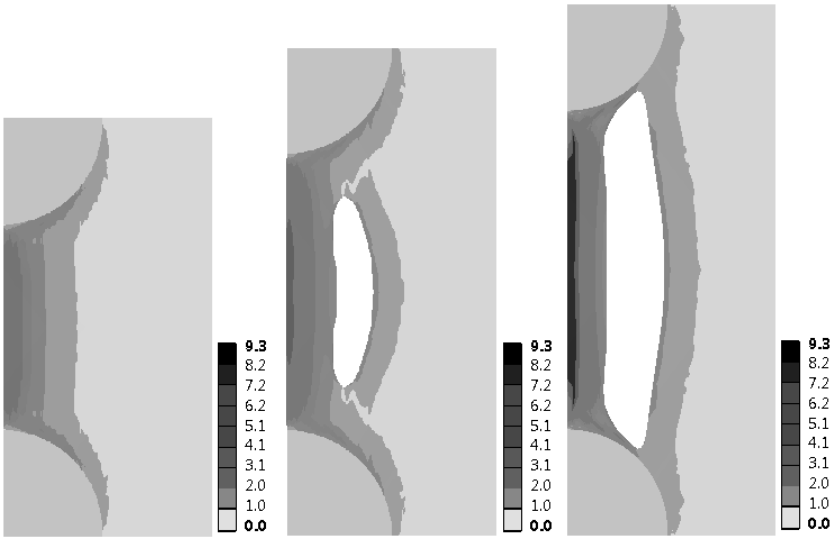

a *b* *c*

Figure 4: Distribution maps λ_e, elongation: *a* - 160%; *b* - 200%; *c* - 250%

The pores in the matrix began to appear at the elongation of 160%; at 250% of the the nanostrand was fully formed; complete destruction of the cell (strand breakage) occurred at approximately 500%.

The results of computer simulation showed that in case of a new strength criterion using matrix breaks occurred not in the gap between the inclusions, but on some removal from it. Thus, the formation of a weakened zone in the form of a "hollow ring" occurred around the gap between the particles, that is quite be interpreted as a possible appearance of the elastic strand between the particles.

As a result, we can say that the formation of strands in an elastomeric composite is possible in the event that an anisotropic change of matrix strength properties will occur during deformation. And this is quite possible due to the reorientation of polymer molecular chains.

Acknowledgements

This work is executed at a financial support of RFBR Grants: 16-08-00756 and 16-08-00914.

References

[1] Pechkovskaya K.A. Carbon black as a rubber amplifier. M.: Chemistry, 1967, 214 p. (in Russian)

[2] Kraus G. Reinforcement of elastomers by carbon black // Rub. Chem. Tech., 1978, V. 51, N 1. P. 297–321.

[3] Moshev V.V. Garishin O.K. Structural mechanics of dispersed filled elastomeric composites //Achievements in Mechanics, 2005, V. 4, N 2, P. 3–36. (in Russian)

[4] *Kuperman F.E. To the question about the mechanics of rubber reinforcement by carbon black // XXIV Symposium "Problems of Tires and rubber composites": Proceedings. Moscow, 2013, P. 171–190. (in Russian)*

[5] *Chvalun S.N. Polymeric nanocomposites // Nature (Priroda), 2000, N 7, P. 22–30. (in Russian)*

[6] *Garishin O.C., Moshev V.V. Damage model of elastic rubber particulate composites // J. Theoretical and Applied Fracture Mechanics. 2002. V. 38. P. 63–69.*

[7] *Dohi H., Kimura H., Kotani M., Kaneko T., Kitaoka T., Nishi T., Jinnai H. Three-Dimensional Imaging in Polymer Science: Its Application to Block Copolymer Morphologies and Rubber Composites // Polymer Journal, 2007, V. 39, N 8, P. 749–758.*

[8] *Morozov I.A., Lauke B., Heinrich G. Quantitative microstructural investigation of carbon-black-filled rubbers by AFM // Rubber chemistry and technology, 2012, V. 85, P. 244-263.*

[9] *Morozov I.A. Structural-Mechanical AFM Study of Surface Defects in Natural Rubber Vulcanizates // Macromolecules, 2016, V. 49, N 16, P. 5985–5992.*

[10] *Garishin O.C., Moshev V.V. Structural rearrangement in dispersion-filled composites: influence on mechanical properties // Polymer Science. Ser. A, 2005, V. 47, N 4, P. 403–408.*

Sokolov Alexander Konstantinovich Institute of Continuous Media Mechanics UB RAS, Perm, Russia
Oleg Konstantinovich Garishin, Institute of Continuous Media Mechanics UB RAS, Perm, Russia
Svistkov Alexander L'vovich, Institute of Continuous Media Mechanics UB RAS, Perm, Russia, Perm State National Research University, Russia

Studies of fracture in shear of a constrained layer

Ulf Stigh, Anders Biel

ulf.stigh@his.se

Abstract

Cracks normally propagate in the opening mode associated with a state of local symmetry at a crack tip. However, the micro- or macrostructure of a material or structure sometimes forces cracks to propagate in a shearing mode. Irrespective of the actual material studied, fracture in shear is frequently associated with the formation of a large number smaller sigmoidal-shaped cracks in the propagation direction of the major crack. Propagation of the major shear crack is accomplished by coalescing the sigmoidal-shaped cracks. Experiments show that the formation of sigmoidal cracks due to shear loading leads to a normal separation of the joined substrates. Theoretical studies show that constraining the local opening of the sigmoidal cracks increases the fracture resistance for the propagation of the major crack. In the present study, experiments with a ductile adhesive loaded in shear and where the normal separation is constrained are presented. The experiments are evaluated using the path independent J-integral. The associated cohesive law shows that considerable normal compressive stress develops in the adhesive during macroscopic shear loading. It is also concluded that by ignoring the normal separation in the evaluation of the experiments, the strength of the adhesive is underestimated. Thus, the procedure developed in earlier studies is conservative from a strength analysis perspective. The present technique might be possible to extend to other materials to reveal their properties in shear fracture

1 Introduction

Cracks are observed to propagate in shear under special circumstances, cf. e.g. [1]. Two different crack propagation mechanisms are observed on a smaller length scale: For some ductile materials, fibrils form and governs the fracture process through the stretching of the fibrils. In other materials, the shear crack is observed to be governed by a process of nucleation, growth and coalesce of smaller cracks, cf. e.g. [2]. These minor cracks appear to propagate in a state of local symmetry, i.e. with crack faces opening in the direction of the maximum tensile principal stress. In pure shear, in 45° relative to the direction of propagation of the major shear crack. If any of the minor cracks is not inhibited to grow in this direction, it will take over the role as the major crack and crack kinking occurs. However, if stiffer layers of material inhibit the propagation, the minor cracks form sigmoidal shapes in a shear

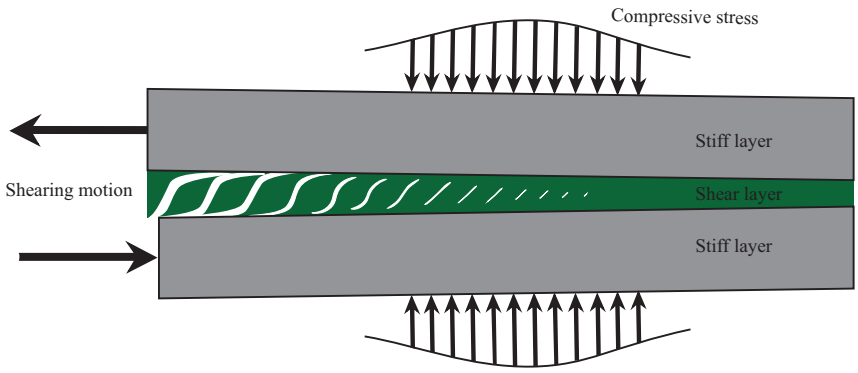

Figure 1: Shear crack propagation by nucleation, growth and coalesce of shear hackles. A shear crack propagates from left to right in this sketch of the fracture process. The shear hackles open up at the left due to their expansion.

layer, cf. Fig. 1. These are known as Riedels in soils, clay and rock, [3], shear hackles in composite materials, [4] and adhesive layers, [5].
During the fracture process, the shear hackles open-up and thus induce an expansion of the layer in which the shear crack propagates. The expansion increases during the fracture process and reaches a maximum at the tip of the growing shear crack. Far from the shear crack-tip, the fracture process is not initiated and the layer is not expanded. Thus, the expansion varies from a maximum at the shear crack-tip to a minimum far from the tip. This indicates that the constraints of the surrounding material influence the amount of expansion. With a soft surrounding, the expansion is expected to be large and with a stiff surrounding, the expansion is small. Due to the expansion of the surrounding material, a compressive stress is expected to act on the layer with shear hackles. Energetically, this means that part of the work performed to shear the layer is consumed to expand the surrounding material. From this, it can be expected that the work needed to fracture the layer in shear should increase as the stiffness of the surrounding material increases since more energy is needed to expand the layer. The shear layer also has to perform work against any source of compressive stress that acts over the layer. Thus, a compressive stress acting to close the shear hackles is expected to increase the work needed to fracture the layer, i.e. the apparent fracture energy. Thus, some care has to be exercised in measuring the fracture energy in shear J_{IIc} or J_{IIIc}, cf. [9].
In many materials showing this fracture process, the geometrical sizes and load levels are extreme. In polymeric adhesive layers, the mechanism can be studied experimentally under reasonable conditions. Appropriately designed and loaded specimens can force a major crack in the adhesive to propagate in a shearing mode at a reasonable load level and in a stable manner, cf. [6]. The findings from studies of shear fracture in adhesive layers is expected to be useful as an initial outset for studies of shear fracture in other materials.
A theoretical study shows the influence of constraining the expansion an elastic-brittle layer, cf. [7]. The study is based on linear elastic fracture mechanics and the principle of local symmetry. It shows that the work needed to fracture a brittle layer in shear is about 35% larger if the constraint is completely inhibited. Experimental studies indicate this effect for engineering adhesives. For tough adhesives, a more

constrained experimental set-up gives about 30% increased fracture energy, [8], and by actively constraining the expansion, the fracture energy increases by about 50%, [9].
By the expansion, there is no direct contact between the crack faces in the wake of a shear crack-tip. This means that Coulomb friction is not expected to play a major role in the fracture process. However, some distance from the crack tip, the crack faces may come into contact due to compressive loads and this may play an important role in a structural fracture process. Estimates of the effect are given in [10] and [11].
In the present paper a summary is given of some recent studies of shear fracture of structural adhesive layers. The next section introduces the method based on the path independent J-integral to be used to connect the shear fracture process to the external loads on test specimens. A cohesive zone model is used to quantify the shear properties of the shearing layer. It should be noted that no assumption on the shape of the cohesive law is assumed, it is only assumed that the same cohesive law governs the behaviour of the entire layer. The shape is a direct result from the experiments. The third section gives design guidelines for experimental methods to measure cohesive laws; especially for shear. Some experimental results are given in section 4 and the paper ends with a discussion and some conclusions.

2 Theory

The theoretical foundation is based on the path-independent J-integral given by

$$J = \int_S \left(U \mathrm{d}y + T_i u_{i,x} \mathrm{d}S \right), \tag{1}$$

in a planar state in the $x-y$-plane where no variation of the fields is allowed in the z-direction. The counter clockwise integration path is denoted S; $\mathbf{T}$ and $\mathbf{u}$ are the traction vector acting on the interior of S, and the displacement vector, respectively; U is the strain energy density, cf. [12] and [13]. Index notation is used with Einstein's summation convention and a comma indicating partial differentiation. If the material is homogeneous in the x-direction, i.e. if U is not explicitly dependent of x, the integral is path independent. This can be shown by evaluating the integral for a *closed* path S not surrounding any object that would change the potential energy if the object is moved in the x-direction. With the help of the divergence theorem, $J = 0$ results. Moreover, the integral gives the configurational force on any object residing inside S, [14]. From these results two conjectures can be drawn: 1) the integration path S can be chosen arbitrarily and Eq. (1) gives the same configurational force as long as S contains the same energy-changing objects and 2) the sum of J for all energy-changing objects in an elastic field is zero. Thus, the configurational forces are in equilibrium in the same way as ordinary forces are in equilibrium, cf. e.g. [15]. These results are useful in the design of test specimens to measure cohesive laws.
Equation (1) is based on the existence of a strain energy density U. This appears as a serious limitation of the applicability of the integral. However, as long as no

unloading takes place, a pseudopotential can take the place of U. That is, the stress can formally be derived by differentiating U with respect to the strain. By this, the applicability of the J-integral is extended to inelasticity when no unloading takes place.
A cohesive zone located in a plane $y = \text{constant}$[1] is governed by a cohesive law,

$$\sigma = \frac{\partial \bar{J}}{\partial w} \tag{2}$$

$$\tau = \frac{\partial \bar{J}}{\partial v} \tag{3}$$

where $\bar{J}$ is a potential for the cohesive normal stress σ in the y-direction, positive when opening the cohesive zone, and the cohesive shear stress τ in the $x-$direction. The conjugated separations are w in the y-direction, denoting the opening and v in the x-direction, denoting the shear. A direct application of Eq. (1) shows that $\bar{J} = J$. This result is derived in [13] for pure opening and it is readily extended to a mixed loading giving Eqs. (2) and (3). An alternative derivation is given in [16].

3 Design of specimen

The energy changing objects identified in test-specimens are boundaries and loading points. Taking the x-axis horizontally, and choosing S to closely encircle a traction free boundary, Eq. (1) shows that a free horizontal boundary does not contribute to J. Similarly, a stress free vertical boundary does not contribute to J. Practically, this can often be achieved by allowing for some overhang at loading points and supports.
Any horizontal boundary between different materials, i.e. a jump in U in the y-direction, does not contribute to J. This is shown by considering that the first term in the integrand of Eq. (1) does not contribute if S is chosen to follow the interface closely on each side. The second term does not contribute either. This follows from the continuity properties of $\mathbf{T}$ and $\mathbf{u}$, cf. [17].
A vertical force P acting on an otherwise free horizontal boundary contributes with J_{P} to J. This is shown by applying Eq. (1) to the boundary.

$$J_{\mathrm{P}} = \frac{P\theta}{b} \tag{4}$$

Here θ is the rotation of the loading point and b is the out-of-plane width of the specimen, cf. [16].
These results are applied to the modified end notched flexure (ENF) specimen, cf. Fig. 2. The specimen consists of two steel bars, i.e. the substrates, and an adhesive layer terminated the distance a from the left support. In an ordinary ENF-specimen, the loading F, Δ is applied at the centre between the supports. By

[1] It can be helpful to consider Fig. 1 with a horizontal x-axis directed to the right and a vertical y-axis directed upwards.

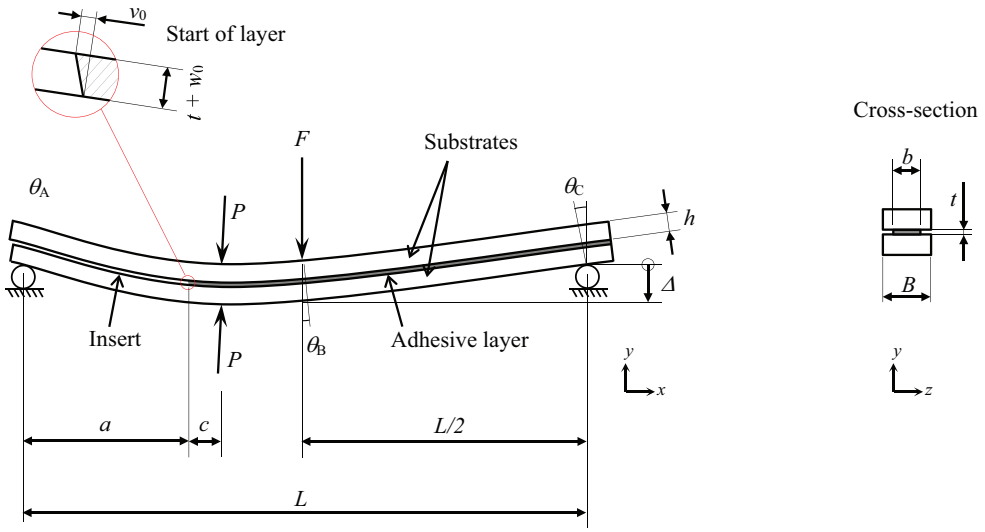

Figure 2: Deformed modified end notched flexure specimen.

gradually increasing the prescribed deflection Δ, the fracture process is initiated at the left end of the layer and eventually a shear crack is formed. The process is stable if the length a is long enough. For a brittle layer, the condition is $a/L > 0.35$ and a somewhat shorter a can be chosen if the layer is tough, cf. [6]. Here, the specimen is modified by a pair of forces P applied close to the left end of the layer, the distance c in Fig. 2. These forces limit the expansion of the shearing layer. In an experiment, P is applied first and kept constant thereafter Δ is gradually increased.

4 Experiments and results

Experiments with the rubber based commercial structural adhesive DowBetamate-5096 are presented in [16]. A brief summary is given here. Cohesive laws are unique for a specific layer thickness. In this study the thickness $t = 0.3$ mm. Two different crack lengths are used $a = 300$ and 350 mm, respectively. The substrates are made of tool steel with a distance L =1 m between the supports. Non of the experiments suffers inelastic deformation of the substrates or instability of crack propagation although the shorter a violates the stability condition for brittle adhesives in [6]. The experiments are performed quasistatically at a loading rate $\dot{\Delta} = 2$ mm/min in a servo hydraulic testing machine (Instron 8802). It is expected that the loading rate influences the evaluated data, cf. e.g. [18]. During the experiments, the expansion w_0 and the shear v_0 at the crack tip are measured using LVDTs. Repeated experiments are performed at five different values of the constraining force $P = 0$, 1.25, 2.50, 3.75, and 5.00 kN.

Figure 3 shows J vs. v and w_0 vs. v_0, respectively with $P = 5$ kN. Although two different specimen geometries are used, i.e. $a = 300$ and 350 mm, there is no sign of this difference in the evaluated data. This supports that the evaluation procedure gives data for the *layer* and not for the specimen, as expected. The red curves are least square adaptions to the experimental data.

The J-curves show a parabolic shape for small v indicating a linear elastic response

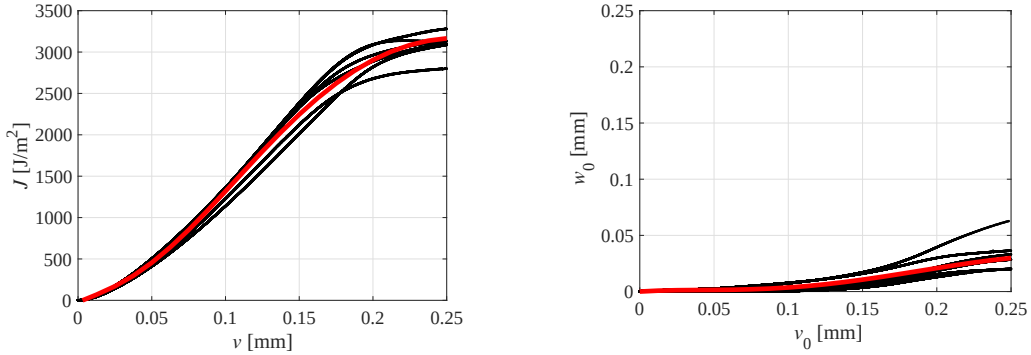

(a) (b)

Figure 3: a) Evaluated J vs. v and b) measured w_0 vs. v_0 for $P = 5$ kN. Black curves: experimental data; red curves: adapted curve. Data from [16]. Note that the $J - v$-relation is assumed to be the same for the entire layer, i.e. the index 0 is dropped on v in the left graph.

for small deformation. This part ends at $v \approx 0.035$ mm irrespective of the level of constraining force P. The shape of the next section of the J-curves corresponds approximately to a cohesive law with linear hardening plasticity. This phase ends when the expansion w_0 becomes considerable. With a larger P this occurs later in the loading history. After this, J continues to increase but with a negative second derivative corresponding to a softening cohesive law, cf. Eq. (3). At $w \approx 0.25$ mm, the J-curve levels out corresponding to zero shear stress and a shear crack has formed.

The w_0 vs. v_0 curves in Fig. 3b shows that the expansion is considerable at fracture even at $P = 5$ kN which is the maximum constraining force in the experimental series, cf. [16]. To derive a cohesive law for pure shear, i.e. for $w = 0$, an extrapolation method is needed. The following procedure is developed in [16]. For 20 consecutive values of v, values of J and w are derived from the adapted J vs. v curves and the w_0 vs. v_0 curves exemplified in Fig. 3. Lines are adapted to the J and w data for each value of v. Each line is extrapolated to $w = 0$ giving a value of J. This gives 20 values of J vs. v for pure shear, i.e. $w = 0$. Figure 4a shows the result. It shows a maximum at $J_{\mathrm{IIc}} = 3.2$ kN/m, i.e. the fracture energy is considerably larger in pure shear than the value 2.1 kN/m evaluated from the experimental series with $P = 0$, cf. [16].

The black curve is a least square adaption. Differentiation of this according to Eq. (3) gives the cohesive law $\tau(v)$ in Fig. 4b. The cohesive shear strength is $\hat{\tau} = 22$ MPa. This is also larger than the value derived from the experiments with $P = 0$ if they are evaluated by ignoring the expansion. This erroneous evolution yields the shear strength 16 MPa. Thus, ignoring the expansion of the layer in the evaluation yields smaller values of the fracture energy and cohesive strength.

The extrapolation procedure also provides an evaluation of the cohesive normal stress for pure shear deformation. The slope of each of the 20 lines adapted to the J vs. w data, is the corresponding normal stress according to Eq. (2). The result is shown as circles in Fig. 4b. A considerable compressive stress develops in

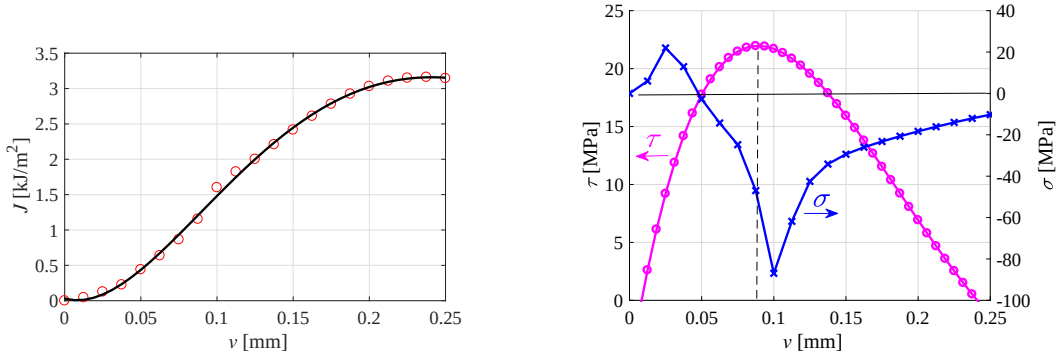

(a) (b)

Figure 4: a) Derived J vs. v for pure shear, i.e. $w = 0$. Circles: extrapolated data; black curve: least square adaption. b) Cohesive law for pure shear. Purple curve: Shear stress vs. shear; Blue curve: Normal stress vs. shear. Data from [16].

conjunction with the formation of the shear hackles, i.e. $\sigma \approx$ -85 MPa at $v = 0.1$ mm. When the shear hackles grow, the layer becomes less stiff in compression, and the compressive stress decreases. However, some compressive stress remain when the shear crack has formed at $v \approx 0.25$ mm. This can be a result of debris of the layer left in the wake of a propagating crack and supporting normal stress.
The positive normal stress derived at small values of v can be an artefact of the extrapolation procedure. As shown in Fig. 3b, w_0 develops very slowly with v_0 at the start of an experiment. This results in large relative deviations between the data and the adapted curves for small values of v, i.e. for $v \lesssim 0.05$ mm. As discussed above, it is expected that the layer responds elastically for $|v| \lesssim 0.035$ mm. As the elastic response must be derived from a strain potential to satisfy basic thermodynamics, and since $\tau = 0$ is the only possibility for $v = 0$ and $w > 0$, $\sigma = 0$ is the only possibility for $w = 0$ and $v > 0$ due to the symmetry of the elastic stiffness matrix resulting from the existence of a potential. Thus, the positive σ for $v \lesssim 0.035$ mm in Fig. 4b is most likely an artefact of errors developed in the extrapolation procedure for small v, cf. [16].

5 Discussion and conclusions

Normally, materials do not fracture in shear. Without a layered structure confining crack propagation to shear, as in the cases of composite materials and adhesive joints, or due to a considerable compressive stress, as is the case in tectonic plates, crack kinking occurs. Cracks prefer mode I, cf. e.g. [1]. In many cases of shear fracture, shear hackles develop during the fracture process. These force the crack tip to open up, i.e. crack opening occurs even if the external loads and the geometry suggest a state of pure shear. This un-symmetry is given by the material behaviour. Since crack opening occurs, friction cannot develop in the close vicinity of the crack-tip. Friction can however develop some distance from the crack tip if large compressive loads act.
The experimental method developed in [9] and the evaluation procedure developed

in [16] yield data for a cohesive zone model of a thin layer fracturing in shear by the development of shear hackles. A modified ENF-specimen is used and evaluated based on the path- independent properties of the J-integral. After extrapolation of the experimental data to a state of pure shear deformation, the cohesive laws for shear stress vs. shear and normal stress vs. shear are derived. The results show larger fracture energy and strength than evaluated by ignoring the expansion. This indicates that earlier results ignoring this expansion are conservative in a design situation; they underestimate the cohesive strength and fracture energy of the adhesive layer.
The effect of constraining the expansion is larger than expected from a theoretical analysis, cf. [7] and [16]. This is attributed to the considerable toughness of the adhesive that invalidates a direct analysis based on linear elastic fracture mechanics. Thus, it is indicated that toughness increases the effect of constraining the expansion. From a designers point of view, it is interesting to note that different engineering methods to improve joints and composites by e.g. adding mechanical fasteners such as rivets in adhesive joints or stitching the layers together in composite materials have an unexpected effect to improve the shear strength by constraining the expansion.
The mechanism presented here might shed some light on the size-effect of the delamination strength noted in e.g. [19].

Acknowledgements

The authors are grateful to the Knowledge foundation for financial support for part of this study.

References

[1] K.B. Broberg. Cracks and fracture. Academic Press, San Diego, 1999

[2] U. Stigh, A. Biel, T. Walander. Shear strength of adhesive layers - Models and experiments. Engineering Fracture Mechanics. 129:67-76, 2014.

[3] W. Riedel. Zur mechanik geologischer brucherscheinungen. Zentralblatt für Mineral, Geologie und Paläontologie, 354-368, 1929.

[4] M.D. Gilchrist, N. Svensson. A fractographic analysis of delamination within multidirectional carbon/epoxy laminates. Composites Science and Technology, 55:195-207, 1995.

[5] H. Chai. Shear fracture. International Journal of Fracture, 37:137-159, 1988.

[6] K.S. Alfredsson, U. Stigh. Stability of beam-like fracture mechanics specimens. Engineering Fracture Mechanics, 89:98-113, 2012.

[7] Z.C. Xia, J.W. Hutchinson. Mode II fracture toughness of a brittle adhesive layer. International Journal of Solids Structures, 31:1133-1148, 1994.

[8] F.A. Leone Jr, D. Girolamo, C.G. Dàvila. Progressive damage analysis of bonded composite joints. NASA/TM-2012-217790, 2012.

[9] U. Stigh, A. Biel. Shear properties of an adhesive layer exposed to a compressive load. Procedia Materials Science. 3:1626-1631, 2014.

[10] L.A. Carlsson, J.W. Gillespie Jr, R.B. Pipes. On the analysis and design of the end notched flexure (ENF) specimen for mode II testing. Journal of Composite Materials, 20:594-604, 1986.

[11] C. Fan, P.-Y. Ben Jar, J.-J.Roger Chen. A unified approach to quantify the role of friction in beam-type specimens for the measurement of mode II delamination resistance of fibre-reinforced polymers. Composites Science and Technology 67 (2007) 989-995.

[12] G.P. Cherepanov. The propagation of cracks in a continuous medium. Journal of Applied Mathematics and Mechanics, 31(3):503-512, 1967.

[13] J.R. Rice. A path independent integral and the approximative analysis of strain concentration by notches and cracks. ASME Journal of Applied Mechanics, 88:379-386, 1968.

[14] J.D. Eshelby. The force on an elastic singularity. Philosophical Transactions of the Royal Society of London A244:87-112, 1951.

[15] D. Svensson, K.S. Alfredsson, U. Stigh, N. Jansson. Measurement of cohesive law for kink-band formation in unidirectional composite. Engineering Fracture Mechanics 151:1-10, 2016.

[16] A. Biel, U. Stigh. Strength and toughness in pure shear of constrained layers. Submitted.

[17] U. Stigh. Applications of equilibrium of configurational forces for the measurement of cohesive laws. Proceedings of the 17th European conference on composite materials, Münich 2016.

[18] T. Carlberger , A. Biel, U. Stigh. Influence of temperature and strain rate on cohesive properties of a structural epoxy adhesive. International Journal of Fracture 155:155-166, 2009.

[19] M.R. Wisnom. On the increase in fracture energy with thickness in delamination of unidirectional glass fibre-epoxy with cut central plies. Journal of Reinforced Plastics and Composites, 2:897-909, 1992.

Ulf Stigh, University of Skövde, Sweden
Anders Biel, University of Skövde, Sweden

On Structure of Electrohydrodynamic Flows Caused by Field-enhanced Dissociation in Various System Configurations

Y. K. Stishkov, S. A. Vasilkov

s.vasilkov@spbu.ru

Abstract

If a dielectric liquid become charged in the external electric field, it starts moving and an electrohydrodynamic (EHD) flow emerges. There are several charge formation mechanisms that are active in the strong electric fields. Unlike the surface one (the charge injection), the volumetric mechanism (the field-enhanced dissociation) is poorly studied. The latter can take place both near metallic electrodes and solid insulation and leads to EHD flows with different structures. Thus, the present study examines a number of EHD systems and characterizes these cases by means of computer simulation. The computations are based on the complete set of electrohydrodynamic equations employing commercial software package COMSOL Multiphysics. The results show specifics of the charge formation and flow structures.

1 Introduction

Electrohydrodynamic (EHD) flows in isothermal incompressible dielectric liquids emerge under the action of the Coulomb force that takes place whenever the net electric charge exists in the presence of the electric field. The flows are typically studied in systems with inhomogeneous electric field with pointed electrodes and can correspond to several mechanisms of charge formation, namely, charge injection (the surface mechanism) and field-enhanced dissociation (the volume one, the relative increase in dissociation rate under the action of strong electric field).

Structures of the EHD flows of the injection type have been studied quite well both with the use of computer simulation and experiments in various systems [1, 2, 3, 4]. On the contrary, the flows caused by the field-enhanced dissociation [5] have been investigated only in a few works and mostly by means of computer simulation [6] or in comparatively weak electric fields [7]. However, as the work [8] has demonstrated good agreement between experimental and calculated velocity fields of the flows of the type, the simulation technique is verified and can be used for further studies.

Considering the electrode systems with pointed electrodes, for example, needle plane or blade-plane configurations, the maximum of the electric field strength and, conse-

quently, that of the injection current or the increase in dissociation rate are located at the tip apex. The flows in the both cases have similar kinematic structures [6]: they develop from the pointed electrode towards the plane. The main difference between the two charge formation mechanisms (that the injection is the surface one and the dissociation is volumetric) does not allow for experimental identifying the dominant mechanism.

To study EHD flows caused by field-enhanced dissociation under secured absence of injection, the works [8, 9] considered original EHD system that creates the region of the strong electric field far from the electrode metal surfaces: the field is strengthened inside a cylindrical hole made in a dielectric flat barrier that is situated between two plane electrodes. In this case, the flow emerges near solid insulation and its structure differs from those observed in systems with pointed electrode. The diversity of flow localizations and structures is of interest, therefore, the present work studies and analyzes them in case of the sole action of the volumetric charge formation mechanism.

First, the paper considers a blade-plane system (Fig. 1a) in which the injection-type flows are often investigated and analyzed. Next, a system with a blade-shape barrier is examined and EHD flow is shown to emerge here (Fig. 1b). Both systems form a region of strong electric field at the tip but differ in the material of the blade. The latter sets conditions for the EHD flow with completely different structure. Further, two systems with axial symmetry are considered: the system with the hole in the barrier as discussed above (Fig. 1c) and a system with a hollow tube electrode slightly protruding from the insulating top (Fig. 1d). The latter system partially reproduces the electric field distribution in the bottom half of the former one but uses the metal electrode instead of solid insulation.

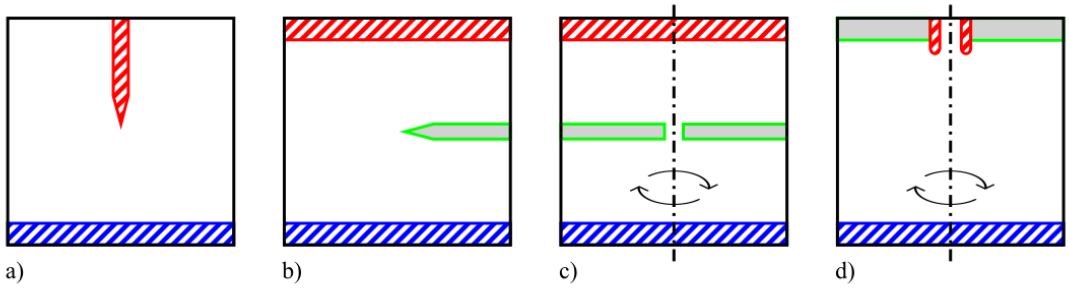

Figure 1: Schematic (not to scale) illustrations of the EHD system configurations: the blade-plane system (a), the dielectric blade system (b), the system with the hole in the barrier (c), and the slightly protruding hollow tube-plane system (d).

The geometries of the first and the third system correspond to those used in other studies, namely, in [10] and [8]. The second system is similar to the third one but the barrier has the shape of the blade from the first system. The last one has dimensions of the bottom half of the third one. Distances from the blade tip, the barriers and the tube electrode are nearly 10 mm. The blades are 10 μm sharp, the diameters of the hole and the tube are approximately 1 mm; curvature radii of the hole edges and the tube end are 0.07 mm and 0.1 mm correspondingly. The present study focuses

mainly on the flow structures and qualitative effects; however, certain quantitative results are of interest too but can differ since the sizes are different.
Analysis of all these cases, on the one hand, allows us to emphasize the variety of possible structures of EHD flows caused by field-enhanced dissociation and, on the other hand, to reveal their general regularities.

2 Simulation technique

The present work includes computer simulation of an EHD flow with the corresponding technique described in [6]. The computations were carried out using software package COMSOL Multiphysics based on the finite element method. The complete set of equations (as in [6]) was solved for the case of the two species of univalent ions with equal mobility and diffusion coefficient values. The dissociation intensity, the part of the source function for transport equations, is $W_0F(p)$ where W_0 is that in the absence of electric field and F is the relative increase in the dissociation rate [5]:
$F(p) = \frac{I_1(4p)}{2p}, p = \frac{e^2}{2k_BT}\sqrt{\frac{E}{4\pi\varepsilon\varepsilon_0 e}}$
Here I_1 is the modified Bessel function of the first kind, e is the elementary electric charge, k_B is the Boltzmann constant, T is the temperature, E is the electric field strength, ε is the relative electric permittivity, ε_0 is the electric constant.
All the considered configurations can be simulated using 2D models with axial or plane symmetry. The following assumptions and approximations are used thought all the models: all the system are closed, consist of electrodes (the shaded regions in Fig. 1) and dielectric surfaces (the remaining ones). Boundary conditions on the surfaces of the electrodes are the voltage (0 or 30 kV), zero velocity, zero flux for the ions of the same polarity (no injection current) and the free passage of the ions of opposite polarity (complete neutralization). Dielectric surfaces use condition $E_N = 0$, zero velocity, and no flux of ions conditions.
Since there is no injection on the electrodes, the only mechanism of charge formation is the dissociation enhanced by the field. The working liquid properties correspond to those of the mixture of transformer oil and cyclohexanol (see [11]) with the low-voltage conductivity of $0.92 \cdot 10^{-8}$ S/m.

3 Results and Discussion

3.1 Metallic blade

To start with, consider blade-plane electrode system that is frequently used to study EHD flows of injection type. Now, the case of field-enhanced dissociation is examined. The curvature radius of the blade tip is as small as 10 μm and thus produces strong electric field. As it can be seen from the simulation results (Fig. 2), the electric field strength exceeds $4{\cdot}10^{-7}$ V/m and the relative increase in the dissociation rate is higher than 10 at a distance of 0.1 mm from the blade (the maximum is greater than 2000).

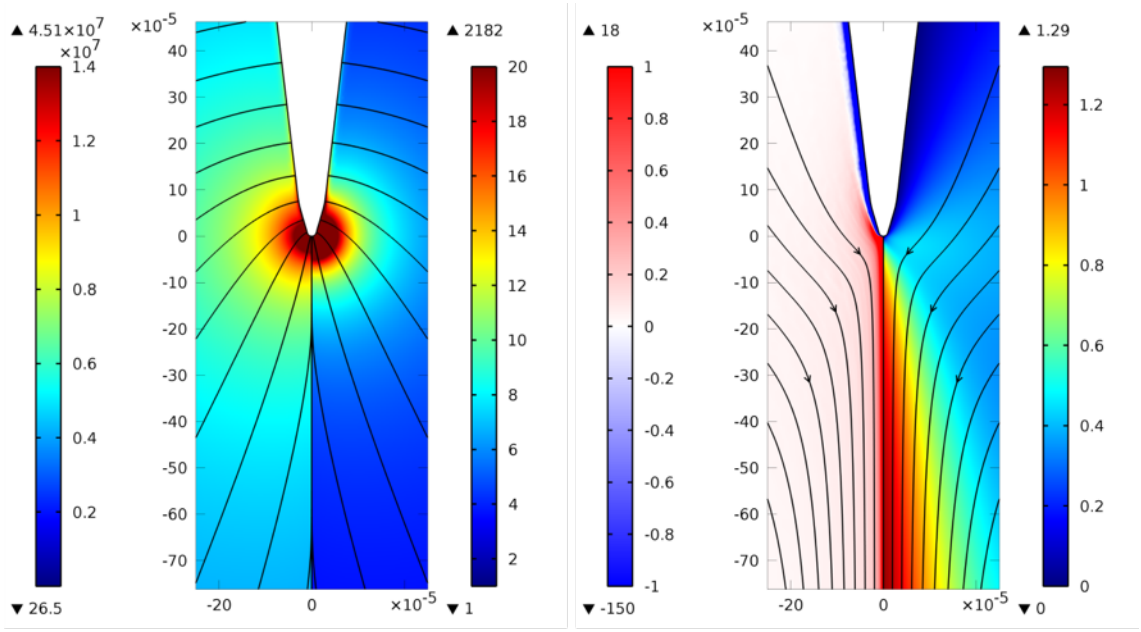

Figure 2: Distribution of quantities near the tip of the metallic blade: (a)п»„the electric field strenght (left) and the relative increase in the dissociation rate (right) near the tip of the blade, and the electric field lines; (b)п»„the distribution of the space charge density (left) and that of EHD flow velocity (right) near the tip of the blade and the streamlines.

The EHD flow in Fig. 2 is directed from the blade towards the plane and has typical structure that qualitatively coincides with that of the already studied injection EHD flows [10].The reason for this is the following: In the region of non-uniform and strong electric field, the counter ions move to the surface of the electrode whereas the ions of the same polarity escape into the bulk. This causes a layer of homocharge to form outside the heterocharge layer (that of the deficit of the ions of the same polarity where the dissociation and recombination rates are unbalanced). Therefore, the Coulomb force pulls the liquid downward just as in the case of injection and forms the observed flow. The space charge density exceeds 10 C/m^3 within approximately 10 μm thin charged jet and becomes much smaller but nonzero in the neighbor regions. The velocity profile is much wider (Fig. 2b) due to the effect viscosity; and the speed exceeds 1 m/s.

3.2 Dielectric blade

To isolate the field-enhanced dissociation from the injection, the works [8, 9] use the dielectric barrier of special design and shows the EHD flow to exist near the barrier. The key feature of the system is the location of the region of the strong electric field far from electrode surfaces, which makes the injection charge formation in the region impossible. The way how the solid insulation changes the electric field distribution is the accumulation of the electric charge on its surface, which results in screening the normal component of the electric field. Therefore, the present simulation technique

uses condition $E_N = 0$ (the component has been screened) on dielectric surfaces.

Consider a blade of the same shape as in previous section but made from solid dielectric. It has the greatest impact on the electric field if it is placed horizontally in the middle of the gap. The electric field lines go around its surface, and a region of the strong electric field (up to $2 \cdot 10^{-7}$ V/m) and enhanced dissociation emerges near the tip (Fig. 3a). The distributions of |E| and F are very similar to those observed in the case of the metal blade but the direction of the field is completely different: electric field lines are perpendicular to the metal surface and are parallel to that of solid insulation. The positive and negative ions move along the electric field lines away from the region of enhanced dissociation and, in the contrast to the case of metal electrode, form the positive net charge above the dielectric blade (Fig. 3b) and the negative net charge bellow it (not shown in Fig. 3). The Coulomb force acts along the field lines and causes the liquid to flow from the tip along the surface of the blade towards its body. Compared with the previous case, the flow has the opposite direction.

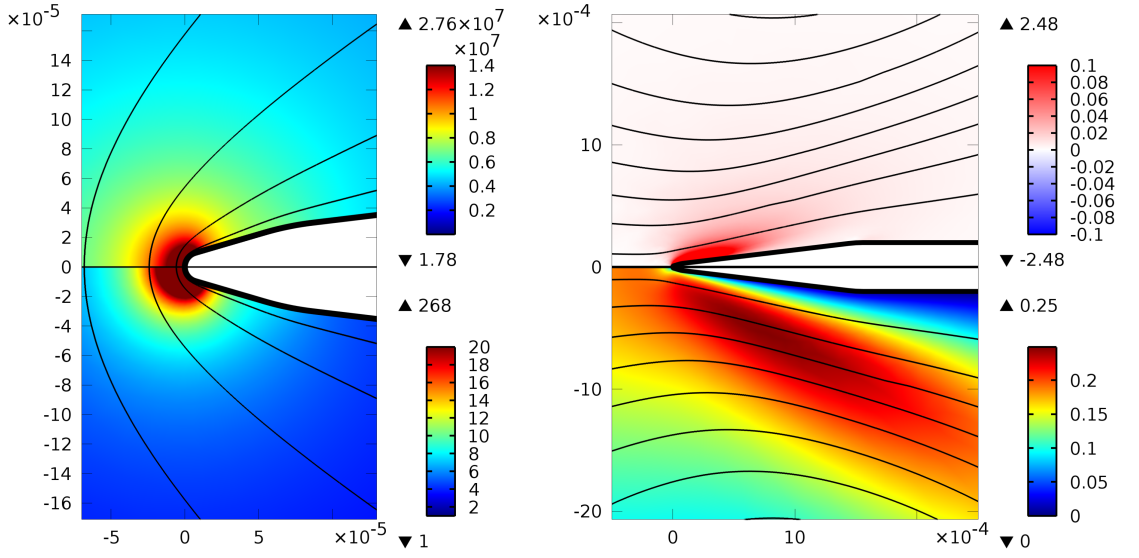

a) b)

Figure 3: Distribution of quantities near the tip of the dielectric blade: (a)п»„the electric field strength (top) and the relative increase in the dissociation rate (bottom) and the electric field lines; (b)п»„the density of the space charge (top) and the velocity magnitude (bottom) and the streamlines.

Similar space charge distributions and flow structures can be generally expected near the sharp edges of solid insulation when the local increase of the electric field strength is produced by the accumulated charge. The latter can happen if the initial (when the dielectric surfaces are uncharged) electric field lines pass through the insulation. This means it should be placed between the electrodes.

3.3 Barrier with the hole

Next, consider and analyze the flow structure in the more complicated system used in [8]. The system consists of two flat parallel electrodes and a dielectric plate (barrier) having a small circular hole. The barrier is placed between the plates and splits the chamber filled with a dielectric liquid into two equal parts, with the hole remaining the only link to connect them. The charge accumulates on the barrier surface, screens the normal component of the electric field, and moves the electric field lines to the hole (the only available way). As a result, a region of the strong electric field emerges inside the hole (Fig. 4) that enhances the dissociation rate and provides EHD flow formation. The work [8] confirmed experimentally that the EHD flow (Fig. 4) does form in this system and has the following structure: the liquid spreads out radially along the barrier and then comes to the hole from the bulk along the cell axis. Let us examine what is happening taking into account the features noted for the system with the dielectric blade.

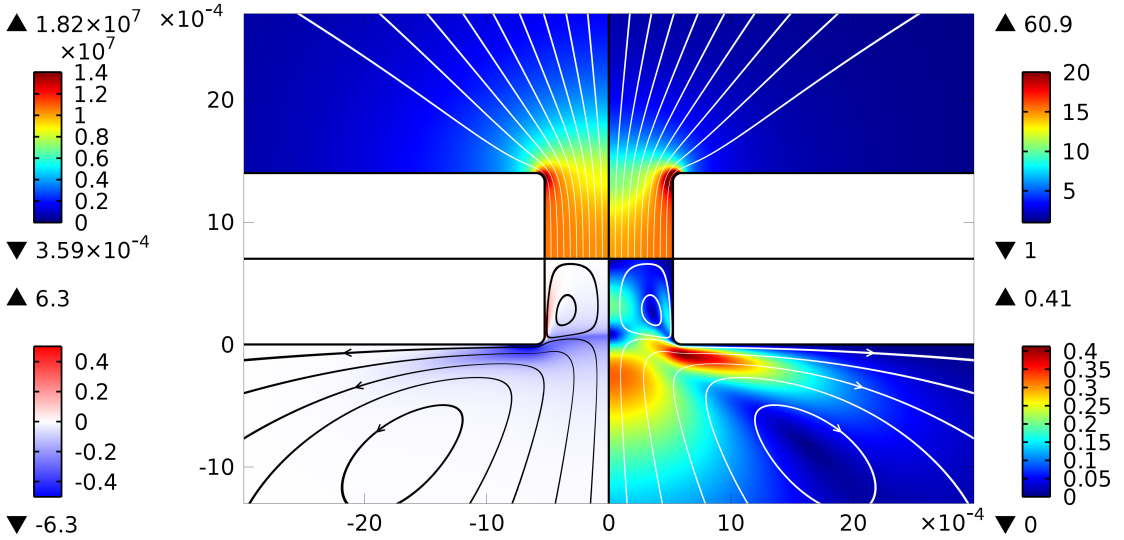

Figure 4: Computed distribution near the hole: the electric field strength and lines (upper left quarter), the relative increase in the dissociation rate with and field lines (upper right quarter), the space charge density and the streamlines (lower left quarter), the velocity magnitude and the streamlines (lower right quarter).

As can be seen from Fig. 4 (where a small area near the hole is shown), the electric field strength is increased in the entire hole, but the maximum values are observed at its edges. The dissociation intensity is distributed in a similar way. Drawing an analogy with the dielectric blade, it is worth noting that the edge of the barrier (the scale of the order of 1 mm) in Fig. 4 plays the role of the end of the blade in Fig. 3. However, it is not sharpened like a blade but blunted (taking into account axial symmetry, the barrier edge forms the hole). In turn, the edges of the hole at the top and bottom surfaces of the barrier (the scale of the order of 0.1 mm) are pointed, and physical processes in close proximity to them are also similar to those at the tip of the dielectric blade. This means there are two "edges" of different scales in the systemп»„the edge of the barrier as a whole and the sharp corners at the edges of

the hole.

The electrical charge moves apart at the both scales. On the scale of the whole hole, a region of positive charge appears above it (not shown in Fig. 4) and that of the negative charge – bellow (Fig. 4). On the scale of the edges of the hole, the two oppositely charged regions appear on different sides of the sharp corner. A small area of positive charge can be seen in Fig.4 at the bottom corner that contributes to the formation of a vortex inside the hole. The complementary region of negative charge enhances the effect of charge separation on the scale of the hole and contributes to the onset of the flow outside the hole.

It should be noted that both the maximum field strength and relative increase in the dissociation rate are smaller than those in the system with the dielectric blade, however, the flow is more intense.

3.4 Slightly protruding hollow tube electrode

Finally, consider a system close to the dielectric barrier with the hole when a slightly (0.1 mm) protruding hollow tube electrode is inserted into the hole. In this case, the electric field distribution is configured mostly by the metal electrode rather than by accumulated charge on the barier.

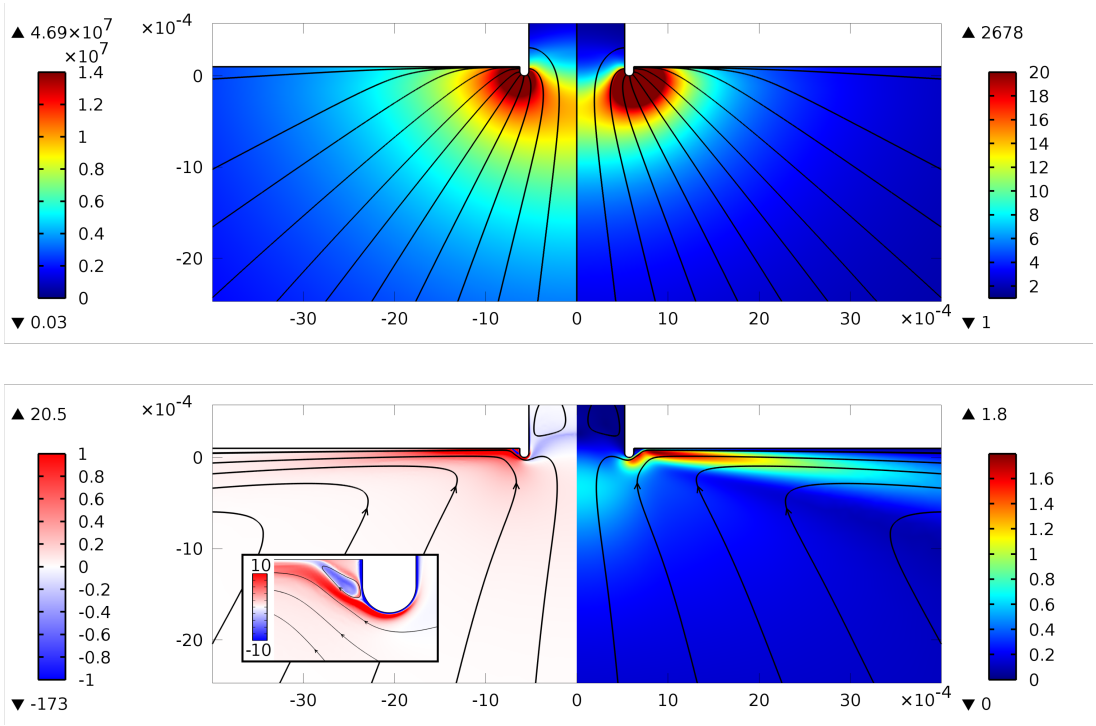

Figure 5: Distribution of quantities near the tube end: (a)п»„the electric field strength (left) and the dissociation intensity enhancement (right) near the end of the tube and the electric field lines; (b)п»„space charge density (left) and velocity magnitude (right) near the end of the tube and the streamlines; (b) also shows an enlarged fragment of the space charge distribution near the in the immediate vicinity to the electrode.

The edges of the tube play the role of sharp dielectric corners in the previous system; the maximum electric field strength and the increase in the dissociation rate are close to those observed in the system with the metal blade. The electric field lines start on the electrode surface at a right angle; they go downward from the very end of the tube (where the field is strongest) and radially along the barrier from its sidewall (where the field is slightly weaker). It would be difficult to predict the direction of the EHD flow if one studied electric field distribution only. Figure 5 shows the flow to be directed along the surface of the barrier right as in the case of the previous system.

As can be seen from the enlarged part of near-electrode region in Fig. 5, there appear a bipolar structure, heterocharge and homocharge layers, and the highest space charge density is produced at the bottom of the electrode. The Coulomb force acts downward here whereas the liquid actually moves to the left in Fig. 5 (away from the axis). Charged bellow the electrode, the liquid shifts and then accelerates radially along the dielectric surface. The EHD flow has the structure as in the system with the hole in the barrier but the specifics of the charge formation and flow intensity (more than 1 m/s) is as in the system with the metal blade.

If the hollow tube is extended from the barrier at a considerable distance, one should expect the system as a whole to be similar to that of needle-plane and the liquid to move toward the counter electrode through the bulk. The simulation results show that the dielectric barrier plays the key role in the present system configuration and changes the flow direction. The possible mechanisms how the barrier influences the flow include the following. First, if the liquid starts moving at some angle to the surface of the barrier under the action of the resultant Coulomb force, the hydrodynamic effects (as the Coanda effect) can redirect the flow along the surface. Second, if the liquid starts moving along the barrier away from the electrode, it transports the charge in the same direction, which enhances the tangential component of the net Coulomb force (a kind of positive feedback takes place). This shows that both electrostatic and hydrodynamic effects contribute to the formation of the EHD flow along the barrier.

4 Conclusions

The paper has studied numerically EHD flows caused by the field-enhanced dissociation in slightly conducting liquids. A number of EHD system configurations have been examined and allow concluding the following:

EHD flows of the dissociation type can emerge near both pointed electrodes and dielectric barriers. The latter additionally requires the accumulated charge to form a localized region of the strengthened electric field. Practically, almost every configuration of dielectric barriers that partially splits the interelectrode gap could lead to the formation of EHD flows of the dissociation type. The flow is always directed away from the region of the enhanced dissociation and follows the electric field lines. In the case of п»„classicalп»„ metal electrodes protruding considerably from any insulation walls, EHD flows are directed toward the counter electrode through the bulk and their structures is qualitatively similar to those of injection EHD flows. If the dielectric barrier edges cause the flows, the same high-voltage processes result in

different space charge distribution and flow structure: the Coulomb force acts upon the oppositely charged regions at the both sides of the edge and accelerates the liquid along the insulation surface away from this edge. If a pointed metal electrode is situated near an insulation surface, a number of electrostatic and hydrodynamic effects can cause the EHD flow to develop along the surface; the direction of the flow can be at a right angle to the direction towards the counter electrode.

Acknowledgements

Research was carried out using computer resources provided by Resource Center "Computer Center of SPbU" (http://cc.spbu.ru).

References

[1] Y. K. Stishkov, A.A. Ostapenko, п»„Electrohydrodynamic Flows in Liquid Dielectricsп»„, Leningrad: Izdatelп»„stvo Leningradskogo universiteta, 1989.

[2] Y. K. Stishkov and V. A. Chirkov, п»„Features of electrohydrodynamic flows in needle-plane electrode system,п»„ 2008 IEEE Int. Conf. Dielectr. Liq., pp. 1п»„3, Jun. 2008.

[3] I. Ashikhmin, Y. K. Stishkov, Y. Donskov, п»„Experimental study of EHD flows in symmetric electrode system in wide range of low-voltage conductivitiesп»„, International Journal of Plasma Environmental Science and Technology, 10 (1), pp. 1-5, 2016.

[4] J. Shrimpton, Charge Injection Systems. Berlin, Heidelberg: Springer Berlin Heidelberg, 2009.

[5] L. Onsager, п»„Deviations from Ohmп»„s Law in Weak Electrolytes,п»„ J. Chem. Phys., vol. 2, no. 9, pp. 599п»„615, 1934.

[6] Y. K. Stishkov and V. A. Chirkov, п»„Formation of electrohydrodynamic flows in strongly nonuniform electric fields for two charge-formation modes,п»„ Tech. Phys., vol. 57, no. 1, pp. 1п»„11, Jan. 2012.

[7] Y. Suh and K. Baek, п»„Competition between the bulk and the dissociation layer in electrohydrodynamic flow of dielectric liquid around coplanar electrodes,п»„ Phys. Rev. E, vol. 87, no. 2, p. 23009, Feb. 2013.

[8] V. A. Chirkov, Y. K. Stishkov, and S. A. Vasilkov, п»„PIV Investigation of EHD Flow Caused by Field-enhanced Dissociation,п»„ in Proc. of 10th Conf. French Soc. Electrost. SFE 2016, pp. 1п»„4, 2016.

[9] V. Chirkov, D. Komarov, Y. Stishkov, and S. Vasilkov, п»„Numerical and experimental study of an EHD flow near solid-dielectric surface,п»„ Proc. 11-th Int. Conf. Mod. Probl. Electrophysics Electrohydrodynamics, pp. 122п»„126, 2015.

[10] A. Gazaryan, A. Sitnikov, V. Chirkov, Y. Stishkov, п»„A Method for Estimation of Functional Dependence of Injection Charge Formation on Electric Field Strengthп»„, in Proc. Electrostatics Joint Conference, pp.1п»„8, 2016.

[11] S. A. Vasilkov, V. A. Chirkov, Y. K. Stishkov, п»„Study on high-voltage conductivity provided solely by field-enhanced dissociation in liquid dielectricsп»„, Journal of Electrostatics, 88, pp. 81-87, 2017.

Y. K. Stishkov, St. Petersburg State University, St. Petersburg, Russia
S. A. Vasilkov, St. Petersburg State University, St. Petersburg, Russia

Four-ion model of an electrohydrodynamic flow in the two-wire electrode system

Yu. Stishkov, R. Zakirianova

y.stishkov@spbu.ru, st016889@student.spbu.ru

Abstract

The paper presents the results of computer simulation of the formation and development of EHD flow in a symmetric electrode-wire system in a closed long channel on the basis of the complete set of EHD equations with four types of ions taken into account. This implements the model of an electrochemical-type EHD converter and allows one to investigate the effect of an external load on its operation. The simulation results are the main characteristics of the through EHD flow of the injection type. The emerging flow was analyzed at different initial ratios of the injection currents, the forced and passive viscous parts of the flow in the closed channel were identified. The extinction of injected ions in the channel is analyzed at different initial ratios of the injection currents at the electrodes.

1 Introduction

An EHD converter is a device that can be used to convert the energy of the electric current into the mechanical energy of a working fluid flow. The structure of an electrohydrodynamic flow of injection type is defined by the electrophysical and electrochemical properties of the working fluid, as well as the electrode-liquid contact parameters. The electrochemical asymmetry of the electrode-liquid contact is required in the symmetrical electrode system to pump fluid through the system, which can be accomplished by means of electrodes of different materials, or various coatings of electrodes, or a liquid with electron-acceptor impurities. In these cases, four types of ions are present in the liquid: those appearing on the electrodes as a result of injection, and the ones dissociated in the volume. These ions, which ensure the intrinsic conductivity of the liquid, can have different properties.

Earlier studies analyzed the structure of the EHD flow in a symmetrical electrode system and identified the effect of the injection intensity on each of the electrodes on the kinematic and dynamic structures of the EHD flow in an open channel [1, 2]. The numerical calculation of computer models of the process of formation and development of an EHD flow, which were implemented within the framework of a two-ionic formulation, has shown that a charge plug can form in the electrode

region under certain conditions. This inhibits the through pumping of the liquid, but can be eliminated by selecting the impurity composition of the liquid so that the injection proceeded on the surfaces of both electrodes [3]. Previously, the EHD flow was calculated numerically in the model of an open short channel, and the effect of the level of low-voltage fluid conductivity [4] and dielectric walls on the flow structure was examined [5].
In a symmetrical electrode system with injection occurring on both electrodes, four types of ions are generated in the liquid: positive and negative ions, which emerge due to either the injection on the electrodes or the dissociation in the volume. In this connection, presented here are the results of computer simulation of the process of formation and development of EHD flow in a symmetric electrode-wire system in a closed long channel on basis of the complete set of EHD equations with four types of ions taken into account. The paper implements the model of an electrochemical-type EHD converter, which allows investigating the effect of an external load on its operation. The simulation yielded the main characteristics of the through-hole EHD flow of the injection type.
A feature of the model with a closed channel is the possibility of analyzing the processes of mutual recombination of injected and dissociated ions. In addition, the model allows taking into account the effects of the uncompensated charge on the cyclic development of EHD flows, as well as the differences in the properties of injected and dissociated ions.

2 Simulation technique

The set of EHD equations contains the Navier-Stokes equation (1), the continuity equation (2), the electrostatic equations (3) and (4), the Nernst-Planck equation for the four ion varieties (5). The considered complete set of EHD equations includes four Nernst-Planck equations - two for injected ions, two for dissociated ions:

$$\gamma\frac{d\vec{v}}{dt}+\gamma\left(\vec{v},\nabla\right)\vec{v}=-\nabla p+\eta\Delta\vec{v}-\rho\nabla\varphi \tag{1}$$

$$div\left(\vec{v}\right)=0 \tag{2}$$

$$div\left(\vec{E}\right)=\frac{\rho}{\varepsilon\varepsilon_0} \tag{3}$$

$$\vec{E}=-\nabla\varphi \tag{4}$$

$$\frac{dn_i}{dt}+div\left(n_i(z_ib_i)\vec{E}-D_i\nabla n_i+n_i\vec{v}\right)=g_i, i=1,\ 2,\ 3,\ 4 \tag{5}$$

$$\rho=\sum_{k=1}^{4z_ien_i} \tag{6}$$

Here $\vec{E}$ is the electric field strength, ρ is the space charge density, φ is the electric potential, n_1 is the concentration of positive injected ions, n_2 is the concentration of negative injected ions, n_3 is the concentration of positive dissociated ions, n_4 is the concentration of negative dissociated ions, g_i is the source function, ε is the relative

electric permittivity, b_i is the ion mobility, D_i is the diffusion coefficient, z_i is the ion valency; ε_0 is the electric constant, e is the elementary electric charge, t is the time; i subscript indicates the ion species, γ is the mass density, $\vec{v}$ is the fluid velocity, p is the pressure, η is the dynamic viscosity. In general, the properties of particles may differ, but the paper assumes them the same. In addition, it should be noted that the ions were univalent, that is, $|z_i|= 1$.

In the problem, we consider the injection and dissociation mechanisms of charge formation with allowance for recombination. The injected ions recombine with one another and with dissociated ions of the opposite sign. Dissociated ions are produced in the volume and recombine with one another and with injected ions. The right-hand side of equations (5) is supplemented with a term describing the death of particles in the volume, and that of (5) for $i = 3,\ 4$ - a term describing the volumetric source of ion generation W:

$$\rho = \alpha_r n_1(n_2 + n_4) \tag{7}$$

$$\rho = \alpha_r n_2(n_1 + n_3) \tag{8}$$

$$\rho = W - \alpha_r n_3(n_2 + n_4) \tag{9}$$

$$\rho = W - \alpha_r n_4(n_1 + n_3) \tag{10}$$

Here W is the dissociation intensity, α_r is the recombination coefficient. The coefficient of recombination of i and k species is determined by the following formula $\alpha_{rik} = \frac{e(b_i+b_k)}{\varepsilon\varepsilon_0}$.

In a liquid with intrinsic conductivity in the absence of an external electric field, the formation of ions occurs due to the thermal motion of the molecules. The equilibrium concentration of ions, which form due to dissociation, is determined by the condition that the rates of dissociation and recombination are equal. The equilibrium concentration is determined through the low-voltage conductivity and is given in this problem as initial equilibrium value $n_0 = \frac{\sigma_0}{2eb}$.

The source function for positive and negative particles in this problem will be the same. The dissociation coefficient in the absence of an external electric field is determined through the equilibrium concentration and is written as $W_0 = \frac{\sigma_0^2}{2eb\varepsilon\varepsilon_0}$.

The Wine effect in the problem is not considered, that is, we assume the dissociation intensity to be constant and equal to the dissociation coefficient in the absence of an external field $W = W_0$. Thus, the source functions in equations (5) for $i = 3,\ 4$ can be written as follows:

$$\rho = W_0 - \alpha_r n_3(n_2 + n_4) \tag{11}$$

$$\rho = W_0 - \alpha_r n_4(n_1 + n_3) \tag{12}$$

The diffusion coefficient was determined by the Einstein relationship $D_i = \frac{k_B T_0}{eb_i}$, where k_B is the Boltzmann's constant, T_0 is the system temperature. The liquid properties are: $b_i = 10^{-8}\ \frac{m^2}{V\cdot s}$, $D_i = 2.59\ cdot10^{-10}\ \frac{m^2}{s}$, $|z_i|= 1$, $\gamma = 950\ \frac{kg}{m^3}$, $\eta = 4.75 \cdot 10^{-3}\ Pa \cdot s$, $\sigma_0 = 3 \cdot 10^{-11}\ \frac{S}{m}$.

A symmetrical wire-wire electrode system in a closed channel was considered (Fig. 1). By virtue of the symmetry of the model about the horizontal axis passing through the electrodes, only half of the model was calculated. The two-dimensional problem was

considered since the wire lengths are much larger than the interelectrode distance. The geometric dimensions were as follows: $W = 6\ cm$, $H = 0.75\ cm$, $L = 1\ cm$, $d = 0.1\ cm$, $r = 0.025\ cm$ is the radius of electrodes.

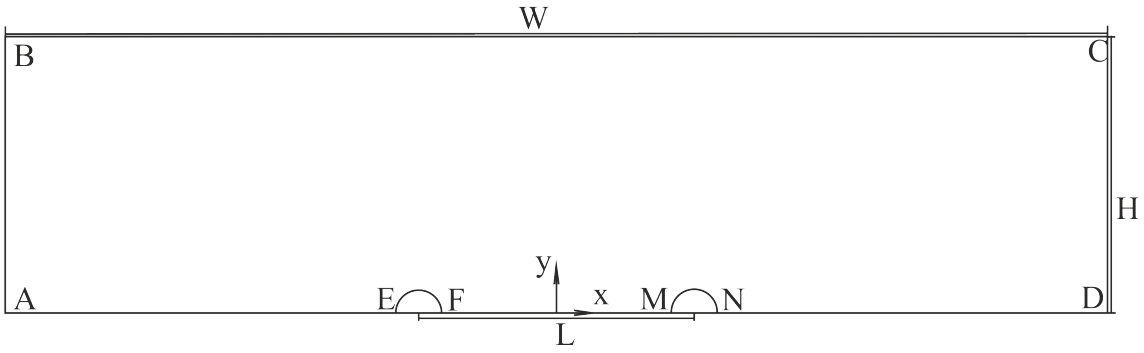

Zakirianova 1: Geometry and boundary conditions.

The channel closure was effected with the help of an original boundary condition, which makes it possible to transfer the values of the unknown functions from the right-hand boundary of the channel to the left-hand one. The choice of boundaries is determined by the direction of the through flow.
Electric potentials $\pm U_0 = \pm 10\ kV$ were specified for the Poisson equation at electrode boundaries EF and MN. The condition of the normal component of the electric field strength being zero is set as $\vec{N} \cdot \vec{D} = 0$on dielectric wall BC. In this case, it is assumed that the charge on the walls shields the field, and the normal component of the field is zero. The condition for transferring charge flux $\rho\vec{v}$ from boundary CD to boundary BA is used as a condition for the closure of the channel.
Flux of ions of the corresponding sign, $\vec{j_i} = f_i(\vec{E})$, and the extinction of ions of the opposite sign, which was set by equation: $\vec{j_i} \cdot \vec{N} = -(n_i(z_i b_i)\vec{E} - D_i \nabla n_i + n_i \vec{v}) \cdot \vec{N}$, were set for the Nernst-Planck equations for the injected ions at electrode boundaries EF and MN. The extinction of the negative injected and dissociated ions was determined at boundary EF, that of the positive injected and dissociated ions was determined at boundary MN. At channel boundary AB, the fluxes of different sorts of ions were set equal to the corresponding fluxes at boundary CD, which were determined by equation $-\vec{j_i} \cdot \vec{N} = (n_i(z_i b_i)\vec{E} - D_i \nabla n_i + n_i \vec{v}) \cdot \vec{N}$. The isolation condition was specified by equation $-\vec{j_i} \cdot \vec{N} = 0$at upper boundary BC and lower boundaries AE, FM, and ND. The free passage of ions was set on right-hand boundary CD. The injection current at the electrodes is given in the form of a quadratic polynomial in the local electric field strength according to formula

$$\vec{j_i} = \left(A \cdot |\vec{E}| + B \cdot |\vec{E}|^2\right) \cdot \vec{N} \tag{13}$$

where A and B depend on the material of the electrodes and impurity additives to the liquid. The injection current on the left-hand electrode was considered in the problem to be greater than on the right-hand one. This determined the direction of the through flow from left to right. The injection functions were chosen in such a way that the initial injection current densities on the left-hand electrode were two or three times higher than on the right-hand electrode.

The adhesion condition $\vec{v} = 0$ was specified for the Navier-Stokes equation at the upper and lower boundaries and on electrodes EF and MN. An incoming fluid flow, whose velocity was equal to that of the flow at boundary CD ($\vec{v} = \vec{v}_{right}$), was set at boundary AB. At boundary CD, there is the outflow with the pressure equal to that pressure at boundary AB, without viscous resistance, following the equation $\left[\mu\left(\nabla\vec{v} + (\nabla\vec{v})^T\right)\right] \cdot \vec{N} = 0$.
The non-stationary problem was solved. The initial conditions are voltage switching, fixed liquid with conductivity equal to the equilibrium value.

3 Results and discussion

At the initial moment, there is no fluid flow, a voltage of 10 kV is applied to the electrodes. After that, the counter flows from both electrodes form in the interelectrode gap, with the flow velocity from the left-hand electrode higher than from the right-hand one. When jets from different electrodes meet, a more intense jet from the left-hand electrode blows a counter jet into the region behind the electrode. So, the through flow forms in the interelectrode gap and in the rest of the channel; the flow rate of the liquid through the channel cross section is sustained. Fig. 2 shows that the process of balancing the flow in a closed channel lasts about 10 seconds, and then the flow rate remains constant. The time is longer than that of crossing of the interelectrode gap by the charged jet. The time dependence of the injection currents on the electrodes also displays regions of attaining the steady state: the current from the left-hand active electrode decreases, and that from the right-hand passive electrode increases. These processes are associated with the formation of charged structures in the bulk, which affect the surface field strength, and therefore, the injection currents. When homocharges form at the electrodes, the injection current of positive ions decreases, and that of negative ions increases. As the smaller, positively-charged jet propagates to the counter electrode, the injection currents increase slightly. After the flux of positively charged ions closes the interelectrode gap, the injection currents decrease. If the injection currents are balanced, the moving charges of the positive and negative ions will be equal and the jet at the outlet of the channel will be neutral. In our case, the injection current of positive ions is approximately one and a half times larger than that of negative ions.
Fig. 3 represents the successive stages of the formation of the EHD flow in a closed channel. The positive space charge is seen to propagate from the right-hand electrode, dominant in the interelectrode gap, into the region behind the electrode. After the stream of the positive charge reaches the right-hand boundary, the smaller charged jet passes to the left side of the cell and the flow attains a steady state. The so-called through EHD flow of injection type forms in the steady state. It is characterized by a thin charged jet, which flows from the active electrode, crosses the interelectrode gap, and becomes a wafer-shaped bipolar charged structure in the region behind the electrode. This prevents the formation of charge plugs and provides some acceleration of the liquid into the region behind the electrode. In general, the flow in the channel can be divided into two parts: the forced flow in the region of the interelectrode gap, where the current lines crowd to the central plane

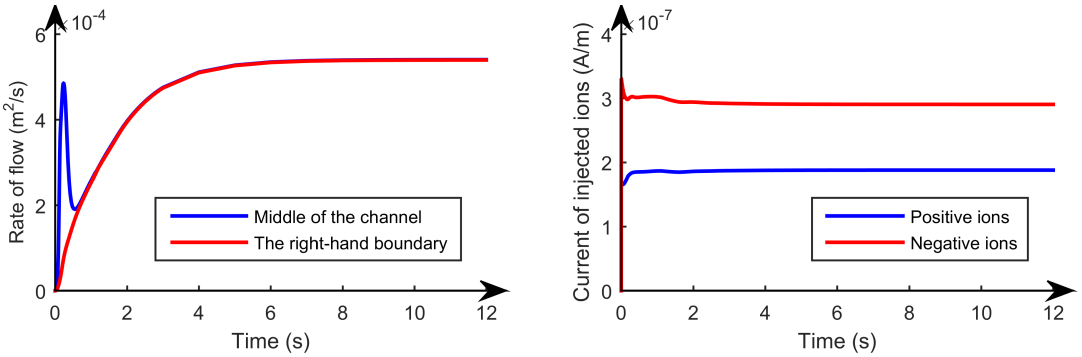

Zakirianova 2: Time dependences of fluid flow rate in different parts of the channel (on the left) and injection currents with a ratio of injection currents of 2:1 (on the right).

and the profile is of Gaussian shape, and the passive viscous flow elsewhere. Intense liquid acceleration occurs in the forced region(see Fig. 3 and Fig. 4).

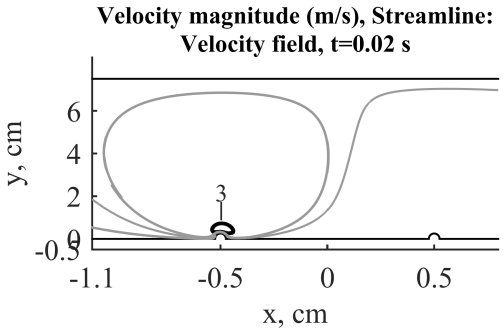
Velocity magnitude (m/s), Streamline:
Velocity field, t=0.02 s
y, cm
x, cm

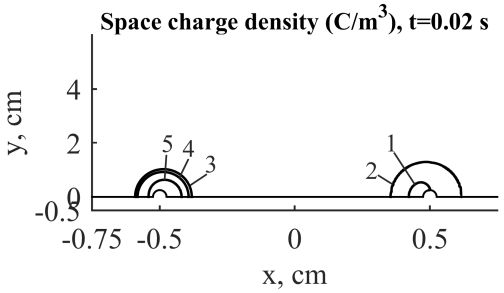
Space charge density (C/m3), t=0.02 s
y, cm
x, cm

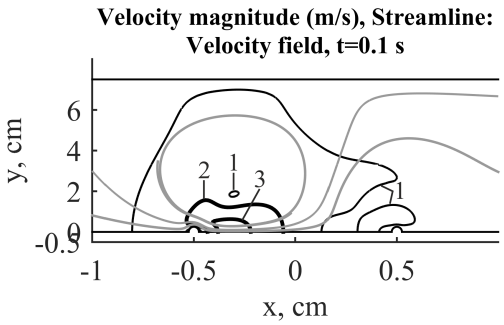
Velocity magnitude (m/s), Streamline:
Velocity field, t=0.1 s
y, cm
x, cm

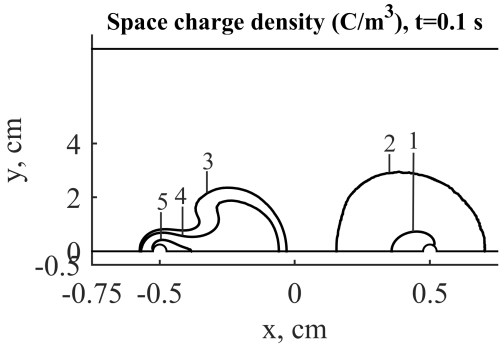
Space charge density (C/m3), t=0.1 s
y, cm
x, cm

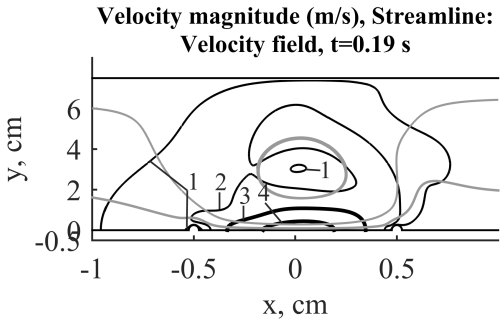
Velocity magnitude (m/s), Streamline:
Velocity field, t=0.19 s
y, cm
x, cm

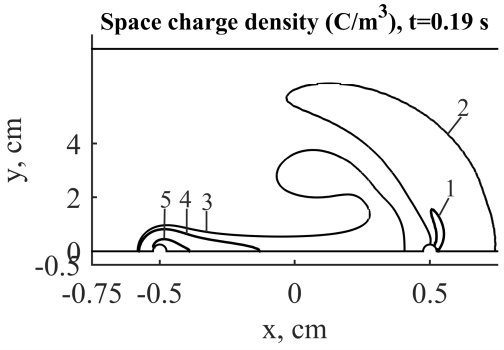
Space charge density (C/m3), t=0.19 s
y, cm
x, cm

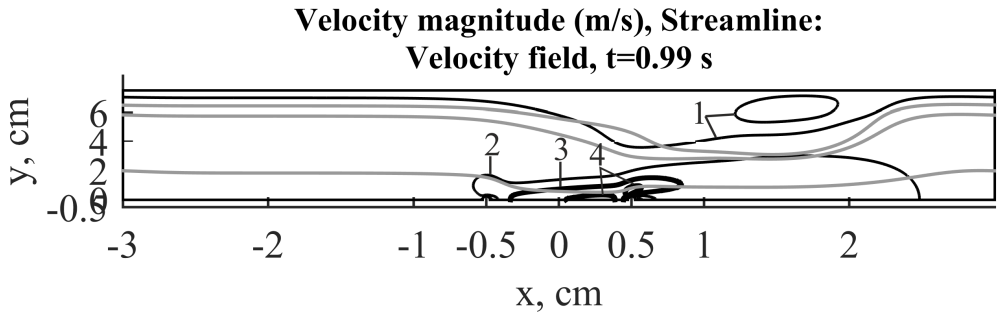
Velocity magnitude (m/s), Streamline:
Velocity field, t=0.99 s
y, cm
x, cm

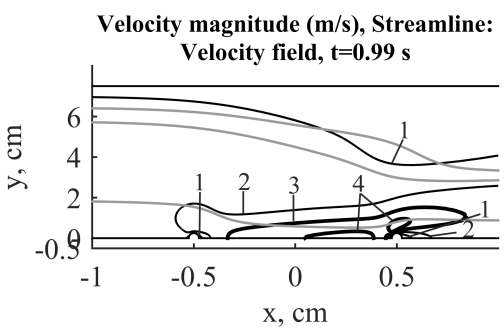
Velocity magnitude (m/s), Streamline:
Velocity field, t=0.99 s
y, cm
x, cm

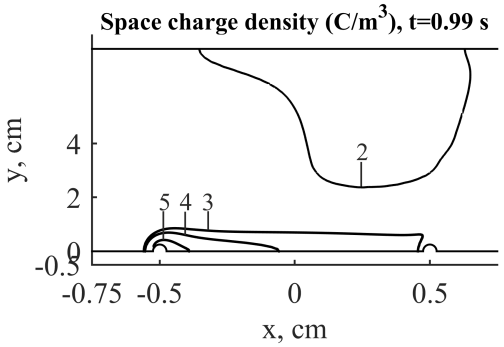
Space charge density (C/m3), t=0.99 s
y, cm
x, cm

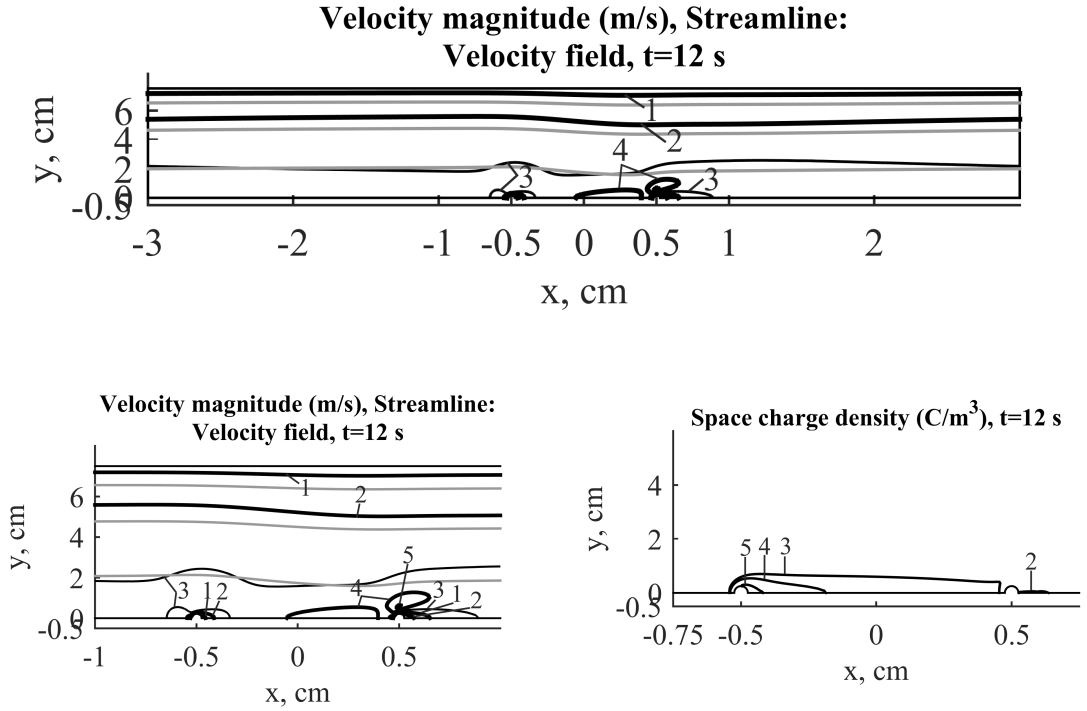

Zakirianova 3: Isolines of the flow velocity distribution and the liquid flow line, the distribution of the space charge at successive instants of time (ratio of injection currents 2: 1). On the velocity distribution plots: 1 - 0.01 m/s, 2 - 0.05 m/s, 3 - 0.1 m/s, 4 - 0.15 m/s, 5 - 0.19 m/s. On the diagrams of the distribution of the density of the space charge: 1 - -0.002 mC/m3, 2 - -0.2 mC/m3, 3-1 mC/m3, 4-2 mC/m3, 5-3 mC/m3.

Fig. 4 shows longitudinal velocity distributions along the central plane of the channel and velocity profiles at different flow levels at the last instant of time. The streamlines are parallel to the walls of the channel in the region of passive viscous flow, the flow velocity decreases slightly along the channel and the velocity profile has a typical parabolic shape. Between these areas, there is the transition area, within which the flow passes from the forced state to the passive one. This region is characterized by a discharge of liquid into the region behind the electrode. Judging from the longitudinal velocity distributions, the length of the transition region corresponds approximately to the size of the interelectrode gap.

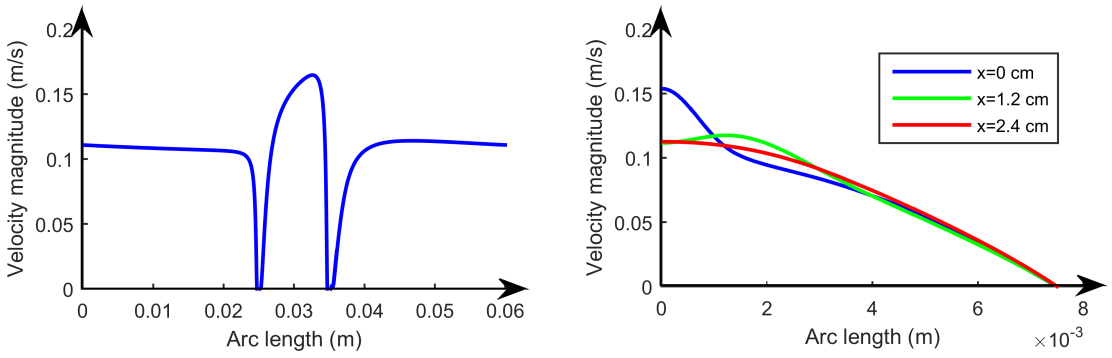

Zakirianova 4: Linear longitudinal (on the left) and transverse (on the right) velocity distributions at the last instant of time (ratio of injection currents 2:1).

Let us analyze the mechanisms of liquid discharge. Fig. 5 shows the longitudinal distributions of the concentration of injected ions at the initial ratio of the injection currents on the left-hand and right-hand electrodes of 2:1 and 3:1, respectively. The positive injected ions of type 1 are seen to be produced on the active electrode and to propagate across the interelectrode gap. There is an intense decrease in the concentration of positive ions within the interelectrode gap due to recombination with negative type 3 conduction ions. Negative ions of type 2 are produced on the passive electrode, therefore the recombination processes go faster. The recombination processes can be seen to occur throughout the entire channel. However, the injected ions do not have enough time to completely recombine in the gap behind the negative electrode and the injected ions are transferred from the right-hand boundary to the left-hand one. However, the concentration decreases by a factor of e at a distance of 1 cm from the right-hand electrode. With the initial ratio of currents of 3:1, the concentration of injected ions that are transferred to the left boundary of the channel is somewhat smaller than the initial ratio of injection currents of 2:1. Also, the concentrations of injected ions of different signs that reach the boundary of the channel are equal at initial ratio of injection currents of 3:1.

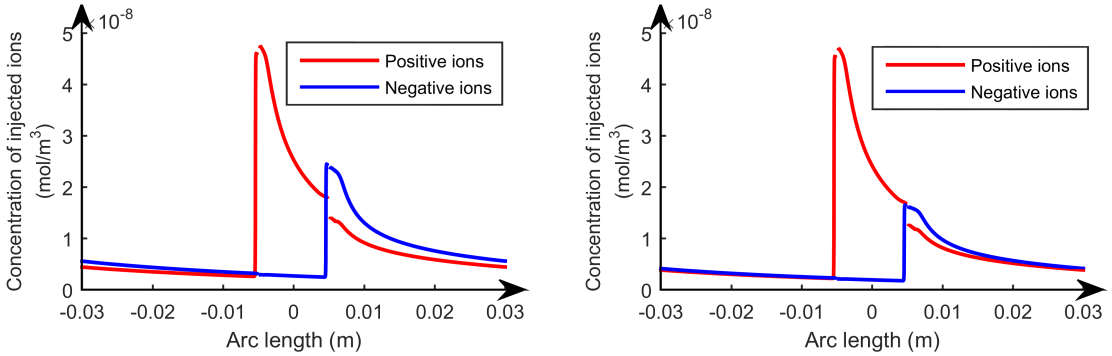

Zakirianova 5: Longitudinal distributions of the concentration of injected positive and negative ions at different initial injection levels (2:1 on the left and 3:1 on the right.

Fig. 6 presents the time dependences of the injection currents on the active and passive electrodes at different initial ratios of the injection currents. The injection

currents in the process of balancing the flow are seen to tend to 1.9:1 at the initial ratio of injection currents of 3:1, and to 1.6:1 at 2:1. At the same time, the average space charge (Fig. 6) circulating through the channel at the initial ratio of 2:1 is half that at the initial ratio of 3:1. Therefore, it is preferable to select the nearest injection currents, with the average flow rate practically unchanged over the channel.

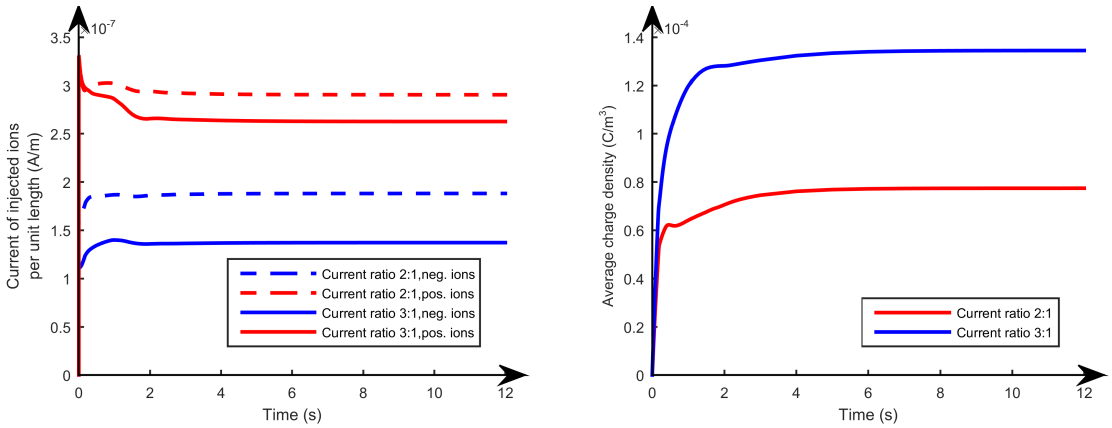

Zakirianova 6: Time dependences of injection currents at the initial ratio of injection currents of 2:1 and 3:1 and the average charge density.

Conclusions

The computer simulation of EHD-flows of injection type from the electrodes of wire-wire type in a closed channel, which is substantially longer than the interelectrode gap, is carried out. A liquid, where four types of ions are present, is considered. The advantage of the model is the possibility of the direct analysis of recombination processes and the study of effect of load and uncompensated space charge on the development of through EHD flows in a closed channel. The structure of the EHD flow is analyzed inside and outside the interelectrode gap.

The model allows one to precisely select the optimum injection function on the electrodes for implementation of the through flow. The results are compared for the initial ratio of injection currents of 2:1 and 3:1; in the first case, the average density of the space charge circulating through the channel decreased almost twofold and the flow rate did not change. Therefore, for the practical application of such a system, it is preferable to choose the nearest initial injection currents that ensure the through flow regime.

References

[1] Buyanov A. V., Stishkov Yu. K., Kinematic Structure of Electrohydrodynamic Flow in “ Wire-Wire”and “ Wire over Plane”Electrode Systems Placed in a Liquid, Technical Physics, vol. 48, no. 8, pp. 972-977, 2003.

[2] Buyanov A. V., Stishkov Yu. K., Peculiarities in the Structure of Electrohydrodynamic Through Flow in a Symmetric Electrode System, Technical Physics, vol. 74, no. 8, pp. 120-123, 2004.

[3] Ashikhmin I. A., Stishkov Yu. K., Strukturnyie Osobennosti EGD-techeniy v Simmetrichnoi Sisteme Elektrodov, [Peculiarities in the Structure of EHD-flow in a Symmetric Electrode System], Elektronnaya obrabotka materialov, є 6, pp. 42-51, 2009.

[4] Ashikhmin I. A., Stishkov Yu. K., Influence of the Level of the Low-voltage Conduction on the Structure of the Through Electrohydrodynamic Flow in a Symmetric Electrode System, Surface Engineering and Applied Electrochemistry, vol. 50, no. 3, pp. 246-252, 2014.

[5] Ashikhmin I. A., Stishkov Yu. K., Effect of Insulation walls on the Structure of Electrodynamics Flows in a Channel, Technical Physics, vol. 57, no. 9, pp. 1181-1187, 2012.

Yu. Stishkov, St. Petersburg State University, Universitetskaya nab. 7-9, St. Petersburg, Russia
R. Zakirianova, St. Petersburg State University, Universitetskaya nab. 7-9, St. Petersburg, Russia

On the selection of snapshot computation for Proper Orthogonal Decomposition in structural dynamics

S. Tegtmeyer, A. Fau, P. Bénet, U. Nackenhorst
stefanie.tegtmeyer@ibnm.uni-hannover.de

Abstract

The analysis of structural dynamic systems usually involves a large number of finite elements and time steps. In order to save computational resources, model order reduction (MOR) approaches have been developed. The Proper Orthogonal Decomposition (POD) is one MOR technique, which defines from a training stage, so called snapshot computation, a reduced basis in which the dynamic equations may be solved easily and quickly. In this contribution, the efficiency of POD in terms of computational cost and accuracy is investigated depending on the load considered during the training stage for dynamic applications.

1 Introduction

In civil or mechanical engineering, dynamic systems are often studied using the finite element method (FEM). This leads to the discrete system of equations $M\ddot{x}(t) + D\dot{x}(t) + Kx(t) = f(t)$, where x is the set of degrees of freedom (dofs) defining the system, i.e. x contains the displacement in each direction for all the nodes and for any time t. $f(t)$ is the time depending loading and M, D, K are the mass matrix, viscous damping matrix and stiffness matrix respectively. They are here considered as constant and symmetric. Despite powerful computational capabilities, some analyses and design problems still cannot be solved within a reasonable computing time using standard methods when the number of dofs N becomes very large. It is then advisable to construct reduced models which approximate the behaviour of the original model by much less dofs while maintaining an acceptable accuracy [12, 10].
Different model order reduction (MOR) approaches have been proposed in the literature [3]. They are based on Galerkin projection onto a subspace of the Sobolev FEM space. This space may depend on the time step t for non-linear problems [12]. The reduced system for the displacement approximation $\tilde{x}$ reads

$$\Phi^T M \Phi \ddot{\tilde{x}}(t) + \Phi^T D \Phi \dot{\tilde{x}}(t) + \Phi^T K \Phi \tilde{x}(t) = \Phi^T f(t), \tag{1}$$

where Φ is a transformation matrix defining the reduced space and the number of dofs is significantly smaller.
Modal basis contains the natural eigenforms of the structure [9, 4]. As this basis is orthogonal with respect to the scalar product of M and K, the dynamic system turns to be diagonal, which reduces drastically the computational cost [12]. The load-dependent Ritz method avoids to compute the eigenvalue problem, which may be costly [7]. Condensation methods, such as Guyan method or dynamic condensation, are explored in [11]. From the comparison between alternative MOR techniques for quasi-static cases [5], or for the frequence response analysis of proportional and non-proportional damped systems [13], Proper Orhogonal Decomposition (POD) appears as an interesting alternative.
POD defines a basis from the result $\{x_T(t)\}$ of a first simulation referred to as the training stage, as summarized in figure 1.

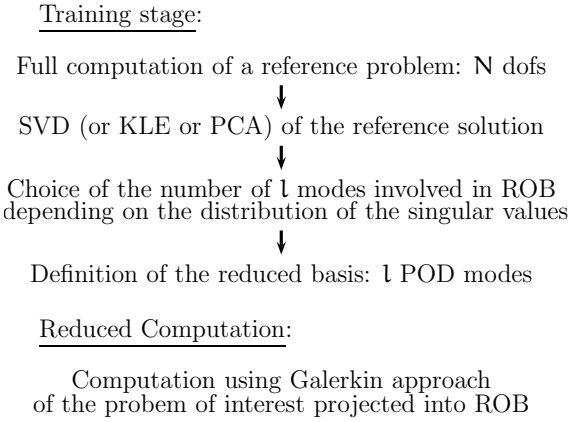

Figure 1: Schematic representation of the POD steps (ROB: Reduced Order Basis)

Using for example singular value decomposition (SVD), a space-time decomposition of the snapshot matrix $X_T(p,t)$ representing the results $\{x_T(t)\}$ provides a set of left singular vectors L and right singular vectors R [5] as $X = (x_1, x_2, ..x_n) = L\lambda R^T$. λ is pseudo diagonal, L and R are orthogonal. By normalizing the singular vectors, this decomposition is unique. L and R describe the space and time dependences of the solution respectively. As the space part of the problem is generally the most computationally costly, POD is based on the space matrix considering l vectors of the matrix L. The decomposition could also be provided by principal component analysis (PCA) or by Karhunen-Loève expansion (KLE) [8].
Once the number l of space modes has been chosen depending on the required accuracy [6], the reduced problem is computed on the basis of POD modes. POD coefficients which represent the time dependence are computed, while the space dependence of the deformation of the structure is described by the POD modes. Updating POD basis during the computation has been proposed by several authors e.g. [1]. Some drawbacks of POD is that the full model still needs to be computed during the training stage, and that the accuracy of the computation largely depends on the training stage characteristics such as its loading or boundary conditions.
An open question is which training problem has to be considered to establish the POD basis for the problem of interest. This question includes time interval to be

considered for the training stage, the loading with respect to time as well as the position of the applied load. Some authors propose for dynamics to consider the first time steps of the problem of interest to establish the ROB, without a detailed investigation, a time length corresponding to the fundamental period of vibration is heuristically suggested in [5]. But it has been outlined that this time has not been optimised. In this contribution, the influence of the time interval and the loading case of the training problem on the POD approximations is investigated. Computational savings offered by POD strategies are also explored to evaluate the potential interest of this approach for dynamic applications.

2 Investigation of POD for dynamic computations

To explore POD capabilities depending on different training stage strategies, a cantilever model with length 25 m, height 1.45 m, and width 3 m is used as structural example. A linear elastic material behaviour with Young's modulus of 210 GPa, Poisson's ratio of 0.3, and mass density of 7850 $\frac{\text{kg}}{\text{m}^3}$ is considered.

2.1 Load cases and numerical discretization

The model is studied under different load cases causing bending (B) and/or normal tension and compression (C), as illustrated in figure 2. For the bending load case, the force is applied at the free end once and in subsequently computations at different positions (load cases B_1 and B_2). Different loads with respect to time are taken into account, e.g. a Heaviside step, a Dirac impulse, or a harmonic loading, see figure 3. For the analysis, the dynamic response of the centre point at the free end section is considered as quantity of interest.

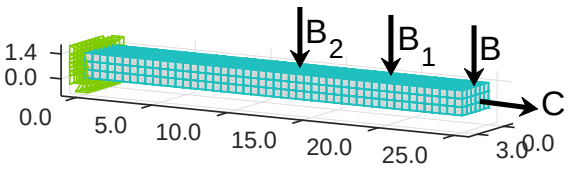

Figure 2: FE model with positions of applied loads

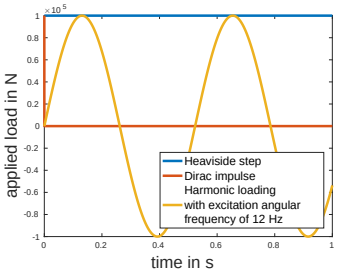

Figure 3: Applied loads with respect to time

The model is discretized using three-dimensional eight-node finite elements with linear shape functions resulting in 4284 dofs. Time integration is performed using an explicit central difference scheme to avoid numerical damping due to implicit solvers and to obtain an accurate estimation of the dynamical response. The time interval of 10 s is divided into 100 000 time steps, leading to a time step interval of 10^{-4} s to guarantee a stable solution of the explicit solver.

2.2 Training stage: Snapshot time window and number of reduced dofs

At first, the influence of the POD training interval on the accuracy of the POD computation considering the same kind of loading is investigated. The results obtained are depicted in figure 4 for a harmonic loading with excitation angular frequency of 325 Hz. A training interval of 0.01 s is too small to gather enough information on the system behaviour for POD construction, see figure 4 (a). The amplitude of the POD approximated response is too small and the response frequency is too high independently of the number of dofs considered in the reduced model. Therefore, the training interval is successively increased. For a smooth, continuous loading, like the harmonic loading, already a training interval of 0.025 s provides good results, if the system is reduced to 10 or 50 dofs, compare figure 4 (b). Using less dofs results into inaccurate approximations. Augmenting the time interval, less dofs are required to obtain a good approximation with the reduced model as illustrated in figure 4 (c). For a non-smooth loading, like the Dirac impulse loading, the time interval of the training stage needs to be increased to at least 0.05 s. It is possible to use only one dof in the reduced system, if the training interval has been large enough.
The required training interval is relatively small, here 0.05 s represents less than 10 % of the period of the first eigenfrequency.

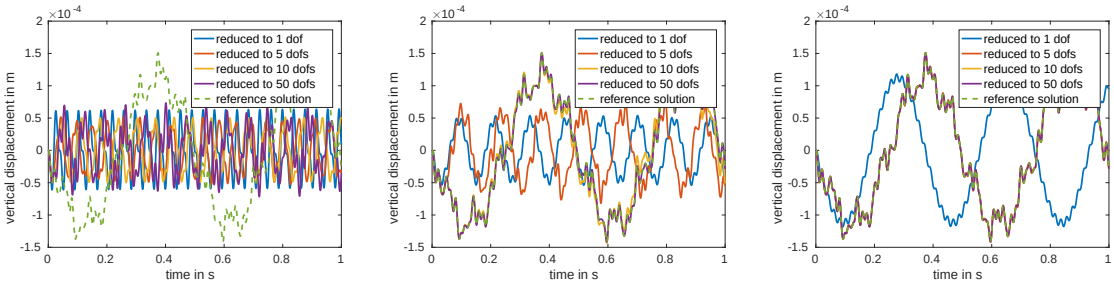

(a) $\Delta t_{Training} = 0.01\,\mathrm{s}$ (b) $\Delta t_{Training} = 0.025\,\mathrm{s}$ (c) $\Delta t_{Training} = 0.05\,\mathrm{s}$

Figure 4: POD dynamic responses under harmonic loading with excitation angular frequency of 325 Hz using different training intervals $\Delta t_{Training}$. The reference solution is computed using a modal subspace reduced model of 100 dofs.

To evaluate the approximations obtained when the applied load of the snapshot compuation and the target computation differ with respect to time, a mean relative error is defined as

$$e_{rel} = \frac{1}{nsteps} \sum_{t_i=1}^{nsteps} \frac{|u_{ref}(t_i) - u_{red}(t_i)|}{|u_{ref}(t_i)|},$$

comparing u_{ref} the reference solution computed with modal subspace reduced model of 100 dofs to u_{red} the solution of the POD reduced model for the centre node at the free end over the whole number of time steps ($nsteps$).
If the aim is to compute the system under a Dirac impulse load case, POD modes from snapshots of a Heaviside step or harmonic loading lead to non-sufficient approximations, see figures 5 (a) and (b). On the other hand, POD modes computed

from snapshots of a Dirac impulse loading can be applied successfully for target computations under Heaviside step and harmonic load cases if the training interval is chosen large enough, see figure 5 (c).
The accuracy of POD approximation using snapshot computations from Heaviside step or harmonic loading, compare figures 5 (a) and (b), converge to a limit with respect to the training time interval, while using the Dirac impulse as load case, the approximation can still be improved by using a larger training time interval as depicted in figure 5 (c). This is due to the range of frequencies excited by the different load cases. The Heaviside step and harmonic loading only excite a specific range of frequencies whereas the Dirac impulse loading excites theoretically all frequencies. Therefore, more information about the dynamic behaviour of the model is captured in the Dirac snapshots which can then be extracted by SVD.

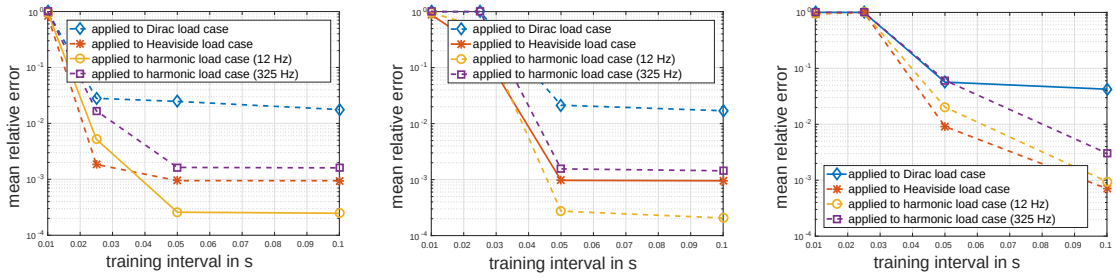

(a) Harmonic loading (12 Hz) snapshots

(b) Heaviside step snapshots

(c) Dirac impulse snapshots

Figure 5: Comparison of the applicability of snapshot computations from different load cases for reduced models with 25 dofs

2.3 Comparison of POD bases

To have a better understanding of the method's behaviour, the POD subspace appearing from SVD of the snapshot computations are compared. In figure 6 the first 50 POD modes obtained from a computation with a Dirac loading within a time interval of 0.1 s are compared to POD modes obtained for the same loading but a smaller time interval by computing the scalar product of each vector pair. A light white point symbolises a scalar product of zero, i.e. these vectors are orthogonal, whereas a dark black point marks a scalar product close to one, i.e. these vectors are collinear. The POD modes from a training stage of 0.01 s and 0.1 s differ, only about 5 similar modes are observed. While enlarging the training time interval, the POD modes converge to a final set of modes. Even for a non-harmonic loading, enlargement of the time interval will not change the determined set of POD modes.

POD modes represent the space dependence of the training stage. Therefore, considering a pure bending load case as training stage, first POD modes are similar to the first pure bending eigenmodes, see figure 7. Similarly, for a longitudinal compression deformation as training problem, the first POD modes correspond to the first eigenmodes describing this kind of deformation. For POD computation considering

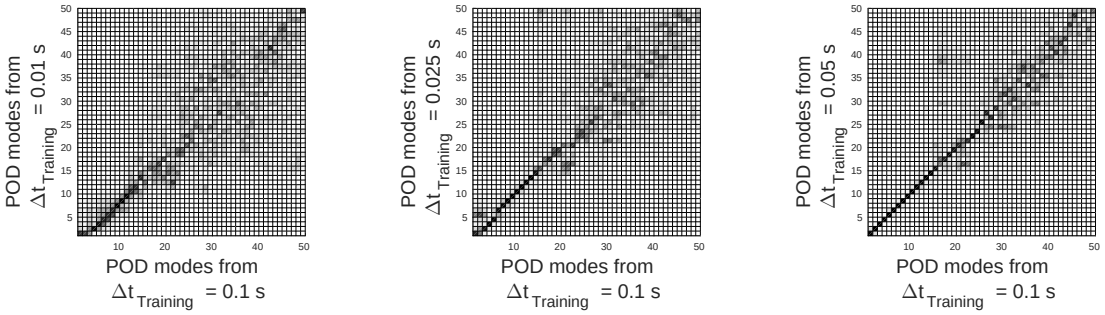

Figure 6: Comparison of POD modes from different training intervals under Dirac loading

B and C load coupled, the eigenmodes corresponding to a bending and compression deformation are extracted by the POD computation.

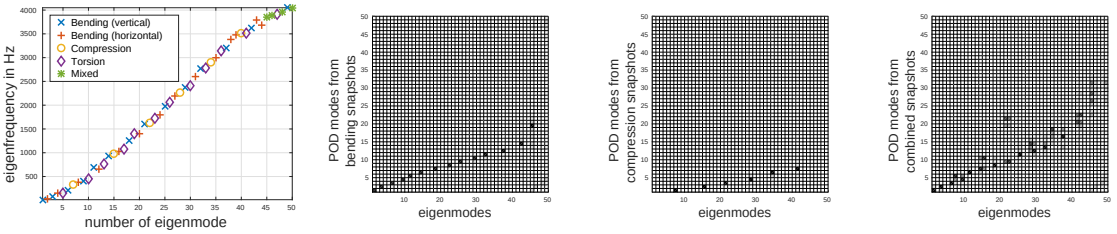

Figure 7: Comparison POD modes from a training interval of 0.1 s with eigenmodes

When modifying the position where the bending load is applied the extracted POD modes differ. 12 modes computed from 10 000 snapshots are similar for load case B and B_1 and only 9 modes are similar for load case B and B_2. Similar are the first POD modes which correspond to the pure bending eigenmodes.
Hence, the application point of the load has a large influence on the definition of the POD basis, and subsequently on the accuracy of the POD computation.

2.4 POD computational effort

Finally, the required computational effort is compared. For the reduction process a singular value problem needs to be computed and the original system is transformed by a Galerkin projection onto a subspace. The computation times for the reduction are presented in figure 8. The more snapshot computations are used and the more dofs the reduced system consists of, the larger the computational times. The computations of snapshots are not considered here.
In figure 9, the computational times for solving the full system and the reduced systems are compared for a time interval of 10 s, corresponding to a computation of 100 000 time steps. The computational effort of the reduced systems here includes the snapshot computations, the reduction process as well as the solution of the reduced system. The number of dofs of the reduced model contributes only slightly to the computational times compared to the snapshot computations.
The savings with respect to the number of snapshot computations are presented in figure 10. For a large number of time steps, POD is clearly more efficient than solving

the full system directly. The advantage of the reduced model depends directly on the required number of time steps for the training time interval and the number of time steps of the target computation. This factor equals to the computational savings. The computational effort of the singular value decomposition and the projection onto the subspace are insignificant. However, for this linear example modal decomposition performs better than POD.

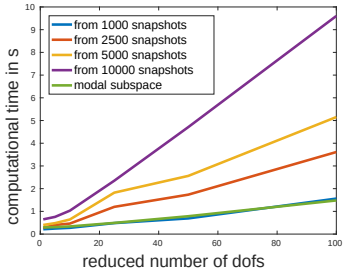

Figure 8: Computational times to reduce the system by SVD

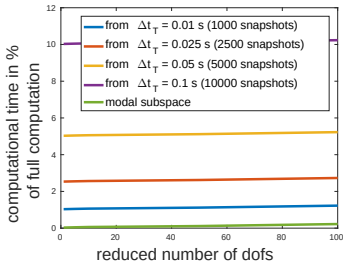

Figure 9: Comparison of computational times for a time interval of 10 s

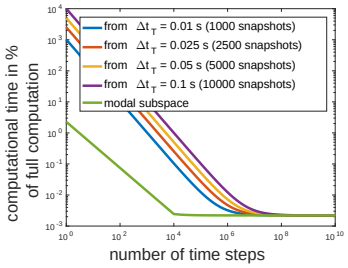

Figure 10: Computational times of reduced models with 100 dofs

3 Conclusion

Here, POD performance has been investigated for linear dynamics, in particular the required characteristics of the training stage have been explored. Concerning the training stage time, it has been seen that a relatively short time, corresponding to less that 10 % of the period of the first eigenmode, is enough to guarantee a good accuracy of the POD approximations. POD computational savings is drastically significant, and becomes larger when the POD computations tackle a long time interval. POD approach seems limited to some load positions which are close to the one of the training stage. Modal decomposition is more flexible regarding different load positions and more efficient in the matter of computational effort in this linear case, but will be reaching its performance limit when including non-linearities. New strategies to overcome that shall be explored in the future.

Acknowledgements

The authors acknowledge the financial contribution from Erasmus and Région Aquitaine Limousin Poitou-Charentes which has funded the stay of Pierre Bénet at the Institute of Mechanics and Computational Mechanics (IBNM), Leibniz Universität Hannover.

References

[1] D. Amsallem *et al.*. A method for interpolating on manifolds structural dynamics reduced-order model, Int. J. Numer. Methods Eng., 80-9, 1241-1258, 2009

[2] K.-J. Bathe. Finite element procedures, Springer, 1996.
[3] B. Besselink *et al.*. A comparison of model reduction techniques from structural dynamics, numerical mathematics and systems and control, Journal of sound and vibration, 332, 4403-4422, 2013.
[4] E.J. Davison. A Method for Simplifying Linear Dynamic Systems, IEEE Transactions on automatic control, 11, 93-101. 1966.
[5] S. Eftekhar Azam, S. Mariani. Investigation of computational and accuracy issues in POD-based reduced order modeling of dynamic structural systems, Engineering Structures, 54, 150-167, 2013.
[6] G. Kerschen *et al.*. The Method of Proper Orthogonal Decomposition for Dynamical Characterization and Order Reduction of Mechanical Systems: An Overview, Nonlinear Dynamics, 41, 147-169, 2005
[7] P. Krysl. Dimensional model reduction in nonlinear finite element dynamics of solids and structures, Int. J. Numer. Methods Eng., 51-4, 479-504, 2001.
[8] M. Meyer and H.G. Matthies. Efficient Model Reduction in Non-Linear Dynamics using the Karhunen-Loève expansion and dual-weighted residual methods, Computational Mechanics, 2003, 31, 179-191, 2003
[9] R.E. Nickell. Nonlinear Dynamics by mode superposition, Computer Methods in Applied Mechanics and Engineering, 7, 107-1296, 1976.
[10] C. PrudвГЄhomme *et al.*. Reliable real-time solution of parametrized partial differential equations: Reduced-basis output bound methods. Journal of Fluids Engineering, 124(1):70вГY80, 2002.
[11] Z.-Q. Qu. Model Order Reduction Techniques with applications in finite element Analysis, Springer, 2004.
[12] A. Radermacher, S. Reese. A comparison of projection-based model reduction concepts in the context of nonliner biomechanics, Arch. Appl. Mech., 83, 1193-1213, 2013.
[13] R. Rodriguez Sanchez, M. Buchschmid and G. Müller. Model Order Reduction in Structural Dynamics, Proceedings of ECCOMAS Congress 2016.

Stefanie Tegtmeyer, Leibniz Universität Hannover, Institute of Mechanics and Computational Mechanics, Appelstr. 9a, 30167 Hannover, Germany
Amélie Fau, Leibniz Universität Hannover, Institute of Mechanics and Computational Mechanics, Appelstr. 9a, 30167 Hannover, Germany
Pierre Bénet, Ecole Nationale Supérieure de Mécanique et d'Aérotechnique (ISAE-ENSMA), Poitiers, France
Udo Nackenhorst, Leibniz Universität Hannover, Institute of Mechanics and Computational Mechanics, Appelstr. 9a, 30167 Hannover, Germany

Multi-fluid modelling of suspension filtration in the near-wellbore zone of injection wells

Kristina I. Tolmacheva, Sergei A. Boronin, Andrei A. Osiptsov, Rail R. Galeev, Boris V. Belozerov, Andrei A. Yakovlev, Alexander N. Sitnikov
kristina.tolmacheva@skolkovotech.ru

Abstract

Injection wells are widely used in the oilfields to maintain reservoir pressure and increase ultimate recovery of hydrocarbons. During injection, water adsorbs solids admixtures from wellbore walls and fine particles from the pores, which results in the flow of suspension in the near-wellbore zone. Suspended particles are trapped in pores, which results in a permeability damage and, as a result, in a decrease in the injectivity of the well. In order to maintain the injection flow rate (injectivity), one needs to either increase the pumping pressure or to introduce additional water cleaning equipment on the surface. Both results in an increase in the cost of field development. To optimize the process of water injection, it is proposed to use a combined approach based on modeling of suspension filtration in porous media with account for permeability damage and recovery.

1 Introduction

For suspension filtration in a porous medium, there is a number of models developed earlier and published in open literature. One of the most frequently used models is a so-called the deep-bed filtration model [1]. The suspension flow is described using three-continua approach (carrier fluid, suspended particles and trapped particles). The key concept of deep-bed filtration model is a parallel-pathway model of a porous medium. In pathways of the first type with a small pore radius, only plugging of suspended particles occurs, and in the pathways of the second type, particles can only deposit. Continuum of trapped particles is separated into two classes, namely plugged and deposited particles. The rates of these two processes are expressed by different formulae. The rate of plugging is proportional to the product of suspended particle concentration, the particle velocity and a linear function of the concentration of the trapped particles. The rate of plugging contains two tuning parameters, usually referred to as the trapping coefficient and the trapping parameter. The rate of deposition is proportional only to concentration of suspended particles. Therefore, the deep-bed filtration model contains three tuning parameters for describing particle trapping and four tuning parameters in closure relation for permeability.

The rate of particle trapping and the closure relation for permeability may have different functional forms. An overview of these dependencies obtained theoretically and experimentally are presented in [2]. The number of tuning parameters in these correlations fall in the range from one to five. The most frequently used correlation between the permeability and the concentration of trapped non-colloidal particles has the power law form (e.g., see [3]). For colloidal particles, the formula for trapping coefficient is obtained in [4] by a pore-scale micromodel of particle transport using Happel's cell approach. The formula is valid only for particles not larger than several micrometers.
In [5] criteria for the particle capture due to direct interception, straining in constrictions and wedging in crevices were proposed. The trapping coefficient is claimed to be proportional to the initial porosity, particle and pore diameters, but the coefficient of proportionality is not estimated. In [1] and [5] the reversal effect to the particle trapping, namely the particle mobilization or entrainment, was studied. The key finding of these studies is that there exists a critical velocity of mobilization, below which the mobilization of particles does not occur. Above this velocity, the rate of mobilization is proportional to the concentration of trapped particles and the flow velocity. The coefficient of proportionality is a tuning parameter, which is called the mobilization coefficient.
Existing models for suspension filtration with non-colloidal particles contain two tuning parameters for describing the mobilization rate and minimum two tuning parameters involved into the expression for the trapping rate.
The key goal of the present study is to decrease a number of tuning parameters by taking into account different physical effects, peculiar to the particle transport (such as trapping and mobilization). In order to do so, we present a development of the multi-fluid model of suspension filtration in a porous medium [6]. Fluid fluxes through large pores of the porous medium and narrow pores of the packed bed of deposited particles are explicitly taken into account, by introducing two permeabilities (for the matrix of the porous medium and for the packed bed of the trapped particles). These are the key novel features, which distinguish the proposed model from the classical deep bed filtration approach [1, 3]. The model predictions are compared with laboratory data sets on the contamination of core samples. The most recent progress in the model development is mainly in taking into account particle mobilization, compressibility of the fluid and two-phase filtration (oil/water). Applications of the model are primarily in the oil and gas industry: drilling mud invasion and cleanup in the near-wellbore zone, fines migration in porous medium, suspension filtration in propped hydraulic fractures as well as permeability damage and recovery in the near-wellbore zone of injection wells, which are used to maintain the reservoir pressure.

2 Formulation of the problem

The present study is aimed at the development of a novel model for suspension filtration in porous media with account for the particle transport. The novelty of the model stems from the fact that porous media formed by the trapped particles have a finite porosity and permeability, so that the clean fluid can filtrate through

these pore channels [6]. The following two porosities are introduced: ϕ_c is the porosity of the medium formed by a porous matrix and the total volume of trapped particles, while ϕ_t takes into account (additionally to ϕ_c) small channels between trapped particles (see Fig. 1a):

$$\phi_c = \phi_0 - \frac{\sigma}{C_{max}}, \qquad \phi_t = \phi_0 - \sigma. \tag{1}$$

Here, ϕ_0 is the initial porosity and C_{max} is the maximum concentration of random close packing.

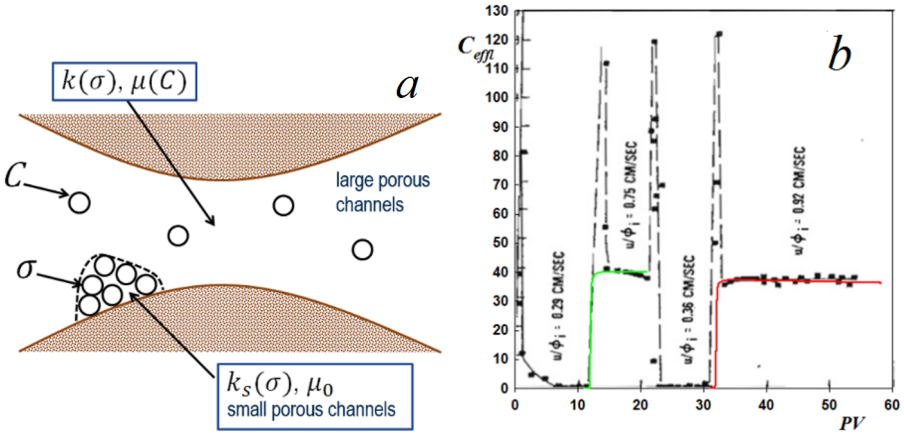

Figure 1: The sketch of suspension filtration in a porous medium (a) and the effluent concentration of suspended particles ($\cdot 10^6$) against the number of pore volumes injected. Black curve - experiment, blue curve - numerical simulation with fitted tuning parameters, red curve - numerical simulation with the same values of tuning parameters and the mobilization velocity (b).

The particle-laden filtration is described using the three-continua approach with different continua being a carrier fluid, suspended particles and trapped particles. Mass balance equations for a two-phase particle-laden suspension are as follows:

$$\frac{\partial}{\partial t}[\rho_\gamma^f s_\gamma(\phi_t - C\phi_c)] + \frac{\partial}{\partial x}(\rho_\gamma^f u_\gamma^f) = 0, \quad \gamma = 1,2 \tag{2}$$

$$\frac{\partial}{\partial t}\ (\phi_c\ s_\gamma C) + \frac{\partial}{\partial x} u_\gamma^p = -q_\gamma, \quad \gamma = 1,2 \tag{3}$$

$$\frac{\partial \sigma}{\partial t} = q_1 + q_2 \tag{4}$$

Here, ρ_γ^f is the fluid density, s_γ is the phase saturation, C and σ are the concentrations of suspended and trapped particles, respectively; u_γ^f and u_γ^p are filtration velocities of the carrier fluid and the particles, q_γ is the rate of particle trapping and mobilization.

The filtration velocities of particles u_γ^p and carrier fluid u_γ^f are expressed in terms of the suspension filtration velocity in large porous channels u_γ and in small porous channels u_s with taking into account the volume fraction of suspended particles C. The carrier fluid flows both through large (with the permeability k) and small (with

the permeability k_s) pore channels. Particles move only in large pore channels. Darcy laws are given below:

$$u_\gamma = -\frac{kk_\gamma}{\mu_\gamma}\frac{\partial p}{\partial x}; \qquad u_s = -\frac{k_s k_\gamma}{\mu_{\gamma,0}}\frac{\partial p}{\partial x} \tag{5}$$

$$u_\gamma^p = Cu_\gamma; \qquad u_\gamma^f = (1-C)u_\gamma + u_s \tag{6}$$

Here, k_γ is the relative permeability, μ_γ is the suspension viscosity, $\mu_{\gamma,0}$ is the fluid viscosity, p is the fluid pressure.
The permeability of small pore channels formed in the pack of trapped fines $k_{s,0}$ is defined after [7]:

$$k_{s,0} = (1-C_{max})\frac{r_h^2}{k_{kc}} = \frac{(1-C_{max})^3 d_p^2}{180C_{max}^2} \tag{7}$$

Here, k_{kc} is the Kozeny constant, which is usually found to be close to 5, and r_h is the hydraulic radius, defined as the ratio of the free volume to the wetted area. If a medium can be considered as a system of channels, r_h, $r_h = (1-\phi)d_p/6\phi$, $k_{s,0}$ can be calculated from (7).
Permeabilities of large and small pore channels are defined after [3, 8] with taking into account formulae for porosities (1). The suspension viscosity is defined as the function of the concentration of suspended particles C [9].

$$k = k_0\Big(1-\frac{\sigma}{\phi_0 C_{max}}\Big)^3, \quad k_s = k_{s0}\Big(\frac{\sigma}{\phi_0 C_{max}}\Big)^3, \quad \mu_\gamma = \mu_{\gamma,0}\Big(1-\frac{C}{C_{max}}\Big)^{-1.89} \tag{8}$$

In the present study, we suppose that both the plugging and the deposition are described by the source term $q_{t,\gamma}$ which is called the trapping rate [5]. The rate of mobilization $q_{m,\gamma}$ is described after [1]. Then the formulae for $q_{t,\gamma}$ and $q_{m,\gamma}$ are given below:

$$q_{t,\gamma} = Cu_\gamma\lambda, \quad q_{m,\gamma} = \alpha\sigma(u_\gamma - u_{crit,\gamma})\Theta(u_\gamma - u_{crit,\gamma}) \tag{9}$$

Here, λ and α are the trapping and mobilization coefficients, which should be tuned against the experimental data, $u_{crit,\gamma}$ is the critical velocity of mobilization, which can be defined theoretically.
Consider the problem of the entrainment of a spherical particle from the plane surface into a laminar flow. Forces acting on the particle include the buoyancy force F_b, the adhesion F_a, the friction F_f and the drag F_d. The adhesion force is defined after the following formula obtained experimentally [10]:

$$F_a = c_1 d, \qquad c_1 = O(10^{-5}) \tag{10}$$

Here, d is the particle diameter. The relation (10) is in agreement with the theoretical formula for the adhesion force acting on a non-colloidal particle in the vicinity of a plane surface in a fluid.

The drag force acting on a particle in the vicinity of the round tube wall is defined after [11, 12]:

$$F_d = 1.7 \cdot 6\pi\mu d^2 \frac{U}{R} \tag{11}$$

Here, U is the flow filtration velocity, R is the tube radius.
We assume that the friction force is proportional to the net vertical force acting on the particle, so that following relation holds:

$$F_f = k(F_a + F_b) = k(c_1 d + \frac{\pi}{6}\Delta\rho g d^3) \tag{12}$$

Below we assume that $k = 1$. A particle mobilization occurs when the force balance is reached:

$$F_d = F_f; \qquad 1.7 \cdot 6\pi\mu d^2 \frac{u_{crit}}{R} = c_1 d + \frac{\pi}{6}\Delta\rho g d^3 \tag{13}$$

$$u_{crit} = \frac{R}{6 \cdot 1.7\mu}\Big(\frac{c_1}{\pi}\frac{1}{d} + \frac{\Delta\rho g}{6} d\Big) \tag{14}$$

As a result, we decreased a number of the tuning parameters in the expression for mobilization from two to one (the mobilization coefficient α) and used a minimum number of the tuning parameter in the formula for the trapping rate (only the trapping coefficient λ).

3 Numerical implementation and validation

The numerical solution is carried out using a finite-difference approach and a uniform staggered grid. In case of incompressible fluids, the equation in terms of the pressure is obtained by summing up the Eqs. (2)-(4) and expressing the velocities according to Darcy laws (5)-(6). The hyperbolic transport equation for the suspended particles (sum of Eqs.(3)) is approximated using the first-order up-wind scheme. The equation for the concentration of the trapped particles (4) is solved using the first-order Euler method.
For validation of the expressions for the critical velocity (14) and the rate of mobilization (second Eq. (9)) we carried out numerical simulations and compared the results against the experimental data [1]. Authors carried out the experiments with the flow of a clean fluid through the dirty pack of glass beads and presented the effluent particle concentration as a function of pore volumes injected. We obtained a good agreement between the expression (14) and the experimental value for the mobilization velocity reported in [1] ($0.448 cm/s$ and $0.58 cm/s$, respectively). Then we tuned the mobilization coefficient by minimization of the discrepancy between the simulations and the experiment. It was obtained that the best agreement is achieved by taking into account both the mobilization and the trapping effects. The results of the modeling with $\lambda = 10 m^{-1}$ and $\alpha = 8.3 \cdot 10^{-3} m^{-1}$ are shown in Fig. 1b. For validation of the formula for the trapping rate (first Eq. (9)), the comparison of the numerical simulations with the contamination experiments [13] is conducted.

The experimental data profiles of the trapped particle compares concentration obtained after filtration of the suspension in the different porous samples. The trapping coefficient λ was tuned for each experiments in the framework of the classical and proposed models. It was obtained that the new model provides a better description of the trapped particle concentration in zones of the large particle accumulation close to a maximum value $\sigma = C_{max}\phi_0$ (Fig. 2).

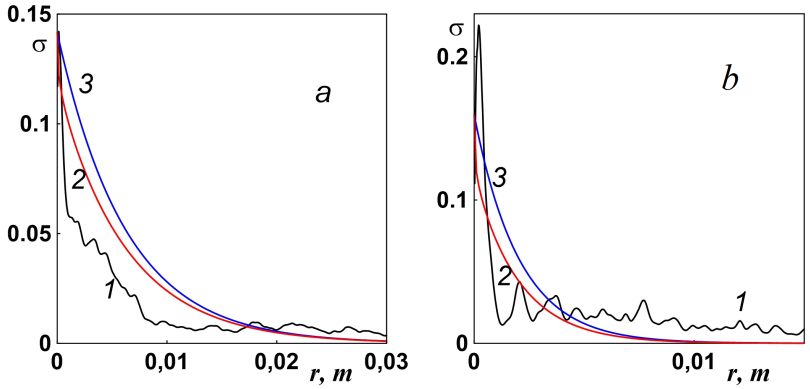

Figure 2: The concentration of trapped particles corresponding to the experiments with Bentheimer (a) and Castlegate (b) samples. Curve *1* - the experiment, *2* - simulations using new model, *3* - classical model.

4 Results and discussion

For the modelling of contamination and clean up of a porous medium in the vicinity of injection wells, we carried out numerical simulations. The input parameters corresponding to field conditions. The typical range of the field parameters is presented in Table 1.

Parameter	Dimension	Value range
Permeability of near-wellbore zone	mD	0.1 – 10
Porosity	non-dim.	0.1
Debit of injection well	m^3/day	50-600
Linear velocity near wellbore	m/s	0.1 – 10
Suspended particles volume concentration	non-dim.	10^{-5} – 10^{-3}
Water viscosity	CP	0.67
Oil viscosity	CP	1.33

Table 1: The field parameters of fluids and injection wells.

The results of simulation of contamination and clean up of a near-wellbore zone are shown in Fig. 3a. At the first stage, the flow of suspension is from left to right (injection) and particles can only be trapped. At the second stage the flow is reversed from right to left (production) and the particle-free fluid mobilizes the trapped particles. In Fig. 3b we present a simulation of the similar sequence, but

with the velocity decreased from 1 to 0.1 m/s and the trapping coefficient increased from 1 to 10 m^{-1}. Note the similarity in profiles of the trapped particle concentration and permeability for these two cases, while the penetration distances are different (5 and 0.5 m). It is found that in the both simulations the permeability is almost completely restored, while the period of clean up is significantly smaller than that of injection.

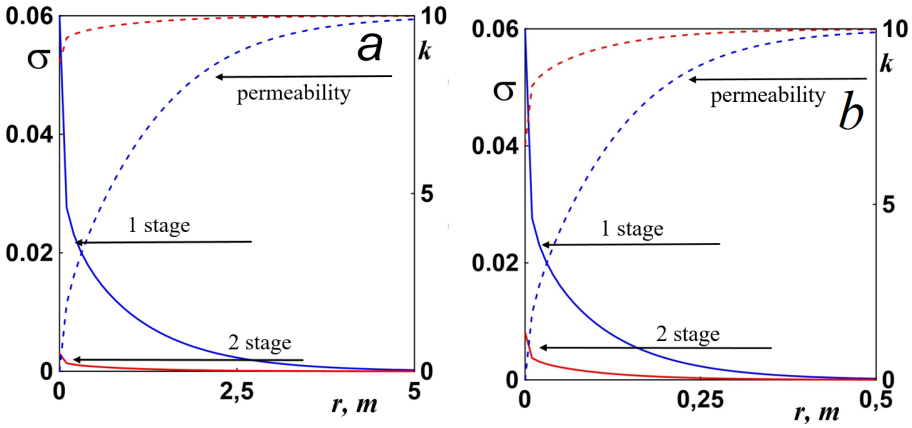

Figure 3: The trapped particle concentration (solid lines) and permeability (dashed lines) as a function of coordinate (with 0 being the injection well). Stage 1 - contamination with $\lambda = 1m^{-1}, t = 60s$, stage 2 - clean up with $\alpha = 0.1m^{-1}, t = 30s$ (a); stage 1 - contamination with $\lambda = 10m^{-1}, t = 60s$, stage 2 - clean up with $\alpha = 1m^{-1}, t = 20s$ (b).

We also simulated the filtration process taking into account both particle trapping and mobilization at all flow stages (Fig. 4). Note that the time of injection and production are the same, but permeability is not restored to its initial value.

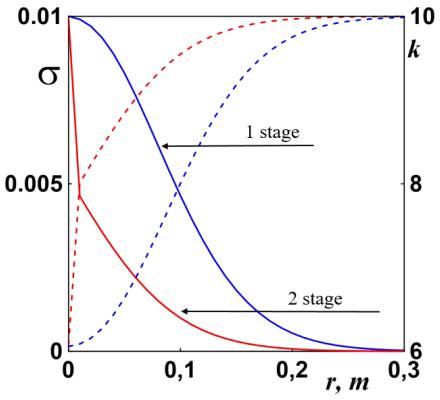

Figure 4: The trapped particle concentration (solid lines) and permeability (dashed lines) as a function of coordinate. Stage 1 - $\lambda = 100m^{-1}, \alpha = 10m^{-1}, t = 10s$, stage 2 - $\lambda = 100m^{-1}, \alpha = 10m^{-1}, t = 10s$.

5 Conclusions

The model of multiphase filtration of suspension in porous media is developed. The key novel element of the model is taking into account the flow of particle-free fluid in pore channels formed by trapped particles. The number of tuning parameters of the model is reduced from five (typical of the classical deep-bed filtration model reported in the open literature) to two. The expression for the critical mobilization velocity is established by considering the balance of forces acting on a single particle touching a plane wall.
The model is validated against a number of lab tests on contamination and cleanup of rock cores. It was demonstrated that the novel model provides a better description of the zones with large accumulation of trapped particles as compared to that obtained using the classical model with the same number of tuning parameters. An expression for the critical velocity of mobilization yields a good agreement with experimental data. Numerical simulations of cyclic injection and cleanup regimes in a porous media in the vicinity of an injection well are carried out. A comparison of the cases with taking into account only trapping, only mobilization, or both effects was carried out.

Acknowledgements

Startup funds of Skolkovo Institute of Science and Technology are gratefully acknowledged. The authors are grateful to the management of Gazpromneft for financial support of this work and the permission to publish.

References

[1] Gruesbeck, C. and Collins, R.E. Entrainment and deposition of fine particles in porous media. Society of Petroleum Engineers Journal, V. 22-06, pp. 847-856, 1982.

[2] Zamani A., Maini B. Flow of dispersed particles through porous mediaвЃ¶deep bed filtration, Journal of Petroleum Science and Engineering, V. 69вЃ¶1, pp. 71-88, 2009.

[3] Boek, E.S., Hall, C., Tardy, P.M.J. Deep Bed Filtration Modelling of Formation Damage due to Particulate Invasion from Drilling Fluids, Transport in Porous Media, V. 91-2, pp. 479вЃ¶508, 2012.

[4] Rajagopalan R., Tien C. Trajectory analysis of deepвЃ¶bed filtration with the spherein-cell porous media model, AIChE Journal, V. 22-3 pp. 523-533, 1976.

[5] Herzig J. P., Leclerc D. M., Goff P. L. Flow of suspensions through porous media вЃ¶ application to deep filtration, Industrial and Engineering Chemistry, V.62вЃ¶5, pp. 8-35, 1970.

[6] Boronin, S. A., Osiptsov, A. A., and Tolmacheva, K. I. Multi-fluid model of suspension filtration in a porous medium, Fluid Dynamics, V. 50-6, pp. 759-768, 2015.

[7] Carman P.C. Fluid flow through granular beds, Transactions, Institution of Chemical Engineers, London, V. 15, pp. 150-166, 1937.

[8] Barenblatt G. I., Yentov V. M., Ryzhik V. M. The theory of the unsteady filtration of liquid and gas, NASA STI/Recon Technical Report N. V. 78, 1977.

[9] Scott K. J. Hindered Settling of a Suspension of Spheres: Critical Evaluation of Equations Relating Settling Rate to Mean Particle Diameter and Suspension Concentration, Council for Scientific and Industrial Research, 1984.

[10] Zimon A. D. Adhesion of dust and powder, Springer Science and Business Media, 2012.

[11] Brenner H., Happel J. Slow viscous flow past a sphere in a cylindrical tube, Journal of Fluid Mechanics, T. 4, N. 2, pp. 195-213, 1958.

[12] Goldman A. J., Cox R. G., Brenner H. Slow viscous motion of a sphere parallel to a plane wallвЃ Y I Motion through a quiescent fluid, Chemical engineering science, V. 22.4, pp. 637-651, 1967.

[13] Mikhailov D., Ryzhikov N., Shako V. An Integrated Experimental Approach to Determining How Invaded Mud Components Modify Near-Wellbore Properties (Russian), Society of Petroleum Engineers, 2014.

Kristina Tolmacheva, Skolkovo Institute of Science and Technology, Nobel str. 3, Skolkovo Innovation Center, Moscow, Russia, 143026

Impact Of The New Vibroexcitation Method To The Screening Process Intensification Of Bulk Materials

Vavilov Andrey Vladimirovich, Ph. D., Associate professor, Doudkin Mikhail Vasilyevich, Doc. tech. sciences, Professor, Kim Alina Igorevna, PhD student, Guryanov Georgiy Alexandrovich, Ph.D.,Professor, EKSTU. D. Serikbaev, Kazakhstan, Ust-Kamenogorsk
AVavilov@yandex.kz

Abstract

The article presents the results of applied research in the field of processing of bulk materials. Namely, screening with the use of new principles of operation of the sorting devices. The result of the work of the authors in this direction is the creation of new technical solutions, which implement the principle of complex excitation of the material on the screen. The principal feature of this solution is that the material acts as the main dynamical phase excitation and additional phase excitation of different forms of orientation. As a result of intensification of both stages of screening, increases the production capacity of the screen. Also as a result of more efficient use of the surface of the sieve can be reduced by metal and power consumption. These conclusions are confirmed by experimental data.

The need for many industries in the machines for bulk materials sorting (screens) of various structures is very high. The confirmation is the fact that just outside of the CIS, manufacturing of screens employs more than 300 enterprises and companies, 90of which - large, including 32 firms located in the USA, 16 - in the UK, 11 - in the Federal Republic of Germany; 6 - in Japan [1, 3].

Literature and patent analyses of recent years show that the interest in screens improvement, the establishment of new structures and new screening ways are increased noticeably. The main development screens trends are intended to achieve the following objectives: improving the efficiency of the screening; improving of performance, reliability and durability of the operation; extension of the scope and technological capabilities.

One of the new, and perhaps the most perspective development directions of screening equipment, at present day, in our opinion, are the screens "with complex excitation of the material." Sometimes the term "dynamic excitation" is used [2]. At the same time this trend can not only create new sorting machines, but also upgrade the existing ones.

The term "screening with complex excitation" called the process when the particles of the bulk material affects several exciting factors such as vibration and rotational motion, or vibration, impact force, etc. One example of complex impact on the screened material is spiral vibrating screen design [3]. This screen is an aggregate that combines the principles of drum and vibrating screens.

An example of screening with complex effect on the material can be generally considered any material excitation methods, when the particles are forced to complex composite movement, while in "no sieve rumble" separation does not occur in the monolayer, but in the "thick layer" of material.

No sieve screen (or vibration segregation qualifier) вЃЌквЃЌis a new and perspective solution in the area of вЃЌквЃЌscreening [4]. This development offered by team composed of: Blekhman I.I., Weisberg L.A., Yakimova K.S. and others. This classifier allows solving technological problems of fine classification, beyond the capabilities of conventional screens. In contrast to screens, this classifier do not have problems with sieve wear and clogging of their holes; vibration intensity (energy consumption) - less. In contrast to vibro-flatness separation, the separation does not take place in a monolayer, and in the "thick layer" of material, that provides high performance and possibility of small materials classification.

New excitation principles of bulk material are used in screens using ВкKroosherВњ technology, the screen has the properties of multifrequency resonance oscillation system. Moreover, among the claimed benefits are large capacity, high screening efficiency, guaranteed effect of self-cleaning screens, etc. This type of screen can also be attributed to the screen with complex excitation.

The undoubted example of using the principle of complex material excitation is the development of vibro-blow screens, which are also continuously improved. So, recently, it is proposed to initiate screening surface by "double" blows. Despite the constructive simplicity of the screen, the implementation of vibro-blow mode is available only in certain combinations of structural and dynamic parameters. There are more examples of screening technologies using complex excitation (including the steeply inclined screens, etc.). At the same time these examples are enough to draw a conclusion about the prospects of the use of the principle of complex excitation in the development of new designs of vibrating screen.

Considering the urgency of the research areas in the D.Serikbaev East Kazakhstan State Technical University (EKSTU) research in this area is conducted for several years. The result of this work is series of new solutions for the use of relatively simple designs for devices that implement the principle of complex material excitation on the screenвЃЌЄs sieve (hereinafter SS - screening surface). The proposed solutions can be used in any type of flat vibrating screens.

All the below results were obtained in the framework of the state budget R & D "Technology of crushing and screening using new methods for bulk materials processing" (customer - MES).

As is known, the essence of the screening process is that the material is sieved on the screenвЃЌЄs sieve in two steps occurring simultaneously and continuously. In the first step the fine grains pass through the thickness of the material to the SS, and the second - through the sieve holes. The effectiveness of the screening process can be enhanced due to the intensification of one or both stages of the process. But the

intensification of the first stage of screening is the most promising way to improve the screens performance.

For this purpose, initially, we proposed new screen design, feed elements (FEs) are fixedly mounted above the screen surface, made in the form of rods, mounted on separate frame (Innovation patent of RK вҺЦ25647, V07V 1/40, publ. 16.04.2012, Bull. number 4). This design allows intensifying the process of mixing the material on the SS, which speeds up the passage of the lower particles class to the sieve. One disadvantage of this solution is decrease of material flow rate (i.e. lost productivity) due to the fact that FEs are the "resistance" of the flow and inhibit it. Material mixing on the sieve is increased, but not enough. The difference in the particles velocities of bulk material with respect to each other activates the process of passing particles of bottom fraction to the sieve surface over the entire layer of bulk material, but the upper fraction begins to accumulate near each rod, which in turn reduces the overall efficiency of the screening process, and as a consequence it reduces screening productivity.

To eliminate this drawback, design with dynamic FEs was proposed, which is communicated an oscillatory motion by its own vibration actuator, or by screen box oscillations (the design protected by innovative patents of the RK - [5, 6]). That is, the fundamental feature of this solution is that the material is affected by basic dynamic phase of excitation generated by the main drive vibration screen, and additional phase of excitation (generated by FEs) of different forms of orientation.

Intensification of screening stages is provided by: firstly, active motion of FE relatively bulk material particles, resulting in an inhomogeneous behavior of individual material monolayers (active mixing); secondly, more efficient sieve loading that allows creating the conditions to maximize pushing and mixing forces. At the same time, the increasing spread of the kinetic parameters of particles material behavior should have a positive impact on both screening stages.

As a result of the two screening stages intensification, the productivity increases. Also as a result of more efficient surface use is possibility of metal consumption reduction, and as a result, screen power consumption. The main advantage of the proposed screening method is that it can be used for the modernization of all types of flat screens.

To check the proposed solutions, a number of theoretical and experimental studies were carried out. There is developed the mathematical probability model of screening process using a new method of bulk material excitation. The laboratory experimental setup (physical model) was manufactured (fig. 1). A number of researches on computer visualization of the proposed models were done. The obtained data show that the use of renewable energy leads to intensity increasing of lower grade passage of bulk material to the sieve on 6.6 ... 13.3% (fig. 2).

Moreover the required screening performance is increased by 10 ... 17%. Electricity costs are increased by only 5 ... 7%. Currently, the research is continuing in this direction, in order to conduct the experiment on the development of a new industrial device design for screening process intensification. Thus, it can be concluded that authors proposed a new way to improve the efficiency of the screening process (by appropriate design of new units), which has a significant effect on the screening process kinetics and the concentration state of fine particles in the granular layer;

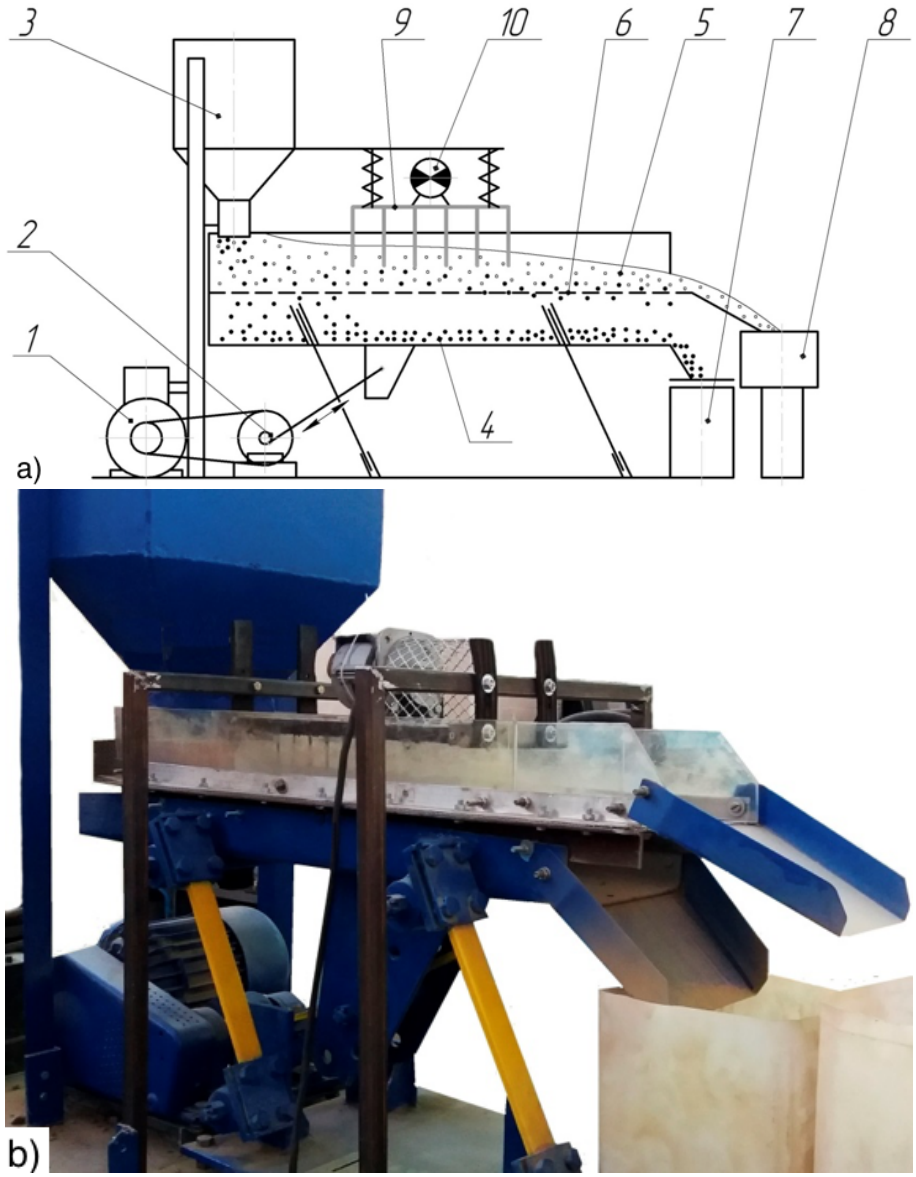

Figure 1: The concept of vibroscreen with additional feed elements (FEs): a) Concept of horizontal vibroscreen: 1 вГУ motor, 2 вГУ vibration generator, 3 вГУ bin, 4 вГУ undersize product, 5 - bulk material, 6 вГУ sieve, 7 вГУ container for undersize product, 8 - container for oversize product, 9 вГУ feed elements (FEs), 10 - generator; b) The experimental installation of the new vibroscreen)

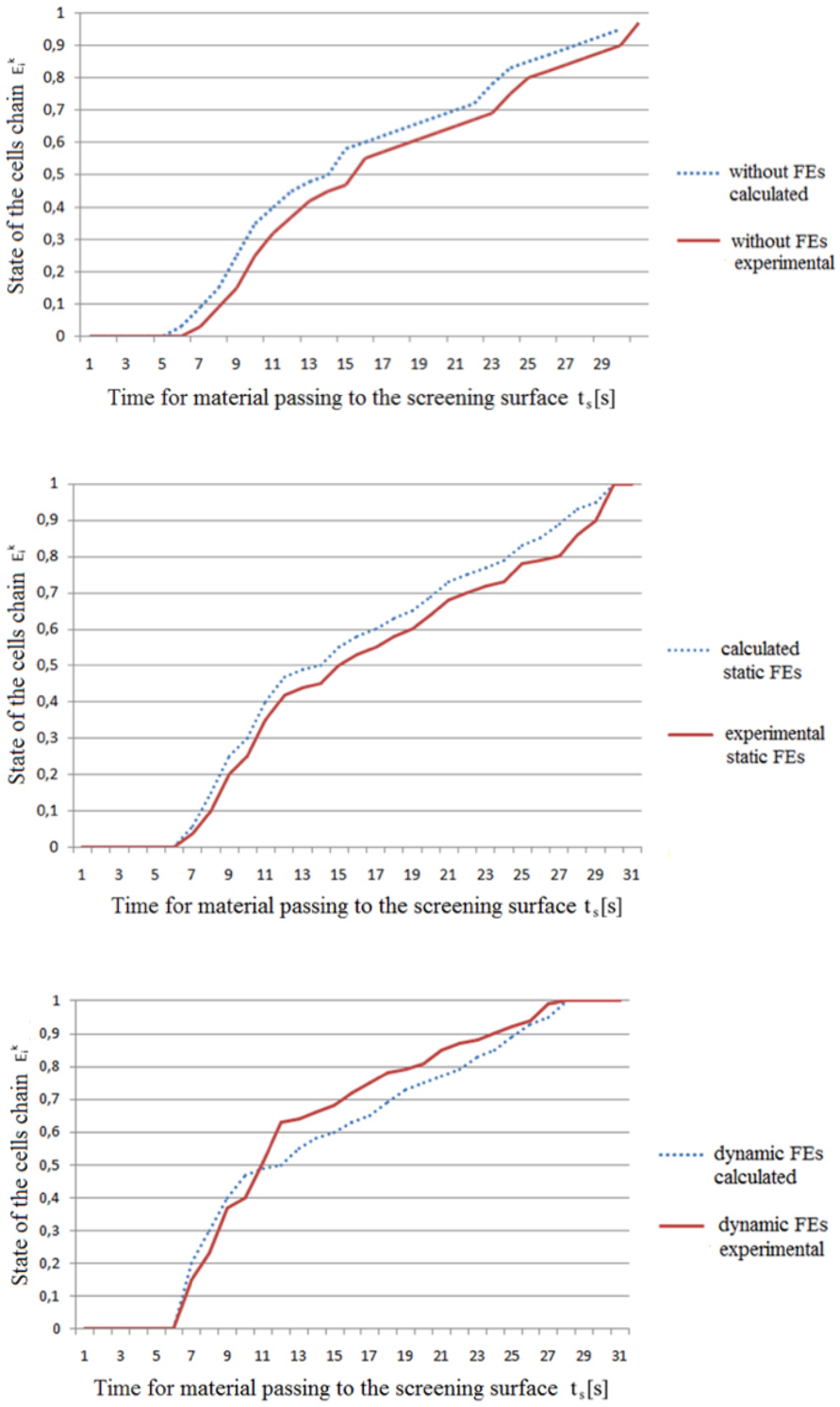

Figure 2: Comparison of theoretical results with experimental studies of the chain state of screened fraction in the 6th vibroscreen cell: a) Without feed elements (FEs); b) With static feed elements (sFEs); c) With dynamic feed elements (dFEs).

it increases the overall screening efficiency due to acceleration of the first phase of screening, i.e. time acceleration of particulate material passage to the sieve.

References

[1] Ivanov A.I. Modern vibrating screens NGO "RIVS" // Mining Journal. 2008. Special Edition. P. 16 - 21.

[2] Ogurtsov V.A. Screening processes of bulk building materials: modeling, calculation and optimization. // Abstract of the thesis for the degree of Doctor of Technical Sciences. - Ivanovo. - 2010.

[3] Vavilov A.V, Surashov N.T., Yelemes D.E. Spiral vibrating screens. // Monograph. Almaty: KazNTU, 2010. 126 p.

[4] Blekhman I.I., Blekhman L.I., Weisberg L.A., Vasilkov V.B., Yakimova K.S. Vibration effects - experiment, theory, use the enrichment of ores and recycling. // Proceedings of the final conf. as a result of the implementation of federal program "Research and development in priority areas of Russian scientific and technological complex for 2007-2012". Moscow: 2009.

[5] Doudkin M.V., Vavilov A.V., Guryanov G.A., Kim A.I. Vibrating Screen. // Innovation patent of the RK вҺЦ 31145. IPC V07V 1/40. Publ. 05.16.2016, Bull. вҺЦ5.

[6] Doudkin M.V., Vavilov A.V. etc. // Innovation patent of the RK вҺЦ 2015 / 0842.1 from 08.07.2015

Specifics of charge accumulation on and transport along the interface between a low-conducting liquid and a solid perfect insulator

S. A. Vasilkov, D. A. Nechaev, Yu. K. Stishkov
d.nechaev@2014.spbu.ru

Abstract

Presently, solid insulation is an essential part of various high-voltage systems including the case of electrohydrodynamic ones. The latter use the Coulomb force to put dielectric liquids in motion and thus their characteristics strongly depend on the electric field distribution. When the solid insulation has much smaller electrical conductivity than that of the liquid, its surfaces accumulate electric charge in a thin layer in the liquid near the interface, which changes the electric field configuration and is difficult to account for in computer simulation. Therefore many works use simplified boundary conditions on the insulation surfaces like the absence of the normal component of the electric field. However, the key problem is that the charge takes time to accumulate and remains mobile in the tangential field, thus the simplified condition should be validated. The present study considers an EHD system, employing an insulating barrier, characterizes the layer of the accumulated charge and checks the applicability of the simplified boundary condition by means of computer simulation. The results show when the simplified condition can be invalid resulting in different total current and electric field distribution.

1 Introduction

Electrohydrodynamic (EHD) systems use the strong electric field to charge dielectric liquids and to put them in motion via the Coulomb force [1]. The characteristics of the systems fundamentally depend on both charge formation mechanisms and the electric field distribution, and the latter is even more essential than the former because it controls the intensity of the charge formation.

The electric field configured by metal electrodes is easily accounted for with the use of up-to-date computer simulation techniques. However, recent studies use solid insulation in EHD systems for various purposes (for example, to generate wall jets [2] or to change the electric field distribution [3,4]) with increasing frequency. Introduced in the region near or between the electrodes, solid insulation accumulates electric charge on its surface (the electrical conductivity of the solid insulation is assumed to be much smaller than that of the liquid) and thus affects the electric

field in an EHD system. The charge remains in a very thin layer of liquid in immediate proximity to the surface and screens the normal component of the electric field in the liquid outside the layer. The key problem is that the charge takes time to accumulate and remains mobile in the tangential field, which complicates simulation of the EHD systems like that.
The accumulated charge in the tangential electric field can cause both the onset of electroconvection and the migration charge transport. These processes are mostly considered on a micro scale, with the liquid motion referred to as induced-charge electroosmotic flow [5,6]. In the case of low-conducting (dielectric) liquids and macro scales the effect of the accumulated charge transport is yet to be investigated.
The phenomena concerning the electrical double layer (EDL) are similar to those discussed and are extensively being investigated (in [7-8], for instance). In the case of accumulated charge, the total charge density per surface unit can be much greater than that in the case of EDL, therefore, disregarding the effects of the accumulated charge transport could be erroneous.
The aim of the present study is to examine the applicability of the simplified boundary condition used in computer simulation on the insulating walls when the electric field distribution is mainly determined by the accumulated charge [3]. The simplest boundary condition states that the normal component of the electric field is absent ($E_N = 0$). This assumes the charge to be totally accumulated, immobile, and located in infinitely thin layer. The works [3,4] rely on it to study the electric current passage and the EHD flow caused by the field-enhanced dissociation in a low-conducting liquid with raised conductivity. The present paper uses geometry from the work [3] and compares the results of utilizing the simplified and more complete models (the latter disregards field-enhanced dissociation, liquid flow, and assumes the solid insulators to be perfect).
In fact, several studies (e. g. [9, 10]) have already used more complete models of charge accumulation on the surfaces of the solid insulation (side boundaries) but they focused neither on the layer structure nor on the effect of the accumulated charge onto the total current or the electric field distribution.
That is why, just after the description of the mathematical model, the present paper studies an 1D system „HV electrode – slightly conducting liquid – solid perfect insulator – grounded electrode“ to characterize the layer of the accumulated charge and to check the impact of model parameters (the low-voltage conductivity of the liquid, the mobility of ions, and the voltage). Then, the more complicated 2D geometry of the EHD system from [3] is considered.

2 Mathematical model

The present work deals with the current passage through the system that consists of both liquid and solid insulation. Since the electric field distributions and the charge accumulation at the liquid-surface interfaces are of main interest, the mathematical model disregards liquid motion to avoid excessive complicacy. Due to the same reason, a pure conduction model—without the field-enhanced dissociation and the injection—is considered with the two species of ions that are univalent and have equal properties.

Thus, the conduction is described by the following set of equations:

$$\mathrm{div}\,(E) = \rho/\varepsilon\varepsilon_0 \tag{1}$$

$$\partial n_i/\partial t + \mathrm{div}\left(\vec{j_i}\right) = W_0 - \alpha_r n_1 n_2 \tag{2}$$

where E is the electric field, ρ is the electric charge density, ε is the dielectric permittivity, ε_0 is the vacuum permittivity, n_i is the concentration of positive (negative) ions, t is the time, $\vec{j_i}$ is the flux density of positive (negative) ions, W_0 is the intensity of dissociation, α_r is the recombination coefficient.

The electric field, the space charge density, the ion flux, the intensity of dissociation and the recombination coefficient are defined as follows:

$$\vec{E} = -\nabla\varphi \tag{3}$$

$$\rho = e\,(n_1 - n_2) \tag{4}$$

$$\vec{j_i} = \mathrm{sign}\,(Z_i)\,n_i b\vec{E} - D\nabla n_i \tag{5}$$

$$W_0 = \sigma^2/(2eb\varepsilon\varepsilon_0) \tag{6}$$

$$\alpha_r = 2eb/(\varepsilon\varepsilon_0) \tag{7}$$

Where φ is the electric potential, e is the elementary electric charge, Z_i is the ion charge number, b is the ion mobility, D is the diffusion coefficient, σ is the liquid conductivity.

According to the Einstein relation, the diffusion coefficient is proportional to the ion mobility:

$$D = bk_bT/e \tag{8}$$

where k_b is the Boltzmann constant, T is the temperature.
The present study employs computer simulation to solve (1-2) with regard to (3-8). The computations were carried out using software package COMSOL Multiphysics® based on the finite element method.

3 One-dimensional approach

Charge accumulation time
Consider the system consisting of two infinite layers – that of liquid dielectric (the barrier) and that of perfect solid insulation. If the voltage applied, the electric charge will accumulate in the liquid at the surface of the barrier until the electric field in the liquid becomes zero. Obviously, the symmetry of this system allows us to solve the problem in one-dimensional approach. The geometry and the boundary conditions of the model are shown in Fig. 1. L is the thickness of the liquid layer, H is the thickness of the solid layer.
The dielectric permittivities of the liquid, ε_H, and that of the solid, ε_L, equal 2 and are of no interest for the present study. V_0 is the voltage applied to one of

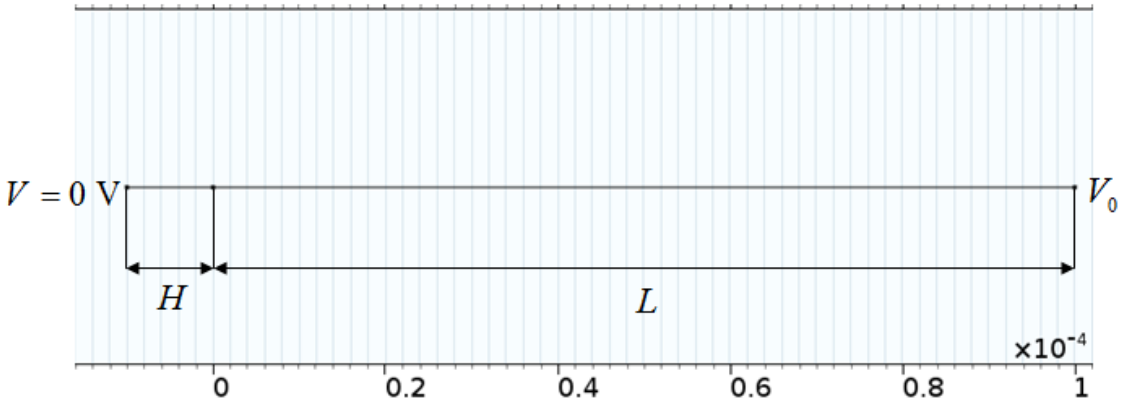

Figure 1: The scheme of the problem.

the electrodes, another one is grounded. σ_0 is the conductivity of the liquid. The voltage, the conductivity and the mobility of ions are the parameters that are varied. This problem can be solved without Nernst-Planck equation (2) in terms of electrostatics (1). The condition of the end of the charge accumulation on the surface of solid insulator:

$$\rho_s = \varepsilon\varepsilon_0 E_H = \varepsilon\varepsilon_0 \frac{V_0}{H}, \tag{9}$$

where ρ_s is the surface charge density on the solid insulator.
Considering the equation (9) and the Ohm's law, we get the expression of ρ_s versus time:

$$\rho_s = \frac{V_0 \varepsilon_H \varepsilon_0}{H} \left(1 - e^{-\alpha t}\right) \tag{10}$$

Where the characteristic time τ of charge accumulation is

$$\tau = \frac{1}{\alpha} = \frac{\varepsilon_0 \left(L\varepsilon_H + H\varepsilon_L\right)}{\sigma H} = \frac{\varepsilon_0 \varepsilon_H L}{\sigma H} + \frac{\varepsilon_0 \varepsilon_L}{\sigma} = \tau_{RC} + \tau_{relaxation} \tag{11}$$

The equation (11) shows that the characteristic time τ is the sum of the two terms. The first term is the RC-time, the characteristic time of the barrier capacitance charging through the resistance of the liquid layer. The second term is the characteristic time of charge relaxation in the liquid dielectric. If the liquid layer is much thicker or much thinner than the barrier, the first or the second term can be neglected. Otherwise, they both are of importance.
When the accumulated charge is located within a thin layer ($<< H$) close to the barrier surface, the characteristic time of the charge accumulation will remain nearly the same. Therefore, for further calculations involving the Nernst-Planck equation (2), it is reasonable to use tenfold characteristic time as the time when charge accumulation reaches stationary value.

Parametric study

To allow for further investigations of more complicated 2D models, the impact of the system parameters should be estimated in the 1D approach now. Fig. 2 shows

the electric field distributions in the liquid, and the distributions of the accumulated space charge are very similar. The electric field is as strong as in the barrier in the close proximity to its surface (the left end), and drops down almost to zero within 1 μm. The point where the electric field is twice weaker shows the characteristic layer thickness that also has the interpretation of a distance where the half of the total net charge is located closer to the barrier surface.

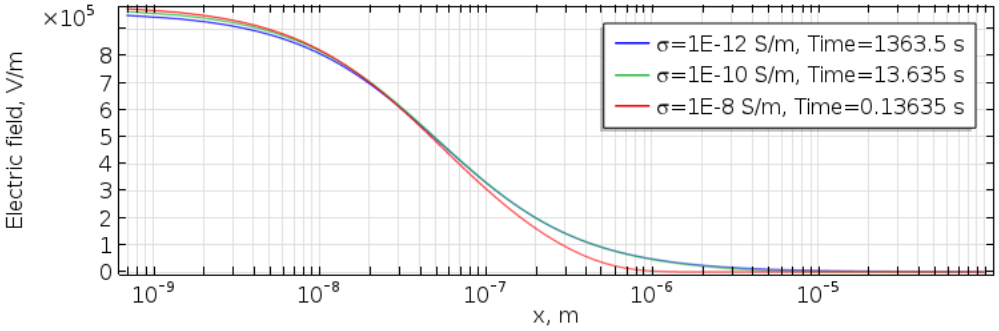

Figure 2: Different conductivity.

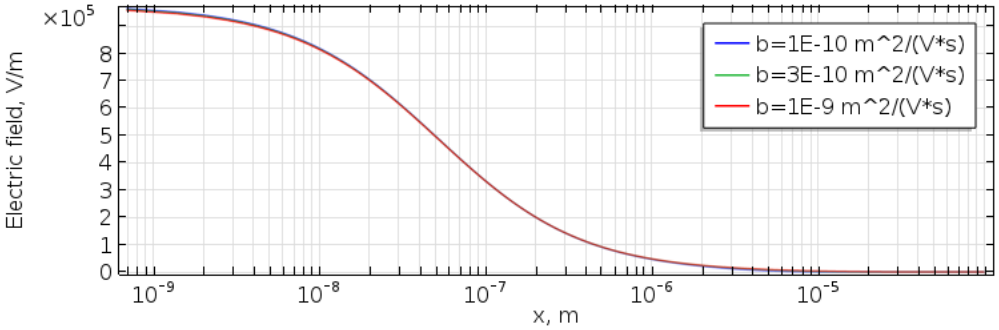

Figure 3: Different mobility of ions.

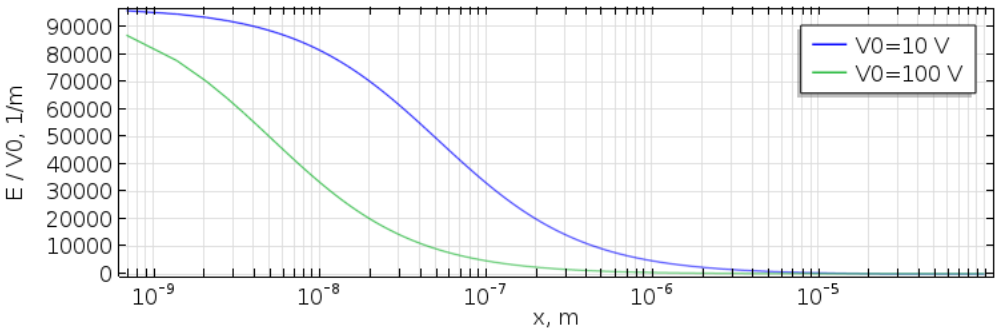

Figure 4: Different voltage.

Figure 5: The results of parametric study.

As it can be seen in Fig. 2a, the value of the liquid conductivity has almost no impact on the layer size and influences the electric field distribution only at the distances on the order of $1\mu m$. However, according to (11), it takes much more time for the charge to be accumulated. The Fig. 2b shows the absence of any effect of the ion mobility at all. This is the outcome of the Einstein relation (8). Nevertheless, if

the tangential electric field exists, the impact of the ion mobility can be significant. The absolute value of the electric field to be screened has the strongest influence and can cause the layer to change the thickness in a wide range of values (Fig. 2c); the stronger the field, the thinner the layer.

4 Realistic geometry

Computer model

The next step of the present study is to consider more complicated system from [3] where the charge transport along the interface is possible. The not-to-scale geometry of the system is shown in the Fig. 3. The system consists of two flat parallel electrodes and a dielectric plate (barrier) having a small circular hole. The barrier is placed between the plates and splits the chamber filled with a dielectric liquid into two equal parts, with the hole remaining the only link to connect them. The charge accumulates on the barrier surface, screens the normal component of the electric field, and moves the electric field lines to the hole (the only available way). As a result, a region of the strong electric field emerges inside the hole, which was used to study the field-enhanced dissociation phenomenon both experimentally and numerically. The computer model in [3] used liquids with the low-voltage conductivity ranging from nearly 10^{-9} S/m to 10^{-8} S/m and the simplified boundary condition $E_N = 0$ that needs validation.

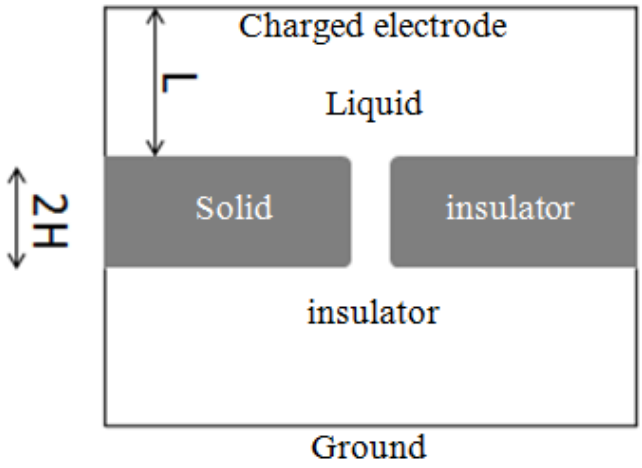

Figure 6: The schematic not-to-scale illustration of the EHD system used in [3].

The system has axial symmetry, thus a 2D axisymmetric model can be implemented. Moreover, there is a horizontal plane of symmetry, so it is reasonable to build geometry only with a quarter of system shown in Fig. 3.

The geometry and the boundary conditions of the computer model are shown at the Fig. 4. The finite-element model for this geometry accounts for steep gradients of the ion concentrations near the surfaces of the solid insulation.

Results

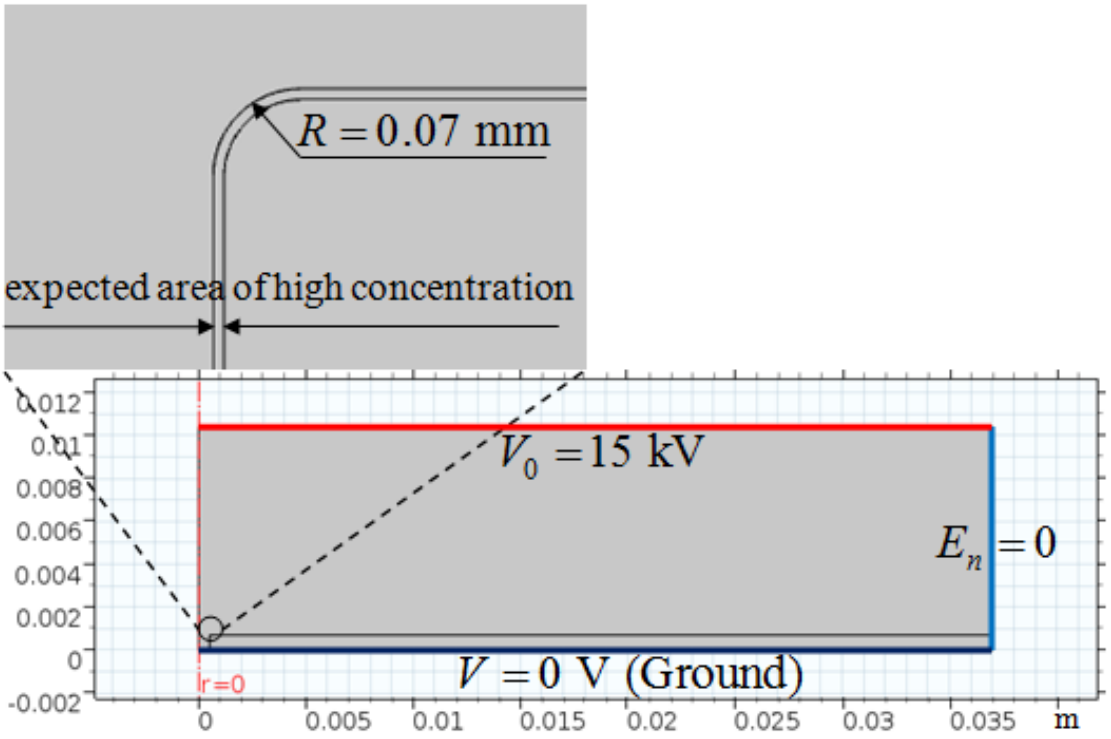

Figure 7: The geometry and the boundary conditions of the computer model.

The most convenient quantities to compare the simplified model and the more complete one are the total current and the electric field distribution. To obtain the results in the case of the simplified boundary condition $E_N = 0$, equation (1) was solved and the total current was calculated using the Ohm's law. In the case of the more complete model, the current is the integral of the current density computed basing on both the ion distributions and that of the electric field.

Figure 5 shows the relative increase of the total current compared to the simplistic model. It is clearly seen that the currents are equal at 10^{-8} S/m, differ slightly at 10^{-9} S/m and dramatically at lower values of the liquid conductivity. At 10^{-12} S/m the current in the more complete model becomes more than a hundred times higher than in the simplified one. Consider the distributions of the electric field normalized to the electric field value in the barrier in case of the absence of the hole (Fig. 6). Figure 6a shows the distribution for the case of the simplistic model where the normal component of the electric field is set to zero on the barrier surface. This model is incapable of computation the electric field strength distribution inside the barrier so it is zero here. In the rest of the model (in the liquid) all electric field lines pass through the hole and there is a region of the strong electric field inside. Comparing Fig. 6a and 6b, one can note that the electric field distributions agree well and just a few electric field lines pass through the barrier instead of the hole. The Fig. 5 shows that this effect is negligible. However, in the case presented in Fig 6c, the difference is apparent: most of the electric field lines pass through the barrier, which means that the normal component of the electric field close to the

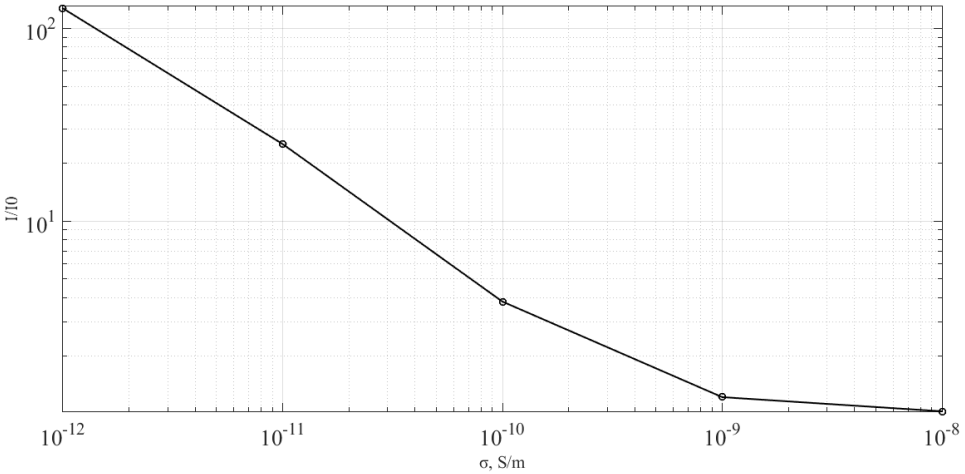

Figure 8: The comparison of models by current.

barrier is not completely screened. Moreover, the electric field strength distribution in the hole differs greatly from the cases presented in Fig 6a and 6b.
These results can be explained by the following: there appears a tangential component of the electric field at the solid-liquid interface, which cause the accumulated charge to migrate along the surface. If the time of the charge accumulation (11) is short, the effect of the charge transport is negligible (the case of Fig. 6b). Otherwise, the charge „slips“ along the barrier to the hole, providing the higher currents and reducing the screening of the normal component of the electric field in the liquid near the interface (the case of Fig. 6c).
Basing on the results, the limit of the applicability of the boundary condition lies in the interval between 10^{-9} S/m and 10^{-8} S/m. However, the limit can shift towards the low-conductivity region in Fig. 5 due to a number of factors. Firstly, if the field-enhanced dissociation is accounted for, it increases the effective value of the conductivity in the region of the strong field. Secondly, the ion mobility that determines the intensity of the charge transport along the barrier may decrease if the ion is very close to the surface.

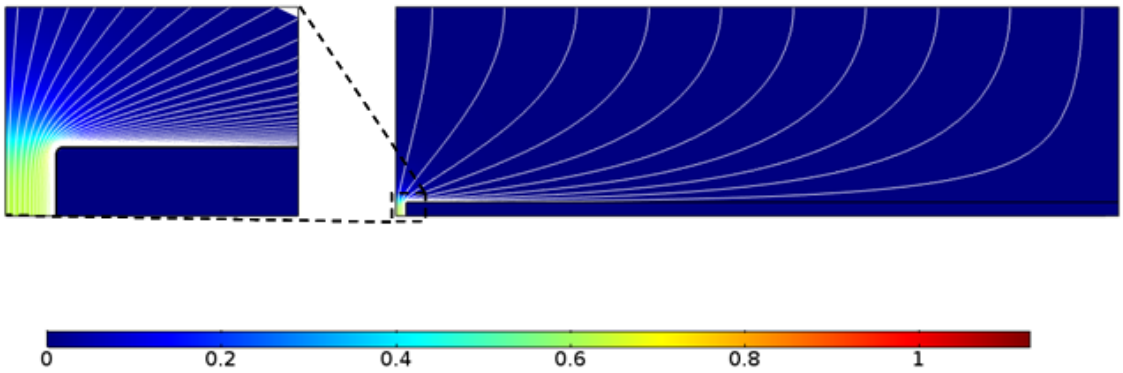

Figure 9: The distribution of the normalized electric field, the case of the full screening of electric field by solid insulator.

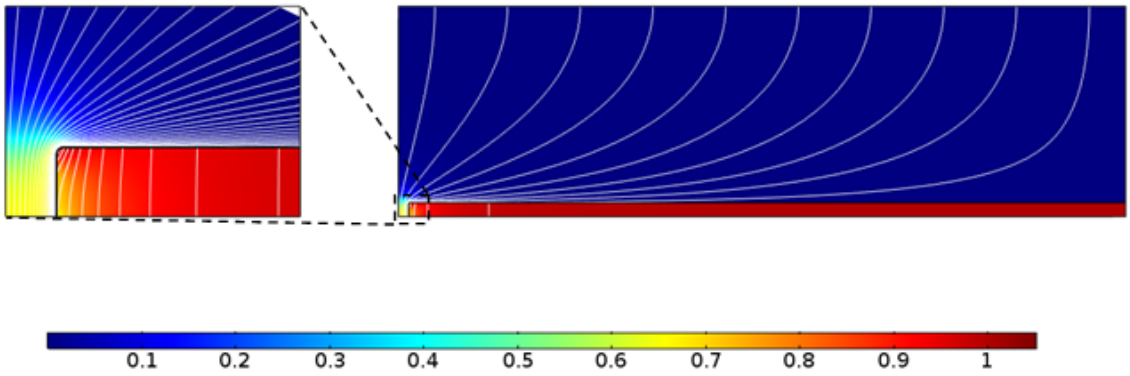

Figure 10: The distribution of the normalized electric field, $\sigma = 10^{-8}\ S/m$.

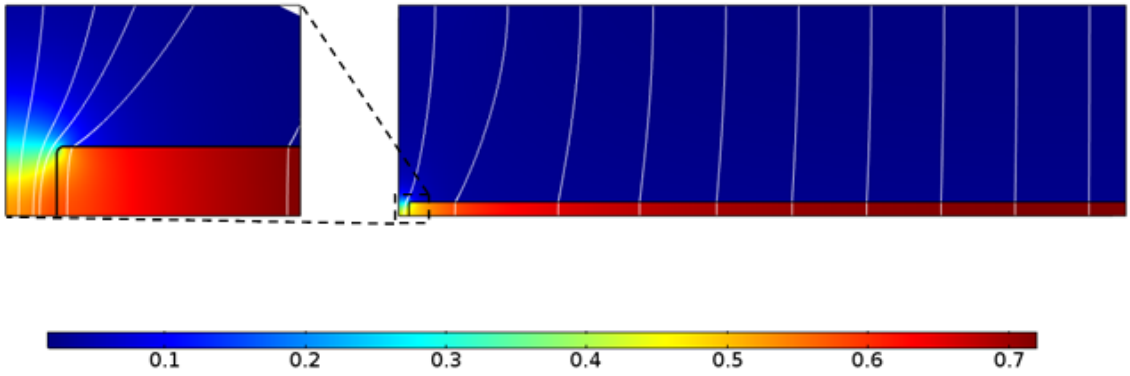

Figure 11: The distribution of the normalized electric field, $\sigma = 10^{-12}\ S/m$.

Figure 12: The results of parametric study.

5 Conclusions

The problem of the electric field screening by the accumulated charge on the interface between the dielectric liquid and solid perfect insulator was studied by means of the computer simulation. The results of the calculations allow concluding the following. Considering liquid dielectrics and strong electric fields (on the order of $10^7 V/m$), the

thickness of the charged layer depends on the electric field strength, the conductivity affects only the time of the charge accumulation, and the ion mobility has no effect at all in the case of the 1D approach.
However, when there is the charge transport along the surface (2D model) the steady-state electric field distribution depends on the conductivity. The result shows that the simplified model of the considered EHD system employing the boundary condition $E_N = 0$ can be used if the liquid conductivity is equal to or higher than 10^{-8} S/m. Otherwise, the electric field distribution and the total current do not correspond to the more complete model.
Accounting for the field-enhanced dissociation should extend the applicability limits of the simplified model. Also, the impact of the ion mobility is yet to be investigated.

6 Acknowledgements

Research was carried out using computer resources provided by Resource Center „Computer Center of SPbU“ (http://cc.spbu.ru).

References

[1] A. I. Zhakin, „Electrohydrodynamics“, Phys. Usp 55, 465–488 (2012).

[2] C. Louste, M. Daaboul, and H. Romat, „Experimental Study of a Plane Turbulent Wall Jet Induced by a Dielectric Barrier Injection in Dielectric Liquid“, no. 7, pp. 106–109, 2008.

[3] S. A. Vasilkov, V. A. Chirkov, and Y. K. Stishkov, „Study on high-voltage conductivity provided solely by field-enhanced dissociation in liquid dielectrics“, J. Electrostat., vol. 88, pp. 81–87, 2017.

[4] V. Chirkov, D. Komarov, Y. Stishkov, and S. Vasilkov, „Numerical and experimental study of an EHD flow near solid-dielectric surface“, Proc. 11-th Int. Conf. Mod. Probl. Electrophysics Electrohydrodynamics, pp. 122–126, 2015.

[5] T. M. Squires and M. Z. Bazant, „Induced-charge electro-osmosis“, J. Fluid Mech., vol. 509, no. 2004, pp. 217–252, 2004.

[6] Y. Daghighi and D. Li, „Induced-charge electrokinetic phenomena“, Microfluidics and Nanofluidics, vol. 9, no. 4–5. Elsevier Ltd, pp. 593–611, 2010.

[7] J. Cabaleiro, T. Paillat, and G. Touchard, „Transient electrical double layer dynamics in a quiescent fluid“, IEEE Trans. Dielectr. Electr. Insul., vol. 21, no. 1, pp. 171–178, 2014.

[8] M. El-Adawy, J. M. Cabaleiro, T. Paillat, O. Moreau, and G. Touchard, „Experimental determination of space charge density associated with flow electrification phenomenon: Application to power transformers“, J. Electrostat., vol. 67, no. 2–3, pp. 354–358, 2009.

[9] I. A. Ashikhmin and Y. K. Stishkov, „Simulation of dynamic current-voltage characteristic in the symmetric wire-wire electrode system placed into channel with low-conducting liquid“, Proc. 10-th Int. Conf. Mod. Probl. Electrophysics Electrohydrodynamics, pp. 122–126, 2012.

[10] I. A. Ashikhmin and Y. K. Stishkov, „Effect of insulating walls on the structure of electrodynamic flows in a channel“, Tech. Phys., vol. 57, no. 9, pp. 1181–1187, 2012.

S. A. Vasilkov, D. A. Nechaev, Yu. K. Stishkov, St. Petersburg State University, 7/9 Universitetskaya nab., St. Petersburg, 199034 Russia

The Lateral Stability problem and Numerical Simulation of a Slender Delta Wing during Self-excited Wing Rock

Yang XiaoLiang, Liu Wei, Chai ZhenXia, Ge MingMing

yangxlnudt@sina.com

Abstract

The Lateral stability problem of modern combat aircraft in high angle of attack is an important issue ralated to flying safety. This investigation foucus on the sideslip behaviors of a slender delta wing during self-excited wing rock. The nonlinear double degree of freedoms aerodynamics model is established for governing the coupling movement in combined free-roll and free-sideslip motion. Then, a numerical investigation is conducted on the dynamic characteristics of an 80FF delta wing in combined free-roll and free-sideslip by solving flow governing equations and Euler rigid-body dynamics equations simultaneously. Implicit, upwind, flux-difference splitting, finite volume scheme and the second-order-accurate finite difference scheme are employed to discrete and solve these governing equations. The governing equations of fluid and movements are solved alternately with a coupling method, either loosely coupling or tightly coupling, both coupling methods are discussed. Well-regulated sideslip oscillation is observed as expected. The sideslip behaviors are mostly affected by the roll oscillatory properties, i.e., the frequencies and phases. The loosely coupling method achieved considerably efficiency and accuracy. The behaviors of double DOFs motion are more complicate than that of single DOF wing rock.

1 Introduction

One of the most common dynamic phenomena experienced by slender wing aircraft flying at high angles of attack is the one known as wing rock. Wing rock is a complicated motion that typically affects several degrees of freedom (DOF) simultaneously[1]. As the name implies, the primary motion is an oscillation in roll, however, the roll characteristics are significant influenced by other coupling motion DOFs. During data analysis, ref[2] and [3] found that some aircrafts proved stable in wind tunnel are unstable in flying test, they think that the dissimilarity of DOFs should account for the phenomenon. Double DOFs motion in combined free-roll and free-sideslip is a common form of coupling wing rock, as Figure 1 depicted.

This is something like Dutch roll, but they are essentially different. Dutch roll is a concept come from disturbance flow and can be described by linear aerodynamic model, however, couping wing rock in combined free-roll and free-sideslip is essentially nonlinear aerodynamic problem under high angle of attack. The concept of vortical lift force has made delta wing the most popular configuration incorporated in modern combat aircraft. With the help of advance control systems, moreover, it becomes more and more feasible for combat aircraft to maneuver in high angle of attack. As the delta wing is the main function plate of lift force and actual configuration of modern combat aircraft, the delta wings oscillating in roll at low speed and high attack angle regime have received a substantial volume of experimental [4]-[6] and computational [7]-[10] research work. However, asymmetrical leading edge vortexes and its fiercely interactions dominant the flowfield, nonlinear aeroforce and moment vary complicately. Owing to the difficulties lying in experiment designing and measuring, these work mainly focus on single DOF wing rock. To the authorrss knowledge, compared with the researches of single DOF wing rock, the numerical investigation about delta wing in this kind of double DOF motion is seldom addressed in published literature. In this paper, we study the double DOFs motion characteristics of the 80rr swept sharp-edged delta wing in combined free-roll and free-sideslip numerically, compare roll characteristics with that of single DOF wing rock, discuss the coupling regime between free-roll and free-sideslip and the flow mechanism sustaining double DOFs wing rock.

2 Model and Methods

2.1 Delta wing model and mesh

An 80° swept-back, sharp-edged delta wing model is incorporated in this investigation. In Figure 2, an O-H topology is employed to mesh the delta wing. The computational domain extends 2.5 chord lengths forward from the wing apex and 5 chord lengths backward from the wing tailing edge. The radius of the computational domain is 4 chord lengths. The minimum grid size in the normal direction to the wing surface is 1.0×10^{-4} chord length on the whole solid surface.

2.2 Flow governing equations

The unsteady, three-dimensional, compressible, full Navier-Stokes equations in strongly conservative form have been used. The equations have been written in a fixed inertial frame of reference and transformed to the computational domain using a generalized time-dependent transformation(ξ, η, ζ, t). The dimensionless form is given as:

$$\frac{\partial Q}{\partial t} + \sum_k \frac{\partial E_k}{\partial k} = \sum_k \frac{\partial E_{vk}}{\partial k} \qquad k = \text{ɔ}, \text{ȷ}, \text{ɪ} \tag{1}$$

$$Q = J^{-1}(æ, æu, æv, æw, æe)^T \tag{2}$$

Where Q is conservation variables, t means time, E and Ev are the inviscid and viscid fluxes in the ξ, η, and ζdirections, respectively. The detail definitions of the inviscid and viscid fluxes are in ref [11].

2.3 Rigid body dynamics equations

The relevant DOFs in this study are roll and sideslip. Both of roll and sideslip equations are second order autonomous ordinary differential equations in time. The rolling equation is written in the body-axes frame of reference to keep the roll-axis moment of inertia constant throughout the entire motion. While the sideslip motion equation is written in the inertial frame of reference. They are given as follow:

$$\begin{cases} I_{xx}\ddot{\text{Œ}} = C_l \\ m\,\ddot{z_o} = C_z \end{cases} \tag{3}$$

The rolling angle Œ is defined positive when the left-hand side (pilot view) of the wing moving down-wards, the variable z_0 represent the z-component of mass center in the inertial frame of reference and its positive direction coincide with the coordinate.C_l and C_z are coefficients of roll moment and transverse force respectively. The parameters I_{xx} and m represent dimensionless roll moment of inertial and mass of the delta wing respectively, written as:

$$I_{xx} = \frac{2\tilde{I}_{xx}}{\tilde{\text{æ}}_\infty \tilde{S}\tilde{c}^3} \quad , \quad m = \frac{2\tilde{m}}{\tilde{\text{æ}}_\infty \tilde{S}\tilde{c}} \tag{4}$$

The superscript '$\sim$' represents variables with dimension. None of the structural damping is considered in this paper.

2.4 Solution algorithm

The implicit, finite volume scheme is used to solve the unsteady, three dimensional, compressible, full Navier-Stokes equations. The Nonoscillation, contains No free parameters and Dissipative (NND) flux-difference splitting scheme[12] is employed to discretize the inviscid fluxes, while the second-order accurate central difference scheme is applied to the discretization of the viscous fluxes which are linearized in time, eliminated in the implicit operator and retained in the explicit terms. The Spalart-Allmaras (SA) model is employed to evaluate the turbulence influences of leeward vortical flow.

The Lower-Upper Symmetric Gauss-Seidel (LU-SGS) scheme is employed to enhance the efficiency of time integration, besides a dual-time-step method [13] which is a Newton-like sub-iteration process is employed to reduce the effect of the inherent time lag in applying the boundary conditions and reduce the factorization error for unsteady-state calculations.

A second-order-accurate finite difference scheme [14] is applied to discretize the rigid-body dynamics equations (3), including roll equation and sideslip equation.

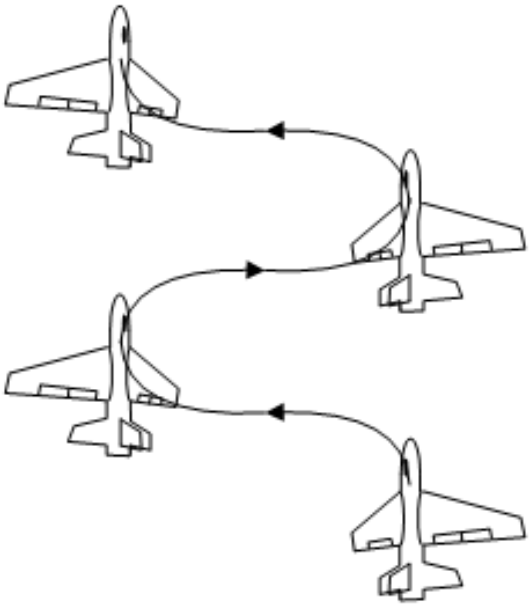

Figure 1: Schematic of aerocraft in combined free roll and free sideslip motion

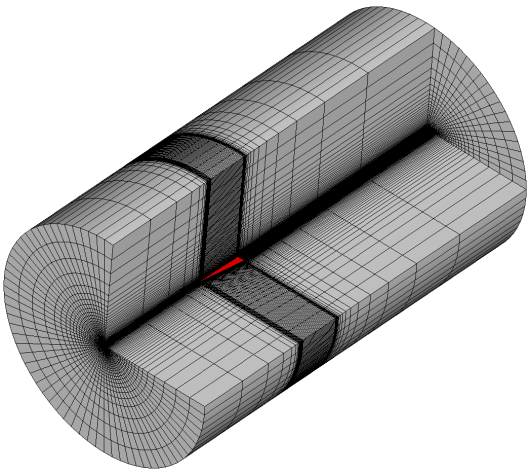

Figure 2: The 80° swept delta wing model and space computational grid distribution

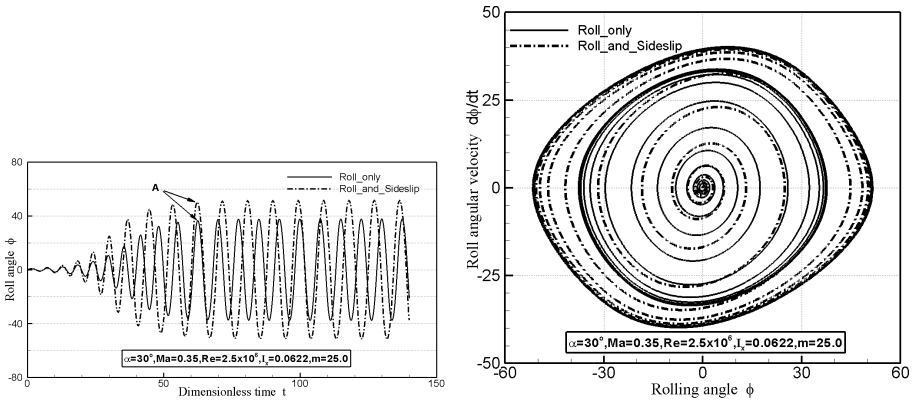

Figure 3: the comparison between roll only and combined roll and sideslip wing rock

3 Results and Disscussions

The nonzero lateral force of rocking delta wing indicates deterioration of lateral stability, accordingly, a sideslip motion is expected to observed as a result. The lateral motion of delta wing during wing rock is evaluated simultaneously.

3.1 Dynamic behaviors of multi-DOFs oscillation

With the nonlinear aerodynamic model established in section 2, the double DOFs motion simulation of the 80ғт delta wing in combined free-roll and free-sideslip is conducted. For manifesting the characteristics of combined free-roll and free-sideslip motion, the roll history curve and phase curve of the double DOFs motion are compared with that of single DOF wing rock. As Figure 3(a) depicted, double DOFs motion built limit cycle oscillation and its roll amplitudes significantly greater than that of single DOF wing rock, indicates that sideslip motion has an influence on the amplitudes characteristics of wing rock. Figure 3(b) draws the phase curves, both single DOF wing rock and double DOFs wing rock in combined roll and sideslip exhibit limit cycle amplitudes in roll, but the later motion built a larger area with limit cycle phase curve, uncover the fact that sideslip has substantially influence on roll amplitudes.

Focus on the frequency characteristics of the roll oscillation history curve, it can be found that the period time are slightly expanded with the influence of sideslip motion, it indicates that double DOFs wing rock in combined free-roll and free-sideslip has larger limit cycle amplitudes and lower frequencies than that of single DOF wing rock. Form startup at the balance angle to limit cycle amplitude achieved a time span is needed. It is interesting that the time spans of the two motions with different DOFs are almost equivalent in spite of different amplitudes and frequencies, as the symbol ʀѳAʀç in Figure 3(a) depicted.

In order to study the rock mechanism of the double DOFs motion in combined free-roll and free-sideslip, nine typical positions in the positive rolling procession ($\omega_x > 0$) are extracted to demonstrate the interaction between the leeward vortical structures and delta wing. As Figure 4 depicted (pilot view), it describes the unsymmetrical evolution of leeward vortexes in the sectional plane (x/c=0.57), wo

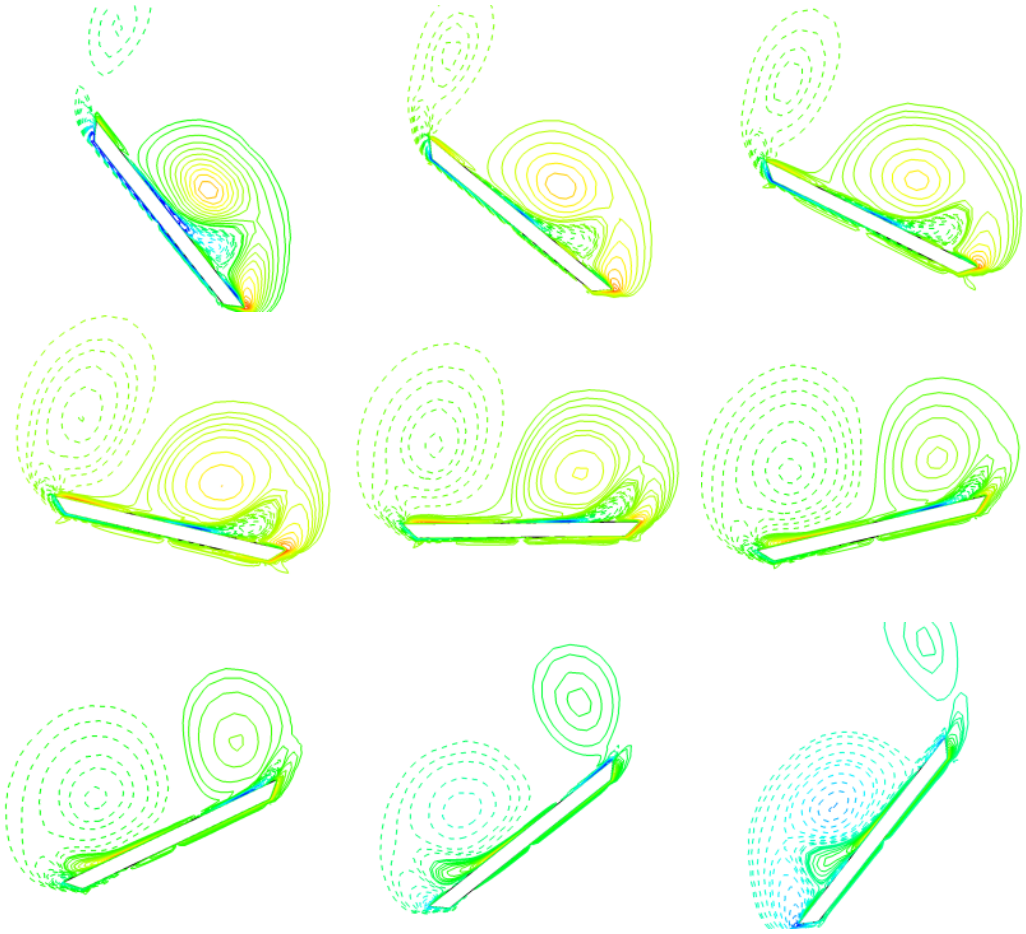

Figure 4: The evolution of sectional (x/c=0.67) streamwise vorticity in positive rolling procession

represent dimensionless sideslip velocity. In the picture, streamwise vorticity are drawn by ISO lines, color represents its magnitude and dash line represnts minus value.

The evolution procession can be mainly divided into three stages. First stage, Figure 4(a) (d), delta wing preserves minus roll angle, left leading edge moves upward and right leading edge moves downward (pilot view), it indicates that the washing effect leads effective attack angle increase at right side and an decrease at left side, as a result, the right leading edge vortexes dominate the leeward flow field of delta wing. As the delta wing rolling right, leading edge vortexes strength increase unsymmetrically on both side across the body symmetry, left side increase rapidly and right side increase slowly. The asymmetrical increase reduced the unsymmetry distribution of pressure, consequently, asymmetrical moment decrease, although roll angular velocity keep increase, the accelerate become more and more smaller. Figure 4(e) is the second stage, the delta wing located about 0° roll angle. As the vortexes movement lag behind the delta wing roll, vortexes preserve unsymmetrical distribution at a symmetrical location. It is critical that turns the delta wing roll unstable at large attack angles. The third stage, Figure 4(f) (i), delta wing preserves positive roll angle, leeward vortexes experience a reverse procession of first stage, leading edge

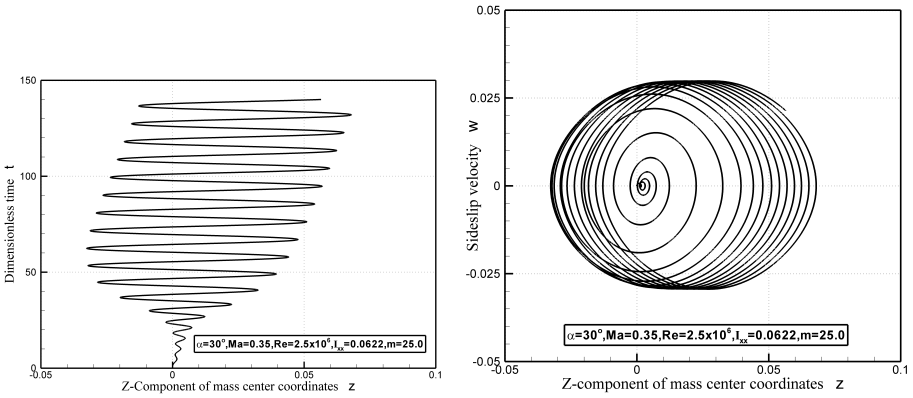

Figure 5: The lateral behaviors of delta wing in double DOFs motion

vortexes strength decrease asymmetrically as the delta wing rolling right on both side across the body symmetry plane, dominant vortexes structure shift from right side to left side. Down washing effect essentially eliminate attack angle decrease with roll angle increase, which makes the left leading edge vortexes almost preserve its strength during the third stage. On the other hand, at the right side, up washing effect collaborate with right roll effectively diminished the right leading edge vortexes strength, whatrss more, the right leading edge vortexes move away from the leeward surface of delta wing. All of these cause an opposite moment and preserve a increase trend, which makes right roll of delta wing slow down till stop.
For evaluting the behaviors of couple method, the results of loose couple method and tight couple method are compared. In fact, the time history curve almost coincide, no significant discrepancy is observed, including ampliudes and frequencies. Considering the efficiency, the loose couple method is employed to conduct the following massive simulation

3.2 Lateral oscillation

The lateral motion is focused. A typical oscillation is observed. Along with the oscillation in rolling, the sideslip motion is excited. After several periods, approximately invariant amplitudes are built with a fixed frequency, as Figure 5(a) depicted. Compared with the wing span, the amplitude of sidesliping displacement is about 0.1 chord length which is not significant. Dissimilarly, the lateral motion is not oscillating around a fixed balance position. The average position of sideslip shift right slightly. Consequently, the phase curve could not form a limit cycle, as Figure 5(b) depicted.

3.3 Coupling regime

Considering the significant influence of sideslip on roll oscillation, the coupling regime of the double DOFs motion in combined free-roll and free-sideslip is discussed also.Figure 6 draws the time history curves of roll angular velocity and sideslip velocity, the conclusion can be drew that sideslip velocity and roll angular velocity of double DOFs wing rock are almost in same frequencies and opposite phase, which

indicates that the couple regime of double DOFs motion is right sideslip during left rolling and left sideslip during right rolling. In Figure 4, we find that when roll motion achieve its amplitudes, sideslip velocity almost equal to zero. In the first stage, leeward leading edge vortexes induced suction region on the right side of delta wing and generated right side-force that makes delta wing sideslip right. In third stage, the suction region shift from right side to left side, the right sideslip velocity decelerates till zero along with the right roll stop. A similar procession can be inferred in the negative procession ($\dot{l}_x < 0$) of roll oscillatory. So the complete story of coupling procession during a period time is drew in Figure 7 and the coupling regime can be conclude as right sideslip during left rolling and left sideslip during right rolling.

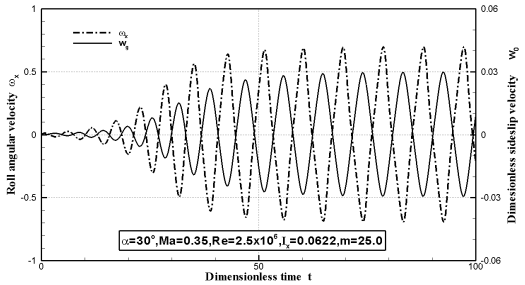

Figure 6: the time history curves of sideslip velocity and roll angular velocity

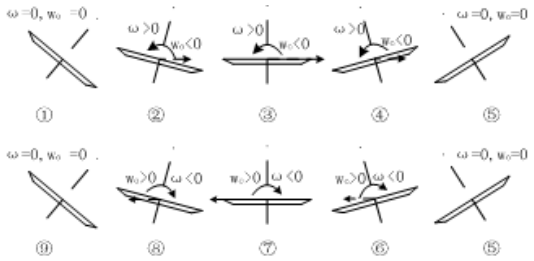

Figure 7: Schematic of the coupling regime of free-roll and free-sideslip

In single DOF wing rock, with definitely incidence angle, sideslip angle and attack angle fully depend on roll angle. With the influence of sideslip, extra hysteresis phenomena induced. As Figure 8(a) depicted, sideslip angle loops hysteretically with roll angle that is different from single DOF wing rock. The sideslip angle definitely increases during positive roll procession and decreases during negative roll procession, the increment versus roll angle achieve limit cycle oscillation eventually, as Figure 8(b). The situation of attack angle is similar to sideslip angle, hysteresis effect is induced by sideslip motion, nevertheless it has a more complicate hysteresis curve which looks like a beautify butterfly as Figure 9 depicted.

4 Summary

Dynamic characteristics of an 80° delta wing in double DOFs wing rock are investigated numerically and the lateral behavior is focused. Results show that sideslip

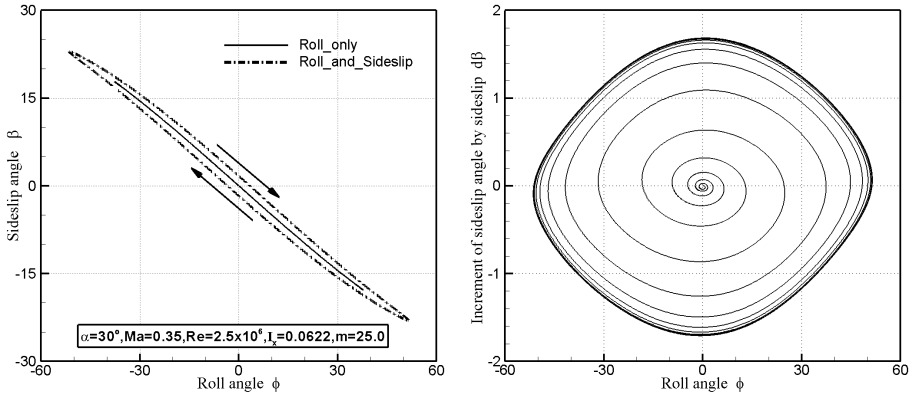

Figure 8: Influence of the coupling effects in combined roll and sideslip motion on sideslip angle

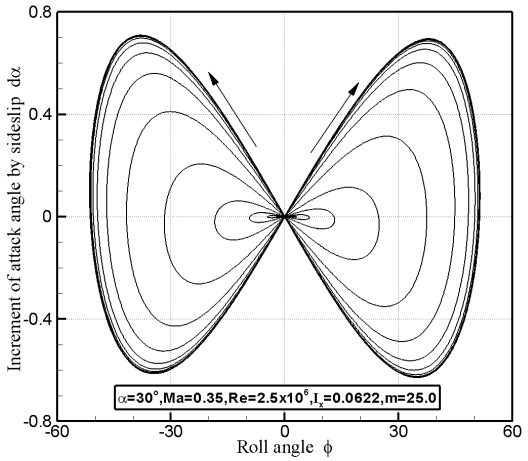

Figure 9: increment of attck angle VS roll angle

motion has an influence on the rolling amplitudes; Asymmetric oscillation of vortices is the flow mechanism sustaining wing rock of slender delta wing in combined free-roll and free-sideslip; Right sideslip during left rolling and left sideslip during right rolling are the coupling regime of slender delta wing in combined free-roll and free-sideslip motion; with the influence of sideslip, attack angle and sideslip angle lag behind the roll angle is observed, the asymmetrical characteristics of flow structures and hysteresis effects are enforced during coupling wing rock; the loose couple method can achieve the same accuracy as that of tight couple method and can achieve high efficiency.

References

[1] J. Nelson R C, Pelletier A. The unsteady aerodynamics of slender wings and aircraft undergoing large amplitude maneuvers. Progress in Aerospace Sciences 2003; 39(2-3): 185-248.

[2] JIA Quyao. Investigation on aerodynamic relation between real flight and wind

tunnel [J]. Journal of Experiments in Fluid Mechanics, 2006. 20(4): p. 87 93. (in Chinese)

[3] JIA Quyao , YANG Yinong , CHEN Nong. The influence of Reynolds number on dynamic aerodynamics correlation between real flight and wind tunnel [J]. Journal of Experiments in Fluid Mechanics, 2007, 21(4): 91 96. (in Chinese)

[4] L.E. Nguyen, L.P. Yin, and J.R. Chambers, ґөSelfinduced wing rock of slender delta wing,ґç AIAA paper 81-1883, Aug. 1981.

[5] B.N. Pamadi, D.M. Rao, and T. Niranjana, ґөWing rock and roll attractor of delta wing at high angles of attack,ґç AIAA paper 94-0807, 1994.

[6] Ericson, L., ґөWing rock analysis of slender delta wings, review and extension,ґç AIAA paper 95-0317, Jan.1995.

[7] X.Z. Huang, and E.S. Hanff, ґөNon-linear rolling stability of a 65ґг delta wing model at high incidence,ґç AIAA paper 99-4102, 1999.

[8] N.M. Chaderjian, and L.B. Schiff, ґөNavier-Stokes prediction of large-amplitude forced and free-to-roll delta-wing oscillations,ґç AIAA paper 94-1884, 1994.

[9] O.A. Kandil, and M.A. Menzies, ґөEffective control of computationally simulated wing rock in subsonic flowґç. AIAA paper 97-0831, 1997.

[10] W. Liu, H.X. Zhang, and H.Y. Zhao, ґөNumerical simulation and physical characteristics analysis for slender wing rock,ґç Journal of Aircraft, vol.43, no.3, pp. 858-861. 2006.

[11] Blazek J. COMPUTATIONAL FLUID DYNAMICS: PRINCIPLES AND APPLICATIONS. 1st ed. Amsterdam, London, New York, Oxford, Paris, Shannon, Tokyo: ELSEVIER SCIENCE Ltd, 2001.

[12] Q. Shen, and H.X. Zhang, ґөA new upwind NND scheme for Euler equations and its application to the supersonic flow,ґç in Proceedings of Asia Workshop on CFD, Sichuan, China, 1994.

[13] A. Jameson, ґөTime dependent calculations using multigrid with application to unsteady flows past airfoils and wings,ґç AIAA paper 91-1596, 1991

[14] W. Liu, H.X. Zhang, and H.Y. Zhao, ґөNumerical simulation and physical characteristics analysis for slender wing rock,ґç Journal of Aircraft, vol.43, no.3, pp. 858-861. 2006.

[15] Z Hanxin, L Wei,X Yufei, Y Youda. On the rocking motion and its dynamic evolution of a swept delta wing [J]. ACTA AERODYNAMICA SINICA, 2006. 24(1): p. 5-9. (in Chinese)

[16] Liu, Wei, Zhang HanXin, and Zhao HaiYang, Numerical Simulation and Physical Characteristics Analysis for SlenderWing Rock[J]. Journal of Aircraft, 2006. 43(3): p. 858-861.

Yang XiaoLiang, Changsha , China
Liu Wei, Changsha , China
Chai ZhengXia, Changsha , China
Ge MingMing, Changsha , China

Skin-effect of redistribution of dissolved hydrogen in metals under tension

Yuriy A. Yakovlev, Dmitriy E. Mansyrev, Sergey V. Polyanskiy

yura.yakovlev@gmail.com

Abstract

Plastic deformation is accompanied by structural rearrangement of the material. Prediction and diagnosis of such adjustment is an important task, since for structural materials, the plastic deformation precedes the destruction.

One of the important features of plastic deformation is the redistribution of natural hydrogen that is inside metals. This process is associated with a number of mechanical phenomena, ranging from the diffusion of hydrogen into the zone of tensile stresses and ending with a change in the size of the structural elements of the metal and the appearance of new structural defects.

Studies show that there is a good correlation between the concentration of diffusively mobile hydrogen and the value of plastic deformation, in many cases they are linearly related.

The report describes a new effect, discovered by the authors in the process of investigating specimens broken with different degrees of plastic deformation. A careful study of the distribution of hydrogen concentrations shows that all changes that are associated with plastic deformation occur in the surface layer of about 1 mm in thickness. Thus, this result gives evidence submitted on the surface nature of the damage accumulation during plastic deformation. On the one hand, this is the basis for developing methods of technical diagnostics of damage by the state of a thin layer. On the other hand, the obtained data makes it possible to develop methods for reducing the damage in plastic deformation by treating the metal surface.

1 Introduction

The strong influence of hydrogen on the strength and other mechanical characteristics of metals was found approximately 150 years ago. In the cracks of cast iron castings, hydrogen gas has been found, and since then any new technology for the production of metals and many other materials has faced to the problem of the destructive effect of hydrogen at an increasingly low level of its concentrations in the solid material.

At the beginning of the 20th century, in connection with the mass production of rolled steel, we had to fight with flocken - discontinuities in the rolled steel.

Causing this disease mass relative hydrogen concentration in the steels of the order of 4 ppm. Then metallurgists faced the brittleness of aluminum alloys already at the concentration level of about 0.4 ppm. "Hydrogen problems" arose in the production of titanium, zirconium, heat-resistant nickel alloys.

Simulation is one of the main ways to find out the cause of hydrogen embrittlement. Hydrogen has a strong effect on the strength of metals, and so many works are devoted to modeling this effect.

Several basic approaches can be distinguished: taking into account the influence of hydrogen on the nucleation and movement of dislocations, taking into account the influence of hydrogen on the development of cracks, taking into account the internal pressure of hydrogen in the metal and "physical approaches" based on taking into account the potential energy of hydrogen interaction with the material matrix.

The motion and formation of dislocations and their influence on local plasticity near the top of cracks lead to local plasticity because of the very high concentration of dislocations. The mechanism of local hydrogen plasticity (HELP) was first described in the work of a scientific group from the University of Illinois [1]. Later, in [3] and [4, 5], on the basis of physical considerations on the potentials of hydrogen interaction with dislocations, the defining equations of the material were proposed that simulate local changes in material properties at the mouth of the microcrack.

At the same time, calculations performed by the authors of the model in [3] show that significant changes in mechanical properties in HELP occur at local relative mass concentrations of hydrogen of the order of 10000 ppm, which is an unattainably high concentration for most metals. Steel even at much lower concentrations independently crack up to complete failure without any external load.

The calculation of local plasticity in the theoretical examination of a crack with a spherical vertex shows that the local concentrations of hydrogen are only 100 times higher than the average [6]. Given that the averages are usually about ppm, the local concentrations do not exceed 100 ppm. Thus, the verification calculation does not confirm that under the influence of external mechanical loads, local accumulation of hydrogen is possible, which is necessary for triggering physical mechanisms of local plasticity.

There is still a whole series of uncertainties about which the authors of the model write, in particular, there is a nonlinear dependence of the internal potential on the magnitude of the stresses and hydrogen concentration, and since huge local concentrations that are many times larger than those observed in practice are considered, all the nonlinearities play a big role.

It was noted in [7] that the HELP model requires huge computational resources for solving any applied problem, therefore, the only way out is to use the continuum model of dislocation development. Such a replacement is often inadequate and the authors propose to use the growth criterion of the submicrocrack, that is, reduce all the hydrogen problems to modeling the development of a crack and to reduce crack resistance.

The peeling model (HEDE) [8] is a similar HELP. The difference lies in the fact that HEDE takes into account the decrease in the energy of formation of free fracture surfaces with increasing local hydrogen concentration.

Standard modeling of the development of hydrogen-induced cracks, taking into ac-

count the reduction in fracture toughness, is also a common approach. At the same time, the model does not relate to real physical mechanisms of hydrogen influence. In addition, it turns out that the consideration of the same model in problems of different dimensions yields strongly differing results [9, 10].
To model hydrogen fragility, molecular dynamics is also used [11, 12], but because of the smallness of the modeled ensembles, it allows us to describe only micromechanisms at the apex of a microcrack or dislocation. The same disadvantage is possessed by the quantum mechanical approach [13, 14] because of the large heterogeneity of real metals, it can be used only to describe the behavior of cracks in ideal crystals or to model the behavior of individual microcracks and dislocations.
A new approach to modeling materials containing hydrogen was proposed in [15]. Experimental studies have shown that under the influence of external loads hydrogen changes its binding energy [16]. Therefore, a separate description of hydrogen transport inside the material in isolation from its stress-strain state is too crude. In [15] proposed a model of a continuous medium, which takes into account the mutual influence of hydrogen on the mechanical properties of the medium and the stress-strain state of the medium on the binding energy and hydrogen transfer.
In all models, a uniform concentration of hydrogen is considered throughout the entire volume of the material, with the exception of defects.
It remains an open question whether artificial saturation with hydrogen can be used in carrying out experimental studies. With the help of this method, practically all the experimental results were obtained. But modern manifestations of hydrogen embrittlement are of a complex nature and are observed under conditions when there is no hydrogen or its ions in the medium surrounding the material. Moreover, in welded joints it is observed in the purest form, and in other cases (for example, when turbine blades are destroyed) they speak of "hydrogen-induced destruction". Experimental data show that, due to the limited capacity of hydrogen traps, it is difficult to expect that its distribution along internal traps does not depend on the way it enters the solid.
Thus, clarifying the effects associated with the redistribution of hydrogen under the action of loads is an important task for both mechanics and technical diagnostics.

2 Experimental research

Model experiments were carried out on samples of aluminum alloy AMC. The choice of metal was made in such a way that the diffusion of hydrogen had practically no effect on its distribution. It is known that at room temperature there is practically no hydrogen diffusion in aluminum alloys. The diffusion coefficients are very small and the initial concentrations of hydrogen persist for years.
We have specially chosen a conventional plate 15 mm thick, obtained by rolling from a casting. The surface of the plate was not previously processed. Samples were prepared from the plate for mechanical testing. The drawing, which is presented in Fig.1.
Samples were subjected to low cycle fatigue tests on a tensile machine. The loading cycle was not symmetrical from 0 to $1.05\sigma_{0.2}$. As a rule, the samples were kept for 3-10 thousand cycles before failure.

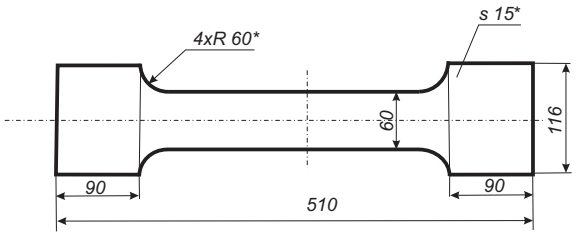

Figure 1: Samples of the AMC alloy for mechanical testing

After the destruction, the volume distribution of hydrogen in the samples was studied. Onlynatural hydrogen was studied. We did not any hydrogen charging or saturation. The sources of hydrogen were: the atmosphere of the laboratory and internal natural hydrogen, which was redistributed under the influence of mechanical loads.
Samples were cut from the broken samples in order to analyze the hydrogen content, had the form of parallelepipeds with a height of 8-15 mm and a section of 6x6 mm^2. The cutting scheme is shown in Fig.2.

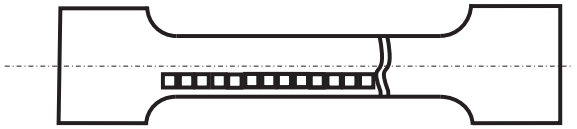

Figure 2: Scheme cutting specimens for measuring the concentration of hydrogen

Samples were cut in two ways:
1. With a portion of the flat rolling surface;
2. With the removal of 1 mm from the outer surface
Cutting was done with a manual saw to prevent overheating of the samples. The cut samples were investigated by hot vacuum extraction using the industrial hydrogen analyzer AV-1.
The procedure for measuring, sample preparation and the principle of operation of the analyzer is described in detail in [Pol1, Pol2, Pol3].
The results of measurements, hydrogen concentration depending on the removal of samples from the line of rupture are shown in Fig.3 and Fig.4. In Fig.3. The results for samples with part of the rolled surface are given. In Fig.4. The results for samples with the removed surface of rolled products are given.
A comparison of the graphs shows that there is a purely surface effect of the uneven distribution of hydrogen as a result of cyclic loading and plastic deformations [16]

3 Discussion of results

Skin effect of the distribution of hydrogen under the influence of external mechanical loads, which we found, is not described in the literature
As a rule, special saturation with hydrogen in solutions of electrolytes is used for research. There are four main ways of saturation:
1. In gaseous hydrogen [20]

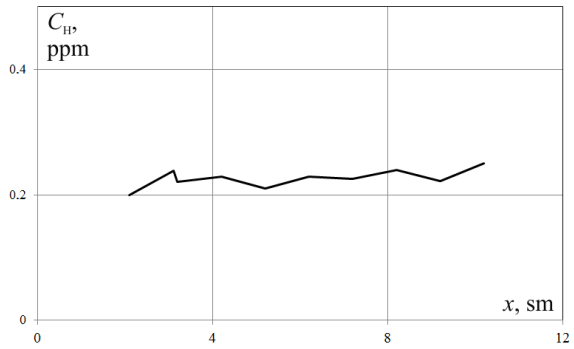

Figure 3: Distribution of hydrogen for samples with a surface layer of rolled metal

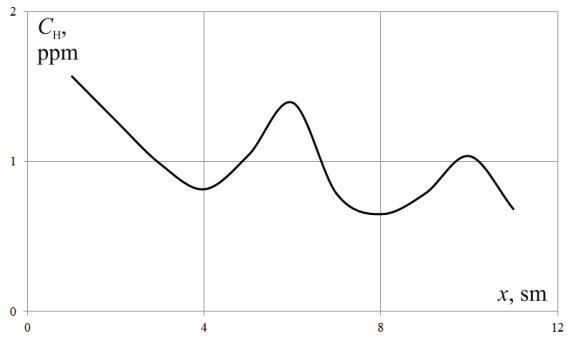

Figure 4: Distribution of hydrogen for samples with a removed surface of rolled products.

2. In acid solution due to corrosion or stress corrosion [20] 3. Cathodic hydrogen charging [20]

4. In electrolyte associated with near-neutral pH SCC, simulating sea or ground water or the environment of transported natural gas [21]. For example, [21] - test Standard set of test conditions for a consistent evaluation of the pipeline and pressure vessel steels and compares test results from different laboratories pertaining to the results of the treatment of H_2S.

At such a saturation, the hydrogen concentration is tens of times higher than the natural one, therefore in all ref.([22, 23], etc.) the skin effect of hydrogen distribution under the influence of external mechanical loads did not manifest itself.

The unevenness of the concentrations that we detected in the case when the surface layer of rolled metal was not removed is due to the well-known effect of Portevin-Le Chatelier. This effect leads to inhomogeneity in the appearance of plastic deformations and this is often found in aluminum alloys.

New in this experiment is the skin nature of the changes that occur with this effect. Concentrations of natural hydrogen in metals are related to their structure. The limiting saturation with hydrogen is characteristic for aluminum alloys. That is, the natural concentration of hydrogen, with a given alloy structure, is extremely saturated. This is due to the fact that the solubility of hydrogen during crystallization of aluminum alloys falls approximately 4 times and hydrogen expelled from the melt is concentrated in various structural defects.

A significant increase in the average hydrogen concentration observed by us (see

Fig. 3,4) can be associated only with the appearance of a large number of defects (microcracks, pores, bundles).
It follows from our results that these defects are localized in a thin layer of thickness less than 1 mm as a result of a significant (35%) plastic deformation. The rest of the volume of material does not experience similar devastation.
Thus, the skin effect of the distribution of hydrogen concentration is related to the skin effect of plastic deformation. We managed to find work that describes the skin effect of plastic deformation [24].
On the one hand, this is an important result for the mechanics. It explains the large influence of surface tension forces on plastic deformation [25], on the other hand, it is still not discussed and is not modeled either in the theory of mechanics of solid or in the numerous hydrogen embritlements models that was described in the introduction.
Accounting for the skin effect in modeling and strength calculations can significantly increase the accuracy of calculations and the adequacy of mechanical models.

4 Conclusions

As a result of the carried out experimental studies, the skin effect of the distribution of natural hydrogen concentrations for plastic deformation under the action of cyclic loading was first discovered.
The observed effect agrees well with the skin effect of residual stresses during plastic deformation, which was discovered 100 years ago but did not receive a theoretical description.
Modeling the skin effect will make it possible to obtain more adequate results when calculating the strength of metal structures and machine components.

Acknowledgements

The financial support of the Russian Foundation for Basic Research, grants 15-08-03112 РФ and 17-08-00783 РФ, is acknowledged.

References

[1] Birnbaum H.K., Sofronis P. Hydrogen-enhanced localized plasticity вЃY a mechanism for hydrogen-related fracture , Mat. Sci. and Eng.: A. 176(1-2) 1994. вЃY p. 191-202.

[2] Sofronis P., Liang Y., Aravas N. Hydrogen induced shear localization of the plastic flow in metals and alloys , European J. of Mech. A. Solids. 20(6) 2001. вЃY pp. 857-872.

[3] Sofronis P., Liang Y., Aravas N. Hydrogen induced shear localization of the plastic flow in metals and alloys , European J. of Mech. A. Solids. 20(6) 2001. вЃY pp. 857-872.

[4] Delafosse D., Magnin T. Interfaces in stress corrosion cracking: a case study in duplex stainless steels , Solid State Phenomena. 59-60 1998. вЃY p. 221-250.

[5] Delafosse D., Magnin T. Hydrogen induced plasticity in stress corrosion cracking of engineering systems , Eng. Fract. Mech. 68(6) 2001. вЃY pp. 693-729.

[6] Taha A., Sofronis P. A micromechanics approach to the study of hydrogen transport and embrittlement. Eng. Fract. Mech. 68(6) 2001. вЃY p. 803вЃY837.

[7] Ignatenko A.V., Pokhodnya I.K., Paltsevich A.P., Sinyuk V.S. Dislocation model of hydrogen-enhanced localizing of plasticity in metals with BCC lattice , The Paton Weld J. (3) 2012. вЃY pp. 15-19.

[8] Varias A.G., Massih A.R. Simulation of hydrogen embrittlement in zirconium alloys under stress and temperature gradients , J. of Nuclear Mat. 279(2-3) 2000. вЃY p. 273-285.

[9] Alvaro A., Olden V., Akselsen O.M. 3D cohesive modelling of hydrogen embrittlement in the heat affected zone of an X70 pipeline steel , Int. J. of Hydrogen Energy. 38(18) 2013. вЃY p. 7539-7549.

[10] Alvaro A., Olden V., Akselsen O.M. 3D cohesive modelling of hydrogen embrittlement in the heat affected zone of an X70 pipeline steel. Part II , Int. J. of Hydrogen Energy. 39(7) 2014. вЃY p. 3528-3541.

[11] Wen M., Xu X.-J., Omura Y., et al. Modeling of hydrogen embrittlement in single crystal Ni , Computational Materials Science. 30(3-4) 2004. вЃY pp. 202-211.

[12] Song J., Curtin W.A. A nanoscale mechanism of hydrogen embrittlement in metals , Acta Materialia. 59(4) 2011. вЃY pp. 1557-1569.

[13] Serebrinsky S., Carter E.A., Ortiz M. A quantum-mechanically informed continuum model of hydrogen embrittlement , Journal of the Mechanics and Physics of Solids. 52(10) 2004. вЃY pp. 2403-2430.

[14] Daw Murray S., Baskes M.I. Semiempirical quantum mechanical calculation of hydrogen embrittlement in metals , Phys. Rev. Lett. 50 (17) 1983. вЃY p. 1285-1288.

[15] Indeitsev D., Semenov PЎ. About a model of structural-phase transformations under hydrogen influence , Acta Mechanica. 195. 2008. вЃY p. 295-304.

[16] A.M. Polyanskiy, V.A. Polyanskiy, D.B. Popov-Diumin "Diagnostics of mechanical condition of materials by method of high-temperature hydrogen vacuum-extraction", Proceedings of the Sixth International Congress on Thermal Stresses, vol. 2, Vienna, Austria, (2005) 589-592

[17] A.K. Belyaev, A.M. Polyanskiy, V.A. Polyanskiy, Ch. Sommitsch, Yu. A. Yakovlev, Multichannel diffusion vs TDS model on example of energy spectra of bound hydrogen in 34CrNiMo6 steel after a typical heat treatment, Int. J. of Hydrogen Energy, 41(20), (2016), 8627-8634.

[18] D.Yu. Andronov, D.G. Arseniev, A.M. Polyanskiy, V.A. Polyanskiy, Yu.A. Yakovlev, Application of multichannel diffusion model to analysis of hydrogen measurements in solid, Int.l J. of Hydrogen Energy, 42(1), (2017), 699-710.

[19] Polyanskiy, A.M., Polyanskiy, V.A., Yakovlev, Yu.A. Experimental determination of parameters of multichannel hydrogen diffusion in solid probe, Int. J. of Hydrogen Energy 39(30), (2014), 17381вЃ“17390.

[20] ISO 16573:2015 Steel - Measurement method for the evaluation of hydrogen embrittlement resistance of high strength steels

[21] TM0284 N. S. Evaluation of pipeline and pressure vessel steels for resistance to hydrogen-induced cracking , Houston, TX: NACE. вЃ“ 2003.

[22] A.A. Saleh, D. Hejazi, A.A. Gazder, D.P. Dunne, E.V. Pereloma, Investigation of the effect of electrolytic hydrogen charging of X70 steel: II. Microstructural and crystallographic analyses of the formation of hydrogen induced cracks and blisters, Int.l J. of Hydrogen Energy, 41(28), (2016), 12424-12435

[23] Y. Mine, K. Koga, K. Takashima, Z. Horita, Mechanical characterisation of microstructural evolution in 304 stainless steel subjected to high-pressure torsion with and without hydrogen pre-charging, Materials Science and Engineering: A, 661(20), (2016), 87-95

[24] Brick R. M., Phillips A., Smith A. J. Quenching Stresses and Precipitation Reaction in Aluminum-Magnesium Alloys, Trans. AIME. 117, (1935), 102.

[25] N. R. Kudinova, V. A. Polyanskiy, A. M. Polyanskiy, Yu. A. Yakovlev, Contribution of Surface Tension Energy during Plastic Deformation of Nanomaterials , Doklady Physics, 61(10), (2016), 514вЃ“516.

Yuriy A. Yakovlev, Institute for Problems in Mechanical Engineering RAS, V.O., Bolshoj pr., 61, St. Petersburg, 199178, Russia

Dmitriy E. Mansyrev, Peter the Great Saint-Petersburg Polytechnic University, Polytechnicheskaya, 29, St. Petersburg, 195251, Russia

Sergey V. Polyanskiy, Institute for Problems in Mechanical Engineering RAS, V.O., Bolshoj pr., 61, St. Petersburg, 199178, Russia

Theoretical and Numerical Analysis of the flow separation criterion for hypersonic nonequilibrium flow over

Ming Zeng, Xiaoyu Zhao, Mingming Ge, Xiaoliang Yang, Wei Liu

ming_z@163.com

Abstract

Through combining the triple-deck theory in the analytical treatment of shock wave boundary layer interactions and the numerical simulation of hypersonic nonequilibrium flow over compression corner, the influence factors on flow separation are analyzed, and a criterion parameter to predict whether the separation occurs is proposed. The criterion parameter (S) is the product of the powers of the corner angle, the freestream Mach number and Reynolds number, and the Chapman-Rubesin parameter. It is based on the existing formula of the incipient separation angle for calorically perfect gas flow, but the reference temperature and the corresponding viscosity in the calculation of Chapman-Rubesin parameter are determined by the reference enthalpy with chemical equilibrium assumption, which introduces the high-temperature gas effects. The powers in the criterion parameter (S) and the critical value of S for incipient separation are determined through large number of numerical simulations of hypersonic nonequilibrium compression corner flow for 3 corner angles (15, 18 and 24 degree), where the 12 freestream Mach numbers range from 8 to 35, the 36 gas densities are corresponding to the altitudes from 30 to 65km, the freestream Reynolds numbers range from 104 to5×10^6.

Key Words: hypersonic, nonequilibrium flow, compression corner flow, flow separation, numerical simulation

1 Introduction

Shock waveïCboundary-layer interaction is an important flow phenomenon that exists widely in the flow over control surface or in the inlet of the hypersonic vehicle. The flow in these areas can be simplified to a compression corner flow. The occurrence of Shock waveïCboundary-layer interaction will produce local peak pressure and peak heat flux. Moreover, when the shock is strong enough, the separation of the boundary layer occurs, which will make the wave structure of the flow field complicated, the increase the peak value of wall pressure and heat flux further, change the aerodynamic load of the hypersonic vehicle control surface, and increase the

drag. The separation of the boundary layer in the inlet will seriously deteriorate the flowfield quality, and cause the loss of the engine intake. Therefore, it is very important to obtain the separation criterion of hypersonic compression corner flow. Under hypersonic conditions, dissociation and even ionization of the high temperature air take place in the boundary layer. This causes the decrease of the temperature and therefore the decrease of gas viscosity, which results in less loss of the gas kinetic energy, and the increase of the gas ability to overcome the adverse pressure gradient. This means that the chemical reaction of the high temperature gas may delay the flow separation as compared with the calorically perfect gas[1].
The study of flow separation criterion has been done by many researchers through theoretical analysis, experimental research, and numerical simulation. The initial separation criterion proposed is the incipient separation angle. Under a given flow condition, the boundary layer will separate only when the angle of the compression corner exceeds a certain critical value (called the incipient separation angle). The incipient separation angle has many influencing factors, including the flow type of the boundary layer (laminar or turbulent), the freestream Mach number and the Reynolds number, and the wall temperature [2]. In 1967, through correlation analysis of the experimental data, Neeham [3] $\sim$ [5] gave the approximate formula of the incipient separation angle for hypersonic laminar boundary layer

$$Ma_\infty \theta_{is} = K\emptyset^{1/2} \tag{1}$$

where θ_{is} is expressed in radians, the coefficient K is taken as 1.13, and the $\emptyset$ is the viscous interaction parameter

$$\emptyset = Ma_\infty^3 \sqrt{C_{\mathrm{REF}}} \Big/ \sqrt{Re_{L\infty}} \tag{2}$$

C_{REF} in the above equation is Chapman-Rubesin parameter

$$C_{\mathrm{REF}} = \frac{\mu_{\mathrm{REF}}}{\mu_\infty} \frac{T_\infty}{T_{\mathrm{REF}}} \tag{3}$$

where T_{REF} is the reference temperature in the boundary layer and μ_{REF} is the corresponding viscosity of the gas.
As a pioneering work in the theoretical analysis of the shock waveïCboundary-layer interaction, Lighthill [7], Stewartson [8] and Neiland [9] proposed the triple-deck theory and established the governing equation of the disturbance flow field in the late 1970s. The local disturbance field is organized into a vertically layered structure: an outer layer external to the boundary layer consisting of potential disturbance flow associated with the viscous displacement effect of the underlying deckћња middle layer of negligible shear-stress-perturbation rotational inviscid disturbance flow occupying the outer 90 percent of the incoming boundary layer thickness; a thin inner layer of viscous disturbance flow within the linear portion of the velocity profile that is interactively coupled with the local pressure field. Triple-deck theory provides a basic theoretical explanation for the upstream influence and free interference phenomenon. Inger (in 1994) [6] [10] solved the governing disturbance flow equations

yielded by this triple-deck theory and derived the incipient separation angle 00, in which the coefficient K is taken as 1.26.
With the arrival of the computer age, the CFD numerical simulation of the flow field based on Navier-Stokes equations becomes an extensively effective method. The numerical study of the high temperature real gas effect on shock waveïCboundary-layer interaction [13, 14, 15, 16, 17] is also being carried out. John [18] assessed the suitability Eq. (1) through numerical simulations for flows with different freestream to wall temperature ratio and at low and high enthalpy conditions. It is pointed out in [19] that Eq. (1) can successfully fit a great deal of experimental data if K=1.4∼1.5 is used in the formula.
Neeham's fitting coefficient applies to the case of small Ma_∞ `, Inger's fitting coefficient applies to the case of larger $Ma_\infty$ `. John included the high temperature gas effects in some of the numerical simulations, however, the detail conditions of the freestream are not taken into account, such as the freestream velocity and gas density. Considering that the velocity and density may influence the flow thermochemical state in the boundary layer and the shock intensity, which will further affect the adverse pressure gradient and the corresponding flow separation characteristics, it can be concluded that Ma_∞ ` is not an inclusive parameter to distinguish the flow condition for the determination of appropriate value of coefficient K in Eq. (1).
In the present work, the incipient separation angle formula (1) is transformed into a formula of separation criterion parameter: $S = Ma_\infty^m Re_{L\infty}^{1/4} C_{\mathrm{REF}}^{-1/4} (T_\infty/T_s)^n \theta_B^l$. The values of the power m, n and l and the critical value of S corresponding the incipient separation are determined by the combination of theoretical analysis and numerical simulation of nonequilibrium compression corner flow. Theoretical analysis is mainly about the influence of chemical reactions on the distribution of temperature and the corresponding viscosity in the boundary layer, on the shock intensity, and on the upstream propagation of the adverse pressure gradient. The nonequilibrium flow simulations are carried out for three compression corners (with angle of 15, 18, and 24 degree) in wide range of hypersonic flight condition, 12 freestream Mach numbers (8, 10, 13, 15, 18, 20, 23, 25, 28, 30, 33, 35) and 36 gas densities (corresponding to the atmosphere at altitude from 30 to 65km) are taken as the case conditions.

2 Theoretical analysis

2.1 Separation Criterion Parameters Based on Triple-Deck Theory

According to Eq. (1), flow separation occurs when the compression corner angle θ_B is greater than or equal to θ_B, namely

$$\theta_B \geq \theta_{is} = \frac{K\emptyset^{1/2}}{Ma_\infty} \tag{4}$$

In practice, the Mach number and Reynolds number may change during the flight, while the shape of the vehicle does not change generally, that is, θ_B keeps constant. For convenience in the prediction of separation, we reform Eq. (4) into

$$\frac{Ma_\infty \theta_B}{Ø^{1/2}} \geq \frac{Ma_\infty \theta_{is}}{Ø^{1/2}} = K \tag{5}$$

From the above equation, we know that for a given corner angle $`_B$ , the flow separation occurs when $\left(Ma_\infty `_B / Ø^{1/2}\right) \geq K$. So a separation criteria parameter can be defined as

$$S_0 = \frac{Ma_\infty \theta_B}{Ø^{1/2}} \tag{6}$$

In the above equation, $S_0 = \frac{Ma_\infty \theta_B}{\chi^{1/2}}$ is a hypersonic similarity parameter which reflects the intensity of the corner-generated shock and the corresponding adverse pressure gradient, and the viscous interaction parameter $Ø$ reflects the pressure increment caused by hypersonic viscous interaction, which can also reflect the flow ability to resist the adverse pressure gradient,. So the separation criterion parameter S_0 is an index of the adverse pressure gradient relative to the flow ability to withstand it. Thus the greater the separation criterion parameter S_0 , the more prone of the flow to separation.
For ease of use, the separation criterion parameter S_0 can also be expressed directly as a function of the freestream Mach number and Reynolds number

$$S_0 = Ma_\infty^{-1/2} Re_{L\infty}^{1/4} C_{\mathrm{REF}}^{-1/4} `_B \tag{7}$$

when , $S_0 > S_{0,is} = K = Ma_\infty \theta_{is} / \chi^{1/2}$ the flow separation occurs.

2.2 Introduction of the Effects of High Mach Number and High Temperature

The separation criterion parameter S_0 in Eq. (7) is defined based on the results of triple-deck theory for calorically perfect gas. Considering the change of temperature distribution by chemical reactions and the limitation of the first-order approximation in the triple-deck theory under very high Mach number conditions, Eq. (7) is modified as follows.
The Chapman-Rubesin parameter is usually determined using the reference temperature method under the assumption of calorically perfect gas. The reference temperature is a function of the freestream Mach number and the wall temperatureħə

$$\frac{T_{\mathrm{REF}}}{T_\infty} \cong 0.50 + 0.039 Ma_\infty^2 + 0.5 \frac{T_w}{T_\infty} \tag{8}$$

The corresponding viscosity is generally determined by Sutherland formula. Considering the chemical reactions in hypersonic flow and the effects on temperature, the reference enthalpy method is used instead of the reference temperature method. The reference enthalpy in the plate boundary layer is

$$h_{\mathrm{REF}} \cong 0.50\,(h_\infty + h_w) + 0.22 \times \sqrt{Pr}\,(H_\infty - h_\infty) \tag{9}$$

where H_∞ is the total enthalpy of the freestream and h_w is the static enthalpy at wall. It can be seen that the influence of wall temperature is taken into account already. To determine the reference pressure in the boundary layer, the viscous interaction should be taken into account. In the strong interaction zone (when $\varnothing > 3$)

$$p_{\mathrm{REF}} \cong p_\infty \times (0.514\varnothing + 0.759) \tag{10}$$

In the weak interacting zoneħïwhen $\varnothing > 3$ ħĸ,

$$p_{\mathrm{REF}} \cong p_\infty \times \left(1 + 0.31\chi + 0.05\chi^2\right) \tag{11}$$

With the reference enthalpy and the reference pressure, the reference temperature T_{REF} can be determined with chemical equilibrium assumption, and the corresponding equilibrium chemical composition can be obtained. Then the viscosity of the multicomponent gas mixture can be calculated from the species viscosity by means of mixture rules [20]. Note that the viscous interaction parameter $\varnothing$ is needed in calculating the reference pressure with Eq. (10) and Eq. (11), however $\varnothing$ is also related to C_{REF} [see Eq.(2)]. So the above process to determine the reference temperature T_{REF} and the parameter C_{REF} requires the iteration. In general situation, two to four iterations are enough to meet convergence.

It can be seen from Eq. (7) that the increase of Mach number, the decrease of Reynolds number, and the increase of compression angle will promote the flow separation. The reason why the the decrease of Reynolds number promotes separation is that it leads to the thickening of the boundary layer and the increase of wall friction. There are several aspects of the influence of Mach number increase. On the one hand, the increase of Mach number means the increase in shock intensity and the adverse pressure gradient. On the other hand, the Mach number increase means the increase in flow kinetic energy and the ability to withstand the adverse pressure gradient. Moreover, as Mach number increases, the subsonic region in the boundary layer is reduced, so the range for the propagation of adverse gradient decreases. In combination, the Mach number increases will suppress the flow separation.

The influence of Mach number is embodied by $Ma_\infty^{-1/2}$ in Eq. (7), which is based on the triple-deck theory with first-order approximation and the calorically perfect gas assumption. This result is obtained in the case where the streamline expansion effect under very high Mach number conditions is omitted and $\varnothing$ is not much greater than 1. It is pointed out in [6] that the upstream influence distance and the incipient pressure will decrease if the streamline expansion effect is considered, which means that the extent of suppressing flow separation by the increase Mach number should be stronger than what Eq. (7) reflects. So the power of Ma_∞ in Eq. (7) can be modified to embody the above effects.

The increase in $`_B$ will increase the shock intensity and the adverse pressure gradient, therefore promote flow separation. Considering that the extent of increase in adverse

pressure gradient due to the increase of $\grave{}_B$ may be stronger under very high Mach number conditions, the power of $\grave{}_B$ can also be adjusted.
In addition, considering the wide range of hypersonic flight altitude which means the variation of freestream temperature, and the freestream temperature variation in hypersonic or high enthalpy tunnel, it is necessary to analyze the effects of freestream temperature on the flow separation. The effect of the increase in freestream temperature is twofold. On the one and, the temperature rise causes the Reynolds number to decrease and thus promotes separation. On the other hand, the freesteam temperature rise at unvarying Mach number also means the increase in the flow kinetic energy and an enhancement of the ability to withstand the adverse pressure gradient. The effect to promote separation by temperature rise through the decrease of Reynolds number has been reflected by $Re_{L\infty}^{1/4}$ in Eq. (7) already. Here the effect to suppress separation by temperature rise through the increase in kinetic energy should be added. In the present work, the effects of freestream temperature on separation are introduced into the separation criteria parameter formula by means of the ratio of freestream temperature to the air temperature at standard conditions. Based on the above analysis, Eq. (7) is modified, adjusting the power of Ma_∞ and $\grave{}_B$ in to m and l respectively, and introducing T_∞/T_s , the ratio of the freestream temperature to that at standard conditions, with the power of n. Namely, an improved separation criterion parameter is defined as

$$S = Ma_\infty^m Re_{L\infty}^{1/4} C_{\mathrm{REF}}^{-1/4} \left(T_\infty/T_s\right)^n \, \grave{}_B^l \tag{12}$$

The values of m, n and l are determined by numerical simulations of nonequilibrium compression corner flow over wide range of Mach number, Reynolds number with various freestream temperature and corner angles.

3 Numerical Analysis

3.1 Governing Equations and Numerical Methods

The governing equations for the flow field are the two-dimensional Navier-Stokes equations coupled with the vibrational and chemical kinetics, which are solved to obtain the steady state solution of the flow field. A finite difference method is used in the calculation. All inviscid terms are discretized with AUSMPW+ scheme [21]. The viscous terms are discretized with center difference scheme.The inviscid fluxes are discretized implicitly while the viscous terms explicitly. The implicit parts of the differential equations are disposed in two steps with the LU-SGS approach [22]. The details of the flow field governing equations are described in [23].
The total length of the compression corner model is 0.6096m, of which the length of the front plate is 0.3048m. The computational mesh (Figure 1) is 131 $\times$81 with 131 points along the surface and 81 points in the flowfield normal to the body, only half of the grid points in both directions are shown for clarity. Refined grids are used near the leading edge, the corner and the position of peak pressure. Exponential stretch is used from the wall. The first normal grid height at the wall is 6.096×10^{-5}m.

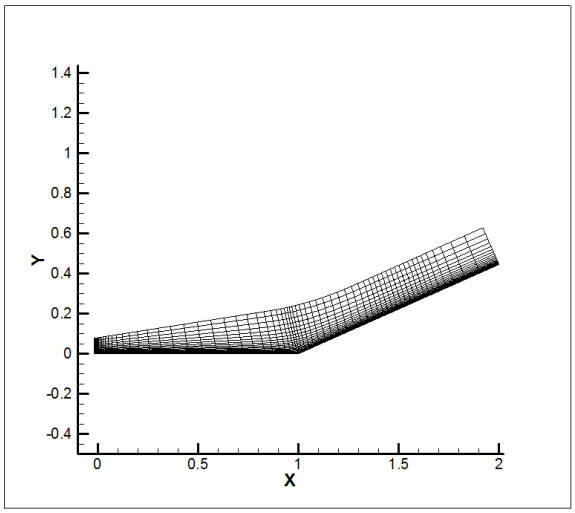

Figure 1: Computational mesh

3.2 Case Conditions

The compression corner angle, freestream Mach number and temperature of the calculation cases are listed in Table 1. For any one case condition (a set of given corner angle, freestream Mach number and temperature) in Table one, flow simulation is carried out with various freestream density. The density values are those of the atmosphere at altitude of 30km to 65km. Through changing the density step by step (the corresponding change of the altitude is 1 km in one step), the density value just corresponding the incipient separation is identified, so is the separation criterion parameter value [by Eq.(7)] at incipient separation, denoted as $S_{0,is}$. With the values of $S_{0,is}$ under each set of case condition, the change of with the freestream Mach number and temperature and the corner angle is analyzed, and the values of the powers in the improved formula of separation criterion parameter [Eq. (12)] are determined.

3.3 Analysis of the Numerical Results

The calculation results of all cases show that the decrease of freestream Mach number and temperature, the increase of the freestream density and the corner angle, will promote the flow separation. Take 18deg compression corner at Mach number of 15 and altitude of 45km as an example, the flowfield pressure distribution and the streamline in the recirculation zone for three different freestream temperauture (100K, 300K, and 500K) are given in Figure 2. The separation zone for the case of $T_\infty = 100$K is obviously larger than the cases with higher T_∞.

Table 1 Freestream Mach number and temperature of the calculation cases

Corner angle (deg)	Mach number	Freestream temperature(K)
15	8, 10, 13, 15, 18, 20, 23, 25	100, 200, 300, 500
18	10, 13, 15, 18, 20, 23, 25, 28	100, 200, 300, 500
24	20, 23, 25, 28, 30, 33, 35 100,	200, 300, 500

There are obvious differences in the values of separation criterion parameter [see Eq. (7)] at incipient separation $S_{0,is}$ for the calculation cases. Take the 15deg compresses

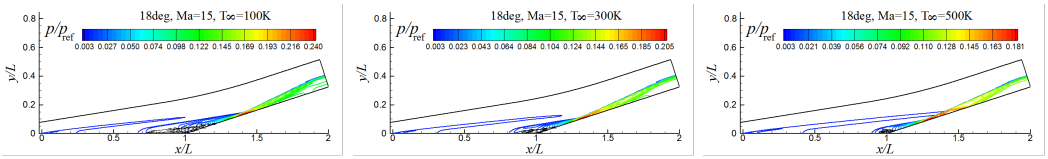

Figure 2: Pressure contour and separation zone streamline at different freestream temperature(18eg corner, Ma=15)

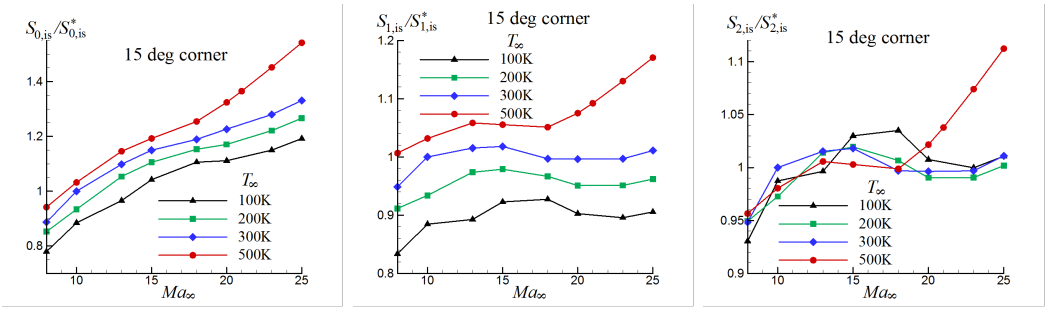

Figure 3: 15deg corner, Variation of separation criterion parameter with freestream Mach number and temperature

corner flow as an example, when the Mach number increases from 8 to 25, increases from 1.13 to 1.74 for the case of $T_\infty = 100$K, while from 1.01 to 1.94 for the case of $T_\infty = 300$K, and from 1.05 to 2.25 when $T_\infty = 500$K. Figure 3(a) gives the variation of the normalized incipient separation parameter (namely $S_{0,is}/S^*_{0,is}$) with Mach number for the 15deg corner flow at different freestream temperature. $S^*_{0,is}$ is the value of incipient separation criterion parameter at $Ma_\infty = 10$ and $T_\infty = 300$K , which is 1.457.

After the analysis of the change of $S_{0,is}$ with Mach number, the separation criterion parameter is modified to

$$S_1 = Ma_\infty^{-0.8} Re_{L\infty}^{1/4} C_{\mathrm{REF}}^{-1/4} \tag{13}$$

Figure 3(b) shows the change of $S_{1,is}/S^*_{1,is}$) with freestream Mach number and temperature. $S^*_{1,is}$ (= 0.7308) is the value at Ma_∞ =10 and $T_\infty = 300$K. It can be seen that the change range of $S_{0,is}$ with Ma_∞ is much smaller than that of $S_{0,is}$, especially for the case of $T_\infty = 300$K and $Ma_\infty = 10\sim25$, the change of $S_{0,is}$ is within 1.5%.

Both Figure 3(a) and Figure 3(b) show that $S_{1,is}$ increases with the freestream temperature. So the separation criterion parameter is further modified to

$$S_2 = Ma_\infty^{-0.8} Re_{\mathbf{L}\infty}^{1/4} C_{\mathrm{REF}}^{-1/4} \left(T_\infty/T_s\right)^{-0.1} \tag{14}$$

where = 288.15K, the temperature of atmosphere at standard conditions. Figure 3(c) shows the change of $S_{2,is}/S^*_{2,is}$ with freestream Mach number and temperature, where $S^*_{2,is}$ (= 0.7278) is the value at Ma_∞ =10 and $T_\infty = 300$K. It can be concluded from Figure 3(c) that the freestream temperature effects on flow separation are reflected by introducing (T_∞/T_s) into Eq.(14).

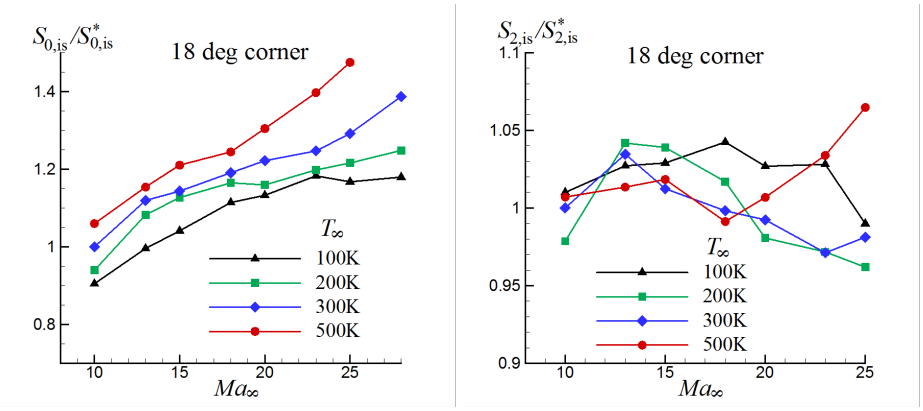

Figure 4: Figure 4 18eg corner, Variation of separation criterion parameter with freestream Mach number and temperature

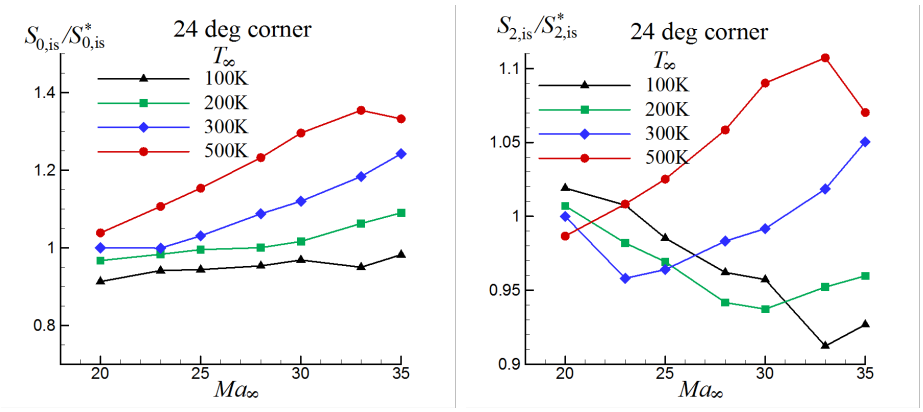

Figure 5: Figure 4 24deg corner, Variation of separation criterion parameter with freestream Mach number and temperature

However, for the case of $T_\infty = 500$K, the incipient separation criterion parameter increases obviously when the Mach number is greater than 23 (corresponding to the flow velocity greater than 10 km /s). This can be seen in Figure 3 (a) to Figure 3(c), with the three parameters, $S_{0,is}$, $S_{1,is}$, and $S_{2,is}$. Such phenomenon may be related to the start of some chemical reaction mechanism at very high speed.

Figure 4 and Figure 5 show the variation of $S_{0,is}/S^*_{0,is}$ and $S_{2,is}/S^*_{2,is}$ with freestream Mach number and temperature for 18deg and 24deg compression corner respectively. In Figure 4, $S^*_{0,is}$ (= 1.4215), $S^*_{2,is}$ (= 0.7125) are the values at Ma_∞ =10 and T_∞ = 300K. In Figure 5, $S^*_{0,is}$ (= 1.6299) and $S^*_{2,is}$ (= 0.6635) are the values at Ma_∞ =10 and $T_\infty = 300$K. The effects of the modification of the separation criterion parameter [in Eq .(14) and (14)] are also shown in 18deg and 24deg compression corner flows. However, for the case of $T_\infty = 500$K, the incipient separation criterion parameter increases significantly when the Mach number is greater than 23 for 18deg compression corner or greater than 30 for 24deg compression corner flow, which is similar to the 15deg compression corner case.

The comparison between the values of incipient separation criterion parameter for the three compression corner flows show that the incipient separation criterion parameter decreases as the corner angle increases. This indicates the necessity to

introduce the angle into the formula separation criterion parameter. Based on the existing numerical data, the definition of separation criterion parameter is further revised to

$$S = Ma_{\infty}^{-0.8} Re_{L\infty}^{1/4} C_{\mathrm{REF}}^{-1/4} \left(T_{\infty}/T_s\right)^{-0.1} \theta_B^{1.2} \tag{15}$$

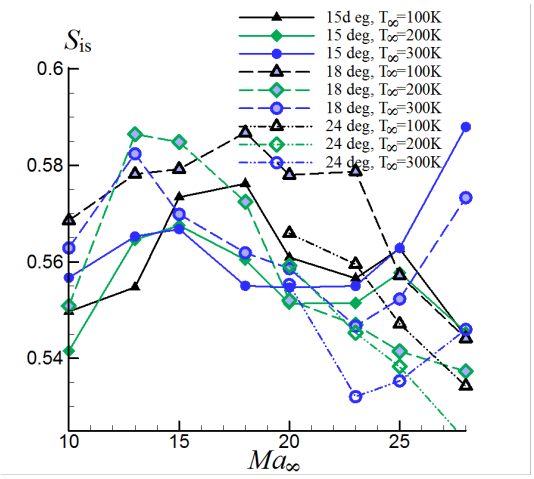

Figure 6: Variation of separation criterion parameter with corner angle, freestream Mach number, and temperature

Figure 6 shows the variation of the value of the incipient separation criterion parameter with the Mach number (10 to 28), corner angle (15deg, 18deg, and 24deg), and the freestream temperature (100K, 200K and 300K). The variation range of S_{is} is 0.525∼0.565 , within 8%. For the case of T_{∞} = 500K, the change of S_{is} is basically in the range, except for the very high Mach number (greater than 23 for 15deg and 18deg corner, and greater than 30 for 24deg corner).

4 Conclusion

(1) Based on the incipient separation angle formula yielded by the triple-deck theory with calorically perfect gas assumption, a separation criterion parameter (S_0) is proposed. S_0 is an index of the adverse pressure gradient relative to the flow ability to withstand it. So the larger the parameter is, the more prone of the flow to separate.
(2) The high temperature real gas effects on flow separation are introduced through the use of reference enthalpy and chemical equilibrium assumption to determine the reference temperature, and the modification of separation criterion parameter formula to $S = Ma_{\infty}^{m} Re_{L\infty}^{1/4} C_{\mathrm{REF}}^{-1/4} \left(T_{\infty}/T_s\right)^{n} \theta_B^{l}$. The values of the power in the formula and the incipient separation criterion parameter value are determined through a large number of nonequilibrium compression corner flow simulations. The present results for the power values are m=-0.8, n=-0.1, and l=1.2. For most of the case, the value range of the incipient separation criterion parameter is $S_{is} = 0.540 \sim 0.585$.

(3) Considering that only three different corner angles are taken in the simulation and analysis, more work is needed to determine the power value of the angle in the separation criterion parameter. For the case with even larger corner angle, the corresponding slope of the flow deflection angle (tan $`_B$ ) can be used instead of $`_B$. The determination of the power values of the freestream Mach number and temperature also need further in-depth work.

Acknowledgements

The research is funded by the National Natural Science Foundation of China (11572348).

References

[1] Tian H, Ye Y D, Jiang Q X, etc. Investigation of real gas effects on local flow separation of lifting body rudder. Acta Aerodynamica Sinica, 2015, 33(3): 330-337. (in Chinese). DOI:10.7638/kqdlxxb-2014.0106

[2] Li S X. Complex flow dominbated by shock-wave-boundary-layer interactions. Beijing: Science Press, 2007. (in Chinese)

[3] Needham D A. Laminar separation in hypersonic flow [Ph.D. thesis]. London: University of London, 1965.

[4] Needham DA, Stollery JL. Boundary-layer separation in hypersonic flow. 4th Aerospace Sciences Meeting. AIAA Paper 1966: 66ïC455.

[5] Needham DA. A Note on Hypersonic Incipient Separation. AIAA Journal, 1967, 5 :2284-2285.

[6] Babinsky H, Harvey J K. Shock wave boundary layer interactions. Cambridge: Cambridge University Press, 2011.

[7] Lighthill J. On boundary-layers upstream influence: II Supersonic flows without separation. Proceedings of the Royal Society, London. 1953, A , 217: 478ïC507.

[8] Stewartson K, Williams P G. Self-induced separation. Proceedings of the Royal Society, London. 1969, A, 312: 181ïC206.

[9] Neiland Y. Towards a theory of separation of a laminar boundary layer in supersonic stream. Fluid Dynamics,1969, 4(4): 33-35.

[10] Inger G R. Scaling of incipient separation in supersonic/transonic speed laminar flows. AIAA Journal, 1994, 33: 178-181.

[11] Rizzetta D P, Burggraf O, Jensen R. Triple-deck solutions for viscous supersonic and hypersonic flow past corners. J. Fluid Mech. 1978, 89(3): 535-552.

[12] Napolitano M, Werle M J, Davis R T. Numerical technique for the triple-deck problem. AIAA Journal, 1979, 17(7): 699-706.

[13] Davis J P, Sturtevant B. Separation length in high-enthalpy shock/boundary interaction. Phys Fluids. 2000, 12(10): 2661-2687.

[14] Marini M. Analysis of hypersonic compression ramp laminar flows under sharp leading edge conditions. Aerospace Sci Technology, 2001, 5: 257-271.

[15] Di Clemente M, Marini M, Schettino A. Shock wave boundary layer interaction in EXPERT flight conditons and Scirocco PWT. AIAA 2005-3411.

[16] Di Clemente M, Marini M, Di Benedetto S, Schettino A, Ranuzzi G.. Numerical prediction of aerothermodynamic effects on a re-entry vehicle body flap configuration. Acta Astronaut, 2009, 65:221-239.

[17] Wang D F. Study of hypersonic viscous intereaction including high-temperature gas effects [Master of Enginerring Thesis]. Changsha: National University of Defense Technology. 2011. (in Chinese)

[18] John B, Kulkarni V. Numerical assessment of correlations for shock wave boundary layer interaction. Computers & Fluids, 2014, 90: 42ïC50.

[19] Inger G R. Theory of heat transfer in shock/laminar boundary-layer interactions. Journal of Thermophysics and Heat Transfer. 1998, 12(3): 336-342.

[20] Anderson J D Jr. Hypersonic and High Temperature Gas Dynamics 2nd ed. AIAA Education Series. Reston, Virginia: AIAA, 2006.

[21] [Kim K H, Kim C, Rho O H. Accurate computations of hypersonic flows using AUSMPW+ scheme and shock-aligned grid tehnique. AIAA 98-2442, 1998.

[22] Stoll P, Gerlinger P, Bruggermann D. Domain decomposition for an implicit LU-SGS scheme using overlapping grids. AIAA 97-0770, 1997.

[23] Zeng M. Numerical rebuilding of free-stream measurement and analysis of nonequilibrium effects in high-enthalpy tunnel [Ph D Thesis]. Beijing: Institute of Mechanics, CAS. 2007. (in Chinese)

Ming Zeng, Changsha , China
Xiaoyu ZHAO, Changsha , China
MingMing Ge, Changsha , China
XiaoLiang Yang, Changsha , China
Wei Liu, Changsha , China

The Role of synchronization in Transition to Two-dimensional and Three-Dimensional Turbulence

Dmitry Zhilenko, Olga Krivonosova

jilenko@imec.msu.ru

Abstract

Turbulent flows of a viscous incompressible fluid in a layer between rotating concentric spheres under the action of the modulation of the velocity of one of the spheres have been studied experimentally and numerically. We used an algorithm of numerical solution based on a conservative finite difference scheme of the discretization of the Navier–Stokes equations in space and semi-implicit Runge–Kutta scheme of the third order integration accuracy in time. Discretization in space was performed on grids nonuniform in radial and meridional directions with concentration near the boundaries and equatorial plane. The experimental setup consisted of two coaxial spheres. The space between the spheres was filled with silicone oil to which aluminum powder was added for visualization of flows. The rotation velocity was periodically varied. Agreement was shown to be between the experimental and calculated results, including the integral properties of turbulent flows. The possibility of the formation of turbulence with spectra qualitatively similar to spectra obtained in measurements in the upper atmosphere is established: with the slope close to -3 at low frequencies and close to $-5/3$ at high frequencies and with the negative longitudinal velocity structure function of the third order. It has been shown that such spectra are formed in the regions of a flow that are strongly synchronized under the action of the modulation of the rotational velocity.

1 Introduction

Large-scale flows in the atmosphere occur in the presence of fast rotation of the Earth, and their properties are usually explained within the concept of вЃЁtwo-dimensionalвЃЉ turbulence [1, 2]. In two-dimensional turbulence, two inertial intervals are usually identified corresponding to energy transfer at low wave numbers and enstrophy transfer at high wave numbers [3]. The inertial interval of energy transfer from high to low wave numbers (inverse cascade) is described by the same Kolmogorov relation as in three-dimensional turbulence [4] for the dependence of the

energy spectrum $E(k)$ on the wave number $k : E(k) \sim k^{-5/3}$. In the inertial interval of enstrophy transfer from low to high wave numbers (direct cascade), this dependence has the form $E(k) \sim k^{-3}$. The direction of the cascade is determined by the sign of the third order longitudinal velocity structure function [5], which is defined as $D_{LLL} = \langle [u(l) - u(l')]^{-3} \rangle$, where u is the velocity at the spatially separated points l and l' and angular brackets mean averaging over the ensemble of realizations. The negative and positive signs of D_{LLL} correspond to the direct and inverse cascades, respectively. Conclusions of the theory of two-dimensional turbulence were confirmed in numerous results reviewed in [6, 7]. At the same time, measurements of the horizontal velocity of the wind in the EarthвЃ™s atmosphere revealed an anomalous location of spectral regions that is inconsistent with the theory of two-dimensional turbulence. In particular, spectra of turbulence with a slope of -3 begin at scales larger than $700km$ and are limited by a strong peak at a scale of $10^4 km$. Spectra with a slope $-5/3$ were detected at scales smaller than $500km$ [1]. Analysis of third order structure functions in [2] showed that only one of these regions with the slope of -3, corresponds to two-dimensional turbulence. This indicates the direct energy transfer cascade in both spectral regions under consideration. Despite the existing explanations [1, 8, 9], reasons for the inverse position of spectral regions, as well as the possibility of reproducing this phenomenon under laboratory conditions, are as yet unclear.

Both viscous dissipation [10] and vertical motions, which are components of Large-scale circulation [6], prevent twoBædimensional turbulent flows in the atmosphere. Large-scale circulation also exists in turbulent flows induced by the rotation of the boundaries of the spherical layer, which is responsible for the motion of viscous incompressible fluid between them [11]. It is exactly why the model spherical Couette flow is studied in this work for the qualitative simulation of processes in the atmosphere. By analogy with Baroud [12], we chose the case of the counter rotation of spheres. Under stationary boundary conditions, oppositely directed vortices with an interface between them are formed in the meridional plane of such a flow (see Figure 1, which is similar to Figure 1 in [13]). A similar circulation can be observed in the case of the rotation of only the inner sphere in the presence of altitude-inhomogeneous external heating [14] , typical of the atmosphere. In spherical layers the formation of turbulence with a high correlation dimension occurs by the increase in the rotation velocity of one of the boundaries [11, 15] as well as by their modulation [16]. The spectrum of developed turbulence in the latter case depends on the parameters of force action [17].

The dependence of the type of the azimuthal velocity spectra on the frequency and amplitude of the modulation of the rotation velocity of one of the spheres is determined in this work experimentally and numerically.

2 Methods of calculation and experiment. Field of study

An isothermal flow of a viscous incompressible fluid is described by the NavierвЂ“Stokes and continuity equations:

$$\frac{\partial U}{\partial t} = U \times rotU - grad\left(\frac{p}{\rho} + \frac{U^2}{2}\right) - \nu rotrotU, divU = 0 \quad (1)$$

where U, p, ν, and ρ, are the velocity, pressure, viscosity, and density of the fluid. These equations are numerically solved in a spherical coordinate system with the radial (r), polar (θ), and azimuthal (φ) directions, in which the impermeability and no-slip boundary conditions have the form $u_\varphi(r = r_k) = \Omega_k(t) r_k \sin(\theta)$, $u_r(r = r_k) = 0$, $u_\theta(r = r_k) = 0$, $k = 1, 2$, where u_φ, u_r, and u_θ are the azimuthal, radial, and polar components of the velocity; and $k = 1$ and 2 correspond to the inner and outer spheres, respectively. We used an algorithm of numerical solution [18] based on a conservative finite difference scheme of the discretization of the NavierвЂ“Stokes equations in space and semi-implicit Runge–Kutta scheme of the third order integration accuracy in time. Discretization in space was performed on grids nonuniform in r and θ directions with concentration near the boundaries and equatorial plane and the total number of nodes $5.76 \cdot 10^5$. This algorithm was used for calculations with both stationary [11] and periodic [19] boundary conditions. Spectra of pulsations of the square of the azimuthal velocity component u_φ (minus the average value determined for the entire sample) were calculated at points $1 - 7$ shown in Figure 1 (θ and φ are constant and only r is varied). To this end, u_φ time series with a length of no less than 72000 points were written with a time step $\triangle t = 0.015 - 0.025s$. D_{LLL} was obtained using the dependence of u_φ on the azimuth angle φ during 16 rotation periods ($0 \leq \varphi \leq 32\pi$). All calculations were performed for the initial and boundary conditions corresponding to the experimental conditions.

The experimental setup consisted of two coaxial spheres. The outer radius of the inner sphere was $r_1 = 0.075m$ and the inner radius of the outer sphere was $r_2 = 0.150m$. The space between the spheres was filled with silicone oil. The rotation velocity was periodically varied by the law $\Omega_k(t) = \Omega_{k0}(1+A_k \sin(2\pi f_k t+\psi_k)$ with an accuracy of no worse than 0.5% (where A_k and f_k are the amplitude and frequency of modulation; Ω_{k0} is average angular velocity of rotation; initial phase ψ_k is arbitrary). The modulation frequencies $f_1 = 0.01 - 0.1Hz$ and $f2 = 0.01 - 0.02Hz$ were no higher than the average rotation frequencies of the spheres ($\Omega_{10}/2\pi = 0.59Hz$, $\Omega_{20}/2\pi = 0.32Hz$). The measurements of u_φ were performed near the outer sphere at a distance of $0.078m$ from the equator plane and at a distance of $0.105m$ from the rotation axis (near point 7 in Figure 1). The experiments were performed at Reynolds numbers $Re_1 = \Omega_{10} r_1^2/\nu = 412.5 \pm 0.5$ and $Re_2 = \Omega_{20} r_2^2/\nu = 900 \pm 1$. At these Reynolds numbers in the absence of modulation, a periodic flow with the frequency $f_0 = 0.0376Hz$ is formed in the layer; this flow referred to as initial is a result of mutual synchronization of individual linear modes [13]. The initial flow has the form of traveling azimuthal waves with the wave number $m = 3$. The modulation of the rotation velocity of one of the boundaries leads to the flow induced synchronization. With an increase in the amplitude of modulation at a

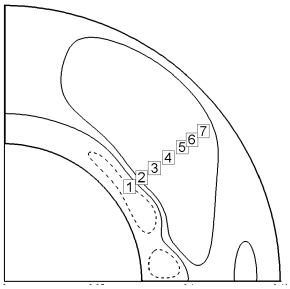

Figure 1: Calculated stream functions Ψ (in $[m^3/s]$)) in the meridional plane of the axisymmetric steady state flow at $Re_2 = -900, Re_1 = 414$: $\Psi_{max} = 6 \cdot 10^{-6}, \Psi_{min} = -6 \cdot 10^{-6}$, and $\triangle\Psi = 6 \cdot 10^{-6}$. Dashed lines are negative value contours. Points $1 - 7$ are located at the relative distance $l = (r - r_1)/(r_2 - r_1) = 0.135, 0.246, 0.359, 0.484, 0.611, 0.7, 0.803$ from the inner sphere with a deviation of 0.206π from the equatorial plane.

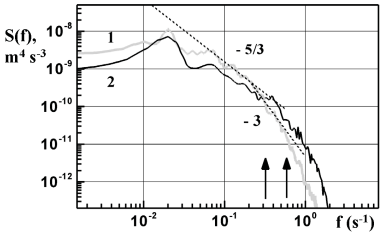

Figure 2: u_φ^2 spectra obtained in the 1 experiment and 2 calculation for point 7 in the case of the modulation of the inner sphere velocity with $f_1 = 0.01Hz$ and $A = 0.163$. The left and right vertical arrows correspond to the average frequencies of rotation of the outer and inner spheres, respectively.

fixed frequency, the initial flow is destroyed. Turbulence appears at the transition from mutual synchronization to induced synchronization [16].

3 Results

With an increase in the amplitude in the case of the modulation of the rotation velocity of the inner sphere, the spectra can be transformed to the form characteristic of two-dimensional turbulence. For example, in the case of the modulation of $\Omega_1(t)$ at $f_1 \leq f_0$ (Figure 2), the spectra obtained both from measurements and numerically exhibit a pronounced segment with a constant slope of $-5/3$ at low frequencies $(0.06-0.27Hz)$ and a segment with a constant slope of -3 at high frequencies $(0.27-0.8Hz)$. At an increase in the amplitude of the modulation of $\Omega_2(t)$, the spectra are modified to the form qualitatively corresponding to the spectra of atmospheric turbulence [1] with a slope -3 at frequencies below $0.1Hz$ and $-5/3$ at higher frequencies $(0.1 - 0.31Hz)$ (Figure 3a). Under the condition $f_k \leq f_0$, the form of the spectrum depends on the position of the point at which the azimuthal velocity is calculated. The most characteristic differences in the form of the spectra at points $1-7$ (Figure 1) are observed in the case of $\Omega_2(t)$ modulation. In particular, near the outer sphere and at a certain distance from it (points $7-3$), the observed spectra are typical to atmospheric turbulence, whereas the spectrum observed near the inner sphere (point 1) has a constant slope of $-5/3$ and is typical to three-dimensional

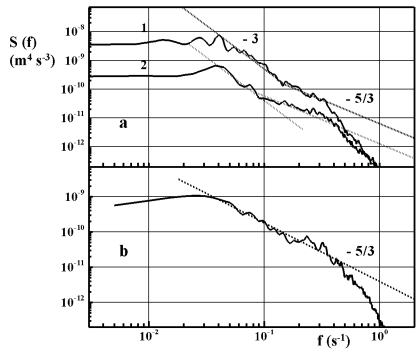

Figure 3: u_φ^2 spectra at points (a) 7 and (b) 1 obtained in the (1) experiment and (2) calculation in the case of the modulation of the velocity of the outer sphere with $f_2 = 0.02Hz$ and $A = 0.2$.

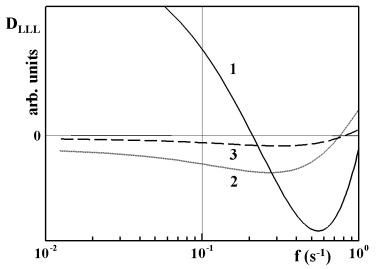

Figure 4: Approximation of the thirdBæorder longitudinal velocity structure function for (1) $f_1 = 0.01Hz, A = 0.163$ and (2, 3) $f_2 = 0.02Hz, A = 0.2$ at points 7 (1, 3) and 1 (2).

turbulence (Figure 3b). We tried to determine the direction of the energy cascade in the cases corresponding to the spectra, shown in Figures 2 and 3, from the sign of the third order longitudinal velocity structure function D_{LLL}. Sign of D_{LLL} alternates with a period of $2\pi/3$, because large-scale coherent structures [11] characteristic of the initial flow are held in the turbulent flow. Similar large-scale coherent structures in the upper layers of the atmospheres of planets (e.g., Venus) were assumingly interpreted as Rossby waves [20]. For this reason, to determine the sign of D_{LLL}, the results of the calculation were approximated by sixth order polynomials.

Figure 4 shows the dependence of D_{LLL} on the frequency f given by the expression [21] $f = \langle u_\varphi \rangle / l$, where $0 < l < 32\pi$ and $\langle u_\varphi \rangle$ is the average velocity at a distance of $rsin\theta$ from the axis. We first consider flows for which the observed spectra were typical to two-dimensional (Figure 2) and three-dimensional (Figure 3b) turbulence. In the former case (Figure 4, line 1), transition from positive D_{LLL} values to negative is observed at $f = 0.2Hz$. At the same frequency, transition from a slope of -3 to a slope of $-5/3$ is observed in the experiment (Fig. 2, line 1). In the latter case (Fig. 4, line 2) $D_{LLL} < 0$. Both of these cases confirm the correctness of the estimate of the sign of D_{LLL}. In the case of atmospheric turbulence (Figure 4, line 3), $D_{LLL} < 0$ in the frequency range corresponding to the segments of the spectrum with both slopes of -3 and $-5/3$.

The level of turbulence of the entire flow as a whole is determined by the behavior of its kinetic energy, which is represented in the form of the sum of the azimuthal (E_φ) and meridional (E_ψ) components taken as integrals over the entire volume of the spherical layer: $E_\varphi = \int u_\varphi^2$ and $E_\psi = \int (u_r^2 + u_\theta^2)$. Thus, the modulation of the rotation velocity of one of the spheres results in the suppression of turbulence in the azimuthal direction of motion. Synchronizations between $\Omega_k(t)$ and E_φ, E_ψ (treated as frequency and/or phase locking) are significantly different for inner and outer

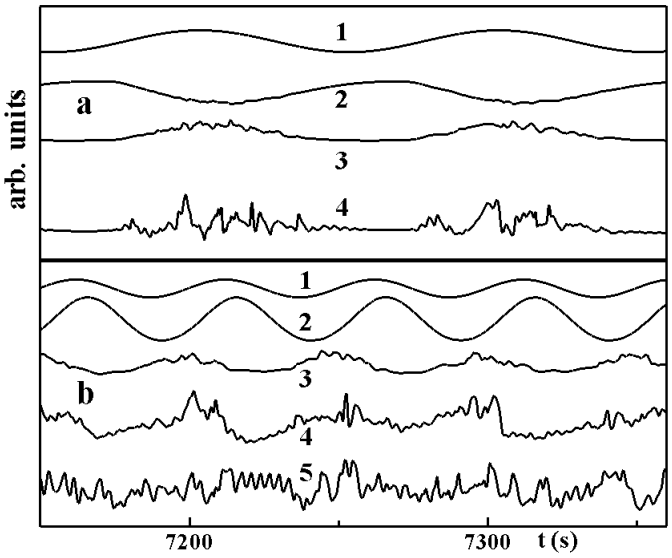

Figure 5: Fragments of the time dependence of various calculated quantities (in arbitrary units) for (a) $f_1 = 0.01Hz, A = 0.163$ and (b) $f_2 = 0.02Hz, A = 0.2$: (1) Ω_i, (2) E_φ, (3) E_ψ, (4) u_φ at point 7, (5) u_φ at point 1, $rms(df)/\Omega_1 = 0.256, 0.130, 0.274$ for cases corresponding to Figs. 3a, 3b, and 4b, respectively.

sphere modulation. In the former case, E_ψ varies almost in phase with the variation of $\Omega_1(t)$ (Figure 4a), whereas in the latter case, the smallest phase shift is observed between $\Omega_2(t)$ and E_φ (Figure 5b). Since E_φ values are two orders of magnitude higher than E_ψ, the above results indicate that synchronization of the flow induced by the modulation of $\Omega_2(t)$ is stronger. As is seen, the level of synchronization between $\Omega_2(t)$ and u_φ is nonuniform in the thickness of the layer of the fluid (Figure 6b): a correlation between the velocity of the sphere and the velocity of the flow is observed at points far from the inner sphere (line 4) and is not observed near the inner sphere (line 5). We calculated the instantaneous frequency differences df between $\Omega_k(t)$ and u_φ. According to [22], the instantaneous frequency and phase are defined as $\chi(t) = \partial\Psi(t)/\partial t$ and $\Psi(t) = \arctan(y(t)/x(t))$, respectively. Here, $x(t)$ is the velocity signal and $y(t)$ is the orthogonal complement to $x(t)$, which is calculated as the Hilbert transform of the series $x(t)$. The minimal root mean square frequency difference $rms(df)$ between $\Omega_k(t)$ and u_φ(the strongest synchronization) is observed near the outer sphere at its modulation (Figure 5). Thus, the strongest synchronization corresponds to spectra of turbulence with the form typical to the upper layers of the atmosphere. The largest frequency difference is observed near the inner sphere at the modulation of the outer sphere. This means that the weakest synchronization corresponds to three-dimensional turbulence. The comparison of the two cases considered above indicates that the effect of the modulation of the outer sphere on the flow is limited by the region of circulation induced by its rotation (points $3-7$ in Figure 1). All presented facts indicate that the appearance of the spectrum of turbulence with slopes of -3 and $-5/3$ at low and high frequencies, respectively, is possible only in the region with strongest synchronization between the rotation velocity and the velocity of the flow.

The results obtained for the model flow under consideration imply that the form of spectra of turbulence in the upper layers of the atmosphere is explained by the induced synchronization of the periodic part of atmospheric flows (e.g., Rossby waves) by an external periodic action with a longer period. Since the main source of the energy for all atmospheric processes is solar heat, seasonal variations of this quantity can be considered as such a periodic external action on the atmosphere.

4 Conclusions

The results of the performed experimental and numerical studies have shown that a decrease in the modulation frequency is accompanied by an increase in differences in the behaviors of the azimuthal and meridional components of the kinetic energy of the flow. The former component remains periodic, whereas the latter component changes the periodic behavior to chaotic. The suppression of turbulence of the azimuthal kinetic energy of the flow promotes the formation of quasi-two-dimensional turbulence. Spectra characteristic of two-Bædimensional turbulence with a constant slope of $-5/3$ and an inverse cascade ($D_{LLL} > 0$) at low frequencies and with a slope -3 and a direct cascade ($D_{LLL} < 0$) at high frequencies have been observed in the case of the modulation of the inner sphere velocity. At a modulation frequency below the frequency of the initial periodic flow, the form of the spectra is spatially nonuniform. In the case of the modulation of the outer sphere velocity, spectra with the qualitative form characteristic to turbulence in the upper layers of the atmoBæsphere with a constant slopes of -3 and $-5/3$ at low and high frequencies, respectively, are observed in the region of circulation induced by the outer sphere. For both segments of the inertial interval $D_{LLL} < 0$. The form of the spectrum near the inner sphere is characteristic of threeBæ-dimensional turbulence: the segment with a constant slope of $-5/3$ presents and $D_{LLL} < 0$. It has been found that the level of synchronization between the rotation velocity of the boundary and the velocity of the flow is different in all flows considered above. The lowest and highest levels of synchronization are observed where spectra are similar to spectra of three-Bædimensional and atmospheric turbulence, respectively.

Acknowledgements

This study was supported by the Russian Foundation for Basic Research, project no. 16-05-00004.

References

[1] K. S. Gage and G. D. Nastrom, J. Atmos. Sci., 43, 729, 1986.

[2] E. Lindborg, J. Fluid Mech., 388, 259, 1999.

[3] R. Kraichnan, Phys. Fluids 10, 1417, 1967.

[4] A. N. Kolmogorov, Dokl. Akad. Nauk SSSR 32, 19, 1941.

[5] U. Frisch, Turbulence: The Legacy of A.N. Kolmogorov. Cambridge Univ. Press, Cambridge, 1995.

[6] S. D. Danilov and D. Gurarii, Phys. Usp. 43, 863, 2000.

[7] G. Boffetta and R. E. Ecke. Ann. Rev. Fluid Mech. 44, 427, 2012.

[8] H. Xia, D. Burne, G. Falkovich, and M. Shats, Nature Phys. 7, 321, 2011.

[9] A. Vallgren, E. Deusebio, and E. Lindborg, Phys. Rev. Lett. 107, 268501, 2011.

[10] A. E. Gledzer, E. B. Gledzer, A. A. Khapaev, and O. G. Chkhetiani, J. Exp. Theor. Phys. 113, 516, 2011.

[11] D. Yu. Zhilenko and O. E. Krivonosova, Tech. Phys. 55, 449, 2010.

[12] C. N. Baroud and H. L. Swinney, Physica D 184, 21, 2003.

[13] D. Yu. Zhilenko, O. E. Krivonosova, and N. V. Nikitin, 42, 886, 2007.

[14] I. M. Yavorskaya, Izv. Akad. Nauk SSSR, Mekh. Zhidk. Gaza 2, 15, 1975.

[15] Yu. N. Belyaev, A. A. Monakhov, S. A. Shcherbakov, and I. M. Yavorskaya, JETP Lett. 29, 295, 1978.

[16] D. Yu. Zhilenko and O. E. Krivonosova, Fluid Dyn. 47, 452, 2013.

[17] S. N. Gordienko and S. S. Moiseev, J. Exp. Theor. Phys. 89, 880, 1999.

[18] N. Nikitin, J. Comp. Phys. 217, 759, 2006.

[19] D. Yu. Zhilenko and O. E. Krivonosova, Tech. Phys. Lett. 39, 84, 2013.

[20] A. S. Monin, Hydrodynamics of Atmosphere, Ocean and EarthвЃЄs Depths Gidrometeoizdat, St.BæPetersburg, [in Russian],1999.

[21] G. S. Golitsyn, Dokl. Phys. 52, 376, 2007.

[22] V. Anishchenko et al., Nonlinear Dynamics of Chaotic and Stochastic Systems. Springer, Berlin, 2002.

Dmitry Y. Zhilenko, Krgiganovski str. 2/21, 51, Moscow, Russia
Olga E. Krivonosova, Krgiganovski str. 2/21,51, Moscow, Russia